

Carlos Chastre · José Neves ·
Diogo Ribeiro · Maria Graça Neves ·
Paulina Faria *Editors*

Advances on Testing and Experimentation in Civil Engineering

Materials, Structures and Buildings

Springer Tracts in Civil Engineering

Series Editors

Sheng-Hong Chen, School of Water Resources and Hydropower Engineering,
Wuhan University, Wuhan, China

Marco di Prisco, Politecnico di Milano, Milano, Italy

Ioannis Vayas, Institute of Steel Structures, National Technical University of
Athens, Athens, Greece

Springer Tracts in Civil Engineering (STCE) publishes the latest developments in Civil Engineering - quickly, informally and in top quality. The series scope includes monographs, professional books, graduate textbooks and edited volumes, as well as outstanding PhD theses. Its goal is to cover all the main branches of civil engineering, both theoretical and applied, including:

- Construction and Structural Mechanics
- Building Materials
- Concrete, Steel and Timber Structures
- Geotechnical Engineering
- Earthquake Engineering
- Coastal Engineering; Ocean and Offshore Engineering
- Hydraulics, Hydrology and Water Resources Engineering
- Environmental Engineering and Sustainability
- Structural Health and Monitoring
- Surveying and Geographical Information Systems
- Heating, Ventilation and Air Conditioning (HVAC)
- Transportation and Traffic
- Risk Analysis
- Safety and Security

Indexed by Scopus

To submit a proposal or request further information, please contact:
Pierpaolo Riva at Pierpaolo.Riva@springer.com (Europe and Americas) Wayne Hu
at wayne.hu@springer.com (China)

Carlos Chastre · José Neves · Diogo Ribeiro ·
Maria Graça Neves · Paulina Faria
Editors

Advances on Testing and Experimentation in Civil Engineering

Materials, Structures and Buildings



Springer

Editors

Carlos Chastre 

CERIS

Department of Civil Engineering
NOVA School of Science and Technology
Universidade NOVA de Lisboa
Lisbon, Portugal

Diogo Ribeiro 

CONSTRUCT-LESE
School of Engineering
Polytechnic of Porto
Porto, Portugal

Paulina Faria 

CERIS

Department of Civil Engineering
NOVA School of Science and Technology
Universidade NOVA de Lisboa
Lisbon, Portugal

José Neves 

CERIS

Instituto Superior Técnico
Universidade de Lisboa
Lisbon, Portugal

Maria Graça Neves 

CERIS

Department of Civil Engineering
NOVA School of Science and Technology
Universidade NOVA de Lisboa
Lisbon, Portugal

ISSN 2366-259X

ISSN 2366-2603 (electronic)

Springer Tracts in Civil Engineering

ISBN 978-3-031-23887-1

ISBN 978-3-031-23888-8 (eBook)

<https://doi.org/10.1007/978-3-031-23888-8>

© The Editor(s) (if applicable) and The Author(s), under exclusive license to Springer Nature Switzerland AG 2023

This work is subject to copyright. All rights are solely and exclusively licensed by the Publisher, whether the whole or part of the material is concerned, specifically the rights of translation, reprinting, reuse of illustrations, recitation, broadcasting, reproduction on microfilms or in any other physical way, and transmission or information storage and retrieval, electronic adaptation, computer software, or by similar or dissimilar methodology now known or hereafter developed.

The use of general descriptive names, registered names, trademarks, service marks, etc. in this publication does not imply, even in the absence of a specific statement, that such names are exempt from the relevant protective laws and regulations and therefore free for general use.

The publisher, the authors, and the editors are safe to assume that the advice and information in this book are believed to be true and accurate at the date of publication. Neither the publisher nor the authors or the editors give a warranty, expressed or implied, with respect to the material contained herein or for any errors or omissions that may have been made. The publisher remains neutral with regard to jurisdictional claims in published maps and institutional affiliations.

This Springer imprint is published by the registered company Springer Nature Switzerland AG
The registered company address is: Gewerbestrasse 11, 6330 Cham, Switzerland

Foreword by Caspar Groot

In the field of Civil Engineering, important reasons for testing are the need for data regarding (performance) characterization, functioning of systems and the evaluation of durability. Basic testing areas are physical, mechanical and chemical testing. Apart from materials choice, design, on-site work procedures and maintenance are especially environmental factors which play a role regarding functioning and durability of civil engineering systems, such as moisture and salt supply, temperature variation, exposure to fire, dynamic loads and soil settlements.

In “Advances on Testing and Experimentation in Civil Engineering—Materials, Structures and Buildings”, the modern developments in this wide field of testing are treated in 17 chapters.

A main observation with regard to this collection of novel test techniques is that it shows the enormous influence of the developments in micro-electronics and computers over the past decades. Mini-sensors, transport of measuring data to data loggers or directly to computers and the processing of data through adequate programs changed the testing world of Civil Engineering from point measurements to a continuous assessment of properties, enabling the monitoring, the functioning and the state of materials, structures and buildings.

Examples of presented novel testing methods, using the mentioned modern technical developments range from Remote Inspection, detecting concrete damage using a drone to a Structural Health Monitoring system for civil engineering structures, from NDT measuring of real time deformation to sophisticated accelerated weathering testing, from acoustic testing to a modelling tool for lighting systems.

Less striking at first sight but certainly important are as well the influence of specific social developments on testing. Examples, stemming from the current emphasis on the reuse of materials, the prevention of the occurrence and application of hazardous substances, such as regarding pollutants, that may end up in the environment, are treated in this book.

In conclusion it may be stated that, as a result of the significant progress in testing techniques (in hard and soft ware), it has become more effective, useful and attractive to control the quality of production processes, the functioning of systems and the monitoring of durability in Civil Engineering.

Caspar Groot
Former Chair of Rilem TC's
TU-Delft/NL
Delft, Netherlands

Foreword by J. G. Dai

The sustainability of structures and infrastructure systems plays a critical role in supporting the continuous growth of the economy and our social well-being in a region. Such a sustainability goal is being greatly challenged by a huge inventory of ageing structures and infrastructure systems built in the last century and the ever-increasing demand for carbon neutrality, which is expected to be achieved by the mid-twenty-first century on a global scale. Our civil engineering community has the responsibility to make our structures and infrastructure systems more resilient while minimizing the embodied and operation energy and the associated carbon footprint during their life cycle. On the other hand, our built environment is exposed to increased risks of various natural hazards such as hurricanes, wind storms, flooding and fire, which are caused by global warming and extreme climate change, and other potential manmade disasters.

All the above call for the development of a comprehensive approach to deal with design, construction, inspection and maintenance, demolition or recycling for a wide spectrum of structural systems and materials. In the past few decades, we have seen huge progress made along this line, including the development of more environmentally, durable and higher-performance materials, non-destructive inspection and health monitoring technologies, repair and strengthening methods, as well as recycling and reusing solutions. Spreading widely these state-of-the-art technologies are certainly beneficial to the economically and environmentally sustainable future.

This book is a collection of new material technologies and various advanced analysis and testing methods for both materials and structures under different mechanical and/or environmental loadings. I believe that these latest reports are very useful for our professionals and students in civil and other relevant engineering disciplines to promote the sustainability of our building and infrastructure systems.

I would like to convey my sincere thanks to the editorial team led by Dr. Carlos Chastre for its dedication to the highest publication quality.

Jian-Guo Dai
Professor of Structural Engineering
Department of Civil and Environmental
Engineering
The Hong Kong Polytechnic University
Hong Kong, China

Preface

Testing and experimentation are essential to support the design of civil engineering infrastructures and buildings, and to understand the phenomena involved. Over the last years, testing and experimentation in civil engineering have assumed increasing importance in a wide range of applications, providing reliable information for the decision-making process during the life cycle. The experimental activities are performed in the laboratory or in situ. They typically allow an enhanced characterization of the behaviour of systems and their components, supporting the stakeholders to find more reliable and sustainable solutions. Currently, the literature lacks a contribution that provides general and foundational knowledge across these topics, and this book aims to fill this gap.

The book presents the recent advances on testing and experimentation in civil engineering, especially in the branches of materials, structures, buildings, geotechnics, transportation, hydraulics and natural resources. It is divided into two volumes, one dedicated to materials, structures and buildings, and the other one dealing with geotechnics, transportation, hydraulics and natural resources. Both volumes include advances in physical modelling, monitoring techniques, data acquisition and analysis, and provide an invaluable contribution for the installation of new civil engineering experimental facilities.

This volume covers the areas of materials, structures and buildings, pointing out the most recent advances on testing and experimentation in several main domains of these areas.

The initial part is dedicated to new developments on materials testing, from environmental requirements to durability of common to more innovative materials and the ones using residues. Laboratory and in situ tests, as well as equipment needed to estimate the behaviour and durability of construction materials are presented, updating the most important technological advances. The following part is dedicated to new developments on testing structures, including in situ tests related to static load tests, dynamic tests and long-term monitoring strategies, as well as laboratory tests of adhesive joints. Additionally, dedicated shake table and blasting testing schemes are described. Recent applications of drone technologies for the inspection and monitoring of civil structures are also presented. The last part is dedicated to new

developments on characterization of buildings. It includes testing, with the support of modelling, to assess building pathology and new requirements, acoustic comfort, fire safety, visual comfort and energy consumption.

These chapters of the book provide a holistic and comprehensive overview of testing and experimentation. They are addressed to professionals willing further improvement in their scientific and technical understanding, and skills in these specific areas of civil engineering.

Lisbon, Portugal

Carlos Chastre

Lisbon, Portugal

José Neves

Porto, Portugal

Diogo Ribeiro

Lisbon, Portugal

Maria Graça Neves

Lisbon, Portugal

Paulina Faria

Acknowledgments

The editors would like to express their sincere gratitude to professionals and organizations that directly or indirectly contribute to the realization of this Book. To the Springer Tracts in Civil Engineering Editors, Prof. Shenghong Chen, Prof. Marco di Prisco and Prof. Ioannis Vayas, for accepting this book proposal in a challenging and innovative thematic in the field of experimentation in Civil Engineering. To the Springer Editor, Dr. Pierpaolo Riva, for all the advice and prompt support in addressing all the questions during the Book preparation. To the experts, Prof. Caspar Groot and Prof. Jian-Guo Dai, for addressing the foreword and critical review of the Book contents. To the educational institutions NOVA School of Science and Technology (FCT NOVA), Instituto Superior Técnico (IST), School of Engineering of Polytechnic of Porto (ISEP) and National Laboratory for Civil Engineering (LNEC), as well as the Civil Engineering Research and Innovation for Sustainability (CERIS) and Institute of R&D in Structures and Construction (CONSTRUCT), which are financed by Foundation for Science and Technology (Portugal) through UIDB/04625/2020 and UIDB/04708/2020, respectively, for providing the necessary conditions for the development of the Book edition. To all the authors of the Book chapters, for the extraordinary commitment with the objectives of the publication and their enthusiasm to be part of this project. Finally, the co-editors would like to thank all the readers of this book for their interest and passion in the most recent advances in testing and experimentation in Civil Engineering.

Contents

Part I Materials

1	New Trends on Bio-cementation and Self-healing Testing	3
	Rui Micaelo, Paulina Faria, and Rafaela Cardoso	
2	Testing Durability on Construction Materials	29
	Carlos Chastre, Paulina Faria, José Neves, Marco Ludovico-Marques, Hugo Biscaia, and Lina Nunes	
3	Innovative Durability Tests on Construction Materials	53
	Carlos Chastre, Paulina Faria, José Neves, Marco Ludovico-Marques, Hugo Biscaia, and Lina Nunes	
4	Testing of New Composites Incorporating Recycled Materials	75
	Jorge de Brito, Pedro Raposeiro da Silva, and José Neves	
5	New Environmental Requirements	103
	Isabel M. Martins and Helena M. Silva	

Part II Structures

6	Remote Inspection and Monitoring of Civil Engineering Structures Based on Unmanned Aerial Vehicles	123
	Diogo Ribeiro, Ricardo Santos, Rafael Cabral, and Rui Calçada	
7	Laboratory Tests on Structural Adhesive Joints	145
	Hugo Biscaia and Carlos Chastre	
8	Shake Table Testing Techniques: Current Challenges and New Trends	173
	Paulo X. Candeias, António A. Correia, and Gidewon G. Tekeste	

9	Experimental Research and Development on Blast Resistant Structures	199
	Gabriel Gomes, Hugo Rebelo, Válter Lúcio, Corneliu Cismasiu, and José Mingote	
10	Load Tests on Bridges	219
	Mário Pimentel, Joaquim Figueiras, Carlos Félix, Filipe Cavadas, Emanuel Tomé, Carlos Rodrigues, and Bruno Costa	
11	Dynamic Testing on Railway Bridges	241
	Diogo Ribeiro, Cássio Bragança, Artur Silva, and Rui Calçada	
12	An Automated Tool for Long-Term Structural Health Monitoring Based on Vibration Tests	269
	Daniel Soares, Rharã de Almeida Cardoso, Flávio de Souza Barbosa, and Alexandre Abrahão Cury	

Part III Buildings

13	Innovative Approach on Building Pathology Testing and Analysis	293
	Nuno M. M. Ramos and Pedro F. Pereira	
14	Testing for New Requirements for Building Coatings	307
	Paulina Faria and M. Rosário Veiga	
15	New Trends in Acoustic Testing in Buildings	333
	Julieta António, António Tadeu, and João Dias Carrilho	
16	State-of-the-Art and Future Insights into the Material's Fire Behaviour Tests	351
	Miguel Chichorro Gonçalves and António Leça Coelho	
17	A Modelling Tool for Lighting Systems Based on Visual Comfort and Energy Consumption—Case Study of a Residential Building	375
	Luis G. Baltazar and João Tapadas	

Contributors

Rharã de Almeida Cardoso University of Juiz de Fora, Juiz de Fora, Minas Gerais, Brazil

Daniel Soares University of Juiz de Fora, Juiz de Fora, Minas Gerais, Brazil

Julieta António CERIS, Department of Civil Engineering, University of Coimbra, Coimbra, Portugal;
Itecons, Coimbra, Portugal

Luis G. Baltazar NOVA School of Science and Technology, Universidade NOVA de Lisboa, Caparica, Almada, Portugal

Hugo Biscaia Department of Mechanical and Industrial Engineering, UNIDEMI, NOVA School of Science and Technology, Universidade Nova de Lisboa, Lisbon, Portugal

Cássio Bragança Department of Structural Engineering, Federal University of Minas Gerais, Belo Horizonte, Brazil

Jorge de Brito CERIS, Department of Civil Engineering, Architecture and Georesources, Instituto Superior Técnico, Universidade de Lisboa, Lisboa, Portugal

Rafael Cabral CONSTRUCT-LESE, Faculty of Engineering, University of Porto, Porto, Portugal

Rui Calçada CONSTRUCT-LESE, Faculty of Engineering, University of Porto, Porto, Portugal

Paulo X. Candeias National Laboratory for Civil Engineering (LNEC), Lisbon, Portugal

Rafaela Cardoso CERIS, Instituto Superior Técnico, Universidade de Lisboa, Lisboa, Portugal

João Dias Carrilho Itecons, Coimbra, Portugal;
CERIS, University of Coimbra, Coimbra, Portugal

Filipe Cavadas Faculty of Engineering, University of Porto, CONSTRUCT-LABEST, Porto, Portugal

Carlos Chastre CERIS, Department of Civil Engineering, NOVA School of Science and Technology, Universidade NOVA de Lisboa, Lisbon, Portugal

Corneliu Cismasiu CERIS, Department of Civil Engineering, NOVA School of Science and Technology, Universidade NOVA de Lisboa, Lisbon, Portugal

António Leça Coelho Universidade Lusófona do Porto, Porto, Portugal

António A. Correia National Laboratory for Civil Engineering (LNEC), Lisbon, Portugal

Bruno Costa Faculty of Engineering, University of Porto, CONSTRUCT-LABEST, Porto, Portugal

Alexandre Abrahão Cury University of Juiz de Fora, Juiz de Fora, Minas Gerais, Brazil

Pedro Raposeiro da Silva CERIS, Department of Civil Engineering, Instituto Superior de Engenharia de Lisboa, Instituto Politécnico de Lisboa, Lisboa, Portugal

Flávio de Souza Barbosa University of Juiz de Fora, Juiz de Fora, Minas Gerais, Brazil

Paulina Faria CERIS, Department of Civil Engineering, NOVA School of Science and Technology, Universidade NOVA de Lisboa, Lisbon, Portugal

Carlos Félix School of Engineering, Polytechnic of Porto, CONSTRUCT-LABEST, Porto, Portugal

Joaquim Figueiras Faculty of Engineering, University of Porto, CONSTRUCT-LABEST, Porto, Portugal

Gabriel Gomes CINAMIL, Academia Militar, Instituto Universitário Militar, Lisbon, Portugal

Miguel Chichorro Gonçalves Faculdade de Engenharia, Universidade do Porto, Porto, Portugal

Válter Lúcio CERIS, Department of Civil Engineering, NOVA School of Science and Technology, Universidade NOVA de Lisboa, Lisbon, Portugal

Marco Ludovico-Marques INCITE, Escola Superior de Tecnologia do Barreiro, Instituto Politécnico de Setúbal, Setúbal, Portugal

Isabel M. Martins Laboratório Nacional de Engenharia Civil, Lisbon, Portugal

Rui Micaelo CERIS, Department of Civil Engineering, NOVA School of Science and Technology, Universidade NOVA de Lisboa, Lisbon, Portugal

José Mingote NATO Counter IED Centre of Excellence, Madrid, Spain

José Neves CERIS, Department of Civil Engineering, Architecture and Georesources, Instituto Superior Técnico, Universidade de Lisboa, Lisboa, Portugal

Lina Nunes CE3C and Structures Department, National Laboratory for Civil Engineering, Lisbon, Portugal

Pedro F. Pereira CONSTRUCT-LFC, Faculty of Engineering (FEUP), University of Porto, Porto, Portugal

Mário Pimentel Faculty of Engineering, University of Porto, CONSTRUCT-LABEST, Porto, Portugal

Nuno M. M. Ramos CONSTRUCT-LFC, Faculty of Engineering (FEUP), University of Porto, Porto, Portugal

Hugo Rebelo CINAMIL, Academia Militar, Instituto Universitário Militar, Lisbon, Portugal

Diogo Ribeiro CONSTRUCT-LESE, School of Engineering, Polytechnic of Porto, Porto, Portugal

Carlos Rodrigues Faculty of Engineering, University of Porto, CONSTRUCT-LABEST, Porto, Portugal

Ricardo Santos CONSTRUCT-LESE, School of Engineering, Polytechnic of Porto, Porto, Portugal

Artur Silva CONSTRUCT-LESE, Faculty of Engineering, University of Porto, Porto, Portugal

Helena M. Silva Laboratório Nacional de Engenharia Civil, Lisbon, Portugal

António Tadeu CERIS, Department of Civil Engineering, University of Coimbra, Coimbra, Portugal;
Itecons, Coimbra, Portugal

João Tapadas Department of Civil Engineering, NOVA School of Science and Technology, Universidade NOVA de Lisboa, Lisbon, Portugal

Gidewon G. Tekeste Civil Engineering Department, University of Aveiro, Aveiro, Portugal

Emanuel Tomé Faculty of Engineering, University of Porto, CONSTRUCT-LABEST, Porto, Portugal

M. Rosário Veiga Department of Buildings, National Laboratory for Civil Engineering, Lisbon, Portugal

Part I

Materials

Chapter 1

New Trends on Bio-cementation and Self-healing Testing



Rui Micaelo , Paulina Faria , and Rafaela Cardoso

Abstract In the last decade, a significant effort was made by research institutions and industry to change ordinary construction materials into green, smart, adaptive, and advanced materials. Green materials (for example bio-cement) are developed to reduce carbon footprint and waste, using biological agents replacing common binders. Smart materials can monitor their condition and respond to state changes as designed. Examples of smart materials are composite materials that can heal autonomously after structural damage occurs. Nevertheless, despite the disposition of the construction industry to accept innovations being at high, these green and smart materials will only prevail if they prove to be sustainable and useful in the long-term. To this, they need to be adequately characterized and the benefits in comparison with conventional materials assessed. However, the standardized methods and apparatus used to characterize the conventional materials are often not adequate to these materials, either because of their atypical composition, therefore requiring different tests (e.g., chemical analysis) or lack of standardized methods to evaluate the specific property. This chapter describes and discusses the recent developments in the testing of green materials such as bio-cemented and self-healing materials.

Keywords Self-healing · Bio-cementation · Characterization · Soils · Asphalt · Cementitious materials

R. Micaelo () · P. Faria

CERIS, Department of Civil Engineering, NOVA School of Science and Technology,
Universidade NOVA de Lisboa, Lisbon, Portugal

e-mail: ruilbm@fct.unl.pt

P. Faria

e-mail: paulina.faria@fct.unl.pt

R. Cardoso

CERIS, Instituto Superior Técnico, Universidade de Lisboa, Lisboa, Portugal
e-mail: rafaela.cardoso@tecnico.ulisboa.pt

1.1 Introduction

Bio-cementation, also known as Microbially induced calcite precipitation (MICP), consists in promoting the precipitation of calcium carbonate from bacteria metabolic activity, whose most stable mineral form is calcite. Bio-cement minerals are precipitated around bacteria communities living in the pores and discontinuities of the media to be treated. This filling effect improves the hydraulic properties and overall stiffness of the treated medium. The bio-cement layer precipitated adheres to surfaces and, therefore, bonds are created and strength increases. The improvements achieved depend on the amount of bio-cement, and also on the continuity and geometry of the precipitated layer. Urease-producing bacteria are used, selected in accordance with the medium to be treated, to ensure they survive in local environmental conditions while the treatment is in progress. They can be stimulated to grow (bio-stimulation), or can be added in controlled dosages (bio-addition). Investigation of soil treatment based on MICP (resistance to erosion, resistance to liquefaction, slope stability) showed that it is a viable alternative to traditional techniques. In addition to MICP, microorganisms that produce iron oxides or other minerals alternative to calcium carbonate also have potential and have been evaluated in construction materials. Other applications in Civil Engineering are crack sealing and stone consolidation by external treatments or the development of self-healing materials.

In general terms, a self-healing material is defined as a material that can heal damage and recover properties of the undamaged state. For example, vernacular air lime mortars are known by its self-healing ability due to calcium carbonate dissolution, transport and re-precipitation. The mechanism leading to self-healing can be intrinsic of the material (autogenic) or engineered, and can occur autonomously after damage or upon an applied stimulus. These properties and the actual design strategy of self-healing (e.g. release of healing agents) are often used to classify the self-healing system.

In the last decades, a considerable research effort has been made to provide conventional materials (polymers, paints, concrete, asphalt, etc.) with self-healing properties. Some of these materials have intrinsic self-healing capacity but in fact with low impact on durability because of the limited extent of recovery that can be obtained, or the long time required to complete the healing process. Nevertheless, not many of these engineered materials have already reached the commercial market of construction materials and structures. Most self-healing mechanisms have not been entirely understood because of the complex physical and chemical interactions and reactions involved in it. On the other hand, adding or promoting self-healing properties should not compromise other valuable properties of the material (e.g. a paint that repairs autonomously scratches on coated surfaces but has the colour faded sooner than conventional paints would be less appealing to most buyers).

Bio-cements and self-healing materials are examples of recent innovations in construction industry. Green, smart, adaptative, or advanced materials need to be adequately characterized, and the benefits in comparison with conventional materials assessed to ensure market acceptance in the long-term. However, testing these

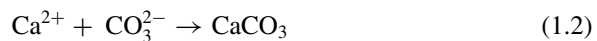
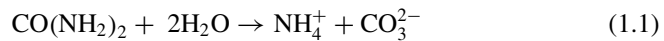
materials is not straightforward. This chapter describes and discusses the recent developments in the testing of bio-cemented and self-healing materials, particularly soils and bituminous materials.

1.2 Testing of Bio-cemented Materials

1.2.1 General Aspects of Bio-cementation

The first studies on using MICP in Civil Engineering applications appeared at the end of the twentieth century [1]. This technique can be used in porous materials, such as soils, and to seal discontinuities, as long as there is enough space for bacteria to survive, and their adhesion to the material surfaces could occur. Urease producing bacteria are used because the precipitation of calcium carbonate requires the combination of carbonate ions from the hydrolysis of urea and calcium ions, both present in the environment or supplied in the feeding solution (aqueous solution containing the urea and the calcium source). The calcium source used is usually calcium chloride, but can be calcium phosphate [2, 3].

The hydrolysis of urea ($\text{CO}(\text{NH}_2)_2$), in parallel with acid-base reactions promoted by pH rise, results in ammonium NH_4^+ and carbonate ions CO_3^{2-} (Eq. (1.1)). The precipitation of calcium carbonate (CaCO_3) occurs in the presence of calcium ions (Ca^{2+}) (Eq. (1.2)).



Several different bacteria can be used for bio-cementation, for example *Bacillus cereus*, *Bacillus sphaericus*, *Bacillus pasteurii* or *Sporosarcina pasteurii*, *Myxococcus xanthus* and *Shewanella* [4]. The choice is done as function of the environmental conditions of each particular case and bacteria survival to them. *Sporosarcina Pasteurii* species is the most popular because it is non-pathogenic, exists naturally in soils, has high urease activity and survives to high pH. Bacteria dosages are usually defined to be around 10^8 cells/mL [5].

MICP is being investigated for treating mainly sandy soils, improving their mechanical and hydraulic properties (improving foundation soil load bearing capacity) and erosion protection [2, 6, 7], for consolidating stone surfaces [8] and to heal cracks and protect the surface of concrete [9, 10]. In both cases the treatment is done by adding bacteria mixed with a feeding solution (by submersion or injection) to the materials to be treated, as it will be discussed next. Apart from being applied for treating sandy soils, the efficacy of iron-based bioproducts and bioproducts resulting from mixed microbial cultures have also been tested to treat the surface of historic materials, such as clayish-based, limestone and cementitious [11]. The use

of bacteria in fresh mortar, concrete or bituminous to create self-healing materials is another application. The mixture between soil (sands with some clay percentage) and bacteria and feeding solution was also used for brick production [12].

When treating soils (mainly sands), the solution with bacteria and feeding solution can be added by gravity keeping a low water head [13], or by injection, where the fluid is introduced under relatively low pressures [7]. Submersion is done for concrete and stone, mainly to treat surfaces against weathering and erosion, and eventually providing them resistance to chemical attack [14]. However, this type of treatment can hardly be reproduced on site, where a spray or brushing are options.

The most novel aspect worth to discuss is the fact that bio-cementation relies on bacterial activity and this is the main difference between using MICP or other biotechnologies and traditional techniques for the same purpose. Bacteria are living organisms sensitive to temperature and pH changes, and uncertainty exists on their survival when the treatment is in progress, and also on their efficiency (therefore, on the amount and homogeneity of bio-cement produced). Monitoring the treatment is necessary to assess bacteria activity, namely by measuring urease enzyme, or the chemical components indicating progress of the chemical reaction (urea and ammonium in the case of MICP, that is the most advance biotechnology of the previously mentioned). For this biotechnology, the quantification of calcium carbonate content (CCC) can also be done to confirm that precipitation has occurred, but is an indirect measurement of bacteria activity and is done in small amount of material because it is a destructive method.

The tests performed to assess the efficiency of the treatment on bio-cemented materials, proportional to the amount of bio-cement produced, are identical to those done on the materials treated using such known techniques. Standard tests are performed, and for this reason they will not be explored here and only some examples will be presented. Depending on the volume treated, homogeneity must be evaluated and that is usually done by collecting small samples of material for specific laboratory testing (mineralogical analysis, mercury intrusion porosimetry tests, calcium carbonate content) or by non-destructive testing (electrical resistivity, ultrasonic pulse velocity) through detecting changes in a given mechanical or hydraulic property. The identification of calcite, as the mineral form of calcium carbonate present, is an indicator of durability [14] but there is still limited experience on this treatment to have data on durability.

1.2.2 Monitoring Bacteria Activity

Monitoring bacteria activity should be done in real-time or time-lapse, making it possible to update the design of the solution along with the treatment. It can be performed by quantitative methods in which small samples of effluent fluid are extracted from the material and their chemical composition is analysed to detect and quantify indicators of bacterial activity, such as ammonium and urea, and also enzyme urease. The tests must be done after sample extraction, therefore on the

treatment site, or samples must be preserved (usually frozen) when transported to the laboratory.

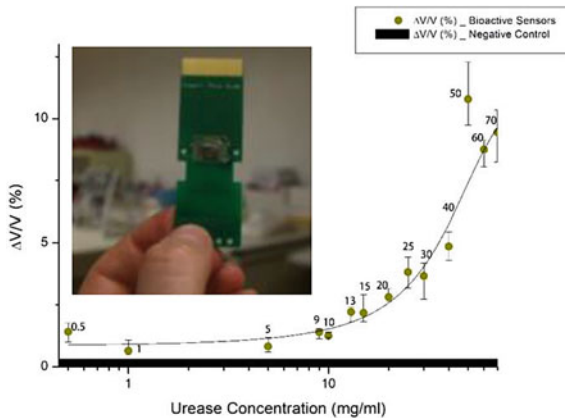
When ammonium or urea are measured, the estimation of bacteria activity considers stoichiometric calculations based on the Eqs. (1.1) and (1.2). By measuring the ammonium (NH_4^+) it is possible to estimate the amount of hydrolysed urea and the concentration of carbonate (CO_3^{2-}). Ammonium concentrations can be found using expedite methods such as ammonium strips (the same used for quality control of water in fish water tanks), or when using Nessler reagent colorimetric method [15]. In Nessler method a fixed amount of liquid is mixed with known amount of Nessler reagent and optical density at 425 nm is measured after 1 min of reaction and compared with calibration values, which are similar measurements performed with varying concentrations of this reagent without any NH_4^+ . This method detects NH_4^+ concentrations ranging between 0 and 0.5 mM.

The concentration of enzyme urease present in the effluent fluid can also be measured. The quantity of urease present in the purge fluid can be assumed to be proportional to bacterial activity, and therefore to the quantity of calcium carbonate that precipitates. The main disadvantage of measuring proteins such as urease is the fact that they are specific for each organism, and therefore knowledge must exist on the target protein and its specific combination antibodies. Protein detection is usually done using classical approaches such as high-performance liquid chromatography and gas chromatography, which require large processing time and trained personnel [16]. Recently, a biosensor able to measure urease concentration from *Canavalia ensiformis*, similar to that of *S. Pasteurii*, was presented and is under development to be used in real case. Biosensor-based devices can be highly sensitive and target selective, besides being fast, user-friendly, easy to implement, portable and cost-beneficial. The main disadvantage is the need of investigation to make it target selective and the need of previous treatment of the effluent fluid before placing it in the sensor.

Figure 1.1 shows the magnetoresistive (MR) biosensor developed for measuring enzyme urease [16]. It operates based on ELISA (enzyme-linked immunosorbent assay) method, which is a competitive-binding affinity essay usual in such type of sensors. Basically, for the sensor developed, a solution of magnetic label conjugated to an antibody via streptavidin-biotin interaction, mixed with the effluent fluid, flows through a microfluidic system, which is connected with the biosensor (Fig. 1.1). The magnetic nanoparticles label the urease in the sample because they are attached to the urease via the antibody. The sensor detects these nanoparticles if they get immobilized on the sensor surface (Fig. 1.1). Readings are made after washing with water flow, to be sure that only the nanoparticles attached to the urease proteins linked to the sensor are detected. The biosensor presented is optimized for purified urease (*C. ensiformis*); its calibration for urease concentrations varying between 0.5 and 70.0 mg/ml is presented in Fig. 1.1.

CCC can also be measured in small amounts of material (about 5 g), by washing the sample with 0.5 M HCl solution until all CaCO_3 is dissolved (the dissolution is complete when no more CO_2 gas bubbles are released). In this case the CCC is determined with Eq. (1.3), where m_i and m_f are the initial and final dry masses.

Fig. 1.1 Urease biosensor: magnetic biosensor on printed circuit board (PCB) and calibration curve for purified urease (adapted from [16])



$$CCC = \frac{m_f - m_i}{m_i} \quad (1.3)$$

CCC can be estimated indirectly from stoichiometric calculations using the Eqs. (1.1), (1.2) and after quantifying ammonium and the concentration of CO_3^{2-} ions.

Although the presence of calcium carbonate indicates bacteria activity, the study must go further to identify its mineral form because calcite is the one intended because it is insoluble, and therefore ensures durability. The three polymorphs of calcium carbonate minerals are calcite, vaterite and aragonite.

There is uncertainty on the chemical conditions necessary to generate each form of calcium carbonate; however, some studies indicate that high pH favours calcite formation [17, 18]. Analysis done on Scanning electron microscope (SEM) images is useful to visually identify these forms, but X-ray diffractometry (XRD) is more precise on this identification. The presence of calcium carbonate is not linked to bacterial activity directly, but the presence of these minerals indicates that the hydrolysis of urea took place, because bacteria catalyse this reaction. Recent studies had shown that vaterite changes to calcite along time, depending on pH and the presence of large amounts of urea and calcium ions [19, 20], although some studies indicate that the calcium carbonate mineral form is associated to bacteria species, or to the interaction between bacteria and the minerals from the substrate (limestone substrates favour calcite, which is not observed in silicate stone) [21]. Recent developments are being done using microfluidic devices to investigate in laboratory the mechanisms of calcite precipitation under different conditions [20, 22, 23].

1.2.3 Tests Performed on Bio-cemented Soils

Bio-cementation treatment in soils is a volumetric treatment, in which large quantities of bacteria and feeding solution are injected, in a circulating system, allowing to

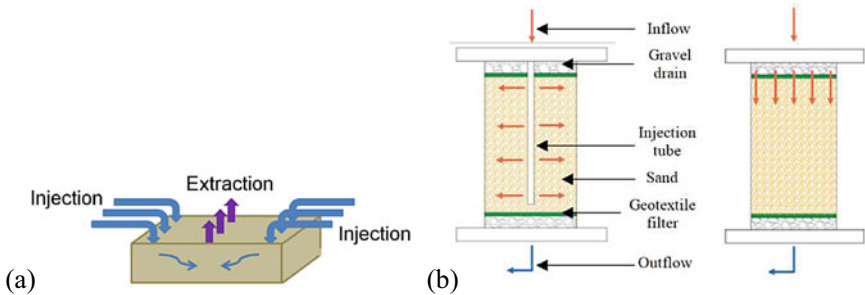


Fig. 1.2 General configurations of bio-cementation treatment in soils: **a** in situ tests; **b** experimental tests [24]

recover part of the injected fluid (scheme in Fig. 1.2 for in situ tests and some standard laboratorial test setups). Homogeneity is achieved by increasing the number of injection points and decreasing the distances between the injectors and the collectors. Final injection of clean water is necessary to clear ammonium and chlorides from the soil, as they are contaminants. Collected fluids can be tested to detect bacterial activity, as already described.

Samples prepared in laboratory or collected in situ must be tested to characterize the treated material by adopting standard tests (unconfined compression tests [6], triaxial tests [19], dynamic tests [12], resonant column tests [25], permeability tests [5, 12, 26]) quantifying the strength and stiffness earned with the treatment, or permeability reduction. It is always important to relate the tested parameters with the amount of calcium carbonate precipitated, so CCC must be determined as well. XRD tests and sometimes SEM images are often performed to identify the mineral form of calcium carbonate found. Mercury intrusion porosimetry (MIP) tests can also be done, usually for research purposes. They present the pore size distribution curves and this distribution is affected by the concentration of precipitate clogging the pores, and therefore reducing their size.

Heterogeneity can be measured by non destructive geophysical tests (electrical resistivity tests and sonic tests), or by geotechnical characterization tests (cone penetration tests—CPT—or Menard pressiometer tests, Standard penetration tests—SPT). A good example of in situ treatment and its evaluation is the work done by Van Passen et al. [7], who have performed the treatment in a tank ($8.0 \times 5.6 \times 2.5$ m) filled with sand. The authors have performed non destructive testing using shear wave velocity measurements, detecting high heterogeneity. It is well visible in Fig. 1.3a, showing a photograph of the treated volume which remained intact after water washing the entire treated sand. This treated volume exhibits the path of the circulating treatment fluid. CCC was measured in samples collected in several places confirming the heterogeneity found.

Gomez et al. [27] have performed the treatment in sand dunes to provide them resistance to erosion. Treatment was mainly superficial by aspersion the bacteria and feeding solution in a large area (4 cells 4.0×2.4 m each). They were able to form

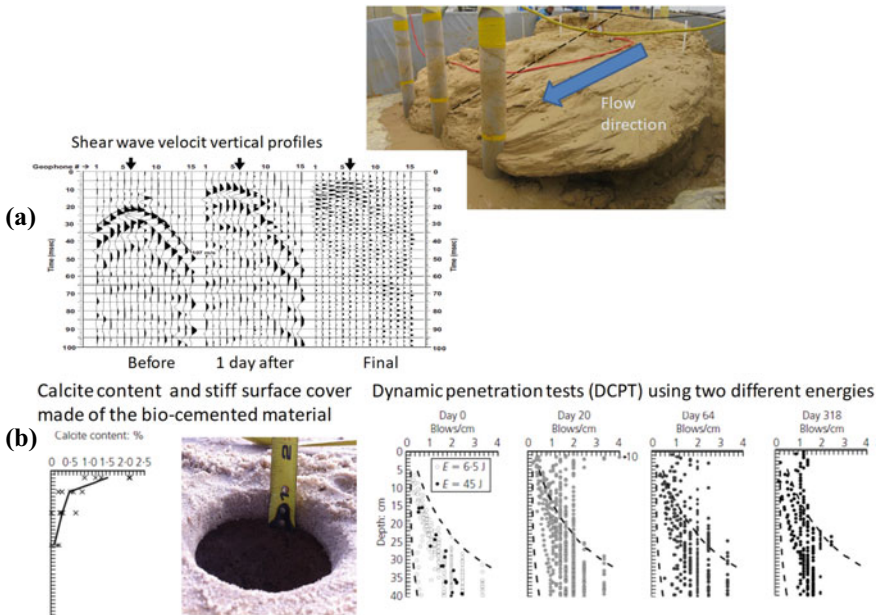


Fig. 1.3 Some examples of heterogeneity evaluation using in situ tests: **a** adapted from [7]; **b** adapted from [27]

a protective stiff crust, illustrated in Fig. 1.3b. In situ tests were also performed to evaluate the treatment, in this case dynamic cone penetration tests (DCPT). These tests are similar in concept to load bearing capacity tests, which can also be an alternative to evaluate the treatment effects on soil strength and stiffness.

Electrical resistivity tests are not as usual as sonic tests because they are not precise. Electrical resistivity will decrease due to wetting and the presence of the chemicals supplied with bacteria and feeding solution, independently from the precipitation of calcium carbonate. It will be sensitive to this precipitation only if there is a significant change in voids ratio, which means that huge amounts of precipitate must occur. Therefore, it may help tracking the fluids injected in terms of spatial distribution, but not the bio-cement location itself in the soil. Nevertheless, it can be useful for monitoring the treatment. Recently, the circulation of electrical current in soils, similar to what is being done in electrokinetic treatments, has been used to promote homogeneity during laboratory testing [28] but this is not an economical method for in situ cases.

Resistance to erosion is completely different from the resistance to liquefaction; however, both resistances are increased due to the presence of calcium carbonate precipitate bonding the particles of sand. In the first case erosion is caused by water drag forces (tensile stresses) and, therefore, shear strength must be increased with the treatment. This is achieved because these are adhesion bonds, so they provide true cohesion to soils. When it concerns liquefaction, first the soil must be saturated

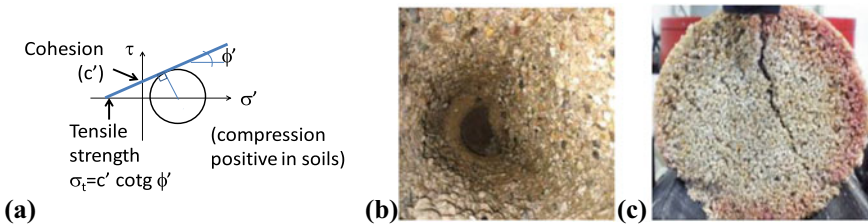


Fig. 1.4 Resistance to erosion and liquefaction: **a** relationship between cohesion and tensile strength using Mohr-Coulomb envelope; **b** coarse soil after an erosion test using water jet, adapted from [29]; **c** tensile strength evaluated indirectly through Brazilian splitting tests (adapted from [30])

and water pressures (hydrostatic) must rise creating a buoyancy force larger than effective stress. This can be considered similar to applying inner tensile stresses, separating the soil particles. In this case the bonds will provide tensile strength to soil, which is linked to true cohesion (see the Mohr-circle in Fig. 1.4a), but they are not the same. Due to the fact that both resistances are due to the presence of calcium carbonate bonds, both can be evaluated in similar ways. The easiest test is to perform erosion tests by using water jet with controlled pressure (Fig. 1.4b), measuring the penetration depth of the jet along time (erosion rate) and eventually the mass of the eroded material [29]. Tensile tests can also be done, or tensile stress can be found indirectly through Brazilian splitting tests, as it was done in sand samples by Cardoso et al. [30] (Fig. 1.4c).

1.2.4 Tests Performed on Bio-cemented Surfaces and Discontinuities

When bio-cementation is used to treat other porous materials, such as stone and cement-based materials like mortar and concrete, a surface treatment intends to provide a protective cover against erosion, chemical attack [31], water absorption, or to seal cracks and discontinuities. The latter has been applied in stone [9, 32–34], concrete [35–37] and mortar [38]. Some usual treatment setups for applying external bio-cementation treatment in surfaces and in cracks are presented in Fig. 1.5.

Electro-chemical interaction at the interface, in the contact surface, is responsible for adhesion. Adhesion is higher in hydrophilic surfaces [39] and is affected by the minerals present (for example, calcite precipitation is higher on calcite substrates than on silicate substrates [40]). The tests done on treated surfaces depend on the purpose of the treatment (against biological or chemical attack [37], impact or erosion [41], water absorption [11]). The most common tests performed on surfaces are presented in Table 1.1 and can be divided into tests to measure physical properties and tests to measure mechanical properties. The bio-cement coat is itself a porous material and, then, this protective porous layer may contribute to increase vapor transport by

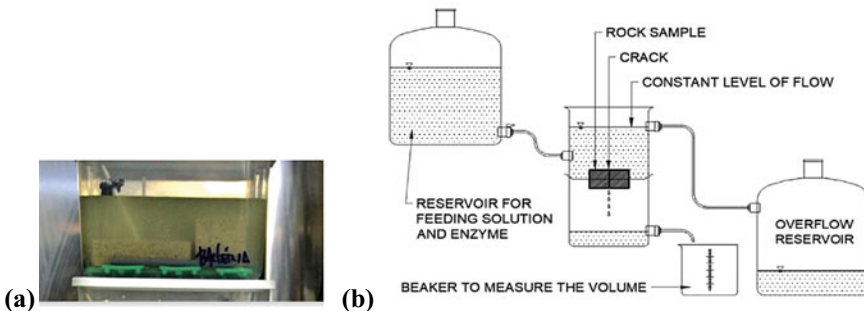


Fig. 1.5 Some usual setups of bio-cementation treatment for: **a** submersion for surface protection; **b** forcing fluid circulation through a discontinuity to seal it [34]

Table 1.1 Some usual tests performed to measure physical and chemical properties on treated surfaces

Property	Test	
Mechanical	Stiffness	Ultrasonic pulse velocity
	Stiffness and strength	Destructive tests performed on samples extracted after the treatment
	Strength	Pull-off
	Surface cohesion	Resistance to perforation using milling cutter with different diameters
Physical	Porosity	Water uptake by capillarity/water absorption
	Porosity/cracking	Infiltration tests
	Roughness	Roughness meter
Chemical	Alkaline agents	Submersion in solutions with known concentration
	Sulphate agents	
Other	Freeze-thaw cycles	Environmental loads
	Temperature cycles	

diffusion, therefore affecting water uptake properties [4] or other secondary effects. It is also worth to note that colour is important, particularly when the treatment is done for repair and consolidation of historical constructions. Colour change can be measured using a trichromatic chromameter, for example [31].

Roughness is an important parameter for bio-cement adhesion to the surfaces, as when any another traditional technique is used for the same treatment purpose. Roughness promotes bacteria fixation [42]. This is particularly important when the treatment is done using fluid flow because it can wash away the bacteria and precipitate [33] and is also a concern when injecting bacteria in soils. The effect of substrate roughness on bio-cementation was investigated by many authors mainly when researching its potential as a crack sealing technique, combining roughness and width (in cracks with 0.20 mm width [43], between 0.15 and 1.64 mm [38] and

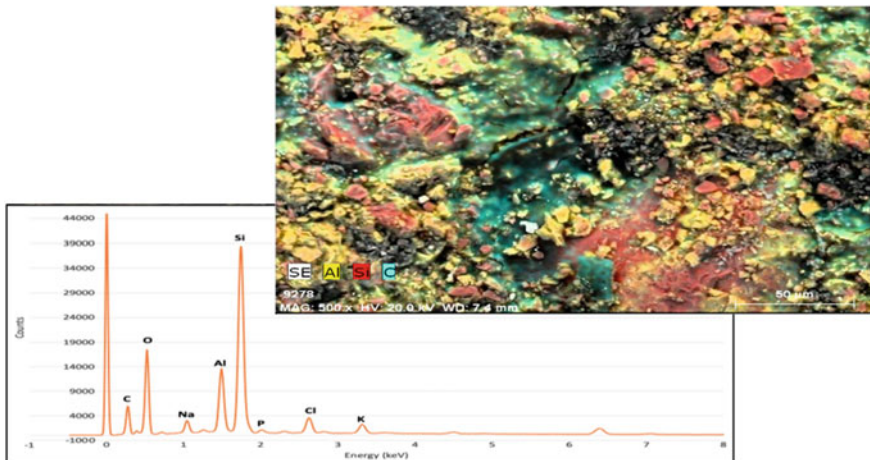


Fig. 1.6 SEM-EDS micrograph (500 \times magnification) of a brick sample treated with E.coli + Fe bioproduct with the EDS elemental distribution map (yellow = Al, red = Si and blue = C) and respective EDS spectrum [11]

with width varying between 1 and 2.5 mm [44]). Several methods can be used to visualize the treated surfaces, such as SEM-EDS (Fig. 1.6).

On cracked material, the treatment effect is not only superficial. In laboratory experiments, a challenge is to pre-crack samples with the defined width. Both prismatic and cylindric samples are commonly used; in the latter, the samples are frequently previously cut in slides and pre-cracked individually. The cracks' width is measured initially and after defined periods; several methods, such as binocular microscope, are used.

Infiltration tests are the most common tests performed to evaluate crack sealing effectiveness [34, 44, 45], in which a water pound is created and water level is monitored along time. These tests are also permeability tests (variable water head). Some cases are presented in the literature describing in situ permeability tests which were performed after bio-cementation treatment, mainly on rock masses [1]. Wiktor and Jonkers [46] have used this treatment to seal the cracks of a concrete slab in a car parking. Basically they have recreated an infiltration test by installing a small pound above the damaged area and forcing the flow through the cracks of a solution with bacteria and feeding solution (Fig. 1.7a). The evaluation of treatment efficiency was made visually by checking water presence in the lower face of the slab. Cardoso et al. [47] have done a similar procedure in a laboratory to seal the cracks of a reinforced concrete beam (Fig. 1.7b); however, an impervious paint was necessary for the lateral walls of the beam to force vertical circulation of the fluid. In this case sealing was evaluated when the water level of the reservoir installed remained constant. The steel bars presented corrosion in this particular case, probably because pH was reduced during the treatment. This may be a secondary effect to consider in real cases.

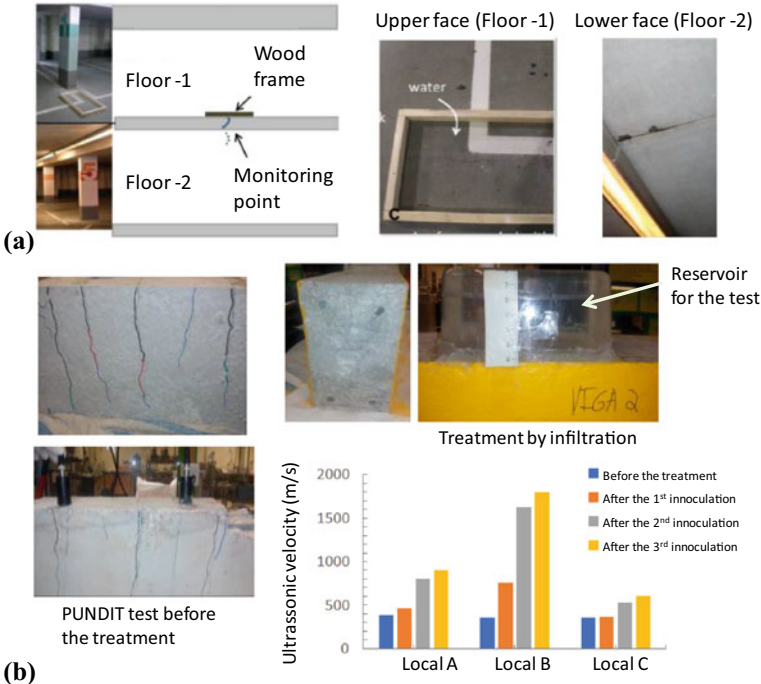


Fig. 1.7 Crack sealing evaluation: **a** in situ test in a parking slab [46]; **b** in situ test in a reinforced concrete beam [47]

When strength increment is intended with the bio-cementation treatment, for example for repair and consolidation works [32, 37], destructive tests can also be performed. Tensile strength can be measured through tensile strength tests and indirectly through Brazilian splitting tests. Shear tests along the crack can also be performed to measure shear strength. These tests are usual when evaluating the strength of treated cracks using standard sealing materials [41]. As when evaluating homogeneity in soils, non destructive tests can also be performed to evaluate the treated materials. Examples are the measurement of ultrasonic pulse velocities [32].

Finally, other cases exist in which fresh cementitious mortar and concrete or ceramic pastes are mixed with bacteria and feeding solution, for bio-formulated products. In the first case bio-cement will be produced along with cement hydration products [48, 49]; alternatively, it can be produced to seal cracks when damage occurs [41] and encapsulated bioproducts are activated. In the first case the precipitated calcium carbonate is not acting as the cement mineral itself but rather in conjunction with the hydrated cement minerals. The tests performed in such materials are equivalent to those performed in standard cementitious materials, conjugated with deeper analysis of the microstructure by SEM imaging and MIP tests, and by chemical and mineralogical composition. The second is the case of self-healing materials, which will be discussed below for the case of bituminous materials.

1.3 Testing of Self-healing Materials: Bituminous Materials

1.3.1 General Aspects

This section is about the recent developments in the testing of self-healing materials, in which asphalt self-healing systems are used as a reference. Nevertheless, many of the achievements and the unsolved problems with testing of self-healing bituminous materials are common to other self-healing construction materials, such as Portland cement mortars and concrete, and even to ceramic products.

Intrinsic self-healing ability of asphalt¹ during the periods between traffic loads has been acknowledged for a long time now, and it has a positive effect on service life [50]. After the occurrence of damage, wetting and interdiffusion mechanics act to recover the initial strength. However, on open cracks, healing is preceded by flow to bring in close contact the crack surfaces [51]. The bitumen is very stiff in the in-service temperature range; therefore, the healing-based mechanisms are very slow and only small recoveries can be achieved under traffic action. To accelerate intrinsic healing, two self-healing asphalt systems have been proposed: induction heating and incorporation of encapsulated rejuvenators. As illustrated in Fig. 1.8, both systems act by decreasing the viscosity of the bitumen, through the temperature increase caused by an alternating electromagnetic field or the diffusion of low-viscosity oil from capsules [52]. Induction heating is an autogenous stimulated healing technique while encapsulated rejuvenators is an autonomous healing technique. Figure 1.9 shows the expected effect of these techniques on the service life of asphalt pavements.

Induction heating, presented earlier, attracted more research, and is closer to be considered completed and qualified for the operational environment [53]. Heating through microwave energy has been also proposed and investigated, which is referred by some as microwave induction heating [54]. Internal heating of bituminous mixture melts the bitumen which contributes to healing cracks. However, this changes the microstructure of the material in damaged and undamaged regions with undetermined

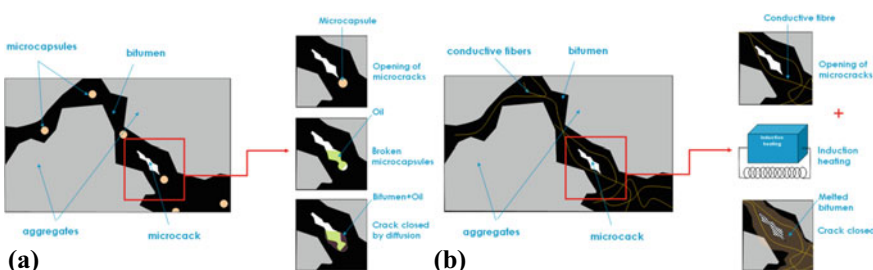
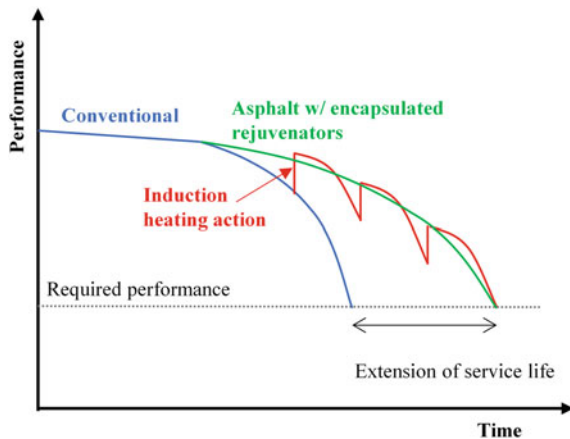


Fig. 1.8 Mechanisms of asphalt self-healing: **a** rejuvenators; **b** induction healing [52]

¹ In this chapter the European terminology of bituminous materials is used: “bitumen” designates the binder and “asphalt” designates the mixture.

Fig. 1.9 Effect of self-healing techniques on asphalt performance and service life



consequences. Currently, the main limitations of using this technique are: (1) when to apply induction heating to maximize the pavement's service life and, (2) how many times can induction heating be implemented with high efficiency.

Differently, asphalt healing with encapsulated rejuvenators has been proven in the laboratory but not demonstrated under operational conditions (road environment). The most investigated topic under this subject is the type and characteristics of capsules, which is primarily a function of the fabrication method. Three methods have been proposed: (1) saturating porous sand with the rejuvenator and coating the sand particles [55], (2) the ionotropic gelation method (crosslinking of sodium alginate with calcium ions) [56] and, (3) *in situ* polymerisation of urea-formaldehyde or other polymers [54]. There are several issues identified with this technique that need further investigation, such as: (1) the adequate size and strength of capsules to each type of asphalt; (2) how long the asphalt's service life can be extended if the capsules can only assist crack healing once; (3) if the area around the broken capsule is less susceptible to future microdamage (cracking, disintegration).

For a thorough review on asphalt healing, namely the theoretical concepts and the research and development work performed up to now, is recommended [53, 54, 57].

Asphalt industry will only absorb these innovative asphalt self-healing techniques if they prove technically and economically effective. The standardized methods and apparatus used in asphalt practice are often not adequate to these materials, either because of their atypical composition, therefore requiring different tests, or due to lack of standardized methods. In the following subsections, it is discussed briefly the tests used to investigate crack healing and to characterize new constituents and typical asphalt properties.

1.3.2 *Self-healing Research and Assessment*

Investigation of the asphalt self-healing phenomenon and effectiveness extends over several orders of magnitude, from nano- to macro-scale, and the purpose of the analysis and the testing methods used vary with it. At the macro-scale, testing can serve both the purpose of research, as well as of performance assessment and quality control. Differently, smaller scale investigations concentrate on understanding healing mechanisms.

- (1) *Nano-scale* (10^{-9} – 10^{-6} m): at this scale, the analysis focuses on the composition, interaction and mobility of the molecular structures and functional chemical groups. Fracture and damage are associated with broken links between these elementary structures, namely the stiffer ones, and strength recovery with the reestablishment of broken bonds. This investigation addresses mainly the intrinsic healing mechanisms of bitumen.

The bitumen's chemical composition is characterized in terms of the SARA fractions (Saturates, Aromatics, Resins and Asphaltenes) determined with chromatography methods, and the chemical evolution monitored through Fourier-Transform Infra-Red spectroscopy (FTIR) [58]. At the nano-scale, bitumen is a composite material with several microstructures establishing stable and unstable bonds between them, which determine the macro-behaviour of the material. The effect of temperature on rheological behaviour, the wetting and diffusion mechanisms, the effect of oxidative reactions are common research topics [53]. Attenuated Total Reflectance (ATR)-FTIR has also been used to detect the extent of rejuvenator's diffusion in asphalt [59].

SEM and Atomic Force Microscopy (AFM) can provide complementary information to chemical composition. These techniques give information (type, micromechanical properties) on the superficial microstructures of bitumen which can be used to build fundamental models of bitumen's behaviour [54]. However, there is not yet a consensus on the interpretation of features identified in these high-resolution images, and how they are related with healing mechanisms.

- (2) *Micro-scale* (10^{-6} – 10^{-3} m): a significative part of the damage healing process (flow and crack closure), which is the main target of asphalt self-healing techniques, occurs under this scale. Nevertheless, full strength recover depends on completion of wetting and diffusion mechanics along crack surfaces. Two imaging techniques, fluorescence microscopy (FM) and X-ray computed tomography (CT), are commonly used for this research purpose. FM is commonly used to analyse the distribution of additives in bitumen (e.g. polymers), and in self-healing studies to investigate the distribution of capsules in bitumen and, eventually, the rejuvenator release from open capsules and crack closure [60]. CT is a powerful non-destructive imaging technique to characterize the internal microstructure of composite materials with a high resolution (up to a few microns) and has been used to characterize the distribution of capsules in asphalt and to monitor damage and healing under different conditions. For

example, Micaelo et al. [56] compared crack closure on asphalt specimens with and without capsules containing sunflower oil and Garcia et al. [61] analysed the effect of damage and induction heating on the internal aid voids structure of asphalt specimens.

- (3) *Meso/macro-scale* ($>10^{-3}$): at this broad scale group, many testing methods have been used in asphalt self-healing studies. In general, the mechanical properties of the bituminous material are compared in different states (undamaged, damaged, and healed) to determine the self-healing technique performance. The size of the specimen depends on the selected test method, varying from a few millimetres to several decimetres. Bitumen, bituminous mastic or asphalt have been used in testing. Currently, these tests are adaptations of conventional and standardized test methods, and there is not a firm method accepted by the scientific and industrial community. Differently, field testing focuses on the overall performance of asphalt pavements, not exclusively on self-healing properties, that allows the use of conventional test methods.

The two most used self-healing testing methods are fatigue- and fracture-healing methods, which have been implemented with numerous testing configurations (monotonic or cyclic loading; tension, shear or flexion stress states; disk-, cylindrical- and prismatical-shaped specimens). In the fatigue-healing method, the specimen is first subjected to cyclic loading until a certain damage level is attained, then to a healing method and, finally, loaded again. In the fracture-healing method, the specimen is usually loaded to induce large damage, such as the specimen broken in two halves, then subjected to a healing method and, finally, loaded again to failure. The healing method of induction heating is to expose the specimen to electromagnetic or microwave induction for a certain period and then allow the specimen to cool down to room temperature before retesting. The damaged specimens with encapsulated rejuvenator are allowed to rest for a certain period under defined temperature conditions.

Often, in the fracture-test, loading occurs under low-temperature conditions to avoid wide and spread deformation in the specimen during the first loading stage. This means that fracture-tests assess the ability to heal a single large crack, which, nevertheless, does not resemble damage in real conditions. Cracking is a slow-progressive process which initiates with microcracks that coalesce into macro-cracks and ultimately leads to failure. Fatigue tests are intended to simulate this (slower) damage evolution in the material, that is more complex to characterize and, thus, to measure the effect of self-healing.

Hence, some previous studies reported different conclusions on the efficiency of the same self-healing technique from experimental results of fracture- and fatigue-healing tests, which may be related with the tests attributes. In [62, 63] it was studied the effect of alginate capsules containing sunflower oil on the self-healing properties of dense asphalt. The fracture-healing test results (Fig. 1.10a) showed that with 0.75%^M of capsules it was possible to recover about 50% of initial strength in 3-point bending after 80 h of healing time. On the contrary, the fatigue-healing test results (Fig. 1.10b) did not show an improvement of fatigue resistance after resting

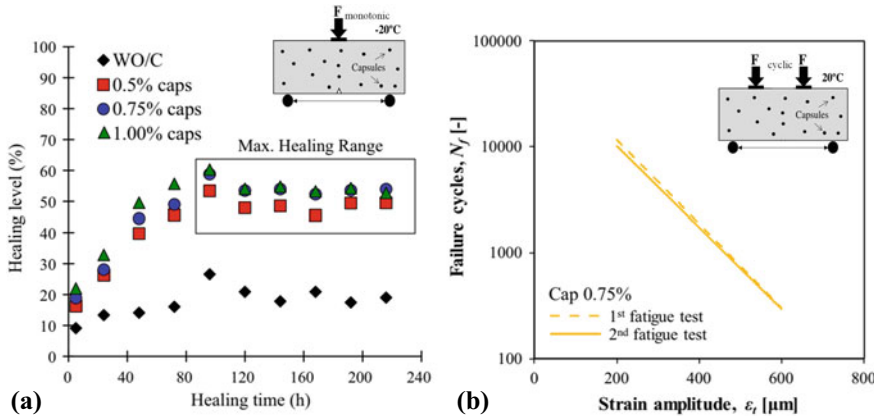


Fig. 1.10 Testing of asphalt self-healing induced by encapsulated rejuvenators with fracture-test **a** and fatigue-test **b** (adapted from [62, 63])

(96 h) in specimens with and without capsules. One possible reason for this is that the softening power of rejuvenator and the crack healing have opposite effects on mechanical behaviour; however, the softening effect is hidden when the mechanical test is performed under low-temperature conditions.

Besides the type of loading test, many other test conditions, including the preparation of specimens, are important for the healing response. It is accepted that the higher the damage level, the least effective the self-healing technique will be. However, the conditions that optimize healing performance would hardly be the same with induction heating and encapsulated rejuvenators. The level and characteristics of damage imposed to specimens will change with the loading mode, deformation level, loading frequency/rate, introduction of periodic rest periods and/or the load interrupting condition. Also, bituminous materials are very sensitive to test temperature and ageing level. In addition, different analysis methods can be applied to the same test methods, which can result in different conclusions. For example, in fatigue-healing tests, one method to quantify healing performance (HI) is with Eq. (1.4), where N_f^1 and N_f^2 are the number of cycles to reach a defined damage level in the first and the second loading stage, respectively. This healing index is determined to each specimen and the average value determined for the set of tested specimens under the same conditions (load level, frequency, etc.). Differently, considering that fatigue testing results show typically large variation, in [61] a reference fatigue life of the material, under certain loading conditions, was first determined by fitting a Weibull statistical distribution to a set of specimens. So, Eq. (1.5) is adopted to determine the healing index (HI) of each specimen, where N_f is the total number of cycles to failure (before and after healing) of specimen and $N_{0.5}$ is the number of cycles to failure with a probability of 50%.

$$HI = \frac{(N_f^2)}{(N_f^1)} \quad (1.4)$$

$$HI = \frac{N_f - N_{0.5}}{N_{0.5}} \quad (1.5)$$

1.3.3 Characterization of New Constituents

Asphalt and their constituent materials (bitumen, aggregates, and reclaimed asphalt) are required to comply with defined physical, geometrical, chemical, rheological and/or performance requirements. In Europe different hot-mix asphalt types are defined through standards EN 13108-1 to -7, the bitumen with EN 12591, EN 14023 or EN 13924, and the aggregates with EN 13043. Common additives used by asphalt industry, such as waxes, fibres, and pigments, are not covered by these standards; however, their use is allowed.

For (electromagnetic) induction heating, conductive particles (steel fibres, scraps or grit) are added to asphalt, whereas capsules or fibres containing rejuvenators (see Fig. 1.11) are added in the other self-healing technique.

The properties and methods used in the literature to characterize these additives are listed in Table 1.2. Often, the characterization of steel particles is very simple and only covers density and size. Differently, capsules containing rejuvenators are characterized to a greater extent and using advanced techniques (e.g. SEM). Testing of capsules is more intense because the technique is being investigated to determine its viability. Also, as the rejuvenator is a commercial product (light oil) with defined properties, the characterization effort focuses essentially on its compatibility with the bitumen. Many conventional bitumen tests are used to evaluate the effect of rejuvenator on bitumen. One relevant property that has not yet been investigated is leaching behaviour. Some rejuvenators are chemical products with important health and safety issues. In the future, capsules containing rejuvenators for the asphalt industry will be a commercial product and it can be expected that many of these properties are included in the product specifications.

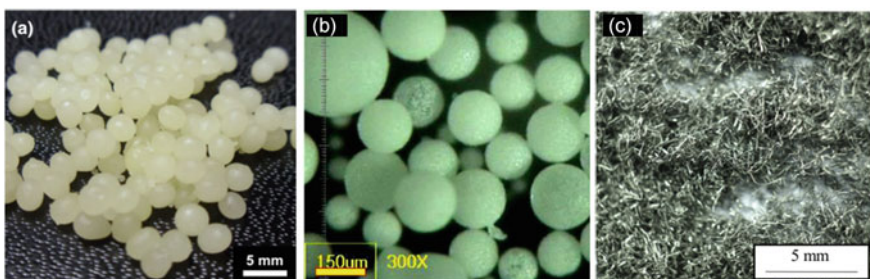


Fig. 1.11 **a** Calcium-alginate capsules [62]; **b** urethane resin capsules [64]; **c** steel wool [65]

Table 1.2 Properties and test methods for steel particles and capsules containing rejuvenators

Property		Steel particles	Capsules/fibres w/rejuvenators
Geometrical	Gradation	<ul style="list-style-type: none"> – Sieve analysis – Optical microscopy (fibres) 	<ul style="list-style-type: none"> – Microscopy (SEM, fluorescence or optical) – Laser particle size analysis
	Particle shape	<ul style="list-style-type: none"> – Optical microscopy 	<ul style="list-style-type: none"> – Microscopy (SEM, fluorescence or optical)
Physical	Density	<ul style="list-style-type: none"> – Pycnometer 	<ul style="list-style-type: none"> – Water pycnometer – Method of discharging kerosene – Estimated from compositional data
	Water absorption	NR	NR
	Thermal stability	NR	<ul style="list-style-type: none"> – Thermogravimetric analysis
	Electrical resistivity	<ul style="list-style-type: none"> – Multimeter – Resistance tester 	NR
Chemical	Composition	NR	<ul style="list-style-type: none"> – FTIR – Compositional data
Mechanical	Compression strength	NR	<ul style="list-style-type: none"> – Monotonic compression test (capsules)
	Tension strength	NR	<ul style="list-style-type: none"> – Monotonic tensile test (fibres)
Rejuvenator-bitumen compatibility	Dispersion	NA	<ul style="list-style-type: none"> – Fluorescence microscopy
	Chemical composition	NA	<ul style="list-style-type: none"> – FTIR – SARA composition
	Consistency	NA	<ul style="list-style-type: none"> – Needle penetration – Softening point
	Ductility	NA	<ul style="list-style-type: none"> – Ductility tensile test
	Viscosity	NA	<ul style="list-style-type: none"> – Capillary tube viscometer (absolute) – Rotational viscometer (dynamic)
	Rheological behaviour	NA	<ul style="list-style-type: none"> – Complex modulus and phase angle (dynamic shear rheometer)
	Low-temperature behaviour	NA	<ul style="list-style-type: none"> – Bending beam test

NR—not reported; NA—not applicable

1.4 Performance and Durability

General, empirical, and fundamental requirements are set to asphalt in European standards EN 13108-1 to -7 to ensure that, as part of the pavement structure, it can withstand traffic loading under different environmental conditions for the design period. General and empirical requirements are mostly related to composition, volumetry, and performance in simulation and (long used) empirical-base tests. Fundamental requirements are based on fundamental mechanical properties, such as stiffness. Often, a combination of these requirements is used in practice.

Adding or promoting self-healing properties should not compromise other valuable properties of asphalt, such as the stiffness, resistance to permanent deformation and water sensitivity. The literature mentions that conventional and standardized test methods are used to assess asphalt with conductive particles or encapsulated rejuvenators in comparison with conventional asphalt. Next, some test methods and results commonly used on asphalt (bitumen tests are not considered) are briefly summarized.

- (1) *Stiffness*: the stiffness modulus of asphalt is a basic mechanical property used in the pavement design and it is determined under cyclic loading in temperature-controlled conditions. Several tests that differ in applied loading and geometry of asphalt specimen can be used. Important issues are not anticipated when using these tests with any asphalt modified for self-healing purposes.

One of the most used tests is the Indirect Tensile (IT) test that applies indirect tension to cylindrical specimens, namely because specimens can be manufactured in the laboratory or extracted from pavement sites and can be of variable size (diameter and thickness). According to standard EN 12697-26, several load cycles (haversine waveform) are applied along the vertical diameter (see Fig. 1.12a), with the amplitude adjusted to achieve a target peak transient horizontal deformation. The horizontal deformation is measured with two linear variable differential transformers mounted opposite one another in a rigid frame. The stiffness modulus (Sm) is calculated for each loading cycle with Eq. (1.6), where ν is the Poisson's ratio, Z is the amplitude of horizontal deformation and h is the mean thickness of the specimen. The test is repeated over two perpendicular diameters for each specimen, and the results of the stiffness modulus averaged. The test temperature is usually between 15 and 25 °C.

$$Sm = \frac{F \times (\nu + 0.27)}{Z \times h} \quad (1.6)$$

For example, Fig. 1.12b compares the results of the IT test to porous asphalt specimens with and without steel fibres and calcium alginate capsules [67]. This study concluded that both additives increase the stiffness modulus, and the effect is cumulative. Previous research reported similar conclusions to the effect of steel fibres; however, similar capsules decreased the stiffness of dense asphalt [68]. A similar reduction effect of these type of capsules on stiffness modulus

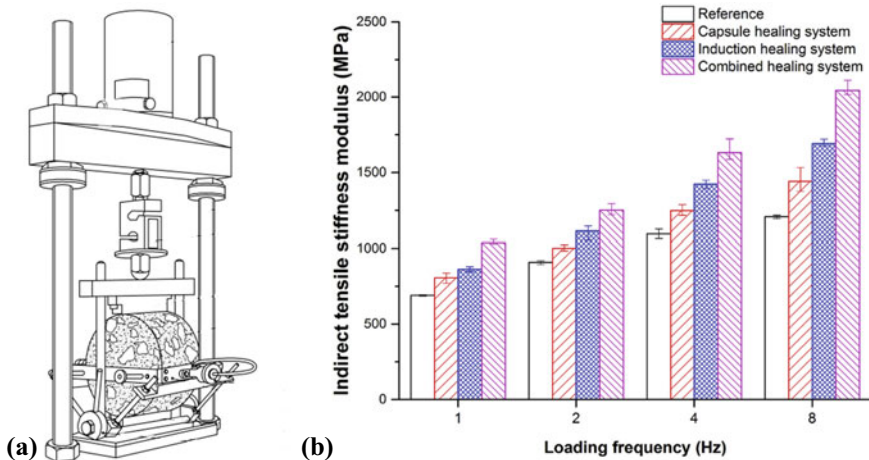


Fig. 1.12 **a** IT test configuration defined in EN 12697-26 [66]; **b** asphalt stiffness measured with the ITS test [67]

was reported in Micaelo et al. [63] based on a different test configuration (4-point bending).

- (2) *Resistance to permanent deformation:* deformation accumulation with traffic loading on wheel paths (rutting) is one of the most important pavement distresses, which for encapsulated rejuvenators can be even more challenging if part of the rejuvenator is released to asphalt during the first years after opening to traffic. Its evaluation is based on three different test types: (i) cyclic compression tests without or with small lateral confinement; (ii) triaxial cyclic compression test; and (iii) wheel-tracking test. The triaxial test determines “true” deformation properties of asphalt whereas the other tests are performance related. From these, the wheel-tracking (WT) test is the most used because it simulates traffic loading. In this test, the susceptibility to permanent deformation is determined from the rut depth (RD) evolution with repeated passes of a loaded wheel at the test temperature. In Europe, the test is performed following the European standard EN 12697-22 that defines the use of different equipment depending on the specimen size. The specimen is conditioned in air or in water depending on the device used at a constant temperature (40–60 °C) (see Fig. 1.13a).

For example, in Micaelo et al. [63] the effect of calcium alginates capsules on the resistance to permanent deformation of dense asphalt at 60 °C with the WT test was studied (see Fig. 1.13b). Specimens with different amounts of capsules showed strong rutting resistance like reference mixture, and it increased after resting for 5-days at 20 °C. From this, the researchers suggested that damage due to shear deformation could also be partly healed.

- (3) *Particle loss and water damage:* loss of aggregate particles is a common distress seen in asphalt surfaces after several years, which is caused by weak binder-aggregate adhesion especially in presence of water. Water can cause bitumen

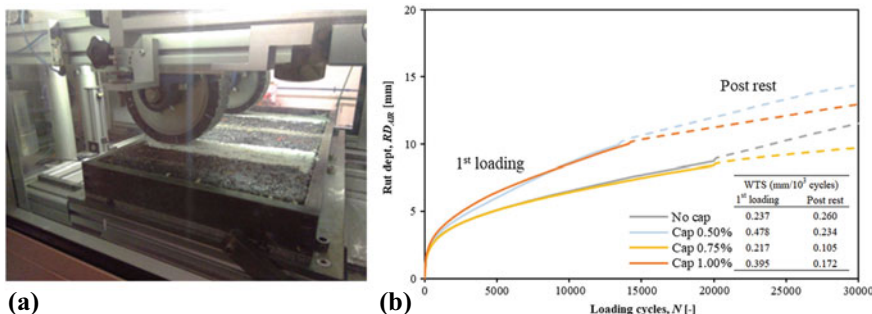


Fig. 1.13 **a** Specimen being tested with small-device (EN 12697-22); **b** WT test results [63]

debonding from aggregate particles by several mechanisms (displacement, detachment, film rupture and blistering and pitting) [69], and moisture-induced damage extends to non-superficial layers when water can ingress the pavement. Besides, the cohesion strength of bituminous mastic and the interlocking aggregate structure are also very important to avoid loss of particles. Hence, open-graded mixtures, such as porous asphalt, can be susceptible to particle loss in dry conditions.

Conventional testing used to assess water-induced damage susceptibility of asphalt involves one of two types of methods: (1) immersing coarse aggregate fractions coated with bitumen in the water, under static or dynamic agitation conditions, at a certain temperature, and determining the bitumen loss by visual assessment at defined times; (2) comparing a mechanical property (e.g. tensile strength, stiffness, etc.) of asphalt specimens conditioned in air and water for a defined period. Both methods are performance related tests and do not provide intrinsic properties of material; however, the latter is often adopted in specifications because as-built asphalt is tested.

According to the EN 12697-12 a set of specimens is divided in two subsets, with one set maintained in air and the other stored in water and, following the conditioning time, the specimens are submitted to the mechanical test (compression or indirect tensile). The number of specimens and the conditions used for conditioning the specimens vary with the mechanical test used. The ratio of the compression strength or the indirect tensile strength of the water conditioned subset to that of the dry subset is calculated. This test method is similar to the previous test procedure based on Marshall stability [70].

Experimental evaluation of the susceptibility to particle loss of porous asphalt is a conventional test procedure in Europe. In the test procedure specified in EN 12697-17 a minimum of 5 cylindrical specimens are submitted to 300 turns in the Los-Angeles-machine drum (without metal balls) and the particle loss is calculated from comparing the initial and final weight of specimens. The test is performed with specimens conditioned at 15–25 °C of temperature. Although not foreseen in this

test procedure, it can also be used to evaluate moisture-damage susceptibility if two differently conditioned (dry and wet) sets of specimens are tested.

In the literature regular use of these test methods is reported on various asphalts containing steel particles and capsules containing rejuvenators. Surprisingly, previous studies [65, 68] on the effect of steel particles and calcium-alginates capsules on water susceptibility and particle loss showed, in general, that both constituents do not weaken asphalt.

1.5 Conclusions and Prospect

The construction industry employs several materials that have been investigated to produce reinforced materials by bio-cementation or to boost natural self-healing capacity. This happens because constructions represent large investments that are expected to serve satisfactorily for many decades with minimal maintenance requirements and, in many situations, maintenance is hardly feasible.

Some of the most usual methods and apparatus used to characterize the biocements and self-healing materials are presented, some of them based on conventional materials when adequate, or others adapted to assess specific requirements due to atypical compositions and expected performances. The lack of standardized methods to evaluate specific properties is also discussed based on examples.

A particular aspect of such materials is the need to understand how they behave providing learning tools to tailor multifunctional materials for different and more durable applications. This implies multiscale analysis and specific tests, possible with the knowledge of transdisciplinary teams bringing fundamental concepts such as biology, chemistry and multiphysics.

Acknowledgements The authors would like to acknowledge the support of FCT for the partial funding of this work under the strategic project UIDB/04625/2020 from the research unit CERIS.

References

1. Phillips A, Gerlach R, Lauchnor E, Mitchell A, Cunningham A, Spangler L (2013) Engineered applications of ureolytic biomineratization: a review. *Biofouling: J Bioadhesion Biofilm Res* 29:715–733
2. Akiyama M, Kawasaki S (2012) Microbially mediated sand solidification using calcium phosphate compounds. *Eng Geol* 137–138:29–39
3. Xu J, Du Y, Jiang Z, She A (2015) Effects of calcium source on biochemical properties of microbial CaCO_3 precipitation. *Front Microbiol* 1–7
4. Cardoso R, Pedreira R, Duarte S, Monteiro G, Borges H, Flores-Colen I (2016) Chap 5-biocementation as rehabilitation technique of porous materials. In: de Freitas VP, Costa A, Delgado J (eds) *Building pathology and rehabilitation*. Springer, pp 99–120
5. Al Qabany A, Soga K, Santamarina C (2012) Factors affecting efficiency of microbially induced calcite precipitation. *J Geotech Geoenvironmental Eng* 138:992–1001

6. Al Qabany A, Soga K (2013) Effect of chemical treatment used in MICP on engineering properties of cemented soils. *Geotechnique* 63:331–339
7. Van Paassen L, Ghose R, van der Linden T, van der Star W, Van Loosdrecht M (2010) Quantifying biomediated ground improvement by ureolysis: large-scale biogROUT experiment. *J Geotech Geoenvironmental Eng* 136:1721–1728
8. Jimenez-Lopez C, Rodriguez-Navarro C, Pinar G, Carrillo-Rosúa FJ, Rodriguez-Gallego M, González-Munoz MT (2007) Consolidation of degraded ornamental porous limestone by calcium carbonate precipitation induced by microbiota inhabiting the stone. *Chemosphere* 68:1929–1936
9. De Muynck W, De Beliea N, Verstraete W (2010) Microbial carbonate precipitation in construction materials: a review. *Ecol Eng* 36:118–136
10. Achal V, Mukerjee A, Reddy MS (2013) Biogenic treatment improves the durability and remediates the cracks of concrete structures. *Constr Build Mater* 48:1–5
11. García-González J, Pereira AS, Lemos PC, Almeida N, Silva V, Candeias A, Juan-Valdes A, Faria P (2020) Effect of surface biotreatments on construction materials. *Constr Build Mater* 241:118019
12. Raut SH, Sarode DD, Lele SS (2014) Biocalcification using *B. pasteurii* for strengthening brick masonry civil engineering structures. *World J Microbiol Biotechnol* 30:191–200
13. Montoya BM, DeJong JT, Boulanger R (2013) Dynamic response of liquefiable sand improved by microbial-induced calcite precipitation. *Geotechnique* 63(4):302–312
14. De Muynck W, Debrouwer D, DeBelie N, Verstraete W (2008) Bacterial carbonate precipitation improves the durability of cementitious materials. *Cem Concr Res* 38:1005–1014
15. Harkes MP, van Paassen LA, Booster JL, Whiffin VS, van Loosdrecht MCM (2010) Fixation and distribution of bacterial activity in sand to induce carbonate precipitation for ground reinforcement. *Ecol Eng* 36:112–117
16. Albuquerque D, Cardoso R, Monteiro G, Martins V, Cardoso S (2019) Towards a portable magnetoresistive biochip for urease-based biocementation monitoring. In: Proceedings of 6th IEEE Portuguese meeting on bioengineering (ENBENG 2019). Lisbon
17. Ropp RC (2013) Encyclopedia of the alkaline earth compounds. Elsevier. ISBN: 9780444595508
18. Oral CM, Ercan B (2018) Influence of pH on morphology, size and polymorph of room temperature synthesized calcium carbonate particles. *Powder Technol* 339:781–788
19. DeJong JT, Fritzges MB, Nusslein K (2006) Microbially induced cementation to control sand response to undrained shear. *J Geotech Geoenvironmental Eng* 132:1381–1392
20. Wang Y, Soga K, Dejong JT, Kabla AJ (2019) Microscale visualization of microbial-induced calcium carbonate precipitation processes. *J Geotech Geoenvironmental Eng* 145(9):04019045
21. Mitchell AC, Ferris FG (2006) The influence of *Bacillus pasteurii* on the nucleation and growth of calcium carbonate. *Geomicrobiol J* 23:213–226
22. El Mountassir R, Lunn RJ, Moir H, MacLachan E (2014) Hydrodynamic coupling in microbially mediated fracture mineralization: formation of self-organized groundwater flow channels. *Water Resour Res* 50
23. Felício F, Silvério V, Duarte SO, Galvão A, Monteiro A, Cardoso S, Cardoso R (2019) Preliminary tests on a microfluidic device to study pore clogging during biocementation. In: Proceedings of 7th international symposium on deformation characteristics of geomaterials (IS-Glasgow2019). Glasgow, UK
24. Dias FC, Borges I, Duarte S, Monteiro G, Cardoso R (2020) Comparison of experimental techniques for biocementation of sands considering homogeneous volume distribution of precipitated calcium carbonate. In: 4th European conference on unsaturated soils, E-UNSAT2020. Lisbon, Portugal, p 05004
25. Cabalar AF, Karabash Z, Erkmen O (2018) Stiffness of a biocemented sand at small strains. *Eur J Environ Civ Eng* 1:54
26. Stabnikov V, Chu J, Naeimi M, Ivanov V (2011) Formation of water-impermeable crust on sand surface using biocement. *Cem Concr Res* 41:1143–1149

27. Gomez M, Martinez M, DeJong JT, de Hunt C, Vlaming L, Major D, Dworatzek S (2015) Field-scale bio-cementation tests to improve sands. *Ground Improv Proc Inst Civ Eng ICE* 168(3):206–216
28. Terzis D, Hicher P, Laloui L (2020) Benefits and drawbacks of applied direct currents for soil improvement via carbonate mineralization. In: 4th European conference on unsaturated soils, E-UNSAT2020. Lisbon, Portugal, p 05007
29. Van Paassen LA (2011) Bio-mediated ground improvement: from laboratory experiment to pilot applications. *Geotech Spec Publ* 41165(211 GSP):4099–4108
30. Cardoso R, Pires I, Duarte SO, Monteiro G (2018) Effects of clay's chemical interactions on biocementation. *Appl Clay Sci* 156:96–103
31. Phillips AJ, Cunningham AB, Gerlach R, Hiebert R, Hwang C, Lomans BP, Spangler L (2016) Fracture sealing with microbially-induced calcium carbonate precipitation: a field study. *Environ Sci Technol* 50(7):4111–4117
32. Tiano P, Cantisani E, Sutherland I, Paget JM (2006) Biomediated reinforcement of weathered calcareous stones. *J Cult Herit* 7:49–55
33. Minto JM, MacLachlan E, Mountassir GE, Lunn RJ (2016) Rock fracture grouting with microbially induced carbonate precipitation. *Water Resour Res* 52(11):8827–8844
34. Arbabzadeh E, Cardoso R (2019) Efficiency of biocementation as rock joints sealing technique evaluated through permeability changes. In: 4th International conference on geotechnical research and engineering (ICGRE'19). Rome, Italy
35. Van Tittelboom K, De Belie N, De Muynck W, Verstraete W (2010) Use of bacteria to repair cracks in concrete. *Cem Concr Res* 40:157–166
36. De Belie N, De Muynck W (2008) Crack repair in concrete using biodeposition. In: Proceedings of ICCRR. Cape Town, South Africa
37. Ramachandran SK, Ramakrishnan V, Bang SS (2001) Remediation of concrete using micro-organisms. *ACI Mater J* 98:3–9
38. Choi SG, Wang K, Wen Z, Chu J (2017) Mortar crack repair using microbial induced calcite precipitation. *J Cem Concr Compos* 83:209–221
39. Mitchell J, Santamarina C (2005) Biological considerations in geotechnical engineering. *J Geotech Geoenvironmental Eng* 131(10):1222–1233
40. Rodriguez-Navarro C, Rodriguez-Gallego M, BenChekroun K, Gonzalez-Munoz MT (2003) Conservation of ornamental stone by *Myxococcus xanthus*-induced carbonate biomineratization. *Appl Environ Microb* 69:2182–2193
41. Sánchez M, Faria P, Ferrara L, Horszczaruk E, Jonkers HM, Kwiecién A, Mosa J, Peled A, Pereira AS, Snoeck D, Stefanidou M, Stryszewska T, Zajac B (2018) External treatments for the preventive repair of existing constructions: a review. *Constr Build Mater* 193:435–452
42. Cheng Y, Feng G, Moraru CI (2019) Micro- and nanotopography sensitive bacterial attachment mechanisms: a review. *Front Microbiol*
43. Kahori H, Bagherpour R (2017) Application of carbonate precipitating bacteria for improving properties and repairing cracks of shotcrete. *J Constr Build Mater* 148:249–260
44. Peng S, Di H, Fan L, Fan W, Qin L (2020) Factors affecting permeability reduction of MICP for fractured rock. *Front Earth Sci* 8:217
45. Wu C, Chu J, Wu S, Guo W (2018) Quantifying the permeability reduction of biogrouted rock fracture. *Rock Mech Rock Eng*
46. Wiktor V, Jonkers HM (2015) Field performance of bacteria-based repair system: pilot study on a parking garage. *Case Stud Constr Mater* 2:11–17
47. Cardoso R, Monteiro A, Flores-Colen I, Monteiro G (2017) Use of biocementation for cracks rehabilitation of different construction materials. In: 3rd International conference on protection of historical constructions (PROHITECH'17). Lisbon, Portugal
48. Ghosh P, Mandal S, Chattopadhyay BD, Pal S (2005) Use of microorganism to improve the strength of cement mortar. *Cem Concr Res* 35(10):1980–1983
49. Jonkers HM, Thijssen A, Muyzer G, Copuroglu O, Schlangen E (2010) Application of bacteria as self-healing agent for the development of sustainable concrete. *Ecol Eng* 36:230–235

50. Bazin P, Saunier JB (1967) Deformability, fatigue and healing properties of asphalt mixes. In: 2nd International conference on the structural design of asphalt pavements, pp 553–569
51. Little DN, Bhasin A (2007) Exploring mechanism of healing in asphalt mixtures and quantifying its impact. In: Self healing materials: an alternative approach to 20 centuries of materials science. Springer Netherlands, Dordrecht, pp 205–218
52. Garcia A, Schlangen E, Van de Ven M (2009) Two ways of closing cracks on asphalt concrete pavements: microcapsules and induction heating. *KEM* 417–418:573–576
53. Xu S, García A, Su J et al (2018) Self-healing asphalt review: from idea to practice. *Adv Mater Interfaces* 5:1800536
54. Sun D, Sun G, Zhu X et al (2018) A comprehensive review on self-healing of asphalt materials: mechanism, model, characterization and enhancement. *Adv Coll Interface Sci* 256:65–93
55. García Á, Schlangen E, van de Ven M, Sierra-Beltrán G (2010) Preparation of capsules containing rejuvenators for their use in asphalt concrete. *J Hazard Mater* 184:603–611
56. Micaelo R, Al-Mansoori T, Garcia A (2016) Study of the mechanical properties and self-healing ability of asphalt mixture containing calcium-alginate capsules. *Constr Build Mater* 123:734–744
57. Liang B, Lan F, Shi K et al (2021) Review on the self-healing of asphalt materials: mechanism, affecting factors, assessments and improvements. *Constr Build Mater* 266:120453
58. Lesueur D (2009) The colloidal structure of bitumen: consequences on the rheology and on the mechanisms of bitumen modification. *Adv Coll Interface Sci* 145:42–82
59. Al-Mansoori T, Norambuena-Contreras J, Micaelo R, Garcia A (2018) Self-healing of asphalt mastic by the action of polymeric capsules containing rejuvenators. *Constr Build Mater* 161:330–339
60. Su J-F, Han S, Wang Y-Y et al (2017) Experimental observation of the self-healing microcapsules containing rejuvenator states in asphalt binder. *Constr Build Mater* 147:533–542
61. Garcia A, Salih S, Gómez-Mejide B (2020) Optimum moment to heal cracks in asphalt roads by means electromagnetic induction. *Constr Build Mater* 238:117627
62. Norambuena-Contreras J, Liu Q, Zhang L et al (2019) Influence of encapsulated sunflower oil on the mechanical and self-healing properties of dense-graded asphalt mixtures. *Mater Struct* 52:78
63. Micaelo R, Freire AC, Pereira G (2020) Asphalt self-healing with encapsulated rejuvenators: effect of calcium-alginate capsules on stiffness, fatigue and rutting properties. *Mater Struct* 53:20
64. Chung K, Lee S, Cho W et al (2018) Rheological analysis of self-healing property of microcapsule-containing asphalt. *J Ind Eng Chem* 64:284–291
65. Ajam H, Gómez-Mejide B, Artamendi I, Garcia A (2018) Mechanical and healing properties of asphalt mixes reinforced with different types of waste and commercial metal particles. *J Clean Prod* 192:138–150
66. BS EN 12697-26 (2004) Bituminous mixtures—test methods for hot mix asphalt—part 26: stiffness. British Standards Institution, London
67. Xu S, Liu X, Tabaković A, Schlangen E (2020) A novel self-healing system: towards a sustainable porous asphalt. *J Clean Prod* 259:120815
68. Al-Mansoori T, Micaelo R, Artamendi I et al (2017) Microcapsules for self-healing of asphalt mixture without compromising mechanical performance. *Constr Build Mater* 155:1091–1100
69. Hunter RN, Shelf A, Read J (2015) The shell bitumen handbook, 6th edn. ICE Publishing, London
70. CRD-C652-95 (1995) Standard test method for measurement of reduction in Marshall stability of bituminous mixtures caused by immersion in water. US Army Corps of Engineers, USA

Chapter 2

Testing Durability on Construction Materials



Carlos Chastre , Paulina Faria , José Neves ,
Marco Ludovico-Marques , Hugo Biscaia , and Lina Nunes

Abstract The durability of construction materials is a key concern and can be related to different actions such as weathering conditions outdoors enhanced by climatic change, chemical and biological attack, abrasion, and other conditions of service over time. Frequently, several actions develop simultaneously, making it difficult to reproduce in situ conditions in laboratory. Furthermore, testing to assess durability depends largely on the nature of the material itself or on the way it has been assembled with other materials. The ageing techniques to assess long-term durability performance of construction materials are based on accelerated durability tests, which include, for example, thermal stress, freeze–thaw cycles, air pressure, salt crystallization, chemical weathering, and ultraviolet radiation. These tests allow the assessment of the materials’ structural integrity, as well as their aesthetics. In this chapter, the main trends on durability tests on construction materials, such as clay-based, cementitious

C. Chastre () · P. Faria

CERIS, Department of Civil Engineering, NOVA School of Science and Technology,
Universidade NOVA de Lisboa, Lisbon, Portugal
e-mail: chastre@fct.unl.pt

P. Faria
e-mail: paulina.faria@fct.unl.pt

J. Neves
CERIS, Department of Civil Engineering, Architecture and Georesources, Instituto Superior
Técnico, Universidade de Lisboa, Lisbon, Portugal
e-mail: jose.manuel.neves@tecnico.ulisboa.pt

M. Ludovico-Marques
INCITE, Escola Superior de Tecnologia do Barreiro, Instituto Politécnico de Setúbal, Setúbal,
Portugal
e-mail: marco.marques@estbarreiro.ips.pt

H. Biscaia
Department of Mechanical and Industrial Engineering, UNIDEMI, NOVA School of Science and
Technology, Universidade NOVA de Lisboa, Lisbon, Portugal
e-mail: hb@fct.unl.pt

L. Nunes
CE3C and Structures Department, National Laboratory for Civil Engineering, Lisbon, Portugal
e-mail: linanunes@lnec.pt

and polymeric composites, natural stone, metals, wood, and bituminous binders and mixtures, will be presented and discussed.

Keywords Biological agents · Bituminous binders and mixtures · Brick · Cementitious composites · Clayish materials · Polymeric composites · Natural stone · Salts · Weathering · Frost · UV radiation · Wood

2.1 Introduction

Durability is defined as “capability of a building or its parts to perform its required function over a specified period of time under the influence of the agents anticipated in service” [1]. The materials’ durability used in buildings and infrastructures is increasingly a key concern. Several degradation forms can be observed in different materials (Fig. 2.1), from different time periods: cultural heritage over 500 years old (Fig. 2.1b), buildings of the last century (Fig. 2.1a, c–e) or of the current century (Fig. 2.1f, g). To prevent these phenomena, a number of strategies have been developed—from the conservation and repair of existing buildings to the durability requirements in new construction products. All these strategies are based on research and development, with the consequent standardization of procedures, tests, and codes, always having in mind the increase of buildings and infrastructures lifespan and the eco-efficiency of its materials. Prior to this analysis, it is necessary to understand the degradation mechanisms, the long-term behaviour of the materials and the connections used in conservation and repair, as well as in new constructions. When construction elements are subjected to different actions, such as the adverse weathering conditions increased by the climatic changes, chemical and biological attacks, abrasion, and other conditions of service over time, their physical, chemical, biological and mechanical performance may be altered.

Ageing techniques to assess the long-term durability performance of building materials are based on accelerated durability tests (ADT), which include, for example, thermal stress, frost weathering, air pressure, water action, salt crystallization, chemical weathering, and ultraviolet (UV) radiation. ADT tests are a fundamental tool, which enables the scientific community and the building materials industry to gain a better understanding of the degradation mechanisms and long-term behaviour of materials and connections, in order to achieve the requirements to ensure the expected lifetime of buildings and infrastructures.

ADT tests accelerate the degradation of materials beyond what is expected in service and allow the assessment of the materials’ structural integrity, as well as their aesthetics. However, in many real cases, several actions develop simultaneously, making it difficult to reproduce *in situ* conditions in the laboratory. Furthermore, testing to assess durability depends largely on the nature of the material itself or on the way it has been assembled with other materials. Test methodologies and equipment have developed as knowledge of the laws of nature (and climate change) has evolved. This means that the requirements for performing ADT tests that have



Fig. 2.1 Degradation forms observed in different materials: **a** render, masonry bedding mortar and brick deterioration; **b** sandstone alveolization; **c** steel corrosion; **d** rammed earth lack of cohesion; **e** timber deterioration; **f** bituminous mixtures cracking; **g** concrete spalling

been satisfactory in the past may no longer be sufficient today or in the near future, what encourages and directs research and development in this area of knowledge [2].

In the current chapter, dedicated to testing durability on construction, after this introduction, some of the most common degradation mechanisms are described, the main durability test standards that apply to these materials are presented, and the equipment traditionally used for accelerated durability tests is shown. These involved the study of timber, earth-based materials, natural stone, mortars and concrete, bituminous binders and mixtures, and bonded connections using FRP composites. In the following chapter, some case studies, in which innovative equipment and test procedures related to the durability of materials and connections were developed, are presented and discussed.

2.2 Mechanisms of Degradation

2.2.1 Wood

Wood is a natural, sustainable, and organic composite characterized by its hygroscopic behaviour, orthotropic constitution, and variable natural durability [3]; it is certainly one of the most rediscovered building materials ever since the early

humans have started to settle and build shelters. The rise of Engineered Wood Products and awareness about sustainable development in recent decades have increasingly expanded the use of timber in construction, either in rehabilitations or new constructions.

However, despite being a traditional material, durability of wooden structures continues to be a challenge. Like other biobased materials, wood can be subject to biological deterioration by fungi and insects. The biological agents, when combined with favourable conditions, can lead to simply aesthetic damage, reduction in indoor air quality, or compromising its resistant load capacity, creating a risk to human health and safety, in addition to an increase of repair and maintenance costs.

Wood, as a natural and hygroscopic material, absorbs or releases moisture according to the ambient conditions, and its durability is intrinsically related to its moisture content (MC). The colonization of fungi on wood requires a series of factors to occur, like moisture content above 20–30%, adequate oxygen source, and favourable temperature/air relative humidity [4]. Meanwhile, subterranean termites form nests in the soil searching for food by building galleries with moist soil and faecal particles and, although they manage to attack timber with low moisture contents, they prefer wood with moisture content above 20% (Fig. 2.2) [5].

2.2.2 Rammed Earth, Cob and Unfired Clay Blocks

Earth has been used as a building material for millennia because it is almost always available. However, it is not a standardized material. Each earth has its own types and contents of clays, silt, sand and coarser aggregates. There are different types of clays but they are highly hygroscopic. Hygroscopicity is beneficial so that earthen products can act as indoor passive moisture buffers. However, it can increase problems of biological development. Due to environmental concerns (low embodied energy, reusability), the use of earth is regaining attention in construction all over the world, and some countries, such as Germany [6], are developing standards to test and label earthen products.

Rammed earth and cob are very common types of monolithic wall building technologies. Rammed earth is made with excavated earth, that is roughly disaggregated, humidified, placed inside formworks in layers, compacted sequentially. Immediately, the formworks can be removed. For cob production an earth mortar is produced with a high content on plant fibres, and portions are placed to form a wall. Each portion can be beaten with a wood stick, and the surfaces of the wall can be regularised by



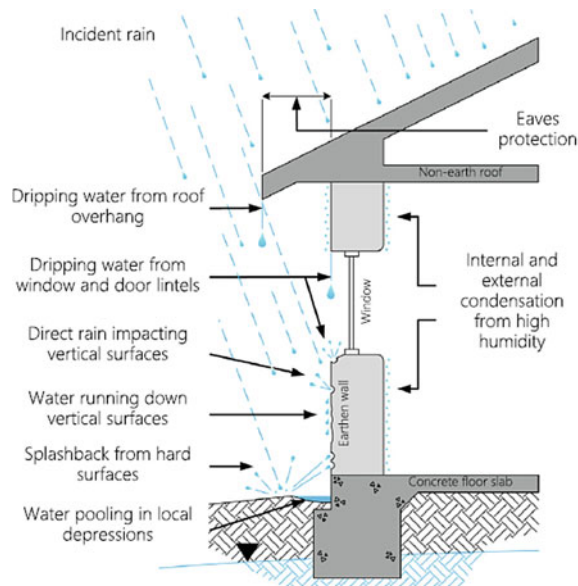
Fig. 2.2 Summary of main wood biodeterioration risk factors

cut. Unfired clay blocks can be made by placing a clayish mortar inside a mould and letting it air-dry (adobe), extruding a clayish paste, cut in blocks and air-dry them (extruded earth blocks, EEB) or placing humidified earth inside a mould that is pressed manually or mechanically (compressed earth blocks, CEB). The clay blocks are used to produce masonries together with a bedding mortar that should have a composition similar to the one of the blocks. The clay is the only material that binds the other aggregates of the earth (silt, sand and, depending on the earth product, coarser particles) on all these (unstabilised) earthen products. Therefore, these products may be highly vulnerable to water (Fig. 2.3). That is why in some cases some low contents of binders, such as lime, or other products, such as natural oils, are added to the earth, or applied on the surface of the earthen products, to increase its durability towards water. When added to the earth mix, the earthen products are designated as stabilised. However, those additions increase the embodied energy of the products, and may constrain reusability and reduce hygroscopicity. Several studies have been made in the last decade to achieve a compromise between the desired performance and expected durability.

2.2.3 Stones

Rocks are mineral-composed porous materials with specific texture, structure, and color. Rock classification encompasses different genesis procedures of this natural material and is based on three main groups: igneous, sedimentary, and metamorphic.

Fig. 2.3 Different possibilities of moisture degradation in a new earth façade [7]



Stones are rock materials extracted from natural outcrops and quarries, cut into blocs, and used as building materials or raw materials for carving-sculptures and other cultural works, being an outstanding testimony of Mankind heritage since Prehistory to nowadays.

Durability of stone building materials depends on weathering evolution and is essentially a physical and mechanical phenomenon, being the water flow inside the pore space the main agent of degradation. Water can be absorbed from underground reservoirs by capillarity, or from rain fall or from deposition of mist liquid droplets on stone surfaces.

Crack and deformation, detachment and features induced by material loss, are the three families of five shown in ICOMOS stone deterioration patterns illustrated glossary [8] with more intrusive effect and influence on stability of structural elements due to fracture and strain damage, and also material loss of cross sections. Salt crystallization-dissolution, freezing–thawing, heating–cooling (thermal shock), wetting–drying, and swelling of clay-minerals in the presence of water, are the main mechanisms responsible for these stone deterioration patterns.

Chlorides, sulphates, nitrates, carbonates, sodium, potassium, and magnesium are the predominant salt ions found worldwide in stone building elements. Alveolization is one of the features induced by material loss with deeper impact due to the extent of cavities and its connections in length and depth, and a close relationship was found between this feature and salts crystallization-dissolution and wind [9, 10].

Discoloration and deposits are the other two patterns that seriously affect more the clarity of contours of facades elements. Acid dissolution of carbonate materials and sulphation of stone surfaces due to industrial pollution are the main mechanisms of chemical weathering that act within the lifetime of the known constructions. Discoloration and deposits like black crusts result from the referred sulphation of stone due to SO_x emissions to atmosphere and its values of layers thickness range between a few micrometers to almost a centimeter. As time goes by, the sulphate layers are removed due to the dissolution and the direct washing out. Stone loss occurs in structural sections, migrating inwards from the surface and revealing a long-lasting effect of decreasing the structural stability. The biological colonization by microbial organisms, algae, fungi and lichens that causes also weathering on thinner outer layers, have also a slow effect of removing deeper structural material. Only the destructive mechanical effect of the roots of higher plants penetrating joints and cracks is faster.

2.2.4 Mortars

Fresh mortars are formulated with (minimum) a binder, an aggregate (such as sand) and water. Other materials can also be added, such as complementary binder or aggregate, additions, namely pozzolans or fibres, and admixtures such as plasticizers that allow to reduce kneading water. Different binders can be used, namely clayish earths, calcium sulphates, such as hemi-hydrated gypsum, construction limes, such

as air limes, natural hydraulic limes or formulated limes, and several different types of cements. The hardening of mortars differs with the type of binder, namely just drying for earth mortars, carbonation for air lime mortars, hydrating for hydraulic binders mortars. Therefore, the minimum age of test differs between mortars: while after drying for earth mortars, generally 28 days for cement mortars, for lime mortars time for carbonation must be ensured before testing. The requirements of mortars depend on the applications, namely defined by the EN 998-1 [11] for several types of renders and plasters and by the EN 998-2 [12] for bedding mortars. Furthermore, masonry mortars are applied intending to increase the walls' durability; therefore, its mechanical-physical properties have to be compatible to the ones of the walls. Working together to protect the walls, frequently the mortars can capture and release moisture and salts coming from those walls. Renders and plasters have different exposures and, therefore, different agents are used to test its durability. Namely, water and abrasion are more common for renders and for joint mortars of unrendered masonry.

2.2.5 *Concrete*

Concrete degradation may have different chemical, physical, or biological causes [13–17]. The chemical degradation of concrete can be caused by sulphate attack, alkali-silica reaction, or other chemical attacks. The sulphates in soil or water can react with the calcium hydroxide of the cement, forming calcium sulphate. This process causes the cement paste to expand and can lead to cracking and deterioration. In turn, certain types of silica present in the aggregates can react with the alkali in cement, producing alkali-silica gel, which is expansive and causes cracking. Concrete can also be damaged by exposure to acidic or alkaline substances, such as industrial waste or cleaning agents. Leaching is another chemical mechanism of degradation, which can occur when water or other liquids containing dissolved substances (such as acids or bases) come into contact with the concrete and dissolve some of its components, such as cement or aggregate. This can weaken the concrete and make it more susceptible to damage.

The chemical degradation mechanisms in case of reinforced concrete include also, the carbonation, and the chloride attack on concrete [13, 14, 18–21]. The carbonation results from the reaction of carbon dioxide from the air with the calcium hydroxide in the concrete, forming calcium carbonate. This process reduces the pH of the concrete and causes it to become more alkaline, which can lead to the generalized corrosion of steel reinforcement bars. The chloride attack on concrete is a form of corrosion that occurs when the chlorides are present in the environment and come into contact with the concrete. This can occur when concrete structures are located near the ocean, or when de-icing salts are used on roads and highways. The chlorides can penetrate the concrete and reach localized parts of the steel reinforcement bars, causing corrosion of the rebar. This can weaken the concrete structure and ultimately lead to its failure.

While bacteria itself does not have a significant effect on concrete, the by-products of certain types of bacteria can be harmful to the concrete. Sulphate-reducing bacteria in untreated sewage can produce hydrogen sulphide, which is then oxidized by aerobic bacteria present in biofilm on the concrete surface to form sulfuric acid. This acid can dissolve the carbonates in the cement and cause a loss of strength in the concrete, as well as producing harmful sulphates. However, nowadays some bacteria are tested to be specifically introduced in concrete for self-healing (see Chap. 5). The growth of plants or other organisms on or within concrete can also contribute to its degradation.

Some common physical causes of concrete degradation include, among others, imposed loads, displacements or deformations, vibration, abrasion, freeze–thaw cycles, fire, thermal expansion and contraction, and shrinkage. Following the concrete production, while curing went on, a slight shrinkage will naturally occur. However, if the concrete is restrained, this shrinkage can cause cracking. Besides, concrete can crack or break if it is subjected to a sudden impact, such as from a falling object or a vehicle collision. If the ground beneath the concrete settles or shifts, it can cause the concrete cracking. Likewise, the surface of concrete can become worn down due to friction or impact. This can be caused by things like foot traffic, vehicle traffic, or the movement of heavy objects on the concrete surface. In turn, when water freezes inside the pores of concrete, it can expand and cause the concrete to crack or spall. This can be a problem in areas with cold winters, as the water can freeze and thaw repeatedly over time. Another physical mechanism can occur with temperature changes, which causes expansion and contraction in concrete, which can lead to cracking. This is more likely to be a problem in fire situations or in areas with extreme temperature fluctuations.

2.2.6 Steel

There are several mechanisms that can cause steel to degrade or weaken over time. These mechanisms include corrosion, stress corrosion cracking, fatigue, wear and tear, and heat damage [22].

Corrosion occurs when the steel is exposed to oxygen and water, leading to the formation of iron oxide. This process can weaken the steel and reduce its strength. Stress corrosion cracking occurs when the steel is subjected to tensile stress and is exposed to an aggressive environment, such as saltwater. Fatigue, or the repeated loading and unloading of the steel, can also cause degradation, as it can lead to cracks forming in the steel, which can eventually cause it to fail. Wear and tear, such as abrasion or impact, can also cause steel to degrade, and exposure to high temperatures for an extended period can weaken or damage the steel.

2.2.7 Bituminous Binders and Mixtures

Bituminous mixtures are traditionally composites essentially made up of aggregates and bitumen. The bitumen is the result of the distillation of crude oil, widely used in road pavements all over the world. Although it is the minority component, the bitumen serves as a binder and plays an essential role in the behaviour of bituminous mixtures. Durability is a global and major concern in relation to road pavements, on account of the alteration of the bituminous mixtures when exposed to the effects of environmental conditions (e.g. oxygen, water, sunlight) and traffic loading. Indeed, most common pavement degradations have to do with durability, such as fatigue cracking and disaggregation. Ageing and moisture damage are the main factors that affect the durability of the bituminous mixtures, assuming that they are adequately designed and constructed. Ageing is primarily a result of the binder and is caused by three factors: volatilisation of the light components during production, transport and placement of the bituminous mixture (short-term ageing, STA); oxidation and steric hardening occurring after the construction throughout the pavement service life (long-term ageing, LTA). The primary effect of ageing is an increase in the binder viscosity and, subsequently, an increase in the stiffness and brittleness of the bituminous mixture, which becomes more prone to cracking and disaggregation [23, 24].

2.2.8 Polymers and FRP Composites

The mechanisms of degradation of polymers and fibre reinforced polymer (FRP) composites are somewhat similar [25–27]. Polymers and FRP composites are susceptible to the degradation due to fire [28], thermal cycles [29, 30], freeze–thaw [31], salt fog [32], UV radiation, microbial attack, moisture [33], chemical attack, stress cracking, wear and tear, impact, fatigue, and creep [34].

Thermal degradation occurs when polymers or FRP composites are exposed to high temperatures, causing them to become brittle and lose their strength. UV radiation can cause the fibres and the polymeric matrix in FRP composites to degrade, leading to a loss of mechanical strength and durability. Microbial attack, or the growth of microorganisms such as bacteria or fungi, can lead to the breakdown of the material. Moisture can penetrate the polymeric matrix of FRP composites, leading to corrosion of the fibres and a loss of mechanical strength. Chemical degradation occurs when polymers are exposed to certain chemicals, such as acids or bases, which can cause them to become brittle and lose their strength. Stress cracking is a form of degradation that occurs when polymers are subjected to tensile stress and are exposed to an aggressive environment, such as oil or gasoline. Wear and tear, such as abrasion or impact, can also cause polymers to degrade. Impact and fatigue can damage the fibres and the polymeric matrix in FRP composites, leading to a loss of strength and durability. Finally, polymers and FRP composites are susceptible to

creep, or deformation under sustained loading, which can lead to a loss of mechanical strength and durability over time.

2.3 Durability Standards

Table 2.1 presents some standards to test durability of some materials and products related to heat, air and pressure, salt crystallization, corrosion, and climatic cycles, while Table 2.2 register the same but related to exposure to laboratory light sources and other actions. Some materials have been previously addressed in Sect. 2.2 while others were not.

In the second column, although the standard is sometimes defined for a specific material, in some cases it can be adapted and also used to test other materials. Some tests are not specific to test durability but can be used to assess performance loss due to artificial aging. That can be the case of NDT mechanical testing, such as dynamic modulus of elasticity or contact angle, performed before and after aging.

Some details are presented below for some materials and products addressed in the Tables 2.1 and 2.2 and for complementary materials.

Timber. Current European normative references address the biological degradation in terms of natural durability, treatability, and exposure conditions during its service life. Natural durability is the natural resistance of a wood species against biological degradation. EN 350 [35] defines classification systems of natural durability for several wood species as well as its treatability. For example, Scots Pine (*Pinus sylvestris L.*), one of the most common wood species in Europe, is classified as moderately/slightly durable against fungi, susceptible of damage due to wood-boring insects, susceptible to termite infestation, easy to treat sapwood, and difficult/extremely difficult to treat heartwood. Meanwhile, EN 335 [36] considers a five-class system, defined as Use classes, to relate the general service life location of the timber element, the exposure to wetting in service, and the occurrence of biologic agents.

Both normative references use the wood relation to water as a parameter to define the guidelines. EN 350 [35] considers that wood species with higher permeability are usually more susceptible to fungal/insects attacks, but, on the other hand, are usually easier to treat. Meanwhile, EN 335 [36] uses the timber element location to define the frequency of exposure to wetting and the occurrence of biological agents. Therefore, many approaches consider moisture content the key to predict the service life of timber structures, along with temperature and air relative humidity. In particular, the wood-water relationships and their role for wood susceptibility to fungal decay has been recently reviewed [37], and the importance of content, state and distribution of moisture in wood was clearly emphasised as key factors for fungal activity.

Table 2.1 Degradation action by heat, air and pressure, salt attack, corrosion, and climatic cycles, applied material or product and standards

Ageing type	Material	Standard
Heat, air and pressure	BB&M	EN 12607-1: 2014. Bitumen and bituminous binders—Determination of the resistance to hardening under influence of heat and air—Part1: RTFOT method
	BB&M	EN 12607-2: 2014. Bitumen and bituminous Binders—Determination of the resistance to hardening under influence of heat and air—Part 2: TFOT method
	BB&M	EN 12607-3: 2014. Bitumen and bituminous binders—Determination of the resistance to hardening under influence of heat and air—Part 3: RFT method
	BB&M	EN 14769: 2012. Bitumen and bituminous binders—Accelerated long-term ageing conditioning by a Pressure Ageing Vessel (PAV)
	BB&M	EN 15323: 2007. Bitumen and bituminous binders—Accelerated long-term ageing/conditioning by the Rotating Cylinder Method (RCAT)
	BB&M	EN 12697-45: 2012. Bituminous mixtures—Test methods for hot mix asphalt—Part 45: Saturation Ageing Tensile Stiffness (SATS) conditioning test
	BB&M	CEN/TS 12697-52: 2017. Bituminous mixtures—Test methods—Part 52: Conditioning to address oxidative ageing
Salt Attack	S, M	EN 12370: 2020. Natural stone test methods. Determination of resistance to salt crystallization
	S, M	EN 14147: 2003. Natural stone test methods. Determination of resistance to ageing by salt mist
	S	ASTM C88/C88M-18. Standard test method for soundness of aggregates by use of sodium sulfate or magnesium sulfate
	S, M	ASTM D5240/D5240M-20. Standard test method for evaluation of the durability of rock for erosion control using sodium sulfate or magnesium sulfate

(continued)

Table 2.1 (continued)

Ageing type	Material	Standard
	S, M	RILEM. Recommended tests to measure the deterioration of stone and to assess the effectiveness of treatment methods. Test V.1a—crystallization test by total immersion (for untreated stone); Test V.1b—crystallization test by total immersion (for treated stone); Test V.2—crystallization test by partial immersion. Test V.3—Frost resistance. Materials and Structures, 13(75), 175–253 (1980)
Corrosion	M&C	ASTM G85-19. Standard practice for modified salt spray (Fog) testing
	M&C	ISO 9227: 2017. Corrosion tests in artificial atmospheres—Salt spray tests
Climatic Cycles	M	EN 1015-21: 2002. Methods of test for mortar for masonry—Part 21: Determination of the compatibility of one-coat rendering mortars with substrates
	S, M	EN 12371: 2010. Natural stone test methods. Determination of frost resistance
	S, M	ASTM D5312/D5312M—12. Standard test method for evaluation of durability of rock for erosion control under freezing and thawing conditions
	C	ASTM C666/C666M-15. Standard Test Method for Resistance of Concrete to Rapid Freezing and Thawing
	S, M	EN 14066: 2013. Natural stone test methods. Determination of resistance to ageing by thermal shock
	S	EN 16140: 2019. Natural stone test methods. Determination of sensitivity to changes in appearance produced by thermal cycles
	S	EN 16306: 2013. Natural stone test methods. Determination of resistance of marble to thermal and moisture cycles
	S, M	ASTM D5313/D5313M—12. Standard test method for evaluation of durability of rock for erosion control under wetting and drying conditions
	S, M	EN 13755: 2008. Natural stone test methods. Determination of water absorption at atmospheric pressure

(continued)

Table 2.1 (continued)

Ageing type	Material	Standard
Exposure to laboratory light sources	S, M	EN 13919: 2002. Natural stone test methods. Determination of resistance to ageing by SO ₂ action in the presence of humidity
	P	ASTM G154—16. Standard practice for operating fluorescent ultraviolet (UV) lamp apparatus for exposure of nonmetallic materials
	P	ISO 4892–1: 2016. Plastics—Methods of exposure to laboratory light sources—Part 1: General guidance
	P	ISO 4892–2: 2013. Plastics—Methods of exposure to laboratory light sources—Part 2: Xenon-arc lamps
	P	ISO 4892–3: 2016. Plastics—Methods of exposure to laboratory light sources—Part 3: Fluorescent UV lamps
Other	P	ISO 4892–4: 2013. Plastics—Methods of exposure to laboratory light sources—Part 4: Open-flame carbon-arc lamps
	M, E	DIN 18947: 2018. Earth plasters—Requirements, test and labelling (in German)
	M, E	EN 15801: 2009. Conservation of cultural property. Test methods. Determination of water absorption by capillarity.
	E, M, S	EN 15802: 2009. Conservation of cultural property. Test methods. Determination of static contact angle. CEN, Brussels
	M	EN 15803: 2009. Conservation of cultural property—Test methods—Determination of water vapour permeability
	M, E	EN 16302: 2013. Conservation of cultural heritage. Test methods. Measurement of water absorption by pipe method
	M, E	EN 16322: 2013. Conservation of cultural heritage. Test methods. Determination of drying properties
	E	DIN 18945: 2018. Earth blocks—Requirements, test and labelling (in German)
	E	HB 195: 2002. The Australian Earth Building Handbook

(continued)

Table 2.1 (continued)

Ageing type	Material	Standard
	E	XP P13-901: 2001. Blocs de terre comprimée pour murs et cloisons: definitions—Spécifications—Méthodes d'essais—Conditions de réception (in French)
	E	NZS 4298: 1998. Materials and workmanship for earth buildings
	E	UNE 41410: 2008. Compressed earth blocs for walls and partitions. Definitions, specifications and test methods (in Spanish)
	S, M	EN 14157: 2017. Natural stone test methods. Determination of the abrasion resistance
	S, M	EN 14146: 2004. Natural stone test methods—Determination of the dynamic modulus of elasticity (by measuring the fundamental resonance frequency)
	S, M	EN 16301: 2013. Natural stone test methods. Determination of sensitivity to accidental staining

Note BB&M—Bituminous binders and mixtures; C—Concrete; M—Mortars; M&C—Metals and Coatings; S—Natural Stone

Table 2.2 Degradation action by exposure to light and others, applied material or product and standards

Action	Material	Standard
Exposure to laboratory light sources	P	ASTM G154-16. Standard practice for operating fluorescent ultraviolet (UV) lamp apparatus for exposure of nonmetallic materials
	P	ISO 4892-1: 2016. Plastics—Methods of exposure to laboratory light sources—Part 1: General guidance
	P	ISO 4892-2: 2013. Plastics—Methods of exposure to laboratory light sources -Part 2: Xenon-arc lamps
	P	ISO 4892-3. Plastics—Methods of exposure to laboratory light sources- Part 3: Fluorescent UV lamps
	P	ISO 4892-4. Plastics—Methods of exposure to laboratory light sources- Part 4: Open-flame carbon-arc lamps

(continued)

Table 2.2 (continued)

Action	Material	Standard
Other	M, E	DIN 18947: 2018. Earth plasters—Requirements, test and labelling (in German)
	S, M	EN 13755: 2008. Natural stone test methods. Determination of water absorption at atmospheric pressure
	M, E	EN 15801: 2009. Conservation of cultural property. Test methods. Determination of water absorption by capillarity
	E, M, S	EN 15802: 2009. Conservation of cultural property. Test methods. Determination of static contact angle
	M	EN 15803: 2009. Conservation of cultural property—Test methods—Determination of water vapour permeability
	M, E	EN 16302: 2013. Conservation of cultural heritage. Test methods. Measurement of water absorption by pipe method
	M, E	EN 16322: 2013. Conservation of cultural heritage. Test methods. Determination of drying properties
	E	DIN 18945: 2018. Earth blocks—Requirements, test and labelling (in German)
	E	HB 195: 2002. The Australian Earth Building Handbook
	E	XP P13-901: 2001. Blocs de terre comprimée pour murs et cloisons: définitions—Spécifications—Méthodes d'essais—Conditions de réception (in French, being revised)
	E	NZS 4298: 1998. Materials and workmanship for earth buildings
	E	UNE 41410: 2008. Compressed earth blocs for walls and partitions. Definitions, specifications and test methods (in Spanish)
S, M	S, M	EN 14157: 2017. Natural stone test methods. Determination of the abrasion resistance
	S, M	EN 14146: 2004. Natural stone test methods—Determination of the dynamic modulus of elasticity (by measuring the fundamental resonance frequency)
	S, M	EN 16301: 2013. Natural stone test methods. Determination of sensitivity to accidental staining

Note M—Mortars; P—Plastics; E—Earth products; S—Natural Stone

Rammed earth, cob and unfired clay blocks masonry. In an area where not much international standards exist, a high effort is being made to standardize how to test durability of earth building products [38]. These products have moderate to low strength and tests are performed to assess if durability to dry abrasion and to abrasion by water spray or water dropping is adequate. Immersion in water before abrasion is unviable for unstabilised earth products, what is clearly a limitation. In fact, earthen products durability mainly depends on resistance to water, although other actions, such as imposed by insects and animals, chemical and thermal may also impact its longevity [7]. Water has a major impact on the durability of earthen wall products since even the strength of earthen buildings is related to their moisture content, and also to drying shrinkage. Therefore, mechanical tests are performed with the earth products at different moisture conditions, to assess its performance when in humid environments and, indirectly, its durability. Furthermore, water can induce high damage not only when it rises from the ground in old walls that have no capillary barrier, but also when the earth walls have a water vapor barrier (namely by a low water vapor permeable render or finishing system) and moisture cannot evaporate, and mainly when it is not protected from the direct action of rainwater. Lack of durability due to rainwater can occur by flood, rainfall-induced erosion and water absorption. Therefore, research studies have been developed on how to assess earth products durability, but few standardised tests exist so far.

For chemically stabilised earth products, test procedures similar to conventional materials can be performed; but that is not the case for unstabilised earth products. From the less to the most aggressive direct tests for earth products, the following can be referred: abrasion by dry brushing, based on the French standard XP P13-901 presented in Table 2.2; water absorption by contact and gravity, based on the German DIN 18945 addressed in Table 2.2, illustrated by Muguda et al. [39]; capillary water absorption, based on the EN 15801 (please see Table 2.2), although for unstabilised earth materials it is advisable to use a net basket with a cloth on the base to support and weight the samples. Capillary rise and absorption by gravity can also be assessed visually and by the damage resulting in earth samples [40]. A very specific test for earth products is the Geelong test simulating water drip addressed on the New Zealand code NZS 4298 (Table 2.2), where the type of sample, angle of impact and eroded depths can also be measured at shorter intervals and not only after 60 min, and the erodibility index is assessed as defined in the Spanish standard UNE 41410 (Table 2.2). Another is the dip test defined by the DIN 18945 (Table 2.2), that assesses the resistance of unstabilised earthen products to damage (loss of mass) whilst suspended and partially immersed in water (10 cm for 10 min), simulating a flood; it can also be applied with several adaptations [38].

Apart from indirect and direct tests to assess earth products durability, namely by accelerate weathering, there are also tests to assess durability by natural weathering exposure. However, these tests are only representative by comparison between earth products exposed during the same period and in the same conditions because climatic conditions are not reproducible, and to follow the effect of weathering with time.

Stones. Stone weathering can be assessed by means of mineralogical properties, physical and mechanical behaviour. The former is associated with parameters of absorption, movement of water inside the pores/empty space and drying. The latter depends on stress (compression and tension)-strain parameters and related ultrasonic pulse velocities. The determination of resistance of stone to ageing by artificial accelerated cycles of: salt, mainly sulphates but also chlorides, is carried out according to RILEM (1980), EN 14147, ASTM C88/C88M-18, EN 12370, ASTM D5240/D5240M –20; freezing–thawing is performed following the EN 12371 and ASTM D5312/D5312M–12; for thermal shock by heating–cooling, the procedures are in EN 14066, EN 16306 and EN 16140; wetting–drying is carried out following ASTM D5313/D5313M–12; SO₂ in the presence of humidity as reported in EN 13919. Regarding abrasion resistance of indoor flooring the EN, 14157 and EN 16301 can be used, the latter also when considering aesthetical aspects. All the previous standards and test specifications are defined in Tables 2.1 and 2.2.

Mortars. Being artificial stones, some durability testing for mortars is similar to stone; being similar to the matrix of a concrete, some testing is similar to concrete. Depending on the mortar application, specific durability tests can be performed, namely direct tests such as resistance to abrasion based on the German standard for earth plasters DIN 18947 (Table 2.2) and specific for renders performed after accelerated cycles defined by the EN 1015–21 (Table 2.1), to assess the effect as vapour barrier according to the EN 15803 and EN 16322 (Table 2.2), and outdoor tests performed in situ before and after natural weathering exposure, such as the water absorption under low pressure following the EN 16302 (Table 2.2), the ultrasonic pulse velocity and the resistance by pendular sclerometer, the impact test, the surface cohesion [41].

Bituminous binders and mixtures. Ageing has a major impact on the durability of bituminous binders and mixtures. The ageing process can be simulated in the laboratory through accelerated processes carried out on the bituminous binder or on the bituminous mixture (loose mixture or compacted samples). Before and after each ageing simulation, samples should be tested to quantify the changes to the properties of the bituminous binders and mixtures. Some of the appropriate and common test methods for this purpose are viscosity, penetration, softening point, weight loss, stiffness, and tensile strength. An ageing index is commonly used to analyse the effect of the ageing on the material. Normally, the lower the ageing index, the less the extent of ageing. Table 2.1 presents the current standard tests for the accelerated ageing of bituminous binders and mixtures (BB&M), mostly based on heating of the specimens. To simulate the ageing of the bituminous binder the most used standard tests are: the rolling thin film oven test (RTFOT, EN 12607-1, Table 2.1); thin film oven test (TFOT, EN 12607-2, Table 2.1); rotating flask test (RFT, EN 12607-3, Table 2.1); pressure ageing vessel test (PAV, EN 14769, Table 2.1); and rotating cylinder ageing test (RCAT, EN 15323, Table 2.1). In the case of bituminous mixtures, the following standard tests are used: short-term oven ageing (STOA) and long-term oven ageing (LTOA) (AASHTO R 30, Table 2.1); saturation ageing tensile stiffness (SATS, EN 12697-45, Table 2.1); and conditioning to address

oxidative ageing (CEN/TS 12697-52, Table 2.1). The test methods can be used on specimens from laboratory production or samples taken from the field. Other test methods can be indirectly related to durability, such as water sensitivity (EN 12697-12 [42]), retained Marshall stability (MIL-STD-620A [43]), and moisture-induced damage (AASHTO T283 [44]). The focus of this chapter in relation to bituminous binders and mixtures is solely on ageing simulation.

The RTFOT and PAV are the most common and consensual tests for assessing the STA and the LTA, respectively, of bituminous binders. In the RTFOT the EN 12607-1 (Table 2.1), a thin film of binder is conditioned for 75 min at 163 °C inside a heat-resistant glass container permanently rotating in a circular metal carriage with blown heated air pressure in a special oven. The PAV test, defined by the EN 14769 (Table 2.1), is considered the most reliable LTA method. It consists of a preliminary pre-hardening of the bituminous binder (RTFOT or TFOT), followed by the exposure of a static film to pressurised air at selected temperatures between 8 and 115 °C, during a given period to simulate the changes occurring to the bituminous binder within a pavement in service. Regarding the ageing of bituminous mixtures, the STOA and LTOA tests, following the AASHTO R 30 (Table 2.1) are the most frequently used: the STOA defines the conditioning oven of loose bituminous mixtures for 4 h at 135 °C before compaction; the LTOA establishes the conditioning of compacted bituminous mixtures in the conditioning oven for 5 days at 85 °C. The STOA is regarded as adequately simulating the STA, on account of the plant mixing and compaction. The LTOA is designed to simulate the LTA for approximately 7–10 years of a pavement's service life.

In recent years, advanced research has been conducted in bituminous binders and mixtures to improve ageing methods, overcoming certain limitations identified in the traditional tests, such as the modified rolling thin film oven test (RTFOTM), modified German rotating flask (MGRF), and stirred air flow test (SAFT). The NCHRP Project number 9–36 [45], which was developed in USA to replace RTFOT and PAV tests, concluded that MGRF could be an alternative to the RTFOT for neat and modified bituminous binders. Most recently in EU, new tests have been proposed for bituminous mixtures such as saturation ageing tensile stiffness according to the EN 12697-45 (Table 2.1) and oxidative ageing following the CEN/TS 12697-52 (Table 2.1). The latter consists of two sets of conditioning methods: one for loose bituminous mixtures, for 20 h at 90 °C (similar to the PAV test); and the other for compacted specimens, using a forced flow of oxidant gas for 168 h at 65 °C [46].

2.4 Traditional Equipment for Accelerated Durability Tests

The equipment available on the lab allows accelerated ageing tests to be carried out to reproduce in a few weeks the damage that occurs over many years, namely outdoors. Figure 2.4 shows some of that equipment at Durability Lab (DEC Labs) of Universidade NOVA de Lisboa. This equipment has traditionally been used in accelerated ageing tests of various materials, such as stone, wood, mortar, concrete,

steel, polymers and composite materials, or to study the behaviour of structural connections made with these materials (Fig. 2.4).

From this equipment, the following stand out: (i) climatic chambers with variation in air temperature and relative humidity (Fig. 2.4a) which allow the analysis of the thermodynamic behaviour of materials, composites and connections; using the simulation of different climatic conditions it is possible to evaluate the performance of a given material or bond during its lifetime; (ii) carbonation test chamber (Fig. 2.4b) which allows accelerated carbonation tests of materials under different conditions; (iii) Xenon Arc test chamber (Fig. 2.4c) where it is possible to reproduce the damage caused by the full spectrum of sunlight and rain; (iv) freeze–thaw test chamber (Fig. 2.4d) to analyse the durability to freeze–thaw cycles; (v) cyclic corrosion chamber (Fig. 2.4e) to simulate the same type of environmental changes that occurs in nature and causes the corrosion of metallic materials; this test is distinguished from the salt fog test, by combining periods of salt fog with drying periods and periods of controlled temperature and humidity, during an ageing cycle; (vi) SO₂



Fig. 2.4 Test chambers for accelerated durability tests: **a** Climatic; **b** Carbonation; **c** Xenon Arc; **d** Freeze–Thaw; **e** Corrosion; **f** SO₂ corrosion; **g** Salt fog

test chamber (Fig. 2.4f) that allows simulation tests of the acidic atmosphere; and vii) salt fog test chamber (Fig. 2.4g) which is normally used to verify the degradation of properties of materials and surface coatings or the degradation of structural connections due to salt fog.

2.5 Final Remarks

In this chapter, the typical degradation mechanisms of different construction materials, such as timber, earth-based wall materials, stone, mortars, concrete, steel, bituminous binders, and mixtures, as well as FRP composites were presented. Several standards and test procedures to assess durability of some of these materials were specified, as well as the traditional equipment used for accelerated durability tests.

One of the main focuses of the durability of timber is moisture, as this is the cause of several degradation, namely by ensuring conditions for the development of biological colonisation and damage.

The focus of the durability of earth-based products is the action of water. That is the reason why in some cases earth-based materials are stabilised, namely by additions of low contents of binders, or the surface protected. Therefore, apart from testing durability, for these building products it is mandatory to design and built earthen monolithic and masonry walls in a way to ensure protection from water from the ground, floods, and direct action of rain.

Stone durability, regarding natural and artificial ageing, depends mainly on the movement of water and salts in the pores/empty space, surface deposition also considering pollutants, wetting and drying, heating and cooling processes, biological colonization and their effects on mineralogical, physical and mechanical properties of sound building stones in cultural heritage.

As mortars can have many different types of applications, the specific requirements they should have to ensure durability, and the test procedures to follow, depend largely on the application foreseen. Furthermore, as mortars are applied in direct contact with a substrate they are supposed to protect, the durability of the system substrate-mortar is often more important than the durability of the mortar itself.

The physical, chemical, or biological mechanisms of concrete degradation are potentiated by other factors that can contribute to this degradation, such as the poor-design or construction, the poor-quality of materials, the lack of maintenance, the age of the structure or the extreme environmental conditions. Thus, it is important to consider all these factors when designing, constructing, and maintaining concrete structures to ensure their long-term performance and durability.

Corrosion, stress corrosion cracking, fatigue, wear and tear, and heat damage are some of the mechanisms that can affect steel. Some mainly depend on the exposure while others on the manufacture for application. Therefore, it is essential to consider specificities when conducting durability tests.

Polymers and FRP composites are primarily affected by thermal cycles, freeze-thaw, salt fog, UV radiation, moisture and microbial attack, chemical attack, stress

cracking, wear and tear, impact, fatigue, and creep. Depending on the application that polymers and FRP composites will have on site, several different tests can be performed to assess their durability.

The focus of the durability of bituminous binders and mixtures is ageing. This phenomenon is due mainly to oxidation and volatilization of the bituminous binder. It greatly impacts the properties of bituminous mixtures during the in-service life, mainly on cracking and rutting resistances. The durability becomes more critical when using non-traditional materials. One of the main challenges on accelerated laboratory tests is to simulate the ageing of bituminous mixtures directly related to the local application's environmental conditions: moisture and solar radiation.

Acknowledgements The authors would like to acknowledge the support of FCT for the partial funding of this work under the strategic projects UIDB/04625/2020 and UIDB/EMS/00667/2020 respectively from the research units CERIS and UNIDEMI.

References

1. ISO 15686-1:2011 (2011) Buildings and constructed assets—service life planning—Part 1: General principles and framework. ISO
2. Klyatis LM (2012) Accelerated reliability and durability testing technology, vol 70. Wiley, New Jersey
3. Verbiest M, Nunes L, Jones D, Branco J (2019) Service life design of timber structures. In: Ghiasi B, Lourenço PB (eds) Long-term performance and durability of masonry structures: degradation mechanisms, health monitoring and service life design. Woodhead Publishing Series in Civil and Structural Engineering, pp 311–336
4. Jeffree M (2019) Wood—Building the bioeconomy. The European Confederation of Woodworking Industries, Brussels, Belgium
5. Cruz H, Jones D, Nunes L (2015) Chapter 12-Wood. Materials for construction and civil engineering. Science, Processing and Design. Springer, Switzerland, pp 557–583
6. Ziegert C, Röhlen U, Schroeder H (2020) The success story of earth building standards in Germany. In: LEHM2020—international conference on building with earth. Dachverband Lehm e. V., Weimar, Germany
7. Beckett CTS, Jaquin PA, Morel JC (2020) Weathering the storm: a framework to assess the resistance of earthen structures to water damage. Constr Build Mater 242. <https://doi.org/10.1016/j.conbuildmat.2020.118098>
8. Delgado Rodrigues J, João Revez M (2016) ICOMOS international scientific committee for stone ICOMOS-ISCS: illustrated glossary on stone deterioration patterns=Glossário ilustrado das formas de deterioração da pedra. In: Vergès-Belmin V (ed) Monuments & Sites vol XV. Paris
9. Ludovico-Marques, M., Chastre, C.: Effect of Artificial Accelerated Salt Weathering on Physical and Mechanical Behavior of Sandstone Samples from Surface Reservoirs. In: Makhlouf, A.S.H., Aliofkhazraei, M. (eds.) Handbook of Materials Failure Analysis With Case Studies from the Oil and Gas Industry. pp. 215–233. Butterworth Heinemann - Elsevier, (2016)
10. Ludovico-Marques M, Chastre C (2012) Effect of salt crystallization ageing on the compressive behavior of sandstone blocks in historical buildings. Eng Fail Anal 26:247–257. <https://doi.org/10.1016/j.engfailanal.2012.08.001>
11. EN 998-1:2016 (2016) Specification for mortar for masonry-Part 1: rendering and plastering mortar. In: CEN, European Standardisation Institute, Brussels, Belgium

12. EN 998-2:2016 (2016) Specification for mortar for masonry-Part 2: masonry mortar. In: CEN, European Standardisation Institute, Brussels, Belgium
13. Dyer T (2014) Concrete durability. CRC Press
14. Soutsos M (ed) Concrete durability: a practical guide to the design of durable concrete structures. Thomas Telford Ltd
15. Miron LERD, Koleva DA (2017) Concrete durability: cementitious materials and reinforced concrete properties, behavior and corrosion resistance. Springer
16. Hellmich C, Pichler B, Kollegger J (eds) CONCREEP 10: mechanics and physics of creep, shrinkage, and durability of concrete and concrete structures. ASCE
17. Tanabe T-A, Sakata K, Mihashi H, Sato R, Maekawa K, Nakamura H (eds) (2008) Creep, shrinkage and durability mechanics of concrete and concrete structures, two volume set: proceedings of the CONCREEP 8 conference held in Ise-Shima, Japan, 30 Sept–2 Oct 2008. CRC Press
18. Sarja A, Vesikari E (eds) (1996) Durability design of concrete structures, RILEM TC130-CSL report. E & FN Spon, Chapman & Hall, UK
19. Andrade C, Gulikers J, Polder R (2016) Durability of reinforced concrete from composition to protection. Springer
20. Alexander M (ed) (2016) Marine concrete structures: design, durability and performance. Woodhead Publishing
21. Andrade C, Gulikers J, Marie-Victoire E (eds) (2018) Service life and durability of reinforced concrete structures. Springer
22. Uhlig HH, Revie RW (1985) Corrosion and corrosion control, 3rd edn. John Wiley and Sons Inc., New York, NY, United States
23. Airey GD (2003) State of the art report on ageing test methods for bituminous pavement materials. Int J Pavement Eng 4(3):165–176. <https://doi.org/10.1080/1029843042000198568>
24. Sirin O, Paul DK, Kassem E (2018) State of the art study on aging of asphalt mixtures and use of antioxidant additives. Adv Civil Eng 2018:3428961. <https://doi.org/10.1155/2018/3428961>
25. Davies P, Rajapakse YD (eds) (2018) Durability of composites in a marine environment 2. Springer
26. Miyano Y, Nakada M (2018) Durability of fiber-reinforced polymers. Wiley Online Library
27. Reifsnider KL (ed) Durability of composite systems. Woodhead Publishing
28. Azevedo AS, Firma JP, Correia JR, Chastre C, Biscaia H, Franco N (2022) Fire behaviour of CFRP-strengthened RC slabs using different techniques—EBR, NSM and CREatE. Compos B Eng 230:109471. <https://doi.org/10.1016/j.compositesb.2021.109471>
29. Biscaia HC, Silva MAG, Chastre C (2016) Influence of external compressive stresses on the performance of GFRP-to-concrete interfaces subjected to aggressive environments: an experimental analysis. J Compos Constr 20(2):04015044. [https://doi.org/10.1061/\(ASCE\)CC.1943-5614.0000600](https://doi.org/10.1061/(ASCE)CC.1943-5614.0000600)
30. Gigliotti M, Lafarie-Frenot M-C, Grandidier J-C, Minervino M (2017) Mechanical behavior of organic matrix composites: effect of thermo-oxidative ageing. John Wiley & Sons
31. Yang Y, Silva MAG, Biscaia H, Chastre C (2019) Bond durability of CFRP laminates-to-steel joints subjected to freeze-thaw. Compos Struct 212:243–258. <https://doi.org/10.1016/j.compstruct.2019.01.016>
32. Yang Y, Biscaia H, Silva MAG, Chastre C (2019) Monotonic and quasi-static cyclic bond response of CFRP-to-steel joints after salt fog exposure. Compos B Eng 168:532–549. <https://doi.org/10.1016/j.compositesb.2019.03.066>
33. Biscaia HC, Silva MAG, Chastre C (2014) An experimental study of GFRP-to-concrete interfaces submitted to humidity cycles. Compos Struct 110:354–368. <https://doi.org/10.1016/j.compstruct.2013.12.014>
34. Possart W, Brede M (2019) Adhesive joints: ageing and durability of epoxies and polyurethanes. John Wiley & Sons
35. EN 350:2016 (2016) Durability of wood and wood-based products. Testing and classification of the durability to biological agents of wood and wood-based materials. CEN, European Standardisation Institute, Brussels, Belgium

36. EN 335:2013 (2013) Durability of wood and wood-based products-use classes: definitions, application to solid wood and wood-based products. CEN, European Standardisation Institute, Brussels, Belgium
37. Brischke C, Alfredsen G (2020) Wood-water relationships and their role for wood susceptibility to fungal decay. *Appl Microbiol Biotechnol* 104(9):3781–3795. <https://doi.org/10.1007/s00253-020-10479-1>
38. Medvey B, Dobiszay G (2020) Durability of stabilized earthen constructions: a review. *Geotech Geol Eng* 38(3):2403–2425. <https://doi.org/10.1007/s10706-020-01208-6>
39. Muguda S, Lucas G, Hughes PN, Augarde CE, Perlot C, Bruno AW, Gallipoli D (2020) Durability and hygroscopic behaviour of biopolymer stabilised earthen construction materials. *Constr Build Mater* 259:119725. <https://doi.org/10.1016/j.conbuildmat.2020.119725>
40. Gomes MI, Faria P, Gonçalves TD (2020) Rammed earth walls repair by earth-based mortars: the adequacy to assess effectiveness. *Constr Build Mater* 205:213–231. <https://doi.org/10.1016/j.conbuildmat.2019.01.222>
41. Santos T, Faria P, Silva V (2019) Can an earth plaster be efficient when applied on different masonries? *J Build Eng* 23:314–323. <https://doi.org/10.1016/j.jobe.2019.02.011>
42. EN 12697-12:2018 (2018) Bituminous mixtures. Test methods. Determination of the water sensitivity of bituminous mixtures. CEN, European Standardisation Institute, Brussels, Belgium
43. MIL-STD-620A (1966) Military standard. Test methods for bituminous paving materials. Method 104. Measurement of reduction in Marshall stability of bituminous pavements caused by immersion in water. Department of defense
44. AASHTO T283 (2022) Standard method of test for resistance of compacted asphalt mixtures to moisture-induced damage. AASHTO, American Association of State Highway and Transportation Officials, Washington, D.C., USA
45. Anderson DA, Bonaquist R (2011) Investigation of short-term laboratory aging of neat and modified asphalt binders. NCHRP Report 709, Transportation Research Board, The National Academies Press, Washington, DC
46. Steiner D, Hofko B, Hospodka M, Handle F, Grothe H, Füssl J, Eberhardsteiner L, Blab R (2016) Towards an optimised lab procedure for long-term oxidative ageing of asphalt mix specimen. *Int J Pavement Eng* 17(6):471–477. <https://doi.org/10.1080/10298436.2014.993204>

Chapter 3

Innovative Durability Tests on Construction Materials



Carlos Chastre , Paulina Faria , José Neves ,
Marco Ludovico-Marques , Hugo Biscaia , and Lina Nunes

Abstract Innovation in structures and construction materials demands a more accurate performance analysis during the life cycle. In addition, climatic changes pose new challenges to civil infrastructures that were not so relevant in the past. In most cases, the traditional test methods cannot accurately assess the complex phenomena involved in durability. The modern and complex factors require a different approach to durability analysis. The purpose of this chapter is to present innovative durability tests on construction materials: wood; rammed earth, cob and unfired blocks; natural stone; bituminous binders and mixtures; and Fibre Reinforced Polymers (FRP) to concrete bonded connections. Most of these tests concern the accelerated simulation of the main phenomena involved in durability performance – ageing – of the materials and structures, such as wet-dry cycles, UV exposure, salt water immersion, salt fog cycles, and action of biological agents. The demonstration and validation of the new

C. Chastre () · P. Faria

CERIS, Department of Civil Engineering, NOVA School of Science and Technology,
Universidade NOVA de Lisboa, Lisbon, Portugal
e-mail: chastre@fct.unl.pt

P. Faria
e-mail: paulina.faria@fct.unl.pt

J. Neves
CERIS, Department of Civil Engineering, Architecture and Georesources, Instituto Superior
Técnico, Universidade de Lisboa, Lisbon, Portugal
e-mail: jose.manuel.neves@tecnico.ulisboa.pt

M. Ludovico-Marques
INCITE, Escola Superior de Tecnologia do Barreiro, Instituto Politécnico de Setúbal, Setúbal,
Portugal
e-mail: ludovicomarques@gmail.com

H. Biscaia
Department of Mechanical and Industrial Engineering, UNIDEMI, NOVA School of Science and
Technology, Universidade NOVA de Lisboa, Lisbon, Portugal
e-mail: hb@fct.unl.pt

L. Nunes
CE3C and Structures Department, National Laboratory for Civil Engineering, Lisbon, Portugal
e-mail: linanunes@lnec.pt

durability test methods on construction materials are supported by the description of some case studies based on experimental research.

Keywords Ageing techniques · Accelerated durability tests · Construction materials · Durability · Innovation · Performance

3.1 Introduction

The previous chapter addressed the typical degradation mechanisms of different construction materials, such as timber, rammed earth and unfired clay blocks, stone, mortars, concrete, steel, bituminous binders and mixtures, as well as Fibre Reinforced Polymers (FRP). The main durability standards applicable to these materials were mentioned, as well as the traditional equipment for accelerated durability tests.

In this chapter, some case studies related to innovative durability tests on construction materials are presented. The case studies start with a study related to wood moisture content and monitoring systems, followed by a case study that shows the influence of pressure and distance on spray testing for rammed earth constructions. The next case study addresses the assessment of natural stone durability through an innovative salt ageing cyclic test developed for this purpose. A piece of accelerated test equipment developed to test compacted specimens of bituminous mixtures is the following case presented. This equipment allows the application of UV radiation and drying-wetting cycles to the test specimens during a certain period, to simulate an equivalent ageing process in the field. Finally, with the last case study, the results of some experimental tests performed with a double shear test equipment developed to assess FRP to concrete bonded connections are shown.

3.2 Wood Moisture Content and Monitoring Systems

The moisture content has impacts on most of the physical and mechanical properties of wood, mainly through conditioning dimensional changes, the development of cracks, fungal decay, and insect attacks [1]. It is usually expressed as a function of the material's dry mass (the water mass as a percentage of dry wood mass) and can be measured by direct or indirect methods. The direct method, according to EN 13183-1 [2], is based on gravimetric measurements before and after oven-drying, and it is the most used in laboratory tests. Within the indirect methods, a full range of techniques to estimate the moisture content, from dry to fully water-saturated wood, have been described e.g. [3, 4], including electrical resistance, capacitance, microwave, and spectrometry, among other methods. Although less accurate, indirect methods are usually preferred for measurements in situ, mainly due to their practicality and non-destructive assessment.

The hygroscopic behaviour of wood allows for the estimation of overall moisture content values, associating hygrometric equilibrium curves, temperature, and air relative humidity data [4]. According to Svensson et al. [5], the variation of the moisture content can be characterized by four parameters: Equilibrium Moisture Content (EMC), MC amplitude (A), MC penetration (IMC), and MC gradient (∇ MC). However, the existence of individual zones with an accumulation of moisture within the timber element, resulting in local deterioration, brings the necessity of complete methods to continuously monitor the moisture content.

To control biological deterioration, continuous monitoring, associated with maintenance, can be an alternative to chemical treatments, increasingly limited due to current environmental legislation [6, 7]. One fundamental component for the success of the monitoring is the choice of the data acquisition system [7]. Over the last years, several hygrothermal measurements and monitoring techniques have been developed e.g. [8, 9], highlighting the resistance-type methods. Also, nowadays, automatic data acquisition systems can be easily installed *in situ*. Despite the recognized accuracy of the method, it makes local measurements, implying the previous accurate identification of areas with higher infiltration risks.

The relevance of water content and continuous monitoring as an option to predict future problems related to wooden structure degradation is currently reflected in the number of authors who dedicate their studies to these issues, particularly aiming at the estimation of the service life of timber structures concerning the risk of fungal decay [8]. Within this area, new methods of test and experimental set-ups were identified as needed [10, 11] since new methodological approaches combining techniques from different areas of research could contribute to an optimized use of the material.

An example of this approach is under development [12] simulating the transport of water between wet masonry and wooden beams ends to better understand the periodic wetting and drying of wooden elements also taking into account the specific problems of moisture-exposed brick masonry [13]. The experimental campaign was carried out on three test setups that represent the contact between a timber beam and a support masonry with the following elements: (i) Scots pine timber beam-end with $100 \times 160 \times 100 \text{ mm}^3$ (three samples); (ii) masonry support for the beam; and (iii) six Karsten tubes per test set up applied to the masonry with three configurations for simulating the diffusion of water to the wood. Figure 3.1 shows one of the configurations that simulate absorption in both directions (parallel and perpendicular to the fibres) through Karsten tubes positioned on the back and base of the masonry.

The areas identified with a higher risk of biological deterioration were close to the contact zone between the masonry and the two faces of the beam, reaching easily values above 30% of moisture content. In addition, the drying period, which lasted approximately 30 days, was not enough for the beam to dry to its equilibrium moisture content, with measured values above 20% of moisture content, the threshold considered in the literature for the activation of the biological deterioration process. As expected, fungal development was noted from the early stages of the wetting process (Fig. 3.2).

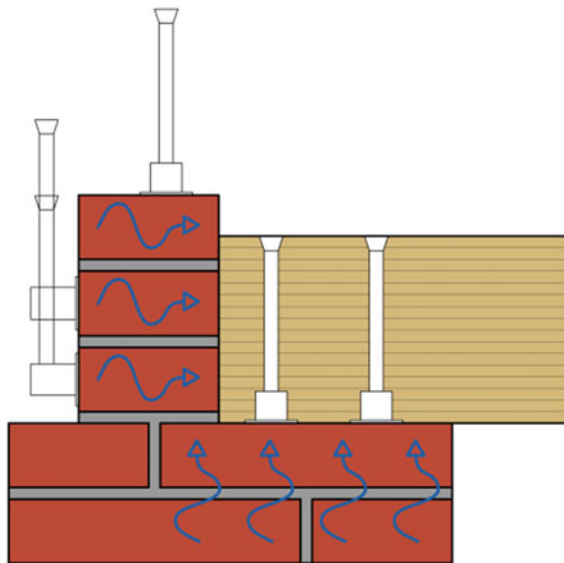


Fig. 3.1 Example of test setup to simulate moisture dynamics at a timber beam ends in contact with masonry (*Image credit Maxime Verbist*)

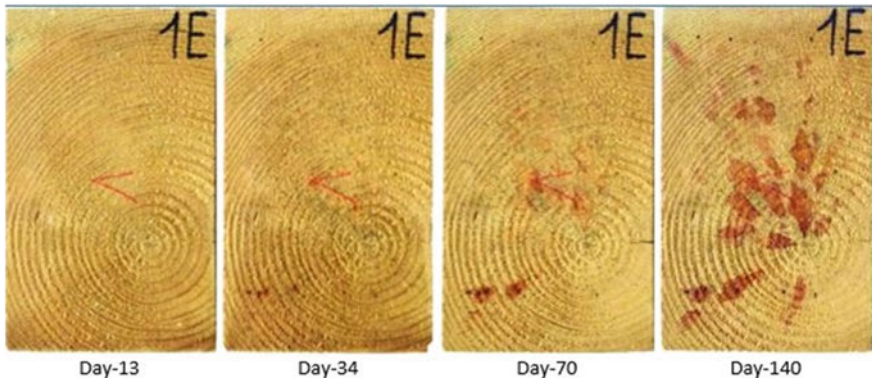


Fig. 3.2 Onset and development of fungi (e.g. moulds) on the transversal (E) surfaces in contact with the wet masonry support during the testing period [9] (*Photos credit Maxime Verbist*)

3.3 Rammed Earth, Cob and Unfired Earth Blocks

In cold climates, the moisture in recently produced rammed earth and cob walls can freeze. To reduce that problem, the production of these types of earth techniques only occurs *in situ* in protected sites, and freeze-thaw tests are carried out to assess the durability of this action. Some of these tests are very aggressive for non-stabilized

earth products and are commonly applied to assess the increase of durability when stabilisers are added [14].

The biological development, by organic growth is another test related to earth products' durability that is also associated to moisture. As earthen products are highly hygroscopic, their moisture content can change easily; therefore, the environmental conditions in which they are in equilibrium are very important to allow comparison of results. Particularly for earth products that include plant fibres, ventilation during drying is extremely important. The vulnerability to biological development can be tested using a method adapted from ASTM D5590-17 [15] of exposure in defined temperature, relative humidity, and ventilation conditions, that has been applied to several materials [16, 17]. The problem is that the colour of earth-based materials does not facilitate visual observation.

For earth products applied with exposure to rain, the spray test, also known as the accelerated erosion test (AET), is very important to assess durability. A surface of a sample of the exposed earthen product is subjected to a defined water spray pressure applied with a defined nozzle at a defined distance (Fig. 3.3). The tested samples perform correctly if erosion does not surpass a defined limit by the period of the test. Several variations of this test exist (modified AET), comprising different spray pressures, distances, or exposed areas [18] and discussion is still ongoing, namely for the revision of the Australian standard HB 195 [19] and mainly because non-stabilized earth products can hardly validate the test.

There are much less destructive tests that can be used to assess the effect of water on durability, namely to evaluate the effect of treatments applied on the exposed surface earth elements. An alternative to the standardised water absorption by Karsten tube test [20], is the contact sponge test (Fig. 3.4) [21]. A sponge occupying all the volume of a Petri dish is wet and placed in contact with the earth's surface to test for a defined period.

The wet sponge mass is registered before the test and results can be assessed by the difference in mass of the sponge, which corresponds to the water absorbed by the earthen surface. An advantage of this test is that, by registering the mass of water

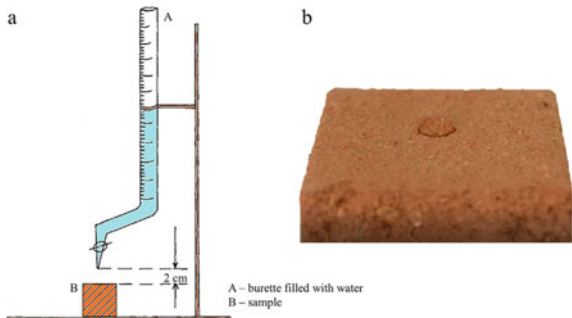
Fig. 3.3 Example of a spray test equipment (without sample) to assess earth products durability to water



Fig. 3.4 Example of the simple contact sponge test applied on adobe and rammed earth samples to assess earth products' water absorption and future durability [21]



Fig. 3.5 Scheme of a simple water drop test and drop of water on an earthen sample surface previously treated [23]



added to the sponge and containing the wet sponge in closed Petri dishes after the test until weighing, the simple test can also be applied *in situ*.

Another simple test that can be used with a similar aim is the contact angle test. This test can be performed with standardized equipment [22] but, when it is not available, it can be performed in a simplified way using a video camera to record the time a drop of water takes to be absorbed (Fig. 3.5) [23].

The results can be expressed by the time for a similar drop to be absorbed by different earthen surfaces. When testing the effect of the addition of stabilisers in the earth mixture or of surface treatments, results can also be expressed by the increase in absorption time in comparison to the reference, non-stabilised or untreated surface.

3.4 Assessment of Natural Stone Durability

3.4.1 Introduction

This section presents a case study with an innovative automatic chamber prototype developed at Universidade NOVA de Lisboa [24] to carry out salt crystallization-dissolution ageing cycles inside the pores of sandstone specimens. It should be noted that the prototype can also be used to test other materials, such as other types of stone and mortars.

The developed experimental apparatus, as well as the summary of the main experimental results are described in the following subsections, showing the efficiency and the potential of the automatic chamber developed to carry out accelerated ageing tests on stone specimens.

The sandstone studied in this research has about 20–25% carbonates and 45–51% quartz and is fine to medium-grained. The specimens revealed porosity values of 18.5% on average and a bulk density of about 2180 kg/m^3 before the ageing tests.

3.4.2 Experimental Apparatus

The automatic chamber prototype developed (Fig. 3.6) can perform salt ageing tests on 30 stone cubic samples of 5 cm-long per tray, based on cycles of immersion within a sodium chloride solution, drying at $60\text{--}100^\circ\text{C}$ and cooling at 20°C . The test program can be selected to follow the standards procedures of RILEM [25] and EN 13755:2008 [26], replacing sodium sulphate with sodium chloride solutions.

The test protocol implemented in the equipment's control system consisted of performing 60 cycles of 24 h, in which each cycle starts with the full immersion of the samples (dissolution) for 2 h within a 10% sodium chloride solution, followed by 20 h of heating at $60 \pm 2^\circ\text{C}$ (crystallization), and ending the cycle with h of cooling.

The full immersion of the sandstone samples is obtained automatically with the 2 h at room temperature (circa 20°C) in 10–14% salt solution. There are two options to fill the trays with salt solutions or deionised water: (1) through the pumping of the water from the bottom reservoirs, or (2) by gravity-flow of the water from the top

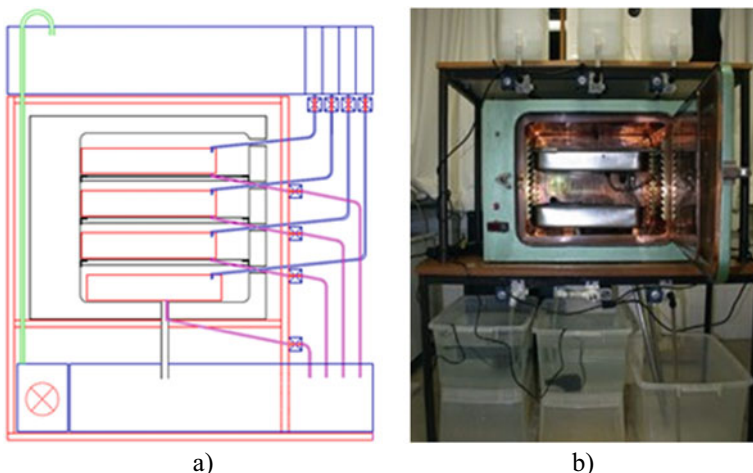


Fig. 3.6 Salt ageing chamber prototype: **a** schematic of the chamber and **b** real image

reservoirs to the trays, using connecting tubes and electrical valves existing below the trays or at the top reservoirs. A warning pipe system avoids that water, or salt solutions to overflow the safety level. After running out of the time programmed for immersion, salt solutions are moved back to the bottom reservoirs or put back into the top reservoirs, passing through the same electrical valves. Then, for 20 h the specimens are dried inside the chamber following the test protocol at 60 ± 2 °C and later are cooled at 20 ± 2 °C for 2 h.

A concentration of 1 ppm/h of ions was obtained in deionised waters after washing at the end of the ageing cycles. The final steps of the experimental procedure are drying the samples in an oven at 60 °C and their storage at 20 °C in a desiccator.

3.4.3 Physical and Mechanical Experimental Procedures

As recommended by RILEM [25] and EN 13755 [26] standards, during the ageing tests the damage assessment was done by visual observation of the failure features on the samples' surfaces, and by the weight records of the remaining mass of the samples' stone, to evaluate the mass loss percentage.

After the ageing tests, the specimens were tested under uniaxial compression until rupture. The tests were carried out under axial displacement control at a rate of 10 µm/s using the servo-controlled press testing machine of the laboratory of structures [27]. The vertical displacements were measured by LVDTs placed between the press plates, and the force by the press load cell. The stress–strain diagrams of sandstone salt-weathered samples were obtained considering the force divided by the contact area of the specimen and the displacement divided by the height of the specimen.

3.4.4 Experimental Results

During the ageing tests, a progressive loss of surface material was observed due to the release of individual grains, detachment of scales and millimetric cavities, which were visible just before the 40th cycle. At the 60th cycle, it was found that the cube edges were completely rounded. The damage assessment done by visual observation showed that granular disintegration was the most important degradation pattern observed (Fig. 3.7).

Figure 3.8a shows the mass loss in percentage recorded on sandstone samples during salt artificial ageing tests, as well as the compressive strength loss in percentage recorded after the uniaxial compression tests, for an identical number of cycles. The average mass loss of sandstone samples ranges up to around 8% at the 60th salt cycle. In turn, the average value of the compressive strength loss as well as the modulus of elasticity loss show an approximate decrease of 60% at the 60th ageing cycle (Fig. 3.8a and b). The experimental tests carried out made it possible to

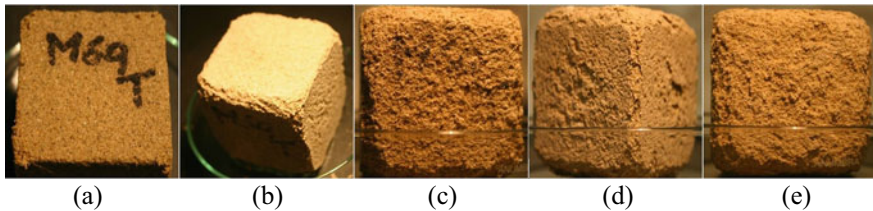


Fig. 3.7 Degradation features during the salt ageing test: **a** after 7 cycles; **b** rounded edges after 30 cycles; **c** and **d** scale detachments after 40 cycles, respectively front and rear; **e** completely rounded edges at 60th cycle

relate the compressive strength (σ_{Nc}) to the number of degradation cycles (Nc) and the initial compressive strength (σ_c) through the following expression:

$$\sigma_{Nc} = e^{-0.014Nc} \sigma_c \quad (3.1)$$

Figure 3.8b shows envelopes of stress-strain diagrams of uniaxial compression tests, obtained during the artificial salt ageing tests. The average value of the compressive strength ranges between 30.9 MPa, before the ageing tests, and 11.8 MPa at the 60th cycle, i.e. a decrease of about 60%.

The study shows the significant degradation effect on sandstone samples due to salt ageing cycles performed by the automatic chamber prototype developed. In addition, it was possible to highlight the importance of basic engineering properties. In particular, the finding that an average mass loss of around 8% could be misleading

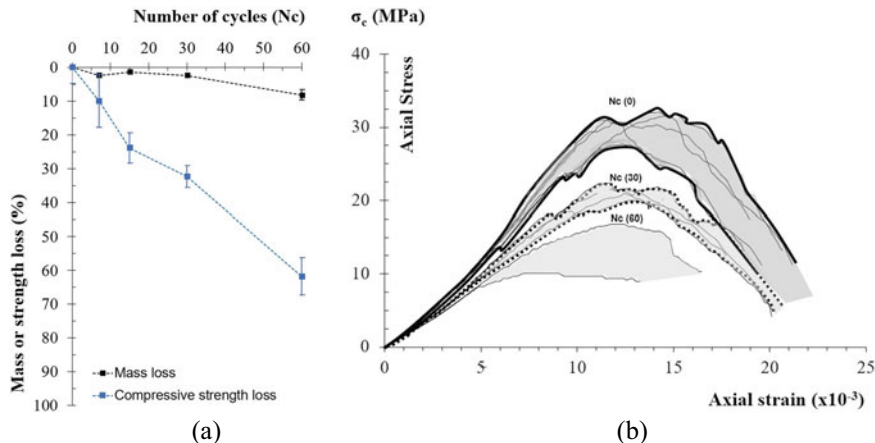


Fig. 3.8 **a** Mass loss (black dots) and compressive strength loss average values (blue dots) during salt crystallisation ageing cycles (Nc); deviation range is shown close to dots; **b** envelopes of stress-strain diagrams obtained on sandstone samples during salt crystallisation ageing at a number of cycles (Nc) of 0, 30, and 60

in relation to the mechanical parameters (compressive strength and modulus of elasticity), which have an average decrease of about 60% reported during the salt ageing test.

3.5 Bituminous Binders and Mixtures

3.5.1 Introduction

In the past, greater efforts have been directed at the development of binder ageing accelerated processes than at the ageing of bituminous mixtures. Furthermore, the study of a binder separately is not sufficiently representative of the global ageing of a compacted bituminous mixture because other properties may also have a significant impact, such as the voids content, the voids interconnection and the binder content. Today, innovation in bituminous binders and mixtures is a constant, with an impact on ageing and improved durability (e.g., nano, self-healing and bio-based technologies). In this context, the development of innovative durability tests for bituminous binders and mixtures is also particularly important. In the case of ageing, methods that are both more accurate and capable of better simulating real field conditions are desirable. Heating, solar radiation, freeze–thaw, and wetting are identified as the most relevant actions that affect ageing, revealing the potential for their incorporation in advanced simulation methods.

3.5.2 TEAGE Description

The Instituto Superior Técnico (IST) of the University of Lisbon has developed an alternative laboratory method designated *TEcnico Accelerated AGEing* (TEAGE), for the long-term ageing (LTA) simulation of compacted specimens of bituminous mixtures. This new approach consists of applying ultraviolet (UV) radiation and drying-wetting cycles to the test specimens during a certain period, to correspond to a specific equivalent ageing process in the field. This period is calculated based on the main environmental conditions at the field location: UV radiation and precipitation. Figure 3.9a shows a general view of the TEAGE prototype installed in the Laboratory of Transport Infrastructures at IST's Department of Civil Engineering, Architecture and Georesources [28, 29].

The TEAGE prototype consists of a conditioning chamber, cooling fans incorporated in the inlet and exhaust chimneys, water control/timer valves and UV lamps (Fig. 3.9b). Test specimens are placed inside the conditioning chamber on a rack where they are subjected to continuous UVB radiation and wetting/drying cycles. TEAGE uses UVB radiation (280–315 nm wavelength) due to its greater ageing

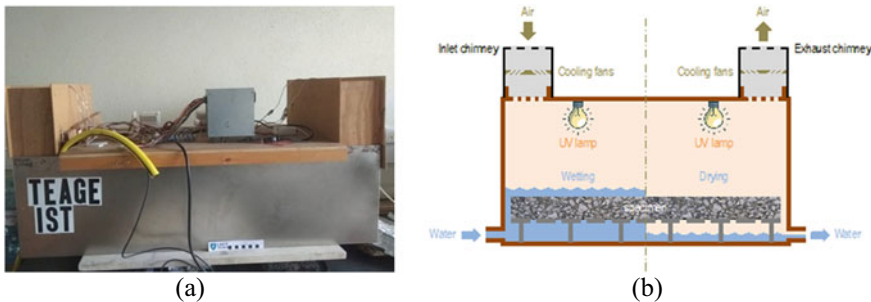


Fig. 3.9 **a** TEAGE prototype; **b** Scheme of the prototype

effect and higher transfer of energy during a shorter conditioning period. UVB radiation is simulated through specific UV lamps. To prevent the overheating of the specimens (above 60 °C) due to the UVB radiation, cooling fans are used to induce a continuous cooling airflow from the inlet to the exhaust chimneys. Lisbon receives an annual energy exposure of 5.7 GJ/m² and the UV lamps' configuration transmits the equivalent of one year of UVB radiation in approximately 100 h. Wetting/drying cycles are applied using automatic control/timer valves that raise the water level inside the conditioning chamber and, at the end of the defined time, allow the water to escape. Simulation of the total precipitation on the pavement is not possible in such a short period. TEAGE assumes that the duration of the immersion in water of the specimens should be equivalent to the days with precipitation greater than 5 mm. For the simulation of 7 years of Lisbon environmental conditions in 30 days, the following TEAGE prototype setup should be implemented: 24 W of UVB radiation; a combination of 4 daily immersion cycles of 40 min per cycle to simulate the real effect of precipitation; and 354 m³/h of cooling airflow. Crucho [30] goes into greater detail on how the TEAGE functions [30].

Although developed for bituminous mixtures, TEAGE can also be adapted for bitumen specimens using only UV radiation. In this approach, a thin film of bitumen deposited on a wide stainless-steel tray is exposed to radiation for the period required to simulate the LTA [28, 29].

3.5.3 TEAGE Results

Exposure to sunlight has a visible effect on the colouring of the bituminous mixtures in wearing courses. Figure 3.10a shows the aspect of dense specimens extracted from a pavement after 1, 3 and 7 years of service life. Similarly, TEAGE specimens show a greyish appearance on the surface that contrasts with the dark grey (off-black) of the unaged specimens. Figure 3.10b shows test specimens after 10, 20 and 30 days of TEAGE ageing that correspond to 2.3, 4.7, and 7.0 years, respectively, of real ageing in a pavement located in Lisbon [28, 29].

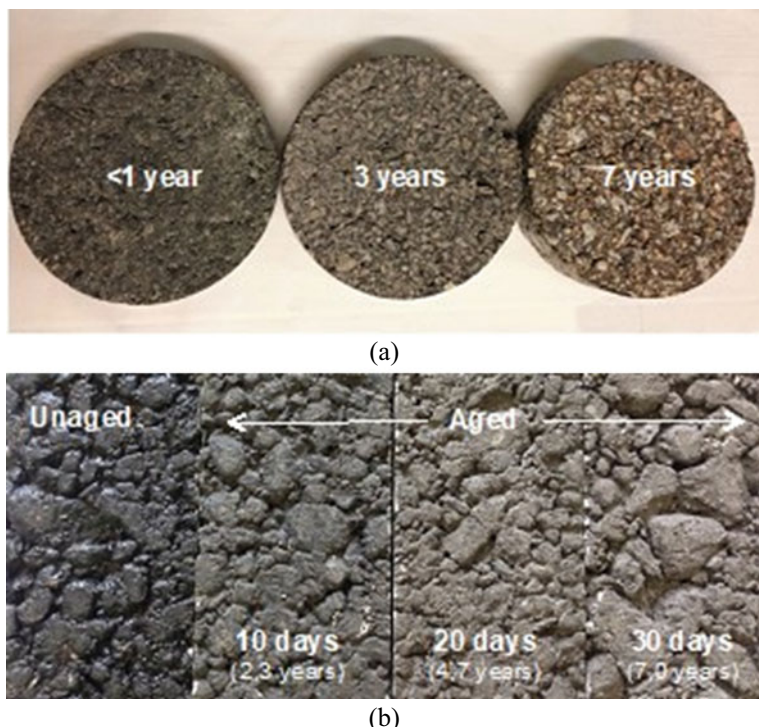


Fig. 3.10 **a** Specimens extracted from the pavement; **b** TEAGE specimens

Stiffness can give an adequate indication of the performance of the bituminous mixtures. The hardened material tends to increase the stiffness. Figure 3.11 presents the results of stiffness tests performed following EN 12697-26 using a four-point bending test on prismatic specimens (Annex B) at 20 °C for several frequencies (1, 3, 5, 10, 20, and 30 Hz). Tests were performed on unaged and aged specimens of a continuously graded and dense bituminous mixture (asphalt concrete, AC 14 surf 35/50, following EN 13108-1). Both long-term oven ageing (LTOA) and TEAGE tests were used for comparison. TEAGE specimens were conditioned for 10, 20 and 30 days that correspond to 2.3, 4.7, and 7.0 years, respectively (Fig. 3.10b). The aged mixtures and the corresponding recovered bituminous binders were tested, and the results were compared. Figure 3.11 shows in general that the aged bituminous mixtures presented a higher stiffness modulus and lower phase angles, which is consistent with the hardening effect of LTA. In addition, results confirm a reasonable correspondence between LTOA and the 7-year ageing simulation in the TEAGE prototype [28, 29].

In general, research carried out on various types of bituminous mixtures (e.g., asphalt concrete, stone mastic asphalt) and using different bituminous binders (neat

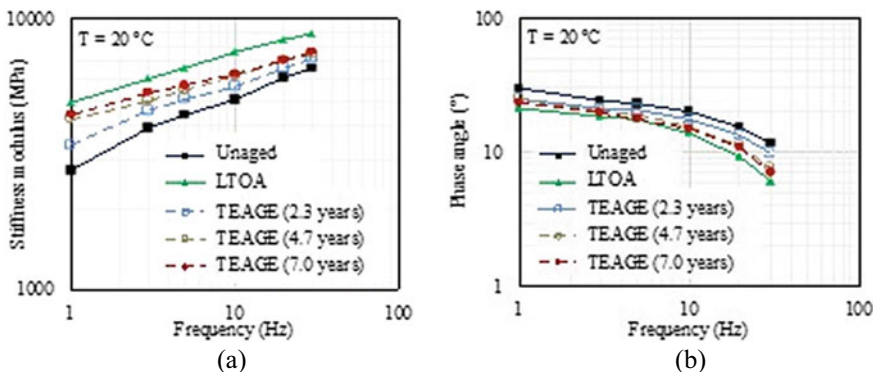


Fig. 3.11 **a** Stiffness modulus; **b** Phase angle

and modified bitumen, including polymer and nano modification) have also validated the TEAGE method as a new approach to the LTA of bituminous mixtures [28, 29].

3.6 Double Shear Tests to Assess FRP to Concrete Bonded Connections

3.6.1 Introduction

The knowledge of the mechanical behaviour of bonded connections has increased in the past decade thanks to several studies carried out by different research groups around the world, e.g., [31–36]. Particularly, the research group at NOVA University of Lisbon has also contributed to that knowledge increase with several developed studies [37–45]. In this section, a brief explanation of how the adhesive law of a bonded connection between a Fiber Reinforced Polymer (FRP) and a concrete substrate is presented.

It should be mentioned that, unlike other cases where international standards give clear guidelines for material testing, there are no standards to be followed in the cases of bonded connections. Therefore, to obtain an adhesion law that may be used to describe a mixed mode condition (i.e. Mode I + II), a novel test setup was developed by Biscaia et al. [46], which consisted of an externally bonded continuous FRP sheet to two opposite concrete surfaces.

In this research, the influence of different environmental conditions such as salt fog cycles, full immersion in 5% salt water, dry–wet cycles, and temperature cycles below the glass transition temperature (T_g) of the adhesive of 68.5 °C (between 7.5 °C and 47.5 °C and between –10 °C and 30 °C) on a bonded connection between Glass (G) FRP composite and a concrete substrate was studied under two different external stresses of 0.5 MPa and 1.0 MPa.

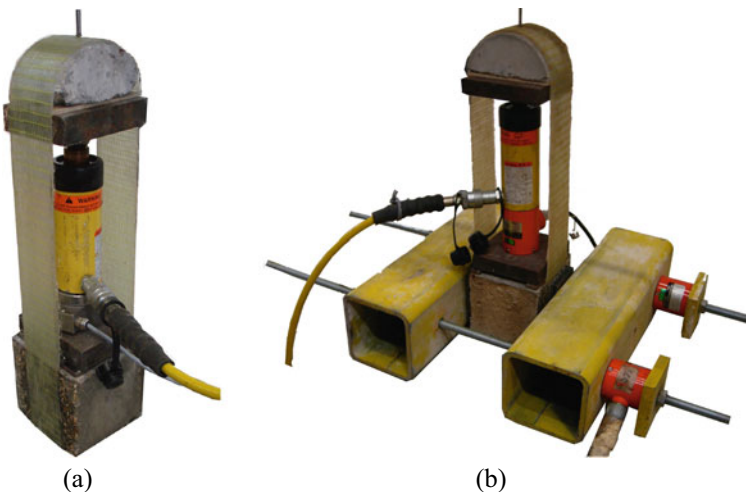


Fig. 3.12 Self-equilibrated double shear tests: **a** free of external compressive stresses; and **b** with an imposed external compressive stress

3.6.2 Experimental Procedure

To characterize the interfacial bond behaviour between two different materials such as concrete and an FRP composite under different mechanical and/or environmental conditions, the conceived double shear test could be very interesting. If on one hand, it allows us to subject the bonded connection to external and controlled pressure, on another hand, it allows us to have specimens with relatively small dimensions which makes them compatible with a large range of existing artificial ageing equipment. The configuration of the double shear tests also allows to development of a self-equilibrated and quite simple test setup (see Fig. 3.12).

Hence, different external pressures should be considered as well as different ageing stages per each environmental condition. Consequently, and aiming to study the influence of different environmental conditions on a bonded connection, the experimental program may involve several specimens. It should be bear in mind also that each situation should be repeated (at least 3 times minimum) which leads to a large experimental campaign to be carried out.

3.6.3 Interfacial Characterization

The main purpose of these double shear tests is to obtain a couple of adhesion laws that may locally describe the interfacial bond behaviour of the bonded connection. Figure 3.13 shows how the adhesive law can be related to the Mohr–Coulomb criterion. Three distinct situations can be identified from Fig. 3.13. The first and easiest

one, lies on the assumption that the bonded connection is subjected to pure Mode II, i.e. free of external stresses ($\sigma_0 = 0$ MPa). In this situation, the relative displacements (or slip, s) of the bonded connection are related to the developed shear (or bond) stresses as shown in Fig. 3.13c, which is usually designated in the literature as the bond-slip law [47–49] of the bonded connection. Here, when the interfacial slips reach s_0 , the interfacial maximum bond stress is reached ($\tau_{\max,0}$) which, in the Mohr–Coulomb criterion is usually denoted as cohesion (c). After this, the bond stresses cannot increase with the interfacial slips and therefore, the interfacial stresses tend to decrease until a zero value. The way that the bond stresses increase and then decrease with the interfacial slips depends on the bonded materials as well as the adhesive types [50–52].

The second situation identified from Fig. 3.13 is the case of a tension external pressure σ_t (see Fig. 3.13b). The reduction of the maximum bond stress is the main difference observed from the first situation. Like the pure Mode II case, after the peak bond stress, the increase of the interfacial slips leads to a zero-bond stress condition as well. The third situation can be observed in Fig. 3.13d or e. In this case, the bonded connection is externally pressured with compressive stress. This is the same case when, for instance, a metallic anchorage plate is used to fix an FRP composite to the substrate and delay, or even prevent, the premature debonding of the FRP composite as documented in the literature [53–55]. The explanation of how the use of a mechanical anchorage could be efficient in a bonded connection is easily explained by the Mohr–Coulomb criterion. Let us first assume that the external pressure is σ_1 . According to this criterion, the increase of the maximum bond stress in the bonded connection is obtained according to:

$$\tau = \tau_{\max,0} + \mu_e \sigma \quad (3.2)$$

where μ_e is the internal friction coefficient of the bonded connection and σ is the external stress (positive in the case of compression). Hence, the maximum bond stress of the externally pressured bonded connection has now enhanced from $\tau_{\max,0}$ to $\tau_{\max,1}$ and, unlike the other two situations, after this peak stress is reached, the increase of the interfacial slip leads to a nonzero bond stress situation herein denoted as residual bond stress (τ_{res}). In the Mohr–Coulomb criterion, this is commonly denoted as dry friction (see the dash-dot line in Fig. 3.13a). So, as long as the compressive external pressure increases, e.g. to σ_2 , the peak and the residual bond stresses will tend to increase, which enhances, consequently, the bond performance of the bonded connection.

3.6.4 Analysis of Some Available Experimental Results

After the time exposure of the specimens to 3000 h, 5000 h and 10,000 h, the double shear tests were carried out. To obtain reference values, unaged specimens were also

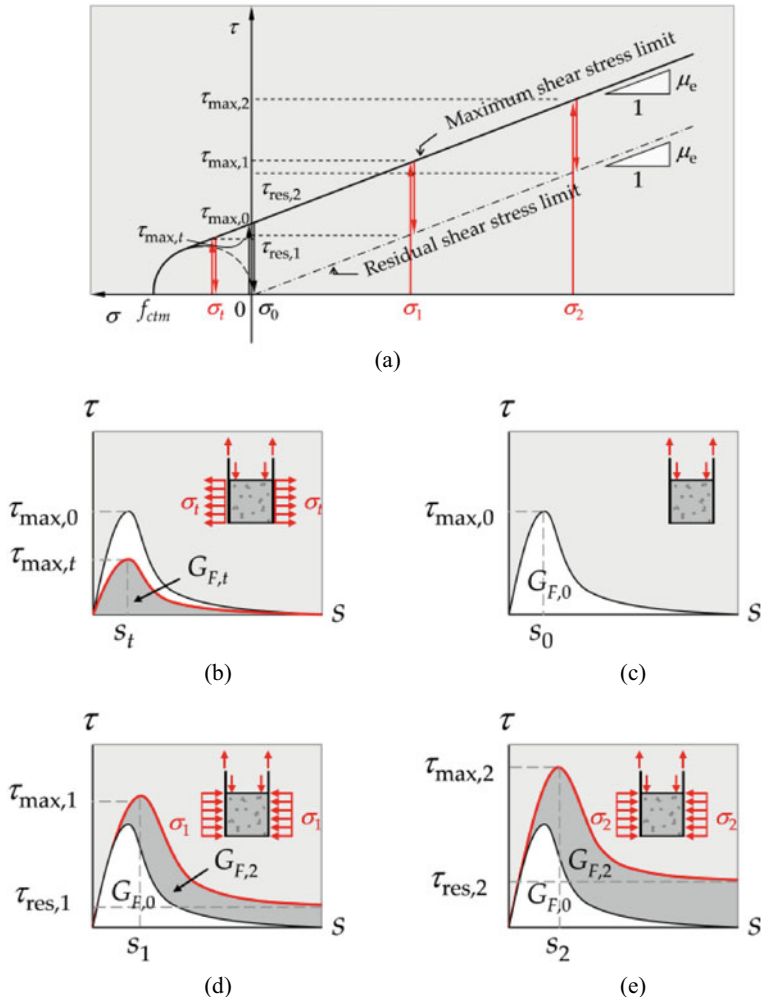


Fig. 3.13 **a** Definition of the couple adhesive law of a bonded connection through the Mohr-Coulomb criterion; **b** influence of a tension external pressure in the adhesive law; **c** adhesive law free of external pressures; **d** influence of the compression external pressure σ_1 in the adhesive law; and **e** influence of the compression external pressure σ_2 in the adhesive law

tested. For the sake of simplicity, only the results obtained for the temperature cycles are presented in Fig. 3.14.

The gain and losses of each property (maximum bond stress at three different external compression pressure of 0 MPa, 0.5 MPa and 1.0 MPa, residual stress and the internal friction coefficient) are shown in Fig. 3.14b. Each result was obtained from the following expression:

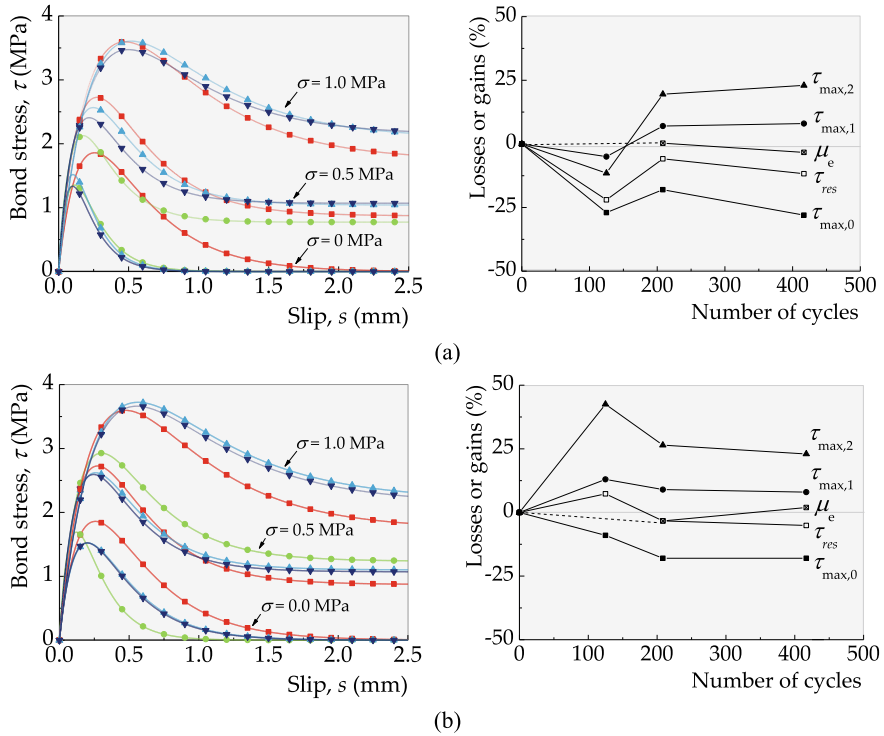


Fig. 3.14 Estimated local adhesive laws and the corresponding evolution of the maximum and residual bond stresses in the temperature cycles between **a** 7.5 °C and 47.5 °C; and **b** -10 °C and 30 °C

$$D = (p_i/p_0 - 1)100\% \quad (3.3)$$

where p_i is the analysed parameter at the end of the i^{th} cycle, i.e., after the ageing exposure, and p_0 is the analysed parameter obtained from the unaged specimens. The calculated variations of each parameter are reflected on the adhesive law (see Fig. 3.14a and c) which is obtained mathematically by the following exponential curve:

$$\tau = A^2 B (e^{-Bs} - e^{-2Bs}) E_f t_f + \tau_{\text{res}} (1 - e^{-Bs}) \quad (3.4)$$

where A and B are constants that are defined from the experimental strain-slip curve of a lengthy bond length; E_f and t_f are, respectively, the modulus of elasticity and the thickness of the FRP composite [56].

These results show that the maximum bond stress of the aged GFRP-to-concrete interface free of external compressive stress has decreased by approximately 25% in both cases. However, the reported ageing conditions had a marginal impact on the interfacial maximum stress when the external compressive stress was increased.

Another interesting result observed from this study was the increase of the internal friction coefficient with the number of the ageing period which is coherent with the increase of the residual stress. In these cases, a such increase may be attributed to some loss of water in the substrate as well as in the adhesive that could increase the internal friction (μ_e) of the bonded connection.

3.7 Final Remarks

In this chapter, several case studies related to innovative durability tests were presented. These were designed to simulate some of the degradation processes occurring on materials such as timber, rammed earth and unfired earth blocks, natural stone, bituminous binders, and mixtures, as well as on the interface of FRP to concrete connection.

In these case studies, it is worth highlighting the performance of accelerated tests that try to simulate in the laboratory the degradation phenomena that affect materials and composites. These phenomena may be motivated by environmental agents (water, salt water, UV, etc.) or by biological agents and are at the base of the most important phenomena of degradation in construction materials for civil engineering infrastructures.

The presentation of the innovative durability tests in this chapter was supported by the description of case studies mainly related to research projects in development. The main challenge in the near future is the worldwide dissemination and implementation of these methods through their standardization.

Acknowledgements Carlos Chastre, Paulina Faria, and José Neves are grateful for the Foundation for Science and Technology's (FCT) support through the funding FCT-IDB/04625/2020 from the research unit CERIS (Centre of Civil Engineering Research and Innovation for Sustainability). Likewise, Hugo Biscaia would like to also acknowledge the support of FCT for the partial funding of this work under the strategic project UIDB/EMS/00667/2020.

References

1. Cruz H, Jones D, Nunes L (2015) Wood. In: Materials for construction and civil engineering. Science, Process Design, pp 557–583. Springer, Switzerland
2. EN 13183-1:2002 (2002) Moisture content of a piece of sawn timber Determination by oven dry method. In: CEN, European Standardisation Institute, Brussels, Belgium
3. Thybring EE, Kymäläinen M, Rautkari L (2017) Experimental techniques for characterising water in wood covering the range from dry to fully water-saturated. *Wood Sci Technol* 52(2):297–329. <https://doi.org/10.1007/s00226-017-0977-7>
4. Dietsch P, Franke S, Franke B, Gamper A, Winter S (2014) Methods to determine wood moisture content and their applicability in monitoring concepts. *J Civ Struct Heal Monit* 5(2):115–127. <https://doi.org/10.1007/s13349-014-0082-7>

5. Svensson S, Turk G, Hozjan T (2011) Predicting moisture state of timber members in a continuously varying climate. *Eng Struct* 33(11):3064–3070. <https://doi.org/10.1016/j.engstruct.2011.04.029>
6. Broda M (2020) Natural compounds for wood protection against fungi—a review. *Molecules* 25(15). <https://doi.org/10.3390/molecules25153538>
7. Palma P, Steiger R (2020) Structural health monitoring of timber structures – review of available methods and case studies. *Constr Build Mater* 248. <https://doi.org/10.1016/j.conbuildmat.2020.118528>
8. van Niekerk PB, Brischke C, Niklewski J (2021) Estimating the service life of timber structures concerning risk and influence of fungal decay—a review of existing theory and modelling approaches. *Forests* 12(5). <https://doi.org/10.3390/f12050588>
9. Brischke C, Rapp AO, Bayerbach R (2008) Measurement system for long-term recording of wood moisture content with internal conductively glued electrodes. *Build Environ* 43(10):1566–1574. <https://doi.org/10.1016/j.buildenv.2007.10.002>
10. Brischke C, Alfredsen G (2020) Wood-water relationships and their role for wood susceptibility to fungal decay. *Appl Microbiol Biotechnol* 104(9):3781–3795. <https://doi.org/10.1007/s00253-020-10479-1>
11. Curling S, Gobakken LR, Cragg S, de Windt I, Willems W, Meyer-Veltrup L, Van den Bulcke J, Melcher E, Humar M, Lanata F, Macchioni N, Palanti S (2017) In: Jones D, Brischke C (eds) Performance of bio-based building materials. pp. 385–481. Elsevier Ltd. <https://doi.org/10.1016/j.buildenv.2021.107844>
12. Nunes L, Verbist M, Lima DF, Branco JM (2021) Preliminary testing of moisture propagation at timber beam-ends in contact with wet masonry. Proceedings 1st International Conference on Moisture in Buildings, London. <https://doi.org/10.14293/icmb210044>
13. Aktas YD, Zhu H, D’Ayala D, Weeks C (2021) Impact of surface waterproofing on the performance of brick masonry through the moisture exposure life-cycle. *Build Environ* 197. <https://doi.org/10.1016/j.buildenv.2021.107844>
14. Muguda S, Lucas G, Hughes PN, Augarde CE, Perlot C, Bruno AW, Gallipoli D (2020) Durability and hygroscopic behaviour of biopolymer stabilised earthen construction materials. *Constr Build Mater* 259:119725. <https://doi.org/10.1016/j.conbuildmat.2020.119725>
15. ASTM D5590–17 (2017) Determining the resistance of paint films and related coatings to fungal defacement by accelerated four-week agar plate assay. In: ASTM international, Pennsylvania
16. Nunes L, Cintura E, Parracha JL, Fernandes B, Silva V, Faria P (2021) Cement-bonded particleboards with banana Pseudostem waste: physical performance and bio-susceptibility. *Infrastructures* 6:86. <https://doi.org/10.3390/infrastructures6060086>
17. Parracha JL, Borsoi G, Flores-Colen I, Veiga R, Nunes L, Dionísio A, Gomes MG, Faria P (2021) Performance parameters of ETICS: correlating water resistance, bio-susceptibility and surface properties. *Constr Build Mater* 272:121956. <https://doi.org/10.1016/j.conbuildmat.2020.121956>
18. Beckett CTS, Jaquin PA, Morel JC (2020) Weathering the storm: a framework to assess the resistance of earthen structures to water damage. *Constr Build Mater* 242:118098. <https://doi.org/10.1016/j.conbuildmat.2020.118098>
19. HB 195 (2002) The Australian earth building handbook. In: Standards, Australia
20. EN 16302:2013 (2013) Conservation of cultural heritage. Test methods. Measurement of water absorption by pipe method. In: CEN, European Standardisation Institute, Brussels, Belgium
21. Ribeiro T, Oliveira DV, Bracci S (2022) The use of contact sponge method to measure water absorption in earthen heritage treated with water repellents. *Int J Architect Herit* 16(1):85–96. <https://doi.org/10.1080/15583058.2020.1751344>
22. EN 15802:2009 (2009) Conservation of cultural property. Test methods. Determination of static contact angle. In: CEN, European Standardisation Institute, Brussels, Belgium
23. Parracha JL, Pereira AS, Velez da Silva R, Almeida N, Faria P (2019) Efficacy of iron-based bioproducts as surface biotreatment for earth-based plastering mortars. *J Cleaner Product* 237:117803. <https://doi.org/10.1016/j.jclepro.2019.117803>

24. Ludovico-Marques M, Chastre C (2016) Effect of artificial accelerated salt weathering on physical and mechanical behavior of sandstone samples from surface reservoirs. In: Makhlof ASH, Aliofkazraei M (eds) Handbook of materials failure analysis with case studies from the oil and gas industry, pp 215–233. Butterworth Heinemann - Elsevier. <https://doi.org/10.1016/B978-0-08-100117-2.00013-3>
25. RILEM (1980) Recommended tests to measure the deterioration of stone and to assess the effective-ness of treatment methods. Mater Constr 13(75):175–253
26. EN 13755:2008 (2008) Natural stone test methods. Determination of water absorption at atmospheric pressure. In: CEN, European Standardisation Institute, Brussels, Belgium
27. Ludovico-Marques M, Chastre C (2012) Effect of salt crystallization ageing on the compressive behavior of sandstone blocks in historical buildings. Eng Fail Anal 26:247–257. <https://doi.org/10.1016/j.engfailanal.2012.08.001>
28. Crucho JML, Picado-Santos LGD, Neves JMCD, Capitão SD (2020) The TEAGE ageing method for asphalt mixtures. Transp Eng 2:100030. <https://doi.org/10.1016/j.treng.2020.100030>
29. Crucho J, Picado-Santos L, Neves J, Capitão S, Al-Qadi IL (2020) Tecnico accelerated ageing (TEAGE) – a new laboratory approach for bituminous mixture ageing simulation. Int J Pavement Eng 21(6):753–765. <https://doi.org/10.1080/10298436.2018.1508845>
30. Crucho J (2018) Development of an accelerated asphalt concrete aging method and utilization of nano-modifiers to improve durability of asphalt concrete. Doctoral thesis, University of Lisbon, Portugal
31. Dai J, Ueda T, Sato Y (2005) Development of the nonlinear bond stress-slip model of fiber reinforced plastics sheet-concrete interfaces with a simple method. J Compos Constr 9(1):52–62. [https://doi.org/10.1061/\(ASCE\)1090-0268\(2005\)9:1\(52\)](https://doi.org/10.1061/(ASCE)1090-0268(2005)9:1(52))
32. Doroudi Y, Fernando D, Nguyen VT, Torres JP (2019) Experimental study on CFRP-to-steel bonded interfaces under quasi-static cyclic loading. J Compos Constr 23(4):04019023. [https://doi.org/10.1061/\(ASCE\)CC.1943-5614.0000945](https://doi.org/10.1061/(ASCE)CC.1943-5614.0000945)
33. Ferracuti B, Savoia M, Mazzotti C (2006) A numerical model for FRP–concrete delamination. Compos B Eng 37(4–5):356–364. <https://doi.org/10.1016/j.compositesb.2005.08.002>
34. Lu XZ, Teng JG, Ye LP, Jiang JJ (2005) Bond–slip models for FRP sheets/plates bonded to concrete. Eng Struct 27(6):920–937. <https://doi.org/10.1016/j.engstruct.2005.01.014>
35. Yuan H, Teng JG, Seracino R, Wu ZS, Yao J (2004) Full-range behavior of FRP-to-concrete bonded joints. Eng Struct 26(5):553–565. <https://doi.org/10.1016/j.engstruct.2003.11.006>
36. Zhou Y-W, Wu Y-F, Yun Y (2010) Analytical modeling of the bond–slip relationship at FRP–concrete interfaces for adhesively-bonded joints. Compos B Eng 41(6):423–433. <https://doi.org/10.1016/j.compositesb.2010.06.004>
37. Biscaria HC, Chastre C (2018) Theoretical analysis of fracture in double overlap bonded joints with FRP composites and thin steel plates. Eng Fract Mech 190:435–460. <https://doi.org/10.1016/j.engfracmech.2017.12.038>
38. Biscaria HC, Chastre C, Silva C, Franco N (2017) Mechanical response of anchored FRP bonded joints: A nonlinear analytical approach. Mech Adv Mater Struct 25(3):238–252. <https://doi.org/10.1080/15376494.2016.1255812>
39. Biscaria HC, Chastre C, Silva MAG (2013) Modelling GFRP-to-concrete joints with interface finite elements with rupture based on the Mohr-Coulomb criterion. Constr Build Mater 47:261–273. <https://doi.org/10.1016/j.conbuildmat.2013.05.020>
40. Biscaria HC, Chastre C, Silva MAG (2013) Linear and nonlinear analysis of bond-slip models for interfaces between FRP composites and concrete. Compos B Eng 45(1):1554–1568. <https://doi.org/10.1016/j.compositesb.2012.08.011>
41. Biscaria HC, Chastre C, Silva MAG (2017) Analytical model with uncoupled adhesion laws for the bond failure prediction of curved FRP-concrete joints subjected to temperature. Theoret Appl Fract Mech 89:63–78. <https://doi.org/10.1016/j.tafmec.2017.01.008>
42. Yang Y, Silva MAG, Biscaria H, Chastre C (2018) CFRP-to-steel bonded joints subjected to cyclic loading: An experimental study. Compos B Eng 146:28–41. <https://doi.org/10.1016/j.compositesb.2018.03.039>

43. Biscaya HC, Micaelo R, Teixeira J, Chastre C (2014) Delamination process analysis of FRP-to-parent material bonded joints with and without anchorage systems using the distinct element method. *Compos Struct* 116:104–119. <https://doi.org/10.1016/j.compstruct.2014.04.021>
44. Biscaya HC, Micaelo R, Teixeira J, Chastre C (2014) Numerical analysis of FRP anchorage zones with variable width. *Compos B Eng* 67:410–426. <https://doi.org/10.1016/j.compositesb.2014.07.031>
45. Yang Y, Silva MAG, Biscaya H, Chastre C (2019) Bond durability of CFRP laminates-to-steel joints subjected to freeze-thaw. *Compos Struct* 212:243–258. <https://doi.org/10.1016/j.compstruct.2019.01.016>
46. Biscaya HC, Chastre C, Silva MAG (2012) Double shear tests to evaluate the bond strength between GFRP/concrete elements. *Compos Struct* 94(2):681–694. <https://doi.org/10.1016/j.compstruct.2011.09.003>
47. Gomez J, Torres L, Barris C (2020) Characterization and simulation of the bond response of NSM FRP reinforcement in concrete. *Materials (Basel)* 13(7). <https://doi.org/10.3390/ma13071770>
48. Li Y, Bielak J, Hegger J, Chudoba R (2018) An incremental inverse analysis procedure for identification of bond-slip laws in composites applied to textile reinforced concrete. *Compos B Eng* 137:111–122. <https://doi.org/10.1016/j.compositesb.2017.11.014>
49. Yuan H, Lu X, Hui D, Feo L (2012) Studies on FRP-concrete interface with hardening and softening bond-slip law. *Compos Struct* 94(12):3781–3792. <https://doi.org/10.1016/j.compstruct.2012.06.009>
50. Biscaya HC, Chastre C, Borba IS, Silva C, Cruz D (2016) Experimental evaluation of bonding between CFRP laminates and different structural materials. *J Compos Constr* 20(3). [https://doi.org/10.1061/\(ASCE\)CC.1943-5614.0000631](https://doi.org/10.1061/(ASCE)CC.1943-5614.0000631)
51. Fernando D, Yu T, Teng JG (2014) Behavior of CFRP laminates bonded to a steel substrate using a ductile adhesive. *J Compos Constr* 18(2). [https://doi.org/10.1061/\(ASCE\)CC.1943-5614.0000439](https://doi.org/10.1061/(ASCE)CC.1943-5614.0000439)
52. Shi J-W, Cao W-H, Wu Z-S (2019) Effect of adhesive properties on the bond behaviour of externally bonded FRP-to-concrete joints. *Compos Part B: Eng* 177. <https://doi.org/10.1016/j.compositesb.2019.107365>
53. Gao L, Zhang F, Liu J, Lu X, Gao H (2019) Experimental and numerical study on the interfacial bonding characteristics of FRP-to-concrete joints with mechanical fastening. *Constr Build Mater* 199:456–470. <https://doi.org/10.1016/j.conbuildmat.2018.12.033>
54. Kang THK, Howell J, Kim S, Lee DJ (2012) A state-of-the-art review on debonding failures of FRP laminates externally adhered to concrete. *Int J Concrete Struct Mater* 6(2):123–134. <https://doi.org/10.1007/s40069-012-0012-1>
55. Moghaddas A, Mostofinejad D, Ilia E (2019) Empirical FRP-concrete effective bond length model for externally bonded reinforcement on the grooves. *Compos B Eng* 172:323–338. <https://doi.org/10.1016/j.compositesb.2019.05.068>
56. Biscaya HC, Chastre C, Silva MAG (2015) Bond-slip model for FRP-to-concrete bonded joints under external compression. *Compos B Eng* 80:246–259. <https://doi.org/10.1016/j.compositesb.2015.06.004>

Chapter 4

Testing of New Composites Incorporating Recycled Materials



Jorge de Brito · Pedro Raposeiro da Silva · and José Neves

Abstract This chapter presents the most recent and innovative testing techniques for evaluation of new composites incorporating recycled materials in civil engineering infrastructures, namely concrete structures and pavements. Recycled materials are commonly used in transport infrastructures through the incorporation in unbound and bound layers of pavement roads and, more recently, in concrete structures as well as various types of mortars. Moisture damage, affinity, durability, and mechanical performance are some important concerns within the conformity assessment of recycled aggregates, binders, asphalt and hydraulic mixes under special climate and traffic conditions. Regarding concrete and mortars, it is important to understand the influence of new recycled materials on their deterioration process. In an infrastructure produced with conventional constituent materials, concrete and mortars will probably deteriorate gradually and not suddenly and catastrophically. Usually, the deterioration process can be more relevant only after some time, depending on numerous factors such as quality of concrete and environmental and durability requirements. Thus, associated with the use of recycled materials, it is essential to determine the infrastructures' performance in measurable terms at the time of its completion and during its service life. Therefore, a detailed survey on the main testing techniques, in relation to the main deterioration mechanisms (physical, mechanical, and chemical processes) of concrete and pavement, is presented.

Keywords Bituminous mixtures · Concrete infrastructures · Deterioration mechanisms · Recycled materials · Road pavements · Testing techniques

J. de Brito · J. Neves

CERIS, Department of Civil Engineering, Architecture and Georesources, Instituto Superior Técnico, Universidade de Lisboa, Lisboa, Portugal
e-mail: jorge.brito@tecnico.ulisboa.pt

J. Neves

e-mail: jose.manuel.neves@tecnico.ulisboa.pt

P. R. da Silva

CERIS, Department of Civil Engineering, Instituto Superior de Engenharia de Lisboa, Instituto Politécnico de Lisboa, Lisboa, Portugal
e-mail: silvapm@dec.isel.pt

4.1 Introduction

Contrary to a common statement, instead of concrete, aggregates are the most consumed product after water. Although aggregates consumption is almost 12 times bigger than that of cement, their environmental impact (EI) is insignificant relatively to cement [1]. If one considers only half of the produced aggregates and cement used for pastes, mortars and concrete without considering the mixing procedure and transportation, the total GWP will be around $2.0113E + 15$ kg CO₂ eq [1]. Thus, the environmental impacts of the main raw materials to produce grouts, pastes, mortars and concrete is at least 710 and 31 times higher than the total emitted CO₂ by “human exhalation” and “all human activities including exhalation” per year, respectively (source of the secondary data [1]).

To reduce the impact of aggregates, using recycled concrete aggregates (RCA) instead of natural aggregates (NA), namely those resulting from construction and demolition waste (CDW), has been proved to be one of the most efficient actions. However, to do so, it is essential to know well the properties of such aggregates, especially since they are believed to have a higher scatter than the properties of NA, which is not necessarily true [2]. Therefore, the next section is dedicated to the discussion of how the RCA's properties differ from those of NA.

The two sections after that concern the properties of concrete made with RCA, in the fresh and the hardened state. There, the highlights deal with the distinct proprieties of RCA that mostly affect the RCA-based concrete characteristics/properties, and the tests that can be performed to closely monitor such situations. It is concluded that, depending on the replacement ratio of NA with RCA, the intrinsic quality of the RCA and adoption of procedures to offset the worst features of RCA, the use of RCA in concrete is perfectly viable, from a strictly technical point of view, without a drastic change in the business-as-usual stance of the industry.

The incorporation of waste materials in bituminous mixtures is also a current research and practice issue aimed at promoting sustainability in pavement engineering. This chapter covers the incorporation of RA from construction and demolition waste in bituminous mixtures, such as coarse and fine aggregates and as filler material. Recycled additions for the modification of the bituminous binder are not included in this chapter. In addition to the most common test methods for the geometrical, physical and mechanical properties of the constituents and the mixture itself, when using recycled aggregates in bituminous mixtures some particularities of the test methods gain particular importance. This chapter focuses, in greater detail, on the cases of affinity between recycled aggregates and bitumen, and the evaluation of the mechanical performance (e.g. water sensitivity, permanent deformation, stiffness, and fatigue).

4.2 Properties of Recycled Concrete Aggregates

The role of aggregates in concrete is extremely important, since, although the cement paste evidences significant strength, it has two main disadvantages, among others: its dimensional instability, caused by high shrinkage and creep and, on the other hand, the cost and environmental impacts of cement. The way to overcome these disadvantages is to add aggregates to the cement paste, thus producing concrete.

Similarly, the use of RCA to replace NA in the production of concrete is seen today as a viable method to continue responding to the referred dimensional instability of the cement paste and, simultaneously, solving a two-fold problem: reuse CDW instead of simply landfilling it (with all the disadvantages in terms of environmental impact) and, on the other hand, cause a decrease in NA consumption, consequently decreasing the negative impact associated with its exploitation (lower consumption of natural resources with all the obvious advantages in terms of environmental impacts).

These RCA result primarily from the processing of inorganic materials previously used in construction (CDW), of which the most appropriate are those from the grinding of hardened concrete.

However, it is essential to know their properties so that their application and performance are based on full knowledge of the material. Thus, to calculate the concrete mix proportions, it is essential to know some properties of the RCA, such as density, water absorption, size distribution, water content and apparent density. It should be noted that, in the case of size distribution, water content and apparent density, the procedure as well as the reference values specific of RCA are common to NA and depend on factors not particular to RCA. Thus, the material properties, and related tests analysed in this chapter, include the essential properties of RCA to produce concrete and mortars, such as density and water absorption.

Regarding the tests used to analyse the referred properties of RCA, it should be noted that they basically follow (except for water absorption) the same procedures used for NA. However, in what concerns the characteristic values of these properties, it is expected that the density of the RCA is lower than that of the NA, considering the amount of mortar adhered to the RCA, which has a high porosity (higher void volume) and thus significantly contributes to a reduction of density. Similarly, the water absorption of RCA is expected to be much higher than that of NA.

4.2.1 Density

Density is the relationship between the mass of a body and its volume. For aggregates, it corresponds to the relationship between the mass and the total volume of the particles including the pores. These pores, in the case of RCA, are a conditioning factor to the referred density, essentially because some aggregates contain denser and more impermeable particles, while others have more porous particles, and still others

contain a mixture of these two types of particles. A particle can also contain voids or pores, some completely closed and isolated from the outside and others connected and in contact with the outer surface.

The RA's density is influenced both by the nature of the original NA (obviously including their porosity) and by the mortar adhered to their surface. Given that the mortar adhered to the surface of the RCA have a lower density than that of the original NA, it is expected that for RCA with more mortar adhered, the density will be lower. Thus, the RCA's pre-processing method (mainly the number of crushing cycles) will mostly condition the amount of mortar on the surface of the coarse RCA and, consequently, their density. On the other hand, the fine fraction of RCA shows less sensitivity to the number of crushing cycles [3, 4], i.e. for the same crushing process conditions, the amount of mortar adhered to the surface of the obtained RCA increases as the fraction size decreases. This higher amount of mortar adhered to the fine RCA and the consequent increase in their porosity (which causes a decrease in density compared to the original fine NA) is clearly one of the main limitations to the use of this fraction of RCA in the production of concrete and mortars. It is therefore essential to find a balanced value for the number of crushing cycles to obtain a high-quality RCA with properties suitable to produce concrete and mortars.

As mentioned above, another essential factor for the density of RCA is obviously the overall quality of the original concrete from which the RCA were obtained. In this sense, and contrary to what would be expected, some authors [5, 6] refer that the variation in both the amount of cement and the compressive strength of the original concrete does not significantly influence the density of the obtained RCA. On the contrary, other authors [3, 7, 8] point out the existence of a direct correlation between the compressive strength of the original concrete and the density of the RCA obtained. Gokce et al. [7] observed a consistent decrease in the density of the RCA obtained from original concrete with equally decreasing compressive strength, thus confirming that the compressive strength of the original concrete has some influence on the quality of the RCA and thus also on its density.

4.2.2 Water Absorption

Water absorption can be defined as the increase of the aggregate mass due to the filling of its water-permeable pores, expressed as a percentage of its dry mass. The water absorption is naturally dependent on the porosity of the aggregates. However, it is always lower than their porosities, both absolute and apparent, because water, or another fluid, will not penetrate all pores, as many of them are not accessible. The amount and speed with which water accesses the interior of the aggregates depends on the size, continuity, and volume of pores. By comparison with cement paste—which due to its viscosity and particle size cannot penetrate to great depth (but only in the larger pores) -, water, in turn, can penetrate more easily the aggregate particles.

The water absorption of RCA is a property that cannot be disregarded in the production of concrete or mortar, in contrast to what usually happens with NA that

present absorption values typically below 1.6%. RCA usually have higher water absorption values than those observed in the original NA, depending essentially on the factors mentioned in Sect. 4.2.1 for density.

Both the crushing process and the washing of the RCA play an essential role on their water absorption. For a RCA subject to a primary + secondary crushing process (instead of just a primary crushing), a significant decrease in the mortar adhered is expected and, consequently, a reduction of the corresponding water absorption will occur [9–11]. Similarly, proper washing of the RCA can significantly contribute to remove the finer particles that increase the RCA's water absorption [4].

As discussed for density, the quality of the original concrete may have some relevance on the water absorption of the obtained RCA. As mentioned in Sect. 4.2.1, it is possible to find published works with somewhat contradictory results, some claiming a significant influence of the compressive strength of the original concrete by reducing the water absorption of the RCA [8, 12], while others refer to a totally null causal link [13, 14]. From the literature, it is possible to state that the water absorption of the RCA is likely to be affected by the compressive strength of the original concrete.

As observed for density, the RCA fine fraction has a higher water absorption than the coarse fraction. The high amount of mortar adhered to fine particles, as well as the cement paste accumulated in this RCA fraction, is presented as one of the main causes for the referred increase in water absorption [6, 15, 16].

4.2.3 *Determination of Density and Water Absorption*

The knowledge of the aggregates' density value is essential for the evaluation of their properties, but it is also fundamental for the mix design of both concrete and mortars. Similarly, the aggregates' water absorption calculation is extremely relevant, as it allows evaluating the amount of water that they can retain inside and, in this way, it is possible to determine the respective amount of water mix correction. For RCA, water absorption can take on extra relevance due to the usually higher values (when compared to NA). In these cases, the effective W/C ratio and workability may be compromised, making it necessary to get corrections to the amount of water added to the concrete or mortars when mixing.

The density and water absorption of the aggregates are determined according to the methodology presented in the European standard EN 1097-6 [17]. The mentioned standard requires separating the test samples in three particle sizes that must be analysed separately: 0.063–4 mm, 4–31.5 mm and 31.5–63 mm.

Regarding the test method, EN 1097-6 [17] divides the fraction presented by two test methodologies:

- Pycnometer method—for aggregates that pass through the 31.5 mm sieve and are retained on the 0.063 mm sieve; however, the test procedures for this methodology vary depending on whether they are fine or coarse aggregates;

- Wire mesh basket method—for aggregates that pass through the 63 mm sieve and are retained on the 31.5 mm sieve.

As mentioned above, the pycnometer method is applied to fractions 0.063–4 mm (fine aggregates) and 4–31.5 mm (coarse aggregates). This difference in the procedure of the test occurs because in sands the operation of removing the surface water is not possible as in coarse aggregates.

4.2.3.1 EN 1097-6 [17] Tests Limitations for Fine RCA

The methodology, presented in EN 1097-6 [17] for the assessment of water density and absorption, has some limitations when the particles to be tested are fine recycled aggregates [18]. In this case, due essentially to the mortar adhered to the surface of the fine particles, it is possible to observe a set of problems that lead to altered results. These limitations can be divided into two groups. The first one is associated with the characteristics of fine recycled aggregates that limit the accuracy of the results obtained. The second group is more associated with the limitations of the outputs of the EN 1097-6 [17] tests, which do not provide an adequate response to the specific needs of using fine recycled aggregates. As a way of solving these problems, in 2001 a first proposal for a new method to determine the density and water absorption of fine RCA appeared. Leite [19] proposed a methodology based on a hydrostatic scale. Despite the evident improvements to the traditional methodology used for natural aggregates, there are still numerous limitations, namely: although the deflocculating process of the finer particles improves relative to the original method, it is observed that some extremely fine materials still represent a problem for the release of the occluded air; on the other hand, this method still does not present a solution for the water absorption relative to the initial instant of the process.

4.2.3.2 New Methodology to Determine the Density and Water Absorption of Fine RCA

In 2013, Rodrigues et al. [18] presented a new method to determine the water absorption of fine RCA. The authors proposed the use of the pycnometer method combined with the hydrostatic scale used by Leite [19] and the innovation of dispersing the particles using sodium hexametaphosphate [(NaPO₃)₆]. To avoid the particles flocculation and with clear advantages in the process of release of the occluded air in the samples, the fine aggregates are dispersed in a solution of sodium hexametaphosphate diluted in distilled water with a concentration of 1 g/L [18]. The proposed test method is thus divided into two distinct but complementary phases, namely:

- Phase 1—Application of the pycnometer method: this phase is almost identical to the one in EN 1097-6 [17] for the “Pycnometer method for fine aggregates (0.063–4 mm)”. The main difference lies in the preparation of the fine RCA sample, which



Fig. 4.1 Left: Sample immersed in sodium hexametaphosphate solution; right: Submersion of the set (sample, sieves, and support) for hydrostatic weighing

is immersed in a diluted solution of 1 g/L sodium hexametaphosphate in distilled water for 24 h (Fig. 4.1).

- Phase 2—Application of the hydrostatic scale method (Fig. 4.1): this phase consists of a methodology adapted from Leite [19] proposal and EN 1097-6 [17].

According to this, in the first phase (pycnometer method), it is possible to determine more accurately the absolute overall water absorption values and the density of the fine RCA. With the second phase (hydrostatic scale), it is viable to know the water absorption first values (2–3 min after immersion), as well as its variation over time. This new methodology is now in common use, with excellent results in the dispersion of fine RCA particles and in the contribution to the release of air from the samples. In addition, it is also worth noting the possibility of knowing the initial water absorption values, coinciding with the most critical phase of absorption, which, in these aggregates, assumes special relevance.

4.3 Fresh Recycled Aggregate Concrete Properties

The characterisation of concrete in the fresh state is a fundamental tool to control the production of concrete, as it has a significant impact on its performance in the hardened state.

4.3.1 Fresh Concrete Density

The compacted fresh concrete density is directly related to the density of its components as well as of its compactness. In the concrete composition, the fraction corresponding to the aggregates is predominant, thus justifying the greater influence of the aggregates' density on this property. It can thus be said that the difference between the fresh density of a conventional concrete with NA and that of a concrete with RCA results from the difference in density between RCA and NA, as they represent the largest portion of the constituents. In addition, the RCA's more angular shape causes an increase in concrete voids, which may also contribute to the decrease in fresh density of this type of concrete compared to the conventional one. As abovementioned, the low density and mortar adhered to the surface of the RCA are the main causes for the decrease of fresh density of concrete produced with RCA. Similarly, the increase in the substitution ratio of NA with RCA contributes to the decrease of fresh concrete density.

The compacted fresh concrete density is determined according to the methodology presented in the European standard EN 12350-6 [20]. The methodology presented in this standard may not be applicable to very stiff concrete that cannot be compacted by normal vibration. The compacted fresh concrete density test allows the evaluation of the compactness of concrete in the fresh state and the drawing of conclusions on its porosity in the hardened state. The test procedure is simple and begins by filling a rigid container of 10 L of capacity, in two layers properly compacted using, for example, a mechanical vibrator. Finally, the container and its contents are weighed to determine its mass. The compacted fresh concrete density is calculated using Eq. (4.1):

$$D = \frac{m_2 - m_1}{V} \quad (4.1)$$

where: D—fresh concrete density (kg/m^3); m_1 —mass of the empty container (kg); m_2 —mass of the container filled with compacted concrete (kg) and V—container volume (m^3).

The variation in compacted fresh concrete density between concrete with RCA and its equivalent with NA can be significant. However, it is possible to find values usually below 5% of variation (see Table 4.1). For example, Xiao et al. [21] found a 5% decrease in the fresh density of concrete with 100% RCA compared to a reference concrete with 100% NA. Etxeberria et al. [11] refer to a 3.3% decrease in concrete with 100% replacement of coarse NA with coarse RCA. On the other hand, Dong et al. [22] show a variation of only 0.8%, but for a replacement ratio of 50% recycled coarse aggregates. Marinković et al. [23], like Xiao et al. [21] and Verian et al. [24], present a difference of approximately 4.8% but for a replacement ratio of 65%, while the rest refer to a replacement ratio of 100% (Table 4.1).

Table 4.1 Compacted fresh concrete density, for different substitution ratios of NA with RCA

Fresh concrete's density	Reference values		
	Maximum	Minimum	Average
D _{RC,0%}	2420	2366	2398
D _{20%}	2400	2359	2378
D _{50%}	2390	2340	2355
D _{100%}	2340	2246	2287

Sources Marinković et al. [23], Xiao et al. [21], Verian et al. [24], Dong et al. [22] and Fonseca et al. [25]

4.3.2 Workability

Concrete workability is one of the most tested properties of fresh concrete. This control can be done expeditiously by using the Abrams funnel, easily carried out on site without using complex laboratory equipment.

With this test, it is also possible to qualitatively assess the effective W/C ratio. It is thus possible to detect possible errors in the mix proportions and validate, for instance, the coarse RCA water absorption compensation method.

In order to compare the performance of concrete produced with RCA with that of concrete with NA, it is important to know the water absorption of the aggregates and to correct the mixing water while maintaining the effective W/C ratio as constant as possible. To compensate for the RCA higher water absorption, there are three possible ways:

- To increase the binder's content, a measure with some environmental limitations and that increases the overall cost;
- To increase the apparent W/C ratio, which can lead to lower performance of the RCA concrete, both mechanical and durability wise;
- To use plasticizers or superplasticizers.

The measures described have direct consequences on the quality of concrete. According to Bravo et al. [26], the increase of W/C ratio leads to a worse mechanical and durability performance, while the increase in binder content and the use of plasticizers are solutions that result in higher economic costs.

Therefore, to maintain the same workability between a concrete with RCA and an equivalent concrete with NA, it is usual to compensate for the greater water absorption of the RCA. There are two widely used methodologies:

- Pre-saturate the RCA;
- Add an extra amount of water during mixing, in order to compensate for the water absorbed by the RCA.

Ferreira et al. [27] showed that the pre-saturation of the RCA is detrimental to the mechanical performance of concrete and, in particular, to the durability performance, thus being preferable to compensate the absorption by adding water to the mix. Poon et al. [12] reached the same conclusion, stating that to pre-saturate RCA is harmful to concrete. Despite the higher economic costs, the use of plasticizers or superplasticizers is also a very effective technique to compensate for the workability loss due to the high RCA water absorption. This solution allows adding a smaller amount of compensating water to the mix, thus increasing the performance of the produced concrete [28].

Workability, using the slump test, is determined according to the methodology presented in the European standard EN 12350-2 [29]. The concrete is placed inside the Abrams funnel in three layers of identical depth, each compacted with 25 strokes. After the compaction process, the funnel is lifted, causing the concrete to slump by its own weight. The test result is given by the slump measure from the difference between the height of the mould (300 mm) and the highest point of the specimen after demoulding.

In terms of workability, there are some relevant differences between concrete produced with NA or RCA. Thus, as RCA have a higher water absorption than NA, it is expected that a concrete that incorporates the first ones will present less workability than an equivalent concrete with NA only and the same W/C ratio.

Taking into account the effect of the W/C ratio on the workability of concrete produced with RCA, it is worth noting the work of Leite [19], who evaluated the effect of RCA on concrete with different W/C ratios. The author refers the reduction of slump with the increase of W/C ratio, which is justified by the smaller amount of cement present in the mix. Cement, due to its reduced size, behaves as a lubricant for the mix in the fresh state. The author also stresses the high variability associated with the workability test with the Abrams funnel. Leite [19] justifies this variability with the higher roughness of RCA compared to NA, also allowing for lower slumps, which is explained by the fact that RCA absorb a higher amount of water than NA.

On the other hand, the density of RCA also influences the workability of concrete. The workability tests using the Abrams funnel carried out by Carrijo [30] indicate a tendency to reduce workability with the decrease in the density class of the RCA used. This behaviour in the fresh state of concrete with RCA is related to the greater water absorption of RCA and their lower density.

As the other parameters mentioned, the fine RCA content also influences the workability of concrete. Solymar [31] studied the workability of concrete, based on the slump flow test, and observed that, as the content of fine RCA increased, the slump flow decreased. The author justifies this by stating that the use of fine RCA increases the friction between the aggregate particles and, therefore, increases the consistency of concrete (consequently decreasing its workability).

4.4 Hardened Recycled Aggregate Concrete Properties

The differences between the properties of RCA and NA (referred to in Sect. 4.4.2) will necessarily cause a different behaviour between concrete produced with RCA and NA. In this sense, a survey on the testing techniques and performance levels of the main properties in the hardened state of concrete produced with RCA compared to concrete with NA is presented in the following subsections.

4.4.1 Density

Several factors significantly contribute to the decrease in density of concrete with RCA, in addition to the reduction of the density of RCA compared to NA, namely: the substitution ratio of NA with RCA, the overall quality of the RCA and the age of the test.

The hardened concrete density is determined according to the methodology presented in European standard EN 12390-7 [32]. This standard specifies a method to determine the density of hardened concrete. It is applicable to lightweight, normal-weight and heavyweight concrete. It differentiates between hardened concrete in the following states: as received, water saturated and oven dried.

Accordingly, with the aforementioned European standard it is possible to determine the mass and volume of hardened concrete specimens and hence calculate the respective density. The density calculation is performed based on the determined values of the mass and volume of the specimen using Eq. (4.2):

$$D = \frac{m}{V} \quad (4.2)$$

where: D—density relating to the condition of the specimen (as received, water saturated or oven dried) and the method to determine the volume (kg/m^3); m—mass of the specimen determined (as received, water saturated or oven dried) at the time of the test (kg) and V—specimen volume (obtained by water displacing or using designated dimensions) (m^3).

In general, it is possible to state that the density of concrete produced with RCA decreases with the increase in the substitution ratio of NA with RCA. Accordingly, Pereira-de-Oliveira et al. [33] conducted a study involving only coarse RCA replacing coarse NA (with replacement ratios of 0%, 20%, 40% and 100%). The authors reported a decrease (albeit moderate) in the density of concrete with the increase of the replacement ratio, with a higher variation, compared to the reference concrete, for the higher replacement ratio at 28 days. The authors also reported a reduction in density from 7 to 28 days of only 0.7% (excluding the higher replacement ratio).

Pereira-de-Oliveira et al. [33] highlighted the importance of the density of the coarse RCA themselves (which is lower than that of the coarse NA) on the density of the produced concrete.

4.4.2 Compressive Strength

In general, it is possible to state that the use of RCA instead of NA causes a decrease in the concrete compressive strength. This decrease in strength is attributed essentially to three main factors [24, 34]: increase in concrete with RCA of the effective W/C ratio caused basically by the higher water absorption of RCA and its flat and angular shape. In other words, the compressive strength of concrete with RCA depends both on the properties and amount of RCA, and on the W/C ratio, NA substitution ratio, amount and quality of the mortar adhered to the RCA's surface, as well as, as mentioned above, the origin and pre-processing mode of RCA [24, 34].

However, these strength differences tend to be more significant mostly for concrete of higher strength classes (usually classes outside the usual and recommended application range for RCA) or when the RCA density is much lower than conventional NA's. On the other hand, when the substitution ratio increases, the lower strength of RCA compared to NA's, due to the mortar adhered, causes a decrease in the concrete compressive strength. It can therefore be said that, as a general rule, by keeping the size distribution curve of RCA equal to that of NA, controlling the replacement ratio and maintaining the workability of the identical concrete, the differences between the strength of concrete with RCA and a reference mix (with NA only) will be minimal. For example, Evangelista and de Brito [35] indicated a limit of 30% of substitution ratio of fine NA with fine RCA for the concrete compressive strength loss not to be significant.

Regarding strength development over time, it should be noted that some authors mention an increase in this property at older ages compared to reference concrete with NA only [4, 24, 35]. The authors point out the influence of the amount of mortar adhered to the RCA's surface and the consequent presence of non-hydrated old cement that will react with water at older ages and thus increase the mix compressive strength [24, 36].

Regarding the influence of the RCA's own mechanical performance on the concrete compressive strength, it should be noted that, for conventional concrete, its strength depends essentially on the strength of the cement paste. In these cases, the strength of the aggregates assumes a secondary role without negatively influencing the concrete strength. However, for particular cases such as lightweight aggregates or RCA (due essentially to the mortar adhered), where their strength approaches approximately half of the common value of cement paste, the strength of concrete becomes more dependent on the strength of the aggregates [3].

The hardened concrete compressive strength is determined according to the methodology presented in the European standard EN 12390-3 [37]. This test intends to evaluate the strength capacity of concrete when subjected to a uniform compression stress. The test specimen shall be a cube, cylinder or core and must remain, until the test date, in a wet chamber. Before carrying out the test, the surface moisture must be removed. The specimen properly positioned in the loading apparatus is subjected to the application of a load at a constant rate between 0.2 and 1 MPa/s, until failure. After the test, it is necessary to inspect the specimen to find out whether a satisfactory or unsatisfactory failure occurred according to Figs. 1, 2, 3 and 4 of EN 12390-3 [37]. The compressive strength is then calculated by Eq. (4.3):

$$f_c = \frac{F}{A_c} \quad (4.3)$$

where: f_c —compressive strength, in N/mm²; F —maximum load at failure, in N; and A_c —cross-sectional area of the specimen on which the compressive force acts, in mm².

According to what has been presented, the compressive strength of concrete produced with RCA depends on numerous factors, which results in innumerable contradictory published results. In this sense, for example Etxeberria et al. [11] refer that, for a concrete with RCA to reach the same level of strength as its equivalent with NA, it would be necessary to increase the amount of cement, making this RCA a solution that is not economically viable or sustainable. The authors present these conclusions based on a study in which they obtained a decrease in compressive strength of approximately 25% for concrete with 100% coarse RCA compared to a reference concrete with the same amount of cement and W/C ratio. Referring now to the properties of RCA that influence the concrete strength (mentioned at the beginning of this sub-section), the paste adhered to RCA used by Etxeberria et al. [11] was of very low quality and hence the obtained variation. The authors also stated that, for lower replacement ratios (for example, around 20%), the decrease in concrete strength is very low.

Similarly, Yaprak et al. [38] obtained a compressive strength decrease of approximately 35% between a reference concrete and a concrete with 100% fine RCA. The authors also emphasize the greater porosity and water absorption of the adhered mortar, which leads to a higher W/C ratio of the mix and to a weaker cement paste/RCA connection, as the main causes for the results obtained. On the contrary, Rao et al. [39] presented higher values (of compressive strength at 7 days for concrete with 50% and 100% coarse RCA instead of NA) than those of the respective reference concrete. In this case, the authors emphasize the high-water absorption and the rough texture of RCA, as the main reason for the best cement paste/AR connection. Conversely, Chandra [6] refers that for substitution ratios of NA with RCA up to 30%, no relevant differences were observed in compressive strength.

4.4.3 Splitting Tensile Strength

Concrete splitting tensile strength depends on several composition parameters, such as with cement content or W/C ratio, increasing with the first and decreasing with the second. The aggregate/paste transition zone is another conditioning factor of this property. Other conditioning factors may be the aggregates' type and quality, as well as the paste microstructure (not only in the transition zone). Mehta and Monteiro [40] reported that the microstructure properties in the transition zone tend to affect more the tensile strength than the compressive strength. It can be said, however, that the trends identified for compressive strength, in particular those related to W/C ratio, are maintained for tension, although in a less noticeable way.

As with the compressive strength, it is expected that the tensile strength of concrete with RCA decreases with the increase in substitution ratio of NA with RCA, attributing this behaviour to the lower tensile strength of the latter, which in turn is due to the mortar adhered to the RCA. Despite this trend, the surface of RCA, which is normally rougher than that of NA, contributes favourably to the tensile strength of concrete. However, the increase in W/C ratio to compensate for the loss of workability of these mixes, traditionally attributed to the greater water absorption capacity and surface roughness of RCA compared to NA's, causes the decrease in tensile strength.

Some authors [11, 41] thus refer that concrete with RCA presents a tensile strength equivalent to that of conventional concrete, i.e. they state that the presence of RCA is more relevant for compressive strength than for tensile strength. These authors emphasize the good interconnection between the aggregates and the mortar matrix, improved by the increased water absorption of the AR. Etxeberria et al. [11] state that the effect of the adhered mortar to the RCA's surface assumes a very relevant role creating a weak spot (in the transition zone aggregate/cement paste) for compressive strength failure to occur. However, when creating that smoother transition between aggregate/cement paste, it causes an increase in tensile strength.

However, the negative influence of the increase in the fine RCA replacement ratio on the evolution of the tensile strength should be noted. In this case, a slight decrease in this property compared to a reference concrete (with NA only) is expected. Verian et al. [24] show differences up to 10% in tensile strength between concrete with RCA and with NA, depending naturally on the substitution ratio of NA with RCA.

The hardened concrete splitting tensile strength is determined according to the methodology presented in the European standard EN 12390-6 [42]. This standard specifies a method to determine the splitting tensile strength of cylindrical test specimens of hardened concrete. This test is usually performed on cylindrical test specimens with 150 mm diameter and 300 mm height, subjected to a wet curing process by immersion in water at 20 ± 2 °C until the test age. The rate used to apply the load should be 3.5 kN/s, within the range of 0.05 ± 0.01 MPa/s as per EN 12390-6 [42]. The cylindrical specimen is subjected to a compressive force, applied over a narrow

section along its entire length using two steel loading pieces in contact with the specimen by means of two strips of pressed cardboard. The splitting tensile strength is then calculated by Eq. (4.4):

$$f_{ct} = \frac{2 \times F}{\pi \times L \times d} \quad (4.4)$$

where: f_{ct} —splitting tensile strength, in N/mm²; F —maximum load at failure, in N; L —specimen contact line length, in mm; d —cross section dimension, in mm.

This test also makes it possible to observe the failure surface of the test specimen. Therefore, it is possible to observe/validate the uniform distribution of the aggregates in the solid matrix throughout the entire specimen without particle agglomeration or the occurrence of any segregation or exudation phenomena. It is also possible to check whether the failure surface always crosses the aggregates and whether any form of failure occurs through the interface area between the aggregates and the cement paste, which may provide a good indication of the quality of the aggregates/paste transition zone.

4.4.4 Modulus of Elasticity

In theoretical terms and according to simplified regulatory forecasting models, the modulus of elasticity depends almost exclusively on compressive strength. Thus, for equal compressive strength values, equivalent moduli of elasticity are expected, both for concrete with RCA and NA. However, the experimental value of the modulus of elasticity, both for concrete with RCA and NA, depends on the proportion of the individual modulus value of the various components and their percentages by volume. In other words, in concrete containing aggregates with higher mechanical strength values, the modulus of elasticity tends to increase. On the other hand, this value tends to decrease with the increase of the amount of cement paste and with the increase of porosity of concrete. Therefore, Assié [43] mentioned, in his work, that, in a concrete formulated with conventional aggregates, the modulus of elasticity of the mortar phase presents a value between approximately 6 and 25 GPa, about 3–15 times lower than the modulus of elasticity of the aggregates (60–100 GPa).

In the particular case of concrete with RCA, the main conditioning factor of this property is associated with the modulus of elasticity of the RCA itself. The modulus of elasticity of RCA is usually lower than that of NA, thus it is expectable that the modulus of elasticity of concrete (with RCA) is also lower than that of an equivalent reference concrete (with NA only). However, it is possible to find published results of the modulus of elasticity of concrete with RCA with significant variations and naturally very associated with the quality of the used RCA. For example, while Xiao et al. [21] referred in their study that concrete with 100% RCA modulus of elasticity showed a reduction of approximately 45% by comparison with a reference concrete (with NA only), other authors showed reductions of only 20% [44]. The most likely

cause for the differences presented is the quality of the aggregates, proving the more significant influence of the aggregates on concrete modulus of elasticity than that of the cement paste, which in the case of concrete with AR assumes a relevant role.

The determination of the secant modulus of elasticity can be carried out according to LNEC E 397 [45] specification on cylindrical specimens with 150 mm diameter and 300 mm height, subjected to the wet curing process by immersion in water at 20 \pm 2 °C up to test age. The specimens must be instrumented with two strain gauges, in diametrically opposite positions. The secant modulus of elasticity is determined by applying loading—unloading cycles where the stress should vary between 0.5 and 1 MPa and up to 1/3 of the ultimate compressive strength, registering the initial and final strains obtained. The test ends when the difference in the average of the strain variations between two consecutive cycles is less than 10%. The secant modulus of elasticity (E_c) is then determined, according to the LNEC E 397 [45] specification, by Eq. (4.5):

$$E_c = \frac{\Delta\sigma}{\Delta\varepsilon} = \frac{\sigma_a - \sigma_b}{\varepsilon_{a,n} - \varepsilon_{b,n}} \times 10^{-3} \quad (4.5)$$

where: E_c —secant modulus of elasticity, in GPa; σ_a —maximum applied stress, in MPa; σ_b —initial stress, in MPa; $\varepsilon_{a,n}$ —strain for σ_a measured in the umpteenth load cycle; $\varepsilon_{b,n}$ —strain for σ_b measured in the umpteenth load cycle.

The dynamic modulus of elasticity can be determined using the ultrasound pulse velocity test (UPV), according to EN 12504-4 [46] and ASTM C597 [47] using, for example, 15 × 15 × 15 cm or $\phi 15 \times 30$ cm test pieces. After determining UPV (V), density (ρ) and considering the Poisson's ratio (μ) of concrete, it is possible to estimate the dynamic modulus of elasticity (E_d) based on Eq. (4.6), referred to in Sect. 5.1 of ASTM C597 [47]:

$$V = \sqrt{\frac{E_d(1 - \mu)}{\rho(1 + \mu)(1 - 2\mu)}} \quad (4.6)$$

This method of determining the dynamic modulus of elasticity is because the UPV waves in a concrete element can be correlated with its elastic properties through Eq. (4.6). Considering that UPV depends, almost exclusively, on the elastic properties of the material and not so much on its size, this method is also used to assess the quality of concrete in general [48].

As presented at the beginning of this section, the modulus of elasticity of concrete is fundamentally influenced by the modulus of elasticity of the cement paste and aggregates, as well as by the connections established between these two phases. Coarse RCA are more deformable than the original rock due to the mortar adhered to their surface, which makes its overall stiffness lower. In this case, the modulus of elasticity in concrete with coarse RCA is obviously lower than that of an equivalent reference concrete. Comparing RCA concrete with the respective reference concrete (with NA only), the trends mentioned for compressive strength remain for

the modulus of elasticity, albeit in a more pronounced way, i.e. the higher the substitution ratio of NA with RCA, the greater the decrease in the modulus of elasticity [21, 49].

For the use of fine RCA in substitution of fine NA, it is found that, for example, Evangelista and de Brito [35] obtained a reduction in the secant modulus of elasticity with the increase of the substitution ratio (consistent with that mentioned for coarse RCA). The authors found that, for concrete with 30% fine RCA, the secant modulus of elasticity reduction was not very high, but that for 100% replacement of fine NA with fine RCA, this becomes significant. Thus, the authors refer that, for small incorporation ratios, it is possible that the concrete stiffness is not very influenced by fine RCA. Similarly, Pereira et al. [50] obtained a decrease in the secant modulus of elasticity with the increase in the incorporation ratio of fine RCA, with average reductions between 13 and 19%, for concrete with 100% of fine RCA.

4.4.5 Shrinkage

The phenomenon of concrete shrinkage represents, in a simple way, its dimensional variation without any type of loading. There are several types of shrinkage that can occur alone or simultaneously. They are usually subdivided into plastic, drying, autogenous, thermal, and carbonation shrinkage [51–53].

In the case of concrete produced with RCA, a rise in the total shrinkage with the increase in the substitution ratio of NA with RCA (both coarse and fine) is expected. As mentioned before, the total shrinkage of concrete is strongly conditioned by two main factors [48]: amount of cement paste and W/C ratio.

The amount of mortar adhered to the surface of RCA, associated with the cement paste of the new concrete, necessarily causes an increase in the total paste volume and, consequently, an increase in total shrinkage [24, 35]. The influence of fine RCA on total shrinkage is more negative than of coarse RCA. Fine RCA have a higher relative amount of mortar adhered to them, which implies more water absorption and greater total shrinkage. Verian et al. [24] referred higher values of total shrinkage of concrete with coarse RCA, between 20 and 50%, in relation to the respective reference concrete, while concrete with fine RCA presented on average values from 70 to 100%.

The determination of the total shrinkage strain can be carried out according to the LNEC E 398 [54] specification on prismatic test specimens. This test makes it possible to determine the variation in the dimensions of the concrete specimens over time, which may be positive or negative (shrinkage or expansion) depending on the curing conditions. The test starts immediately after demoulding, at 24 h, keeping the test specimens at an ambient temperature of 20 ± 2 °C and a relative humidity of $50 \pm 5\%$ during the entire testing period. Using a deflectometer enables recording the variation in length between the two metallic pins glued to the specimen's surface, compared to the standard bar supplied with the deflectometer (Fig. 4.2).



Fig. 4.2 Total shrinkage test

The metal pins are glued to the specimen's surface immediately after demoulding, using a (high resistance and quick drying) two-component epoxy-based glue and with the support of a standard bar, in order to position the metal pins correctly. To determine total shrinkage, the difference between the length of a specimen after drying under controlled conditions and its length immediately after demoulding is measured. Through Eq. (4.7), the total shrinkage value at a given moment can be obtained:

$$\varepsilon = \frac{d_f - d_i}{d_i} \quad (4.7)$$

where: ε —total shrinkage value at a given moment, in mm/mm; d_i —initial distance measured by the deflectometer, in mm; d_f —distance measured by the deflectometer at a given moment, in mm.

Total shrinkage consists of the dimensional variation of concrete, a phenomenon that occurs from the end of compaction until reaching the limit of balance with the environment with constant hygrometric conditions and without any applied stress. When restricted, shrinkage can result in cracks that impair the appearance of concrete and make it more vulnerable to degradation mechanisms, thus affecting its durability. Shrinkage depends on several factors, but in the particular case of concrete with RCA it is clearly one of the most affected properties by the incorporation of this type of aggregates. The mortar adhered to the surface of RCA has a capacity to restrict the deformation (shrinkage) of the cement paste significantly less than that of NA. In addition, it is also worth mentioning the influence of fine RCA, which, because of their higher percentages of mortar adhered, have an even lower ability to restrict the deformation of the cement paste. However, Evangelista and de Brito [35] pointed out that the fine RCA's ability to retain water can be beneficial, as it supplies water to the concrete crystalline structure and thus ensures the continuation of cement's hydration reactions. Thus, the authors refer that, in the case of concrete with fine RCA, a lower or even zero total shrinkage in the first ages is expected, evolving only in more advanced ages (after the referred absorbed water is consumed) in a similar way to concrete with coarse RCA and reaching, at these ages, values naturally higher than those obtained in a reference concrete.

4.4.6 Durability Properties

The durability of construction materials are detailed in Chap. 5 —*Innovative Durability Tests on Construction Materials*. Therefore, only a brief context in terms of durability performance for concrete produced with RCA is presented here.

Although the requirements in terms of durability properties of concrete with RCA are the same as for a conventional concrete, the quality of RCA is clearly different from that of conventionally used NA. In this sense, it can be said that its properties in the hardened state with respect to durability may still be slightly different from those presented by conventional concrete. The main differences between RCA and NA are based on the amount of mortar adhered to the surface of RCA and the consequent change in their water absorption and stiffness. More water absorption may also lead to an increase in the effective W/C ratio, which can alter the formulation of concrete with RCA. These differences can substantially affect the durability of concrete with RCA when compared to a conventional concrete with NA only, namely the development of its microstructure and consequently the effect of carbonation and chloride penetration, among other actions.

For concrete with RCA, once again, the high porosity of RCA negatively influences the performance in terms of the durability of the respective concrete. As they are more porous, concrete with RCA will have a greater water absorption, which is expected to increase with the increase in the RCA incorporation ratio. Several research works, such as Kou and Poon [55], Matias and de Brito [56], and Rao et al. [39], concluded that absorption by both capillarity and immersion was higher in concrete with RCA. Maleševe et al. [57] obtained an absorption value about 44% higher for concrete with 100% replacement of NA with RCA and 22% higher for concrete with 50% replacement, compared to reference concrete with NA only.

Regarding chloride penetration, it is expected that, as the substitution ratio increases, there will be a lower resistance of concrete with RCA to the diffusion of chloride ions. This trend can be justified by the greater permeability of these mixes compared to a reference concrete with NA only, which increases with the substitution ratio. The greater permeability of these mixes is a consequence of the high porosity of the RCA's adhered mortar. This property of hardened concrete is an important indicator of the durability of this material. It depends on the same factors as water absorption and, naturally, shows similar trends. Therefore, as concrete produced with RCA has the worst characteristics of porosity and absorption, it is expected to present worse performance in terms of resistance to the chloride penetration [58]. Gomes [59] found that, in concrete with coarse RCA substitution ratios of 50%, the resistance to chloride penetration decreased only 5.6% compared to the reference concrete with NA only. On the other hand, Olorunsogo [60] observed greater chlorides diffusion from concrete with RCA compared to a reference concrete, with increments between 41 and 87% in concrete with 100% substitution ratios.

Carbonation consists of the reaction of carbon dioxide (CO_2) present in the atmosphere with minerals from hydrated cement, a reaction that occurs under certain hygrometric conditions. The substitution of NA with RCA expectably leads to a

decrease in resistance to carbonation, evidenced by the increase in the depth of CO₂. This behaviour is fundamentally justified by the greater porosity of RCA compared to NA. The increase in mixing water, in order to compensate for the greater absorption of AR, also contributes to a reduction of the resistance to carbonation, taking into account the greater porosity that it causes in hardened concrete. In fact, several research studies show that this property can be significantly affected by the replacement of NA with RCA [58]. It is also expected that the use of fine RCA instead of fine NA increases the carbonation of concrete even more sharply than when replacing coarse NA with coarse RCA [58].

4.5 Testing Bituminous Mixtures Incorporating Recycling Aggregates

4.5.1 Materials and General Testing

Bituminous mixtures can incorporate RA as coarse or fine aggregates but also as filler material. These RA can have different origins than waste materials, and most commonly are derived from CDW. Recycled concrete aggregate (RCA) and reclaimed asphalt pavement (RAP) obtained from CDW are the most current RA used in bituminous mixtures. RCA are the RA obtained exclusively from crushing of demolished concrete structures. RAP is the waste material removed from asphalt pavements (milling or crushing) and may end up being rejected or used in surplus mixes during the production phase [61]. Other waste materials from industrial activities can also be considered, mainly fulfilling the purpose of filler aggregates in bituminous mixtures (e.g. quarry waste, plastic, glass, brick, tiles and other ceramic products). The diversity of RA, in terms of quality and homogeneity, could have a great impact on some properties that are critical to the bituminous mixture performance.

The aggregates are an important component of a bituminous mixture, with a significant impact on the performance of the mixture itself. They make up roughly 95% of the weight of the bituminous mixture components. Neves et al. [62, 63] presented an extensive description of the aggregate test methods for the latest technical specifications for civil engineering applications. For roads, airfields and other trafficked areas, the specifications for aggregates for bituminous mixtures and surface treatments are laid out in EN 13043 [64]. The main properties of the aggregates are classified in geometrical, physical and chemical categories. In general, these properties and the corresponding test methods are also applicable to RA. The geometrical properties are important and must take into consideration the size, grading, fines content, fines quality, and shape of the aggregates. The physical properties have to do with resistance to fragmentation (Los Angeles), resistance to wear (micro-Deval), particle density and water absorption, bulk density, polishing, resistance to surface abrasion and resistance to abrasion from studded tyres for application in surface courses, and affinity to the bituminous binder. In the event of the bituminous mixture

incorporating RA, the chemical requirements gain greater importance. In addition to a general petrographic description, evaluation of contaminators and volume stability are important in the case of the use of RA coarse aggregates. Identical requirements must be met in the case of filler aggregate, taking into account the same purposes: grading, density, voids of dry compacted filler, harmful fines, and water susceptibility. The evaluation of the aggregate durability is also particularly important and freeze–thaw and thermal shock resistances are some of the most important properties for this purpose.

Aggregate density and water absorption are currently ascertained in accordance with EN 1097-6 [17], as described in detail in Sect. 4.2.3. Generally speaking, RA tend to exhibit high porosity and, consequently, lower density and higher water absorption than NA. This is particularly the case for RCA, due to the presence of old cement mortar. There is a correlation between the water absorption and the required bituminous binder content established by the mixture design. Accordingly, the application of RA in bituminous mixtures can lead to the non-advantageous increase in the binder content. Thus, particular attention to density and water absorption is recommended. The alternative methods presented in Sect. 4.2.3 can also be adopted.

4.5.2 Affinity Between Recycled Aggregates and Bitumen

The diversity of RA, in terms of quality and homogeneity, could have a considerable impact on some properties that are critical to the bituminous mixture's performance. This is true for the affinity between aggregates and bitumen. EN 12697-11 [65] specifies the procedures for determining the affinity between aggregate and bitumen and the influence thereof on the susceptibility of the aggregate-bitumen combination to stripping.

Susceptibility to stripping can be considered as an indirect measure of the power of the bitumen to adhere to RA, or of different bitumen types to adhere to a single recycled aggregate. The procedures can also be used to evaluate the effect of moisture on a given aggregate-bitumen combination with or without different types of adhesion agents. Different test methods are mentioned in EN 12697-11 [65], but the rolling bottle method is extremely common. The affinity is expressed by visual record of the degree of bitumen coverage on non-compacted bitumen-coated mineral aggregate particles after performing the test during a total of 24 h rolling time. When testing RA, it is recommended to make additional observations after 48 h and 72 h for a more accurate evaluation of the binder coverage.

Figure 4.3 shows examples of RCA samples after 6 h (Fig. 4.3a), 24 h (Fig. 4.3b) and 72 h (Fig. 4.3c) of testing in the bottle rolling machine, thus allowing for a visual identification of the bitumen coverage [66]. Generally speaking, a tendency towards decreased affinity between RCA and bitumen is observed.

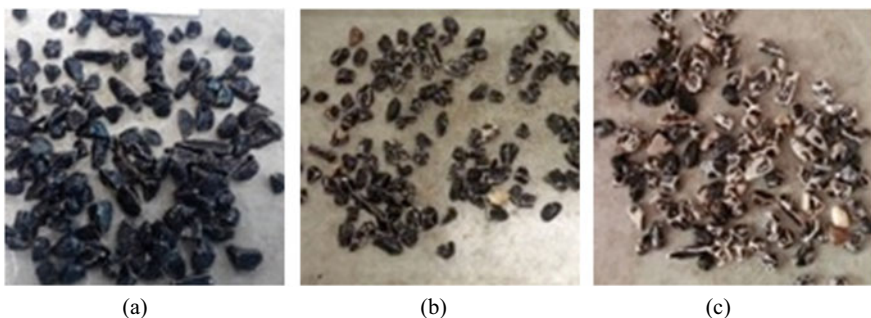


Fig. 4.3 Evolution of the affinity between RCA and bitumen in the rolling bottle method: **a** 6 h; **b** 24 h; and **c** 72 h [66]

4.5.3 Evaluation of Mechanical Performance

The design and quality control based on mechanical performance gains particular importance in the context of the utilisation of non-traditional materials in civil engineering applications. The fact that RA do not meet the requirements established for NA should not compromise their application if long-term performance is ensured and validated. In addition to the economic and environmental advantages of the utilisation of RA in bituminous mixtures, the majority of researchers and designers confirm that simply by incorporating adequate RA in the composition of the different types of bituminous mixtures does not significantly compromise, in general, their mechanical performance for the diverse applications in road pavements [67–69]. For example, in the case of RCA, due to the more angular shape and textural roughness of the particles, there is usually an increase in the resistance to the permanent deformation of the bituminous mixture.

The mechanical and durability test methods for the long-term evaluation of the performance of bituminous mixtures that incorporate RA are also adequate: determination of water sensitivity, susceptibility to permanent deformation, stiffness evaluation, and resistance to fatigue. The Marshall test based on EN 12697-34 [70] is a quite common empirical method used in the design and quality control that could also be adapted to bituminous mixtures with RA.

Test specimens are frequently manufactured in laboratory by impact or gyratory compaction in cylindrical moulds and by roller compactor in prismatic moulds. The adjustment of the compaction energy where RA are utilised is admissible. The tests can also be applied to specimens extracted from pavements.

Unsatisfactory durability related to susceptibility to water action is one of the main problems reported when incorporating RA into bituminous mixtures. The American standard MIL-STD-620A—method 104 (CRD-C 652-95)—deals with water sensitivity assessment based on the comparison between Marshall stability of two groups of test specimens [71]: the first group (unconditioned) is immersed in water at 60 °C for 30 min; the second group (conditioned) stays in a water bath at 60 °C for 24 h.

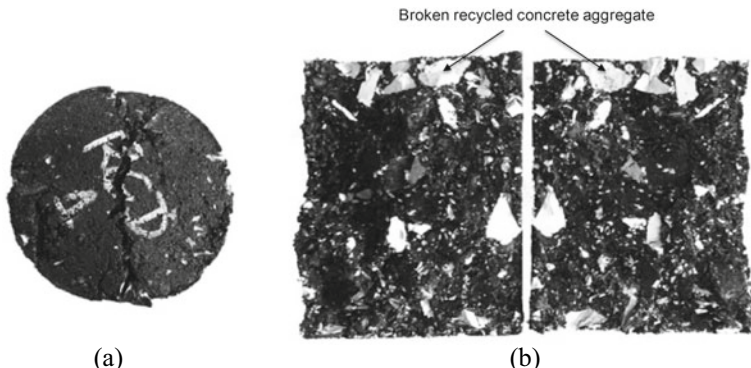


Fig. 4.4 Type of failure of a RCA bituminous mixture after the indirect tensile strength test for the determination of water sensitivity [66]

The retained Marshall stability (RMC) is the ratio between conditioned and unconditioned stabilities, expressed as a percentage, and it is the indicator of moisture susceptibility. The European standard EN 12697-12 [72] describes the water sensitivity test based on the indirect tensile strength ratio (ITSR), which is calculated as the ratio of the indirect tensile strength of wet (water conditioned) specimens (ITS_w) to that of dry specimens (ITS_d), expressed as a percentage.

The maximum tensile stress applied to test specimens is determined in accordance with EN 12697-23 [73]. Figure 4.4a illustrates the typical failure “combination” that is generally obtained after breaking when RA are incorporated in the mixtures. This failure is characterised by a limited tensile break line and larger deformed areas close to the loading strips. Figure 4.4b shows a view of the surfaces of the open specimen, on which the broken RCA are fairly visible. The breakage of particles is a common characteristic of RA.

The susceptibility to permanent deformation is commonly assessed by the wheel-tracking test in accordance with EN 12697-22 [74]. This test assesses the rut depth formed by a standard wheel during load cycles. Different size devices and specimens conditioning could be selected. The temperature conditioning for measuring rut depth is 60 °C but other temperatures could be more suitable where some types of RA are utilised, depending on the local conditions and the pavement layer for the mixture.

Stiffness is an all-important property that influences the structural behaviour of the road pavement. EN 12697-26 [75] specifies different methods for assessing the complex stiffness modulus, including bending tests and direct and indirect tensile tests. The tests are performed under a given fixed temperature, controlled loading and type of specimen and support. The four point bending test—4 PB—is quite common and performed on prismatic specimens in controlled loading (different range of frequencies) and temperature (based on local experience) conditions.

The specifications for resistance to fatigue are laid out in EN 12697-24 [76], following the very similar principles of the stiffness test [75]. Fatigue is a very important factor for the performance of a bituminous mixture in a pavement under

the repeated passage of traffic loads over time. 4 PB is also a quite common test procedure for assessing the fatigue behaviour of bituminous mixtures incorporating RA.

Other test methods for mechanical evaluation of bituminous mixtures incorporating RA are suitable. In each case, the most adequate conditions for loading and temperature of test specimens must be evaluated taking into account the presence of RA. Durability tests can also be performed according to the methods described in Chaps. 2 and 3.

4.6 Conclusions

This chapter presents and discusses the main properties and respective test methodologies of recycled aggregates (RA), as well as their effect on concrete production. The main constraint of recycled concrete aggregates (RCA) is the mortar adhered to their surface. It is possible to see throughout this chapter that this adhering mortar significantly affects the performance of the concrete produced with RCA, causing an increase in porosity, an increase in water absorption and a decrease in the stiffness of these aggregates. On the other hand, it is worth noting the greater influence of the fine component of these aggregates on the worst performance of concrete. However, the performance of concrete produced with RCA depends not only on the aforementioned RCA properties, but also on the NA's substitution ratio. Naturally, for higher replacement ratios, their impact on the concrete performance is more negative.

However, there are a set of potential methodologies that allow improving the quality of RCA and reducing their less positive impact on some of the concrete properties, namely:

- Improve the collection/crushing process through, for example, the use of a primary and secondary crushing procedure as it is usual in NA; these improvements can decrease the amount of adhered mortar with the consequent decrease in their absorption and permeability and, on the other hand, improve the particles' shape;
- Use of supplementary cementitious materials as partial cement replacement, as a way to improve the workability of concrete, reduce its shrinkage and decrease its permeability, by limiting the penetration of the main degradation mechanisms, among others.

It is, however, possible to conclude that the use of RCA is feasible for concrete production, with no specific conditions regarding their characterisation. However, some attention is necessary to adapt the properties and characteristics of these aggregates to an adequate intended performance of concrete.

Laboratory testing of bituminous mixtures incorporating RA from CDW was also described herein with the main focus on recycled concrete aggregates and reclaimed asphalt pavement. The most common test methods are similar to NA's in terms of the geometrical, physical and mechanical requirements. In the case of RA, special attention should be given to the density and water absorption. Taking into account

the diversity of the RA, in terms of quality and homogeneity, susceptibility to stripping is useful for measuring the adherence of the bitumen to the RA. However, more accurate and objective methods should be given preference for this purpose, such as the rolling bottle method with longer observation periods. The design and quality control of bituminous mixtures incorporating RA should be mostly supported by mechanical and durability tests that evaluate the long-term performance of the bituminous mixtures. The most current tests are water sensitivity, susceptibility to rutting, stiffness, and resistance to fatigue.

Acknowledgements The authors are grateful for the Foundation for Science and Technology's support through funding FCT-IDB/04625/2020 from the research unit CERIS (Center of Civil Engineering Research and Innovation for Sustainability).

References

1. de Brito J, Kurda R (2020) The past and future of sustainable concrete: a critical review and new strategies on cement-based materials. *J Cleaner Product* 281
2. de Brito J, Kurda R, da Silva PR (2018) Can we truly predict the compressive strength of concrete without knowing the properties of aggregates? *Appl Sci* 8(7):1095
3. Nagataki S, Gokce A, Saeki T, Hisada M (2004) Assessment of recycling process induced damage sensitivity of recycled concrete aggregates. *Cem Concr Res* 34(6):965–971
4. Silva RV, de Brito J, Dhir RK (2014) Properties and composition of recycled aggregates from construction and demolition waste suitable for concrete production. *Constr Build Mater* 65:201–217
5. Hansen TC, Narud H (1983) Strength of recycled concrete made from crushed concrete coarse aggregate. *Concr Int* 5(1):79–83
6. Chandra S (2004) Implications of using recycled construction demolition waste as aggregate in concrete. In: Limbachiya MC, Roberts JJ (eds) Proceedings of the international conference on sustainable waste manage and recycling: construction demolition waste. UK: Thomas Telford, pp 105–14
7. Gokce A, Nagataki S, Saeki B, Hisada M (2011) Identification of frost-susceptible recycled concrete aggregates for durability of concrete. *Const. and Building Materials* 25(5):2426–2431
8. Andreu G, Miren E (2014) Experimental analysis of properties of high performance recycled aggregate concrete. *Constr Build Mater* 52:227–235
9. Hansen TC (1992) Recycling of demolished concrete and masonry. E&FN Spon, London
10. Juan MS, Gutiérrez PA (2009) Study on the influence of attached mortar content on the properties of recycled concrete aggregate. *Constr Build Mater* 23(2):872–877
11. Etxeberria M, Vázquez AM, Barra M (2007) Influence of amount of recycled coarse aggregates and production process on properties of recycled aggregate concrete. *Cem Concr Res* 37(5):735–742
12. Poon CS, Shui ZH, Lam L, Fok H, Kou SC (2004) Influence of moisture states of natural and recycled aggregates on the slump and compressive strength of concrete. *Cem Concr Res* 34(1):31–36
13. Hasaba S, Kawamura M, Torli K, Takemoto K (1981) Drying shrinkage and durability of concrete made from recycled concrete aggregates. Japanese Concrete Institute 3:55–60
14. Katz A (2004) Treatments for the improvement of recycled aggregate. *J Mater Civ Eng* 16(6):597–603
15. Poon CS, Chan DX (2006) Feasible use of recycled concrete aggregates and crushed clay brick as unbound road sub-base. *Constr Build Mater* 20(8):578–585

16. Katz A (2003) Properties of concrete made with recycled aggregate from partially hydrated old concrete. *Cem Concr Res* 33(5):703–711
17. EN 1097–6: Tests for mechanical and physical properties of aggregates, Part 6: Determination of particle density and water absorption. Comité Européen de Normalisation (CEN): Brussels, Belgium (2013)
18. Rodrigues F, Evangelista L, de Brito J (2013) A new method to determine the density and water absorption of fine recycled aggregates. *Mater Res* 16(5):1045–1051
19. Leite, M.: Evaluation of the mechanical properties of concrete made with aggregates recycled from construction and demolition waste [Thesis]. Porto Alegre: School of Engineering, Federal University of Rio Grande do Sul (in Portuguese) (2001).
20. EN 12350–6: Testing fresh concrete; Part 6: Density. Comité Européen de Normalisation (CEN): Brussels, Belgium (2019)
21. Xiao J, Li J, Zhang C (2005) Mechanical properties of recycled aggregate concrete under uniaxial loading. *Cem Concr Res* 35(6):1187–1194
22. Dong JF, Wang QY, Guan ZW (2013) Structural behaviour of recycled aggregate concrete filled steel tube columns strengthened by CFRP. *Eng Struct* 48:532–542
23. Marinković S, Radonjanin V, Malešev M, Ignjatović I (2010) Comparative environmental assessment of natural and recycled aggregate concrete. *Waste Manage* 30(11):2255–2264
24. Verian KP, Ashraf W, Cao Y (2018) Properties of recycled concrete aggregate and their influence in new concrete production. *Resour Conserv Recycl* 133:30–49
25. Fonseca N, de Brito J, Evangelista L (2011) The influence of curing conditions on the mechanical performance of concrete made with recycled concrete waste. *Cement Concr Compos* 33(6):637–643
26. Bravo M, de Brito J, Pontes J, Evangelista L (2015) Mechanical performance of concrete made with aggregates from construction and demolition waste recycling plants. *J Clean Prod* 99:59–74
27. Ferreira L, de Brito J, Barra M (2011) Influence of the pre-saturation of recycled coarse concrete aggregates on the fresh and hardened properties of concrete. *Mag Concr Res* 63(8):617–627
28. Pacheco J, de Brito J, Ferreira J, Soares D (2017) Dynamic characterization of full-scale structures made with recycled coarse aggregates. *J Clean Prod* 142(4):4195–4205
29. EN 12350–2: Testing fresh concrete; Part 2: Slump test. Comité Européen de Normalisation (CEN): Brussels, Belgium (2019)
30. Carrijo P (2005) Analysis of the influence of the density of coarse aggregates from construction and demolition waste on the mechanical performance of concrete (Master's thesis). Universidade de São Paulo, São Paulo, Brazil (in Portuguese)
31. Solymar M (2005) Classification of recycled sands and their applications as fine aggregates for concrete and bituminous mixtures (PhD thesis) Fachbereich Bauingenieurwesen Der Universität Kassel, Kassel, Germany
32. EN 12390–7: Testing hardened concrete; Part 7: Density of hardened concrete. Comité Européen de Normalisation (CEN): Brussels, Belgium (2019)
33. Pereira-de-Oliveira L, Nepomuceno MCS, Castro-Gomes JP, Vila MFC (2014) Permeability properties of self-compacting concrete with coarse recycled aggregates. *Constr Build Mater* 51:113–120
34. Santos S, da Silva PR, de Brito J (2019) Self-compacting concrete with recycled aggregates – A literature review. *J Build Eng* 22:349–371
35. Evangelista LR, de Brito J (2007) Mechanical behaviour of concrete made with fine recycled concrete aggregates. *Cement Concr Compos* 29(5):397–401
36. Kurad R, Silvestre JD, de Brito J (2017) Ahmed H. Effect of incorporation of high volume of recycled concrete aggregates and fly ash on the strength and global warming potential of concrete. *J Cleaner Product* 166:485–502
37. EN 12390–3: Testing hardened concrete; Part 3: Compressive strength of test specimens. Comité Européen de Normalisation (CEN): Brussels, Belgium
38. Yaprak H, Aruntas HY, Demir I, Simsek O, Durmus G (2011) Effects of the fine recycled concrete aggregates on the concrete properties. *Int J Phys Sci* (10):2455–2461

39. Rao M, Bhattacharyya S, Barai S (2011) Influence of field recycled coarse aggregate on properties of concrete. *Mater Struct* 44(1):205–220
40. Mehta PK, Monteiro PJM (2005) Concrete microstructure, properties and materials, McGraw-Hill, USA, p 684
41. Kang THK, Kim W, Kwak YK, Hong SG (2012) The choice of recycled concrete aggregates for flexural members. In: 18th international association for bridge and structural engineering congress on innovative infrastructures, Seoul, Korea
42. EN 12390–6: Testing hardened concrete; Part 6: Tensile splitting strength of test specimens. Comité Européen de Normalisation (CEN): Brussels, Belgium (2009)
43. Assié S (2004) Durabilité des bétons autoplaçants (Thèse de doctorat). L’Institut National des Sciences Appliquées de Toulouse, Toulouse, France, p 254
44. Maruyama I, Sogo M, Sogabe T, Sato R, Kawai K (2004) Flexural properties of reinforced recycled beams. In Proceedings of international RILEM conference on the use of recycled materials in buildings and structures 1:525–535
45. LNEC E 397: Hardened concrete, determination of the modulus of elasticity of concrete in compression. National Laboratory in Civil Engineering (LNEC—Laboratório Nacional de Engenharia Civil): Lisbon, Portugal, (In Portuguese), (1993)
46. EN 12504–4: Testing concrete; part 4: Determination of ultrasonic pulse velocity. Comité Européen de Normalisation (CEN): Brussels, Belgium (2004)
47. ASTM C597–09: Standard test method for pulse velocity through concrete. ASTM International. West Conshohocken (2009)
48. Mindess S, Young JF, Darwin D (2003) Concrete. 2nd edn, Pearson Education, Upper Saddle River, New Jersey
49. Kou SC, Poon CS, Chan D (2004) Properties of steam cured recycled aggregate fly ash concrete. In: International RILEM conference on the use of recycled materials in buildings and structures, Barcelona, Spain, pp 590–599
50. Pereira P, Evangelista LR, de Brito J (2012) The effect of superplasticizers on the mechanical performance of concrete made with fine recycled concrete aggregates. *Cement Concr Compos* 34(9):1044–1052
51. Neville AM (1995) Properties of concrete. Harlow, Pearson
52. Illston JM, Domone PL (2001) Construction materials, their nature and behaviour. third edition, Spon Press, UK, 554
53. Jensen OM, Hansen PF (2001) Autogenous deformation and RH-changes perspective. *Cem Concr Res* 31(12):1859–1865
54. LNEC E 398: Hardened concrete, determination of shrinkage and of swelling. National Laboratory in Civil Engineering (LNEC—Laboratório Nacional de Engenharia Civil): Lisbon, Portugal, (In Portuguese), (1993)
55. Kou S, Poon C (2012) Enhancing the durability properties of concrete prepared with coarse recycled aggregate. *Constr Build Mater* 35:69–76
56. Matias D, de Brito J, Rosa A, Pedro D (2013) Mechanical properties of concrete produced with recycled coarse aggregates - Influence of the use of superplasticizers. *Constr Build Mater* 44:101–109
57. Malešević M, Radonjanin V, Marinković S (2010) Recycled concrete as aggregate for structural concrete production. *Sustainability* 2(5):1204–1225
58. Evangelista LR, de Brito J (2010) Durability performance of concrete made with fine recycled concrete aggregates. *Cement Concr Compos* 32(1):9–14
59. Gomes M, de Brito J (2009) Structural concrete with incorporation of coarse recycled concrete and ceramic aggregates: durability performance. *Mater Struct* 42:663–675
60. Olorunsogo F (2002) Performance of recycled aggregate concrete monitored by durability indexes. *Cem Concr Res* 32:179–185
61. EN 13108–8: Bituminous mixtures. Material specifications. Part 8: Reclaimed asphalt. Comité Européen de Normalisation (CEN): Brussels, Belgium (2016)
62. Neves J, Picado-Santos L, Diogo AC (2015) Chapter 5 - Bituminous binders and mixtures. In: Gonçalves MC, Margarido F, Editor S (eds). Springer

63. Neves J, Diogo AC, Freire AC, de Brito J (2015) Chapter 20 - aggregates. In: Gonçalves MC, Margarido F, Editor S (eds). Springer
64. EN 13043: Aggregates for bituminous mixtures and surface treatments for roads, airfields and other trafficked areas. Comité Européen de Normalisation (CEN): Brussels, Belgium (2013)
65. EN 12697-11: Bituminous mixtures. Test methods. Determination of the affinity between aggregate and bitumen. Comité Européen de Normalisation (CEN): Brussels, Belgium (2020)
66. Neves J, Lameirão J, Freire AC (2019) Physical and mechanical properties of warm mix asphalt composed by recycled concrete aggregates. In: 7th international conference on bituminous mixtures and pavements. CRC Press, pp 194–200
67. Martinho FCG, Picado-Santos L, Capitão SD (2018) Feasibility assessment of the use of recycled aggregates for asphalt mixtures. Sustainability 10:1737
68. Rahman MT, Mohajerani A, Giustozzi F (2020) Recycling of waste materials for asphalt concrete and bitumen: a review. Materials 13:1495
69. Tarsi G, Tataranni P, Sangiorgi C (2020) The challenges of using reclaimed asphalt pavement for new asphalt mixtures: a review. Materials 13:4052
70. EN 12697-34: Bituminous mixtures. Test methods. Marshall test. Comité Européen de Normalisation (CEN): Brussels, Belgium (2020)
71. CRD-C 652-95: Standard test method for measurement of reduction in Marshall stability of bituminous mixtures caused by immersion in water (Formerly MIL-STD-620A, Method 104, 13 January 1966). Construction Criteria Base, Handbook for Concrete and Cement, Whole Building Design Guide, <http://www.wbdg.org> (last accessed 2020/11/20)
72. EN 12697-12: Bituminous mixtures. Test methods. Determination of the water sensitivity of bituminous specimens. Comité Européen de Normalisation (CEN): Brussels, Belgium (2018)
73. EN 12697-23: Bituminous mixtures. Test methods. Determination of the indirect tensile strength of bituminous specimens. Comité Européen de Normalisation (CEN): Brussels, Belgium (2017)
74. EN 12697-22: Bituminous mixtures. Test methods. Wheel tracking. Comité Européen de Normalisation (CEN): Brussels, Belgium (2020)
75. EN 12697-26: Bituminous mixtures. Test methods. Stiffness. Comité Européen de Normalisation (CEN): Brussels, Belgium (2018)
76. EN 12697-26: Bituminous mixtures. Test methods. Resistance to fatigue. Comité Européen de Normalisation (CEN): Brussels, Belgium (2018)

Chapter 5

New Environmental Requirements



Isabel M. Martins and Helena M. Silva

Abstract In the construction sector, overall policies on resource efficiency and the circular economy have as one of their objectives the shift from the use of natural materials to industrial by-products and materials recovered from waste. In this context, the assessment of the presence of hazardous substances in construction products and the corresponding implications for the environment—soil, air and water—as well as for health is an increasingly relevant topic. This chapter presents the environmental regulations related to the presence of hazardous substances in construction materials, the current developments in harmonized test methods for environmental monitoring of these materials as well as the perspectives regarding European environmental limit values for pollutants. Furthermore, environmental criteria for construction materials based on environmental product declarations, ecolabels and other schemes, intended to inform citizens about environmental performance, are also addressed.

Keywords Construction materials · Environmental assessment · Hazardous substances · Leaching · Ecotoxicity · Eco-labels

5.1 Framework

The built environment is responsible for 50% of all extracted materials and 35% of the European Union (EU)'s total waste generation [1]. Over the last decade, the European policies concerning the construction sector have emphasized the necessity of improving the efficiency of resources by keeping them in the economy for longer periods. Against this background, the recovery of materials, both by-products and waste, had become the focus for the development of a secondary building materials market.

I. M. Martins · H. M. Silva
Laboratório Nacional de Engenharia Civil, Lisbon, Portugal
e-mail: imartins@lnec.pt

H. M. Silva
e-mail: hmsilva@lnec.pt

Currently, the European Green Deal [2], the new policy framework of the EU, comprises a set of initiatives, namely the new Circular Economy Action Plan [3] and the Renovation Wave [4], which accounts for actions to make construction more sustainable. On this subject, it is worth mentioning that it is crucial to reduce and assess the content of contaminants in order to increase the confidence in secondary materials.

In Europe, regardless of whether primary or secondary raw materials were used in construction products, the Construction Products Regulation (CPR) [5] applies, provided the construction products are covered by harmonized European standards (hEN) or European Assessment Documents (EAD).

Since the replacement of the Construction Products Directive (CPD 89/106/EEC) [6] by the Construction Products Regulation (CPR) in 2013, it is mandatory to issue a declaration of performance (DoP) for construction products to bear the CE marking that allows the free circulation within the EU's single market [7].

5.2 Assessment of the Release of Dangerous Substances under CPR

The performance of construction products goes far beyond ensuring its mechanical resistance and durability through its working life. In fact, the aspects of the protection of public health and the environment are a global concern and must also be addressed. To this end, the CPR states that "*Construction works as a whole and in their separate parts must be fit for their intended use, taking into account in particular the health and safety of persons involved throughout the life cycle of the works*" [5]. Furthermore, the CPR in its third basic requirement of construction works (BWR3), named "Hygiene, health and the environment", addresses these issues.

The compliance of a construction product with BWR3, calls for information on the content or emission of 'regulated dangerous substances' and its inclusion in the DoP. This input in DoP is essential for the transition to a cleaner and healthier built environment as it enables the stakeholders to make a more informed choice reducing the risks to the ecosystems and protecting the citizens.

The European Commission has issued the Mandate M/366 to the European Committee for Standardization (CEN), under the subject "*Development of horizontal standardized assessment methods for harmonised approaches relating to dangerous substances under the Construction Products Directive (CPD)—Emission to indoor air, soil, surface water and ground water*" which was carried out by the Technical Committee CEN/TC 351 "*Construction products: Assessment of release of dangerous substances*".

Since it was set, CEN/TC 351 [8] has worked out methodologies and horizontal test methods related to the release (and/or content) of regulated dangerous substances taking into account the emission scenarios (emission to indoor air and release to the soil, surface water and groundwater) and the intended conditions of use of the product.

After verifying the existing assessment methods for substances from an indicative list of regulated dangerous substances, possibly associated with construction products, CEN/TC 351 defined the harmonized methods to be developed and created the following five working groups [8]:

- WG 1 Release from construction products into soil, ground water and surface water;
- WG 2 Emissions from construction products into indoor air;
- WG 3 Radiation from construction products;
- WG 4 Terminology;
- WG 5 Content and eluate analysis in construction products.

To carry out its mission CEN/TC 351 has also taken into account European legislation on chemical substances and environmental policies that cross with construction products legislation [9], namely Regulation (EC) No 1907/2006 “*concerning the Registration, Evaluation, Authorisation and Restriction of Chemicals (REACH)*” [10], Regulation (EC) No 850/2004 “*concerning on persistent organic pollutants*” [11] and Directive 2000/60/EC “*establishing a framework for community action in the field of water policy*” [12].

An overview of the most relevant technical specifications (TS), technical reports (TR) or European standards (EN) published is given in Table 5.1.

It should be noted that different TS are now being draft as harmonized standards, keeping the code number of TS. The following are examples of this coexistence: FprCEN/TS 17459, prEN 16637-1 rev, prEN 16637-2, prEN 16637-3 rev, prEN 17195 rev, prEN 17196, prEN 17197, prEN 17200 rev, prEN 17201, prEN 17331 and prEN 17332. Table 5.2 shows other work in progress from CEN/TC 351.

5.2.1 Indoor Air

The construction products can emit dangerous substances into indoor air, contributing significantly to indoor pollution, and therefore affecting the health of the occupants of the buildings [13]. Concerning the release scenario “emission to indoor air”, CEN/TC 351 published the horizontal reference method EN 16516 “*Construction products: Assessment of release of dangerous substances—Determination of emissions into indoor air*” [14], that applies to volatile organic compounds (VOC), semi-volatile organic compounds (SVOC), very volatile aldehydes and ammonia. The method is based on the use of a reference test chamber with standardized dimensions, climate and ventilation. The emission of compounds is determined 28 days after the installation of the construction product in the chamber. At this time the vapour-phase compounds present in the chamber air are collected and analysed by an appropriate method (GC-MS and HPLC for volatile organic compounds and spectrophotometric methods or any equivalent analytical methods for ammonia) [14].

There is a quite large amount of gaseous organic substances that can be emitted by building materials (such as floorings, particle boards, walls and ceiling finishes,

Table 5.1 Published Standards and guidance documents under harmonization work of CEN/TC 351 [8]

TS/TR/EN	Title
CEN/TR 15855:2009	Construction products—Assessment of release of dangerous substances—Barriers to trade
CEN/TR 15858:2009	Construction products—Assessment of the release of regulated dangerous substances from construction products based on the WT, WFT/FT procedures
CEN/TR 16045:2010	Construction Products—Assessment of release of dangerous substances—Content of regulated dangerous substances—Selection of analytical methods
CEN/TR 16098:2010	Construction products: Assessment of release of dangerous substances—Concept of horizontal testing procedures in support of requirements under the CPD
CEN/TR 16220:2011	Construction products—Assessment of release of dangerous substances—Complement to sampling
CEN/TR 16410:2012	Construction products—Assessment of release of dangerous substances—Barriers to use—Extension to CEN/TR 15855 Barriers to trade
CEN/TR 16496:2013	Construction Products—Assessment of release of dangerous substances—Use of harmonised horizontal assessment methods
CEN/TS 16637-2:2014	Construction products—Assessment of release of dangerous substances—Part 2: Horizontal dynamic surface leaching test
EN 16687:2015	Construction products—Assessment of release of dangerous substances—Terminology
CEN/TR 16797-1:2015	Construction products: Assessment of release of dangerous substances—Guidance on the statistical assessment of declared values—Part 1: Principles and rules of application
CEN/TR 16797-2:2015	Construction products: Assessment of release of dangerous substances—Guidance on the statistical assessment of declared values—Part 2: Technical and statistical background
CEN/TS 16637-3:2016	Construction products—Assessment of release of dangerous substances—Part 3: Horizontal up-flow percolation test
CEN/TR 17105:2017	Construction products—Assessment of release of dangerous substances—Guidance on the use of ecotoxicity tests applied to construction products
CEN/TR 17113:2017	Construction products—Assessment of release of dangerous substances—Radiation from construction products—Dose assessment of emitted gamma radiation
CEN/TS 17195:2018	Construction products: Assessment of release of dangerous substances—Analysis of inorganic substances in eluates

(continued)

Table 5.1 (continued)

TS/TR/EN	Title
CEN/TS 17196:2018	Construction products: Assessment of release of dangerous substances—Digestion by aqua regia for subsequent analysis of inorganic substances
CEN/TS 16637-1:2018	Construction products—Assessment of release of dangerous substances—Part 1: Guidance for the determination of leaching tests and additional testing steps
CEN/TS 17216:2018	Construction products—Assessment of release of dangerous substances—Determination of activity concentrations of radium-226, thorium-232 and potassium-40 in construction products using semiconductor gamma-ray spectrometry
CEN/TR 17304:2018	Construction products—Assessment of release of dangerous substances—Determination of emissions into indoor air of ammonia from cellulose insulation at 90% RH
CEN/TS 17197:2018 + AC:2018	Construction products: Assessment of release of dangerous substances—Analysis of inorganic substances in digests and eluates—Analysis by Inductively Coupled Plasma—Optical Emission Spectrometry (ICP-OES)
CEN/TS 17200:2018 + AC:2018	Construction products: Assessment of release of dangerous substances—Analysis of inorganic substances in digests and eluates—Analysis by Inductively Coupled Plasma—Mass Spectrometry (ICP-MS)
CEN/TS 17201:2018 + AC:2018	Construction products: Assessment of release of dangerous substances—Content of inorganic substances—Methods for analysis of aqua regia digests
EN 17087:2019	Construction products: Assessment of release of dangerous substances—Preparation of test portions from the laboratory sample for testing of release and analysis of content
CEN/TS 17331:2019	Construction products: Assessment of release of dangerous substances—Content of organic substances—Methods for extraction and analysis
CEN/TS 17332:2019	Construction products: Assessment of release of dangerous substances—Analysis of organic substances in eluates
EN 16516:2017 + A1:2020	Construction products: Assessment of release of dangerous substances—Determination of emissions into indoor air

wooden panels and sealants) [9]. EN 16516 [14] gives a non-exhaustive list of volatile organic compounds, included in the following categories: aromatic hydrocarbons, saturated aliphatic hydrocarbons, terpenes, aliphatic and aromatic alcohols, glycols and glycol ethers, aldehydes, acids and esters [14].

For a harmonised assessment of the building product emissions, a working group, under the coordination of the European Commission's Joint Research Centre (EC-JRC), is setting a harmonised list of compounds and their associated European harmonised ‘lowest concentrations of interest (EU-LCI)’ values [15]. The “EU-LCI

Table 5.2 Standards under development (working in progress) by CEN/TC 351 [8]

Draft/Working item	Title
prEN (WI = 00351034)	Construction products: Assessment of release of dangerous substances—Determination of the content of polycyclic aromatic hydrocarbons (PAH) and of benzene, toluene, ethylbenzene and xylene (BTEX)—Gas-chromatographic method with mass spectrometric detection
prEN (WI = 00351035)	Construction products: Assessment of release of dangerous substances—Determination of biocide residues using LC-MS/MS
prEN 17216	Construction products: Assessment of release of dangerous substances—Determination of radium-226, thorium-232 and potassium-40 activity using gamma-ray spectrometry
prEN 17637 (WI = 00351050)	Construction products: Assessment of release of dangerous substances—Dose assessment of emitted gamma radiation Construction products: Assessment of release of dangerous substances—Sampling and qualitative determination of asbestos in construction products
(WI = 00351042)	Construction products: Assessment of release of dangerous substances—Methods for the determination of N-nitrosamines in air samples derived by EN 16516

values are health-based reference concentrations of chemical substances for inhalation exposure used to assess emissions after 28 days from a single construction product during a laboratory test chamber procedure as defined in the EN 16516” [16]. The definition of these values is based on all relevant published toxicological and risk assessment data and in the REACH principles [15]. The up-to-date EU-LCI values are available on the official website of the European Union [16].

Currently, there are three mandatory systems in different Member States for the assessment of VOC emissions to the indoor environment from construction products [17, 18], each of them with its particular criteria. German AgBB scheme is based on pass-fail criteria for 185 compounds established in the German LCI list (EU-LCI values are usually adopted) [19]. The criteria established in the Belgian Royal Decree are similar to the German system, but in this case it is considered the harmonised EU-LCI list [20]. French VOC regulation focuses on a classification system based on the selection of 10 compounds [21–23]. An overview of the German and Belgian limits is given in Table 5.3 and the French classification system is presented in Table 5.4.

In addition, to these mandatory systems, several voluntary labelling schemes for low-emission building materials, with their specific requirements for product evaluation, are used in other European countries [25, 26]. For example, the M1 for low-emission building materials in Finland considers the following parameters: total volatile organic compounds emission < 0.2 mg/m²h; Emission of a single volatile organic compound (VOC) ≤ EU-LCI; Formaldehyde emission < 0.05 mg/m²h, Ammonium emission < 0.03 mg/m²h; The emission of CMR-compounds belonging to category 1A or 1B in Annex VI to Regulation (EC) No 1272/2008 < 1 µg/m³

Table 5.3 Overview of mandatory limit values in Germany [19] and Belgium [20]

After 28 days of testing	German	Belgium
Total Volatile Organic Compounds (TVOC)	$\leq 1000 \mu\text{g}/\text{m}^3$	$\leq 1000 \mu\text{g}/\text{m}^3$
Total Semi-Volatile Organic Compounds (TSVOC)	$\leq 100 \mu\text{g}/\text{m}^3$	$\leq 100 \mu\text{g}/\text{m}^3$
Volatile carcinogen of categories 1A and 1B (according to Regulation No 1272/2008 [24])	$\leq 1 \mu\text{g}/\text{m}^3$	$\leq 1 \mu\text{g}/\text{m}^3$
Toluene	$\leq 900 \mu\text{g}/\text{m}^3$	$\leq 300 \mu\text{g}/\text{m}^3$
Acetaldehyde	$1200 \mu\text{g}/\text{m}^3$	$\leq 200 \mu\text{g}/\text{m}^3$
Formaldehyde	$100 \mu\text{g}/\text{m}^3$	$\leq 100 \mu\text{g}/\text{m}^3$
R value (sum of all Ri values to the COV with LCI)	≤ 1	≤ 1
TVOC without LCI	$\leq 100 \mu\text{g}/\text{m}^3$	-

Ri is given by the ratio Ci/LCII (where Ci is the mass concentration in the air of the reference room and LCII is the LCI value of compound i)

Table 5.4 French classification system (limit values of the emissions classes in $\mu\text{g}/\text{m}^3$) [23]

Substance/Emission class	A +	A	B	C
Formaldehyde	<10	<60	<120	>120
Acetaldehyde	<200	<300	<400	>400
Toluene	<300	<450	<600	>600
Tetrachloroethylene	<250	<350	<500	> 500
Xylene	<200	<300	<400	>400
1,2,4—Trimethylbenzene	<1000	<1500	<2000	>2000
1,4—Dichlorobenzene	<60	<90	<120	> 120
Ethyl benzene	<750	<1000	<1500	>1500
2-butoxyethanol	<1000	<1500	<2000	>2000
Styrene	<250	<350	<500	>500
TVOC	<1000	<1500	<2000	>2000

According to the French regulation: Trichlorethylene, Benzene, Bis(2-ethylhexyl) phthalate and Dibutyl phtalate $\leq 1 \mu\text{g}/\text{m}^3$

and Odour: not odorous [27]. The Danish indoor climate is similar to the German AgBB scheme and includes the evaluation of the release of particles and the odour assessment [13].

Based on the existing labelling schemes, the European Commission has been working on the development of a harmonised labelling scheme for the assessment of VOC emissions from construction products under the CPR. However, until now, no consensual protocol has already been reached. It is expected that within a few years, the CE marking accompanied by DoP may contain classes or levels for the release of dangerous substances based on a harmonised VOC emission label.

Table 5.5 Classes for formaldehyde emissions [28]

Class	Requirements (using test method EN 717-1 [29])	Requirements (using test method EN 16516 [14])
E1	Equilibrium concentration in the air of the test chamber $\leq 0.12 \text{ mg/m}^3$	$\leq 0.12 \text{ mg/m}^3$
E2	Equilibrium concentration in the air of the test chamber $> 0.12 \text{ mg/m}^3$	$> 0.12 \text{ mg/m}^3$

After the publication of the harmonised standard EN 16516 [14] in 2017, the product standards in the EU have started to include the assessment of the “*Emission of dangerous substances into indoor air*” using this harmonized test method. The product standard EN 14041 [28] “*Resilient, textile, laminate and modular multilayer floor coverings—Essential characteristics*” is one example of this inclusion.

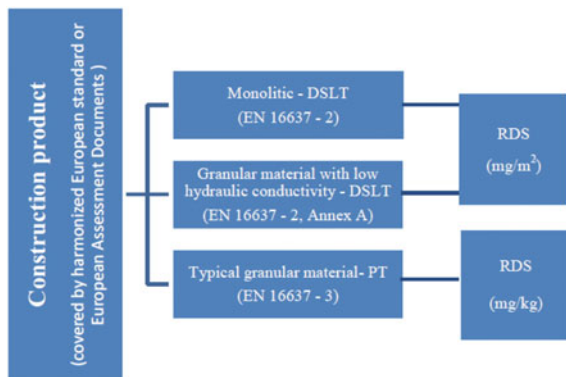
Regarding the levels/classes of emission into indoor air, currently, only the emission formaldehyde classes have been addressed in the construction product standards and therefore in the CE marking (Table 5.5).

5.2.2 Soil and Water

Under outdoor exposure conditions, construction products can potentially release Regulated Dangerous Substances (RDS) to surface water, groundwater and soil through different physicochemical paths related to the construction product characteristics and scenario of exposure. Several contaminants (e.g., biocides, PAH, heavy metals) found in the stormwater can be linked to the use of construction products (e.g., renders, mortars, paints, roofing materials, bricks) [30]. These pollutants may have toxic effects on the environment and, consequently, on human health [31]. To ensure the environmental compatibility of construction products, it is essential to determine the adequate release test applied to the construction product to understand which substances are released and in what amount.

To assess the release of RDS from different construction products into water and soil, CEN/TC 351 developed two harmonized tests: the CEN/TS 16637-2 [32], a dynamic surface leaching test (DSL-T) for determining the release of inorganic and/or non-volatile organic substances from the monolithic, plate or sheet-like construction products or from granular construction products with low hydraulic conductivity whose surface is in contact with a leachant, and CEN/TS 16637-3 [33], an up-flow percolation test (PT) to determine the release of inorganic and/or non-volatile organic substances from common granular construction products [8]. The scheme for choosing the preferred method to assess the release of RDS is presented in Fig. 5.1.

Fig. 5.1 Test for release of RDS from construction products based on CEN/TS EN 16637-1 [36]



In the DSLT, the sample from the construction product is immersed in a leachant for specified periods of time, keeping a specific liquid to area (L/A) ratio. After each period, the leachant is renewed and the collected liquid fraction is analysed for its content.

For the PT test, the granular material is packed in a column and under hydraulically dynamic conditions, using a continuous vertical up-flow that ensure a specific liquid to solid ratio (L/S), different fractions of eluate are gathered for chemical analysis.

It should be mentioned that none of the referred tests covers metals, metallic coatings and organic coatings, since these materials have a different mechanism of release. However, it is expected that future validation works may extend the scope for the use of the method [7]. For construction products not in permanent contact with water (with dry and wet phases), namely façade coatings such as paints, mortars, mineral renders, renders with organic binders, which are subject to changes of physical and chemical properties during the permanent contact with leachant, the laboratory test EN16105 [34] can be applied instead of part 2 or 3 of CEN/TS 16,637 [35].

The eluates obtained from the above-mentioned tests can subsequently be subjected to chemical and ecotoxicological characterization. Concerning chemical analysis, available test methods to determine the released dangerous substances from the construction products have been compiled in the technical report CEN/TR 16045 [7]. The chemical characterization of the eluate is the desirable option, however analysis of the construction product content can also be undertaken when this is the only feasible solution to assess the release of specific compounds. The selected methods are based on test methods from other fields (for example soil quality, characterization of waste and water quality). Based on these existing methods, CEN/TC 351 has prepared technical reports for the analysis of inorganic and organic substances in eluates (see Table 5.1).

For the analysis of specific organic substances in eluates, the technical report CEN/TS 17332 [37] specified the appropriate methods for the determination of individual or groups of substances in aqueous eluates from leaching of construction products. Biocides, bisphenol A, BTEX, dioxins and furans, Dissolved Organic Carbon

(DOC), epichlorohydrin, mineral oil, nonylphenols, PAH, PBDE, PCB, dioxin-like PCB, PCP, phenols and phthalates are covered in this document [37].

Currently, CEN methods have undergone a process of validation for their robustness and are now in the second stage of validation to estimate the precision. As part of the validation work, the Joint Research Centre (JRC) presented a technical report of an interlaboratory comparison of leachates/eluates and the content of substances like biocides, phthalates, mineral oil, polycyclic aromatic hydrocarbons (PAHs) and poly-chlorinated biphenyls (PCBs) from render, sealant, asphalt aggregate and recycled aggregate [38].

The DSLT [32] and PT [33] tests are recent and there is not yet enough data regarding their application in construction products. In Europe, the implementation of these methods will lead to comparable data as opposed to the current situation. A study regarding the use of construction and demolition waste, slags from ferrous metals production, and ashes from coal combustion highlighted the diverse regulations and criteria applied, aiming at protecting the environment when these secondary resources are used as aggregates in construction products.

As the question of whether comparable methods exist at the European level has been overcome, the challenge arises as to which substances are relevant to be tested for a given group of construction products. The target substances should be selected based on the product formulation (chemical constitution and composition of the product). This is not to say that what matters is the content of the substances in the construction product. In reality, this content is a very poor indicator of what can be released and, although, in terms of the production of construction products the control of the content of existent substances is easier to apply, it is not adequate. The information on the chemical composition is useful from a qualitative perspective because it allows checking which substances included in the Indicative List of Regulated Dangerous Substances are present and, therefore, which need to be checked in the eluates [9]. The priority substances are considered based on the European legislation [30, 39, 40], such as water framework directive (2000/60/EC) [12], waste framework directive (2008/98/EC) [41], landfill regulation (Council decision 2003/33/CE) [42], REACH [10], persistent organic pollutants (POP) Regulation No 850/2004 [11] and biocidal products Regulation No 528/2012 [43].

Beyond chemical characterization of the eluates, the ecotoxicological characterization provides additional information because it allows an understanding of the effects that the eluate has on living organisms. The main drivers to conduct these tests are the lack of knowledge of the substances present in the construction products or the fact that the content of some substances is not easy to quantify in the eluate. Usually, the minimum test battery focus on acute ecotoxicity (CEN TR/17105 [44]) and it combines the exposition of organisms from three different trophic levels to the diluted eluate followed by assessment of the observed effects as follows:

- Algae—analysis of growth rate inhibition (EN ISO 8692 [45]);
- Crustacea—evaluation of reduction of mobility after 48 h (EN ISO 6341 [46]);
- Luminescent bacteria: inhibition of light emission (EN ISO 11348-3 [47]).

Special attention must be given to the reported substances labelled as “acute toxicity” category 1, 2 e 3, “carcinogenicity category 1A or 1B, “Germ cell mutagenicity” category 1A or 1B, “Aquatic Acute” category 1 or Aquatic Chronic category 1, 2, 3 or 4 and Reproductive toxicity” category 1A or 1B as per the Regulation EC No 1272/2008 [24, 48]. Since construction products are constituted by complex mixtures of additives (e.g. plasticizers, stabilization agents, pigments, surfactants and solvents), screening methods like gas chromatography coupled with mass-selective detection (GC–MS) or liquid chromatography coupled with mass-selective detection (LC–MS) can be used to identify other relevant organic substances [30].

The technical specifications above mentioned are the basis to implement environmental protection requirements of the Construction Products Regulation, and to ensure soil and water protection. The application of these methods will be recommended not only in a legal context under CPR (CE marking of construction products) but also in voluntary labelling and environmental product declarations.

The harmonized methods permit us to compare the obtained leaching results with national or case-specific limit values [39]. However, and because the leaching behaviour is influenced by several factors (e.g. the geometry of the component and the weather), these results are not directly comparable to the environmental concentrations on the real service conditions. To define reasonable release limit values it is necessary further research to develop suitable models to predict the environmental concentration from the leaching test results [49].

Limit values for leaching from construction products have been introduced in some countries (e.g. Netherlands, Belgium, Denmark, German and Finland) [31, 39]. Nevertheless, the limit values are not comparable, because the selected materials and the release scenarios are different between them. It is expected that the harmonisation work of CEN/TC 351 leads to an uniformization of the criteria on EU level to the assessment of the leaching behaviour of construction products.

5.3 Environmental Labels

The construction sector plays a significant role in the consumption of resources and energy. As already mentioned, environmental awareness of the effects of this sector on pollution and resources depletion has led to the increasing demand for environmentally friendly building materials [39, 50].

To provide relevant information on the environmental performance of materials to all the stakeholders of the construction sector, various environmental labels and declarations have emerged with the objective to promote the choice of products with low environmental impact when compared to others intended for the same use and having similar performance.

The recognition of the commercial benefits of this type of labels/declarations/claims has led to the appearance of a large number of labelling initiatives, each one with its specific criteria. To establish harmonized criteria, definitions and guidelines for the different labels on the market [51], the International

Standardization Organization (ISO) developed standards concerning different types of labels and declarations:

- ISO 14024 [52]—Environmental labels and declarations—Type I environmental labelling—Principles and procedures.
- ISO 14021 [53]—Environmental labels and declarations—Self-declared environmental claims (Type II environmental labelling). It is a declaration of the company and it is not third-party certified.
- ISO 14025 [54]—Environmental labels and declarations—Type III environmental declarations—Principles and procedures.

The type I labels, commonly known as ‘Eco-labels’, form part of an independent (third-party certified) and multi-criteria labelling scheme, which certifies a product that meets a set of criteria based on life cycle considerations [55]. Some of these, applied to several product groups including building materials, are, for instance, *European Ecolabel* (e.g., product group: *Indoor and outdoor Paints and Varnishes*) [56], *German Blue Angel* (e.g., product groups: *Floor Coverings, Internal Plasters, Thermal insulation and Wall paints*) [57], *Natureplus* (e.g., product groups: *insulation materials, wall paints, adhesives*) [58] and *Nordic Swan* (e.g., product groups: *chemical building products, construction and facade panels and floor coverings*) [59].

Besides the type I labels, there is a “Type I-like” label, which focuses only on a single aspect, for example, air quality. Some of these are, for example, the *Eurofins Indoor Air Comfort* [60], *eco-INSTITUT* [61] and *GreenGuard* [62].

Concerning the Environmental Product Declarations—EPDs (Type III environmental declarations), they provide quantitative indicators for the environmental performance based on a life-cycle approach, and they were created for comparing the environmental impact of similar products [55]. To enable this comparison, the Life Cycle Assessment (LCA) should be based on common rules for each group of products, known as Product Category Rules (PCR). Therefore, ISO and European Committee for standardisation (CEN) developed standards with specific requirements for construction products [50]:

- ISO 21930 [63]—Sustainability in buildings and civil engineering works — Core rules for environmental product declarations of construction products and services;
- EN 15804 [64]—Sustainability of construction works—Environmental product declarations—core rules for the product category of construction products.

These standards have been used as a reference for the development of several EPD programmes for construction products, which includes *IBU*, by the *Institut Bauen und Umwelt e.V.* (Germany), the *Global EPD* by *AENOR* (Spain), the *Alliance HQE-GBC/Programme FDES INIES* (France) and *DAP Habitat System* by the *Habitat Cluster* (Portugal) among others [50].

Environmental information related to the construction products is needed to assess the sustainability of construction works. The life-cycle approach is considered in the Construction Product Regulation, namely in the Basic requirements for construction works BRW3 (hygiene, health and the environment) and BRW7 (sustainable use of natural resources). Although it is not referred in the CPR how to demonstrate the conformity with these basic requirements, it states that: “*For the assessment of the sustainable use of resources and of the impact of construction works on the environment the Environmental Product Declarations should be used when available*” [5].

5.4 Future Perspectives

As part of the 2030 Agenda for Sustainable Development Goal of the United Nations, the SDG 12—Ensure sustainable consumption and production patterns, comprised a target related to the protection of natural habitat and human health: “*an environmental sound management of chemicals and all wastes throughout their life cycle would be implemented in order to significantly reduce their release to air, water and soil, protecting human health and the environment from their adverse impacts*” [65]. This objective has not been achieved although several initiatives intended to reach the goal have been developed.

Contrary to expectations, the monitoring indicators at European level that measure the progress towards SDG 12 objectives [66] (see Fig. 5.2) give cause for concern regarding the consumption of toxic chemicals in recent years.

Assuming that this raise of toxic chemicals could affect the construction products, increased demand for faster evaluation procedures regarding the release of hazardous substances could be expected.

It should be pointed out that the new Circular Economy Action Plan [3] foresees the development of methodologies, from 2021 onwards, to track and reduce the presence of substances of concern in recycled materials. It will therefore be important to be aware of these actions in the near future.

Indicator	Long-term trend (past 15 years)	Short-term trend (past 5 years)
Decoupling environmental impacts from economic growth		
Consumption of toxic chemicals	(1)	
Resource productivity and domestic material consumption (DMC)		
⌚ Average CO ₂ emissions from new passenger cars (**)	(2)	
Energy productivity (*)		
Green economy		
Gross value added in the environmental goods and services sector		
Waste generation and management		
Circular material use rate	(3)	
Generation of waste excluding major mineral wastes	(4)	(5)

(*) Multi-purpose indicator. (**) Trends for EU target.

(1) Past 14-year period (2) Past 11-year period (3) Past 13-year period (4) Past 12-year period. (5) Past 4-year period

Legend:

- | | | | |
|--|--|--|--|
| | Significant progress towards SD objectives | | Significant movement away from SD objectives |
| | Moderate progress towards SD objectives | | Moderate movement away from SD objectives |

Fig. 5.2 European indicators monitoring of SDG 12 (adapted from [66])

References

1. European Commission: communication from the commission: roadmap to a resource efficient Europe. COM/2011/571 final (2011)
2. European Commission: communication from the commission: European Green Deal. COM/2019/640 final (2019)
3. European Commission: Communication from the commission: a new circular economy action plan for a cleaner and more competitive Europe. COM/2020/98 final (2020)

4. European Commission: Communication from the commission: a renovation wave for Europe—greening our buildings, creating jobs, improving lives. COM/2020/662 final (2020).
5. Regulation (EU) No^o 305/2011 of the European Parliament and of the Council of 9 March 2011 laying down harmonised conditions for the marketing of construction products and repealing Council Directive 89/106/EEC. Off J Eur Union Ser L 88:5–43 (2011)
6. Council Directive 89/106/EEC of 21 December 1988 on the approximation of laws, regulations and administrative provisions of the Member States relating to construction products. Off J Eur Communities Ser L 40:11.2.1989, 12–26 (1989)
7. Ilvonen O (2013) Assessing release of hazardous substances from construction products—review of 10 years of experience with a horizontal approach in the European Union. *Build Environ* 69:194–205
8. CEN Homepage, <https://standards.cen.eu/>, last accessed 2020/11/21
9. NEN Homepage, https://www.nen.nl/media/Overig/N0403_New_indicative_list__DS_041_051rev12.pdf, last accessed 2020/11/21
10. Regulation (EC) No 1907/2006 of the European Parliament and of the Council of 18 December 2006 concerning the Registration, Evaluation, Authorisation and Restriction of Chemicals (REACH), establishing a European Chemicals Agency, amending Directive 1999/45/EC and repealing Council Regulation (EEC) No 793/93 and Commission Regulation (EC) No 1488/94 as well as Council Directive 76/769/EEC and Commission Directives 91/155/EEC, 93/67/EEC, 93/105/EC and 2000/21/EC. OJ L 396/1 (2006)
11. Regulation (EC) No 850/2004 of the European Parliament and of the Council of 29 April 2004 on persistent organic pollutants and amending Directive 79/117/EEC. OJ L 158, 7–49 (2004)
12. Directive 2000/60/EC of the European Parliament and of the Council of 23 October 2000 establishing a framework for Community action in the field of water policy OJ L 327, 22.12.2000, 1–73 (2000).
13. Harmonisation framework for indoor products labelling schemes in the EU. ECA Report No 27. Publications Office of the EU (2012)
14. EN 16516:2017. Construction products: Assessment of release of dangerous substances—Determination of emissions into indoor air. CEN (2017)
15. Harmonisation framework for health based evaluation of indoor emissions from construction products in the European Union using the EU-LCI concept ECA Report No 29. Publications Office of the EU (2013)
16. European Commission Homepage, https://ec.europa.eu/growth/sectors/construction/eu-lci/values_en, last accessed 2020/11/23
17. Scutaru AM, Witterseh T (2020) Risk mitigation for indoor air quality using the example of construction products—efforts towards a harmonization of the health-related evaluation in the EU International J Hygiene Environ Health 229:113588
18. Scutaru AM, Crump D (2017) EU-LCI Harmonisation framework for the health-based evaluation of VOC emissions to indoor air from construction products. healthy buildings conference, Lublin, Poland. https://ec.europa.eu/growth/sectors/construction/eu-lci/documents-global_sssary_nn, last accessed 21/12/2020
19. Requirements for the indoor air quality in buildings: health related evaluation procedure for emissions of volatile organic compounds (VVOC, VOC and SVOC) from Building Products. Committee for Health-related Evaluation of Building Products. Umweltbundesamt (2018)
20. https://www.umweltbundesamt.de/sites/default/files/medien/355/dokumente/agbb_evaluation_scheme_2010.pdf, last accessed 21/12/2020.
21. Belgish Staatsblad : Arrêté royal établissant les niveaux seuils pour les émissions dans l'environnement intérieur de produits de construction pour certains usages prévus. C—2014/24239 (2014)
22. Arrêté du 30 avril 2009 relatif aux conditions de mise sur le marché des produits de construction et de décoration contenant des substances cancérogènes, mutagènes ou reprotoxiques de catégorie 1 ou 2. JORF n°0122 du 28 mai 2009
23. Décret n° 2011–321 du 23 mars 2011 relatif à l'étiquetage des produits de construction ou de revêtement de mur ou de sol et des peintures et vernis sur leurs émissions de polluants volatils. JORF n°0071 du 25 mars 2011

24. Arrêté du 19 avril 2011 relatif à l'étiquetage des produits de construction ou de revêtement de mur ou de sol et des peintures et vernis sur leurs émissions de polluants volatils. JORF n°0111 du 13 mai 2011
25. Regulation (EC) No 1272/2008 of the European Parliament and of the Council of 16 December 2008 on classification, labelling and packaging of substances and mixtures, amending and repealing Directives 67/548/EEC and 1999/45/EC, and amending Regulation (EC). Off J Eur Union Ser L 353, 31.12.2008, 1–1355 (2008)
26. The building information Foundation RTS Homepage: <https://cer.rts.fi/en/>, last accessed 2020/11/24
27. Dansk Indeklima Mærkning Homepage: <https://indeklimamaerket.dk/in-english/criteria/> last accessed 2020/11/24
28. Harmonisation of indoor material emissions labelling systems in the EU. ECA Report N°24. Publications Office of the EU (2005)
29. EN 14041:2018: Resilient, textile, laminate and modular multilayer floor coverings—Essential characteristics. CEN (2018)
30. EN 717-1:2004. Wood-based panels—Determination of formaldehyde release—Part 1: Formaldehyde emission by the chamber method. CEN (2004)
31. Bandow N, Gartiser S, Ilvonen O, Schoknecht U (2018) Evaluation of the impact of construction products on the environment by leaching of possibly hazardous substances. Environ Sci Europe 30:14
32. Butera S, Christensen TH, Astrup TF (2014) Composition and leaching of construction and demolition waste: inorganic elements and organic compounds. J Hazard Mater 276:302–311
33. CEN/TS 16637–2:2014. Construction products—Assessment of release of dangerous substances—Part 2: Horizontal dynamic surface leaching test. CEN (2014)
34. CEN/TS 16637–3:2016. Construction products—Assessment of release of dangerous substances—Part 3: Horizontal up-flow percolation test. CEN (2016)
35. EN 16105:2011. Paints and varnishes—Laboratory method for determination of release of substances from coatings in intermittent contact with water. CEN (2011)
36. Schoknechta U, Sommerfelda T, Borhob N, Bagdab E (2013) Interlaboratory comparison for a laboratory leaching test procedure with façade coatings. Prog Org Coat 76:351–359
37. CEN/TS 16637–1:2018. Construction products—Assessment of release of dangerous substances—Part 1: Guidance for the determination of leaching tests and additional testing steps. CEN (2018)
38. CEN/TS 17332. Construction products: assessment of release of dangerous substances—Analysis of organic substances in eluates, CEN, 2019
39. García-Ruiz S, Linsinger T, Conneely P, Emteborg H, Held A (2020) Precision of test methods to assess the release of organic substances from construction products Horizontal dynamic surface leaching test CEN/TS 16637–2 horizontal up-flow percolation test CEN/TS 16637–3 content of organic substances CEN/TS 17331 and analysis of organic substances in eluates CEN/TS 17332, Joint Research Centre (JRC) Technical report
40. Wahlström M, Laine-Ylijoki J, Järnström H, Kaartinen T, Erlandsson M, Palm Cousins A, Wik O, Suer P, Oberender A, Hjelmar O (2014) Environmentally sustainable construction products and materials—assessment of release. Nordic innovation. Nordic Innovation Report, No. 3. <https://www.nordicinnovation.org/> last accessed 2020/11/30
41. López-Uceda A, Galvín AP, Ayuso J, Ramón Jiménez J, Vanwalleghem T, Peña A (2018) Risk assessment by percolation leaching tests of extensive green roofs with fine fraction of mixed recycled aggregates from construction and demolition waste. Environ Sci Pollut Res 25:36024–36034
42. Directive 2008/98/EC of the European Parliament and of the Council of 19 November 2008 on waste and repealing certain Directives (Text with EEA relevance) OJ L 312, 22.11.2008, 3–30 (2008)
43. Decision 2003/33/EC. Council Decision of 19 December 2002 establishing criteria and procedures for the acceptance of waste at landfills pursuant to Article 16 of and Annex II to Directive 1999/31/EC. Official Journal L 011, 16/01/2003, 0027—0049 (2003)

44. Regulation (EU) No 528/2012 of the European Parliament and of the Council of 22 May 2012 concerning the making available on the market and use of biocidal products Text with EEA relevance. OJ L 167, 27.6.2012, 1–123 (2012)
45. CEN/TR 17105:2017. Construction products—Assessment of release of dangerous substances—Guidance on the use of ecotoxicity tests applied to construction products. CEN (2017)
46. EN ISO 8692:2012. Water quality—Fresh water algal growth inhibition test with unicellular green algae (ISO 8692:2012). CEN (2012)
47. EN ISO 6341:2012. Water quality—Determination of the inhibition of the mobility of Daphnia magna Straus (Cladocera, Crustacea)—Acute toxicity test (ISO 6341:2012). CEN (2012)
48. EN ISO 11348–3:2008. Water quality—Determination of the inhibitory effect of water samples on the light emission of *Vibrio fischeri* (Luminescent bacteria test)—Part 3: Method using freeze-dried bacteria (ISO 11348–3:2007). CEN (2008)
49. EOTA Technical Report General BWR3 checklist for EADs/ETAs Dangerous substances, Report TR34, EOTA (2015)
50. Bandow N, Jürgens F, Schoknecht U, Bauprodukte BB (2018) Entwicklung von Vergabekriterien für den Blauen Engel mit Hilfe von Auslaugtests, Abschlussbericht, 67/2018, Bundesanstalt für Materialforschung und -prüfung (BAM), Umweltbundesamt Berlin
51. Durão V, Silvestre JD, Mateus R, Brito J (2020) Assessment and communication of the environmental performance of construction products in Europe: Comparison between PEF and EN 15804 compliant EPD schemes. Resour Conserv Recycl 156:104703
52. ISO Homepage, <https://www.iso.org/>, last accessed 2020/12/5
53. ISO 14024:2018. Environmental labels and declarations Type I environmental labelling Principles and procedures. ISO (2018)
54. ISO 14021:2016. Environmental labels and declarations — Self-declared environmental claims (Type II environmental labelling). ISO (2016)
55. ISO 14025:2006. Environmental labels and declarations — Type III environmental declarations — Principles and procedures. ISO (2006)
56. OECD Homepage, <https://www.oecd.org/env/labelling-and-information-schemes.htm>, last accessed 2020/11/30
57. EU Ecolabel Homepage, <http://ec.europa.eu/ecat/>, last accessed 2020/12/1
58. Blue Angel Homepage, <https://www.blauer-engel.de/en>, last accessed 2020/12/1
59. Natureplus Homepage, <https://www.natureplus.org>, last accessed 2020/12/1
60. Nordic Swan Ecolabel Homepage, <https://www.nordic-ecolabel.org/>, last accessed 2020/12/1
61. Eurofins Homepage, <https://www.eurofins.com/consumer-product-testing/industries/construction-building/indoor-air-comfort/>, last accessed 2020/12/1
62. Eco-Institut-label Homepage, <https://www.eco-institut-label.de/en/>, last accessed 2020/12/1
63. UL Greenguard certification Homepage, <https://www.ul.com/services/greenguard-certification>, last accessed 2020/12/21
64. ISO 21930:2017. Sustainability in buildings and civil engineering works — Core rules for environmental product declarations of construction products and services. ISO (2017)
65. EN 15804:2012. Sustainability of construction works—Environmental product declarations—Core rules for the product category of construction products. CEN (2012)
66. UN General Assembly, Transforming our world: the 2030 Agenda for Sustainable Development, 21 October 2015, A/RES/70/1, available at: <https://www.refworld.org/docid/57b6e3e44.html>; last accessed 2020/11/20
67. Eurostat, https://ec.europa.eu/eurostat/statistics-explained/index.php/SDG_12_-_Responsible_consumption_and_production#Responsible_consumption_and_production_in_the_EU:_overview_and_key_trends, last accessed 2020/12/21

Part II

Structures

Chapter 6

Remote Inspection and Monitoring of Civil Engineering Structures Based on Unmanned Aerial Vehicles



Diogo Ribeiro , Ricardo Santos, Rafael Cabral , and Rui Calçada

Abstract This chapter describes recent contributes for the remote inspection and monitoring of civil engineering structures with the support of Unmanned Aerial Vehicles (UAVs). Regarding the remote inspection, dedicated computer-vision methodologies are presented for the automatic detection of cracks and exposed steel rebars on reinforced concrete (RC) structures. Two distinct image processing techniques are used: one based on heuristic features and other based on deep learning. In case of deep learning the stages related to the image database, as well as the training and validation are detailed. Both techniques are successfully applied to the case study of a building facade and a large-scale silo structure. In relation to the monitoring, an innovative methodology for estimating in-plane structural displacements based on video systems and UAVs is presented. As the structure and the UAV are both in motion, the estimation of the absolute structural displacements involves, first, the evaluation of the relative displacements of the UAV-structure based on target tracking, and second, the UAV motion subtraction based on the data derived from an embedded Inertial Measuring Unit (IMU). The validation of the proposed methodology is based on an exploratory test performed in the field, which conducted to very satisfactory and promising results.

Keywords Remote inspection · Monitoring · Unmanned Aerial Vehicle (UAV) · Cracks · Exposed steel rebars · In-plane displacements · Inertial Measuring Unit (IMU)

D. Ribeiro · R. Santos

CONSTRUCT-LESE, School of Engineering, Polytechnic of Porto, Porto, Portugal
e-mail: drr@isep.ipp.pt

R. Santos

e-mail: rps@isep.ipp.pt

R. Cabral · R. Calçada

CONSTRUCT-LESE, Faculty of Engineering, University of Porto, Porto, Portugal
e-mail: up201609762@edu.fe.up.pt

R. Calçada

e-mail: ruiabc@fe.up.pt

6.1 Introduction

The assessment of civil engineering structures is a key instrument for infrastructure managers to evaluate structural integrity and operability, as well as estimating possible maintenance or rehabilitation needs [1].

Typically, the structural condition assessment is performed based on the information provided by inspections complemented by performance indicators derived from Structural Health Monitoring (SHM) systems [2]. Visual inspections require the presence of trained inspectors that directly assess the structural condition based on specific decision-making criteria. This traditional technique is generally time-consuming, laborious, expensive and may put in risk the safety of professionals, particularly on situations of difficult accessibility. In turn, SHM systems allow the continuous monitoring of the structural integrity based on the measurement of physical quantities, such as, accelerations, strains, and displacements, to enhance safety, reliability and reduce the inspection costs. However, these systems have typically limited spatial coverage or require dense instrumentations arrays. Additionally, once installed, the access to the sensors is often restrained, making difficult the regular system maintenance, to detect sensory system malfunctions and noisy signals.

To address some of these problems, digital images and their associated processing techniques have been recognized as key components for improving inspection and monitoring strategies to achieve an automated condition assessment of civil engineering infrastructures [3].

In what concerns the inspection procedures, a recent line of research has been devoted to developing techniques of automated damage identification, including concrete cracks [4], concrete spalling and delamination [5] and steel corrosion [6, 7]. In this domain, two main approaches for damage identification based on digital images are presented in the bibliography: heuristic feature-extraction methods [8] and deep learning-based methods [9, 10].

The heuristic feature-extraction methods are based on the application of filters to images to enhance features of interest. A large part of the early research on vision-based damage detection was focused on identifying concrete cracks based on heuristic filters, particularly edge detection filters, e.g., Sobel gradient filters and the application of the Canny method, which can detect boundaries between image areas that have distinct brightness and reveal textures, enabling the location of the pixels on the crack edges [11]. Another type of heuristic features are the morphological filters which are related to image processing operators based on shape modifications [12]. In a morphological operation, the value of each pixel in the transformed image is based on a comparison of the corresponding pixel in the original image with its neighbours. The most basic morphological filters are dilation and erosion. Dilation adds pixels to the boundaries of objects in an image, while erosion removes pixels on object boundaries. Also, some variants of these morphological filters are used, such as, opening, closing and binarization operations [13]. Image binarization, which allows converting the pixels of a grayscale image to either black or white, is commonly used for crack detection, because dark cracks are generally categorized

as black, whereas lighter image regions appear white [14]. However, the efficiency of heuristic edge detection filters in detecting concrete cracks is particularly affected by perturbations on concrete surfaces, such as roughness, stains, and pockmarks and by external induced noises, such as lighting, distortions, shadows and blurring.

To overcome these limitations, deep learning computer vision methods have been successfully applied in the last few years in vision-based damage detection of civil engineering infrastructures. Several deep learning algorithms are broadly used in computer vision specifically for features learning and classification of images [15], however, the most widely and successfully applied are Convolutional Neural Networks (CNNs) [16, 17]. CNNs were specifically designed for crack identification and involve a training procedure based on a large set of real-world images, representative of cracks and non-cracks scenarios, and the definition of a classification model based on a group of successive layers (convolution, pooling, and fully connected layers) associated to specific mathematical operators [18]. The trained classification model is subsequently applied to new images in which cracks are to be detected. Typically, the training database is based on a transfer-learning concept, i.e., based on the architecture of an existing pretrained CNN (e.g., AlexNet, VGG, ResNet and others) eventually with a modified layout of layers, or based on a newly developed image database. Most databases are updated and augmented in dimension based on the application of data augmentation techniques which allows a considerable upgrade in their efficiency [19]. However, CNNs have demanding hardware requirements and can be extremely time-consuming, especially during training and validation phases, even if advanced GPU processing is available [20].

More recently, some applications are based on the use of Unmanned Aerial Vehicles (UAVs) coupled with computer vision systems for remote structural inspections. These coupled systems demonstrated to be competitive in the damage identification of inaccessible as well as extensive areas, allowing a considerable reduction of costs and execution times, since the inspection requires less technical staff. However, the performance of digital images processing tools depends highly on the image acquisition conditions such as capturing angle, weather conditions and undesired dust on target surface.

In recent years, computer vision-based methods coupled with UAVs have also been tested in field and laboratory applications, as an alternative technology for measuring structural displacements on SHM systems [21, 22].

In contrast to the measurements using a fixed reference point [23], the UAV is a non-stationary reference point and, therefore, its movements considerably affect the measured structure's displacements [24–28]. Changing from a stationary to a non-stationary measuring point poses a major challenge for the signal analysis, particularly in what concerns the development of methods to measure the absolute displacement of the structure instead of the structure-camera relative displacement. Thus, to increase the accuracy of the absolute displacement estimate, several camera motion subtraction techniques have been developed, namely: (i) using digital high-pass filtering [24], (ii) using a stationary background object [25, 26], and (iii) using an Inertial Measuring Unit (IMU) [27, 28].

The most promising and challenging technique is based on the estimation of the UAV motion from the data provided by an IMU, which consists of a set of DC type gyroscopes and accelerometers capable of responding to very low frequency movements (virtually 0 Hz). Precise estimations of the displacements and rotations of the UAV are obtained by the double integration of acceleration measurements or by the simple integration of angular velocities, respectively. Typically, the integration procedure is affected by errors that cause distortions in the baseline signal (drift), which are amplified in the case of double integration [29]. Thus, the success of the integration process requires a baseline adjustment of the signals by applying high-pass filters or using linear, bilinear, or polynomial corrective functions [30]. High-pass filters not only remove the baseline errors but also eliminate the low-frequency content of the signal associated with quasi-static movements.

This chapter presents recent developments on the remote inspection and monitoring of civil engineering structures based on computer-vision techniques and UAVs. A particular attention is given to the development and application of a robust methodology capable of detecting anomalies on RC structures, particularly cracks and exposed steel rebars, as well as evaluating in-plane structural displacements.

6.2 Integrated Methodology for the Remote Inspection and Monitoring of Reinforced Concrete Structures

Figure 6.1 presents an overview of the integrated methodology for the remote inspection and monitoring of RC structures supported by UAVs. The UAV is equipped with a high-precision GPS system, aided by a position correction system Real Time Kinematic (RTK) with the eventual support of a local station. The UAV is also equipped with an IMU and a native camera which provide high-precision georeferenced images.

Based on the georeferenced images collected by the UAV's camera, the post-processing of the images is performed in MATLAB[®] software.

In case of the remote inspection, the developed tool provides two different image processing techniques: one based on heuristic features and other based on Convolutional Neural Networks (CNNs). At this stage, these techniques were specifically designed for the (a) automatic detection of cracks, and (b) exposed steel rebars.

In case of the monitoring, the tool can provide an estimation of the in-plane absolute structural displacements of a precision target fixed to the structure. For this purpose, two computational tools were developed: one for heuristic processing of the video images, and other for the numerical integration of the data derived from the IMU. The video image processing tool aims at estimating the relative displacements between the UAV and the target. In turn, the numerical integration tool allows estimating the movements of the UAV, in particular the displacements and rotations, based on the records from the IMU system. Finally, an estimate of

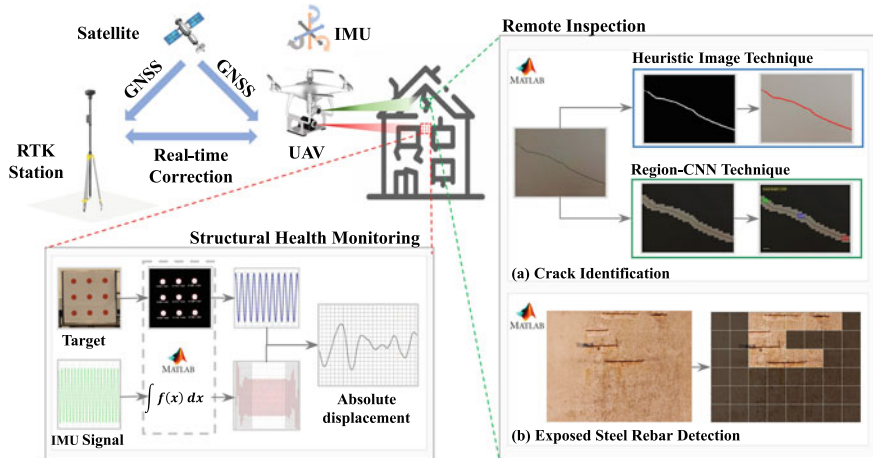


Fig. 6.1 Overview of the integrated remote inspection and monitoring methodology

the absolute displacement of the structure is obtained from the displacements of the video tracking corrected by the UAV's movements.

6.3 Remote Inspection and Automatic Detection of Anomalies Using Unmanned Aerial Vehicles

6.3.1 Strategy

The remote inspection based on UAVs includes three different phases, as shown in Fig. 6.2, namely: (1) recognition of the structure and flight preparation; (2) image collection campaign using UAV, and (3) image processing based on heuristic features or CNNs.

Phase 1, recognition and preparation, typically involves: (i) the collection of project elements and the investigation of the inspection history of the target structure, (ii) a site-visit to assess conditions and possible risk factors (potential flight obstacles, wind exposure conditions, electromagnetic interference, etc.), (iii) obtaining flight permits from the competent national authorities, (iv) selection of the technical staff and flight equipment (drone, camera, etc.), (v) elaboration of a flight plan including the definition of landing/takeoff zones, the flight time, the strategy for collecting images of the structure, the proximity of the drone to the target, among others.

Phase 2, collecting images with UAV, involves, in the first stage, a precision topographic survey of some control points of the structure. This step is essential for the georeferencing and calibration of the collected images. Control points must be located along the entire structure and can be materialized with auxiliary targets, or,

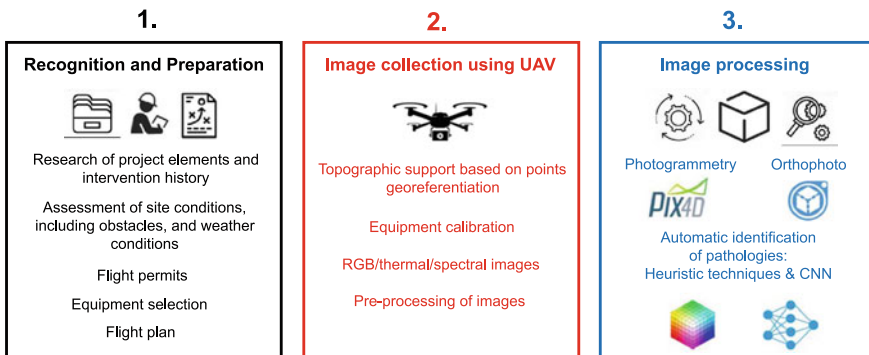


Fig. 6.2 Strategy for remote inspection

alternatively, with remarkable points of the structure. Obtaining the coordinates of the control points involves the definition of ground basepoints, in polygonal, and in line-of-sight with the structure, with the support of GNSS (Global Navigation Satellite System) receivers, preferably with the support of a RTK module, in addition to the use of an electronic theodolite. In the second stage of phase 2, images are captured using a drone equipped with a photographic camera. The drone must meet a set of specifications, namely: wide range of control and operability, endurance to wind loads in the vehicle and camera, stabilization capability, obstacle proximity sensors, positioning accuracy via RTK system, possibility of automatic flight, compatibility with different type of cameras or equipment, high autonomy, high-resolution cameras, and high storage capacity. The collection of images must be done safely, but as close to the structure as possible since shorter distances improve image resolution.

Finally, Phase 3 involves the automatic identification of RC surface anomalies, namely cracks and exposed steel rebars, based on heuristic features or CNNs. The processed georeferenced images may be used to perform a 3D geometric reconstitution of the structure by applying photogrammetry techniques available in software Pix4Dmapper[®] or to perform an orthophoto mosaic of the facade available in software Microsoft Image Composite Editor[®].

6.3.2 Heuristic Techniques

Heuristic image processing for crack detection, involves, first, the detection of the edges, and afterwards, the application of morphological features that enhance their visualization, particularly its tracing precision. Edge detection involves the prior application of a gradient detection filter, which can identify areas of the image with abrupt changes in lightness, based on the gray scale image. Afterwards, the automatic edge detection is performed by applying the Canny method [8], which is able to identify objects in the image by associating them in different clusters, i.e., clusters

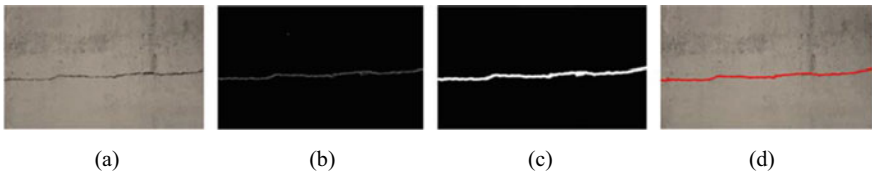


Fig. 6.3 Heuristic feature algorithm for crack detection: **a** original image; **b** Canny method; **c** edges expansion, filling, and erosion; **d** enhanced crack

associated with cracks and the rest of the image. Then, a specific series of morphological features are applied to the edges, particularly, (*i*) the closure, that allows the filling of the crack area, (*ii*) the expansion, that allows the expansion of crack areas in the perspective of aggregation with nearby areas also identified as cracks, (*iii*) the elimination of outliers, to remove objects outside the patterns of the cracks, (*iv*) the erosion, that contracts the crack zones and defines the final contours, and finally, (*v*) the pathology is shown in the image by means of a false color, resulting from the change in the white color of the binary image, and the superimposition on the original image. Figure 6.3 shows the main steps for the automatic crack detection based on heuristic features.

Regarding the detection of exposed steel rebars, in many situations accompanied by visible corrosion phenomena, involves, first, adjusting the brightness of the original image, so that only darker colors are visible. Then, the image is segmented by bands of colors (or channels), and retaining only the G band, in which the darkest colors of the image were concentrated. Based on this image, a color gradient detection filter was applied, followed by edge detection, in a procedure identical to that applied in the detection of cracks but, in this case, with the purpose of detecting the edges of exposed steel rebars. Then, the morphological features of image filling, dilation and erosion are applied consecutively. Lastly, the pathology is shown in the image by means of a false color, resulting from the change in the white color of the binary image, and superimposed on the original image. Figure 6.4 shows the main steps for the automatic detection of exposed steel rebar based on heuristic features.

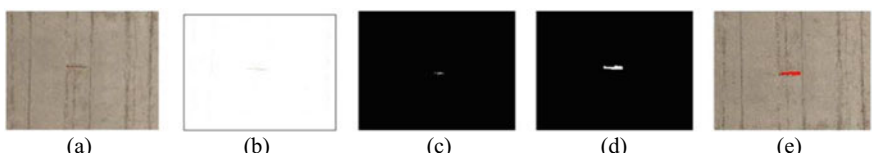


Fig. 6.4 Heuristic feature algorithm for exposed steel rebars: **a** original image; **b** brightness increase; **c** Canny method; **d** edges expansion, filling, and erosion; **e** enhanced crack

6.3.3 Deep Learning Techniques

The process of creating efficient CNNs involves two main steps: first, the constitution of an image database, and second, the training and validation of the network.

The quality of the images database is of utmost importance as well as the ability to cover distinct real environment scenarios. The simulation of non-captured environment scenarios can be performed using data augmentation techniques [19].

For specific situations, such as cracks or exposed steel rebars, a transfer learning strategy based on the selection of a pre-trained neural network can be considered. Typically, transfer learning is preferable than creating a new and dedicated neural network. There are several pre-trained neural networks with distinct architectures composed by multiple layers of artificial neurons (convolution, pooling, and fully connected layers).

In this work, the adopted strategy consists in using AlexNet network, whose architecture is illustrated in Fig. 6.5, which includes a large image database for each damage (20 k images), namely, cracks or exposed steel rebars, to classify an image as anomaly or non-anomaly. Additionally, a sliding window algorithm was used to classify the images on a region-by-region basis (Region-CNN or R-CNN). The sliding window scrolls the image from 227 to 227 pixels, considering a stride equal to 113 pixels, and darkening the regions of the image where no surface anomaly is detected.

6.3.3.1 Image Database

The acquisition of images, both from pathology ridden and intact concrete, involved capturing images in real context and obtaining online images. Typically, the images are captured from several real structures, and taken at several angles, distances, and different times of the day to cover a large diversity of image capture situations. Then, images are divided into 227×227 pixel resolution to be compatible with the pre-trained AlexNet network, using PhotoScape software[®]. All images which after division are not considered valid for classification are discarded.

Finally, it is also necessary to use Data Augmentation techniques to obtain enough images for a robust classifier. Training images can be increased in number by

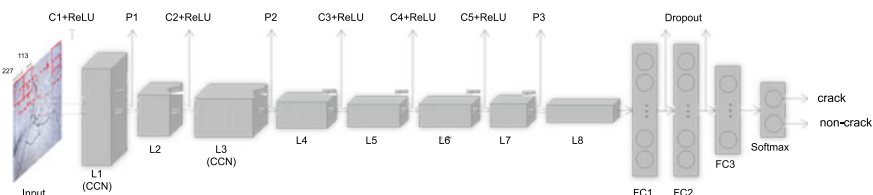


Fig. 6.5 CNN architecture for crack detection. L#: Operation layers; C#: Convolution operations; P#: Max pooling operations; CCN: Cross-channel normalization; FC#: Fully connected layers

geometric transformations, blur, and changes in the colour scale. As for geometric transformations, rotations, translations, and reflections can be applied to the original image in order to take into account the variation of the direction and the angle at which an image can be obtained. The application of blur simulates image capture conditions of insufficient light or motion, while changes in the colour scale are intended to take into consideration variations in white balance or brightness and colour of the pictures.

Figure 6.6 illustrates the process of the database constitution for the case of exposed steel rebars. Data augmentation allowed a seven-fold increase of the original database size, obtaining a sufficient number of valid images for training the CNN. At the end of the process, 40 k images were obtained, 20 k of exposed reinforcement and 20 k of intact concrete.

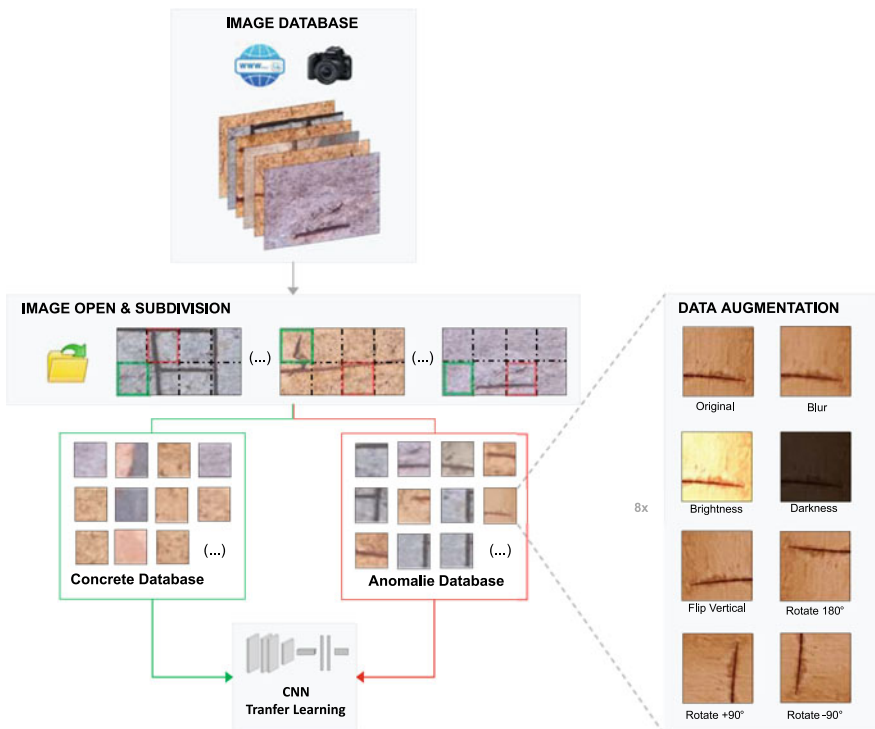


Fig. 6.6 Image database constitution for exposed steel rebars

6.3.3.2 Training and Validation

To perform the CNN training the Deep Learning Toolbox in MATLAB[®] was used, where some of the most popular convolutional neural network algorithms are implemented.

It was decided to use the AlexNet pre-trained network for the training of the CNN used not only because of its good performance, but also due to the reduced training time needed. As the CNN AlexNet is configured for one thousand categories, it was necessary to make small changes to its layers to classify only two categories. For each category, the images were subdivided, with 80% used for training the CNN and 20% reserved for validation. Figure 6.7 shows, schematically, how the process of training a robust classifier works for the case of exposed steel rebars.

6.3.4 Application to Crack Detection

The automatic crack identification methodology, based on both heuristic and CNN techniques, was applied to the remote inspection of the front facade of building F of the School of Engineering of Polytechnic of Porto (ISEP) campus (Portugal). Figure 6.8a shows an overview of the entire facade of the building and the two regions (A and B) where cracks were detected. Figure 6.8b illustrates the UAV, DJI Matrice 600 Pro, equipped with a Zenmuse X5 camera, capturing images of the building facade during a flight.

The distance between the UAV and the facade varied between 3.0 m and 5.0 m. A laser system, installed on the UAV gimbal, recorded at each second and during all flight time the distance between the drone and the facade. This distance is used for the calculation of the pixel dimension, which, posteriorly, enables the evaluation of the crack characteristic, such as the length and thickness. This last option involves a dedicated algorithm that is only associated to the CNN technique.

The images captured on regions A and B were processed using the heuristic and CNN image processing techniques (Fig. 6.9). The heuristic approach allows to detect and highlight in false colour (red) the visible crack, while the CNN approach allows to detect the visible crack, identified by the non-dark zones, as well as automatically characterize its length and maximum/minimum thicknesses with accuracy to the size of the pixel (mm/px).

Region A (Fig. 6.9a) presents a horizontal crack at the interface between the masonry parapet of the roof and the RC edge beam. It is one of the largest cracks detected, measuring 3.23 m in length, and thicknesses values between 1.88 mm and 6.65 mm. In turn, region B (Fig. 6.9b) has a diagonal crack situated near a window opening and presents 0.559 m in length and thicknesses varying between 1.41 mm and 3.95 mm.

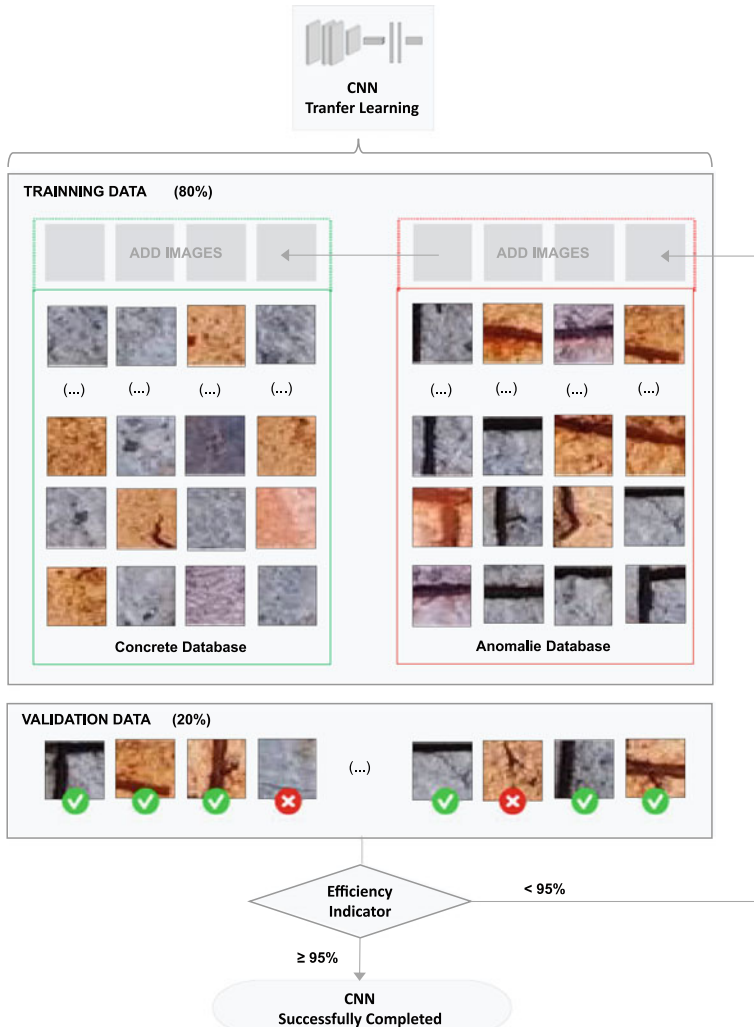


Fig. 6.7 CNN training and validation for exposed steel rebars

6.3.5 Application to Exposed Steel Rebar Detection

The automatic exposed steel rebar detection methodology, based on CNN technique, was applied to an industrial building, entirely built-in reinforced concrete, located in Vila do Conde, Portugal, next to the bank of the Ave river and about 2 km from the Atlantic Ocean [16]. For security reasons, the entrance into the industrial complex was forbidden, due to the advanced state of degradation of the structure and facilities. This limitation determined that the capture zone should be limited to the west side of

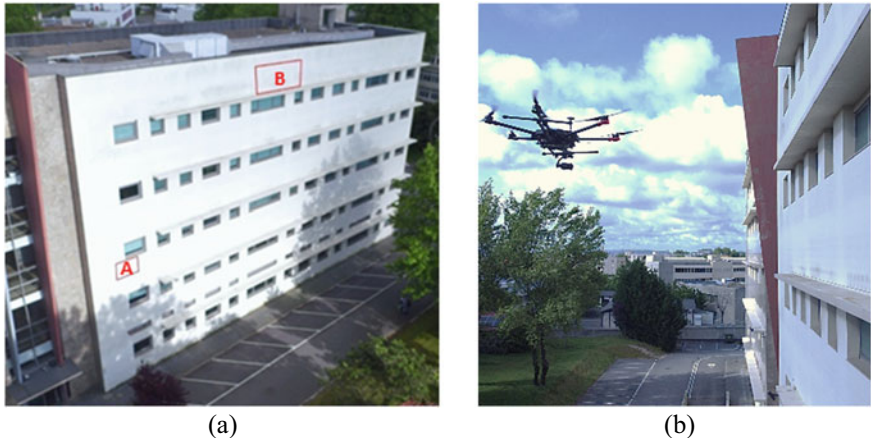


Fig. 6.8 Remote inspection of a building facade on ISEP campus: **a** building overview with identified regions A and B, **b** UAV DJI Matrice 600 Pro during the flight

the structure to operate the drone in safe conditions. Figure 6.10 shows the regions (A and B) where the images were captured.

The images were captured using a DJI Mavic Mini drone with a camera resolution of 4000×2250 pixels. The distance between the UAV and the facade varied between 3.0 m and 5.0 m. The images captured on the identified region were processed using the CNN technique, allowing to detect the exposed steel rebars.

Figures 6.11 and 6.12 show the created orthophoto mosaic from region A and region B, respectively, before and after processing, in which the exposed rebars have been highlighted in red for increased visibility. The few false positives occurrences are highlighted in green colour. The false positives appear in areas of advanced delamination, but still without exposed rebars, leading the algorithm to erroneously classify these positions. The accuracy of the network was equal to 98.33% and 99.60% for regions A and B respectively, which is higher than the validation efficiency.

6.4 Displacement Monitoring Using Unmanned Aerial Vehicles

6.4.1 Strategy

The non-contact displacement monitoring is based on the tracking of a target fixed to the structure using a video system and a UAV. As the structure and the UAV are both in motion, the tracking of the target allows obtaining the UAV-structure relative displacements. Therefore, it is necessary to evaluate and compensate the movements of the UAV to obtain the absolute displacements of the structure [24–28].

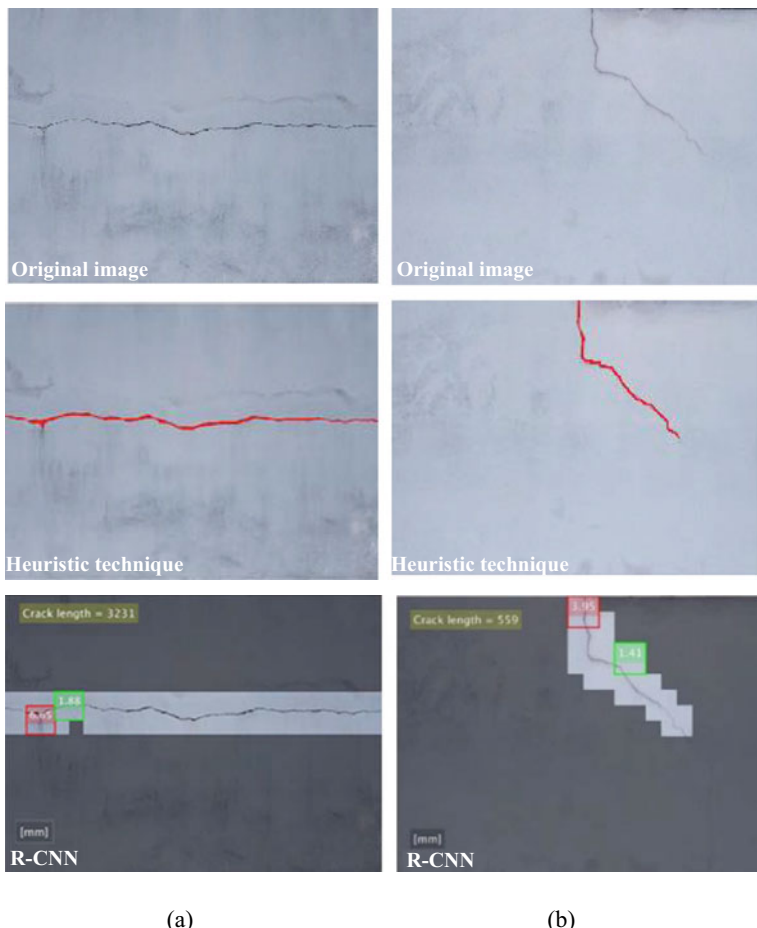


Fig. 6.9 Image processing techniques: **a** region A, **b** region B

Figure 6.13 shows the strategy with the tools developed on MATLAB[®] software for the video target tracking and the compensation of the drone's movements through IMU data. The drone's movement subtraction is based on the data recorded in an Inertial Measurement Unit (IMU) consisting of three accelerometers and three gyroscopes. Based on the acceleration records of the accelerometers and the angular velocity records of the gyroscopes, it is possible to estimate the displacements and rotations of the UAV using numerical integration techniques. The video target tracking is carried out based on the application of heuristic image processing techniques that allow to estimate the target position in each frame of the video.



Fig. 6.10 Silo overview with the identification of the inspection regions (A and B)

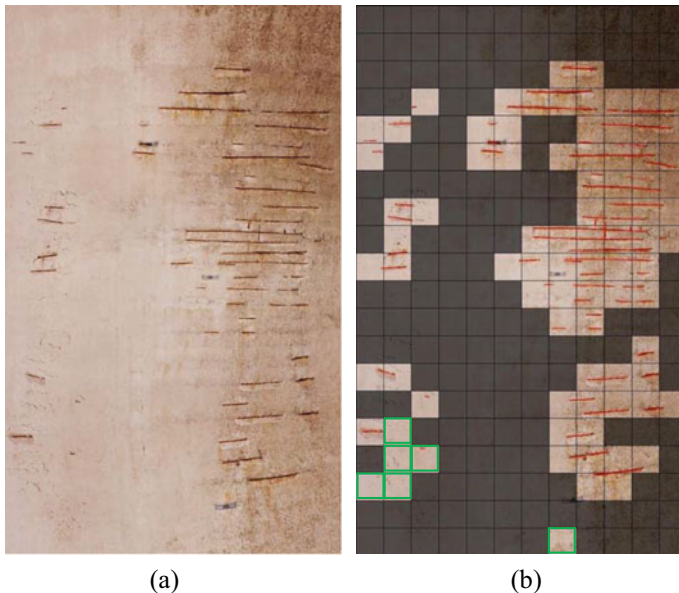


Fig. 6.11 Inspection of region A: **a** original, **b** processed

6.4.1.1 UAV Movements

The degrees of freedom representing the movements of the UAV are illustrated in Fig. 6.14 and refer to the geometric centre of the inertial system: three displacements, according to axes X, Y and Z, and three rotations, α , β and γ , around axis X, Y and Z, respectively. The X axis is perpendicular to the motion plane (target).

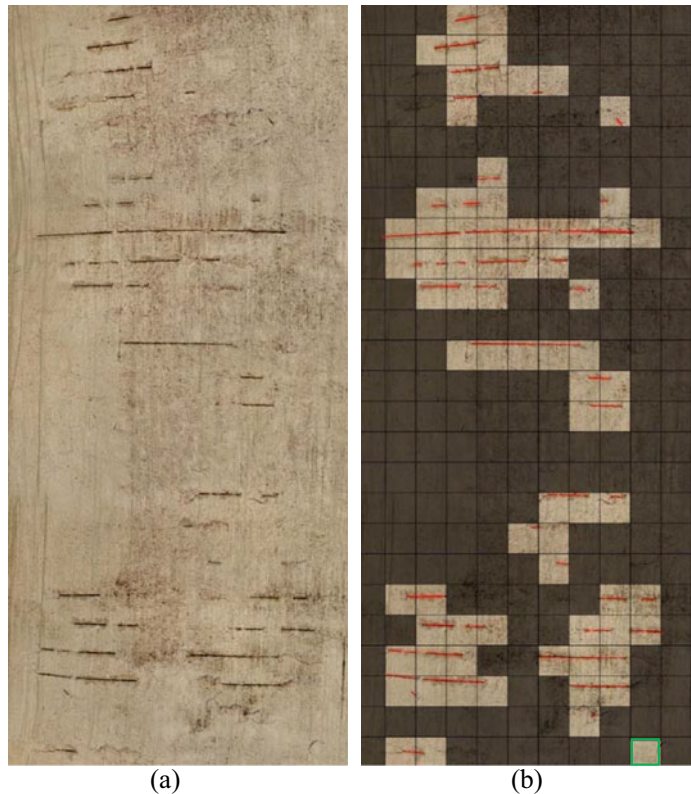


Fig. 6.12 Inspection of region B: **a** original, **b** processed

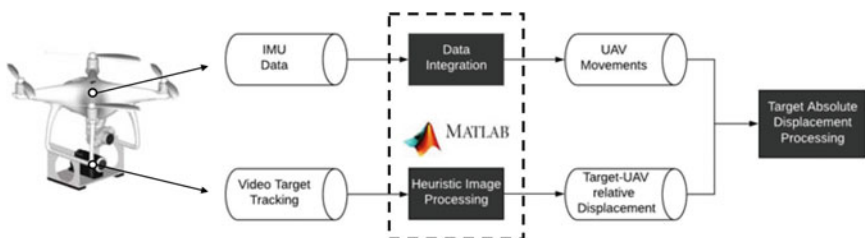
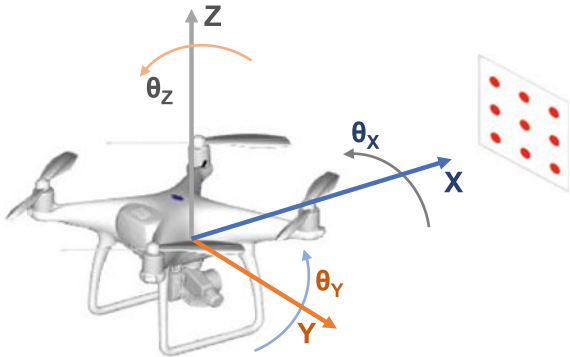


Fig. 6.13 Strategy of the heuristic image processing and numerical integration tools

The value of the virtual displacement of the target in the direction Y due to the movements of the UAV ($\vec{\delta}_{UAV}^{Y,i}$) can be determined from the sum of four terms of the UAV movement, given by Eq. (6.1).

$$\vec{\delta}_{UAV}^{Y,i} = \vec{\delta}_Y^{Y,i} + \vec{\delta}_X^{Y,i} + \vec{\delta}_\alpha^{Y,i} + \vec{\delta}_\gamma^{Y,i} \quad (6.1)$$

Fig. 6.14 Reference degrees of freedom characterizing the movement of the UAV and direction of the target motion



where $\overrightarrow{\delta}_Y^{Y,i}$ is the term resulting from the movement of the UAV in the direction Y, $\overrightarrow{\delta}_X^{Y,i}$ is the term resulting from the movement of the UAV in the direction of axis X, whose approximation or distance to the target indirectly induces a virtual movement of the target in the direction Y, $\overrightarrow{\delta}_\alpha^{Y,i}$ is the term resulting from the rotation of the UAV around axis X, which, due to the fact that the inertial system is distanced from the video system, induces a virtual displacement of the target in the direction Y, and $\overrightarrow{\delta}_\gamma^{Y,i}$ is the term resulting from the rotation of the UAV around axis Z, that also induces a virtual displacement of the target in the direction Y, where all terms refer to time step i.

According to Ribeiro et al. [28], the value of the virtual displacement of the target in the direction of axis Y due to the movement of the drone, at each time step i, can be obtained by the expression of Eq. (6.2).

$$\begin{aligned} \delta_{UAV}^{Y,i} = & \iint_{t_{i-1}}^{t_i} a'_Y(t) \cdot dt \cdot dt + \iint_{t_{i-1}}^{t_i} a'_X(t) \cdot dt \cdot dt \cdot \frac{Q_{i-1}}{D_{i-1}} \\ & + C \cdot \iint_{t_{i-1}}^{t_i} \dot{\alpha}(t) \cdot dt + D_i \cdot \iint_{t_{i-1}}^{t_i} \dot{\gamma}(t) \cdot dt \end{aligned} \quad (6.2)$$

where, $a'_X(t)$, $a'_Y(t)$ are the acceleration records corrected by the rotational effect and according to axes X and Y, respectively; Q_{i-1} is the distance from the centre of the camera sensor to the centre of the target, measured in the direction of axis Y for the time step i-1; D_i and D_{i-1} are the distances from the drone to the target measured in the direction of axis X for the time steps i and i-1, respectively; C is the distance from the gyroscope to the video camera sensor; $\dot{\alpha}$ and $\dot{\gamma}$ are the angular velocities around axes X and Z, respectively. More details about the mathematical formulation can be found in Ribeiro et al. [28].

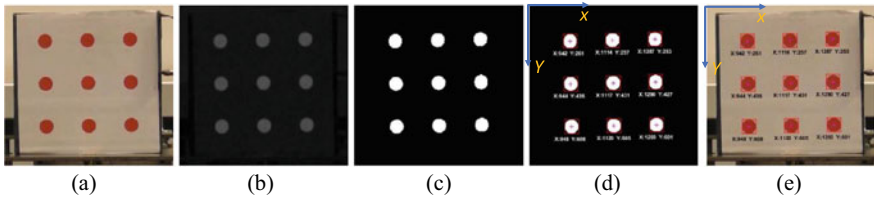


Fig. 6.15 Heuristic image processing for target tracking: **a** original image; **b** subtract red components and gray scale; **c** binary image and filter; **d** label all centroids; **e** overlay original image

6.4.1.2 Target-UAV Relative Displacement

The target tracking methodology is based on the application of morphological operators, particularly on segmentation, which involves the division of each image into regions (sets of pixels) that are similar in a given property, in this case colour. Figure 6.15 shows the ordered sequence of the morphological operators that constitute the image tracking algorithm, with a graphical representation of the effect of its application.

The original RGB image is subjected to a segmentation operation that allowed to separate the background from the red circles of the target. For this purpose, the G and B channels were subtracted from the image and the image was converted to the grayscale.

The resulting image is then converted to a binary image, in black and white. In this step, a filter is also applied to eliminate clusters of white pixels from areas of the image other than the circular areas of the target.

Subsequently, based on the binary image, the coordinates (x, y) of the centroid of the nine circular areas of the target are determined, in pixels. The origin of the referential (x, y) is considered in the upper left corner of the field of vision. In the end, for better visualization, the tracking of the binary image is overlaid with the original image.

Image resolution is calculated for each pair of circular areas at time step i (r_j^i), in px/mm, for a total of 6 values (r_1^i to r_6^i) in the direction of axis X, through the Eq. (6.3).

$$r_j^i = \frac{X_{j+3}^i - X_j^i}{[30 \cdot \cos \cos \gamma_i \cdot (1 - \sin \sin \alpha_i^2)]} \quad j = 1 \text{ to } 6 \quad (6.3)$$

where X_j^i is the coordinates of axis X of the centroid of circular area j , in pixels, at time step i , and α_i, γ_i are the rotations of the UAV-video system, at time step i , in relation to axis X and Z.

Based on the 6 singular values of the image resolution, only the n individual values ($n \leq 6$) less than 3 times the Mean Absolute Deviation (MAD) are considered.

Thus, the image resolution at time step i (r^i), in px/mm, which is variable in time due to the movement of the camera in the direction of the target and due to the perspective distortion, is given by Eq. (6.4).

$$r^i = \frac{\sum_{j=1}^n r_j^i}{n} \quad (6.4)$$

When the image resolution is known, the value of the horizontal displacement of the target at time step i ($\delta_V^{Y,i}$) is obtained through the Eq. (6.5).

$$\delta_V^{Y,i} = \delta_V^{Y,i-1} + \left[\frac{\left(\sum_{j=1}^9 X_j^i - X_j^{i-1} \right)}{9} \times \frac{1}{r^i} \right] \quad (6.5)$$

The image distortion errors, essentially due to barrel and pincushion distortions, were neglected due to the following reasons: (i) the video camera is equipped with very low distortion lens [31], as proved in preliminary laboratory tests with a dedicated calibration target, where maximum errors of the order of 0.03 mm occurring on the lateral sides of the images, were obtained; (ii) the positioning of the target is the most possible at the central region of the image [32].

6.4.2 Application

The exploratory field test consisted of measuring the displacements of a target fixed to a massive RC wall based on the video system and with the UAV in motion. In these circumstances, the target does not move, thus, the virtual displacement of the target estimated by the video system ($\vec{\delta}_V^{Y,i}$) is only due to the movements of the UAV ($\vec{\delta}_{UAV}^{Y,i}$) with opposite direction, conforming to Eq. (6.6).

$$0 = \vec{\delta}_V^{Y,i} + \vec{\delta}_{UAV}^{Y,i} \Leftrightarrow \vec{\delta}_V^{Y,i} = -\vec{\delta}_{UAV}^{Y,i} \quad (6.6)$$

The purpose of the exploratory field test is to validate the inertial system of the UAV, particularly the numerical integration tool, by comparing the displacements obtained through the inertial and video systems. If the inertial system works properly, both displacements values tend to be equal unless the sign. Therefore, in future applications, it will be possible to subtract the displacements of the UAV from the displacements estimated by the video system.

Figure 6.16 shows some details of the field test, namely the location of the target fixed to the wall, the UAV with the on-board video system and the local RTK station. The video was recorded by an DJI UAV, model Phantom 4 Pro with an external video camera from Panasonic, model HC-V380, rigidly connected to the body of the



Fig. 6.16 Experimental layout of the exploratory field test

UAV. The operational distance from the UAV to the target varied between 4.70 m and 5.20 m.

Figure 6.17 shows the records of the horizontal in-plane displacements of the target obtained through the video system and the inertial system (with opposite sign) based on a flight measurement period lasting 84 s. The initial ([0–30] s) and final ([54–84] s) parts of the records were removed because of the distortion effect of the signal resulting from the double integration of the acceleration records [28].

The result shows a good agreement between the displacement records obtained by the video system and the UAV inertial system. In some time intervals, such as between 37 and 43 s, the agreement is actually very good. The relative error between the mean square values (RMS) of the records is equal to + 9.3% using the video system as a reference. In turn, the difference between the peak values of both records is equal to -1.47 mm, which corresponds to a relative error of -15.5%, taking the results of the video system as reference.

6.5 Conclusions

This chapter presented some recent and innovative applications of UAVs on the remote inspection and monitoring of civil engineering structures.

The remote inspection techniques involve the use of heuristic and CNN image processing techniques. Both approaches reveal robustness and efficiency in automatically detecting visible anomaly in RC structures. A dedicated algorithm was also developed to precisely estimate the crack characteristics, particularly its length and thickness. In future works new deep learning detection techniques, such as, mask Region-CNN, will be applied, which will even increase the efficient and robustness of the proposed methodology.

In what concerns the remote monitoring, a non-contact displacement monitoring system is presented. This system is based on the tracking of a target fixed to the structure using a video system and a UAV. As the structure and the UAV are both in motion, the tracking of the target allows obtaining the UAV-structure relative

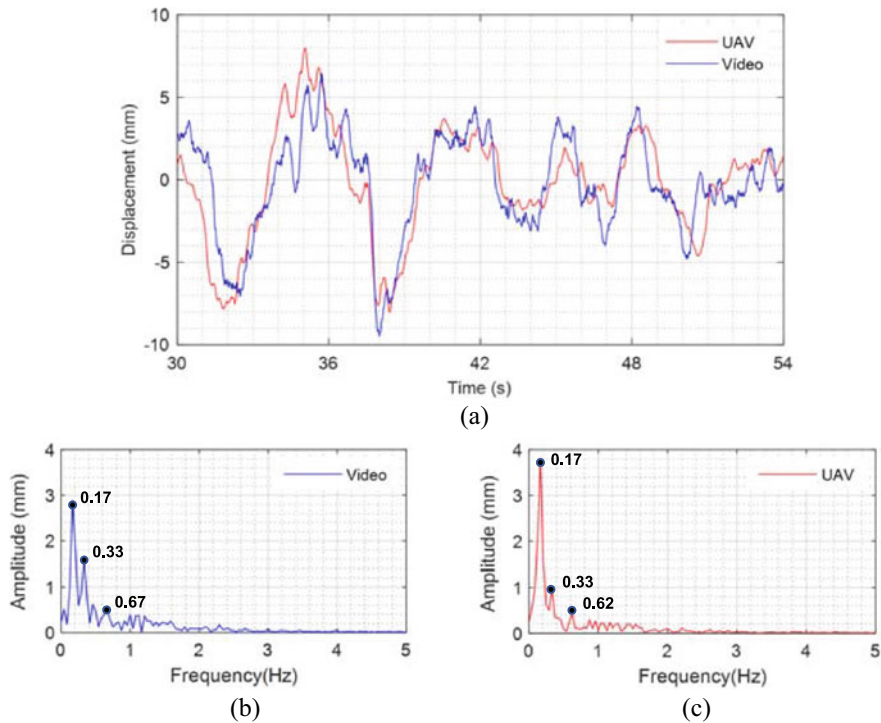


Fig. 6.17 Comparison of displacement records obtained through the video system and the UAV inertial system, and corresponding FFT amplitudes

displacements. Furthermore, an UAV motion subtraction technique was developed based on the data derived from an IMU. The results of an exploratory field test show a good agreement between the displacement records obtained by the video system and the UAV inertial system considering a target fixed to a non-movable structure. Based on these promising results, it will be possible in future applications to subtract the displacements of the UAV from the displacements estimated by the video system on real structures.

Acknowledgements The authors would like to thank the research unit CONSTRUCT (POCI-01-0145-FEDER-007457, UID/ECI/04708/2020, FEDER and FCT/MCTES) – Institute of R&D in Structures and Construction, funded by FEDER funds through COMPETE2020 – Programa Operacional Competitividade e Internacionalização (POCI) – and by national funds through FCT (Fundação para a Ciência e a Tecnologia). Additionally, the supported by the doctoral grant UI/BD/150970/2021 (to Rafael Cabral) - Portuguese Science Foundation, FCT/MCTES.

References

1. Nowogońska B (2020) A methodology for determining the rehabilitation needs of buildings. *Appl Sci* 10(11):3873. <https://doi.org/10.3390/app10113873>
2. Agdas D, Rice JA, Martinez JR, Lasa IR (2016) Comparison of visual inspection and structural-health monitoring as bridge condition assessment methods. *J Perform Constr Facil* 30(3):04015049. [https://doi.org/10.1061/\(ASCE\)CF.1943-5509.0000802](https://doi.org/10.1061/(ASCE)CF.1943-5509.0000802)
3. Spencer BF Jr, Hoskere V, Narazaki Y (2019) Advances in computer vision-based civil infrastructure inspection and monitoring. *Engineering* 5(2):199–222. <https://doi.org/10.1016/j.eng.2018.11.030>
4. Liu Z, Cao Y, Wang Y, Wang W (2019) Computer vision-based concrete crack detection using U-net fully convolutional networks. *Autom Constr* 104:129–139. <https://doi.org/10.1016/j.autcon.2019.04.005>
5. Ijjeah AA, Ullah S, Kudela P (2021) Full wavefield processing by using FCN for delamination detection. *Mech Syst Signal Process* 153:107537. <https://doi.org/10.1016/j.ymssp.2020.107537>
6. Lemos R, Cabral R, Ribeiro D, Santos R, Alves V, Dias A (2023) Automatic detection of corrosion in large-scale industrial buildings based on artificial intelligence and unmanned aerial vehicles. *Appl Sci* 13(3):1386. <https://doi.org/10.3390/app13031386>
7. Bondada V, Pratihar DK, Kumar CS (2018) Detection and quantitative assessment of corrosion on pipelines through image analysis. *Proc Comput Sci* 133:804–811. <https://doi.org/10.1016/j.procs.2018.07.115>
8. Ribeiro D, Santos R, Shibusaki A, Montenegro P, Carvalho H, Calçada R (2020) Remote inspection of RC structures using unmanned aerial vehicles and heuristic image processing. *Eng Fail Anal* 117:104813. <https://doi.org/10.1016/j.englfailanal.2020.104813>
9. Cha YJ, Choi W, Büyüköztürk O (2017) Deep learning-based crack damage detection using convolutional neural networks. *Comput-Aided Civil and Infrastr Eng* 32(5):361–378. <https://doi.org/10.1111/mice.12263>
10. Tran VP, Tran TS, Lee HJ, Kim KD, Baek J, Nguyen TT (2021) One stage detector (RetinaNet)-based crack detection for asphalt pavements considering pavement distresses and surface objects. *J Civ Struct Heal Monit* 11(1):205–222. <https://doi.org/10.1007/s13349-020-00447-8>
11. Hoang ND, Nguyen QL (2018) Metaheuristic optimized edge detection for recognition of concrete wall cracks: a comparative study on the performances of Roberts, Prewitt, Canny, and Sobel algorithms. *Advances in civil engineering*. <https://doi.org/10.1155/2018/7163580>
12. Boato G, Dang-Nguyen DT, De Natale FG (2020) Morphological filter detector for image forensics applications. *IEEE Access* 8:13549–13560. <https://doi.org/10.1109/access.2020.2965745>
13. Li G, Ren X, Qiao W, Ma B, Li Y (2020) Automatic bridge crack identification from concrete surface using ResNeXt with postprocessing. *Struct Control Health Monit* 27(11):e2620. <https://doi.org/10.1002/stc.2620>
14. Kim H, Ahn E, Shin M, Sim SH (2019) Crack and noncrack classification from concrete surface images using machine learning. *Struct Health Monit* 18(3):725–738. <https://doi.org/10.1177/1475921718768747>
15. Dong CZ, Catbas FN (2021) A review of computer vision-based structural health monitoring at local and global levels. *Struct Health Monit* 20(2):692–743. <https://doi.org/10.1177/1475921720935585>
16. Santos R, Ribeiro D, Lopes P, Cabral R, Calçada R (2022) Detection of exposed steel rebars based on deep-learning techniques and unmanned aerial vehicles. *Autom Constr* 139:104324. Article no S0926580522001972. <https://doi.org/10.1016/j.autcon.2022.104324>
17. Sony S, Dunphy K, Sadhu A, Capretz M (2021) A systematic review of convolutional neural network-based structural condition assessment techniques. *Eng Struct* 226. <https://doi.org/10.1016/j.engstruct.2020.111347>.

18. Ali L, Alnajjar F, Jassmi HA, Gochoo M, Khan W, Serhani MA (2021) Performance evaluation of deep cnn-based crack detection and localization techniques for concrete structures. *Sensors* 21(5):1688. <https://doi.org/10.3390/s21051688>
19. Shorten C, Khoshgoftaar TM (2019) A survey on image data augmentation for deep learning. *J Big Data* 6(1):1–48. <https://doi.org/10.1186/s40537-019-0197-0>
20. Nex F, Duarte D, Tonolo FG, Kerle N (2019) Structural building damage detection with deep learning: assessment of a state-of-the-art CNN in operational conditions. *Remote Sens* 11(23):2765. <https://doi.org/10.3390/rs11232765>
21. Hoskere V, Park JW, Yoon H, Spencer BF Jr (2019) Vision-based modal survey of civil infrastructure using unmanned aerial vehicles. *J Struct Eng* 145(7):04019062. [https://doi.org/10.1061/\(ASCE\)ST.1943-541X.0002321](https://doi.org/10.1061/(ASCE)ST.1943-541X.0002321)
22. Yoon H, Hoskere V, Park JW, Spencer BF (2017) Cross-correlation-based structural system identification using unmanned aerial vehicles. *Sensors* 17(9):2075. <https://doi.org/10.3390/s17092075>
23. Ribeiro D, Calçada R, Ferreira J, Martins T (2014) Non-contact measurement of the dynamic displacement of railway bridges using an advanced video-based system. *Eng Struct* 75:164–180. <https://doi.org/10.1016/j.engstruct.2014.04.051>
24. Garg P, Moreu F, Ozdagli A, Taha MR, Mascareñas D (2019) Noncontact dynamic displacement measurement of structures using a moving laser Doppler vibrometer. *J Bridg Eng* 24(9):04019089. [https://doi.org/10.1061/\(ASCE\)BE.1943-5592.0001472](https://doi.org/10.1061/(ASCE)BE.1943-5592.0001472)
25. Ellenberg A, Branco L, Krick A, Bartoli I, Kontsos A (2015) Use of unmanned aerial vehicle for quantitative infrastructure evaluation. *J Infrastruct Syst* 21(3):04014054. [https://doi.org/10.1061/\(ASCE\)IS.1943-555X.0000246](https://doi.org/10.1061/(ASCE)IS.1943-555X.0000246)
26. Yoon H, Shin J, Spencer BF Jr (2018) Structural displacement measurement using an unmanned aerial system. *Comput-Aided Civil and Infrastr Eng* 33(3):183–192. <https://doi.org/10.1111/mice.12338>
27. Abellanosa CB, Lugpatan RPJ, Pascua DAD (2016) Position estimation using inertial measurement unit (IMU) on a quadcopter in an enclosed environment. *Int J Comput Commun Instrum Eng* 3:332–336. <https://doi.org/10.15242/IJCCIE.AE0516306>
28. Ribeiro D, Santos R, Cabral R, Saramago G, Montenegro P, Carvalho H, Calçada R (2021) Non-contact structural displacement measurement using Unmanned Aerial Vehicles and video-based systems. *Mech Syst Signal Process* 160:107869. <https://doi.org/10.1016/j.ymssp.2021.107869>
29. Rocha SM, Feiteira JFS, Mendes PS, Da UP, Silva RFP (2016) Method to measure displacement and velocity from acceleration signals. *Eng Res Appl* 6(6–4):52–59
30. Arias-Lara D, De-la-Colina J (2018) Assessment of methodologies to estimate displacements from measured acceleration records. *Measurement* 114:261–273. <https://doi.org/10.1016/j.measurement.2017.09.019>
31. Panasonic Corporation (2015) Basic owner's manual high-definition video camera: model no. HC-W580 HC-V380. Newark, USA
32. Pan B, Yu L, Wu D, Tang L (2013) Systematic errors in two-dimensional digital image correlation due to lens distortion. *Opt Lasers Eng* 51(2):140–147. <https://doi.org/10.1016/j.optlaseng.2012.08.012>

Chapter 7

Laboratory Tests on Structural Adhesive Joints



Hugo Biscaia and Carlos Chastre

Abstract Since the Greek and Roman times adhesive structural connections have been used to join individual members of a structure to form a complete assembly. In this chapter, a review of the different laboratory tests on structural adhesive joints is given. These tests aim to assess the performance of the adhesive connection when subjected to normal or shear stress, or a combination of these field stresses. The test setup and the corresponding test protocols will also be addressed, as well as their advantages and disadvantages. Finally, some examples of innovative laboratory tests on structural adhesive joints between different materials will be presented and discussed in more detail.

Keywords Structural adhesive joints · Structural adhesive connections · Bond stresses · Structures · Laboratory tests

7.1 Review of Laboratory Tests on Structural Adhesive Joints

The use of epoxy resins with a structural purpose began in the late 60's with L' Hermite and Bresson [1–3], through the use of steel plates bonded to concrete as structural strengthening [1–8], and continued with the emergence of Fiber Reinforced Polymers (FRP) having the same purpose [9–14]. Many were the tests setups used by different researchers, e.g., [15–22], and no universal definition of a test setup for studying the adhesion between two materials exists. Despite of being similar studies, researchers are using different test setups to evaluate the same bond characteristics which may lead, for instance, to different strength capacities [23] which difficult the

H. Biscaia

Department of Mechanical and Industrial Engineering, UNIDEMI, NOVA School of Science and Technology, Universidade NOVA de Lisboa, Lisbon, Portugal

e-mail: hb@fct.unl.pt

C. Chastre ()

CERIS, Department of Civil Engineering, NOVA School of Science and Technology, Universidade NOVA de Lisboa, Lisbon, Portugal

e-mail: chastre@fct.unl.pt

comparisons between the available data. Although the geometry conditions and the same materials are used, the so-called pull-pull and pull-push tests leads to different strengths because the relative displacements between materials is carried out in a different way which influences the interfacial bond stress transfer throughout the bonded length. Therefore, it is of utmost importance to know the advantages and disadvantages of using each test setup as well as the consequences that such choice may have on the final performance of the adhesively bonded connection.

In 2006, Davalos et al. [24] have enumerated a few aspects that could help to nominate a test setup for worldwide use. For instance, considering the enormous variety of commercialized adhesive types, the future standard test setup should focus on the bonded connection instead on the adhesive. This would eliminate one important variable of the problem in the study of the bond characterization between two materials.

In Fig. 7.1 different schematic tests adopted in the literature to evaluate the bond characteristics between two materials under a mechanical load are shown.

The versatility and compactness of the specimens to be tested is an important issue. With this, it is expected that the test setup could be used in a broader range of situations and covering different conditions such as quasi-static loads, cyclic or fatigue loads, creep, durability tests, etc. At the same time, the results obtained from the standardized test setup should be correlated with real structural elements with larger dimensions. Finally, but not less important, the standardized test setup should be as simple as possible to reduce the data acquisition. This will allow researchers to simplify the interpretation of the results, and therefore, facilitate the validation of the experimental findings that can be very useful to define design recommendations with an extreme relevancy in a practice context.

The development and improvement of structural adhesive joints continues through the willing of scientists, designers, and manufacturers to overcome new challenging situations in the construction industry. The aim of this chapter is to contribute to the development of structural adhesive joints, having in mind the improvement of the bond performance of structural joints.

7.2 Case Studies of Structural Adhesive Joints with Different Materials

This section presents several case studies carried out by the authors in which different types of materials such as steel, FRP, concrete, stainless-steel and timber were used to study and develop different structural joints: steel-concrete, FRP-concrete, stainless steel-concrete, FRP-timber, as well as FRP-steel bonded joints. Depending on the specific situations, those adhesive joints were tested in laboratory under different actions—monotonic or cyclic loads, or under adverse environmental conditions—salt fog, temperature variations or high temperatures.

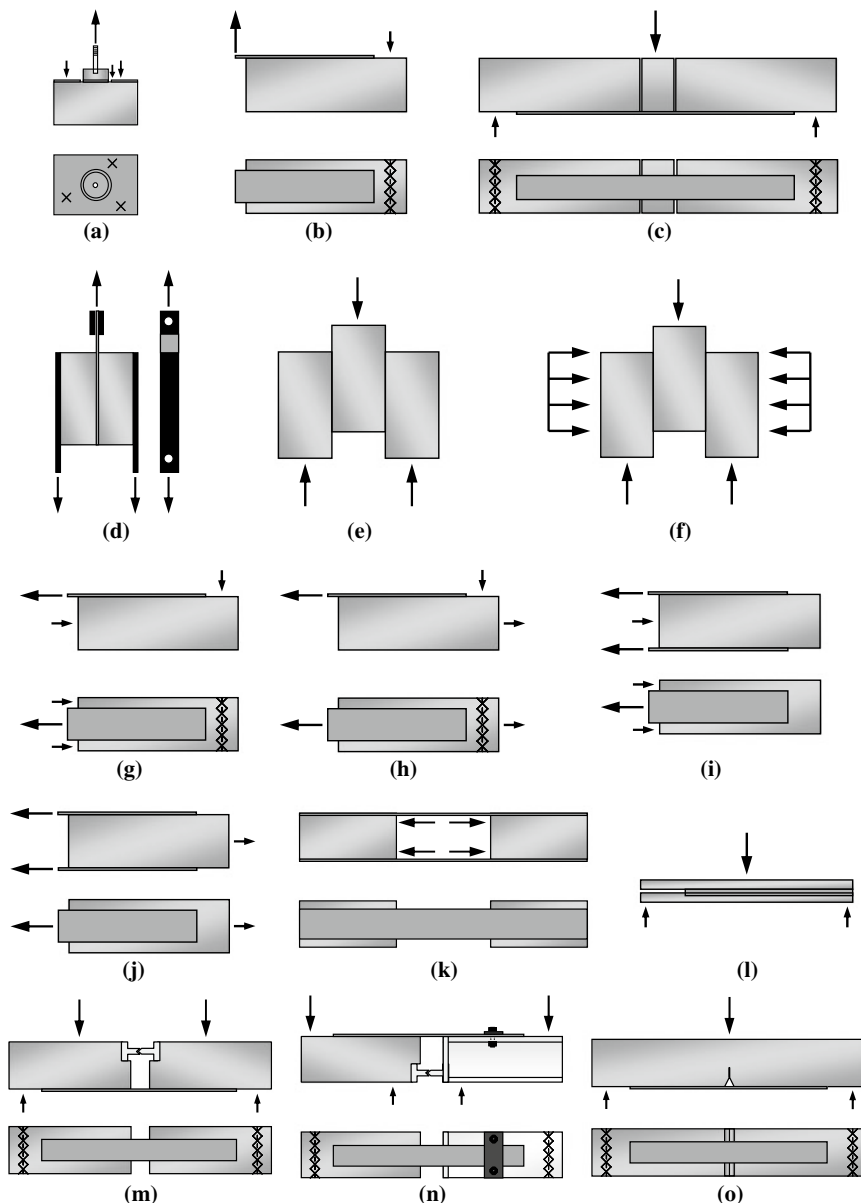


Fig. 7.1 Different schematic tests adopted in the literature to evaluate the bond between two materials under a mechanical load

7.2.1 Steel-Concrete

Chastre [15] have presented a study of the behaviour of steel plates bonded to reinforced concrete elements, which can be used in the strengthening of concrete structural elements, whether or not mechanical anchors are used. The objective of this research work was to investigate the behaviour to monotonic actions and particularly to cyclic loading of steel-epoxy-concrete connection with mechanical anchors. These cyclic actions are of particular interest in structures subject to strong seismicity. The research is mainly based in experimental analysis. The characterization of the materials was carried out as well as six models of the steel-epoxy connection were tested with monotonic loading. The structural bonded steel-epoxy-concrete with and without mechanical anchors connections were tested in twenty-six models, submitted to monotonic or cyclic loads. To carry out the monotonic and cyclic tests it was necessary to develop the test setup shown in Fig. 7.2.

Besides the type of action, other parameters were experimentally studied in the steel-epoxy-concrete connection models. These were the shape of the bonded connection, the type of concrete, the type of epoxy resin, the type of connection—with or without mechanical anchors, and the type of action—monotonic or cyclic.

The characterization of the mechanical properties of the materials used—steel, concrete (A and B) and of the two types of epoxy resins (V and P) was carried out, as well as the tests carried out to characterize the steel-epoxy bond. From the analysis of the results, it was found that the mean values of the tensile strength and the modulus of elasticity of the epoxy resin P were higher than those of epoxy resin V by 37% and 45%, respectively. It was also found that the average bond strength at rupture of the steel-epoxy-concrete connection was 39% higher in epoxy resin P (3.19 MPa) than in epoxy resin V (2.32 MPa).

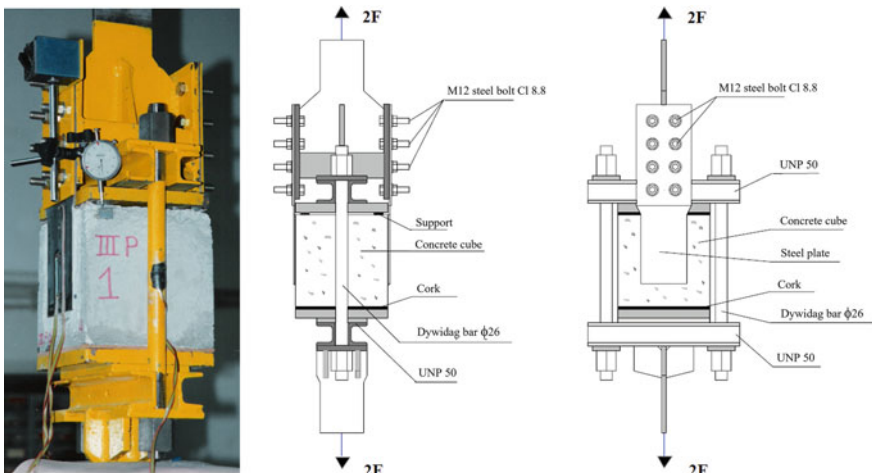


Fig. 7.2 Test setup developed [15] to monotonic and cyclic actions

In the connection tests with mechanical anchors, after the rupture of the steel-resin-concrete connection, it is observed that the connection still has a load capacity greater than 50% of the value of the rupture force of the steel-epoxy-concrete connection, which reveals a more ductile behavior of this type of connection, compared to the connection without mechanical anchors.

It was also observed in the tests, the appearance of a crack involving the entire model and caused by the compression effect of the mechanical anchor on the concrete (an effect similar to “splitting”).

The following is a summary of the main conclusions observed in the tests of the steel-concrete joints [15]:

- (i) Shape of the bonded connection: This influence was not very significant at rupture. However, this may be associated with the small dimensions of the specimens—which were conditioned by the type of test equipment needed to carry out the tests with cyclic loads—and the consequent reduced anchorage length. It can therefore be concluded that this is not the most suitable type of model to test the effect of the shape variation;
- (ii) Type of concrete: In general, this influence was not very significant in bonded connections without mechanical anchors. However, in models with mechanical anchors, the influence of the type of concrete is already considerable at rupture force—about 30% higher in concrete type A. It is therefore concluded that the quality of the concrete fundamentally affects the bonded connections with the mechanical anchors;
- (iii) Type of epoxy resin: The rupture force in the model tested with epoxy resin type P and concrete type A, was 22% higher than the value obtained in the standard model (epoxy resin type V, concrete type A). The quality of the resin therefore seems to affect the bond strength;
- (iv) Type of connection: The models with mechanical anchors and epoxy resin type V presents an average value of the rupture force 46% higher than that of the corresponding models without mechanical anchors. In turn, the models without mechanical anchors, tested under monotonic loads, presents an average bond stress on the rupture between the average value of the steel-epoxy bond and the average value of the concrete mean tensile strength. The rupture in the joints without mechanical anchors is almost always conditioned by the value of the average bond stress in the rupture of the steel-epoxy bond specimens. In turn, the rupture is conditioned by the value of the concrete mean tensile strength in the joints with mechanical anchors.

The average bond stress in the rupture of the joints without mechanical anchors, concrete type A and epoxy resin type V, was 2.66 MPa, while in the corresponding joints with epoxy resin type P, was 3.27 MPa. This stress in the joints with mechanical anchors, concrete type A and epoxy resin type V, was 3.89 MPa. In turn, in the corresponding experimental model with concrete type B, was 2.99 MPa.

The maximum displacement in the connection is about 35% lower in joints with mechanical anchors and the stiffness of the joint at 40% of the

rupture force, was about 114% higher than the corresponding experimental tests without mechanical anchors;

- (v) Type of action: It was found that the yield strength in steel was never exceeded with monotonic loads. The maximum stress reached in the steel was 55% of the yield stress in the joints without mechanical anchors, and 82% of this value in the joints with mechanical anchors. In some connections with mechanical anchors, tested to cyclic actions, a local phenomenon of plastic deformation of the steel plate was observed, which occurred next to the mechanical anchor, in the last displacement cycles, before failure. The joints without mechanical anchors tested to cyclic actions show a great degree of dispersion of the results, and their behavior to cyclic actions cannot be considered satisfactory. In turn, it was verified in the cyclic tests of the joints with mechanical anchors that the connection had a strength loss of 14% relatively to the corresponding joints under monotonic loads. It should be noted that this behavior of the connections was independent of the type of concrete. Therefore, the behavior under cyclic loads of the steel-concrete bonded joints with mechanical anchors can be considered quite reasonable.

7.2.2 FRP-Concrete

This is, perhaps, the most studied case. Therefore, it is not surprising that several test schemes could be found in the literature, e.g. [25–30]. Nevertheless, in this subsection, two test setups are presented. The first one is the 4-point bending test which is a configuration originally proposed by RILEM TC [31] to evaluate the bond between steel ribbed rods and concrete. This test consists of applying an external load to a reinforced concrete hinged beam which is simple supported by a roller and a pinned support. The hinge is placed at the centre of the beam on its compression side whereas the FRP composite is bonded to the soffit of the beam. This test is very useful since the positioning of the compression and tension forces are known during the test and, with one single test, it is possible to monitor two FRP-to-concrete bonded joints at the same time. However, beyond bending, internal shear forces perpendicular to the FRP bonded area develop in this test. If meaningful, these shear forces will influence the debonding of the FRP composite from the concrete tensioned surface and so, the FRP debonding is carried out under a mixed mode, i.e., under fracture Mode I + II.

To avoid the development of internal forces perpendicular to the FRP bonded area and allow the study of an FRP debonding from the concrete substrate under pure fracture Mode II, the single lap shear tests are preferred instead. Nevertheless, the pulling load in this test type should be perfectly aligned with the composite to avoid the development of peeling stresses within the bonded area. Otherwise, the presence of misalignments, will lead to an FRP debonding under a mixed mode once again. Furthermore, this single lap shear can be carried out under two different load conditions that leads to two different designations: (i) pull-pull test; and (ii) pull-push test. In both, the load transmitted to the FRP composite is pulling out the

composite from the substrate and therefore, the difference between both lies on the reaction obtained in the concrete substrate. If this reaction force pulls the concrete substrate, then the test is denoted as a pull-pull test. On the other hand, if the reaction force pushes the concrete substrate, then the test is designated as a pull-push test. As already shown by the authors in [23], if the substrate cannot be considered rigid when compared with the FRP composite, then, for the same specimen, the pull-pull test will lead to a higher bond strength than that obtained from a pull-pull-test. This can be easily explained by the development of bond stresses in both ends of the FRP composite in the pull-pull test whilst the pull-push test originates bond stresses only at the FRP pulled end that tend to migrate towards the FRP free end.

In Fig. 7.3, an overview of these two tests is shown. In the left-hand of this figure (Fig. 7.3a), it is shown the 4-point bending test carried out by Silva et al. [32] to evaluate the bond performance of Glass (G) FRP sheets externally bonded to the tensioned side of a reinforced concrete hinged beam. The monitoring equipment used included two pressure cells (located below the beam) to measure the loads transmitted to the hinged beams; 2 displacement transducers, one to measure the mid-span displacements and another one to measure the vertical displacement of section under the external load; and 13 strain gauges bonded onto the GFRP sheets (6 per bonded surface and another one at the centre and where the GFRP is not bonded to the hinged beam). The purpose of these strain gauges is to allow us to study the bond performance between the GFRP composite and the concrete.

Figure 7.4a shows the setup adopted by Biscaya et al. [30] to simulate the single lap shear test and evaluate the pure Mode II bond performance between a Carbon (C) FRP laminate bonded to a concrete block. This configuration revealed to be quite versatile because it was easy to adapt it to other substrates such as steel or timber, but it also allowed us to test other specimens with different dimensions in which different bonding techniques were used also. This test configuration consists of one steel frame where a hydraulic jack is placed. At the front of the hydraulic jack, a pressure cell is placed which measures the loads transmitted to the CFRP laminate. A mechanical anchorage device with a hollow metallic cylinder with two-piece anchor wedges is

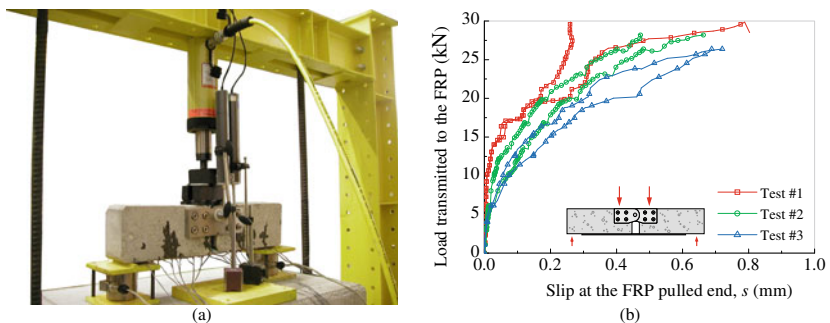


Fig. 7.3 Overview of the: **a** 4-point bending tests to evaluate the FRP-to-concrete bonded joints; and **b** typical load-slip curves

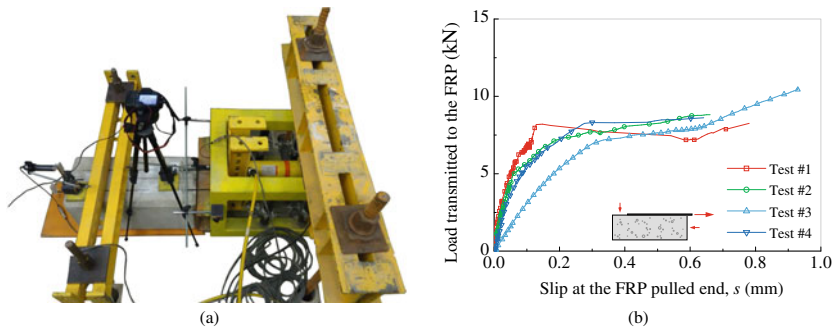


Fig. 7.4 Overview of the: **a** single lap shear tests to evaluate the CFRP-to-concrete bonded joints; and **b** typical load-slip curves

installed next to ensure that the composite can be pulled out when the hydraulic jack starts to work. Two steel profiles were used to fix the specimens and the steel frame to the floor of the laboratory through four Dywidag tie rods (2 per steel profile) which ensured that the specimens or the test setup stayed fixed during the tests. In this case, 2 displacement transducers were used to measure the displacements at both CFRP ends. Since the adopted bonded length varied, the number of strain gauges used to measure the strains in the CFRP laminates also varied. Additionally, a digital camera was also used to take pictures at every 5 s of the test which allowed us to measure the relative displacements between the CFRP laminate and the concrete block through the digital image correlation (DIC) technique. This contactless measuring technique was quite helpful in those cases where the Near Surface Mounted (NSM) bonding technique was adopted since the use of strain gauges bonded to the composite could have decreased the bond capacity between the CFRP and the surrounding concrete.

Figure 7.3b shows the typical load-slip curves obtained from the 4-point bending tests whilst Fig. 7.4b shows the same results obtained from the single lap shear tests. In these two cases the difference of the maximum load transmitted to the FRP composite lies precisely on the FRP composite used in each test. For instance, two layers of GFRP sheets with a nominal thickness of 1.27 mm per layer and with 80 mm width were used in the 4-point bending tests. In the other tests, a CFRP strip with 1.4×10 mm (thickness \times width) was used. Moreover, the bonded length adopted in the former case was 240 mm whereas the load-slip curves shown in the other case correspond to a bonded length of 300 mm. In both cases, the load-slip curve has a nonlinear development until complete debonding. However, unlike the load-slip curves obtained from the single-lap shear tests, the load-slip curves obtained from the 4-point bending tests do not show a plateau which corresponds to the FRP debonding initiation of a sufficient long bonded length, i.e., higher than the effective bond length which, by definition, is the length beyond which the load transmitted to the FRP composite does not increase further. Two main factors may justify this difference on the load-slip curves. One, as already mentioned, lies on the internal shear forces (perpendicular to the bonded area) originated in the 4-point bending

test. At the centre of the hinged beam, the bending of the beam induces compression stresses into the GFRP-to-concrete joint which can improve the bond behaviour of the bonded joints by, for instance, increasing the interfacial maximum bond stress. Moreover, the effective bond length of this GFRP-to-concrete joint was estimated in 275 to 295 mm [32] which is 14,6% to 22,9% higher than the bonded length. Therefore, no plateau could (at least) theoretically be seen in the load-slip curves obtained from the 4-point bending tests shown in Fig. 7.3b.

In the case of the single lap shear tests, the effective bond length was experimentally obtained by changing the bonded length of different specimens. In this particular case, bonded length between 50 and 300 mm were considered which allowed us to obtain an effective bond length of approximately 160 mm [30]. Therefore, being less than the bonded length of 300 mm, it is expected to observe a plateau in the load-slip curve which represents the migration of the interfacial bond stresses towards the CFRP free end.

It is noteworthy to mention that Test #3 in the single lap shear test showed a small load increase after the debonding load was reached, i.e., after the corresponding plateau of debonding load. This can be explained, for instance, observing the failure mode of this specimen in Fig. 7.5a.

Unlike Test #4 where an interfacial failure mode between the CFRP strip and the adhesive (see Fig. 7.5b), the failure model observed from Test #3 allow us to observe a cohesive rupture within the concrete surface close to the CFRP free end. So, as the CFRP began to debonded from the concrete block, the load remains unchanged as the interfacial slips increased. As mentioned, along with this process, the interfacial bond stresses migrate towards the CFRP free end (from the right to the left side of Fig. 7.5a). When these stresses reached the vicinities of the CFRP free end, the adhesion of the CFRP to the concrete improved the stress transfer between the CFRP and the concrete promoting therefore, its rupture and increasing the load capacity of the specimen.

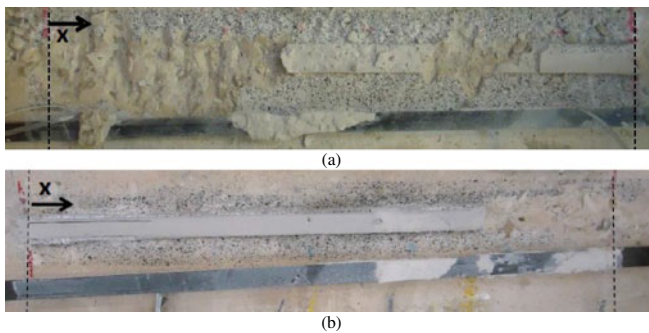


Fig. 7.5 Overview of the failure modes observed in the specimen tested in: **a** Test #3; and **b** Test #4 of the single lap shear tests

7.2.3 Stainless Steel–Concrete

To overcome the corrosion problem associated to steel, the use of stainless steel (SS) on reinforced concrete structures could be a good alternative solution. However, the actual costs associated to the stainless steel may discourage its use. Like stainless steel, CFRP composites are free of corrosion problems, but it has a non-linear and ductile behaviour that makes it, from the structural point of view, very interesting to be used rather than CFRP composites which have linear and fragile rupture behaviour. In a previous work of the authors [33–35] the stainless steel was used to flexural strength different reinforced concrete (RC) T-beams according to different bonding techniques. These T-beams were tested to a 4-point bending test and after being tested, the beams were cut near the supports where they had not reached the cracking bending moment. These parts of the T-beams were then reused to bond stainless steel bars and rods. In the case of the bars, several bonded lengths were externally bonded (EB) to the downside of the T-beams flanges. Figure 7.6a shows the single lap shear test setup adopted to evaluate the stainless steel-to-concrete bonded joints. This test setup is the same used in [30] to evaluate the bond between CFRP strips and concrete (see Fig. 7.6a). In this case however, the T-beams were placed upside down for testing. Like the single lap shear tests of the CFRP-to-concrete bonded joints described in Sect. 2.2, the monitoring equipment used on the tests of the stainless steel bars externally bonded to concrete included: (i) one pressure cell, which was placed between the hydraulic jack and a mechanical anchorage device that was formed by a hollowed metallic cylinder with two-piece anchor wedges (see detailed Fig. 7.6b); (ii) two displacement transducers, one to measure the displacements of the adhesively bonded joint at the stainless steel loaded end, and another one to measure the displacements at the stainless steel free end; (iii) depending of the adopted bonded length, several strain gauges were bonded throughout the bonded length that measured the strains in the stainless steel during the loading; and (iv) a digital camera that took several pictures of the bonded length that, through the DIC technique, allowed us to measure the relative displacements of a pre-selected area of interest of the stainless steel-to-concrete bonded joint.

Regarding this last item, it is important to mention that to avoid the loss of detail and/or definition of the photos, the digital camera took pictures from a limited area of interest near the stainless steel pulled end. Therefore, in those cases where the bonded length was too long, only part of it was monitored. An example can be seen from Fig. 7.7b in which the results at the debonding initiation of the EBR specimen with a bonded length of 800 mm are shown. From this Fig. 7.7b, it is also possible to observe that the DIC measurements led to a slip configuration with too many “peaks and values”. Such results compromise the determination of the local bond behaviour since, e.g, to obtain the bond stresses a second derivative of the slips would be needed to carry out which will magnify their values.

To bypass this issue, the slip distribution at the debonding initiation can be expressed through a mathematical function with continuous first and second derivatives [36]:

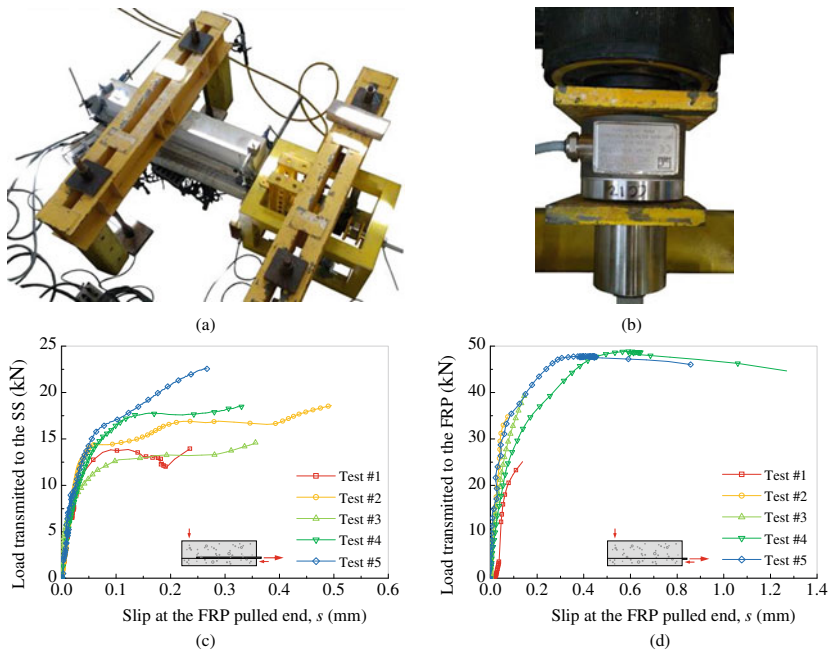


Fig. 7.6 Overview of the: **a** single lap shear tests to evaluate the stainless steel-to-concrete bonded joints; **b** detail of the mechanical anchorage device and the pressure cell; **c** typical load-slip curves obtained from the stainless steel bars EB to concrete; and **d** typical load-slip curves obtained from the stainless steel ribbed rods NSM on concrete

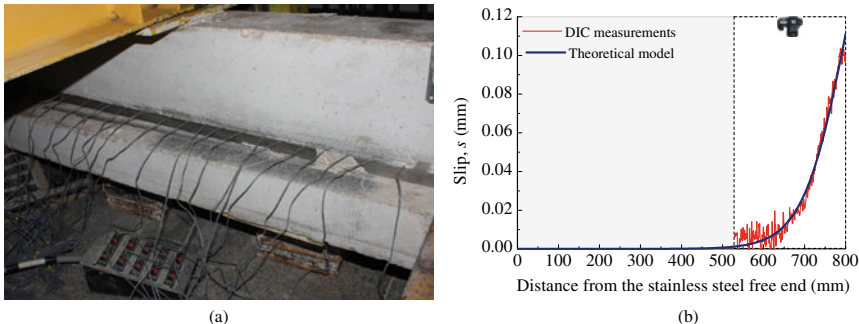


Fig. 7.7 **a** Failure mode observed from the stainless steel EB onto the concrete with a bonded length of 800 mm; and **b** comparison between the slip distribution obtained from the DIC measurements and that obtained from a theoretical fitting curve

$$s(x) = a/(1 + e^{b \cdot (L-x)}) \quad (7.1)$$

where “*a*” and “*b*” are constants to be determined from fitting the curve to the experimental results obtained from the DIC technique; *L* is the bonded length; and *x* corresponds to the direction of the bonded length with origin at the stainless steel free end. If the concrete substrate can be considered rigid when compared with the stainless steel bar, then the bond stresses can be estimated according to [37–39]:

$$\tau(x) = E_{ss} t_{ss} d^2 s / dx^2 \quad (7.2)$$

where E_{ss} and t_{ss} are the Young modulus and the thickness of the stainless steel, respectively.

In the case of the ribbed stainless steel rods, and since the NSM bond technique was adopted in a few number of specimens, the evaluation of the bond between the stainless steel rods and the concrete in these NSM specimens was exclusively based on the DIC measurements. Aiming to obtain the effective bond length and the local adhesion behaviour (i.e, the bond-slip relationship) of the stainless steel rods and the concrete, different bonded lengths were considered also. The results showed that the effective bond length of these NSM specimens was shorter (~71.5%) than that obtained from the EBR specimens. Moreover, and unlike the EBR specimens where the stainless steel bars have debonded from the concrete substrate, classical ruptures of the stainless steel rods could be observed from the NSM specimens with the largest bonded lengths. Despite the different stainless steel used in both situations, the results clearly suggested that the cumulative use of ribbed rods and the NSM bonding technique provides a better bond performance between the stainless steel and the concrete T-beams compared with the use of flat bars EB onto the concrete surface. This can be justified through the global and local bond behaviours obtained from both situations.

From the global point of view, the loads reached in the EBR specimens are much lower than those obtained from the NSM specimens (see Fig. 7.6c and d). Moreover, the shape of the load-slip curves shown in Fig. 7.6c and d are quite similar to those obtained from the CFRP-to-concrete bonded joints shown in Fig. 7.4b. However, an important difference between the load-slip curves obtained from the NSM specimens (see Fig. 7.6d) should be mentioned which lies on the plateau at maximum load transmitted to the stainless steel (or to the CFRP strip in the case of CFRP-to-concrete bonded joints). Hence, the observed plateau in the NSM specimens correspond to the yielding of the stainless steel whereas the plateau at maximum load of the EBR specimens correspond to the debonding load of the stainless steel (or CFRP) from the concrete substrate.

Regarding the local bond behaviour, the maximum interfacial bond stress calculated in the case of the EBR specimens was approximately 9.0 MPa whilst the NSM specimens registered a maximum interfacial bond stress of approximately 16.3 MPa. Furthermore, the estimated local adhesion law obtained from the EBR specimens can be mathematically defined through an exponential function with a first ascending branch followed by a softening branch and ending with zero bond stress. On the

other hand, the local adhesion behaviour of the NSM specimens can be estimated through a tri-linear adhesion law which is characterized by an initial ascending branch followed by a limited plateau (corresponding to the maximum interfacial bond stress) that ends with the initiation of a linear softening branch.

The failure modes observed in the EBR specimens were mainly characterized by the separation of the stainless steel bars from the adhesive. Nevertheless, in the specimens with the largest bonded lengths, the cohesive rupture a superficial layer of concrete could be observed as well in some regions of the bonded length. In the specimens with the shortest bonded length, the adhesive failure between the stainless steel bar and the adhesive was mainly observed. In the middle, i.e., in those cases where the bonded length was not too short nor too long, cohesive ruptures within the concrete were mainly observed. In the case of the NSM specimens, two main failure modes were observed. One, as already mentioned, was characterized by the rupture of the stainless steel ribbed rod which could be observed in those specimens with the largest bonded length whilst the failure modes observed in the other specimens showed a cohesive rupture in the concrete.

7.2.4 FRP-Timber

The present need to preserve ancient timber constructions has led several researchers to look at the potentialities of using FRP composites to repair existing timber structures [40]. Like concrete structures, the FRP composites can be bonded to the timber substrate by means of equivalent bonding techniques such as the EBR or NSM bonding techniques. Furthermore, due to such similarities between both systems (concrete or timber) it is not surprising that the same issues associated with concrete structures can be observed in the case of timber structures. For instance, the FRP composite is prone to debond from the timber prematurely, i.e., when the maximum strain in the FRP composite is too far away from its rupture value. Once again, like concrete structures, as the bonded length increase the load transmitted to the FRP composite increases but until a certain bonded length value which is denoted, as already mentioned, the effective bond length of the FRP-to-timber bonded joint. To evaluate this and other aspects of this type of bonded joints, the local bond behaviour is important to identify. This is a task quite hard to accomplish since we can find several timbers used in construction, and with different degradation levels between them. In addition, the large number of adhesives commercially traded in the construction industry exponentially increases the combinations of CFRP-to-timber bonded joints. Nevertheless, since timber and concrete are materials with different constitutive behaviours under tension or compression, the local bond behaviour of CFRP-to-timber joints should be different from the CFRP-to-concrete bonded joints. In fact, some studies carried out by the authors [30, 41, 42] pointed out that the CFRP-to-timber bonded joints can be modelled through tri-linear or exponential bond-slip relationships in which the softening branch (i.e., after maximum interfacial bond stress) tends to a residual bond stress.

The authors have carried out some studies [41–43] where CFRP-to-timber bonded joints were studied. In the studies with ancient timber [40, 41], the timber used belong to an ancient building built in a small Portuguese coast village called Sesimbra during the nineteenth century. The timber used to carry out these studies was removed from a suspended timber pavement. Initially, the timber was completely unknown but after performing several tests (e.g, the 3-point bending test, compression tests and pull-out tests) to identify the timber, it was found that the timber was a redwood (*Pinus Sylvestris L.*) with a density of 400 kg/m^3 , which can be found in several mountainous regions in the north and centre of Portugal, especially since the nineteenth century.

Three main bonding techniques were analysed. In the first one, the EBR bonding technique was considered, and different bonded lengths were adopted. In the second situation, the NSM bonding technique was tested. Finally, in the last situation a steel plate was pressed against the CFRP free end to delay or even prevent the CFRP premature debonding. To do so, the single lap shear test shown in Fig. 7.8a was adopted.

Although in this case the specimens had smaller dimensions than those already described for concrete (see Sect. 7.2.2 or 7.2.3), the idealized single lap shear test setup allowed us to continue using the same test setup already used for the concrete

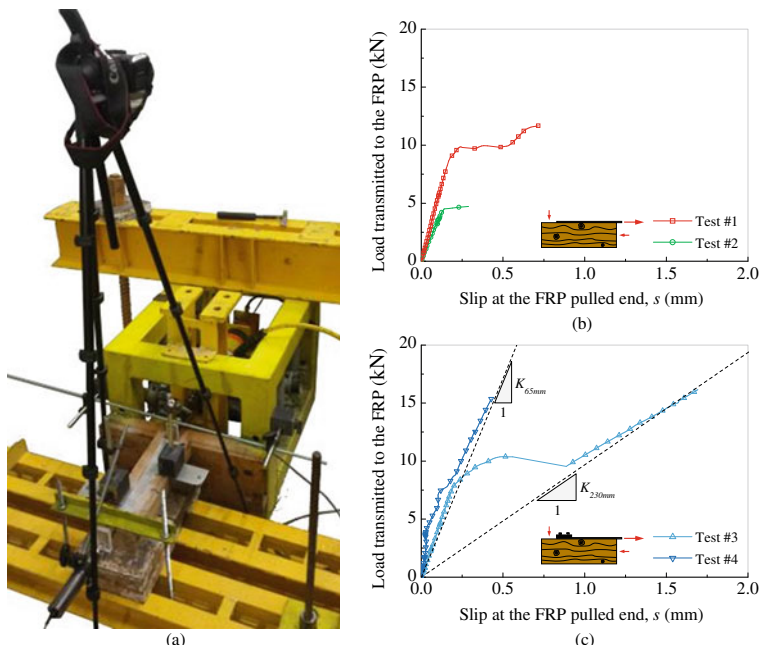


Fig. 7.8 Overview of the: **a** single lap shear tests used to evaluate the CFRP-to-timber bonded joints; **b** load-slip relationship obtained from the EBR specimens with a bonded length of 65 mm (Test #2) and 200 mm (Test #1); and **c** load-slip relationship obtained from the anchored CFRP specimens with a bonded length of 65 mm (Test #4) and 200 mm (Test #3)

specimens. In this situation, the specimens were instrumented similarly to the other previous cases, i.e.: (i) one pressure cell that measure the loads transmitted to the CFRP strip; (ii) two displacement transducers that measured the displacements at both CFRP ends; (iii) several strain gauges bonded onto the CFRP strips that measure the strain throughout the bonded length of the CFRP-to-timber bonded joint; and (iv) a digital camera that capture the displacements of the CFRP strips as well as the displacements of the timber substrate.

The load-slip curves obtained from the single lap shear tests are briefly summarized in Fig. 7.8b and c. In Fig. 7.8b, the results obtained from the EBR specimens free of any mechanical anchorage device and with two different bonded lengths of 65 and 230 mm are shown. Two main differences of the load-slip curves can be seen here. The one with the lowest load transmitted to the CFRP strip corresponds to the EBR specimen with the shortest bonded length (Test #2) whereas the other curve (Test #1) corresponds to the case with the longest bonded length. These results change when a mechanical anchorage device is installed in both specimens and at the CFRP unpulled end (see Fig. 7.8c). Thus, after the initiation of the CFRP debonding, the load-slip curves tend to a linear load-slip relationship that coincides with the axial stiffness (K) of the CFRP strip, i.e.:

$$K = E_f A_f / L \quad (7.3)$$

where E_f and A_f are the Young modulus and the cross sectional area of the FRP composite, respectively. In these cases, the load-slip curves reveal how efficient the use of a mechanical anchorage can be to delay or avoid the CFRP premature debonding from the timber substrate. Still, in these cases where the CFRP strip was anchored to the timber substrate, the rupture of the CFRP laminate was not achieved since the CFRP strip has slipped from the anchorage during the test.

The efficiency of the mechanical anchorage is therefore, a relevant aspect to be considered when the best anchorage device is needed to be identified among several and different types of other possible anchorages. Within this context, Biscaia and Diogo [43] have studied the influence of different mechanical anchorages on the final performance of anchored CFRP-to-timber joints. To that end, the following mechanical anchorage systems were studied: (i) the Externally Bonded Reinforcement On Grooves (EBROG) (see Fig. 7.9b); (ii) the addition of two short superposed metallic L-shapes (see Fig. 7.9c); (iii) the installation of an embedded rectangular hollowed section at the CFRP free end (see Fig. 7.9d); (iv) the addition of 2 or 3 CFRP spike anchors (see Fig. 7.9e and f, respectively); (v) the installation of a steel plate at the CFRP free end (see Fig. 7.9g); and (vi) through a limited embedded length of the CFRP laminate free end across the thickness of the timber (see Fig. 7.9h). As reference, two groups of EBR specimens were also tested. One group had a CFRP strip with 1.4 mm of thickness and another one with 2.8 mm of thickness.

The timber used in this study was bought from a local supplier who knew that it was pine, and no further information was known. Therefore, it was needed to find out the mechanical properties of the timber and to that end the 3-point bending test, the uniaxial compression test and the pull-off tests were carried out. Based on these tests,

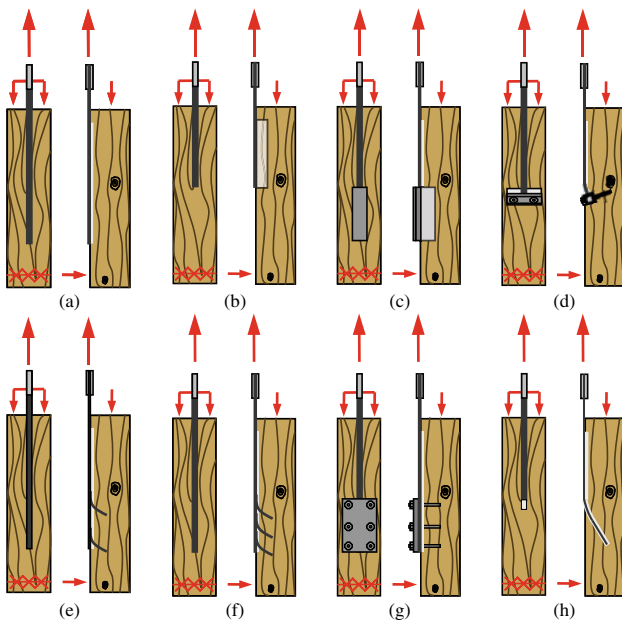


Fig. 7.9 Different analysed anchorage systems: **a** EBR; **b** EBROG; **c** with two small superposed metallic L-shapes; **d** with an embedded rectangular hollowed section; **e** with 2 CFRP spike anchors; **f** with 3 CFRP spike anchors; **g** with a steel plate; and **h** with a limited length of the CFRP laminate free end embedded into the timber

the results allowed us to conclude that the timber was a Scots Pine (*Pinus sylvestris L.*), with an expected average density of 550 kg/m^3 .

All these specimens were tested according to the single lap shear test and the corresponding test setup adopted in this study is shown in Fig. 7.10a. For simplicity, only some load-slip curves are presented. Thus, in Fig. 7.10b and c the load-slip curves obtained from the specimens in which the CFRP unpulled end was embedded into the timber prism are shown. The differences between them lie on the CFRP thickness used in each case. In the former case, i.e., in Fig. 7.10b, the thickness of the CFRP strip was 1.4 mm whilst, Fig. 7.10c shows the results obtained when the CFRP strip has 2.8 mm of thickness. From the point of view of the strengths of the CFRP-to-timber bonded joints, the specimens with the CFRP strip with 1.4 mm-thickness had a better final bond performance than that obtained from their homologous specimens with the CFRP strip with 2.8 mm-thickness. To support this sentence, we can look at the rupture load of each CFRP strip and compare with the maximum load transmitted to the CFRP strip during the test. So, the rupture load of the thinner CFRP was 33.13 kN and the mean value of the maximum load transmitted to the CFRP strip was 26.28 kN ($\text{CoV} = 14.3\%$) which represents 79.3% of the CFRP rupture load. On the other hand, the thicker CFRP reached 29.05 kN which is 48.1% of its corresponding rupture load of 60.45 kN.

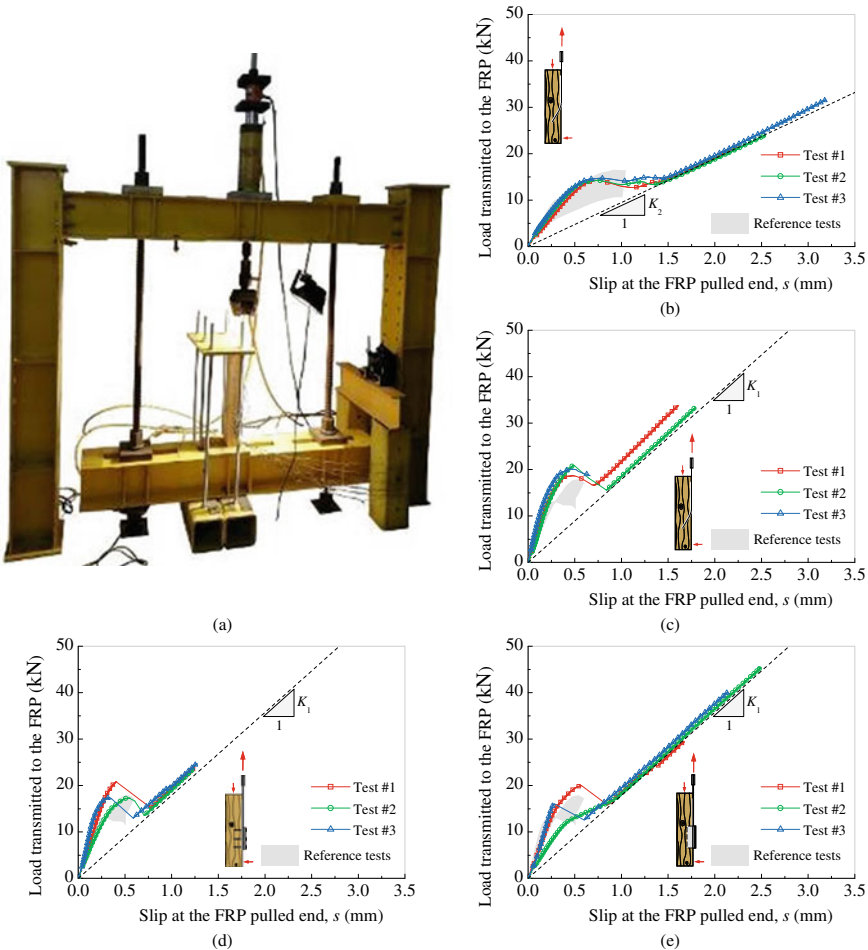


Fig. 7.10 Overview of the: **a** single lap shear tests used to evaluate the CFRP-to-timber bonded joints; **b** load-slip relationship obtained from the specimens where the 1.4 mm-thick CFRP unpulled end was embedded into the timber substrate; **c** load-slip relationship obtained from the specimens where the 2.8 mm-thick CFRP unpulled end was embedded into the timber substrate; **d** load-slip relationship obtained from the specimens where a steel plate was pressured against the CFRP unpulled end; and **e** load-slip relationship obtained from the specimens where two short superposed metallic L-shapes were placed at the CFRP unpulled end

Figure 7.10d shows the load-slip curves obtained from the specimens where the CFRP strip was mechanically anchored with a steel plate installed at the CFRP unpulled end. The efficiency of this anchorage system was not very good because the CFRP strip has slipped from the anchor at an early stage of the test duration.

The mean value of the maximum load reached in this case was 23.95 kN ($\text{CoV} = 2.2\%$) which is approximately only 39.6% of the CFRP rupture load. Two surprising results were also obtained in this study. The first one lies on the specimens where

two short superposed metallic L-shapes were used. In this case, the mean value of the maximum load transmitted to the CFRP strip was 38.33 kN ($\text{CoV} = 17.4\%$). The other one, lies on the inefficiency observed from the use of CFRP spike anchors as a mechanical anchorage (see Fig. 7.9e and f). In this case, and after the CFRP has initiated its debonding from the timber prism, the CFRP spike anchors were not able to transmit the load to the timber core which made impossible to increase the loads once again. Therefore, with 2 and 3 CFRP spike anchors, the mean values of the loads transmitted to the CFRP strip was 18.05 kN ($\text{CoV} = 14.8\%$) and 18.95 kN ($\text{CoV} = 18.4\%$), respectively. In fact, these two results are slightly higher than that obtained from the reference specimens (see Fig. 7.9a) where the mean debonding load was 15.05 kN ($\text{CoV} = 13.8\%$).

Although the mechanical anchorage where the CFRP unpulled end was embedded into the timber prism did not lead to the best performance of the CFRP-to-timber bonded joint, this anchorage has many advantages when compared to the remaining tested anchorages such has its easy application with no need of other materials to make the anchorage. Moreover, it only requires that a hole into the timber substrate and, to avoid stress concentrations, a transition curve between the hole and the timber's surface. However, the main reason that prevented this anchorage to perform best was a few numbers of air voids observed in the adhesive inside the hole.

7.2.5 FRP-Steel

This adhesively bonded joint has gained some scientific developments recently [44–46]. Probably, the main reason to such recent interest lies on the meaningful number of steel bridges needing to be repaired in Europe or in the United States of America [47] where, e.g, after 100 years in service, railway steel bridges were classified absolute or with structural deficiencies and demanding therefore, urgent repair. Hence, to obtain an efficient repair of those existing steel structures, the bond behaviour between the FRP composite and the steel substrate is very important. Like the previous adhesively bonded joints, the FRP-to-steel bonded joints share some aspects with the FRP-to-concrete or timber bonded joints. For instance, the FRP-to-steel bonded joint has an effective bond length which makes the FRP composite prone to debond from the steel prematurely. However, unlike concrete and timber where cohesive ruptures can be observed in the concrete or in the timber, in the case of steel this would not occur, and the yielding of the steel substrate difficulty will occur also. On another hand, the choice of a mechanical anchorage to prevent the premature debonding of the FRP composite from the steel substrate is quite limited because all the anchorages that demands to create holes or grooves in the substrate are not viable solutions. Hence, one main solution is the use of two steel plates that should be used as a grip. This has some implications that designers and/or practitioners must be aware of. One is the change of the local bond behaviour. In this case, the maximum bond stress tends to increase and, after that, the softening will tend to a residual bond stress [48]. Although this seems to benefit the FRP-to-steel bonded joint, too much compression

load may lead to rupture of some FRP fibres which compromise the bond behaviour of the adhesively bonded joint.

The research on this topic can be also conducted considering two main test setups. One is the single lap shear tests in which a steel profile can be used, and within a logic of pulling the FRP composite whereas the steel profile is pushed through a reaction load (see Fig. 7.11). The other way is to carry out double lap shear tests where the loads transmitted to the specimens are both pulling the FRP composite and the steel substrate (see Fig. 7.11). The choice of one or the other one has consequences on the bond performance of the FRP-to-steel joints that cannot be ignored since the interfacial bond transfer between materials occurs within a completely different way. In a practical point of view, this has also implications on how the local adhesive relationship should be calculated [23]. Independently of this and depending on the adhesive type (stiff or ductile), the local adhesive relationship can be described through a triangular or a trapezoidal shape.

To study these bond behaviours between an CFRP laminate and a steel rectangular hollow profile, the authors have carried out some experimental tests [30, 49] that were very useful to complement the bond assessment of the CFRP-to-steel bonded joints through analytical and numerical points of view. These studies [30, 49] had two main objectives. One was to find out how the CFRP-to-steel bonded joint locally behaves and, after that, to improve that bond performance through the installation of a steel

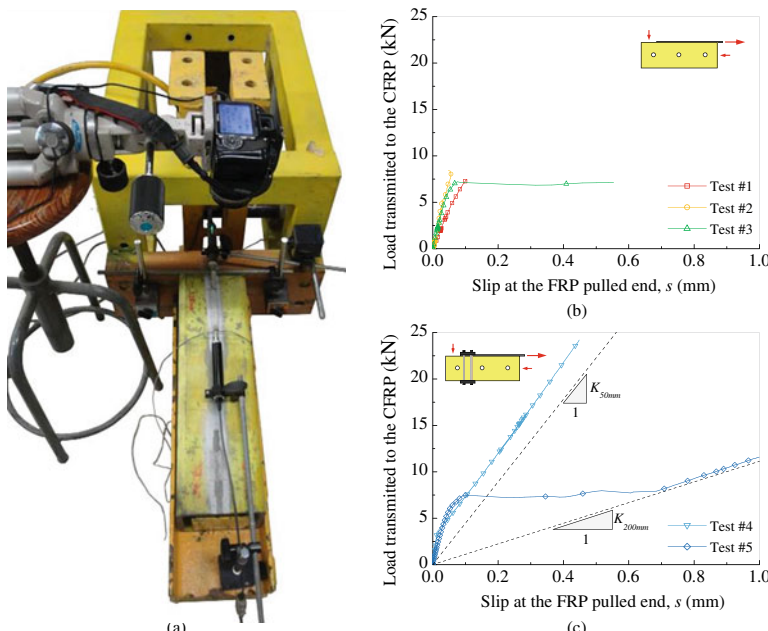


Fig. 7.11 Overview of the: **a** single lap shear tests to evaluate the CFRP-to-steel bonded joints; **b** load-slip relationship obtained from the EBR specimens; and **c** load-slip relationship obtained from the anchored CFRP specimens

plate at the CFRP unpulled end. To do so, the test setup shown in Fig. 7.11 was adopted which is, beyond some minor adaptations to the steel profile, the same test setup that we have used before to study the bond behaviour of the CFRP-to-concrete (see Fig. 7.4a), the stainless steel-to-concrete (see Fig. 7.6a) or the CFRP-to-timber bonded joints (see Fig. 7.8a). The same monitoring equipment used then was also used here which allowed us to test several specimens with different bond lengths (between 10 and 200 mm) and calculate, through a debonding load *versus* bonded length relationship, an effective bond length for the CFRP-to-steel bonded joint of approximately 130 mm.

The load-slip curves obtained from the tests are shown in Fig. 7.11b and c. The tests where no mechanical anchorages were used (see Fig. 7.11b), the load-slip curves have an almost linear behaviour until the debonding load. In Test #3, the observed plateau reveals that the specimens had a sufficient long bonded length which, in this case, was 200 mm. Nevertheless, installing a mechanical anchorage at the CFRP unpulled end, made the strength of the CFRP-to-steel bonded joint to increase significantly (see Fig. 7.11c). The main differences observed from both tests in Fig. 7.11c are due to the different bonded lengths adopted in each specimen. Thus, Test #4 had the same bonded length of Tests #1 and #2 (see Fig. 7.11b) of 50 mm whereas Test #5 had a bonded length of 200 mm. After the CFRP debonding, the load-slip relationships obtained from these two last tests tended to a linear behaviour in accordance to what was already mentioned in 2.4.

The influence of the environmental conditions such as the humidity (with or without salt) and/or the temperature variations on the mechanical properties of the steel, makes quite relevant the study the CFRP-to-steel bonded joints under these conditions. Hence, to clarify some doubts associated to the bond behaviour of the CFRP-to-steel bonded joints under such environmental conditions, the authors have idealized another type of specimens, with smaller dimensions than that shown in Fig. 7.11a that made possible to use a climatic chamber, a salt fog chamber and a universal testing machine equipped with a heater chamber. The limitations of these chambers' dimensions made impossible to adopt the same single lap bonded joints and, in alternative, the double lap bonded joints were chosen. In Fig. 7.12a it is possible to observe these specimens placed in the testing machine. Since four bonded joints are created, a mechanical anchorage was installed in one side of these joints to ensure that the CFRP could debond on the other side of the specimens. Beyond the testing machine, only strain gauges were used to monitor the strains in the CFRP laminates. Due to the symmetry conditions, only one CFRP strip was monitored with several strain gauges. The load-slip curves shown in Fig. 7.11b and c can be considered as reference data that are very useful for comparison with the specimens subjected to an environmental condition. It should be mentioned that the bonded length in these comparisons is very important since it may increase with the environmental condition. Consequently, to make the comparisons with the reference data, the adopted overlapped bond lengths should be sufficient long enough in all the specimens. At the same time however, the dimensions of the chambers cannot be forgotten. Hence, the double lap joints were built with two steel bars with 5 mm-thick and with a 50 mm-width. The length of each steel bar changed but the total length of

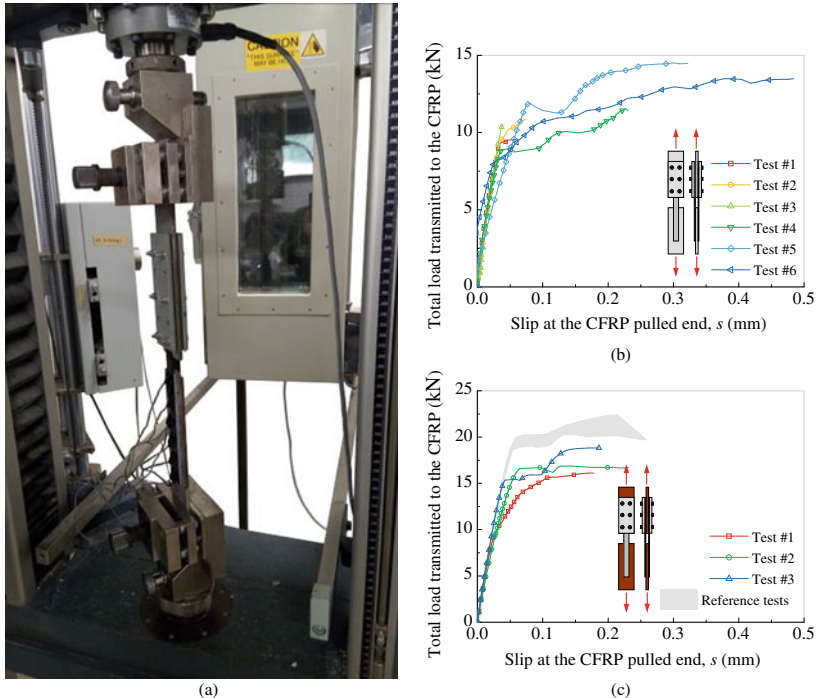


Fig. 7.12 Overview of the: **a** double lap shear tests to evaluate the CFRP-to-steel bonded joints; **b** load-slip relationship obtained from the EBR specimens with short (Tests #1 to #3) and with a sufficient long bonded length (Tests #4 to #6); and **c** comparison between the load-slip relationships obtained from reference (unaged) specimens with aged ones after 5000 h of salt fog exposure

the specimens never exceeded 420 mm length (which includes a 10 mm gap between steel bars).

Figure 7.11b and c show the load-slip curves obtained from the reference specimens and from the specimens submitted to salt fog cycles, respectively. If the load transmitted to the CFRP strip was measured by the 50 kN pressure cell of the testing machine, the determination of the slips has some similarities and differences from the slips determined from the single lap bonded joints. Hence, in both situations, the slips can be determined from the numerical integration of [50]:

$$ds/dx = (1 + \beta) \epsilon_f - (\beta \cdot \alpha_f + \alpha_s) \cdot \Delta T \quad (7.4)$$

where β is the axial stiffness ration between the CFRP laminate and the steel substrate; ϵ_f is the strain of the CFRP composite; α_f and α_s are the linear thermal expansion coefficients of the CFRP laminate and of the steel substrate, respectively; and ΔT is the temperature variation (corresponding to the thermal loading), which is defined according to:

$$\Delta T = T_f - T_i \quad (7.5)$$

where T_f and T_i are the final and the initial temperatures, respectively. In the case of no temperature variations, Eq. (7.4) is reduced in which the interfacial slips exclusively depend on the coefficient β . In this case, this coefficient is $\beta = 0.039$.

Unlike the single lap bonded joints where the CFRP is pulled out and the steel is pushed, the determination of the slips calculated from Eq. (7.4) in the double lap bonded joints (where both materials are pulled out) cannot begin at the CFRP unpulled end towards the CFRP pulled end. If in the case of the single lap bonded joint the CFRP unpulled end has no slip, in the case of the double lap bonded joints such slip condition at the CFRP unpulled end is not verified which avoids therefore, the direct application of Eq. (7.4). Thus, to use Eq. (7.4) and calculate the interfacial slips of the double lap bonded joints it was first identified where the interfacial bond stresses was always zero during the test. Since zero bond stress means zero interfacial slip, the application of Eq. (7.4) can be made from that starting point towards the CFRP pulled end (or unpulled end depending on the value of β).

Carrying out the previous strategy to calculate the interfacial slips, the load-slip curves of the double lap bonded joints shown in Fig. 7.12b revealed a similar behaviour shown in Fig. 7.11b. In fact, the unique difference between them is the test setup since the CFRP laminate and the adhesive used in both situations are the same. However, the strength of the double lap bonded joints is higher than that found in the single lap bonded joints. As already mentioned, this can be easily explained if we keep in mind that unlike the single lap bonded joints where the bond stress transfer begins to develop from the CFRP loaded end towards the CFRP free end, in the double lap bonded joints the bond stress transfer between materials develop in both CFRP ends and increase towards the centre of the joint. Consequently, and from the equilibrium point of view of the adhesively bonded joint, the strength of these double lap bonded joints tend to increase [23].

The influence of the salt fog cycles on the CFRP-to-steel joints is shown through the load-slip curves in Fig. 7.12c. In this case, the 25 mm-width and 1.36 mm-thick CFRP laminate was bonded to the steel bars. Then, the specimens were put inside of a salt fog chamber for 5000 h. Each salt fog cycles consisted on a first period of 6 h of salt fog spray with 5% of salt followed by another period of 18 h in dry conditions at a constant temperature of 35 °C. After the exposure, the specimens had a very rusty aspect.

The corresponding load-slip curves reveals that the strength of the aged CFRP-to-steel bonded joints decreased approximately 18.8%, i.e. from 21.26 kN (mean value obtained from the reference specimens) to a mean value of 17.26 kN. Although the strength of the specimens had decreased, the load-slip curves in both cases (reference and after ageing conditions) have a similar shape. In other words, both cases clearly show an initial linear load-slip relationship and a plateau at maximum load. However, between these two branches, the results may suggest that aged specimens have an accentuated nonlinear transition between those two branches which may be explained by the degradation of the adhesive after the salt fog cycles exposure. In fact, after 5000 h of salt fog exposure, the tensile tests of the adhesive revealed that its strength

has reduced from 21.75 MPa to 12.35 MPa whilst its the rupture strain has increased from 0.33% to 0.45%.

Another study (Fig. 7.13) where the influence of the temperature on the CFRP-to-steel bonded joints was conducted by Biscaia and Ribeiro [51]. Since the temperature tends to increase the effective bond length and considering the dimension limits of the heater chamber of the testing machine, it was possible to conceive a double lap bonded joint with a bonded length of 200 mm.

Different temperature variations were adopted and the initial temperature was $T_i = 20^\circ\text{C}$ (assumed as the temperature when the specimens were manufactured). Figure 7.13a shows one double lap bonded joint placed inside the heater chamber of the testing machine and ready to be tested. The load-slip curves of 5 tests at different temperatures are shown in Fig. 7.13b. These results clearly show that the increase of the temperature has an important impact into the strength of the CFRP-to-steel bonded joint. Such strength decrease is more meaningful when the vitreous transition temperature (T_g) of the resin is reached. In this case, the T_g of the adhesive is, according to the supplier, 62 °C after a curing period of 7 days at 45 °C which was followed during the preparation of the specimens.

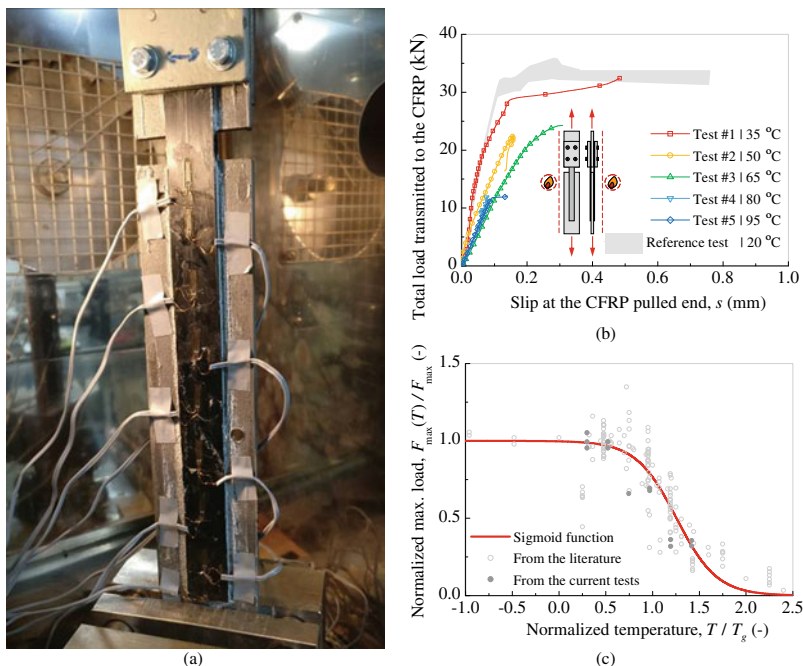


Fig. 7.13 Overview of the: **a** double lap shear tests to evaluate the influence of temperature variations on the CFRP-to-steel bonded joints; **b** influence of the temperature on the load-slip relationships of the CFRP-to-steel bonded joints; and **c** strength predictive curve for CFRP-to-steel bonded joints subjected to temperature variations

To estimate the load capacity of the CFRP-to-steel bonded joints, the following sigmoid function can be empirically considered:

$$F_{\max}(T)/F_{\max} = 1 - 1/\left(1 + e^{-f_1 \cdot (T/T_g - f_2)}\right) \quad (7.6)$$

where F_{\max} and $F_{\max}(T)$ are the maximum loads at room temperature (with no temperature variations) and the estimated maximum load of the CFRP-to-steel bonded joints at a designated temperature magnitude T , respectively; f_1 and f_2 are two dimensionless constants obtained from the experimental data. Based on a wide range of tests found in the literature, Biscaia and Ribeiro [51] the dimensionless parameters f_1 and f_2 were found to be equal to 4.80 and 1.26, respectively. The accuracy of Eq. (7.6) with the all the available experimental data can be seen in Fig. 7.13c. It should be noticed also that no studies were found for too low negative temperatures and therefore, Eq. (7.6) assumes that negative temperatures have no influence on the bond behaviour between an CFRP composite and a steel substrate.

7.3 Final Remarks

The study of structural adhesive joints is fundamental for the evaluation of the structural performance of new materials and constructive solutions, given the different actions to which the structure may be subjected and the safety that must present.

Several case studies carried out by the authors have been presented in which, different types of structural joints are shown, such as: steel-concrete, FRP-concrete, stainless steel-concrete, FRP-timber, and FRP-steel bonded joints, tested in laboratory under different actions or under adverse environmental conditions. In these case studies, it is worth highlighting the different setups presented for the laboratory tests carried out by the authors on structural adhesive joints, which allowed the study of several materials and different joints subjected to monotonic or cyclic loads or adverse environmental conditions, such as salt fog or temperature variations.

There is a multitude of laboratory tests on structural adhesive joints to evaluate the bond characteristics between two materials under mechanical or environmental loads. In this chapter an effort was made to systematize them. However, the technical and scientific community should converge towards a standardization of tests on structural adhesive joints, to avoid different results for the same problem.

Acknowledgements The authors would like to acknowledge the support of FCT for the partial funding of this work under the strategic projects UIDB/EMS/00667/2020 and FCT-IDB/04625/2020, respectively from the research units UNIDEMI and CERIS.

References

1. L’Hermite RL, Bresson J (1967) Beton armé par collage des armatures. In: Les résines de synthèse dans la construction. Colloque RILEM
2. Bresson J (1971) Nouvelles recherches et applications concernant l’utilisation des collages dans les structures. Béton plaqué. In: Annales Inst. Techn. Bât. et T.P, Paris
3. L’Hermite R (1977) Use of bonding techniques for reinforcing concrete and masonry structures. Mat. Constr. 10(2):85–89
4. Johnson RP, Tait CJ (1981) The strength in combined bending and tension of concrete beams with externally bonded reinforcing plates. Build Environ 16(4):287–299
5. Theillout J (1989) Renforcements de structures par la technique des tôles collées. IABSE reports 57/1/57/2, 6
6. Ladher M (1983) Reinforced concrete members with subsequently bonded steel sheets. IABSE reports 46:203–210
7. Cánovas MF (1985) Refuerzo de elementos estructurales de hormigon armado mediante encolado de bandas de acero com adhesivos epoxidicos. In: Informes de la Construcción, vol 37
8. Oehlers D, Ali M (1998) Debonding of steel plates glued to RC flexural members. Struct Eng Mater 1:7
9. Ritchie PA, Thomas DA, Lu L-W, Connelly GM (1990) External reinforcement of concrete beams using fiber-reinforced plastics. In: ATLSS Reports. ATLSS
10. Triantaifillou TC, Plevris N (1992) Strengthening of RC beams with epoxy-bonded fibre-composite materials. Mater Struct 25(4):201–211
11. Meier U, Münger F (1995) Repair of structures through external bonding of thin carbon fiber sheets. IABSE reports 73/1/73/2
12. Chen J-F, Teng J (2001) Anchorage strength models for FRP and steel plates bonded to concrete. J Struct Eng 127(7):784–791
13. Biscaya HC, Micaelo R, Teixeira J, Chastre C (2014) Numerical analysis of FRP anchorage zones with variable width. Compos B Eng 67:410–426
14. Biscaya HC, Micaelo R, Teixeira J, Chastre C (2014) Delamination process analysis of FRP-to-parent material bonded joints with and without anchorage systems using the Distinct Element Method. Compos Struct 116:104–119
15. Chastre C (1993) Behavior of steel-epoxy-concrete connection in structural elements (in Portuguese). IST, Universidade Técnica de Lisboa, MSc
16. Karbhari VM, Engineer M (1996) Investigation of bond between concrete and composites: use of a peel test. J Rein Plast Compos 15(2):208–227
17. De Lorenzis L, Miller B, Nanni A (2001) Bond of FRP laminates to concrete. ACI Mater J 98(3):256–264
18. Bonaldo E, Barros JAO, Lourenço PB (2005) Bond characterization between concrete substrate and repairing SFRC using pull-off testing. Int J Adhes Adhes 25(6):463–474
19. Cao S, Chen JF, Pan J, Sun N (2007) ESPI measurement of bond-slip relationships of FRP-concrete interface. J Compos Constr 11(2):149–160
20. Mazzotti C, Savoia M, Ferracuti B (2009) A new single-shear set-up for stable debonding of FRP-concrete joints. Constr Build Mater 23(4):1529–1537
21. Biscaya HC, Chastre C, Silva MAG (2012) Double shear tests to evaluate the bond strength between GFRP/concrete elements. Compos Struct 94(2):681–694
22. Biscaya HC, Silva MAG, Chastre C (2016) Influence of external compressive stresses on the performance of GFRP-to-concrete interfaces subjected to aggressive environments: an experimental analysis. J Compos Constr 20(2):04015044
23. Biscaya HC, Chastre C (2018) Theoretical analysis of fracture in double overlap bonded joints with frp composites and thin steel plates. Eng Fract Mech 190:435–460
24. Davalos JF, Kodkani SS, Ray I (2006) Fracture mechanics method for Mode-I interface evaluation of FRP bonded to concrete substrates. J Mater Civ Eng 18(5):732–742

25. Aiello MA, Leone M (2008) Interface analysis between FRP EBR system and concrete. *Compos B Eng* 39(4):618–626
26. Kasumassa Nakaba TKT, Hiroyuki Y, Bond Behavior between Fiber-Reinforced Polymer Laminates and Concrete. *ACI Struct J* 98(3)
27. Pan J, Leung CKY (2007) Debonding along the FRP–concrete interface under combined pulling/peeling effects. *Eng Fract Mech* 74(1):132–150
28. Yao J, Teng JG, Chen JF (2005) Experimental study on FRP-to-concrete bonded joints. *Compos B Eng* 36(2):99–113
29. Dai J, Ueda T, Sato Y (2005) Development of the nonlinear bond stress–slip model of fiber reinforced plastics sheet–concrete interfaces with a simple method. *J Compos Constr* 9(1):52–62
30. Bisciaia HC, Chastre C, Borba IS, Silva C, Cruz D (2016) Experimental evaluation of bonding between CFRP laminates and different structural materials. *J Compos Constr* 20(3):04015070
31. TC-RC R (1982) Bond test for reinforcement steel. 1. Beam test. *Mater Struct* 6(32):213–217
32. Silva MAG, Bisciaia HC, Marreiros R (2013) Bond–slip on CFRP/GFRP-to-concrete joints subjected to moisture, salt fog and temperature cycles. *Compos B Eng* 55:374–385
33. Bisciaia H, Franco N, Chastre C (2018) Stainless steel bonded to concrete: An experimental assessment using the DIC technique. *Int J Concrete Struct Mater* 12:9
34. Franco N, Bisciaia H, Chastre C (2018) Experimental and numerical analyses of flexurally-strengthened concrete T-beams with stainless steel. *Eng Struct* 172:981–996
35. Franco N, Chastre C, Bisciaia H (2020) Strengthening of RC beams using stainless steel continuous reinforcement embedded at ends. *J Struct Eng* 146(5)
36. Bisciaia HC, Franco N, Chastre C (2018) Development of a simple bond-slip model for joints monitored with the DIC technique. *Arch Civil Mech Eng* 18(4):1535–1546
37. Wu Y-F, Jiang C (2013) Quantification of bond-slip relationship for externally bonded FRP-to-concrete joints. *J Compos Constr* 17(5):673–686
38. Zhu H, Wu G, Shi J, Liu C, He X (2014) Digital image correlation measurement of the bond–slip relationship between fiber-reinforced polymer sheets and concrete substrate. *J Reinf Plast Compos* 33(17):1590–1603
39. Vaculik J, Sturm AB, Visintin P, Griffith MC (2018) Modelling FRP-to-substrate joints using the bilinear bond-slip rule with allowance for friction—Full-range analytical solutions for long and short bonded lengths. *Int J Solids Struct* 135:245–260
40. Bisciaia HC, Chastre C, Cruz D, Franco N (2017) Flexural strengthening of old timber floors with laminated carbon fiber-reinforced polymers. *J Compos Constr* 21(1):04016073
41. Bisciaia HC, Chastre C, Cruz D, Viegas A (2017) Prediction of the interfacial performance of CFRP laminates and old timber bonded joints with different strengthening techniques. *Compos B Eng* 108:1–17
42. Bisciaia HC, Cruz D, Chastre C (2016) Analysis of the debonding process of CFRP-to-timber interfaces. *Constr Build Mater* 113:96–112
43. Bisciaia HC, Diogo P (2020) Experimental analysis of different anchorage solutions for laminated carbon fiber-reinforced polymers adhesively bonded to timber. *Compos Struct* 243:112228
44. Yang Y, Silva MAG, Bisciaia H, Chastre C (2018) CFRP-to-steel bonded joints subjected to cyclic loading: an experimental study. *Compos B Eng* 146:28–41
45. Yang Y, Bisciaia H, Silva MAG, Chastre C (2019) Monotonic and quasi-static cyclic bond response of CFRP-to-steel joints after salt fog exposure. *Compos B Eng* 168:532–549
46. Yang Y, Silva MAG, Bisciaia H, Chastre C (2019) Bond durability of CFRP laminates-to-steel joints subjected to freeze-thaw. *Compos Struct* 212:243–258
47. Yang Y, Bisciaia H, Chastre C, Silva MAG (2017) Bond characteristics of CFRP-to-steel joints. *J Constr Steel Res* 138:401–419
48. Bisciaia HC, Chastre C (2018) Design method and verification of steel plate anchorages for FRP-to-concrete bonded interfaces. *Compos Struct* 192:52–66
49. Bisciaia HC, Chastre C, Silva C, Franco N (2018) Mechanical response of anchored FRP bonded joints: a nonlinear analytical approach. *Mech Adv Mater Struct* 25(3):238–252

50. Biscaya HC (2019) The influence of temperature variations on adhesively bonded structures: a non-linear theoretical perspective. *Int J Non-Linear Mech* 113:67–85
51. Biscaya HC, Ribeiro P (2019) A temperature-dependent bond-slip model for CFRP-to-steel joints. *Compos Struct* 217:186–205

Chapter 8

Shake Table Testing Techniques: Current Challenges and New Trends



Paulo X. Candeias , António A. Correia , and Gidewon G. Tekeste

Abstract Shake table tests play an important role in the research carried out worldwide to improve existing knowledge on the seismic performance of buildings and other civil engineering structures, including non-structural elements, and also for the seismic qualification of electromechanical equipment. Due to physical constraints, testing of real scale models is usually restricted to small sized structures. For larger structures, reduced scale models are required; otherwise, only substructures can be tested. Each of these approaches presents a different challenge. In reduced scale models, the choice of the scale factor and the similitude law is determined by the type of structure being tested and the relevant phenomena involved. Testing of substructures usually requires an elaborate testing setup in order to impose the necessary boundary conditions. More recently, the development and implementation of hybrid simulations allows carrying out tests on real scale structures combining a physical model on a shake table, where the non linear phenomena occur, with a numerical model in a computer, usually with linear elastic behavior, which can be much larger than the actual testing facility limits. This chapter will address several shake table test methods, focusing on the issues and challenges involved in each one, and the most recent developments on this topic.

Keywords Shake table · Reduced scale model · Substructure · Hybrid simulation

P. X. Candeias · A. A. Correia

National Laboratory for Civil Engineering (LNEC), Lisbon, Portugal

e-mail: pcandeias@l nec.pt

A. A. Correia

e-mail: aacorreia@l nec.pt

G. G. Tekeste

Civil Engineering Department, University of Aveiro, Aveiro, Portugal

e-mail: gidewon.tekeste@ua.pt

8.1 Introduction

Earthquakes are natural events with potential to cause extensive damage to the built environment. In order to mitigate the resulting losses, research is actively carried out in order to increase the knowledge about the seismic behavior of buildings and infrastructures under extreme events, assess their vulnerability and resilience. In the case of existing structures, the research may focus on the development of reinforcement techniques to be applied in seismic risk mitigation strategies, whereas for new structures the research may focus on safer and more resilient design.

Experimental research plays an important role in earthquake engineering. Tests are carried out with physical models, whether using raw materials, protection devices, structural elements or assemblages thereof, substructures or full structures, in increasing levels of complexity. In the end, refined numerical models are developed and calibrated with the experimental results and used to push even further the boundaries of existing knowledge towards less vulnerable and more resilient buildings and infrastructures.

The seismic behavior of real structures is complex. Through performance-based earthquake engineering principles, they are expected to respond in a near linear range for low intensity earthquakes but, to survive an extreme earthquake event, they have to rely on nonlinear behavior and energy dissipation capacity for the design to be economical [1].

To this end, shake table tests are particularly relevant because they allow the simulation, on a controlled environment (the testing facility), of the effects of inertia loads induced by earthquakes. Furthermore, the tests are carried out up to a (near) collapse condition, thus fully exploring the nonlinear response of the structure.

There are many shake table testing facilities spread around the world, most notably in earthquake prone countries. The list of existing shake table testing facilities is long and increasing, as more are built, in an effort to improve the testing capabilities in the earthquake engineering research field. In Tables 8.1 and 8.2 are presented the main characteristics of some of the major shake table testing facilities around the world [2–14].

As can be seen from Tables 8.1 and 8.2, existing shake tables have physical and operational limits, which are different for each case. Due to those limits, if not for economic reasons, the shake table tests of large prototypes are usually carried out using reduced scale models. This topic will be addressed next in this chapter.

In an attempt to overcome some of those limitations, as well as to extend to other effects concurrent with those resulting directly from the earthquake such as soil-structure interaction, newer techniques are being developed, such as testing of substructures with the aid of elaborate testing devices and hybrid simulations. These will be presented later in this chapter.

Table 8.1 Location and physical characteristics of major shake table testing facilities

Shake table	Research infrastructure	Country	Degrees of freedom	Platen surface (m × m)	Platen mass (t)	Maximum payload (t)
E-defense	NIED	Japan	6	20 × 15	N/A	1224
LHPOST	NEES@UCSD	USA	1	7.6 × 12.2	144	2039
UC Berkeley	PEERC	USA	6	6.1 × 6.1	45.4	45.4
6D ST	CCEER	USA	6	2.8 × 2.8	6.4	45.5
1D ST	EUCENTRE	Italy	1	5.6 × 7.0	N/A	140
AZALEE	TAMARIS	France	6	6 × 6	25	100
LNEC-3D	LNEC	Portugal	3	6.4 × 5.6	40	40
EQUALS	UBristol	UK	6	3 × 3	3.8	15
DYNLAB	IZIIS	Macedonia	5	5 × 5	30	40
3D ST	CABR	China	3	6 × 6	N/A	60

8.2 Testing of Reduced Scale Models

A structural model is a physical counterpart of a structural prototype [1, 15]. Prototypes are full sized structures, whether real or conceptual, whereas (physical) models are usually reduced scale, in an attempt to minimize cost and time of production. In the particular case of shake table tests, this is also done so as to cope with their physical and operational limits.

In order to relate the experimental results obtained on the model back to the prototype, a set of similitude conditions and requirements have to be met [1, 15–18]. In the case of shake table tests, the following similitude conditions are particularly relevant: (i) geometric similitude, when geometric characteristics are equally scaled; (ii) kinematic similitude, when homologous particles have homologous velocities; and (iii) dynamic similitude, when homologous parts of a system are subject to homologous net forces. Other similitude conditions might be necessary to consider in case of other physical phenomena, e.g., temperature. Apart from the similitude conditions, the initial and boundary conditions must also be respected in order to achieve similitude between the model and the prototype [19].

Dynamic similitude is the most stringent of the three mentioned above since it implies geometric similitude, through the length (L) dimension, and kinematic similitude, through the time (T) dimension. In itself, it implies force similitude through the mass (M) dimension. Nevertheless, it may still be an insufficient condition to predict the prototype behavior for nonlinear dynamic response [16, 20] since the similitude laws are derived in the elastic range, which may justify discrepancies in predicting inelastic behaviors.

During a shake table test the model will develop internal strains and stresses in response to the external forces. The major external forces are inertia forces (F_I), due to the accelerations imposed by the shake table, and gravity loads (F_G). They can be

Table 8.2 Operational characteristics of major shake table testing facilities

Shake table	Stroke (mm)	Peak velocity (cm/s)	Peak dynamic force (kN)	Frequency range (Hz)	Peak acceleration for given payload
E-defense	± 1000 (H) ± 500 (V)	200 (H) 70 (V)	N/A	0–15	0.9 g (H) 1.5 g (V) (Max. payload)
LHPOST	± 750	180	6800	0–33	1.2 g (400t payload)
UC Berkeley	N/A	N/A	2670 (H) 1335 (V)	0–10	1.5 g (Max. payload)
6D ST	± 300 (H) ± 100 (V)	152 (H) 140 (V)	490 (H) 623 (V)	0–50	1.8 g (60t payload), >1.0 g (100t payload)
1D ST	1000	220	1720	N/A	1.0 g (Max. payload)
AZALEE	± 125 (H) ± 100 (V)	100	N/A	0–100	1.0 g (H) 2.0 g (V) (Max. payload)
LNEC-3D	± 200	70 (T) 60 (L) 50 (V)	700 (T) 500 (L) 1000 (V)	0–40	0.9 g (T) 0.6 g (L) 1.3 g (V) (Max. payload)
EQUALS	300	100	N/A	N/A	1.6 g (H) 1.2 g (V) (10t payload)
DYNLAB	± 125 (H) ± 50 (V)	100 (H) 50 (V)	N/A	0.1–80	3.0 g (H) 1.5 g (V) (bare table)
3D ST	N/A	N/A	N/A	0–50	1.0 g/1.5 g

H—horizontal, V—vertical, T—transverse, L—longitudinal, N/A—not available

expressed in terms of proportionality to ρ (specific mass), L (length), a (acceleration) and g (acceleration of gravity) by Eqs. (8.1) and (8.2):

$$F_I \propto \rho \times L^3 \times a \quad (8.1)$$

$$F_G \propto \rho \times L^3 \times g \quad (8.2)$$

The internal stresses and strains that develop in response to the external forces translate into restoring forces (F_R), which can also be expressed by Eq. (8.3) in terms of proportionality, in this case, to σ (stress), ε (strain), E (elastic modulus) and L^2 (area):

$$F_R \propto \sigma \times L^2 = \varepsilon \times E \times L^2 \quad (8.3)$$

These external and internal forces can be used to define two independent dimensionally homogeneous forms [1, 15]. Starting with the external forces, the ratio between the inertia forces and the gravity forces is expressed by Eq. (8.4):

$$F_I/F_G \propto a/g \quad (8.4)$$

This first form corresponds to the square of the Froude number (Fr) used in dimensional analysis [1, 15]. It expresses the relation between the imposed accelerations (a) and the acceleration of gravity (g). It can also be expressed as $v^2/(L \times g)$, where the symbol v stands for velocity, which is dimensionally equivalent.

The second independent dimensionally homogeneous form can be established by Eq. (8.5) taking the ratio between the inertia forces (F_I) and the restoring forces (F_R):

$$F_I/F_R \propto \rho \times L \times a/E \quad (8.5)$$

This one corresponds to the Cauchy number (Ca) from dimensional analysis [1, 15]. It expresses the relation between the specific mass (ρ), length (L), acceleration (a) and elastic modulus (E). Alternatively, it can be expressed as $\rho \times v^2/E$, where the symbol v stands again for velocity, which is dimensionally the same.

Structural models are divided into three categories depending on their compliance with different similitude requirements [1, 15]: (i) true models, when all the conditions are fulfilled (complete similitude); (ii) adequate models, when first-order conditions, i.e., the conditions related to the main parameters, are fulfilled (“first-order” similitude); and (iii) distorted models, when at least one of the first order conditions is not satisfied (partial similitude).

The difference between true and adequate models is of relevance especially when using dimensional analysis. Here, special insight into a problem can be used to reason that some of the conditions are of “second-order” importance [16].

For shake table tests three types of models are usually considered. The first one is the true replica model, which fully respects both the Froude number and the Cauchy number. This type of model, however, imposes serious restrictions on the physical model material properties [1] because they are required to have either a small elastic modulus or a large specific mass or both [15].

The second type of model is considered an adequate model. Although it also respects both the Froude number and the Cauchy number, it uses additional masses to account for both the inertia effects due to the earthquake loading and the weight due to the acceleration of gravity, therefore lifting some of the restrictions on the physical model material properties that the true replica models impose. These additional masses can be either distributed on the model, or lumped in particular locations, but should always be placed following the notion of tributary areas in order to maintain both translational and rotational inertia. This aspect is particularly important when the model is expected to have a torsional response such as in models with asymmetric

geometry and/or stiffness in plan. These additional masses must also account for any loads, apart from the dead weight, that should be considered to exist during the earthquake (e.g., additional dead loads, fraction of the live loads).

The third type of model is one where the effects of the gravity force can be neglected. Such is the case of models where the mechanisms involved in resisting to the seismic loads are not dependent on the axial loads [15]. This is also considered an adequate model although the Froude number is disregarded and only the Cauchy number is respected.

Table 8.3 presents the scaling factors for earthquake response [1, 15, 19–22]. For each physical quantity, the table presents the symbol assigned (e.g., S), its dimensions (in terms of L, T, M), and the scaling factors (e.g., $S_r = S_p/S_m$, where the subscripts “p” and “m” stand for prototype and model, respectively).

Three special cases arise in this table, the first two in the artificial mass simulation. In the first case, the additional distributed mass can be computed considering an additional specific mass (ρ_a), apart from the model material specific mass (ρ_m), as a function of the prototype material specific mass (ρ_p). Under this condition, the Cauchy similitude requirement yields (Eqs. 8.6 and 8.7):

$$(\rho_m + \rho_a) \times L_m \times g_m / E_m = \rho_p \times L_p \times g_p / E_p \quad (8.6)$$

$$\rho_a = \rho_p \times [(L_r \times g_r / E_r) - (\rho_m / \rho_p)] \quad (8.7)$$

The specific stiffness is computed considering only the model material specific mass (ρ_m), yielding (Eq. 8.8):

$$E_r / (\rho_p / \rho_m) = L_r \times g_r - [E_r / (\rho_p / \rho_a)] \quad (8.8)$$

In the second case, the lumped masses can be computed as additional concentrated mass (m_a). Again, the scaling factor is obtained through the Cauchy similitude requirement (Eqs. 8.9 and 8.10):

$$(m_m + m_a) \times g_m / (L_{m^2} \times E_m) = m_p \times g_p / (L_{p^2} \times E_p) \quad (8.9)$$

$$m_a = m_p \times [(g_r / (L_{r^2} \times E_r)) + (m_m / m_p)] \quad (8.10)$$

The third case arises in the model where gravity forces are neglected. In this adequate model [1, 15], the weight due to the acceleration of gravity is not considered relevant for the overall behavior of the model during the shake table test. For that reason, the specific mass can be scaled directly ($\rho_r = \rho_p / \rho_m$) and the Cauchy similitude requirement yields the acceleration scale factor (a_r) which will depend on the elastic modulus (E_r), specific mass (ρ_r) and length (L_r) scale factors, presented in bold in Table 8.3 (Eqs. 8.11 and 8.12):

$$\rho_m \times L_m \times a_m / E_m = \rho_p \times L_p \times a_p / E_p \quad (8.11)$$

Table 8.3 Scale factors for earthquake response of models

Physical quantity	Symbol	Dimension	True replica model	Artificial mass simulation	Gravity forces neglected
Length	L	L	$L_r = L_p/L_m$	$L_r = L_p/L_m$	$L_r = L_p/L_m$
Area	A	L^2	L_r^2	L_r^2	L_r^2
Volume	V	L^3	L_r^3	L_r^3	L_r^3
Time	t	T	$(L_r/g_r)^{(1/2)}$	$(L_r/g_r)^{(1/2)}$	$L_r/(E_r/\rho_r)^{(1/2)}$
Frequency	f	$1/T$	$(g_r/L_r)^{(1/2)}$	$(g_r/L_r)^{(1/2)}$	$(E_r/\rho_r)^{(1/2)}/L_r$
Displacement	d	L	L_r	L_r	L_r
Velocity	v	L/T	$(L_r \times g_r)^{(1/2)}$	$(L_r \times g_r)^{(1/2)}$	$(E_r/\rho_r)^{(1/2)}$
Acceleration	a	L/T^2	g_r	g_r	$(E_r/\rho_r)/L_r$
Acceleration of gravity	g	L/T^2	$g_r = g_p/g_m = 1$	$g_r = g_p/g_m = 1$	$g_r = g_p/g_m = 1$ (***)
Mass	m	M	$E_r \times L_r^2/g_r$	(**)	$\rho_r \times L_r^3$
Weight	W	$M \times L/T^2$	$E_r \times L_r^2$	$E_r \times L_r^2$	$\rho_r \times L_r^3 \times g_r$ (***)
Force	F	$M \times L/T^2$	$E_r \times L_r^2$	$E_r \times L_r^2$	$E_r \times L_r^2$
Moment	M	$M \times L^2/T^2$	$E_r \times L_r^3$	$E_r \times L_r^3$	$E_r \times L_r^3$
Elastic modulus	E	$M/(L \times T^2)$	$E_r = E_p/E_m$	$E_r = E_p/E_m$	$E_r = E_p/E_m$
Specific mass	ρ	M/L^3	$E_r/(L_r \times g_r)$	(*)	$\rho_r = \rho_p/\rho_m$
Specific stiffness	E/ρ	L^2/T^2	$L_r \times g_r$	(*)	E_r/ρ_r
Pressure	q	$M/(L \times T^2)$	E_r	E_r	E_r
Stress	σ	$M/(L \times T^2)$	E_r	E_r	E_r
Strain	ε	—	1	1	1
Poisson coefficient	ν	—	1	1	1
Curvature	χ	$1/L$	$1/L_r$	$1/L_r$	$1/L_r$
Energy	EN	$M \times L^2/T^2$	$E_r \times L_r^3$	$E_r \times L_r^3$	$E_r \times L_r^3$

(*) Distributed mass, (**) Lumped mass, (***) Neglected

$$a_r = (E_r / \rho_r) / L_r \quad (8.12)$$

In order to illustrate the influence of selecting a particular set of values in the remaining scaling factors and the challenges they pose on the materials used to build the models, Table 8.4 shows three cases (v1, v2, v3) corresponding to different combinations of length and elastic modulus scale factors, which are the same on both true replica models and models where gravity forces are neglected. The first case (v1) illustrates a situation where a material with the same elastic modulus is used in both the prototype and the model. The second (v2) and third (v3) cases illustrate a situation where the elastic modulus in the prototype is 1.5 times higher than in the model. The length scale factor is 2 in the first two cases (v1, v2) and 1.5 in the third

Table 8.4 Scale factor values used for illustration purposes

Physical quantity	True replica (v1)	True replica (v2)	True replica (v3)	Gravity forces neglected (v1)	Gravity forces neglected (v2)	Gravity forces neglected (v3)
Length	2.00	2.00	1.50	2.00	2.00	1.50
Time	1.41	1.41	1.22	2.00	1.63	1.22
Elastic modulus	1.00	1.50	1.50	1.00	1.50	1.50
Specific stiffness	2.00	2.00	1.50	1.00	1.50	1.50
Specific mass	0.50	0.75	1.00	1.00	1.00	1.00
Acceleration	1.00	1.00	1.00	0.50	0.75	1.00

case (v3). Moreover, in the true replica models the acceleration scale factor is always 1.0, due to the Froude similitude requirement, while in the models where the gravity forces are neglected, a specific mass scale factor of 1.0 was used for all cases (v1, v2, v3).

As it can be seen in the true replica models, the specific mass scaling factor is less than one in the first two cases (v1, v2), meaning that a material with a higher specific mass must be used in the model when compared with the prototype. This is a situation that is not always possible to achieve while keeping, e.g., the elastic modulus scale factor, thus requiring the use of additional masses (see Eqs. 8.7 and 8.10) and, therefore, resorting to an artificial mass simulation model. Only in the third case (v3) can a material with the same specific mass be used on both model and prototype but then the elastic modulus scale factor must be equal to the length scale factor and, therefore, smaller in the model when compared with the prototype. This calls for the use of a different material [15] which, in some special cases, is possible to achieve (e.g., [23]).

In the models where gravity forces are neglected, the specific mass scale factor can be set directly. Only the first case (v1) corresponds to using the same material of the prototype to build the model which, in turn, is also the one where the acceleration scale factor is lower. This poses a high demand on the shake table because it implies being able to impose accelerations on the model which are the double of the prototype. In the other two cases (v2, v3) the demands on the shake table are smaller, approaching a scale factor of one, at the cost of increased difficulty in obtaining a suitable material for the construction of the model or in changing the length scale factor.

Figure 8.1 illustrates a reinforced concrete (RC) 1:1.5 reduced scale model of a frame prototype with infill walls tested on the LNEC-3D shake table [24] respecting both the Froude number and the Cauchy number. All the structural materials, concrete, rebars, clay bricks, were made, or selected, according to the geometric scale factor. The elastic modulus scale factor was one. Additional lumped masses were placed on the floor and roof to account for the mass and weight effect, including permanent loads and the quasi-permanent value of the live loads. Discrete distributed

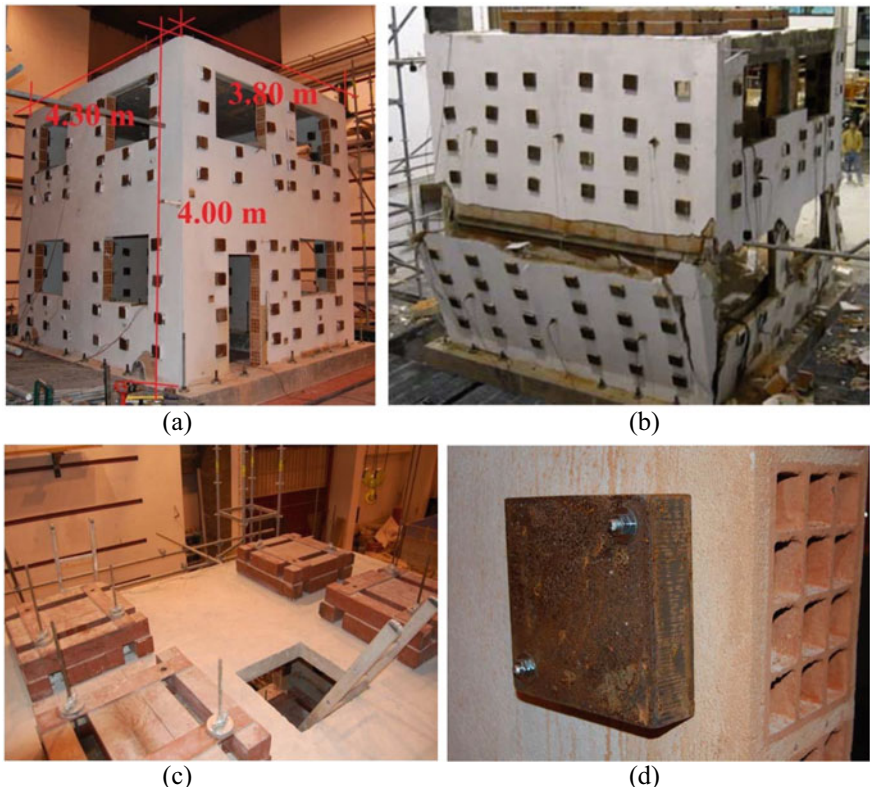


Fig. 8.1 Example of a reinforced concrete 1:1.5 reduced scale model [24]: **a** model dimensions; **b** onset of collapse during shake table test; **c** lumped masses on the roof; **d** discrete distributed mass on the surface of an infill wall panel

masses were placed on the infill walls. Figure 8.1a shows the model placed on the shake table and its global dimensions, Fig. 8.1b the beginning of the collapse mechanism, Fig. 8.1c the lumped masses on the roof and Fig. 8.1d a discrete distributed mass attached to a clay brick.

8.3 Testing of Substructures

When reduced scale testing is not an option and full-scale testing is impossible, there may be the possibility to test a substructure of interest from the full structure. The testing of structural components, or of substructures, requires the adequate fulfillment of their boundary conditions that materialize the interaction between the substructure and the full structure.

On the other hand, the actual implementation of substructure tests will depend on the specific conditions of the laboratory and of the intended test specimen. It may consist on tests of small substructures (e.g., column, damper, isolation device) or more complex ones (e.g., frame or another structural assembly), it may require simple reaction frames and a strong floor or a full-fledged reaction wall test site, it may use one or several actuators, or it may range from a slow simulation up to real-time testing.

Herein, a substructure testing facility is used as an example, consisting on the simultaneous use of a shake table and the surrounding reaction walls, as implemented at LNEC. With such physical conditions, different test setups may be envisaged, which go well beyond the typical shake table test.

For example, a bridge substructure can be tested, with a column or set of columns attached to the shake table and the bridge deck connected to the reaction walls (either directly supported or connected to auxiliary actuators). This type of setup is depicted in Fig. 8.2, although on a different type of substructure, with a test specimen simulating a central column and two half spans to each side of a precast RC industrial building [25]. The column was fixed to the LNEC-3D shake table while the two half beams were connected, through dowels, to corbels placed at the top of the column, on either side, and, on the other end, simply supported on the reaction walls (Fig. 8.2a). The out-of-plane displacements of the beam-column joint were restrained by a steel strut (Fig. 8.2b). The test program included a monotonic test and a cyclic test where in-plane displacements were imposed by the shake table at the base of the column (Fig. 8.2c), while horizontal and vertical reaction forces measured in the beam hinged ends, allowing to obtain both a monotonic force–displacement curve and a cyclic force–displacement curve (Fig. 8.2d).

These experimental tests have revealed two mechanisms: the first was identified by the elastic deflection of the column, as a result of the displacement applied at the base, and highlighted by the global force–displacement curve (Pushover curve); the other was related to the rotation of the beam-column joint. Even for a large displacement input (approximately 180 mm) collapse was not reached for both monotonic and cycling loading. At the end of the monotonic test, beams and dowels have not suffered significant damage, while cracking was found at the end side of the corbel and along the height of the column. From observations after the cyclic test, damage was concentrated mainly in the beam-column connection but it was also observed along the height of the column (flexural cracks in the lower 2 m). Spalling and crushing of concrete on the corbels and beams reduced the moment resisting capacity of the connection.

Focus is also given here to a test setup that simultaneously uses the shake table, one reaction wall and the Testing device for Innovative Masonry infills (TIM), as represented in Fig. 8.3. This test setup was designed for testing RC plane frames infilled with masonry walls, simultaneously subjected to in-plane and out-of-plane dynamic actions in real-time [26, 27]. It can easily be extended to other types of materials, plane frames or infill/cladding components.

This unique testing setup was specifically designed for these tests and is mainly composed of a stiff steel caisson three-dimensional frame which moves rigidly with

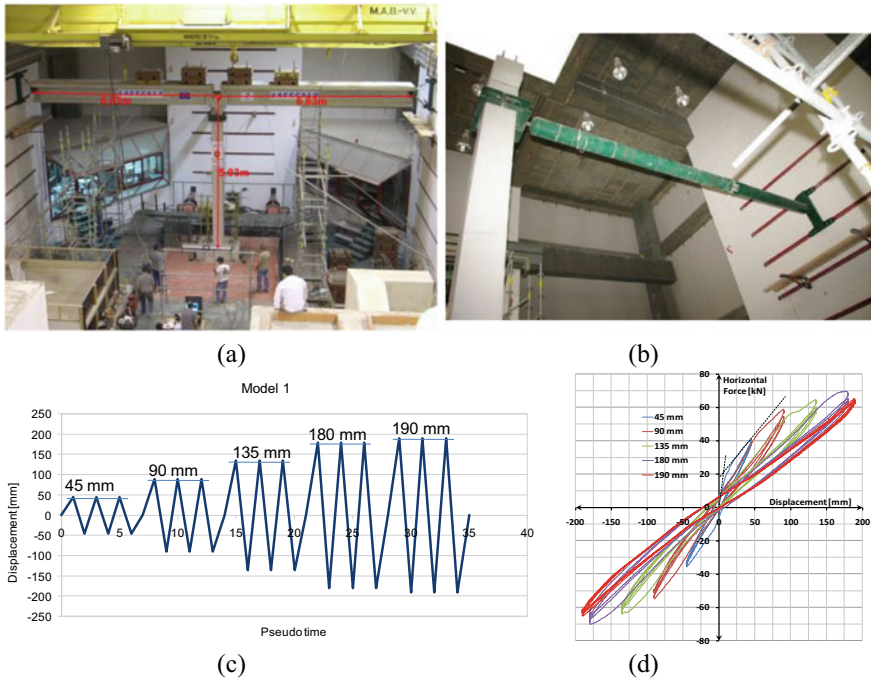


Fig. 8.2 **a** Substructure test of a precast RC frame specimen with one column fixed to the LNEC-3D shake table and two half beams on each side simply supported on the reactions walls (symmetric boundary condition, asymmetric in-plane loading condition); **b** Out-of-plane displacement constraint steel strut and connection devices; **c** Cyclic loading time-history; and **d** Force–displacement cyclic curves

the shake table. It is fixed to the specimen's upper beam in the transverse direction, while a system of rollers allows for an independent motion in the longitudinal direction.

The in-plane motion enforces an interstory drift history on the frame by restraining the upper beam and by imposing the displacement of the shake table on the lower beam. The upper beam is prevented from moving in the longitudinal direction through a strut connection to the reaction wall. This connection between the strut and the reaction wall is performed via a pyramidal support, as depicted in Fig. 8.3c, which distributes the strut reaction on the wall. A long rod then links the pyramidal support to the RC frame upper beam through hinged connectors. All beam-column joints are free to rotate in the plane of the infill, through special hinged base supports.

On the other hand, the out-of-plane motion consists on a rigid-body vibration of both the upper and lower beams, reproducing the story absolute accelerations and thus inducing high-frequency inertia forces perpendicular to the masonry panel and leading to a local vibration of the infill wall. Note that this shake table motion is transmitted to the top beam through the rigid steel caisson structure of TIM. The design of TIM was thus controlled by the requirement of a very stiff behavior in the

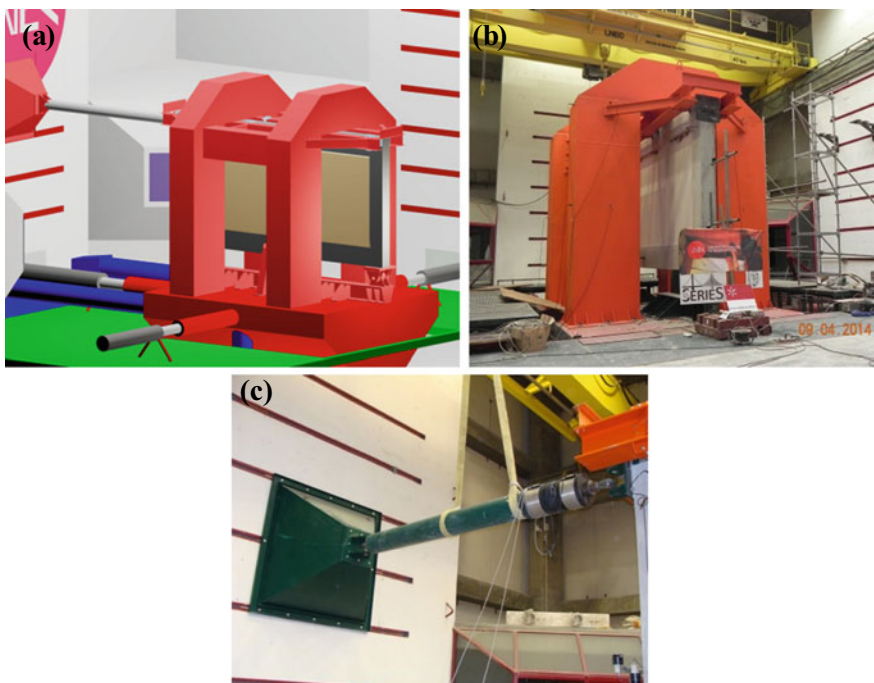


Fig. 8.3 Wall panels' test setup: **a** schematic representation; **b** physical model; **c** strut connection to reaction wall

transverse direction, which was ensured by a vibration frequency for the first mode of vibration above 20 Hz.

The frame and wall panels may have dimensions up to 6.5 m long and 4 m height. The application example shown here corresponds to a couple of specimens with and without a reinforced mortar coating, having external dimensions of 4.8 m by 3.3 m. These specimens were tested simultaneously for in-plane and out-of-plane dynamic actions, representing the response of a given floor frame panel of a RC building (see Fig. 8.4). The target ground motions were applied at the base of a representative building model, shown in Fig. 8.4, in order to obtain the time-histories of the wall panels' motions.

The response history in terms of interstory drift at the floor level for the seismic input considered corresponds to the shake table motion to be applied in the longitudinal direction. On the other hand, the absolute acceleration observed in the out-of-plane direction corresponds to the shake table motion transmitted by TIM to the masonry panel inside the RC frame. Both longitudinal and transverse motions are represented in Fig. 8.4, with two sets for different stages of the test.

The responses in terms of in-plane force and resulting drift in the wall panels are presented in Fig. 8.5a and b for the as-built and strengthened specimens, respectively, for a sequence of test stages. On the other hand, the effect of the bidirectional

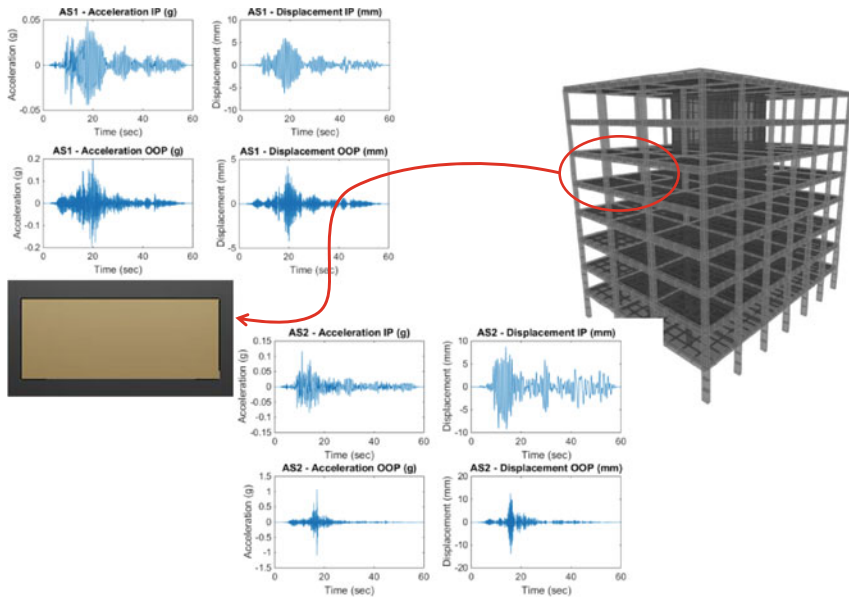


Fig. 8.4 Representative building model for wall panel input definition and resulting in-plane (longitudinal) and out-of-plane (transverse) sets of time-histories

excitation is clearly seen in Fig. 8.5c, with the comparison to the response of the strengthened panel to an in-plane envelope excitation only.

Despite the clear interest of this type of test setup solutions, it would be even more interesting to perform this type of tests using not just predefined input motions but motions that take into account the interaction of the damage evolution with the response of the entire building instead. This would require real-time hybrid simulation approaches, as discussed in the next section of this chapter.

8.4 Hybrid Simulation

8.4.1 Introduction

Hybrid simulation (HS) is a technique for investigating the dynamic response of a structure by dividing it into analytical and physical portions [28]. The analytical portion is modeled in a computational program, whereas the physical portion is tested experimentally. The two portions of the structure interact at interface points throughout the execution of the test. Part of the structure that has complex behavior, or a structural component whose constitutive model is not well established, is typically chosen as the physical model.

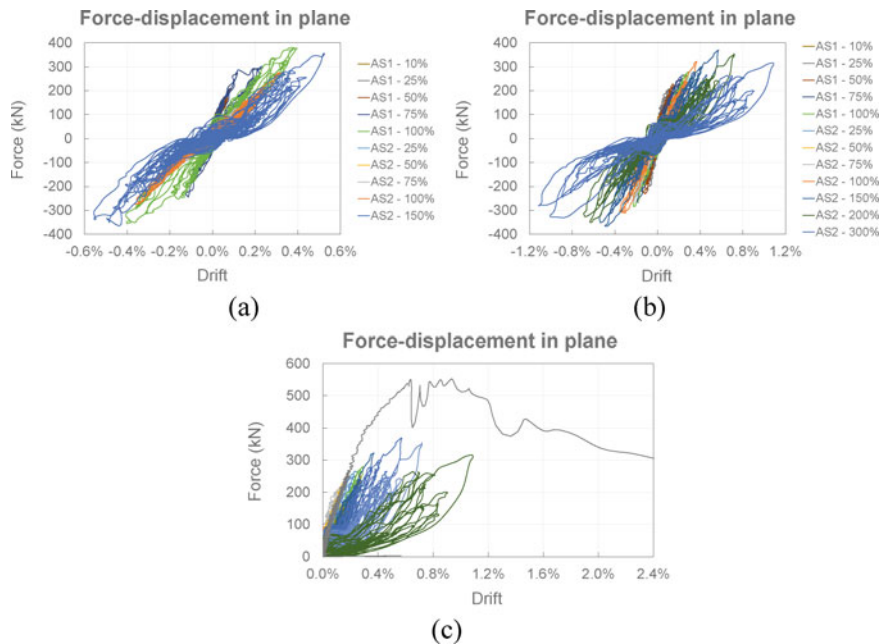


Fig. 8.5 Wall panels' test results: **a** as-built specimen; **b** strengthened specimen; **c** strengthened specimen envelope for in-plane monotonic input (with no out-of-plane action)

Figure 8.6 shows the schematic diagram of a hybrid test of a reference structure comprising a magneto-rheological (MR) damper as the physical substructure. Due to the size of the structure, it may be impractical to conduct the full-scale shake table test. A reduced model of the structure can therefore be tested. However, the response simulation of the structure may be influenced by scaling effects. On the other hand, the hybrid test of the structure can be easily performed by physically testing the MR damper, while the remaining parts are represented numerically. Research done in the past has shown that hybrid testing can reproduce the results of shake table tests [29–31].

8.4.2 Challenges in Hybrid Simulation

The implementation of hybrid simulation is not straightforward due to the challenges in satisfying the boundary conditions at the interface between the two substructures. It may require complex actuator control algorithms which can be challenging for real-time hybrid simulation (RTHS).

The absence of a robust, transparent, extensible, and environment-independent software framework for the implementation of HS has been an important limitation

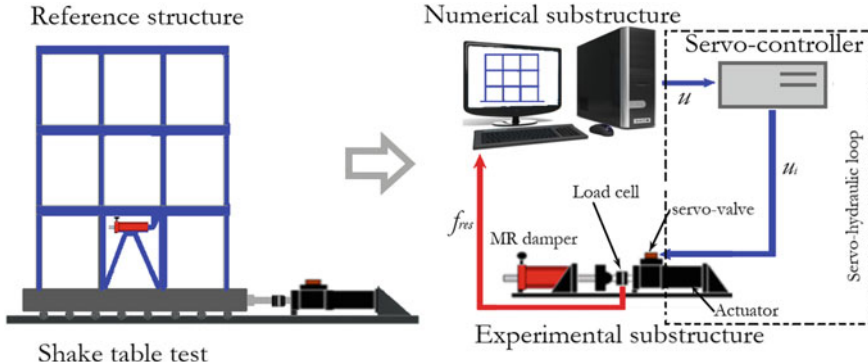


Fig. 8.6 Schematic representation of hybrid simulation

as well. The development of such a framework is very important both for the advancement of the technique and collaboration among research laboratories. Nevertheless, software frameworks such as the OpenFresco [32] and UI-SimCor [33] have been useful in the past. They may still be extended to have the full potential to be used for diverse structural problems and to be able to interface with a wide range of control and data acquisition hardware.

Explicit time integration methods, such as the Newmark method [34], are very efficient and easy to implement, but they can be conditionally stable. They become problematic for stiff problems where very small time-steps are needed for stability conditions. This property can make them prohibitive in some hybrid tests. Additionally, they may not be applicable when massless DOFs exist in a model [32]. Besides, they may result in large unbalanced forces when applied to structures with strong nonlinearity.

On the other hand, implicit algorithms are attractive for nonlinear response simulation, but essentially indeterminate and thus not suitable for RTHS. Implicit methods can also introduce artificial loading and unloading due to their iterative nature. Besides, velocity and acceleration spikes can occur during a RTHS test since the displacement increments within a time-step are not uniform. Nonetheless, the classical implicit methods have been modified, in the past, to be suitable for HS. For instance, the Implicit Newmark Hybrid Simulation (NMHS) algorithm [32] reduces the displacement increments during the iterative process and uses a limited, typically 10, number of iterations without convergence test. The alpha Operator-Splitting (α -OS) integration [35] is, however, a one-step corrector and unconditionally stable algorithm that does require tangent stiffness of the experimental element. This integration has found wide application among the hybrid simulation community, as it is attractive for RTHS. Mixed methods, comprising explicit and implicit schemes, can also be useful when the iterative algorithm fails to converge [36].

Furthermore, integrators in hybrid simulation which possess numerical damping are often favorable since experimental errors can potentially excite higher modes. Among the several developments, the KR- α , which inherits the properties of the

implicit generalized-alpha integration [37], is an attractive method that possesses numerical damping while, at the same time, being unconditionally stable [38]. It is therefore clear that modifying classical integrators, to be suitable for HS, poses a challenge.

Experimental errors in HS, time-delay of a load transfer system, in particular, present a challenge as well. The time-delay of an actuator in RTHS is equivalent to negative damping, meaning energy is added to the system [39]. For obvious reasons, this may lead to instability problems resulting in premature failure of the test specimen and damage of the testing equipment.

To alleviate the effects of time-delay, several delay compensation schemes have been developed in the past two decades. In parallel, error tracking techniques, such as the Tracking indicator (TI) [40], Phase and Amplitude Error Indices (PAEI) [41] and Hybrid Simulation Error Monitor (HSEM) [41–43], have been developed to assist compensation methods and to identify instability instances. The compensation method developed in the early stage of HS uses a third-order polynomial to predict the next time-step command [39]. The Discrete Feedforward Compensation (DFC) scheme was later introduced to compensate for the time-delay [44]. A model-based feedforward approach was also explored in [45]. This method was applied for evaluating the effectiveness of semi-active control in structures.

To tackle the evolutionary nature of time-delay during a hybrid test, some techniques have also been developed. The Adaptive Time Series (ATS) compensator is one of the most effective techniques [46]. This technique updates its parameters at each time-step of integration by solving a least-squares problem. Despite all the work done, actuator time-delay still presents a challenge to HS since no technique can fully compensate for it.

Furthermore, displacement control of an actuator may be inadequate for stiff experimental substructures such as a squat wall. A mixed control technique can be an alternative solution, where the stiff DOFs of a structure are controlled in force while the remaining DOFs are controlled in displacement. On the other hand, in the switch control technique, the controller switches between the displacement and force modes of control. Without loss of generality, the challenge in generating force commands from the conventional displacement-based numerical programs cannot be ignored. The algorithm developed in [47] calculates force commands using an estimated secant stiffness based on the α -OS integration scheme. Similar developments of mixed and switch controls were also implemented in the OpenFresco framework using the Krylov subspace methods [48].

On the experimental side, force control of actuators is inherently unstable, thus adding to the challenge in conducting HS. Hence, equivalent force control approaches such as the mass-controlled [49] and added compliance [50] techniques were developed to tackle it. The latter, which was initially developed to work with the Smith Predictor, was later combined with the ATS compensator [51]. Nonetheless, the added compliance approach can pose difficulties when large forces must be controlled.

Still on the same venue, in substructuring tests that involve significant inertia effects of the experimental substructure, acceleration at the interface boundary may need to be compatible. In this scenario, the accurate tracking of a shake table

acceleration is important. To address this, advanced control algorithms, such as the feedforward-feedback control have been developed. The feedforward-feedback controller implemented in [52] includes the Linear Quadratic Gaussian (LQG) feedback control. Furthermore, in multi-axis hybrid testing [53], as well as in RTHS that combines a shake table and an actuator [54], the coupling of actuators can be problematic. Besides, synchronizing a shake table with an auxiliary actuator can be challenging in RTHS.

8.4.3 Actuator Time-Delay

Experimental errors in hybrid simulation can be categorized as systematic and random. The systematic error, comprising time-delay and gain error, can be difficult to mitigate because they may propagate into the numerical substructure and grow exponentially resulting in instability problems. The time-delay of a hybrid test is essentially the sum of an actuator's delay and a communication delay. In servo-hydraulic actuation, the communication delay is in the order of 1 ms, which is small compared to the response delay of an actuator (20–80 ms).

To demonstrate the precarious nature of the actuator's time-delay, a simulated hybrid test of a SDOF structure, shown in Fig. 8.7a, can be considered. To achieve the worst-case scenario for system instability, the physical portion includes the full stiffness of the structure. Besides, the physical substructure includes a fraction of the viscous damping thus rate-dependent test structure.

For a time-invariant system with time-delay τ , the transfer function of the block diagram shown in Fig. 8.7a can be derived. Substituting the Rekasius equation [55], given by $e^{-s\tau} = (I - sT) \times (I + sT)^{-1}$, into the transfer function, Routh's stability test [55, 56] can therefore be applied to it, and the critical time-delay τ_{crt} can be estimated by Eq. (8.13) as:

$$\tau_{crt} = 2\{\tan^{-1}(\omega_{crt} T_{crt} \pm k\pi)\}/\omega_{crt}, \text{ where } k = 0, 1, 2, 3 \dots \quad (8.13)$$

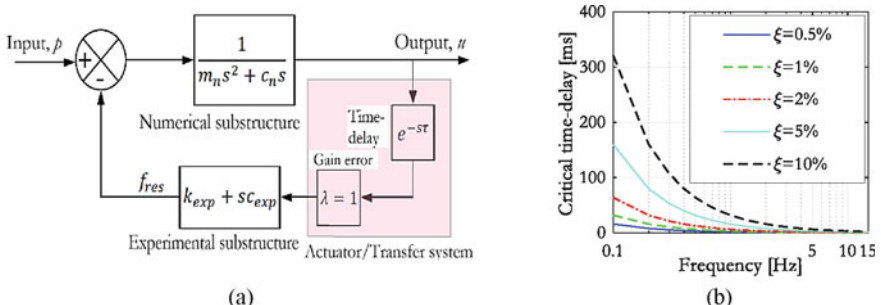


Fig. 8.7 **a** Block diagram of a hybrid test of a SDOF structure; **b** critical time-delay

where T_{crt} is the smallest of the two roots of the characteristic polynomial obtained from Routh's stability test. In Eq. (8.13), ω_{crt} corresponds to T_{crt} and it is calculated by substituting T_{crt} in the characteristic equation of the transfer function. Herein, the relationship between the critical time-delay and the frequency of the SDOF oscillator is evaluated at different ratios of viscous damping, as shown in Fig. 8.7b. For example, $\tau_{crt} = 6.36$ ms when $f_1 = 1$ Hz and $\xi = 2\%$, but becomes 1.27 ms when $f_1 = 5$ Hz.

The critical time-delay of the actuator decreases rapidly with an increasing frequency of the SDOF structure. At higher frequencies, the viscous damping of the structure is less effective in preserving the stability margin since the critical time-delay of an actuator at large frequencies is small regardless of the structure's viscous damping. Conversely, the viscous damping has a remarkable influence on the stability margin in the frequency interval [0,1] Hz. Thus, the role of viscous damping cannot be ignored in reducing the detrimental effect of the time-delay of an actuator. For a MDOF structure with a significant contribution from the higher modes, system instability may be triggered easily because the critical time-delay is small at large frequencies.

8.4.4 Delay Compensation

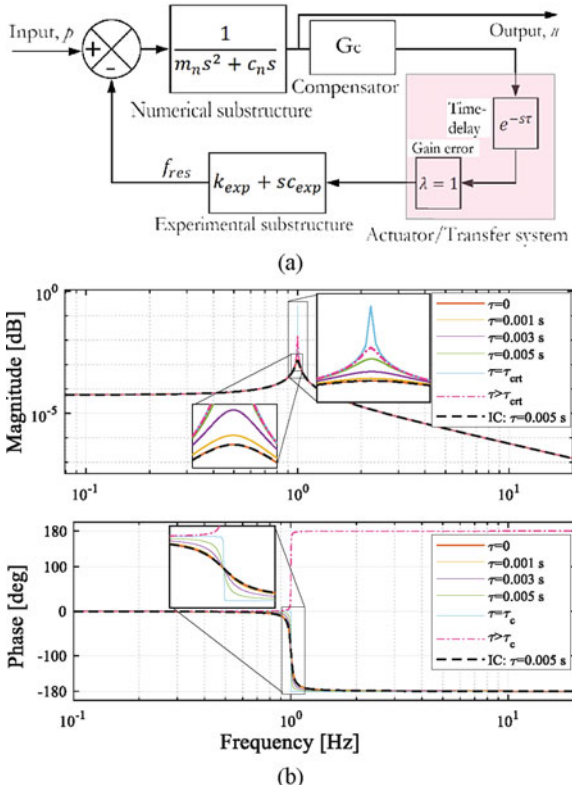
To improve the command tracking of an actuator during RTHS, various delay compensation techniques have been developed to date, as mentioned above. Recalling the hybrid test of the SDOF structure (Fig. 8.7a), the effect of the actuator's time-delay can be reduced by adding a compensator G_C , as shown in Fig. 8.8a. For illustration, taking the natural period of the SDOF oscillator to be 1 s and $\xi = 2\%$, herein, the inverse compensator (IC) [40] models G_C , given by $G_C = z / (\alpha \times z - (\alpha - 1))$, where $\alpha = (\tau + \delta t) / \delta t$ and $\delta t = 1$ ms (controller clock-speed). Figure 8.8b demonstrates that, as the system delay increases, the response of the structure at the resonant frequency increases as well.

For the time-delay of the actuator greater than the critical value, the phase error reaches 360°, meaning positive feedback, thus unbounded response. Assuming $\tau = 5$ ms, i.e., $\alpha = 6$, the IC compensator brings down the deviation of the system dynamics close to zero, as shown in Fig. 8.8b. Nonetheless, this problem does include system nonlinearity, which is often not true in experiments. Hence, a HS framework software must be equipped with adaptive compensation techniques such as the ATS [46].

8.4.5 Hybrid Simulation Including a Shake Table

Substructuring tests in a shake table (aka smart shake table tests) are a class of hybrid simulation that involves a shake table test of a physical substructure while the numerical substructure is modeled in a computational program, as shown in Fig. 8.9.

Fig. 8.8 **a** Block diagram of a hybrid test including a delay compensator; **b** delay compensation in hybrid simulation



A shake table can be used to conduct a hybrid test if its control scheme can interface with external devices. This class of hybrid simulation is suitable for studying soil-structure interaction problems as well as high-rise buildings [38, 56, 57]. Unlike the conventional hybrid test, it may require acceleration compatibility, directly or indirectly, at the boundary between the two substructures [60].

This technique was first demonstrated by conducting tests of a rigid mass, also a SDOF structure, using a small shake table [38, 59]. In [62], a smart shake table test was applied to investigate tuned mass-dampers. It was also suggested for high-rise buildings where the middle part of the building is physically represented while the top and bottom parts are modeled numerically [54]. Since its inception, a great deal of research has been done on the acceleration tracking of a shake table [63]. An adaptive controller based on the Minimal Control Synthesis (MCS) has shown good tracking capabilities for the displacement of a shake table [64]. The inverse transfer function of a shake table has also been used to improve the acceleration errors at the boundary between the two substructures [65].

Direct acceleration control of a shake table is inherently unstable since the shake table can drift even when acceleration is zero [49]. Hence, the position of the shake table should also be controlled. The Acceleration Trajectory Tracking Control

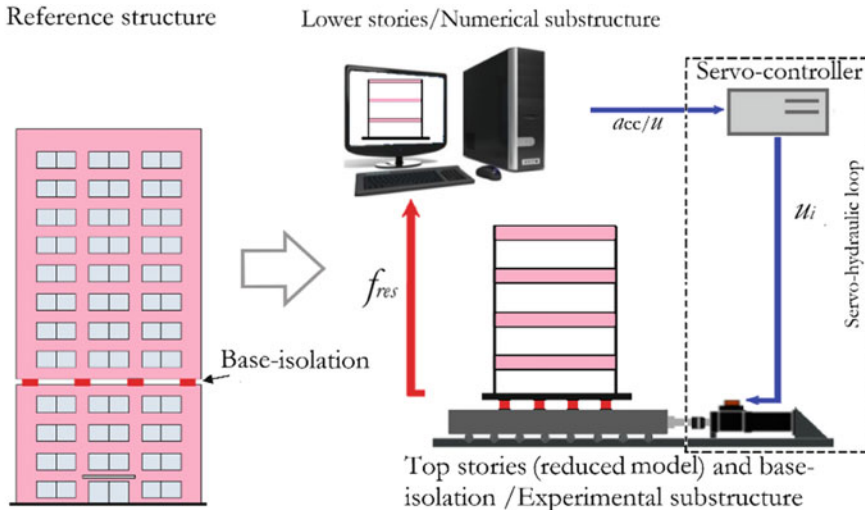


Fig. 8.9 Schematic representation of hybrid simulation in a shake table test

(ATTC), developed in [66], uses a model-based control comprising a feedforward controller, command shaping, Kalman filter, proportional-derivative displacement-based feedback controller, and an intentional time-delay. The latter is applied to the feedback controller making the feedforward command the prime driving source. A similar model-based feedforward-feedback control strategy, which uses the Linear Quadratic Gaussian (LQG) feedback control, was also successful in accurately tracking the acceleration of a uniaxial shake table [67]. This controller was reported to have superior performance compared to the traditional approach, transfer function iteration technique, for acceleration tracking of a shake table.

8.5 Conclusions

Experimental research is a fundamental activity in earthquake engineering, contributing to the seismic vulnerability assessment of buildings and infrastructures. Tests are carried out in controlled environments, exploring the nonlinear behavior of structures up to a (near) collapse condition under earthquake loads, which supply a wealth of experimental data that is later used to develop and calibrate sophisticated numerical models.

There are many shake table testing facilities built around the world, chiefly in earthquake prone countries; a brief list of the major ones was presented. Despite the existing capacities, testing of full-scale large structures is not always possible, circumstances under which reduced scale models have to be used and/or new seismic testing techniques have to be implemented.

Testing of reduced scale models must comply with a set of requirements in order to extrapolate the experimental results back to the real scale models. In the case of dynamic and seismic tests, dynamic similitude, which implies both geometric similitude and kinematic similitude, is quite demanding. Three types of models can be considered, depending on the compliance with the Froude and Cauchy numbers: (i) true replica models fully comply with both Froude and Cauchy numbers but impose serious restrictions on the physical model material properties, making them difficult to use in practice; (ii) adequate models, on the other hand, also comply with the Froude and Cauchy numbers but use additional masses to account for both the inertia effects due to the earthquake loading and the weight due to the acceleration of gravity; and (iii) when the effects of the gravity force can be neglected, additional masses are placed to account only for the inertia effects due to the earthquake loading, meaning compliance only with the Cauchy number.

Scaling factors were presented for all three types of models and the placing of additional masses on adequate models was discussed. These can be either distributed or lumped, but always placed in direct relation with the existing masses or the additional loads required during the shake table test.

Testing of substructures comes up as an alternative to the use of reduced scale models, but it can require a more elaborate testing setup in order to impose the boundary conditions. Examples were presented to illustrate the potential of such tests.

More recently, hybrid simulation is a candidate technique for full-scale testing if its main challenges, such as error propagation, stability, etc., can be restricted. In hybrid simulation, full scale testing can be performed by physically testing the more complex part of a structure in real scale, while the remaining parts are modelled numerically. In addition, hybrid simulation can enable multi-physics response simulation, thus making it versatile.

Shake table testing can also be integrated into hybrid testing, thus establishing a direct link between the two testing techniques. It is expected to see both techniques complement each other in the near future, creating venues for a more reliable and accurate response simulation of buildings and infrastructures.

Acknowledgments This work was partially supported by the European Union Seventh Framework Programme (FP7/2007-2013) under grant agreements 218417-2 (SAFECAST) and 227887 (SERIES), the EU Horizon 2020 programme under Grant Agreement Number 730900 (SERA), and the Portuguese Foundation for Science and Technology (FCT) in the framework of projects PTDC/ECM-EST/3790/2014 - POCI-01-0145-FEDER-016898 (ASPASSI), and PTDC/ECI-EST/6534/2020 (HybridNET).

References

1. Harris HG, Sabnis GM (1999) Structural modeling and experimental techniques, Routledge, ISBN: 9780849324697
2. Nakashima M, Nagae T, Enokida R, Kajiwara K (2018) Experiences, accomplishments, lessons, and challenges of E-defense—tests using world's largest shaking table. Japan Architectural Review. <https://doi.org/10.1002/2475-8876.10020>
3. NHERI@UC San Diego Facilities. The Large High Performance Outdoor Shake Table (LHPOST). <http://nees.ucsd.edu/facilities/>, last accessed 2021/02/01
4. NHERI@UC San Diego Shake Table Specifications, <http://nheri.ucsd.edu/facilities/shake-table.shtml>, last accessed 2021/02/01
5. UC Berkeley Shaking Table, <https://peer.berkeley.edu/uc-berkeley-shaking-table>, last accessed 2021/02/01
6. Center for Civil Engineering Earthquake Research (CCEER), <https://www.unr.edu/cceer/facilities/shake-tables>, last accessed 2021/02/01
7. Calvi GM, Pavese A, Ceresa P, Dacarro F, Lai CG, Beltrami C (2005) Design of a large-scale dynamic and pseudo-dynamic testing facility. IUSS Press, Pavia, Italy. ISBN: 88-7358-026-2
8. Navarra G, Iacono FL, Oliva M, Tesoriere G (2015) A new research facility: the laboratory of Earthquake Engineering and Dynamic Analysis (L.E.D.A.). XXII Congresso—Associazione Italiana di Meccanica Teorica e Applicata—AIMETA 2015. Genoa, Italy
9. Transnational access to European high-class laboratories (2017) SERA Project, <http://www.sera-eu.org/export/sites/sera/home/.galleries/pdfs/SERA-TA-brochure.pdf>, last accessed 2021/02/01
10. SERA PROJECT—Transnational Access Web Portal. <https://sera-ta.eucentre.it/ta-facilities/>, last accessed 2021/02/01
11. Shaking table Azalée, <http://www-tamaris.cea.fr/html/en/tests/azalee.php>, last accessed 2021/02/01
12. Gao C, Yuan X (2019) Development of the shaking table and array system technology in China, Advances in Civil Engineering, vol. 2019, Article ID 8167684, 10 pages, 2019. <https://doi.org/10.1155/2019/8167684>
13. China Academy of Building Research (CABR), <http://www.cabr.com.cn/engweb/Major.htm>, last accessed 2021/02/01
14. Chunyu T, Congzhen X, Hong Z, Jinzhe C (2012) Shaking table test and seismic performance evaluation of Shanghai tower. China Academy of Building Research, Bei San Huan Dong Lu 30#, Beijing, 100013, China. Int J High-Rise Buildings, September 2012, 1(3): 221–228
15. Moncarz PD, Krawinkler H (1981) Theory and application of experimental model analysis in earthquake engineering, Report No. 50., John A. Blume Earthquake Engineering Center, Department of Civil and Environmental Engineering Stanford University
16. Casaburo A, Petrone G, Franco F, Rosa S (2019) A review of similitude methods for structural engineering. Appl Mech Rev May 2019, 71(3): 030802 (32 pages). <https://doi.org/10.1115/1.4043787>
17. Lirola JM, Castañeda E, Lauret B, Khayet M (2017) A review on experimental research using scale models for buildings: application and methodologies. Energy and Buildings 142, 1 (72–110). <https://doi.org/10.1016/j.enbuild.2017.02.060>
18. Addis B (ed.) (2020) Physical models: their historical and current use in civil and building engineering design. First published: 25 September 2020. Print ISBN: 9783433032572, Online ISBN: 9783433609613, <https://doi.org/10.1002/9783433609613>
19. Carvalho EC (1998) Seismic testing of structures (invited lecture). In 11th European Conference on Earthquake Engineering (11ECEE), 53–64. Balkema, Rotterdam, ISBN:9054109823
20. Coutinho CJP (2017) Structural reduced scale models based on similitude theory. PhD Thesis, FEUP, Porto, Portugal
21. Bairrão R, Vaz CT (2000) Shaking table testing of civil engineering structures—the LNEC 3D simulator experience. In 12th World Conference on Earthquake Engineering (12WCEE). Upper Hutt, NZ

22. Candeias PX (2012) Physical modelling, instrumentation and testing. Preparatory Course on Dynamic Experimental Testing, Lisbon, September 23. http://www.series.upatras.gr/sites/default/files/SERIES_LNEC_Training_Course_Session_2_Physical_Modelling_Instrumentation_and_Testing.pdf, last accessed 2021/02/01
23. Tomic I, Penna A, DeJong M, Butenweg C, Correia AA, Candeias PX, Senaldi I, Guerrini G, Malomo D, Beyer K (2020) Seismic testing of adjacent interacting masonry structures. In 17th World Conference on Earthquake Engineering (17WCEE), Sendai, Japan
24. Assessment of innovative solutions for non-load bearing masonry enclosures. Final Report. MASONRY ENCLOSURES Project. User Group Leader: Elizabeth Vintzileou. Seismic Engineering Research Infrastructures for European Synergies (SERIES), July, 2013. http://www.series.upatras.gr/sites/default/files/file/SERIES_MASONRY%20ENCLOSURES_Final%20report.pdf, last accessed 2021/01/01.
25. Toniolo G (2012) SAFECAST project: European research on seismic behaviour of the connections of precast structures. In: 15th World Conference on Earthquake Engineering (15WCEE). Lisbon, Portugal
26. Leite J, Correia AA, Lourenço PB, Vintzileou E, Palieraki V, Candeias P, Campos Costa A, Coelho E (2015) Assessment of innovative solutions for non-load bearing masonry enclosures. Chapter 16 of *Experimental Research in Earthquake Engineering*, Taucer, F. (Ed.), Springer book series Geotechnical, Geological and Earthquake Engineering. https://doi.org/10.1007/978-3-319-10136-1_16
27. Onat O, Correia AA, Lourenço PB, Koçak A (2018) Assessment of the combined in-plane and out-of-plane behavior of brick infill walls within reinforced concrete frames under seismic loading. *Earthquake Eng Struct Dynam* 47(14): 2821–2839. <https://doi.org/10.1002/eqe.3111>
28. Dermitzakis S, Mahin S (1985) Development of substructuring techniques for on-line computer controlled seismic performance testing. In: UCB/EERC-85/04 Report to NSF, University of California, Berkeley, USA
29. Lin Y (2009) Real-time hybrid testing of an MR damper for response reduction. PhD thesis, the University of Connecticut, USA
30. Calabrese A, Strano S, Terzo M (2015) Real-time hybrid simulations vs shaking table tests: case study of a fiber-reinforced bearings isolated building under seismic loading. *Struct Control Health Monit* 22(3): 535–556
31. Chen P, Dong M, Chen P, Nakata N (2020) Stability analysis and verification of real-time hybrid simulation using a shake table for building mass damper systems. *Frontiers in Built Environment* 6
32. Schellenberg A, Mahin S, Fenves G (2009) Advanced implementation of hybrid simulation. In: PEER Report 2009/104 University of California, Berkeley, USA
33. Kwon O, Spencer B, Elnashai A, Nakata N (2007) The UI-SimCor hybrid simulation framework. In: 2nd World Forum on Collaborative Research in Earthquake Engineering, Ispra, Italy
34. Newmark N (1959) A method of computation for structural dynamics. *J Engineering Mechanics, ASCE* 67–94
35. Nakashima M, Kaminosomo T, Ishida M (1990) Integration techniques for substructure pseudodynamic test. In: Proceedings of 4th U.S. National Conference on Earthquake Engineering, pp. 515–524, California, USA
36. Mosqueda G, Ahmadizadeh M (2007) Combined implicit or explicit integration steps for hybrid simulation. *Earthquake Eng Struct Dynam* 36: 2325–2343
37. Chung J, Hulbert G (1993) A time integration algorithm for structural dynamics with improved numerical dissipation: the generalized- α method. *J Appl Mech Trans ASME* 60(2): 371–375
38. Kolay C, Ricles J (2014) Development of a family of unconditionally stable explicit direct integration algorithms with controllable numerical energy dissipation. *Earthquake Eng Struct Dynam* 43:1361–1380
39. Horiechi T, Inoue M, Konno T, Namita Y (1999) Real-time hybrid experimental system with actuator delay compensation and its application to a piping system with energy absorber. *Earthquake Eng Struct Dynam* 28(10): 1121–1141

40. Chen C, Ricles J (2010) Tracking error-based servohydraulic actuator adaptive compensation for real-time hybrid simulation. *J Struct Eng* 136(4):432–440
41. Hessabi R, Mercan O (2011) Phase and amplitude error indices for error quantification in pseudo-dynamic testing. *Earthquake Eng Struct Dynam* 41(10):1347–1364
42. Mosqueda G, Stojadinovic B, Mahin S (2007) Real-time error monitoring for hybrid simulation. Part I: methodology and experimental verification. *Journal of Structural Engineering* 133, 1100–1108
43. Mosqueda G, Stojadinovic B, Mahin S (2007) Real-time error monitoring for hybrid simulation. Part II: structural response modification due to errors. *Journal of Structural Engineering* 133(8), 1109–1117
44. Jung R, Shing P (2006) Performance evaluation of a real-time pseudo-dynamic test system. *Earthquake Eng Struct Dynam* 35(7): 789–810
45. Carrion J, Spencer B, Phillips B (2009) Real-time hybrid simulation for structural control performance assessment. *Earthq Eng Eng Vib* 8(4): 481–492
46. Chae Y, Karim K, Ricles J (2013) Adaptive time series compensator for delay compensation of servo-hydraulic actuator systems for real-time hybrid simulation. *Earthquake Eng Struct Dynam* 42(11): 1697–1715
47. Elkhorai T, Mosalam K (2007) Towards error-free hybrid simulation using mixed variables. *Earthquake Eng Struct Dynam* 36(11): 1497–1522
48. Kim, H (2011) Development and implementation of advanced control methods for hybrid simulation. PhD thesis, University of California, Berkeley, USA
49. Nakata N, Stehman M (2012) Substructure shake table test method using a controlled mass: formulation and numerical simulation. *Earthquake Eng Struct Dynam* 41(14): 1977–1988
50. Sivaselvan M, Reinhorn A, Shao X, Weinreber S (2008) Dynamic force control with hydraulic actuators using added compliance and displacement compensation. *Earthquake Eng Struct Dynam* 37(15): 1785–1800
51. Chae Y, Rabiee R, Dursun A, Kim C (2018) Real-time force control for servo-hydraulic actuator systems using adaptive time series compensator and compliance springs. *Earthquake Eng Struct Dynam* 47(4): 854–871
52. Phillips B, Wierschem N, Spencer B (2014) Model-based multi-metric control of uniaxial shake tables. *Earthquake Eng Struct Dynam* 43(5): 681–699
53. Sadeghian V, Kwon O, Vecchio F (2017) Small-scale multi-axial hybrid simulation of a shear-critical reinforced concrete frame. *Earthq Eng Eng Vib* 16(4): 727–743
54. Shao X, Reinhorn A, Sivaselvan M (2011) Real-time hybrid simulation using shake tables and dynamic actuators. *J Struct Eng* 137(7): 748–760
55. Ebenbauer C, Allgöwer F (2006) Stability analysis for time-delay systems using Rekasius's substitution and sum of squares. In: IEEE Conference on Decision and Control, San Diego, CA, USA
56. Tekeste G, Correia A, Costa A (2017) Stability analysis of a real-time shake table hybrid simulation for linear and non-linear SDOF systems. In: 7th International Conference on Advances in Experimental Structural Engineering, 641–659, Pavia, Italy
57. Tekeste G (2021) Real-time hybrid simulation including a shaking table—development and application to soil-structure interaction. PhD thesis, Civil Engineering Department, University of Aveiro, Portugal
58. Saouma V, Sivaselvan M (2008) Hybrid simulation: theory, implementation and applications. Taylor & Francis, New York, USA
59. Zhang R, Phillips BM, Taniguchi S, Ikenaga M, Ikago K (2017) Performance validation of inter-story isolation through shake table real-time hybrid simulation. In: 16th World Conference on Earthquake Engineering Santiago, Chile
60. Nakata N, Stehman M (2014) Compensation techniques for experimental errors in real-time hybrid simulation using shake tables. *Smart Struct Syst* 14: 1055–1079
61. Igarashi A, Kikuchi Y, Lemura H (2008) Real-time hybrid experimental simulation system using coupled control of shake table and hydraulic actuator. In: 14th World Conference on Earthquake Engineering, Beijing, China

62. Igarashi A et al. (2000) Development of substructured shaking table test method. In: 12th World Conference on Earthquake Engineering, Auckland, New Zealand
63. Stoten D, Gómez E (2001) Adaptive control of shaking tables using the minimal control synthesis algorithm. *Philosophical Transactions of the Royal Society A: Mathematical, Physical and Engineering Sciences* 359(1786): 1697–1723
64. Neild S, Stoten D, Drury D, Wagg D (2005) Control issues relating to real-time substructuring experiments using a shaking table. *Earthquake Eng Struct Dynam* 34(9): 1171–1192
65. Lee S, Park E, Min K, Park J (2007) Real-time substructuring technique for the shaking table test of upper substructures. *Eng Struct* 29(9): 2219–2232
66. Nakata N (2010) Acceleration trajectory tracking control for earthquake simulators. *Eng Struct* 32(8): 2229–2236
67. Phillips B (2012) Model-based framework for real-time dynamic structural performance evaluation. In: NSEL Report Series, Report No. NSEL-031, University of Illinois, USA

Chapter 9

Experimental Research and Development on Blast Resistant Structures



Gabriel Gomes , Hugo Rebelo , Válter Lúcio , Corneliu Cismasiu , and José Mingote

Abstract Structures are usually designed to withstand a broad set of loads (e.g., gravity, wind, temperature changes and earthquakes). However, over the last few decades, wars, terrorist attacks and accidental explosions, have raised up the need to consider blast loads in the construction of relevant public or private infrastructures. The successful design of blast resistant structures requires a deep understanding of the effects of explosions on structures, which can only be achieved by extensive experimental campaigns and comprehensive numerical simulations. This chapter presents an experimental research programme that has been established to assist the development of blast resistant solutions for structures that may be subjected to accidental or intentional explosions on industrial and/or critical/governmental infrastructure and buildings and military/peacekeeping operations infrastructures. The research includes explosive field tests on RC façade panels, strengthened to resist the blast actions or provided with energy dissipation connectors to the main building structure and sacrificial cladding connectors for ventilated façades. These solutions, aim to reduce the blast effects on buildings subjected to accidental or intentional explosions, minimizing injuries and life losses of their occupants.

G. Gomes · H. Rebelo

CINAMIL, Academia Militar, Instituto Universitário Militar, Lisbon, Portugal

e-mail: gomes.gj@exercito.pt

H. Rebelo

e-mail: hugo.bento.rebelo@ulusofona.pt

V. Lúcio · C. Cismasiu

CERIS, Department of Civil Engineering, NOVA School of Science and Technology,
Universidade NOVA de Lisboa, Lisbon, Portugal

e-mail: vlucio@fct.unl.pt

C. Cismasiu

e-mail: cornel@fct.unl.pt

J. Mingote

NATO Counter IED Centre of Excellence, Madrid, Spain

e-mail: jmingote@ciedcoe.org

Keywords Experimental tests • Blast load effects • Façade panels • Energy dissipation connectors • Sacrificial cladding

9.1 Introduction

Research on the effects of explosions in infrastructures has attracted increasingly the interest of many researchers [1–5]. The need to protect infrastructures against explosive attacks in military operations in an expeditionary context is consensual, but the scope of civil application is equally wide, namely in extractive or manufacturing industries (chemical and oil) and critical infrastructures. Whatever the case, military or civilian, the need to protect people and the continuity of operations or business, make it necessary to identify plausible threats and risks and based on these, to assess the consequences of potential attacks or incidents, and to design protective measures consistent with the level of protection intended to be addressed [6].

The results of several research projects (SI4E—Security and Integrity of Strategic Buildings under Accidental or Intentional Explosions, PRINSEF—Protection of Infrastructures and Physical Security, BLADE—Blast T-Walls Performance Optimization Design and PROTEDES—Strategic Building Protection Against Explosions), based on strong experimental and numerical campaigns, allowed, among other findings, to realize that the effects of a close-range explosion outside a building, primarily affect local elements and then might develop into a global failure. This finding constitutes the motivation for the development of protective systems for structural and/or non-structural façade elements that might be directly facing explosions.

The design of a new or the strengthening of existing buildings under blast loading can be done, essentially, following three basic approaches, either standalone or combined: (1) strengthening of structural elements and/or connections; (2) allow existing elements to break and be collected by catching systems, protecting occupants from debris propelling; and (3) shielding a structural element from being directly loaded through the addition of a new, explosion-resistant, outer element sometimes including some kind of energy absorbing mechanism. In this chapter the focus is on the third approach.

9.2 The Blast Loading

An explosion is characterized by the production, in a very short time, of gases at high temperature and extremely high pressures, known as the gas bubble, which expand outwards by pushing the surrounding air [1, 7, 8]. In this process, a small layer of highly compressed air is formed on the wave front, also called the shock wave. Simultaneously, as the hot gas bubble expands, moving away from the focus, the air

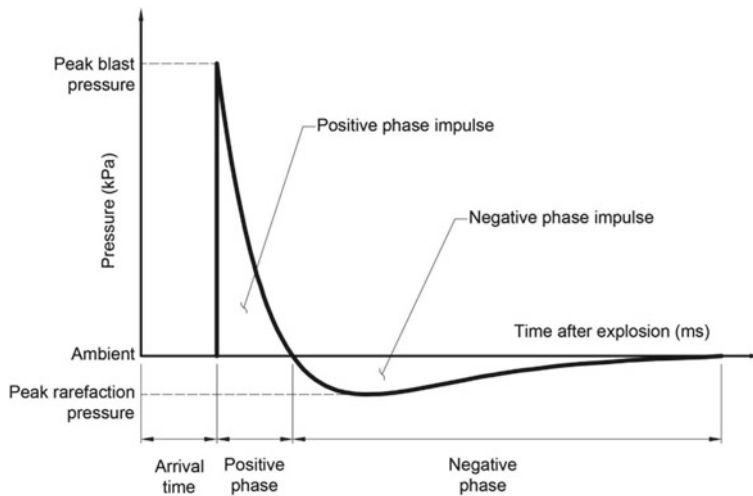


Fig. 9.1 Profile of the shock wave

around the point of explosion cools down and reduces the pressure. In some cases, the gas pressure may momentarily drop below ambient pressure until equilibrium occurs [9].

The shock wave is usually represented, as illustrated in Fig. 9.1, by a time-pressure curve, showing the time dependency of the overpressure's magnitude, i.e., the increase with respect to ambient pressure, inside the region affected by the explosion [7].

The peak pressure is reached instantaneously upon arrival of the shock wave, decaying very rapidly with time. The area under the pressure curve corresponds to the impulse caused by detonation, which in the case of conventional explosions outside buildings is generally the most relevant factor for damage mechanisms.

For the analysis of structures under blast loading, it is necessary to identify the parameters that allow characterizing this load. The main ones are the shape of the wave (shock wave or pressure wave), the incident peak pressure, the positive phase duration, and the impulse. In addition, there are other parameters that may be required, namely the peak reflected pressure, and reflected impulse the peak dynamic pressure the velocity of the shock front and, finally, the blast wavelength.

9.3 High Performance Blast Energy-Absorbing System for Structures

9.3.1 Introduction

Typically, the effects of a close explosion outside a building primarily affect local elements (e.g., a column) and then might develop into a global failure (progressive collapse). To prevent this effect, the research reported here involves the use of an external shielding system linked to the structure using ductile connectors to absorb part of the impulsive energy of the explosion and to transfer the residual part to the floor levels, protecting the columns and masonry walls that, in normal situations, are not designed for protective purposes.

The concept analysed in the experimental tests presented in this section (Fig. 9.2) is intended to ensure that the surface that receives the energy from the explosion is not in direct contact with the elements to be protected, using floor-level Energy-Absorbing Connectors (EAC) with a sufficient stroke to accommodate (by shortening or crushing) the intensity of a given explosion. A couple of similar solutions are reported in the literature [10–13].

When the external element is loaded, it triggers the set of connectors, which absorb the kinetic energy by compressing at a relatively constant stress, reducing the peak forces imparted to the structure. This process allows the partial or total absorption of the kinetic energy transmitted by the explosion (depending on its magnitude and the design of the connecting device), without the outer element transmitting energy to the columns by contact. In case of buildings, a residual part will be transmitted to the structure at the floor level, mobilizing its resistant capacity to horizontal loading.

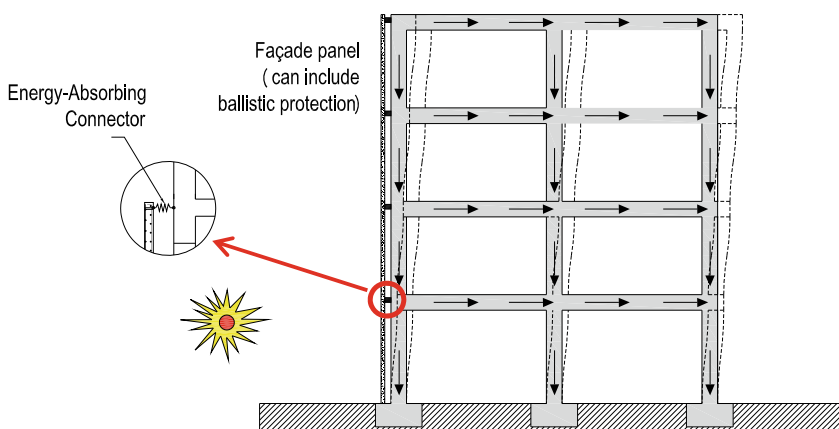


Fig. 9.2 Protection System concept—mobilizing all the structure

9.3.2 Energy Absorbing Mechanisms and Shapes

An energy absorber is a system that converts, totally or partially, the kinetic energy into another form of energy. The conversion of the kinetic energy into energy of plastic deformation depends essentially on the material properties and shape, and the rate of the applied load. Additionally, the peak reaction force of an energy-absorber should be kept below a threshold defined by the resistance of the structure intended to be protected, to avoid unacceptable damages.

The most common type of energy-absorber are thin-walled devices, and several mechanisms can be designed to mitigate the applied kinetic energy. The inversion mechanism [14, 15] is one of the most interesting energy absorber systems and basically involves the turning inside-out or outside-in of a thin circular tube made of a ductile material. Likewise, the dissipation can be obtained by lateral compression, indentation, bending, and lateral crushing of arrays of circular tubes, among others [16–18]. In this section, the experimental study on energy absorber exploring a tube inverter is briefly presented.

9.3.3 Tube Inversion Mechanism

During this research, three tube diameters were used (64×2 , 54×1.5 and 42×1.5 mm) to better understand the inversion mechanism and check the relative importance of the different influencing parameters. The preparatory work was carried out in two stages. In the first stage, (a) the tube was expanded/flared against a die and (b) clamped by welding (Fig. 9.3a and b). The second stage consists of the pre-inversion of the tube (Figs. 9.3c and 9.4). After being inverted the energy absorbing core is ready for free inversion when subjected to dynamic loading.

The pre-inversion process was performed using an MTS 100kN pressing machine. Typical load displacement curves for the two forming phases and the post-inversion load displacement are plotted in Fig. 9.5a. It is interesting to highlight the fact that the

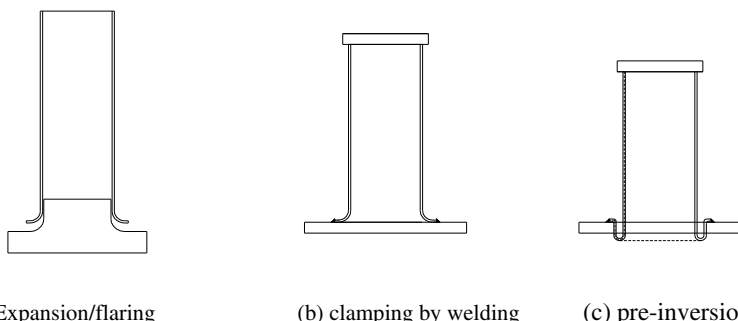


Fig. 9.3 Pre-forming stages

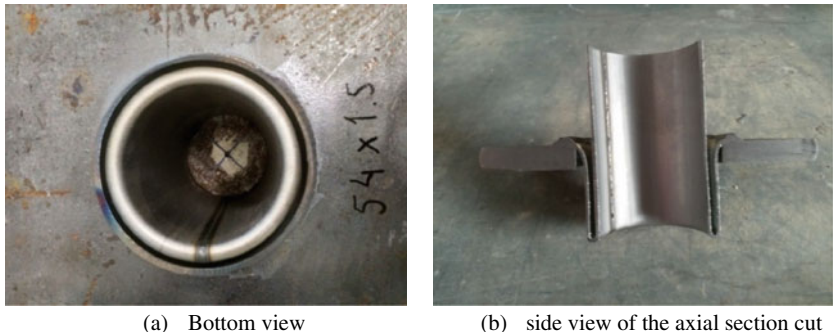


Fig. 9.4 Pre-inversion

forming load against the die is significantly higher than the inversion load. This is a remarkable aspect because this behaviour means that the tube will not buckle locally upon the operating condition (free inversion), since the inversion force is significantly lower than forming force and the resulting stress at the cross section is not enough to cause local buckling and the formation of folds (concertina deformation mode).

Figure 9.5b plots the average force-shortening history for the tested specimens. The steady force, knuckle radius and tensile characteristics of the specimens are presented in Table 9.1.

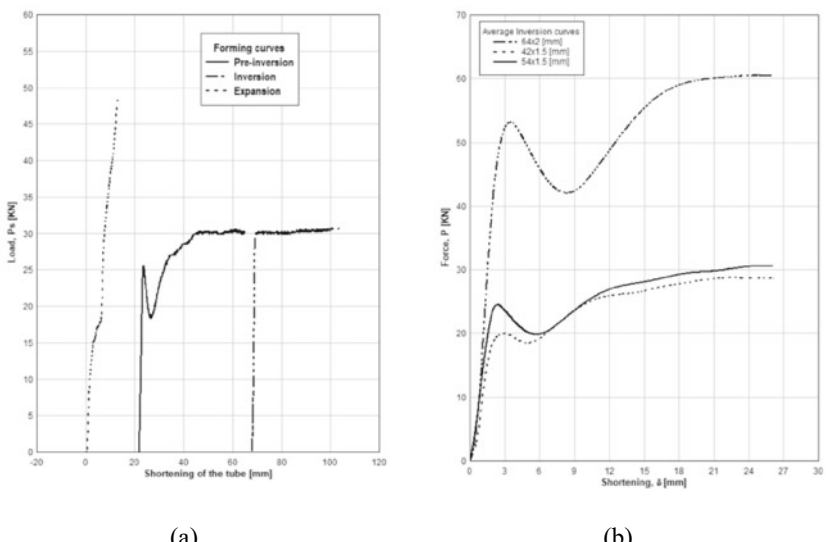


Fig. 9.5 Load-shortening curves; **a** Typical load-displacement curves shape for expansion, pre-inversion, and post-inversion for a steel tube $\varnothing 54 \times 1.5$ mm ($f_y = 376$ MPa); **b** Load-displacement (shortening) history curves for tested specimens

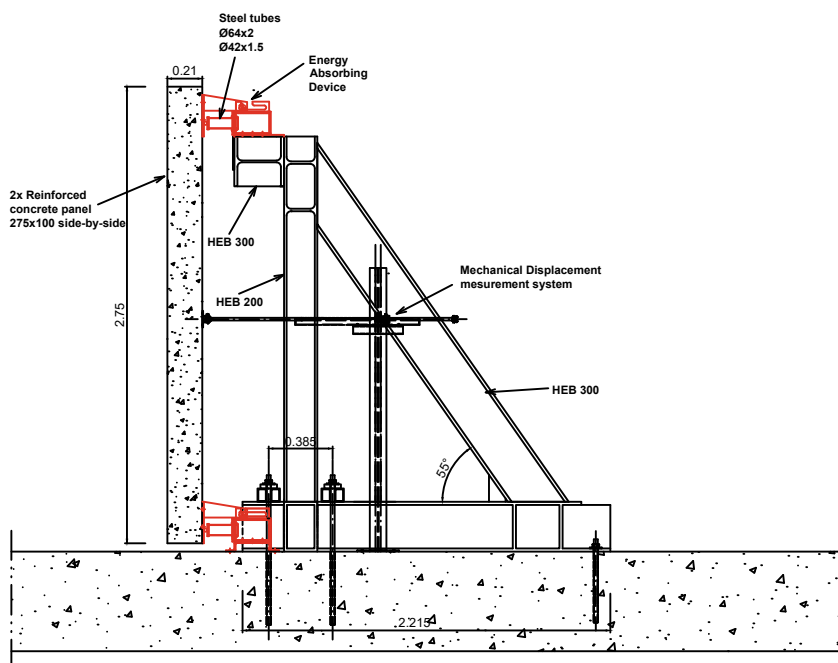
Table 9.1 Mechanical characteristics of the inverted tubes

Specimen	f_y [MPa]	f_u [MPa]	Steady force [kN]	Inversionradius [mm]
$\varnothing 64 \times 2$ mm	371	423	60.45	5.25
$\varnothing 54 \times 1.5$ mm	360	387	30.60	4.25
$\varnothing 42 \times 1.5$ mm	379	401	28.65	4.0

9.3.4 Blast Testing SETUP

The systems were planned to be tested using concrete façade panels in the vertical position (service condition), attached to steel reaction structures (Fig. 9.6) arranged radially, where a cylindrical explosive charge was detonated at the centre. In a final test, sacrificial panels were attached to a Military Type T-Wall System as protective sacrificial layer to evaluate the increase of performance.

Two reaction structures comprising 4 reinforced concrete panels ($2.75 \times 1.00 \times 0.12$ m) attached by connectors at the four corners were used in the case of tube inverters. One of the panels comprises rigid supports and the other three are equipped with EAC. Five blast tests representing typical Vehicle Borne IED in close range were conducted ($Z[m/\sqrt[3]{kg}] = 1.14$ and $Z = 0.64$), replacing each time the energy absorbing cores and the sacrificial panels.

**Fig. 9.6** Blast test setup for inversion tubes

9.3.5 Data from Pressure Gages and Force Sensors

The experimental test has been instrumented with several sensors to extract as much dynamic information as possible. This data will be used next to validate the analytical and numerical models that seek to represent the behaviour of the overall system. The blast testing campaign aimed to validate the application of EAC on a panel element at a real scale and to evaluate the effects of an explosion on the system.

The overpressures were measured by general purpose PCB piezoelectric crystals pressure gages model 113B24 with a measurement range of 6895 kPa and a sensitivity of 0.725 mV/kPa. Figure 9.7 plots the incident overpressure for an explosion of a cylindrical charge ($Z[m/\sqrt[3]{kg}] = 1.14$) at ground level (hemispherical blast wave) over a concrete panel. To avoid noise from records and distort calculations, actual records should not be used directly. Therefore, they were adjusted using the Friedlander curve fit for the positive phase. The adjusted parameters for are indicated in the Table 9.2.

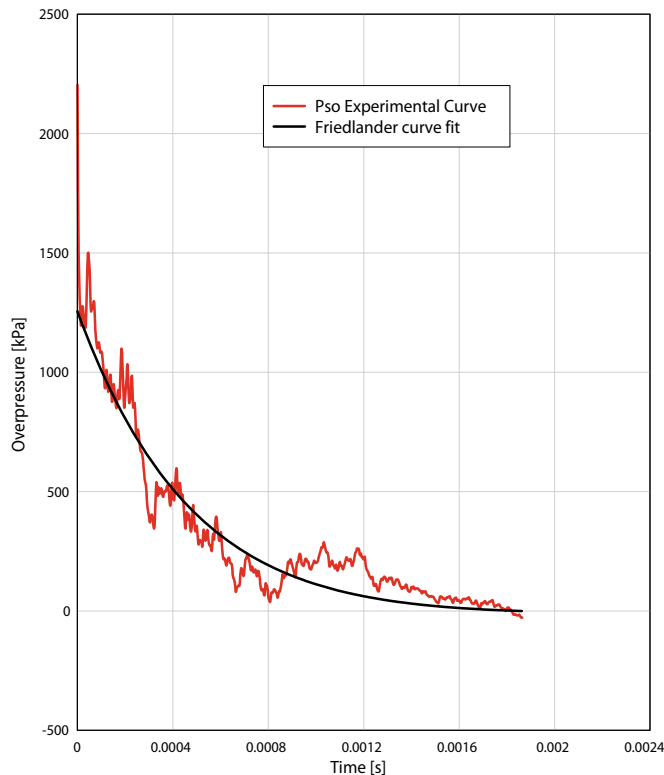


Fig. 9.7 Incident overpressure ($Z[m/\sqrt[3]{kg}] = 1.14$). Explosion at ground level

Table 9.2 Incident overpressure curve parameters: burst at ground level, $Z = 1.14$

P_{so} [kPa]	t_0 [ms]	i_s [kPa.ms]	α [-]
1256,0	1,9	526,82	3,12

P_{so} —Incident peak overpressure; t_0 —Positive phase duration;
 i_s —Incident impulse; α —Friedlander decay parameter

Another blast scenario consisted in an explosion of a cylindrical charge ($Z[m/\sqrt[3]{Kg}] = 0.64$), detonated at 0.8 m high over ground soil. The plot of the incident overpressure and the adjusted Friedlander parameters are given in Fig. 9.8 and Table 9.3.

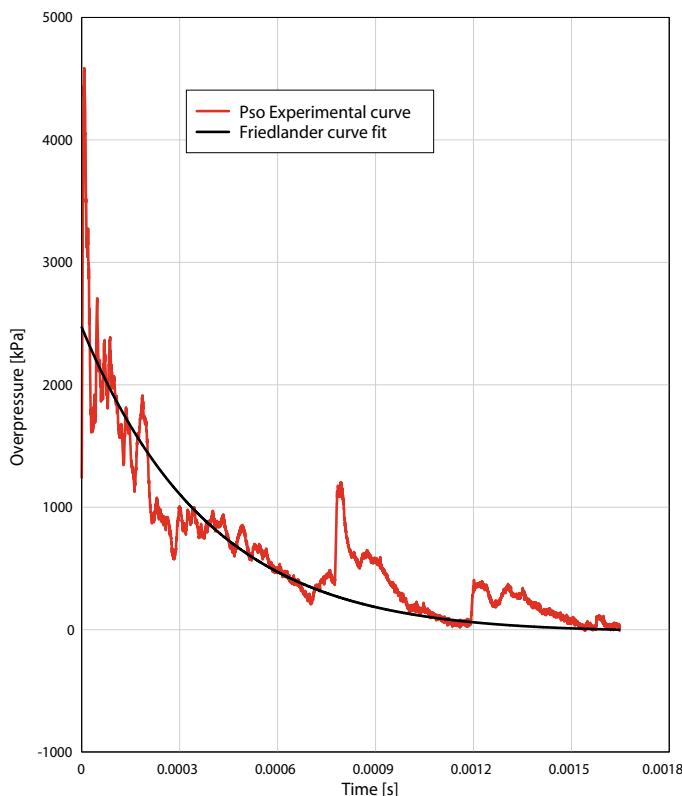


Fig. 9.8 Experimental and Friedlander adjustment of the pressure-time history for $Z = 0.64$

Table 9.3 Incident overpressure curve parameters: bust at 0.8 m height, $Z = 0.64$

P_{so} [kPa]	t_0 [ms]	i_s [kPa.ms]	α [-]
2468,8	1,7	872,8	3,30

Force sensors. Several force sensors were placed in strategic locations to assess the forces transmitted to the supports and further evaluate the effectiveness of the EAC. Two different ICP force sensors models were used: model 200C20 with a sensitivity of 56,2 mV/kN (+/-15%) and a measurement range of 88,96 kN to instrument the EACs; and model 200C50, with a sensitivity of 22,48 mV/kN (+/-15%) and a measurement range of 222,4 kN to record the dynamic reactions at the rigid supports.

When recorded data from the blast test performed using the inversion tubes (#64.05, #548 and #42.15 in Fig. 9.9 and Table 9.4) are compared with the ones obtained using rigid supports, one notes the efficiency of the EACs in the reducing the peak force and the impulse transmitted to the protected structure. At this point it is worth to note that, although an extensive planning was made to monitor all the blast tests, most of the attempts to get accurate force data failed, essentially due to two reasons: (i) very high pressures that caused the rupture or disengagement of the cables' connection during the test; and (ii) rotations of the EAC which made the collected data invalid.

It is also worth to mention that impulse loss that can be observed in Fig. 9.9, considering that the kinetic energy is directly proportional to the square of the impulse, represents a strong reduction in the kinetic energy imparted to the system. The average reduction ratio is 64%.

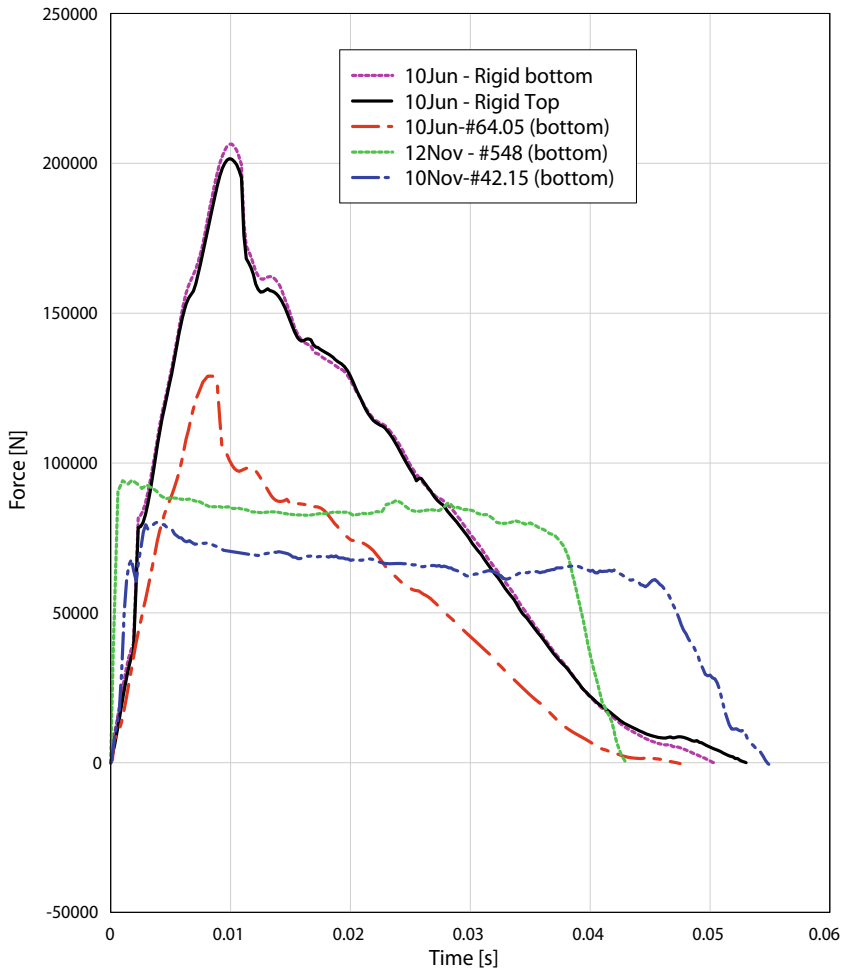
Figures 9.10 and 9.11 illustrate the initial and final state of the EAC inversion based upon two blast tests and specifically the need of an appropriate stroke (inverter length) to absorb the energy imparted to the system.

The outcome of this study, besides the protection of typical structures, was also to evaluate the effect of introducing energy absorbers in Military type Blast T-Walls used in high threat operational context. Figure 9.11 illustrates the use of the EAC as energy absorbing system in Military type Blast T-Walls. Comparing with an unprotected Blast T-Wall, the system performed properly, significantly reducing the damages and avoiding the breach of the T-Wall as shown in Fig. 9.12.

9.4 Explosive Driven Shock Tube Tests on 3D Printed Sacrificial Cladding

Following the same idea of using energy-absorbing cores and sacrificial claddings as described in the previous section, an explosive driven shock tube [19, 20] was used by Rebelo and his colleagues [21] to assess the nonlinear blast response of 3D printed PLA honeycomb when used as the crushable core of a sacrificial cladding solution for Civil Engineering structures.

The experimental campaign employed the small-scale experimental set-up illustrated in Fig. 9.13a. A square section (SHS 80 × 3 mm) explosive driven shock tube was used to generate a planar blast load at its end, resulting from the detonation of a given explosive charge, positioned at a given distance from, or at, its entrance. A schematic representation of the set-up is shown in Fig. 9.13b. A PCB 203B force load

**Fig. 9.9** Force plots at the supports ($Z = 1.14$)**Table 9.4** Parameters of the experimental force-time curves

EAC ID	Panel	Position	Peak force [kN]	Duration [ms]	Total impulse [MN.ms]	Specific impulse [MPa.ms]
Rigid	2B	Bottom	206.6	51	4.239	3.082
Rigid	2B	Top	201.7	53	4.287	3.117
#64.05	2A	Bottom	64.6	47	2.508	1.822
#548	4A	Bottom	46.2	44	3.350	2.430
#42.15	2A	Bottom	40.8	53	2.554	1.880

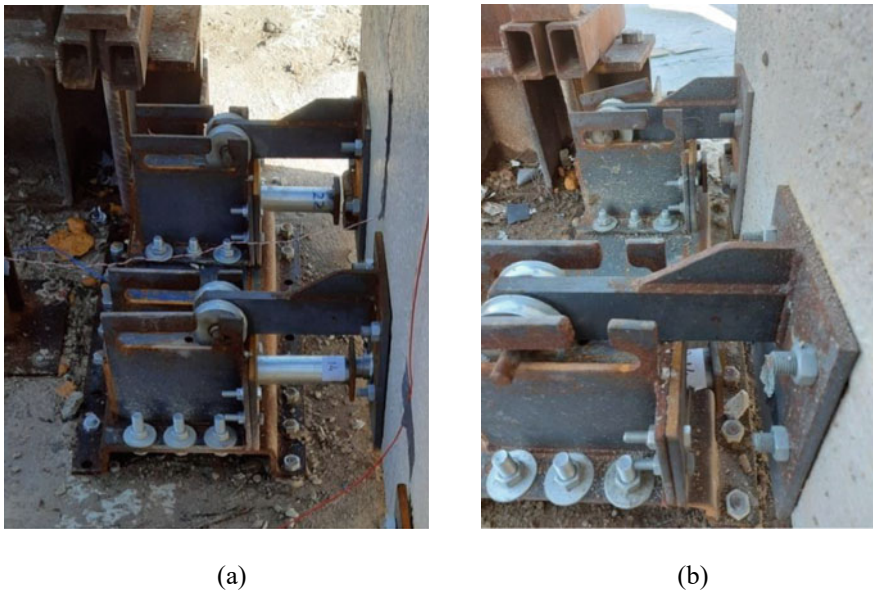


Fig. 9.10 EAC 42 × 1.5 mm Panel 4A under blast at $Z = 1.14$; **a** before the blast test; **b** after the blast test (inverter exhausted)

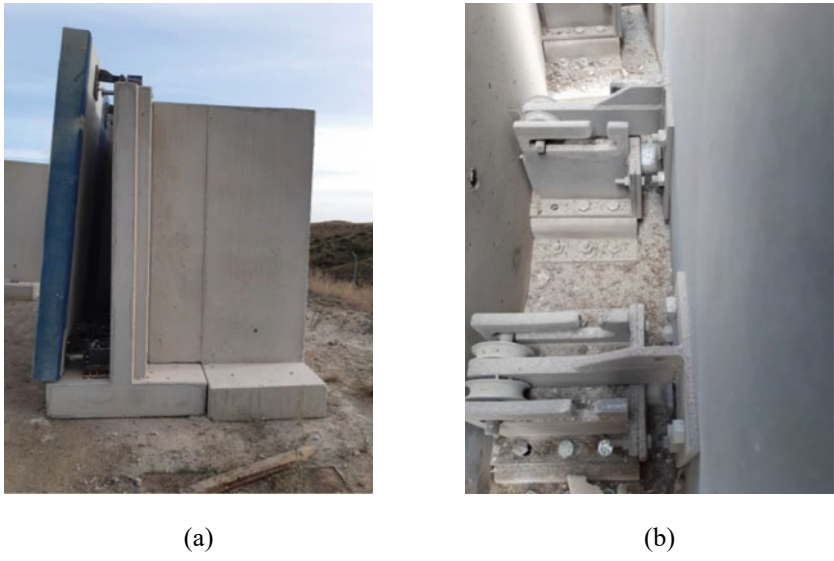


Fig. 9.11 Possible operational application of the energy-absorbing system developed; **a** T-Wall protected system; **b** Post blast plastic deformation of the EAC-blast load correspondent to $Z[m/\sqrt[3]{kg}] = 0.64$



Fig. 9.12 Post Blast result of protected (left) and unprotected (right) T-Walls

cell was placed between the rear plate and the remainder of the set-up to measure the transmitted load with a 1 MHz acquisition rate. A Photron Fastcam SA5 high speed camera was used to measure the displacement of the front plate at 10,000 frames per second. Lastly, it is important to refer that all the obtained measurements were synchronised using a light intensity trigger.

9.4.1 *Instrumentation Overview*

A PCB 203B force load cell (see Table 9.5 for details), was positioned between the rear plate and the remainder of the set-up to record the load transmitted by the sacrificial cladding solution. The schematic representation of the load cell installation is illustrated in Fig. 9.14 the referred sensor is classified as an integrated circuit piezoelectric (ICP) quartz force ring which is well suited for dynamic force measurement applications. To guarantee a correct contact between the sensor and the plates, ensure a linear variation of voltage with force and enable tensile force measurements, a preload must be applied to the sensor. Lastly, an anti-friction washer was used to mitigate damage to the sensor's surface during preload application.

A PCB 102B pressure transducer was used to measure the reflected overpressure on a rigid and fixed boundary (see Table 9.5 for details). Similarly, to the force load cell, the pressure transducer has a piezoelectric element, which generates an electric charge when pressure is applied, and an ICP source follower amplifier that converts the referred charge to a low impedance voltage output.

The deformation of the sacrificial cladding was recorded using a Photron Fastcam SA5 high-speed camera, placed perpendicularly to the loading direction to minimize errors due to out-of-plane movements on the two-dimensional projection of the compression process. As illustrated in Fig. 9.13, two spotlights were placed on either side of the specimen. A white screen was placed in front of the light which

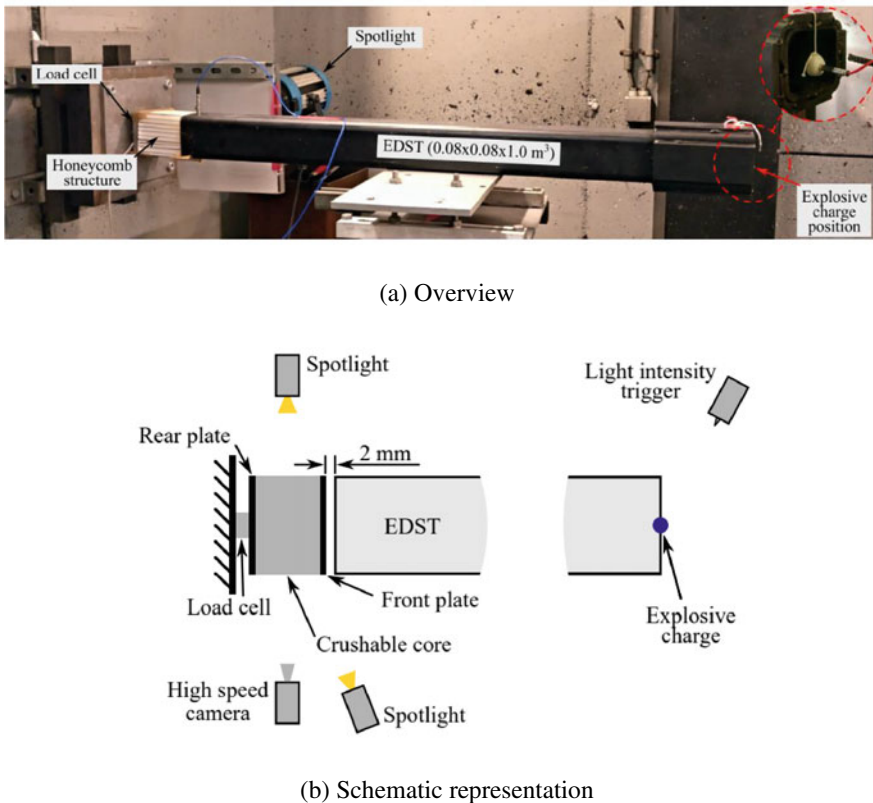


Fig. 9.13 Experimental set-up (Rebelo [21])

Table 9.5 Specification of the PCB transducers

Transducer	Sensitivity	Measurement range	Preload	Stiffness
PCB 203B	56.2 mV/kN	88.96 kN	17.793 kN	4.0 kN/ μm
Transducer	Sensitivity	Measurement range	Max. pressure	Rise time
PCB 102B	0.15 mV/kPa	34,500 kPa	103,000 kPa	$\leq 1 \mu\text{s}$

was positioned behind the set-up and pointed at the high-speed camera to obtain a more homogeneous background. Figure 9.15 shows the two-dimensional projection of the sacrificial cladding solution recorded by the high-speed camera. As illustrated in the referred figure, three different measurements (C_1 , C_2 and C_3) were performed to compute an average imaging magnification of 0.19 mm/pixel. Next, the position of two given points of coordinates X_1 and X_2 were recorded at each frame. Subsequently, the average displacement of the front plate may be determined by means of the difference between the initial and corresponding X coordinate. During the post-processing phase, the image magnification is used to convert the displacement

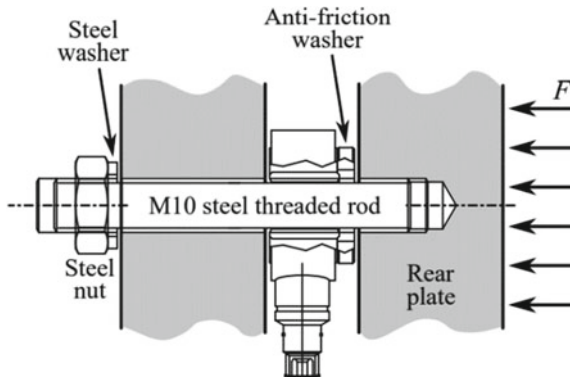


Fig. 9.14 Schematic representation of the PCB 203B load cell installation

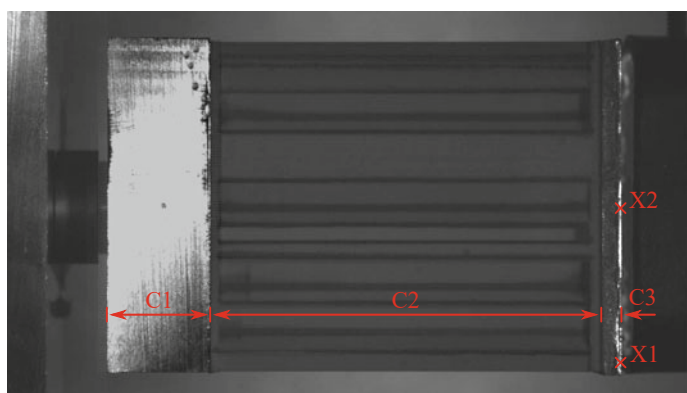


Fig. 9.15 Two-dimensional projection of SC solution on HSC

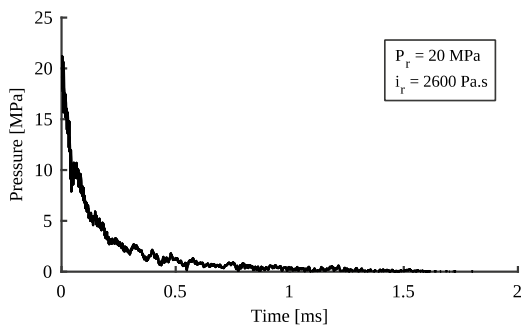
of the plate, while the frame rate enables the conversion of the frame numbers into a time scale. Lastly, the velocity of the front plate was approximated using a typical central difference scheme.

9.4.2 Experimental Results

The average reflected pressure signal from the PCB 102B pressure sensor, attained when a mass of 10 g of C4 is detonated at the entrance of the EDST, as represented in Fig. 9.16.

Figure 9.17 illustrates a side view of the damage evolution in the analysed PLA crushable cores' exterior during blast loading. Each set of images represents frame stops recorded with the HSC at significant time moments. As depicted in the referred

Fig. 9.16 Average reflected overpressure (10 g of C4 at the entrance of EDST)



figure, the fracture pattern is initiated by the crushing of the layers near the top and bottom solid plates, while maintaining relatively intact cells on the lateral surfaces.

Observing the frames in Fig. 9.17, one can see that, the 5 and 7.5% sacrificial cladding solutions are not able to dissipate the explosion kinetic energy, and their localised deformations develop, culminating with the general collapse of the samples. On the other hand, the evolution of the crushing mechanism for the 10% solution, despite growing with strain, led to a final pattern with a large intact zone in the core

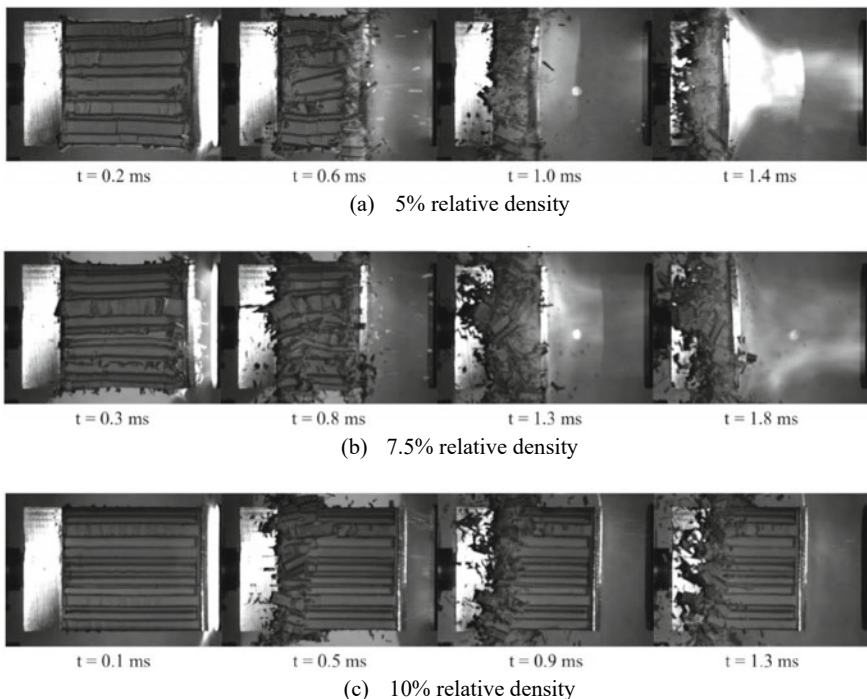


Fig. 9.17 Side view of the sacrificial cladding solutions under dynamic compression

of the sample. This undeformed area confirms that this solution can withstand the blast induced kinetic energy.

The measurements recorded by the force and pressure transducers during the experimental campaign are depicted in Fig. 9.18. The experimental displacement and velocity time histories of the front plate (obtained by digital processing of the images recorded by the HSC) are presented in Figs. 9.19 and 9.20.

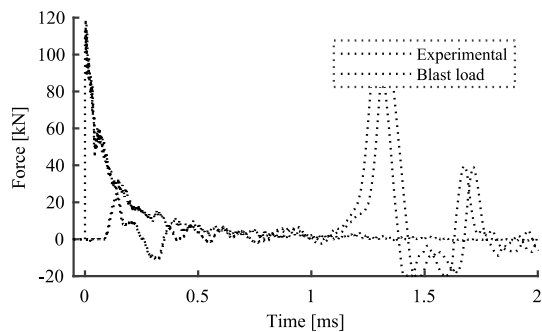
9.5 Conclusions

In this chapter, two highly effective Blast retrofit approaches were testing approaches were presented and each one of them brings different challenges.

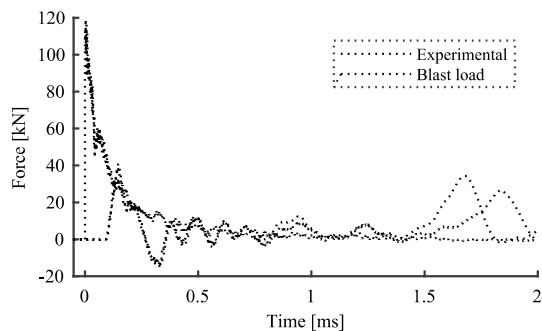
Full scale testing in close range is highly destructive and disruptive for the monitoring system, also inducing a considerable noise in the collected data. In that sense it is recommended to use extra gages to assure that usable data is collected. Furthermore, real scale testing poses all problems of real life such as errors in manufacture of the samples, errors in assembly and mounting, influence of the topography in blast wave propagation, difficulty of using Imagery (High Speed Cameras) for measurements due to the saturation effect of the fireball on the camera sensor. However, cameras are highly useful to record blast wave propagation, which cannot be assumed as planar at short range.

Explosive driven shock tube testing presents some advantages in terms controlling the blast testing parameters. Shock tube can be designed to have the right length to assure the blast wave is planar. Small scale turns also easier to control the manufacture and mounting of the testing samples. Considering that small amount of explosive is used, the fireball does not preclude the use of high-speed cameras for the purpose of record and measuring displacements/crushing. The problem in this type of testing is the difficulty to extrapolate the results to real scale. Scaling in blast testing is a big challenge and frequently leads to wrong conclusions. Therefore, small scale testing is highly effective to characterize materials or structures under high strain rates, allowing also calibrating numerical models, but do not replace full scale testing when evaluating the performance of complete systems.

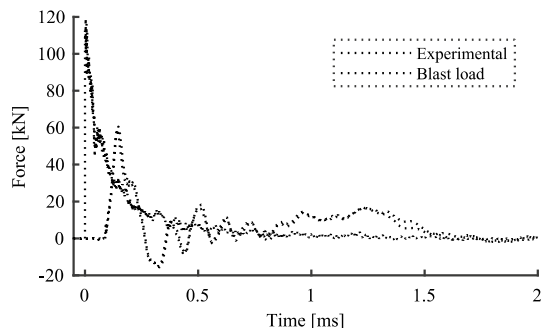
Fig. 9.18 Force-time history dependence on the relative density



(a) 5% relative density



(b) 7.5% relative density



(c) 10% relative density

Fig. 9.19 Displacement time history dependence on the relative density

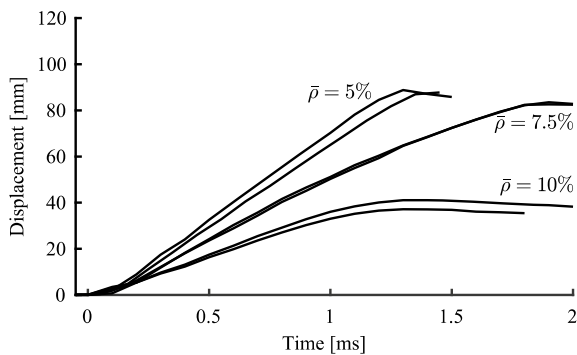
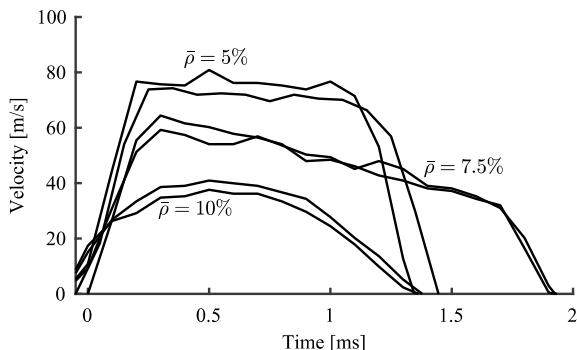


Fig. 9.20 Velocity time history dependence on the relative density



Acknowledgements The information presented in this work is based on and derived from the work and results obtained during the development of the research projects SI4E—Security and Integrity of Strategic Buildings under Accidental or Intentional Explosions funded by Portuguese Army, PRINSEF—Protection of Infrastructures and Physical Security funded by Portuguese Military War College, BLADE—Blast Walls Performance Optimization Design funded by NATO C-IED COE under IED Threat Mitigation Activities, and PROTEDES—Strategic Building Protection Against Explosions funded by the Portuguese funding institution FCT—Fundação para a Ciência e Tecnologia, through Grant SFRH/BD/115599/2016.

References

1. DoD (2014) Structures to resist the effects of accidental explosions. UFC 3-340-02
2. USACE (2008) Single degree of freedom response limits for antiterrorism design, PDC-TR 06-08. Protective Design center, Omaha, Nebraska
3. ASCE, ASCE-SEI 59-11 (2011) Blast protection of buildings
4. Bazan M, Oswald C (2010) Blast design of reinforced concrete and masonry components retrofitted with FRP. San Antonio, TX 78229
5. Cormie D, Mays G, Smith P (2019) Blast effects on buildings, 3rd edn. Thomas Telford, London
6. Gomes G (2016) Reutilização de edifícios para fins operacionais-BlastAssessment. Instituto Universitário Militar, Lisboa. (in Portuguese)

7. Baker W, Cox P, Westine P, Kulesz J, Strehlow R (1983) Explosion hazard and evaluation. Elsevier Science B.V, Netherlands
8. Barros D (1984) Explosivos, artifícios e agressivos químicos. Academia Militar, Lisboa. (in Portuguese)
9. UK MoD, Military Engineering (2008) Force protection engineering, part 2-structures and security systems, vol IX. UK Ministry of Defense
10. Lavarnway D (2013) Evaluating the use of ductile envelope connectors for improved blast protection of buildings. MSc thesis, Case Western Reserve University
11. Wang Y, Liew JYR, Lee SC, Zhai X, Wang W (2017) Crushing of a novel energy absorption connector with curved plate and aluminum foam as energy absorber. *Thin-Walled Struct* 111:145–154
12. Whitney MG (1996) Blast damage mitigation using reinforced concrete panels and energy absorbing connectors. In: Proceedings of the twenty-seventh DoD explosives safety seminar. Las Vegas
13. Pereira V (2017) Sistema Inovador de Protecção de Edifícios face a Explosões, composto por Painéis de Fachada em Betão Armado e Conectores em Aço de Parede Fina com Capacidade de Absorção de Energia. MSc thesis, Universidade de Lisboa. (in Portuguese)
14. Reddy T (1992) Guist and marble revisited—on the natural knuckle radius in tube inversion. *Int J Mech Sci* 34:761–768
15. Guist LR, Marble DP (1966) Prediction of the inversion load of a circular tube. NASA, Tech Note D-3622
16. Baroutaji A, Gilchrist M, Olabi AG (2016) Quasi-static, impact and energy absorption of internally nested tubes subjected to lateral loading. *Thin-Walled Struct* 98:337–350
17. Alghamdi A (2001) Collapsible impact energy absorbers: an overview. *Thin-Walled Struct* 39:189–213
18. Baroutaji A, Sajjia M, Olabi AG (2017) On the crashworthiness performance of thin-walled energy absorbers: recent advances and future developments. *Thin-Walled Struct* 118:137–163
19. Ousji H, Belkassem B, Louar MA, Kakogiannis D, Reymen B, Pyl L, Vantomme J (2016) Parametric study of an explosive-driven shock tube as blast loading tool. *Exp Tech* 40(4):1307–1325
20. Ousji H, Belkassem B, Louar MA, Reymen B, Martino J, Lecompte D, Pyl L, Vantomme J (2017) Air-blast response of sacrificial cladding using low density foams: experimental and analytical approach. *Int J Mech Sci* 128–129:459–474
21. Rebelo HB, Lecompte D, Cismasiu C, Jonet A, Belkassem B, Maazoun A (2019) Experimental and numerical investigation on 3D printed PLA sacrificial honeycomb cladding. *Int J Impact Eng* 131:162–173

Chapter 10

Load Tests on Bridges



Mário Pimentel , Joaquim Figueiras , Carlos Félix , Filipe Cavadas , Emanuel Tomé , Carlos Rodrigues , and Bruno Costa

Abstract This chapter presents an overview on the state-of-the-art procedures for load tests on bridges and on the applicable sensing and data acquisition technologies. Best practices for the planning, preparation and execution of load tests are presented. The discussion is supported by practical applications in which the authors have been involved during the last 20 years. Selected case studies are used to illustrate the role of load tests during commissioning of new bridges, during rehabilitation works and as part of the assessment of existing bridges.

Keywords Bridges · Load tests · Case studies · Structural response · Monitoring

10.1 Introduction

Load tests on bridges constitute a practice as old as building bridges. Historically, load tests were a means to prove the capacity of structures, which until the seventeenth century were built mostly on an empirical basis according to the experience of the builder. With the development of statics and mechanics of materials supporting the understanding of the structural behavior, load testing evolved to produce quantitative information and providing data to verify analytical models. A review on the history of load testing of bridges can be found in [1].

M. Pimentel () · J. Figueiras · F. Cavadas · E. Tomé · C. Rodrigues · B. Costa
Faculty of Engineering, University of Porto, CONSTRUCT-LABEST, Porto, Portugal
e-mail: mjsp@fe.up.pt

J. Figueiras
e-mail: jafig@fe.up.pt

F. Cavadas
e-mail: fcavadas@fe.up.pt

E. Tomé
e-mail: emanuel.tome@fe.up.pt

C. Félix
School of Engineering, Polytechnic of Porto, CONSTRUCT-LABEST, Porto, Portugal
e-mail: csf@isep.ipp.pt

Today two main types of load tests are generally considered: diagnostic (or supplementary) load tests and proof (or proving) load tests. Albeit the numerous guidelines that exist in many countries regulating or providing recommendations for the involved procedures, this is an activity that is difficult to standardize in virtue of the multiplicity of bridge types and circumstances where load testing may be performed. For an overview of the load testing practices and regulations, the reader is referred to [2].

10.2 Types of Load Tests

10.2.1 Diagnostic Load Tests

This type of test is used to supplement theoretical calculations, to validate modelling assumptions and/or to calibrate analysis models in cases where there may be uncertainties about the bridge behavior, a process commonly referred to as “structural identification”. In some references, this type of test is also designated as “supplementary load test” [3, 4].

The test loads are most often achieved using vehicles with controlled weight, or using some kind of ballast load, such as water containers. The latter is more common in footbridges. The upper limit of the load effects must be controlled so that no permanent damage is added to the bridge, the response is kept in the elastic range and the risk of sudden failure is kept negligible. The lower limit must be defined considering the precision of the sensors adopted to measure the relevant structure response variables, such as displacements, rotations or strains. In general, these constraints lead to test load effects in the range of 40–80% of the characteristic value of the live load effect, depending on the structural type, details and constituent materials.

Diagnostic load tests can be performed in the context of assessment of existing bridges, commissioning of new bridges, before and/or after rehabilitation interventions, or even periodically.

Assessment of existing bridges. In the context of bridge safety assessment, diagnostic load tests are a means to determine specific response characteristics of the bridge [5], as per example, the load distribution on multi-beam decks, the load bearing contribution of secondary elements, degree of composite action, identification of arching effects in deck slabs or of partial fixity at the supports [4].

The structural safety evaluation benefits from the use of an updated model supported by a load test, which generally allows less conservative estimates of the load effects. For instance, in the specific context of the fatigue safety assessments, it is shown that small reductions in the stress amplitude spectra can lead to quite significant extensions of the remaining fatigue life [6–8]. Also, detrimental effects can be identified and appropriate actions to fix them can be decided upon interpretation of the test results.

As the safety assessment may involve the extrapolation of the behavior of the bridge from the test load level to the design load level, engineering judgment is required to decide whether some of the beneficial effects evidenced during the test can be relied on. Typical examples of this are the contribution to increase the global stiffness and to the reduction of the load effects in the main load bearing elements of partial end restraint provided by roller supports blocked by corrosion or debris, or of non-load bearing elements, such as kerbs or deck surfacing layers. This process greatly relies on the structural identification procedure to interpret the observed behavior during the test, allowing the identification of the causes for the differences between the measurements and the theoretical estimates. Examples of diagnostic tests performed in the context of the assessment of existing bridges can be found in Refs. [4, 9].

Commissioning of newly constructed bridges. Diagnostic load tests are also valuable just prior to opening of a newly constructed bridge, especially in the case of uncommon bridge types, bridges involving new materials or construction details, or landmark bridges. The objective is to show that the design and construction have been carried out in a satisfactory manner and to acquire reference measurements of the structural behavior. The definition of the test loads follows the principles mentioned above. A notable example of such a diagnostic test is presented in Sect. 10.4.1.

Rehabilitation of existing bridges. In the context of bridge rehabilitation, diagnostic load tests can be used both before and after the rehabilitation. Before the rehabilitation the tests provide the data for the structural identification procedure, allowing the rehabilitation design to be founded on reliable structural models of the bridge. After the rehabilitation, diagnostic load testing can be used to assess the impact of the rehabilitation measures. The definition of the test loads follows the same principles defined above. A remarkable example of this type of test is given in Sect. 10.4.2, other cases are documented in the Refs. [10, 11].

Periodic tests. Periodic diagnostic tests can also be performed in cases where it is of interest to evaluate the evolution over time of the structure response to known loads. This occurs for instance in bridges where damages have been detected and whose impact on the structural safety is unclear. The periodic measurement of the structural response makes it possible to confirm whether or not the damage is progressing and if the structural response is changing. In order to relieve the test logistics and the traffic interruption periods, loading can consist of vehicles with known weight and geometry passing the bridge at controlled speed. A noteworthy example of this type of diagnostic test is presented in Sect. 10.4.3.

10.2.2 *Proof Load Tests*

Proof (or proving) load tests are used to provide a more realistic evaluation of the load-carrying capacity of a bridge than that obtained from a theoretical analysis, especially

in cases where the uncertainties are outsized. This occurs when there are no structural plans to develop the structural models, or whenever the calculation methods are too inaccurate to substantiate the safety assessment. Contrary to diagnostic tests, proof load tests are not conveniently regulated in current standards.

As the goal of the proof load test is to derive directly a safe load carrying capacity without further theoretical analysis, the definition of target proof load is determinant. The involved load levels are much higher than in the diagnostic tests and the related effects should be equal to the factored allowable live load effect. Guidelines on the definition of the proof loads and subsequent load rating are given in [1, 3, 12]. During the test, the load is incremented and the response measured until the stop criteria are met. The loading can be applied by means of special vehicles [13], hydraulic jacks [14] or even prestressing tendons anchored to the ground.

As recommended in Ref. [3], bridges that have been subjected to proof load tests should be inspected periodically after the test because any structural damage incurred during proof load tests can initially be concealed. Careful test planning including risk management provisions is required due to the involved loading levels.

10.3 Planning Load Tests

10.3.1 General

The purpose of this section is to provide guidance on how to perform a load test and to highlight the main aspects to obtain reliable and useful data. One of the aspects that must be taken into account is the effect of temperature variations on the results obtained, which may mask the structural responses that must be identified. Whenever possible, the load test should be carried out when the temperatures on the bridge are closer to a uniform distribution and the variation of the ambient temperature is slower, avoiding, as much as possible, periods of greater insolation.

In order to streamline the bridge loading process, the load vehicles should take, in sequence, the desired static loading positions. In each loading position, vehicles must stop for the shortest possible period, otherwise the test will be very long, allowing the acquisition of the necessary data.

Designing experimental influence lines is relevant to assess in more detail the structural behavior of the bridge. This can be done by using one or more vehicles, side by side, in line or in pairs, crossing the bridge deck at constant speed. It is important that the relative position between vehicles is respected. The record of the bridge behavior during the sudden braking of the trucks, crossing the bridge deck at high speed, can provide information regarding the behavior of the bearings and about restraints to horizontal displacements.

To establish a reference state for the bridge and remove the effect of temperature from the data, measurement periods should be foreseen for the unloaded bridge during which all the measurement systems must remain in operation. Such measurements

should be made at the beginning and at the end of the load test and whenever it is considered appropriate during the test.

10.3.2 Load Test Plan

Before performing a load test on a bridge, it is essential to prepare in advance a detailed work plan to be carried out on site. The plan must be approved by the designer/consultant, the owner and have the contribution of the contractor (if any). A comprehensive test plan should address at least, but not exclusively, the following topics:

Main goals of the load test. The objectives of the test should be stated in accordance with the goals of the designer/consultant or the owner and take into attention the type of structure and its condition. An estimate of the expected results is necessary to design the measurement system and the loading characteristics.

Specification of the measuring system. All the equipment to be used during the load test should be specified, including the parameters to be measured, type of transducers and its location, full range and accuracy of sensors, and data acquisition. Complementary instrumentation available, e.g., permanent monitoring system of the bridge (if any) should be included, identifying the sensors to be used and the procedure to synchronize both permanent and temporary data acquisition systems.

Loading characterization. The load to be applied during the test must be fully characterized. When vehicles are used, this characterization should include their number, type and weight, as well as their arrangement on the bridge deck. Drawings defining the direction of driving and stop position of the vehicles should be provided.

Work plan for the load test. A schedule of the test plan must be available on site, defining the sequence of the load cases, the stop periods of the vehicles on the bridge deck, the loading procedures to record the influence lines, among others. Furthermore, it should include tables, previously prepared to be filled on site, where information of each vehicle should be written (e.g. registration plate, axle loads and total weight), as well as the sequence of all activities performed during the load test (e.g. the start and end time of each loading position or of each influence line).

Complementary observations. Complementary observations should be foreseen such as topographic measurements or visual inspection of the structure, before and after the test. The survey to be carried out using topographic methods should be specified, including the positioning of the topographic targets, the time required to obtain accurate measurements, load cases under observation, among others.

10.3.3 Monitoring System

The monitoring of the structural response during a load test requires the design and installation of a temporary measurement system taking into account the objectives of the load test and the specific requirements defined in the test plan. If the bridge already has its own permanent monitoring system, all sensors of this system, suitable for characterizing the structural behavior, must be in operation, together with the temporary measurement system.

The structural parameters to be observed should characterize the overall bridge behavior, namely span deflections, horizontal bearing displacements, and deck and pier rotations. Local parameters such as deformations, curvatures and crack-openings, among others, must be selected whenever relevant. In addition, measuring the ambient and the bridge temperature is essential since the structure and the monitoring system are both sensitive to thermal variations. Figure 10.1 illustrates some transducers, signal acquisition systems and marks installed on site for a load test.

The measurement of all quantities must be automatic, simultaneous and synchronized. In large bridges, the data acquisition units are usually distributed in local stations, reducing the length of the cables that connect to the transducers, simplifying the installation, while avoiding exposure to noise and reducing possible signal losses. However, for operational reasons, it is convenient to centralize the measurement system, that is, to receive all data in real-time on the same PC. It must also be possible, from this PC, to remotely control the different data acquisition units.

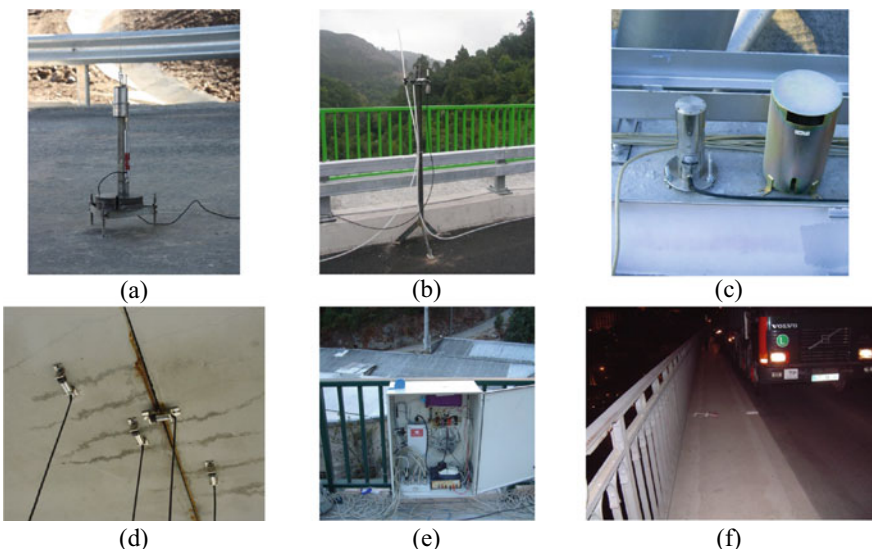


Fig. 10.1 Equipment on site during a load test to measure: **a** deflections with a LVDT, **b** deflections using a hydrostatic leveling system, **c** rotations, **d** crack openings, **e** signal acquisition, and **f** stop position of a vehicle on the deck

The acquisition units can be programmed to operate at a low scan rate when static load positions are tested and turned to high scan rate when the drawing of vehicle influence lines is concerned. Higher scan rates make data processing more time consuming without adding relevant information. Acquisitions with very low scan rates delay testing or limit relevant information.

The accuracy of the measurement system must be compatible with the magnitude of the values to be observed. It is common to use acquisition units of 16-bit or higher analogue-to-digital converters, transducers with a full-scale adjusted to the expected values to be measured and grounded power supplies, reducing the electrical noise. In situations where the electrical noise cannot be reduced to acceptable levels, as it happens sometimes with steel bridges, the fiber optic sensors have undeniable advantages.

To avoid loss of information during the load test, it is essential to establish procedures to protect the collected data. Examples of these good practices are the installation of UPS connected to the central station and at each local station, visualization on real time of the graphical outputs and regular backup of the data during the test.

10.3.4 Report of the Results

The load test report must contain all the relevant information, such the location of all used transducers and its specifications, the load characterization, the test sequence and the results obtained, in graph and table format. The temperature effects on the results should be identified and, if possible, removed from the data.

10.4 Examples

10.4.1 Corgo Bridge

Description of the bridge. The Corgo Bridge (Fig. 10.2) is a prestressed concrete box-girder bridge with a total length of 2790 m, divided into three continuous structures. The Central Sub-Viaduct is a cable-stayed bridge with a 300 m long central span (see Fig. 10.3) and a central suspension system composed of four symmetric semi-fans of 22 stay cables each. The deck holds two carriageways with two traffic lanes each and is constituted by a 28 m wide box-girder. The pylons have a total height of about 193 m and are monolithically connected to the deck. The piers have an octagonal-shaped box cross-section, supporting the deck through pot bearings.

Objectives of the load test. This constitutes an example of a diagnostic load test performed as part of the commissioning of a newly constructed bridge. The main objectives of the load test were essentially the evaluation of the conformity of the built structure with the design assumptions and the establishment of the reference



Fig. 10.2 General view of the Corgo Bridge

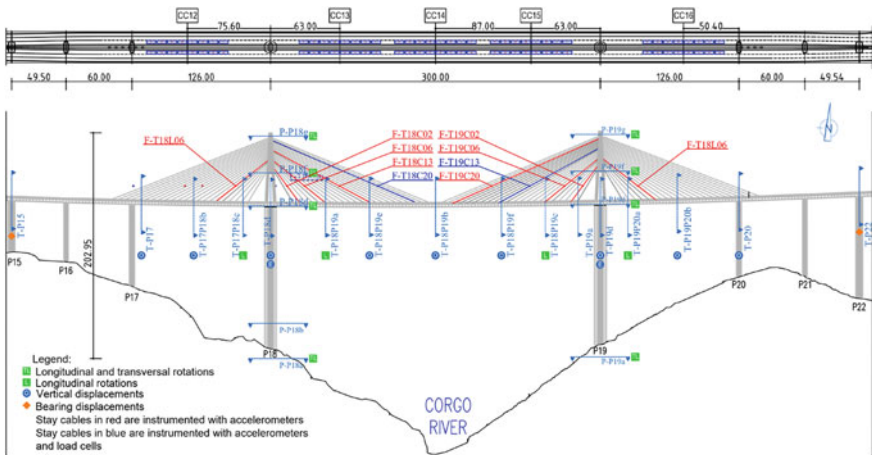


Fig. 10.3 Side elevation of the Central Sub-Viaduct with the location of the monitored sections and with the definition of load cases LC12 to LC16

state of the structural condition by measuring the structural response of the under controlled loads. The test served also to assess the performance of the Structural Health Monitoring (SHM) system installed on the bridge.

Monitoring system. An extensive structural monitoring system was installed in the Corgo Bridge to support the construction phase and follow the service life, with a particular focus on the Central Sub-Viaduct. The schematic layout of the structural monitoring system is shown in Fig. 10.3. The system contemplates the measurement of longitudinal bearing displacements, vertical deflections of the deck (using a hydrostatic levelling system with pressure sensors based on fibre optical technology [15]), rotations, cable forces (2 cables equipped with load cells and 10 with accelerometers), average concrete strains, strains in the steel diagonals, ambient and concrete temperatures, durability indicators (corrosion potential, galvanic current and relative humidity). In the load test, the focus was placed on the longitudinal displacements, vertical deflections, rotations and cable forces. Topographic measurements of the pylons and of the box girder displacements were also performed.



Fig. 10.4 Position of the vehicles during the test: **a** load case LC14 using 16 vehicles; **b** 4 vehicles side-by-side crossing the bridge to obtain the influence lines

Load test plan. The bridge load test comprised several load cases and load levels in order to assess the linearity and repeatability of the structural response of the bridge. Eighteen static load cases involving maximum of sixteen trucks and three crossings of two and four trucks at crawling speed to trace the experimental influence lines were performed (see Fig. 10.4). The load cases comprise both symmetric and eccentric vehicle positioning in the transversal direction of the deck. The vehicles had an average mass of approximately 30 tons distributed by three axles and an averaged total length of 8.5 m.

Results. As discussed in Sect. 10.2.1, in a diagnostic load test a behavioral model of the bridge is necessary to support the critical interpretation and evaluation of the obtained experimental results. In the case of the Corgo Bridge, a dedicated finite element model was adopted [16] and is being used to follow the structural behavior since the construction phase. The calculated and measured girder deflections obtained for load cases LC13 to LC15 are depicted in Fig. 10.5, where the continuous lines are calculated deformed shapes, and the dots represent the measurements at the corresponding locations. Overall, a good agreement between measured and calculated values is observed. A maximum downward deflection of about 128 mm was obtained at the middle of the main span for load case LC14. The influence lines presented in Fig. 10.6 allow the detection of a stiffer behavior of the deck near the pylon P18 compared to that observed near pylon P19. This can be justified by the fact that two different concrete plants and working teams were used during the construction, one on each side of the valley.

Regarding the cable forces, the results obtained for the stay-cables T18C20 and T19C13 (represented in blue in Fig. 10.3) are shown in Fig. 10.7. The continuous lines represent the forces calculated in the stay-cables considering the sixteen trucks moving over the bridge. The dots correspond to the measured values in the static load cases LC12 to LC16, both using accelerometers and load cells.

The analysis of the movements of the pylons made it possible to detect that, contrary to the design assumption, the pot-bearings over the piers P15 P16, P21 and

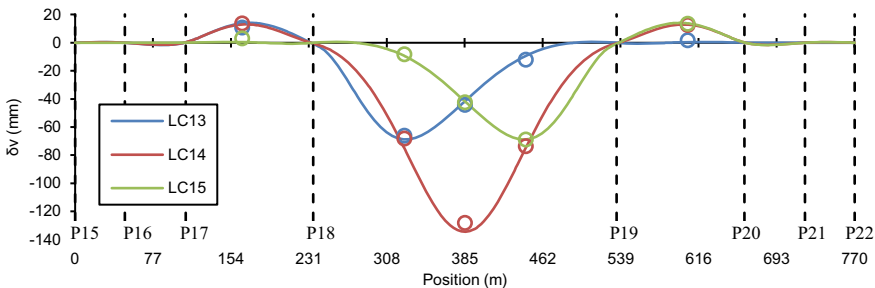


Fig. 10.5 Calculated (lines) versus measured (dots) vertical displacements of the girder for load cases LC13 to LC15

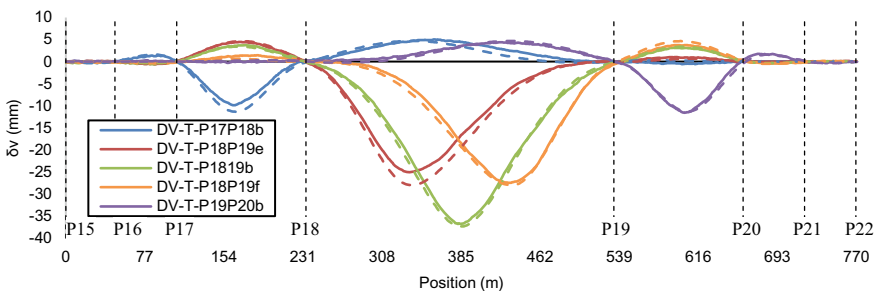


Fig. 10.6 Calculated (dashed lines) versus measured (continuous lines) influence lines of the vertical displacements. The influence lines refer to two pairs of 30 tons trucks crossing the bridge side by side (see Fig. 10.4b)

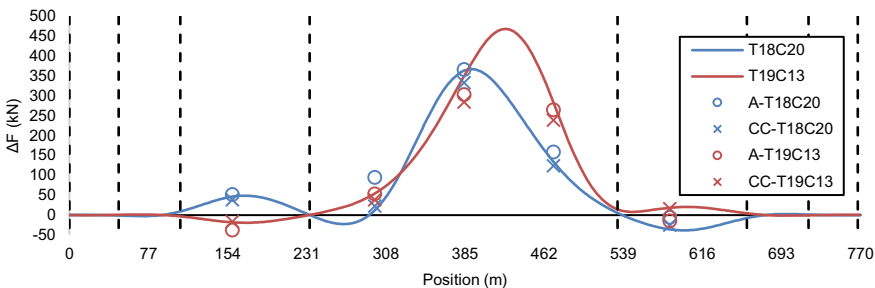


Fig. 10.7 Calculated (lines) versus experimental (dots and crosses) cable forces variations for stay-cables T18C20 and T19C13

P22 were blocked in the longitudinal direction. This was corrected by the contractor before opening the bridge. As shown in Fig. 10.8, in the load cases with a non-symmetrical layout (LC13 and 15) the calculated displacements and rotations of the pylons can only fit the measured values if the relative longitudinal displacements of the deck with respect to the piers are blocked. It should be stressed that the restraint

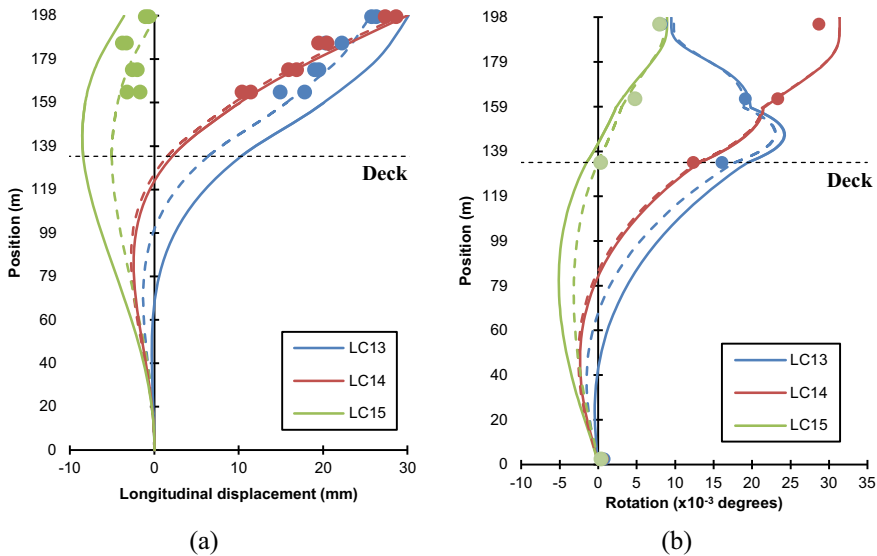


Fig. 10.8 Calculated (lines—free supports; dashed lines—blocked supports) versus measured (dots) **a** lengthwise horizontal displacements and **b** rotations for pylon P18: load cases LC13 to LC15

to the relative longitudinal displacements of the bearings has negligible impact on the displacements and rotations of the girder and in the cable forces, and could have never been detected from the analysis of the vertical deflections of the deck.

Concluding remarks. The importance of diagnostic load testing to evaluate the conformity of the constructed structure with the design assumptions was demonstrated in this case study.

10.4.2 Luiz I Bridge

Description of the bridge. The Luiz I Bridge, opened to traffic in 1886, constitutes a unique example of bridge engineering. Designed by Théophile Seyrig, a former partner of Gustave Eiffel, this metallic bridge consists in a double-hinged arch supporting two decks at different levels, crossing the Douro river in the North of Portugal, between the cities of Porto and Vila Nova de Gaia (Fig. 10.9).

The arch is a 3D truss and exhibits a parabolic geometry in elevation, with a height of 45.1 m and a span of 172 m, being the longest of its type in the world at the time of its construction. The upper deck consists of two 391.25 m-long and 5 m-high truss girders, comprising 13 spans with lengths varying from 11.8 to 50.7 m. It rests over two masonry piers, three metallic towers, two steel posts supported on the arch, and the two end masonry abutments. Structurally the upper deck is integrated with the



Fig. 10.9 Luiz I Bridge: view from the downstream side, with Porto on the left

arch and fixed at the arch crown. The lower deck is constituted by two 3.25 m-high truss girders, with a total length of 174 m, comprising five spans, supported by the masonry abutments and by four steel tie-trusses suspended from the arch. In general, the original bars have “I”, “T” or “box” shaped sections built by assembling plates and angles through riveted connections.

Throughout its life—of more than one century—the bridge was subject not only to minor maintenance and conservation works but also to some functional adaptations. At the beginning of the twenty-first century, the bridge was subjected to a major strengthening and rehabilitation process, in order to allow the integration of the upper deck in the light rail network of Metro of Porto. One of the major operations was the enlargement of the existing upper-deck, from 8.23 to 10.17 m and the replacement of its floor system. The old lightweight concrete pavement was replaced by a metallic grid topped by a cladding steel plate, allowing not only the new railway traffic loads, but also the passage of pedestrians and emergency road vehicles (Figs. 10.10 and 10.11). In addition, critical bars of the upper-deck girders, the arch and the suspension ties, as well as the bracing elements all over the bridge were strengthened.

Objectives of the load tests. Within the scope of this major rehabilitation and strengthening of the bridge, two load tests were carried out: one before (Test 1) and another after (Test 2) the rehabilitation works.

The main objectives of the Test 1 were to: (i) study the mechanics of the bridge behavior, providing an improved insight of the strain/stress distribution among the structural elements; and (ii) provide data for the structural identification procedure, that is, for the development of an accurate numerical model for the analysis of different rehabilitation and strengthening alternatives.

On the other hand, the main objectives of the Test 2 were: (i) the comparison of the bridge response between the two structural conditions, which enabled the assessment of the changes observed in the structural behavior; (ii) to appraise the strengthening solutions and to assess the in-service behavior of the bridge; and (iii) to provide a thorough characterization of the new condition of the bridge in order to establish a baseline for future assessments.

In order to allow a straight comparison of the bridge response between the two conditions, identical location of the instrumented points, as well as a suitable replication of the loading scenarios, were followed in both tests.

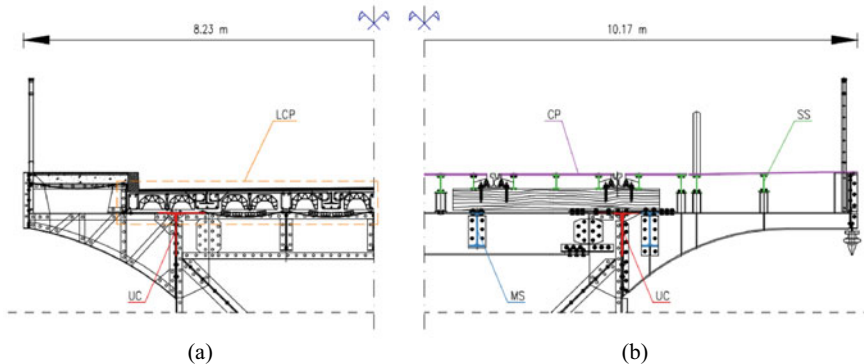


Fig. 10.10 Luiz I Bridge. Cross-sections of the upper-deck floor system: **a** lightweight concrete pavement (LCP) prior to the rehabilitation; **b** steel grid after the rehabilitation, with main stringers (MS) withstanding both the railway traffic loads transferred by the sleepers, and the pedestrians and road emergency vehicles loads supported by the secondary stringers (SS) topped by a cladding plate (CP). After the rehabilitation, the loads are transferred to the nodes of the existing upper-deck upper-chords (UC), through the new crossbeams and cantilevers



Fig. 10.11 Luiz I Bridge. Replacement of the upper-deck floor system **a** removal of the lightweight concrete pavement; and **b** installation of the new floor system

Monitoring systems. The quantities measured in both load tests consisted of vertical displacements (VD) at mid-span of four upper-deck spans and at the arch crown, and of strains in 12 bars cross-sections, namely in the arch chords (4), diagonals (2) and verticals (1), and in the upper-deck chords (3) and diagonals (2) (Fig. 10.12). Although the load tests were performed during the night with the goal of minimizing the effect of the temperature variations in the sensors and in the structural response, the ambient temperature was also recorded.

A temporary hydrostatic leveling system, equipped with electric-based pressure sensors, was installed in the bridge to measure the vertical displacements [17] in both load tests.

The measurement of strains was performed with electric-based foil strain gauges in Test 1 [17]. In Test 2, the strains were collected by FBG sensors, taking advantage of the comprehensive permanent monitoring system installed in the bridge for continuous surveillance of the structural condition after this major intervention [18].

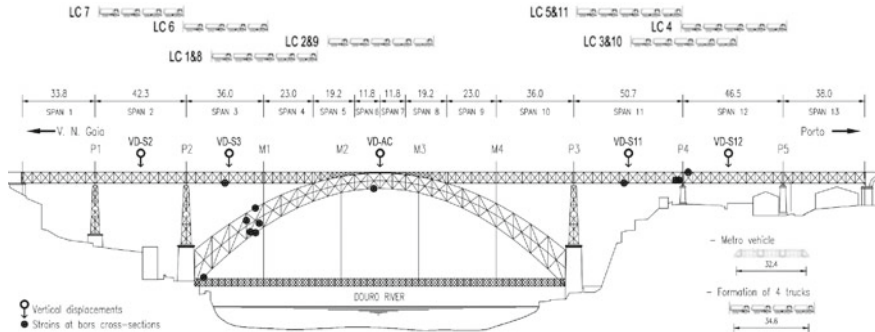


Fig. 10.12 Luiz I Bridge. Measurement system for the two load tests: location and identification of the quantities measured in the load tests. Static load cases

This monitoring system is based on fiber-optic technology, avoiding the drawbacks of electric-based systems installed in steel bridges serving electrified vehicles and significantly simplifying the cable routing in such a large bridge by taking advantage of the multiplexing ability of fiber-optic sensing. This monitoring system, entirely running in Test 2, comprises steel and ambient temperature sensors at 10 points, horizontal displacements transducers at eight points of the upper deck, and strain sensors distributed by pairs at 59 bars cross-sections.

Load tests planning. Before the rehabilitation, the upper-deck served for road crossings, and after the rehabilitation, although it is devoted for railway traffic, it also allows the passage of road vehicles. Therefore, the vehicles used on both tests were three- and four-axles single-unit dump trucks, with an average gross weight of approximately 130 kN, performing two types of loading scenarios on the bridge: static and quasi-static.

The static load cases aimed at maximizing the bridge response by placing the vehicles in critical positions on the bridge (Fig. 10.12), arranged in either a double formation, with the vehicles placed side-by-side centered in the deck (LC1 to LC7), or a single formation placed eccentrically over the deck (LC8 to LC11). The quasi-static load cases aimed at obtaining experimental influence-lines by measuring the response of the structure under a pair of vehicles crossing the bridge side-by-side, at a crawling speed of 5 km/h.

Taking into account the objectives of the tests, the loadings applied in both tests were kept below the legal maximum service loads. For the static load cases, the arrangement of a single formation of trucks leads to an approximate distributed load of 15 kN/m, which corresponds to 80% of the maximum load of a metro vehicle. For the quasi-static load cases, the total load of the rear tandem axles of the trucks was about 95 kN, which corresponds to 50% of the load of an intermediate bogie of a metro vehicle.

Results. A set of 3D finite element (FE) linear elastic models were developed to simulate the bridge condition before and after the rehabilitation assisting the interpretation

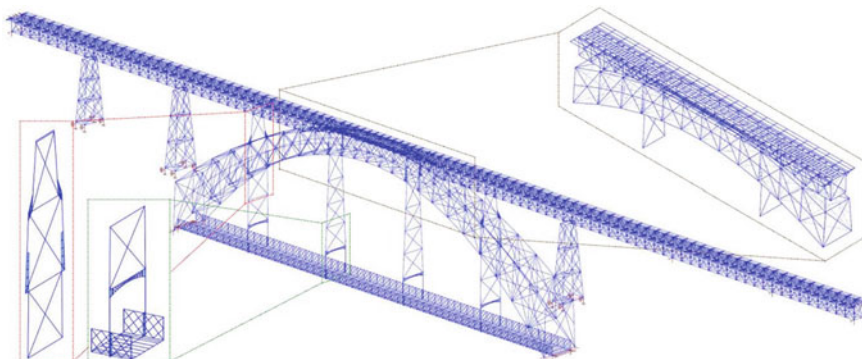


Fig. 10.13 Luiz I Bridge. FE model

of the test results. In particular, the effects of the stiffness of the lightweight concrete pavement (before) or the new deck floor system (after) on the structural behavior are discussed in this section (Fig. 10.13).

Figure 10.14 depicts the maximum values of the vertical displacements of the upper-deck and of the arch crown, recorded in the static load cases in both Test 1 and Test 2. With the goal of assessing the stiffness contribution of the lightweight concrete pavement (Test 1), and the secondary stringers and the cladding plate (Test 2) (see Fig. 10.10), the corresponding numerical estimates calculated from the FE models are depicted over the recorded values.

The experimental results show an average increase of approximately 17% on the deflection of the upper deck (excluding the arch crown), which indicates a corresponding reduction of the upper-deck bending stiffness, as a result of the replacement of the old lightweight concrete pavement by the new steel floor system. However,

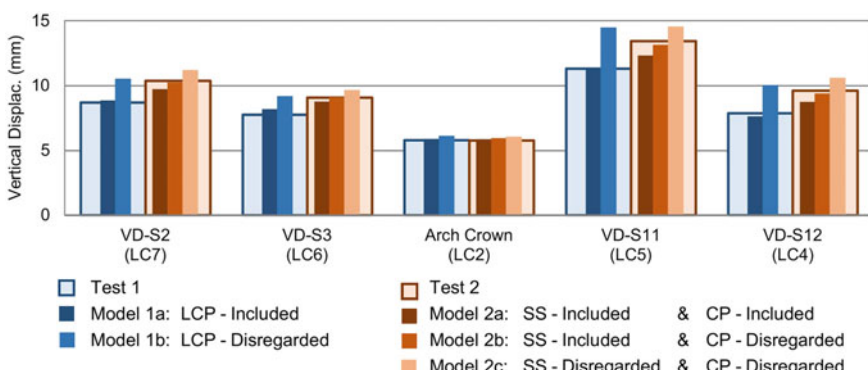


Fig. 10.14 Luiz I Bridge. Measured and estimated vertical displacements for the static loading scenarios conducted in the load tests

this effect on the vertical displacement of the arch crown is negligible, since it is essentially controlled by the arch stiffness.

The differences between the results estimated by Model 1a and 1b confirm the contribution of the lightweight concrete pavement (LCP) to the upper deck stiffness before the rehabilitation.

As for the condition of the structure after the rehabilitation, the numerical estimates clearly show the impact of considering either the cladding plates (CP) or the secondary stringers (SS) on the stiffness of the upper-deck. In addition, the scenario that best fits the experimental results is that simulated in Model 2b, in which the stiffness of the secondary stringers is considered, but not that of the cladding plates.

Figure 10.15 depicts the two strain experimental influence-lines obtained in both tests, for the slow crossing of two dump trucks side-by-side. The first refers to a cross-section of the upper-deck lower-chord, located at the mid-span of the 11th span. The results show that the deformation in the flange is similar in both tests. As, on the one hand, the lower-chords were not intervened, and, on the other, most of the load is transferred by the flange, the results show that the carried force is similar in both tests. The second refers to a cross-section of an upper-deck diagonal, located near pier P4. The results show a reduction in the deformation observed in the flange, which is explained by the strengthening of these bars (performed by attaching two angles to the web free end and two angles to the flange).

Concluding remarks. The Luiz I Bridge, an outstanding example of bridge engineering built in the nineteenth century, was subjected to a major rehabilitation process with the objective of integrating its upper-deck in the light rail network of Metro of Porto. In this context, two load tests were carried out: before and after the rehabilitation. The first test allowed to assess the actual behavior of the bridge, thereby enabling the development of accurate numerical models that supported the design of the rehabilitation solutions. The second test allowed the experimental assessment of the effects of the replacement of the floor system on the bridge behavior, and the evaluation of the effectiveness of the strengthening solutions.

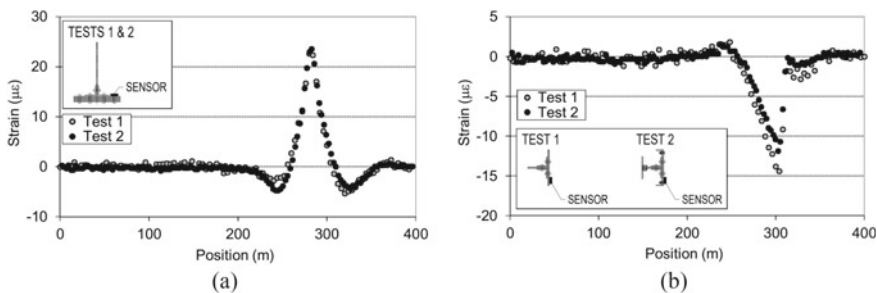


Fig. 10.15 Luiz I Bridge. Experimental steel strains influence-lines measured before (Test 1) and after (Test 2) the bridge rehabilitation at a cross-section of: **a** the upper-deck lower-chord, located at the mid-span of the 11th span; and **b** the upper-deck diagonal, located near pier P4

10.4.3 Foz Tua Bridge

Description of the bridge. The road bridge at the mouth of the Rio Tua serving the EN212 (Trás-os-Montes, Portugal), built in 1940, consists of an arch (78 m-span and 20 m-rise) with a solid rectangular cross-section of unreinforced concrete, and a deck composed of a slab and four reinforced concrete girders. The existence of cracks in certain sections of the arch, which can be associated to construction joints, and the exceptional heavy traffic on the bridge due to the construction works of the Foz Tua Hydroelectric Power plant, recommended a temporary monitoring campaign of the abnormal operational effects on the bridge (Fig. 10.16).

Objectives of the load test. The main objectives of the load test were:

- (i) The assessment of a reference state of the structure, in terms of its response to heavy traffic loads, obtained through strain influence lines in critical sections. Over time, particularly during the period in which the construction of the dam was taking place, these reference influence lines are compared, after normalization, with those obtained during the passage of vehicles of similar configuration. Changes in the condition of the structure, namely the occurrence of certain damages in the arch, would bring to detectable differences.
- (ii) The validation and the calibration of a bridge weigh-in-motion algorithm developed for identification and weighing of heavy trucks crossing the bridge. This system was integrated into an automatic event monitoring system with real-time information available on a web platform. This allows the infrastructure manager to have effective control over compliance with the limits imposed to the traffic loads.



Fig. 10.16 Foz Tua Bridge and the construction site of the Foz Tua Hydroelectric Plant (2012/16)

Monitoring system. The monitoring plan involved the installation of four long gauge strain transducers in each of the six critical sections of the arch for measuring the average deformation of the cracked concrete (Fig. 10.17). In addition, for the detection and weighing of vehicles, strain gauges were installed in the lower fiber of the girders (reinforced with steel plates), at the midspan section of the simply supported deck access span (Section D-T1). These strain gauges make it possible to identify the passage of heavy vehicles, assess their weight, and trigger the recording of the corresponding results.

Test plan. A load test was carried out using a representative vehicle, with known loads and wheelbases, and total weight of 421 kN. A total of six controlled passages were made, three in each direction, using the upstream, center and downstream side of the traffic lane (Fig. 10.18). The strains were measured with an acquisition rate of 50 Hz.

Results. Figure 10.19 shows the measured strains in the deck section (Fig. 10.19a) and in a representative cross-section of the arch (Fig. 10.19b), representing the passage of the vehicle in the center of the traffic lane during the load test. The records obtained during the load test exhibited repeatability in the multiple passages, making it possible to define a reliable reference response.

Regarding the bridge weigh in motion system, the load test results confirmed that the transversal vehicle position within the traffic lane had a significant impact

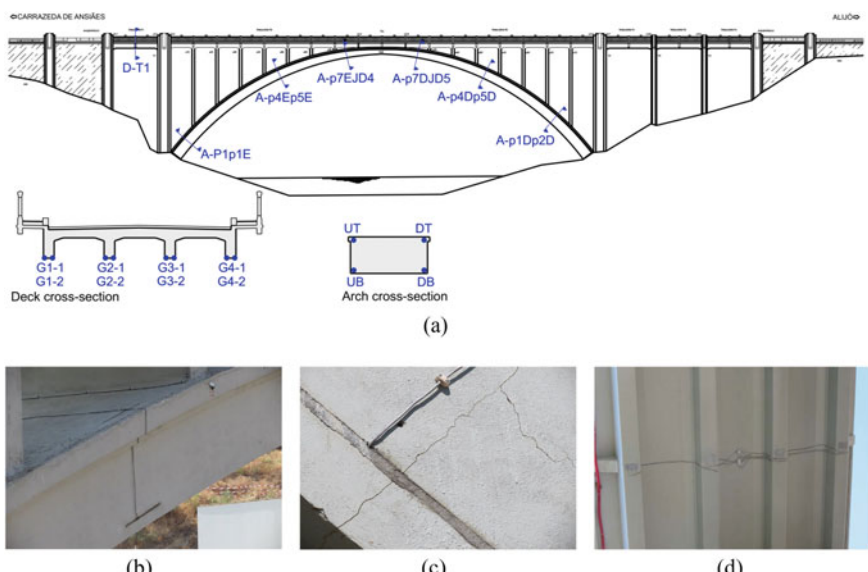


Fig. 10.17 Measurement system: **a** critical arch cross-sections instrumented with four strain transducers and deck cross-section with eight strain gauges for vehicle detection and weighting; **b** a pair of strain gauges embedded in the arch cross-section; **c** detail of a strain transducer intersecting a crack; **d** deck section with eight strain gauges



Fig. 10.18 Load test: **a** general view of vehicle crossing the bridge; **b** vehicle crossing at the downstream side of the traffic lane

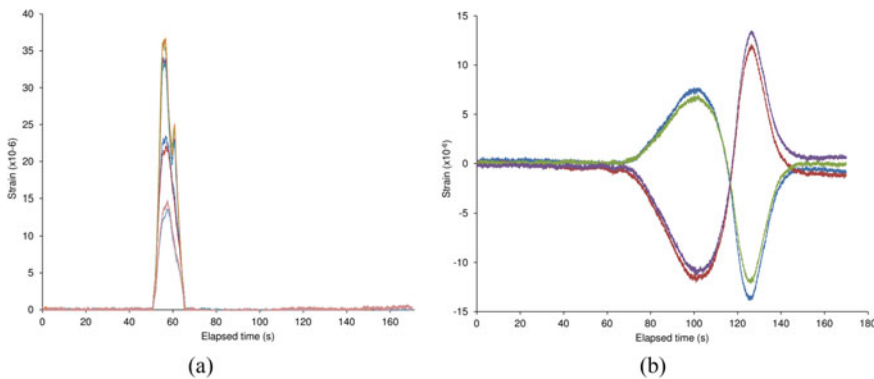


Fig. 10.19 Experimental influence lines: **a** deck cross-section (T-T1) with eight strain measuring points; **b** arch cross-section (A-p4Dp5D) with four strain measuring points

on the strain distribution at the four girders of the deck. Figure 10.20a depicts the transversal distribution of the peak strain values of the eight sensors installed on the deck cross-section, as well as the location of their resultant. It was possible to validate that the strain resultant position is a robust estimator of the vehicle alignment. The peak value of the sum of the measured strains shown in Fig. 10.20b was shown to correlate well with the weight of the vehicle, regardless of its position.

Following a periodic load test policy during the dam construction, experimental influence lines for the passage of similar heavy vehicles were analyzed. More than 6500 vehicles were recorded, supporting the assessment of the structure response over time. In order to automate this analysis, the direction of the vehicles crossing the bridge and their transverse positioning on the deck were identified using the strain records in the simply supported access span. For damage detection purposes, only the vehicles that cross the bridge in the same direction and centered on the traffic lane were considered for comparison. The selection was validated based on the similarity between the normalized strain influence lines recorded in the simply

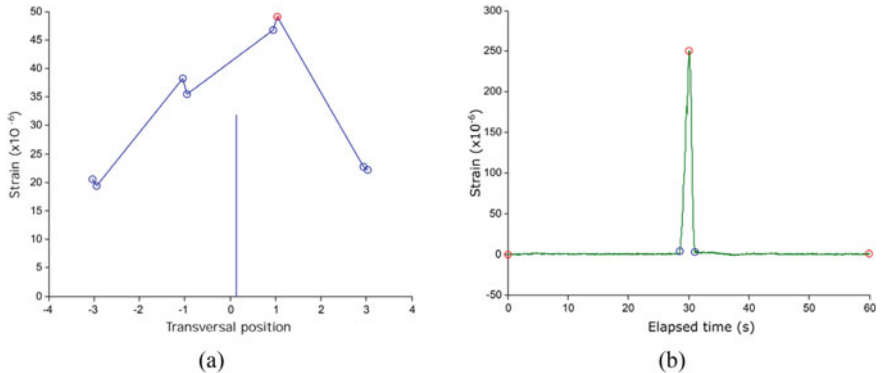


Fig. 10.20 Bridge weigh in motion: **a** profile of the peak strain values across the deck and the respective resultant position (in this case centered on the traffic lane); **b** sum of the influence lines of the measured strains on the deck and peak value used as vehicle weight indicator

supported access span, as shown in Fig. 10.21. The MAC indicator comparing these influence lines is shown in Fig. 10.21b.

The structural health monitoring of the arch was performed comparing the strain records in the different cross-sections of the arch due to the passage of the selected vehicles. Figure 10.22b shows the peaks, maximum and minimum values, of each section of the arch, normalized for the maximum strain, associated with the passage of the selected vehicles. The comparison of the effects of successive vehicles made it possible to detect variations in the arch response. A numerical analysis of the bridge supported the sensitivity of the methodology to different damage scenarios.

Concluding remarks. Foz Tua Bridge has a high patrimonial value and was subjected to exceptional requests resulting from the passage of heavy vehicles during the construction of a dam. The first load test allowed the characterization of the reference

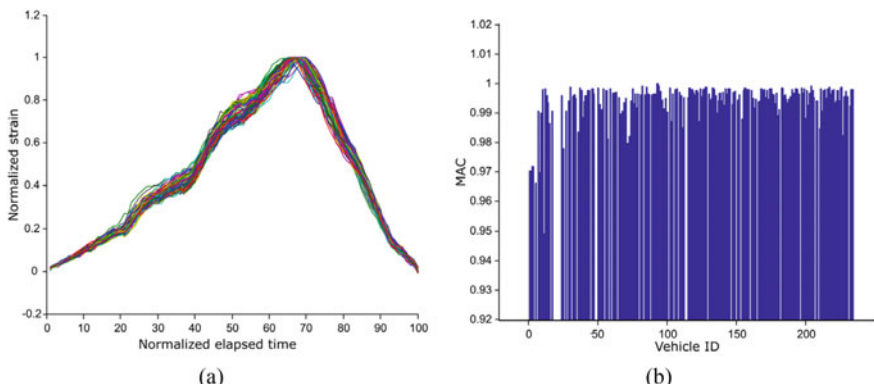


Fig. 10.21 Periodic influence lines measured on the simply supported access span: **a** selected normalized influence lines; **b** MAC of the selected influence line

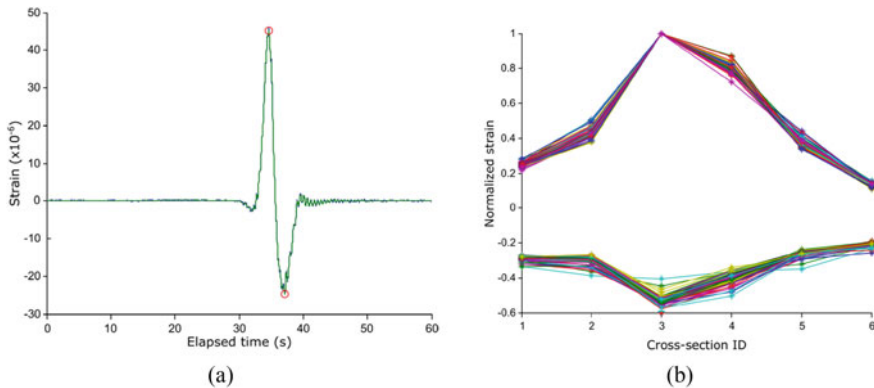


Fig. 10.22 Analysis of the arch response comparing multiple influence lines: **a** maximum and minimum values selected on each influence line; **b** comparison of multiple vehicles effects

behavior of the structure and the calibration of a bridge weigh-in-motion algorithm. During the critical period, periodic load tests with similar loads allowed the comparison of the structural response, which was used as a basis for a structural health monitoring strategy.

10.5 Conclusions

Load testing of bridges are performed in various contexts, ranging from diagnostic testing during the commissioning of new bridges to proof load tests on old bridges. With the developments in sensing, data acquisition technology and processing power, bridge load testing practice evolved to produce detailed information providing structural engineers with a deeper insight on the structural behavior and bridge owners with detailed information regarding the condition of their assets. In this chapter, the types of load tests and the scenarios in which they can be performed were systematized. The best practices and recommendations for load test planning and execution were summarized. Three case studies were described illustrating the potential of load testing and the results that can be achieved.

Acknowledgements The authors acknowledge the financial support by: Base (UIDB/04708/2020) and Programmatic (UIDP/04708/2020) funding of CONSTRUCT financed by national funds through the FCT/MCTES (PIDDAC); and by the project S4Bridges (PTDC/ECI-EGC/31355/2017) financed by FEDER through COMPETE2020-POCI and by national funds through FCT/MCTES (PIDDAC).

References

1. ElBatanouny M, Schacht G, Bolle G (2019) History of load testing of bridges. In: Lantsoght E (ed) Load testing of bridges: current practice and diagnostic load testing, vol 12. CRC Press/Balkema, Leiden pp 9–27
2. Lantsoght E (2019) Current codes and guidelines. In: Lantsoght E (ed) Load testing of bridges: current practice and diagnostic load testing, vol 12. CRC Press/Balkema, Leiden, pp 29–69
3. Highways England (2019) CS 463 Load testing for bridge assessment
4. The Institution of Civil Engineers (1998) National steering committee for the load testing of bridges: guidelines for the supplementary load testing of bridges. Thomas Telford, London
5. American Association of State Highway Transportation Officials (2018) The manual for bridge evaluation, 3rd edn. AASHTO
6. Zhou Y (2006) Assessment of bridge remaining fatigue life through field strain measurement. ASCE J Bridg Eng 11(6):737–744
7. Pimentel M, Brühwiler E, Figueiras JA (2008) Fatigue life of short-span reinforced concrete railway bridges. Struct Concr 9(4):215–222
8. Bayane I, Mankar A, Brühwiler E, Sorensen JD (2019) Quantification of traffic and temperature effects on the fatigue safety of a reinforced-concrete bridge deck based on monitoring data. Eng Struct 196:109357
9. Pimentel M, Figueiras J (2017) Assessment of an existing fully prestressed box-girder bridge. Proc Inst Civ Eng Bridge Eng 170(1):42–53
10. Costa B, Figueiras J (2013) Rehabilitation and condition assessment of a centenary steel truss bridge. J Constr Steel Res 89:185–197
11. Cavadas F, Rodrigues C, Félix C, Figueiras J (2013) Post-rehabilitation assessment of a centenary steel bridge through numerical and experimental analysis. J Constr Steel Res 80:264–277
12. National Cooperative Highway Research Program (1998) Manual for bridge rating through load testing. Research Results Digest, p 234
13. Gutermann M, Schröder C (2015) Loading vehicle BELFA-development and experience gained in 10 years of practice. Bridge Struct 11(1,2):19–31
14. Lantsoght E, Koekkoek R, Hordijk D, de Boer A (2018) Towards standardisation of proof load testing: pilot test on viaduct Zijlweg. Struct Infrastruct Eng 14(3):365–380
15. Rodrigues C, Félix C, Figueiras J (2011) Fiber-optic-based displacement transducer to measure bridge deflections. Struct Health Monit 10(2):147–156
16. Sousa Tomé E, Pimentel M, Figueiras J (2018) Structural response of a concrete cable-stayed bridge under thermal loads. Eng Struct 176:652–672
17. Figueiras J, Félix C, Costa B (2005) Testing and monitoring of a centenary arch bridge. Struct Infrastruct Eng 1(1):63–73
18. Costa B, Figueiras J (2012) Fiber optic based monitoring system applied to a centenary metallic arch bridge: design and installation. Eng Struct 44:271–280

Chapter 11

Dynamic Testing on Railway Bridges



Diogo Ribeiro , Cássio Bragança , Artur Silva, and Rui Calçada

Abstract This chapter describes a set of dynamic tests that are frequently performed in railway bridges during their lifecycle, particularly in the construction, reception, and operation phases. Typically, the dynamic testing of railway bridges involves ambient vibration and free vibrations tests, as well as dynamic tests under the passage of traffic loads. In this scope, the typical framework of the dynamic monitoring system is described, particularly in what concerns the sensor types, data acquisition systems (DAQs), communication protocols and data processing. A special emphasis is given to the data processing techniques which are dedicated to each type of dynamic testing. In case of ambient vibration tests a frequency domain method (EFDD—Enhanced Frequency Domain Decomposition) and a time domain method (SSI—Stochastic Subspace Identification) are detailed. In case of free vibration tests the Logarithm Decrement (LD) and Prony methods are described. For the dynamic test under traffic loads some specific features involving Power Spectrum Density (PSD) functions and train dynamic signatures are used. Additionally, the dynamic tests performed in the Cascalheira bridge, located in the northern line of the Portuguese railway network, are presented as a case study.

Keywords Railway bridges · Dynamic tests · Dynamic monitoring system · Sensors · Data acquisition systems · Data processing · Case study

D. Ribeiro

CONSTRUCT-LESE, School of Engineering, Polytechnic of Porto, Porto, Portugal
e-mail: drr@isep.ipp.pt

C. Bragança

Department of Structural Engineering, Federal University of Minas Gerais, Belo Horizonte, Brazil
e-mail: cassioscb@ufmg.br

A. Silva · R. Calçada

CONSTRUCT-LESE, Faculty of Engineering, University of Porto, Porto, Portugal
e-mail: ajpsilva@fe.up.pt

R. Calçada

e-mail: ruiabc@fe.up.pt

11.1 Introduction

An efficient, safe and reliable railway infrastructure is one of the pillars for the economic development of any country. Among the elements of a railway network, bridges are undoubtedly the structures that deserve more attention in terms of safety, mainly due to the significant traffic actions to which they are subject, and the catastrophic consequences involved in a collapse of such a structure. Thus, infrastructure managers are increasingly interested in the experimental testing and monitoring of bridges envisaging the characterization of their dynamic response, which may provide information to take better decisions about the use and maintenance of these assets [1, 2].

The dynamic tests applicable to railway bridges are mainly the ambient vibration tests, free vibration tests and tests under traffic actions. The ambient vibration tests allow the characterization of the modal parameters, particularly the natural frequencies and mode shapes, while free vibration tests provide accurate estimates of damping coefficients. Typically, these information support the calibration of numerical models of the bridge, which allow the structural assessment under the passage of trains at higher speeds and/or higher axle loads [3]. Furthermore, the tests under traffic actions provide dynamic responses of the train-track-bridge system that can be used to verify the normative criteria related to structural safety, traffic safety and passenger comfort. In addition, these tests provide information for the validation of the numerical models of the bridge, and in cases where a permanent monitoring system is installed, can support the early detection of structural damage [2].

This chapter details the procedures for the performance of different types of dynamic tests on railway bridges, mainly in aspects related to the test preparation, instrumentation and data processing techniques. Also, a case study of experimental testing of a railway bridge will be presented.

11.2 Types of Dynamic Tests

In this section, the main dynamic testing techniques applicable to railway bridges will be discussed, namely ambient vibration tests, free vibration tests and tests under traffic actions. The main fundamentals behind carrying out each test will be presented, as well as the main fields of application. More emphasis will be given to the ambient vibration tests due to the increasing application and refinement of procedures.

11.2.1 *Ambient Vibration Tests*

Description. This test involves the measuring of the structural response (usually in acceleration) to the actions to which they are normally subjected (ambient actions),

such as the wind, the traffic of vehicles circulating on the vicinity of the structure, the traffic of pedestrians, earthquakes of very low intensity (micro-seismicity), the effect of sea waves, etc.

The main advantage of this test is the low economic cost since, in most of the occasions, does not require the use of artificial excitation equipment and does not affect the normal operation of the structure. Additionally, this type of tests is well suitable to identify modes with very low frequencies (below 1 Hz). On the other hand, the measuring system needs to be highly sensitive in order to adequately capture the very low amplitudes of vibration induced by the ambient actions [4].

Sometimes, even with the use of highly sensitive equipment, the amplitudes of vibration generated by ambient actions are significantly reduced to be properly measured, especially in very stiff structures, or its frequency content is limited and insufficient to mobilize a large number of vibration modes, in particular those with higher frequencies. In these circumstances, the external artificial excitation of the structure is generally adopted. The artificial excitation techniques help increasing the vibration levels of the structure, by means of impulse hammers (Fig. 11.1a), human actions (Fig. 11.1b), controlled mass fall, electro-mechanical exciters (Fig. 11.1c), among others. Generally, it is not appropriate to use the trains as forms of excitation when conducting ambient vibration tests, since their added mass considerable interfere with the dynamic properties of the structure.

Test preparation. One of the key points for the success of an ambient vibration test is a careful pre-test planning. The first step consists in the elaboration of a numerical model of the structure, even if simplified, which will provide support for the selection of the mesh of measurement points. For the development of this numerical model, it is essential to resort not only to the project data, but also perform a field visit to the structure aiming at a better understanding of the constructive specificities. In addition, during the visit attention should be paid to the identification of access points, viable locations for installing the sensors and equipment and, if possible, carrying out a set of preliminary measurements to characterize the level of the ambient vibration response.

Once the numerical model has been developed, the selection of the measurement locations must be based on the mode shapes obtained through a numerical modal analysis. Measuring points must always be positioned in locations effectively mobilized

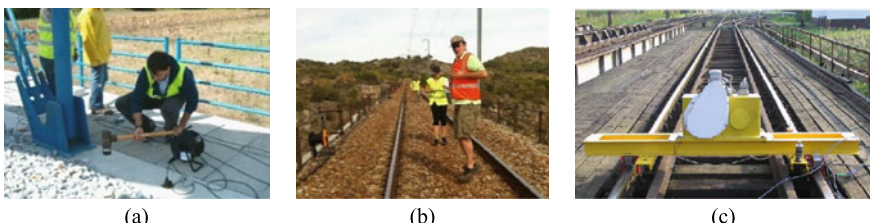


Fig. 11.1 External excitation techniques: **a** impulse hammer [5]; **b** human actions [5]; **c** electro-mechanical exciter [6]

by the modes of vibration to be identified, as well as avoiding positioning a sensor over the nodes (i.e., zero amplitude locations for a specific mode shape). Furthermore, the selected measuring points must allow an adequate distinction between the different mode shapes of the structure, since after the test the modal configurations will only be characterized on the measurement points.

Rodrigues [4] suggests that the quality of a mesh of measurement points can be evaluated by calculating the Modal Assurance Criterion (MAC) parameter (Eq. (11.1)) between the vectors φ_i and φ_j containing, respectively, the numerical modal ordinates of modes i and j extracted from the points where the sensors are proposed to be installed.

$$MAC_{ij} = \frac{|\varphi_i^H \varphi_j|^2}{(\varphi_i^H \varphi_i)(\varphi_j^H \varphi_j)} \quad (11.1)$$

When calculating the Auto-MAC matrix, which correlates the numerical vectors among them, it is desirable that all the values of the main diagonal equal one and the off-diagonal values are zero or less than 0.10 (Fig. 11.2a). As can be seen from Fig. 11.2b, an inadequate choice of the number and location of measurement points may lead to difficulties in distinguishing the different mode shapes.

Another aspect that must be considered when selecting measurement points is the scaling between the modal amplitudes associated to different parts of the structure, that do not necessarily compose the target areas of study. In most of situations, the movements of these non-target regions of the structure induce small amplitude movements on the target areas of study due to structural compatibility. If there are no sensors placed on the non-target regions of the structure, there is no way to scale these small movements, which configurations can be easily confused with the relevant modal configurations of the target areas. The same logic applies to the measurement directions: even if the test is focused on the vertical dynamic behavior of the structure, some sensors must be positioned in the other directions so that

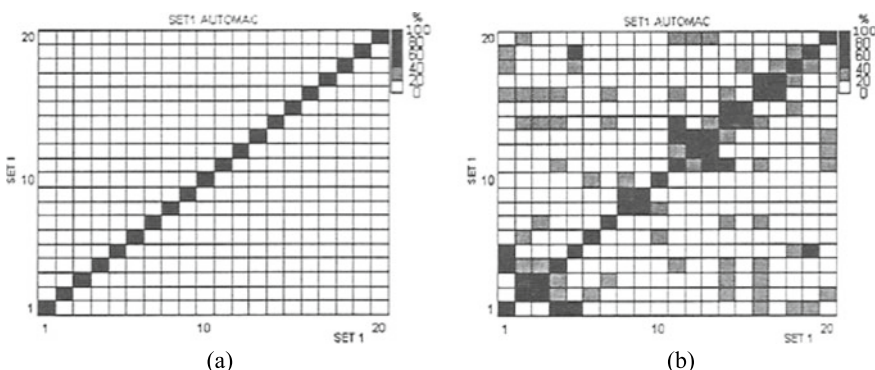


Fig. 11.2 Auto-MAC matrix: **a** adequate mesh; **b** inadequate mesh (adapted from [7])

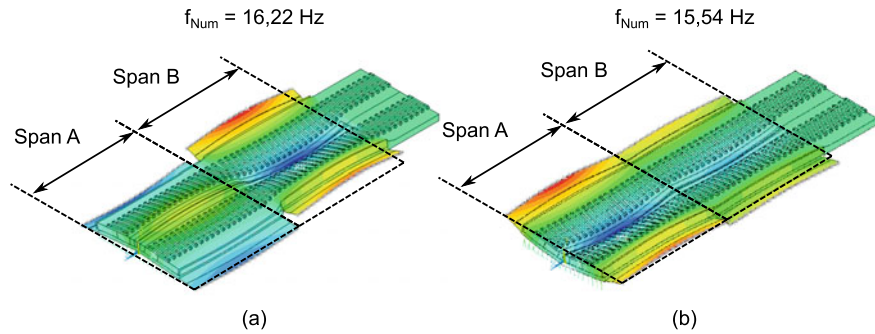


Fig. 11.3 Numerical modal configurations of two vibration modes of Canelas bridge decks, Portugal: **a** span B mode shape; **b** span A mode shape (adapted from [8])

predominantly transverse or longitudinal modes with small vertical movements are not confused with purely vertical modes [5].

The scaling of modes is extremely relevant in the case of railway bridges composed by successive simply supported spans. In these situations, the continuity provided by the railway track between spans guarantees that the mode shapes associated to a specific span exert influence on the others [5]. Figure 11.3 illustrates the torsion mode shapes of the decks of Canelas bridge, Portugal, one related to span B (Fig. 11.3a) and the other related to span A (Fig. 11.3b). Due to the continuity of the track, it is noted that the mode shape associated with span A induces small displacements on span B and with a similar configuration to its own torsion mode shape, as well as a very close frequency value. In this case, installing sensors only in span B would make unfeasible to distinguish between these mode shapes.

In the case of larger railway bridges, it is common to have more measurement points than the number of available sensors. Thus, the test must be performed in several experimental setups, where each setup corresponds to a set of measuring points keeping some fixed reference sensors. Special attention should be paid to the location of the reference sensors avoiding being located on the nodes of the relevant mode shapes. Additionally, it is important that each experimental setup allow a proper spatial visualization of the mode shapes in the post-processing stage.

Figure 11.4 depicts the methodology for carrying out an ambient vibration test in a two-span girder based on a set of reference and mobile sensors. It is assumed a 10-point mesh (1–10) and a total of 4 sensors available. Two different strategies are presented, one using only one reference sensor (Fig. 11.4a) and the other resorting to two reference sensors (Fig. 11.4b). Although adopting more reference sensors implies performing more tests, it is recommended to adopt more than one reference since provides more redundancy in not selecting nodes of the modes of interest [4].

After defining the testing strategy, the next step is to select and prepare the monitoring system. Selecting a monitoring system depends on several factors, such

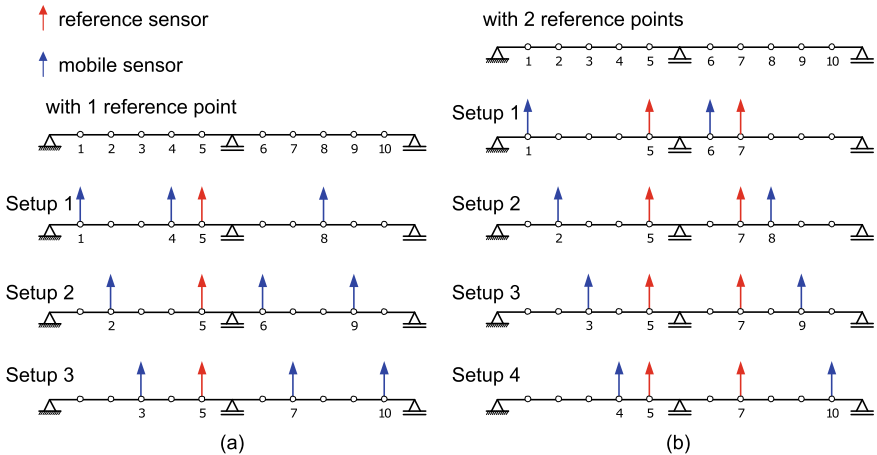


Fig. 11.4 Testing strategies using mobile and reference points: **a** 1 reference point; **b** 2 reference points (adapted from [4])

as, expected vibration levels, frequency range of interest, resolution, communication protocol, ambient conditions, among others, and will be discussed in detail in Sect. 11.3.

11.2.2 Free Vibration Tests

Free vibration tests involve measuring the free-vibration response of the bridge after a sudden release derived from an imposed displacement. Such a procedure can be done by pulling a suspended mass to a cable with a fusible connection until it suddenly breaks [4, 9]. Alternatively, the free-vibration response can be analyzed after the application of an impulsive load, which is usually performed by releasing a free-falling weight that collides with the bridge [10].

Figure 11.5a and b illustrate the free vibration tests performed on the Vasco da Gama bridge and on the runway of Madeira airport, Portugal, in both cases using a suspended weight attached to the structure that was suddenly released. Figure 11.5c depicts a drop weight used by Sampaio et al. [11] to excite some railway bridges on Carajás, northern Brazil.

This type of test is specifically used to accurately identify the modal damping coefficients. This is because the low amplitudes of vibration associated to the ambient vibration tests generally lead to an underestimation of the damping coefficients, since the damping values are remarkably dependent on the vibration amplitudes [3, 4].

The disadvantage of this type of test is the relevant logistics and equipment required to perform it. First, the structure must be out-of-operation to avoid the existence of other interfering sources of vibration. Second, in a larger structure,

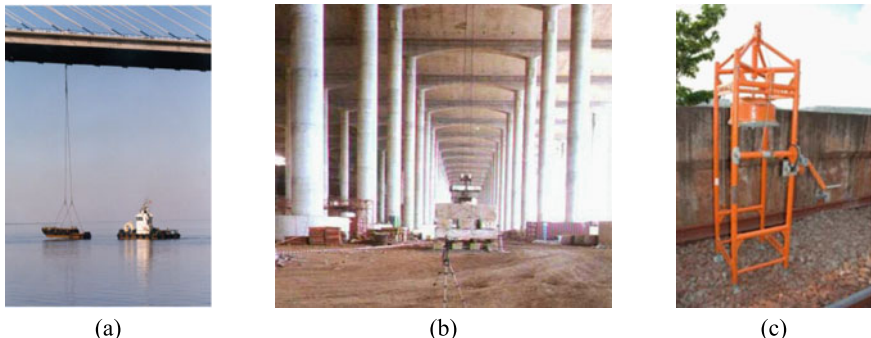


Fig. 11.5 Free vibration tests: **a** Vasco da Gama bridge using a suspended boat [9]; **b** runway bridge of Madeira airport using a suspended massive concrete block [4] and **c** bridge in Carajás line based on a drop-weight system [11]

the installation of the equipment (cables and weights) requires specialized heavy machinery. Finally, the safety risks associated with the sudden release of the stressed cables cannot be ignored. Within this context, it is recommended that this type of test is carried out before the opening of the structure to operation and, therefore, avoiding its interdiction and taking advantage of the available equipment of the contractors [4, 12].

In case of railway bridges, an alternative procedure adopted by several authors [3, 13, 14] to perform free vibration tests, consists on using the free-vibration responses immediately after the last vehicle leaves the bridge or, in cases of short-span bridges, the free-vibration responses that occur between the passage of the successive bogies of the vehicles. This procedure avoids the interdiction of the bridge and all the logistics and equipment required.

11.2.3 Tests Under Railway Traffic

Tests under railway traffic consist of measuring the dynamic responses of the bridge during the passage of railway vehicles. Typically, the response is evaluated both in accelerations and displacements, by means of accelerometers and Linear Variable Differential Transformer (LVDTs). The sensors are positioned on locations where the dynamic effects are expected to be more pronounced due to contributions of the most relevant modes of vibration. Thus, it is usual to install sensors in positions close to 1/2 and 1/4 span sections and comprising both sides of the deck, in case of double lines. Figure 11.6 depicts a typical example of a layout of accelerometers used in a dynamic test under traffic actions.

This type of test is widely used for the validation of numerical models of railway bridges, comparing the measured responses with the ones derived from the numerical simulations comprising the vehicle-structure dynamic interaction problem [3, 15].

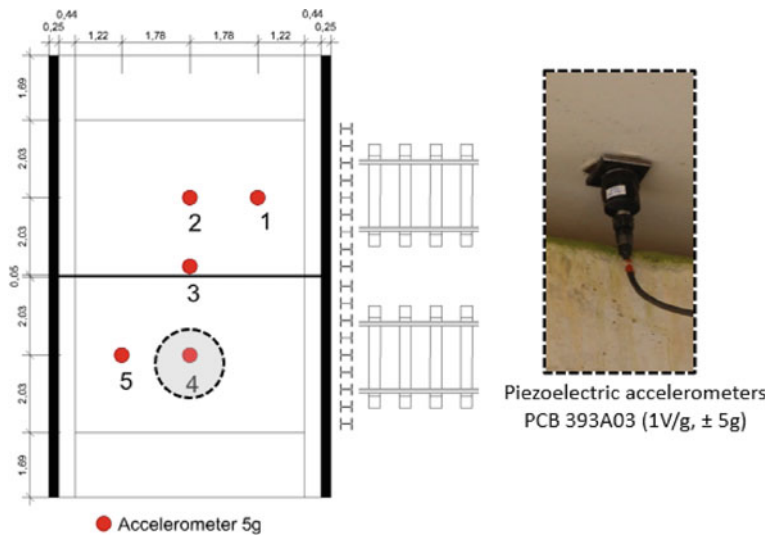


Fig. 11.6 Sensors' layout in a dynamic test under traffic actions

These validated models are used to predict the structural response for new traffic scenarios associated to higher circulation speeds, higher axle-loads, or a combination of both.

11.3 Dynamic Monitoring System

The typical layout of a dynamic monitoring system includes three components, namely the sensors, the data acquisition system, and the communication system (Fig. 11.7). The sensors are responsible for converting physical quantities (displacements, accelerations, strains, etc.) into electrical signals that are read, conditioned and converted into discretized digital signals by the data acquisition systems. The communication systems are responsible for transferring data, in digital format, to a local storage unit or to the cloud, in order to be processed and analyzed. In this section, the specificities of each of these components will be addressed envisaging the dynamic monitoring of railway bridges.

11.3.1 Sensors

In dynamic measurements the main physical quantity to be evaluated is the acceleration or vibration. Thus, this section describes the two most used sensor types capable

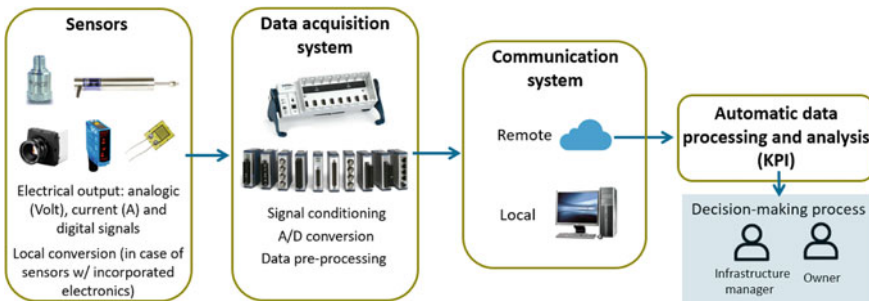


Fig. 11.7 Typical layout of a dynamic monitoring system including sensors, data acquisition, and communication systems

of measuring the accelerations, the piezoelectric accelerometers and the force balance accelerometers.

Piezoelectric accelerometers. These types of sensors are based on the principle of piezoelectricity, which is a property found in quartz crystals and some artificial ceramic materials. When a piezoelectric material deforms, due to the application of a mechanical effort, an electric difference of potential (in Volts) is generated, which is proportional to the stress applied to the crystal [16].

Taking advantage of piezoelectricity, the accelerometers are built by attaching a mass to the piezoelectric crystals, so that the force applied to the crystal, by Newton's second law, will be proportional to the acceleration. Then, a linear relationship between the acceleration and the electric difference of potential in the crystal, whose proportionality constant is known as the sensitivity, is established. Different forms of association between the piezoelectric crystals and the masses can be used to build the accelerometers. The three most common working configurations (compression, shear and bending) are illustrated in Fig. 11.8a.

Compared to other types of accelerometers, the piezoelectric stand out for having high frequency response, high linearity and small size. On the other hand, they have a high impedance, low output range (in Volts) and limitations in measuring movements with very low frequency (less than 0.3–0.5 Hz) and reduced amplitudes.

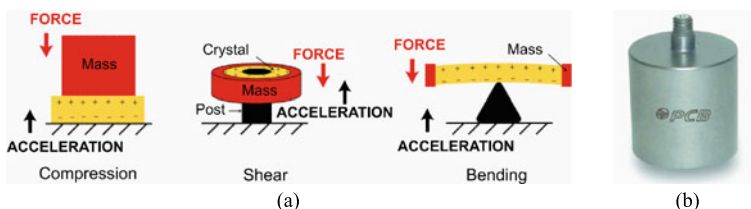


Fig. 11.8 Piezoelectric accelerometers: **a** working configurations (adapted from [16]); **b** PCB® uniaxial accelerometer [17]

Force balance accelerometers. These sensors are composed of a mass suspended by a spring and a servo-type mechanism that controls the position of the mass. When the system is subjected to an acceleration, by inertia, the mass tends to have a relative displacement that is detected by a displacement transducer. Depending on this relative displacement a signal is produced which induces a current in the coil surrounding the mass. With the passage of this current, a magnetic force arises that opposes the movement and keeps the mass in its position. The value of the current necessary to keep the mass static will be proportional to the acceleration of the system [4]. This operating principle is outlined in Fig. 11.9a.

Unlike piezoelectric accelerometers, due to their working principle, servo force balance accelerometers need to be permanently supplied with electrical energy. These accelerometers are able to accurately measure very low frequency vibrations, near DC (≈ 0 Hz), present high sensitivity and, therefore, are recommended for civil infrastructures with very low levels of vibration and low frequency modes of vibration. The considerable higher cost can be highlighted as the main disadvantage in relation to the piezoelectric sensors.

Main accelerometer specifications. Based on the accelerometer datasheet, it is important to know the technical significance of each parameter to select the most suitable device for a specific application. The main specifications to consider are:

- **Sensitivity**—Usually specified in mV/g, it establishes a relation between the level of acceleration and the electrical output of the sensor. For example, an accelerometer with a sensitivity of 10 mV/g when subjected to an acceleration of 1 g will exhibit an electrical difference of potential of 10 mV. Higher values of sensitivity represent an intrinsic ability of the sensor to amplify very low levels of acceleration, as usually happens under ambient actions.
- **Measuring range**—Represents the maximum vibration amplitude capable of being measured with the sensor, usually specified in $\pm g$. These threshold values, if exceeded, leads to signal distortions or clips; however they should not be confused with shock limits, which represent a threshold value that induces damage to the

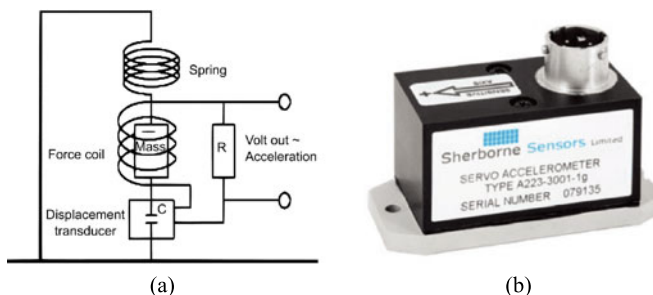


Fig. 11.9 Force balance accelerometers: **a** principle of operation [18]; **b** Sherborne® force balance sensor [19]

sensor. Typically, sensors with a larger measurement range present a reduced sensitivity.

- **Frequency range**—Represents the range of frequencies where the accelerometer can provide accurate measurements, usually specified as a tolerance ($\pm 5\%$, $\pm 10\%$, etc., or even, $\pm 1 \text{ dB}$, $\pm 3 \text{ dB}$, etc.) with respect to the sensitivity at a reference frequency. This frequency range is because the sensitivity of the sensor can only be assumed constant within a certain frequency interval.
- **Linearity**—Measures the deviation between a perfectly linear relation between acceleration and electrical output and the actual sensor response. It is usually specified as a percentage of the full-scale output (% FS).
- **Broadband resolution**—Defined as the root mean square of the output signal without being subjected to any excitation, which allows to quantify the noise level associated with the sensor. It is usually specified in $\mu\text{g RMS}$ or $\mu\text{V RMS}$; however, some manufacturers specify this parameter as a function of the frequency bandwidth in $\mu\text{V}/\sqrt{\text{Hz}}$ or $\mu\text{g}/\sqrt{\text{Hz}}$.
- **Number of axes**—Represents the number of sensitive axes, typically commercial accelerometers can be found in uniaxial or triaxial configurations.

Recommendations for testing of railway bridge. The sensors must have a sensitivity and measurement range compatible with the expected vibration levels of the tested structure. Table 11.1 presents some recommended values for the sensitivity and measuring range of the accelerometers considering different components of the track-bridge system. The recommendations are made for both: Ambient vibration tests and tests under railway traffic.

In addition, the sensor's broadband resolution should be compatible with the ambient vibration levels of the bridge. However, on most occasions, the overall precision of the measuring system is not conditioned by the sensor, but by the A/D conversion at the data acquisition system (see Sect. 11.3.2).

The mounting scheme of the sensors, i.e., the type of attachment of the sensor to the structure, also have a relevant influence on the measured data. The stud mount is the most adequate option since it presents the highest systems' resonance frequency. However, in some structures it is not possible to drill a hole to screw the sensor, which makes this option unfeasible. Therefore, it is recommended to opt for a less

Table 11.1 Recommended characteristics for the accelerometers used in ambient vibration tests and tests under railway traffic

Type of dynamic test	Component	Recommended values	
		Sensitivity (mV/g)	Measuring range (g)
Ambient vibration	Bridge	10,000	± 0.5
Under railway traffic	Bridge	1,000	± 5
	Sleepers	100	± 50
	Rail	10	± 500

invasive mounting scheme that still provide a good fixation, such as the use of adhesives. However, the adoption of several layers of adhesive creates a flexible interface between the sensor and the structure that acts as a vibration filter and distorts the measurements.

11.3.2 Data Acquisition System

Main features. Output signals from transducers are typically analog type. The Data AcQuisition systems (DAQ) allow to transform the output signal of the transducers on digital signals suitable for the interpretation of the dynamic response. The conversion of a continuous analog signal to a discrete digital signal basically involves two main operations, sampling and quantization.

The sampling operation consists in transforming a continuous time analog signal into a discrete data sequence on equally spaced time intervals (Δt). The choice of sampling frequency (f_s) is crucial for the adequate representation of the signal and must respect the Nyquist's theorem (Eq. (11.2)), in which the sampling frequency must be at least twice the highest frequency of interest (f_{\max}). This threshold frequency is commonly known as the Nyquist frequency (f_{Nyq}).

$$f_s = \frac{1}{\Delta t} = 2 \times f_{Nyq} \geq 2 \times f_{\max} \quad (11.2)$$

If the signal contains frequencies higher than the Nyquist frequency, after sampling, these frequencies will be represented as lower frequencies causing a phenomenon usually known as aliasing. In Fig. 11.10 the difference between a signal properly (Fig. 11.10a) and improperly (Fig. 11.10b) sampled is presented in which the effect of aliasing is clear.

To deal with the aliasing phenomenon, the data acquisition systems have built-in analog antialiasing filters, which cut the frequencies above Nyquist, preventing aliasing from occurring. In practice, as there are no ideal filters, it is not possible to cut at an exact frequency and, in general, it is considered that frequencies above 80% of the Nyquist frequency already begin to be affected by the filter. Therefore, it is recommended to adopt a sampling frequency at least 2.4 times higher than the maximum frequency that is intended to be adequately represented.

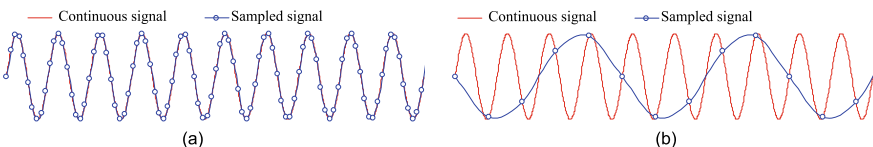
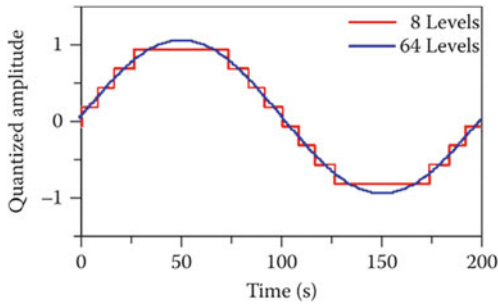


Fig. 11.10 Aliasing error: **a** signal without aliasing; **b** signal with aliasing (adapted from [4])

Fig. 11.11 Quantization operation of a sine-curve for the 3-bit (8 levels) and 6-bit (64 levels) converters (adapted from [20])



The definition of the total acquisition time (t) is also relevant. A rule of thumb normally adopted is to consider an acquisition time greater than 1000 times the period of vibration associated to the lowest frequency (T). If a limited time-domain signal presents an insufficient number of complete cycles, the original signal is distorted in the frequency domain giving rise to leakage errors.

The second step in the analog-to-digital conversion process is the signal quantization. It consists of converting the amplitudes of the continuous analog output into a finite set of integers available in the converter. A converter with a resolution of m bits has the capacity to discretize the range of values of the analog signals, in 2^m levels. As an example, Fig. 11.11 presents the same signal quantized with a 3-bit and a 6-bit converter. As is clear, the greater the number of bits of the converter, the better is the signal.

Typical signal anomalies. Some signal anomalies frequently found in dynamic monitoring are addressed, as well as the possible causes and proposals for corrective/preventive measures [4]:

- **Saturation**—Refer to clippings in the extreme values of signal amplitude, in most cases caused by exposing the sensor to vibration levels outside the measurement range. Sensors with a wider range of measurements should be used.
- **Low signal-to-noise ratio**—In most cases, results from the use of sensors with insufficient sensitivity to detect the vibration levels, making very difficult to adequately distinguish the noise from the response of the structure. Sensors with lower noise levels (broadband resolution) must be considered.
- **Electrical noise**—In measuring systems connected to the electrical supply, noise at frequencies between 50–60 Hz and its harmonics are very frequent. To solve this problem, consider the use of a battery system. However, if there are no structural frequencies close to the electrical noise frequency, consider the use of digital filters.
- **Trends**—These are slow deviations of the mean value of the signal, which do not correspond to any physical modification of the structure. Typically, it manifests as linear trends or even very low frequency components. These trends must be removed through high-pass filters with a cut-off frequency near zero or detrend techniques based on linear or polynomial fit functions.

- **Outliers**—These are atypical values in the signal due to a problem in the analog-to-digital converter and clash with any physical structural response. They can occur either isolate, affecting a single piece of data, or a larger set of data. When dealing with isolated events, they can be corrected by replacing the spurious data by an interpolated value between its adjacent points. When a wider set of data is affected, this interpolation is not possible, and the erroneous portion of the signal must be removed.

11.3.3 Communication System

The communication system main function is to allow local/remote access to the data acquisition system, as well as enabling the transfer of large amounts of data from the acquisition site to the location where the user visualize and analyze the data. Local communication systems generally involve the establishment of a point-to-point communication network, such as RS232, RS485 or USB, which establishes a direct connection between the data acquisition system and a local computer/server. Remote communication systems have shown enormous development, with several commercial solutions already available, from the classic cable type solution supported by Ethernet protocol to the most common ones with access via wireless modem. Wireless networks encompass the traditional protocols, such as GSM (Global System for Mobile Communications) and GPRS (General Packet Radio Service), as well as the most recent Bluetooth, Wi-Fi, and mobile 4G/5G protocols, which can ensure the efficient and cost-effective transfer of large volumes of data (big data).

11.4 Data Processing

In this section, the main data processing techniques applicable to dynamic testing of railway bridges will be discussed. More focus will be given to operational modal analysis techniques, which are applicable to the processing of the ambient vibration test data.

11.4.1 Ambient Vibration Tests

Operational modal analysis (OMA), or output-only modal analysis, consists of a set of modal identification techniques based exclusively on the measurement of the structure responses. This set of techniques can be divided into basically two groups, those based on spectral density functions (frequency domain) and those based on time correlation functions or directly on measured data (time domain).

Rodrigues [4] presents an overview of the main available modal identification techniques. The two most widespread OMA techniques will be here discussed, the Enhanced Frequency Domain Decomposition (EFDD), in the frequency domain, and the Stochastic Subspace Identification (SSI), in the time domain.

Enhanced Frequency Domain Decomposition (EFDD). This method is an advance in relation to the Frequency Domain Decomposition (FDD) method, proposed by Brincker et al. [21], and allows a more accurate estimation of the natural frequencies, mode shapes and damping coefficients. The EFDD is based on the Singular Value Decomposition (SVD) of the Power Spectral Density (PSD) matrix $\mathbf{S}_{yy}(\omega)$, which can be obtained by the Fourier transform of the time-domain correlation functions. Thus, the main diagonal of the PSD matrix is composed by the auto spectral density functions and the out-of-diagonal terms are the cross spectral density functions. The SVD decomposition of the PSD matrix can be summarized by Eq. (11.3):

$$\mathbf{S}_{yy}(\omega) = \mathbf{U}\Sigma\mathbf{V}^H \quad (11.3)$$

in which Σ is a diagonal matrix containing the singular values and \mathbf{U} and \mathbf{V} are similar matrices containing the singular vectors. Brincker et al. [21] demonstrated that, for structures with low values of damping and subject to white noise excitations, the matrix of singular values corresponds to the power spectral density functions of a set of 1 degree-of-freedom (DOF) oscillators, whose singular values and vectors coincide with those of the real structure. Then, the SVD decomposition allows to isolate the contribution of each of the modes of vibration as a 1-DOF system. The main steps of the EFDD method are summarized in Fig. 11.12.

In case of well-separated modes, only the first singular value will have significant magnitude; however, in case of closely spaced modes, one will be identified in the first singular value curve, while the others will be identified in the second and higher

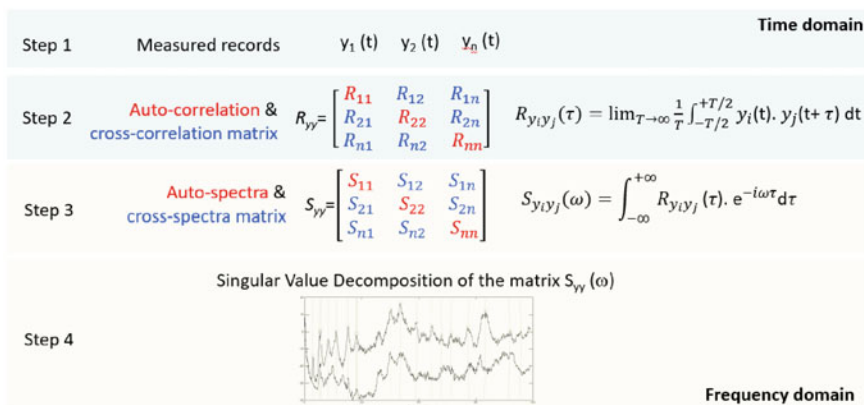


Fig. 11.12 Main steps for the application of the Enhanced Frequency Domain Decomposition (EFDD) method

order singular values curves. The natural frequencies and damping coefficients are obtained through the time domain autocorrelation function calculated by the Inverse Fourier Transform (IFFT) of the singular values around each resonance peak. The selection of the SVD points is based on the similarity between their singular vectors calculated through the MAC parameter. Respecting the assumptions of the method, these functions will be proportional to the decay in free vibration of the 1-DOF oscillator. Thus, the natural frequency can be obtained based on the period of the oscillation and the damping coefficient by adjusting the exponential term ($e^{-\zeta\omega_n t}$) to the decay envelope of the vibration [22, 23].

Stochastic Subspace Identification based on the time series (SSI-DATA). The technique, originally proposed by Van Overschee and De Moor [24], consists of directly fitting a stochastic state-space model of a linear time-invariant system to the response time series given by Eq. (11.4):

$$\begin{aligned} \mathbf{x}_{k+1} &= \mathbf{A}_d \mathbf{x}_k + \mathbf{w}_k \\ \mathbf{y}_k &= \mathbf{C}_d \mathbf{x}_k + \mathbf{v}_k \end{aligned} \quad (11.4)$$

where \mathbf{A}_d is the discrete time state matrix, \mathbf{C}_d is the discrete time output matrix, \mathbf{x}_k is the state vector in the k^{th} time instant, \mathbf{y}_k is the output vector in the k^{th} time instant and \mathbf{w}_k and \mathbf{v}_k are vectors containing the process noise due to disturbances and modelling inaccuracies and measurement noises due to sensor inaccuracies, respectively [22, 25]. It should be noted that Eq. (11.4) implies the premise that the systems input, although unknown, approaches white noise and is condensed in the vectors \mathbf{w}_k and \mathbf{v}_k [22].

From the system of state equations, only the outputs \mathbf{y}_k , which can be measured, are assumed to be known. The identification of the system matrices is based on the calculation of the Kalman filter state estimates $(\hat{\mathbf{X}}_i)$, defined in Eq. (11.5):

$$\hat{\mathbf{X}}_i = [\hat{\mathbf{x}}_i \ \hat{\mathbf{x}}_{i+1} \ \dots \ \hat{\mathbf{x}}_{i+\hat{j}-1}] \quad (11.5)$$

in which $\hat{\mathbf{x}}_i$ are estimates of the state vector. The Kalman filter state estimates are obtained based on the SVD decomposition of a projection matrix, where future outputs are projected on the past outputs. The idea behind the projections is that it retains all information from past time series that is relevant to predict future series [24, 26].

Based on the calculated Kalman filter state estimates, the system matrices can be obtained by Eq. (11.6):

$$\begin{pmatrix} \hat{\mathbf{X}}_{i+1} \\ \mathbf{Y}_{i|i} \end{pmatrix} = \begin{pmatrix} \mathbf{A}_d \\ \mathbf{C}_d \end{pmatrix} (\hat{\mathbf{X}}_i) + \begin{pmatrix} \mathbf{W}_i \\ \mathbf{V}_i \end{pmatrix} \quad (11.6)$$

in which $\mathbf{Y}_{i|i}$ is a Hankel matrix with only one block row. Since a series of estimates of the state vector are calculated, the system above is over defined and needs to be

solved using a least squares approach, with \mathbf{W}_i and \mathbf{V}_i as residuals. Once the system matrices are obtained, the identification problem is solved, since all the physical information, natural frequencies, mode shapes and damping coefficients are derived from \mathbf{A}_d and the matrix \mathbf{C}_d allows transforming the eigenvectors, defined with respect to states, into observable outputs of the physical system [26].

During the SVD decomposition of the projection matrix, the number of non-zero singular values indicate the order of the state-space model that best represents the system. In practice, there will be no null values, since the data is always contaminated by spurious components, so there will be no clear definition of which order should be defined. Thus, it is recommended to estimate the modal parameters assuming different orders of the model and to build the denominated stabilization diagrams. In these diagrams the modes of vibration of the system will be stable for different model orders, while those spurious modes will be non-stable. As a rule of thumb, it is usual to adopt as a stability criterion a maximum variability of 1% for natural frequencies, 5% for damping coefficients and 1% for MAC values [27].

11.4.2 Free Vibration Tests

The free vibration tests aim to obtain realistic estimates of the damping coefficients (ξ) associated to each mode of vibration, based on the free vibration response of the structure. Two techniques will be here discussed, the logarithmic decrement method and the Prony method.

Logarithmic decrement method. This method considers that the free-vibration decay of the acceleration peaks follows an exponential function of the type $Ce^{-\xi_n \omega_n t}$, where C is a constant value, ξ_n is the damping coefficient of mode n , and ω_n is the natural frequency of the mode n . The logarithmic decrement (δ) is defined by Eq. (11.7):

$$\delta = \frac{1}{m} \ln \left(\frac{a_n}{a_{n+m}} \right) \quad (11.7)$$

in which a_n corresponds to the acceleration amplitude of the peak n and a_{n+m} correspond to the acceleration amplitude of the peak $n+m$. Thus, the damping coefficient ξ is simply obtained by $\delta/2\pi$ [10, 28].

An alternative approach, which takes advantage of the automatic curve fitting tools, is to directly fit the exponential decay equation to the peaks of the free-vibration response. As these curve fitting techniques are usually based on the minimization of quadratic errors, based on a least squares approach, it is possible to consider several peaks for the exponential fitting and obtain an optimal curve.

Regardless the adopted strategy, the application of the logarithmic decrement method requires the separation of the free-vibration response of the mode of vibration of interest from the others. In case of structures with well-spaced modes, the mode

of interest can be easily isolated by applying a bandpass filter centered on its natural frequency. In case of closely spaced modes, it may not be possible to separate them, which limits the application of this method.

Another critical aspect when applying the logarithmic decrement method is the part of the free-vibration decay that must be used to calculate the damping coefficient. Malveiro et al. [3] proved a dependence between the damping coefficient and the amplitude of vibration: the greater the amplitude, the greater the damping coefficient tends to be.

Figure 11.13 schematically represents the steps involved in the application of the logarithmic decrement method.

Prony method. The Prony method comes as an alternative to the logarithmic decrement method in the case of existence of closely spaced modes of vibration. The method is based on the decomposition of the signal in a set of exponential decaying sinusoids representative of each frequency of interest by fitting to the data the Eq. (11.8):

$$a[t] = \sum_{i=1}^n A_i e^{-\xi_i \cdot \omega_{0,i} \cdot t} \cos\left(\omega_i \sqrt{1 - \xi_i^2} + \phi_i\right) \quad (11.8)$$

where n is the number of complex exponentials of interest, A_i the amplitude of the i^{th} exponential component, ξ_i the damping coefficient, ω_i the angular natural frequency and ϕ_i the phase angle.

It is recommended to use a bandpass filter to isolate the modes (more than one) to be identified with the Prony method, facilitating the data adjustment of Eq. (11.8). Figure 11.14 schematically illustrates the steps involved in applying the Prony method.

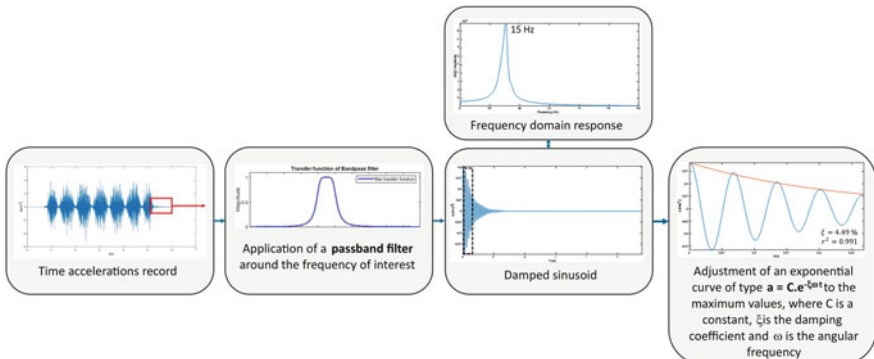


Fig. 11.13 Schematic representation of the application of logarithm decrement method

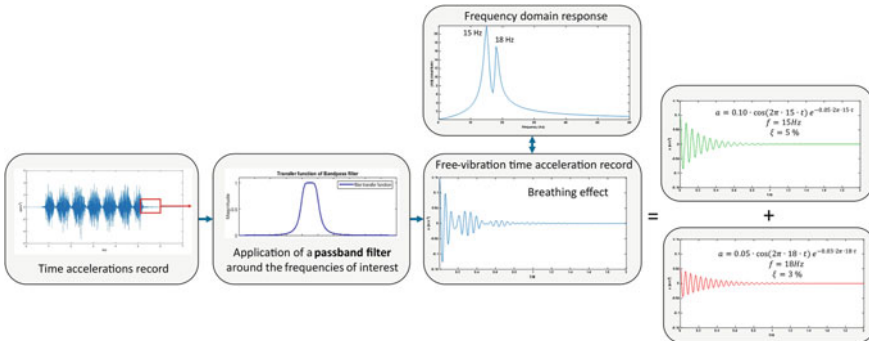


Fig. 11.14 Schematic representation of the application of Prony method

11.4.3 Tests Under Railway Traffic

The interpretation of the results of a test under railway traffic essentially depends on the dynamic behavior of the train-track-bridge system. Thus, the responses of the bridge subsystem are influenced by: (i) bridge dynamics, (ii) vehicle dynamics and vehicle parametric excitation, and (iii) track irregularities and track parametric excitation.

The dynamic behavior of the bridge is governed by its natural frequencies, mode shapes and damping coefficients. Typically, an amplification of the dynamic response of the bridge, or eventually a resonance phenomenon, occur when the parametric excitation of the train loads, due to the regularly spaced groups of axles, equals or get close to one of the natural frequencies of the bridge. Under resonance the response is mainly controlled by the damping coefficient values.

The parametric excitation induced by a train can be characterized by the dynamic signature of the train. This reference parameter depends on the axle loads and distance between axles and is given by Eq. (11.9):

$$S_0(\lambda) = \max_{i=1, N-1} \sqrt{\left[\sum_{k=0}^i P_k \cos\left(\frac{2\pi x_k}{\lambda}\right) \right]^2 + \left[\sum_{k=0}^i P_k \sin\left(\frac{2\pi x_k}{\lambda}\right) \right]^2} \quad (11.9)$$

where λ represents the wavelength, P_k the load value of the k axle, x_k is the distance of the k axle to the first axle of the train and N is the number of axles of the train. As an example, the dynamic signature of an important train in Portugal, the Alfa Pendular train (Fig. 11.15a), is depicted in Fig. 11.15b. The peaks identified correspond to the wavelengths for which the train is more aggressive and, consequently, more prone to excite the railway bridges. The wavelength of 25.4 m is related to the distance between groups of 4 consecutive axles belonging to different vehicle bogies [29].

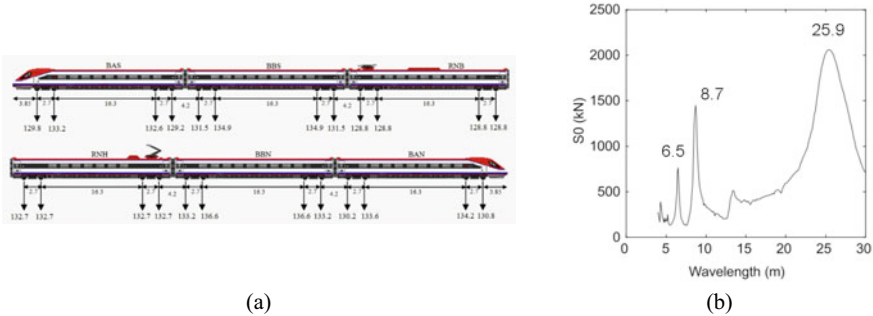


Fig. 11.15 Alfa Pendular train: **a** loading scheme; **b** dynamic signature (adapted from [30])

From the dynamic signature, the frequencies in which the train is more aggressive can be easily accessed by simply dividing the train speed by the wavenumber.

Another relevant source of excitation of the train-bridge system is the track irregularities. As an example, Fig. 11.16a presents the measured irregularities in the northern line of the Portuguese railways close to the bridge over Antuã river [15]. A better understanding of the influence of the track irregularities is provided by a spectral analysis as a function of wavenumber (Fig. 11.16b). Based on the speed of the train, the mobilized frequencies can be estimated by multiplying the wavenumber by the speed.

Once the main dynamic excitation sources are interpreted, the data analysis from a test under railway traffic is usually performed both in time and frequency domains. Usually, time domain responses are used to extract peak values, RMS values, etc. Otherwise, the frequency domain responses are obtained based on Fast Fourier Transforms (FFT) or Power Spectral Density (PSD) functions. The use of PSD is recommended in comparison to a simply FFT, since can typically provide a cleaner spectrum which facilitate the data analysis. The spectral content allows the precise identification of the origin of each excitation source of the bridge.

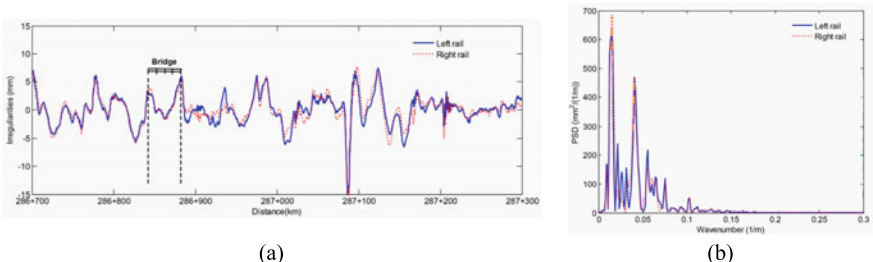


Fig. 11.16 Track irregularities: **a** example of longitudinal profile; **b** power spectral density function [15]

11.5 Case Study

This section presents a case study of a railway bridge in Portugal, the Cascalheira bridge, where ambient vibration tests and dynamic tests under railway traffic were performed. Details about the execution of both types of tests, as well as the data processing and analysis, are also described. More information about the experimental studies performed in the Cascalheira bridge is available in Ref. [13].

11.5.1 Description

Cascalheira bridge is a 11.10 m length short-span bridge located at km 100.269 of the northern railway line in Portugal, that establishes the connection between Lisbon and Porto (Fig. 11.17a). The structure of the deck was completely replaced in 1994, with the aim of increasing the traffic speed. Currently, the maximum allowed speed on this stretch is 160 km/h. The structural solution adopted is a composite filler-beam type, in which the deck is composed by a reinforced concrete slab with embedded steel girders (Fig. 11.17b). The cross-section's width is 11 m and consists of two half-symmetrical and independent decks separated by a longitudinal joint.

11.5.2 Ambient Vibration Test

In the ambient vibration test a technique based on fixed reference points and mobile points was adopted. The test setup consisted of 12 measurement points, involving the use of piezoelectric accelerometers, PCB model 393B12, with a sensitivity of 10 V/g and a measurement range of ± 0.5 g, installed at the lower face of the bridge deck. The time series were acquired in periods of 10 min, with a sampling frequency of 2048 Hz, which was posteriorly decimated to a frequency of 256 Hz. The data acquisition was performed using the cDAQ-9188 system from National Instruments (NI), equipped with IEPE analogue input modules with 24-bit resolution (NI-9234). Since the purpose of this test was to determine the vertical bending and torsion

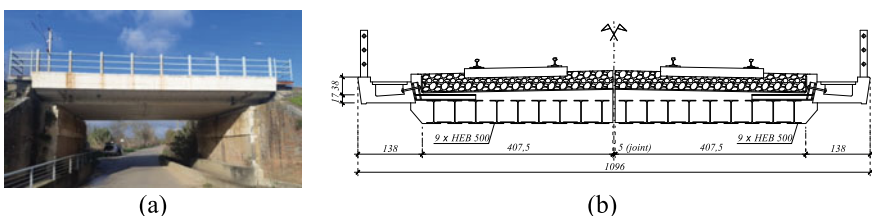


Fig. 11.17 Cascalheira railway bridge: **a** perspective view; **b** cross-section (dimensions in cm)

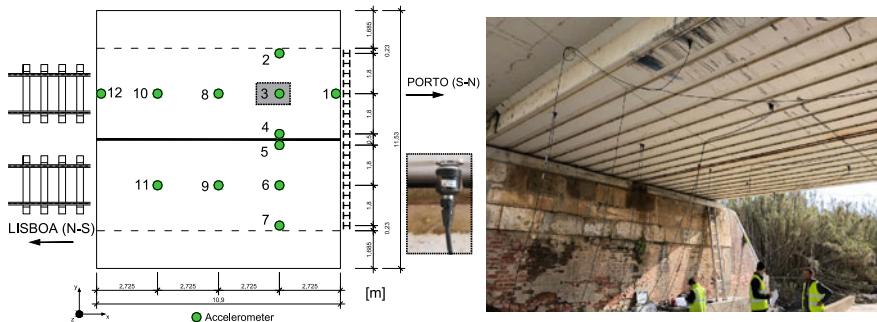


Fig. 11.18 Ambient vibration test: experimental setup including a detail of the accelerometer PCB 393B12 (dimensions in m)

movements, all the accelerometers were installed in the vertical direction. Due to the low acceleration levels of the deck under ambient actions, in some situations additional excitation provided by a non-instrumented impact hammer, at the lower face of the deck, was useful to increase the amplitude of movement of the deck, leading to an increase of the signal-to-noise ratio and, consequently, to a significant improvement of the signal quality.

Figure 11.18 illustrates the experimental configuration of the test setup to identify the modal parameters of the bridge deck. The accelerometers were distributed along the span in the centre of each track, with two accelerometers in the lateral extremities of each half-deck, to distinguish the torsion modes from the vertical ones. Given the constraints to access the upper face of the deck due to traffic, the sensors were installed at the lower face of the deck through magnetic bases, namely on the bottom flange of the steel girders.

The modal identification was performed using the EFDD method available in the ARTeMIS® software [31]. Figure 11.19a shows the first three curves of the average normalized singular values of the spectral density matrices of all test setups, in which is possible to observe the peaks (red dots) corresponding to the four identified global vibration modes depicted in Fig. 11.19b (where, f is the average value of the natural frequency and ξ is the average value of the damping coefficient).

11.5.3 Test Under Railway Traffic

The test under railway traffic aimed to measure the dynamic response of the bridge deck in terms of accelerations caused by the passage of trains. These responses were also used for estimating the bridge damping. Figure 11.20 shows the four measurement points located at the lower face of the deck, in which the vertical accelerations were measured using piezoelectric accelerometers, PCB model 393A03, with a sensitivity of 1 V/g and a measurement range of ± 5 g. For detecting the train axles,

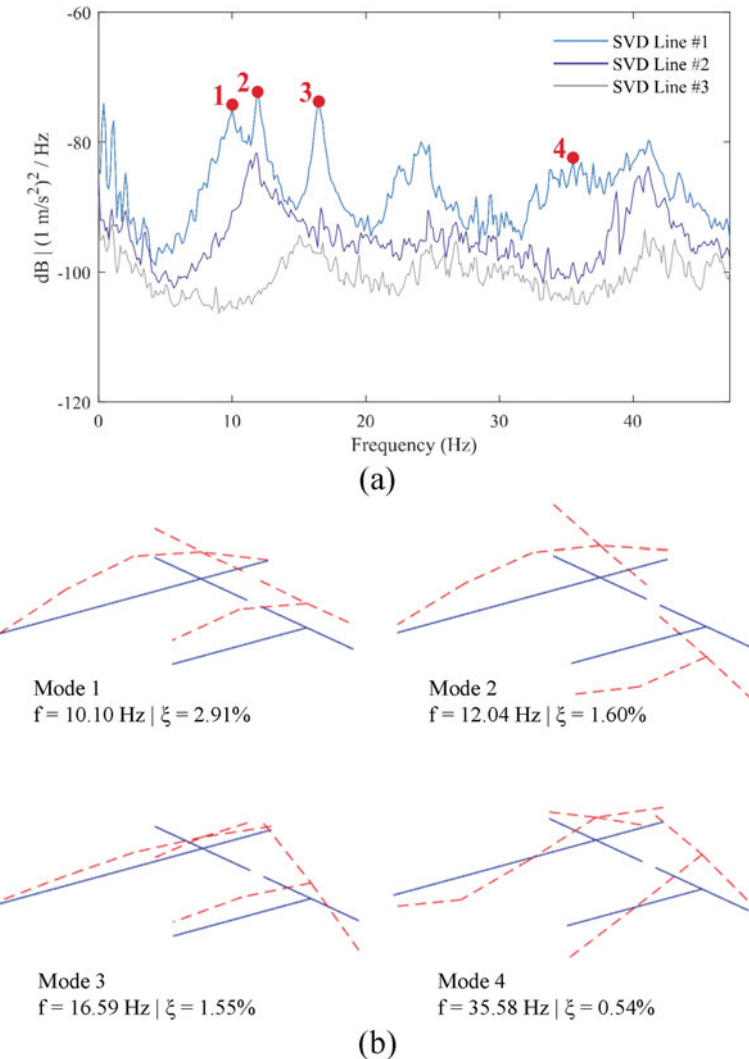


Fig. 11.19 EFDD method: **a** average normalized singular values of the spectral density matrices; **b** experimental modal parameters

two groups of optical sensors were installed on each bridge extremity, including an emitter and a receiver located on opposite track sides (see Fig. 11.20). These optical sensors allowed the detection of the precise time instant that the last train axle leaves the bridge, which is decisive to accurately assess the beginning of the free vibration movement of the bridge, necessary to estimate its damping. The time series were acquired at a sampling rate of 2048 Hz.

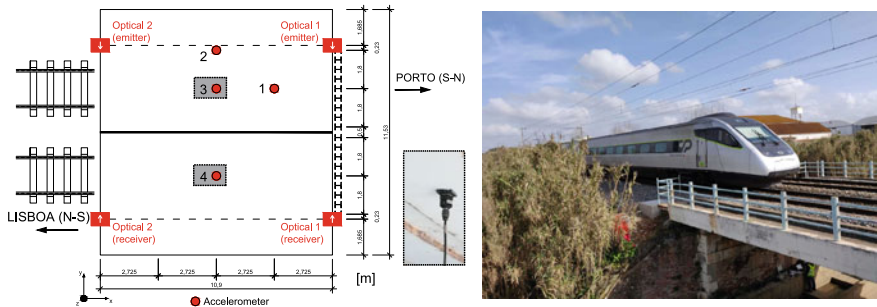


Fig. 11.20 Test under railway traffic: experimental setup including a detail of the accelerometer PCB 393A03 and highlighting the accelerometers located at midspan used to estimate damping

The estimation of the damping coefficients was based on the deck's acceleration responses caused by the train passages, obtained in the two highlighted positions illustrated in Fig. 11.20 (midspan position of each half-deck). For Cascalheira bridge, the free vibration of the structure was not just controlled by the first bending mode, but also by the first torsional mode, whose natural frequencies are close to each other (Fig. 11.19). In these situations, where the natural frequencies of the fundamental bending and torsion modes are close or sometimes merged, which is common in short-span railway bridges, the Prony method shown significant advantages in the estimation of damping coefficients when compared to the LD method [13].

Table 11.2 presents the damping coefficient estimates obtained from the Prony method for modes 1 and 2 and considering the passage of Alfa Pendular train over the bridge at different speeds (110, 135 and 140 km/h). This, proved to be quite similar, attesting the efficiency and consistency of the method. The table also indicates the average damping coefficient values (marked on bold).

Figure 11.21a presents the vertical accelerations time records measured at the accelerometers n°.3 (opposite track) and n°.4 (running track) due to the passage of the Alfa Pendular train at 110 km/h in the Porto-Lisbon direction, and Fig. 11.21b shows the corresponding auto-spectra in the frequency domain. Additionally, Fig. 11.21c depicts the train signature of the Alfa Pendular, highlighting the main frequencies associated with the passage of axles or group of axles.

Table 11.2 Damping coefficients estimates based on the Prony method [13]

Train speed (km/h)	Mode 1			Mode 2		
	f(Hz)	a _{max} (m/s ²)	ξ(%)	f(Hz)	a _{max} (m/s ²)	ξ(%)
110	9.21	0.0774	7.86	11.93	0.0233	4.64
135	9.57	0.0951	6.20	11.46	0.1803	4.76
140	9.55	0.0790	6.01	11.56	0.1899	4.77
	$\bar{\xi} = 6.69\%$			$\bar{\xi} = 4.72\%$		

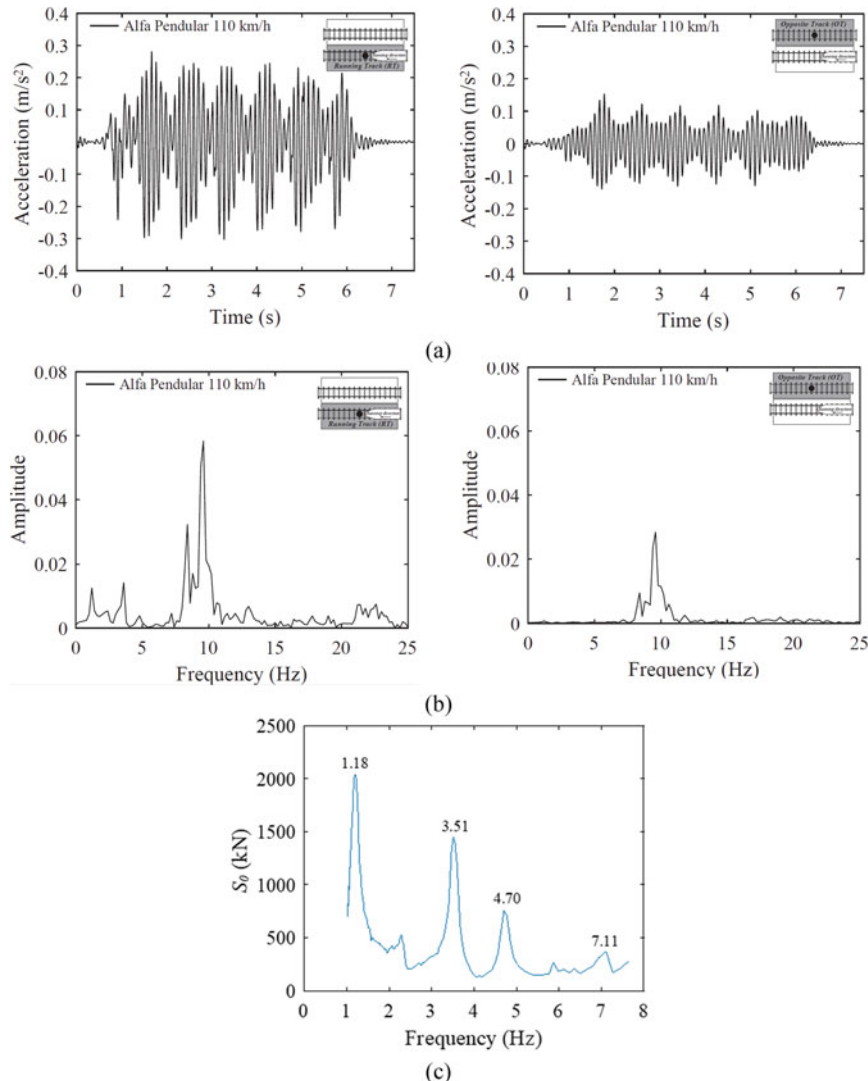


Fig. 11.21 Vertical accelerations records measured at the accelerometers n°. 3 (opposite track) and n°. 4 (running track) due to the passage of the Alfa Pendular train at 110 km/h in the Porto-Lisbon direction: **a** time records; **b** auto-spectra; **c** train dynamic signature

The analysis of the time domain records shows that the maximum acceleration levels on the running track is approximately three times higher than the opposite track. This result also proves the relevant transmissibility effect between the two half-decks due to the transversal continuity of the ballast layer. Also, by analysing the frequency content of the experimental responses, it is possible to observe that the first peaks are associated with the passage of the axles and groups of axles of the

train, in accordance with the train signature, while the highest peaks, around 10 Hz, are associated with the first vibration mode of the bridge.

11.6 Conclusions

This chapter gives an overview of the main types of dynamic testing on railway bridges, particularly the ambient vibration tests, free vibration tests and tests under traffic actions. A special attention was given to the preparation of the tests, layouts, monitoring system, as well as data processing. Concerning the monitoring system, a detailed explanation about the sensors, data acquisition system and communication system, was provided. Furthermore, the data processing involved the use of distinct mathematical techniques, such as the EFDD and SSI methods, in case of ambient tests, DL and Prony methods, in case of free vibration tests, and the analysis of the dynamic responses in the time and frequency domains, in case of test under traffic actions.

In sequence the performance of some of the dynamic tests on real field applications, particularly in the Cascalheira bridge, was presented. The ambient vibration tests proved to be efficient and robust in estimating the modal properties of the structure, namely the natural frequencies, mode shapes and damping coefficients. In the same vein, the tests under railway traffic enabled an accurate assessment of the dynamic structural response in terms of acceleration under passenger trains at speeds between 110 and 140 km/h. The information provided by these tests can be used for the calibration or validation of numerical models, normative verification checks, as well as for structural damage identification.

In conclusion, as future perspectives, with the rapid advancement of new technologies, great advances are expected in the dynamic testing of railway bridges. With regard to sensors, the use of wireless accelerometers based on Wi-Fi technology is increasingly common. Promising applications of non-contact measurement technologies, based on computer vision, have indicated potential in the application of these techniques. With regard to data interpretation and decision making, with the evolution of artificial intelligence techniques, it is expected an increase in the use of automatic damage identification methodologies based on dynamic responses for SHM applications.

Acknowledgements The authors would like to thank the research unit CONSTRUCT (POCI-01-0145-FEDER-007457, UID/ECI/04708/2020, FEDER and FCT/MCTES)—Institute of R&D in Structures and Construction, funded by FEDER funds through COMPETE2020—Programa Operacional Competitividade e Internacionalização (POCI)—and by national funds through FCT (Fundação para a Ciência e a Tecnologia).

References

1. Bien PEJ, Zwolski CEJ (2007) Dynamic tests in bridge monitoring-systematics and applications. In: Conference proceedings of the society for experimental mechanics series IMAC-XXV: Conference & Exposition On Structural Dynamics, Orlando, Florida, USA
2. Meixedo A, Santos J, Ribeiro D, Calçada R, Todd MD (2022) Online unsupervised detection of structural changes using train-induced dynamic responses. *Mech Syst Signal Process* 165
3. Malveiro J, Ribeiro D, Calçada R, Delgado R (2014) Updating and validation of the dynamic model of a railway viaduct with precast deck. *Struct Infrastruct Eng* 10:1484–1509
4. Rodrigues J (2004) Identificação Modal Estocástica: Métodos de Análise e Aplicações em Estruturas de Engenharia Civil (Stochastic modal identification: analysis methods and applications in civil engineering structures). (in Portuguese), Porto, Portugal
5. Ribeiro D (2012) Efeitos dinâmicos induzidos por tráfego em pontes ferroviárias: modelação numérica, calibração e validação experimental (Traffic-induced dynamic effects on railway bridges: numerical modeling, calibration and experimental validation). (in Portuguese), Porto, Portugal
6. Bornet L, Andersson A, Zwolski J, Battini J-M (2015) Influence of the ballasted track on the dynamic properties of a truss railway bridge. *Struct Infrastruct Eng* 11:796–803
7. Ewins DJ (2009) Modal testing: theory, practice and application. Wiley, Baldock, England
8. Carvalho M (2011) Comportamento dinâmico de uma ponte ferroviária de pequeno vão para tráfego de alta velocidade (Dynamic behavior of a short span railway bridge for high speed traffic). (in Portuguese), Porto, Portugal
9. Cunha A, Caetano E, Delgado R (2001) Dynamic tests on large cable-stayed bridge. *J Bridg Eng* 6:54–62
10. Lorenzoni F, De Conto N, da Porto F, Modena C (2019) Ambient and free-vibration tests to improve the quantification and estimation of modal parameters in existing bridges. *J Civ Struct Heal Monit* 9:617–637
11. Sampaio R, Chan THT (2015) Modal parameters identification of heavy-haul railway RC bridges-experience acquired. *Struct Monit Maint* 2:1–18
12. Farrar CR, Duffey TA, Cornwell PJ, Doebling SW (1999) Excitation methods form bridge structures. In: Proceedings of the 17th international modal analysis conference Kissimmee, Florida, USA
13. Saramago G, Montenegro PA, Ribeiro D, Silva A, Santos S, Calçada R (2022) Experimental validation of a double-deck track-bridge system under railway traffic. *Sustainability* 14:5794
14. Malveiro J, Ribeiro D, Sousa C, Calçada R (2018) Model updating of a dynamic model of a composite steel-concrete railway viaduct based on experimental tests. *Eng Struct* 164:40–52
15. Ticona Melo LR, Ribeiro D, Calçada R, Bittencourt TN (2020) Validation of a vertical train-track-bridge dynamic interaction model based on limited experimental data. *Struct Infrastruct Eng* 16:181–201
16. PCB piezotronics: sensing geometries for piezoelectric accelerometers. https://www.pcb.com/sensors-for-test-measurement/accelerometers/sensing_geometries. Last Accessed 03 Jan 2022
17. PCB piezotronics: accelerometers. Vibration sensors. <https://www.pcb.com/sensors-for-test-measurement/accelerometers>. Last Accessed 04 Jan 2022
18. Kumar DP, Pal K (2006) System level simulation of servo accelerometer in simulink. *J Phys Sci* 10:143–150
19. StrainSense limited: servo accelerometers. Force Balance Accelerometers, UK. <https://www.strainsense.co.uk/sensors/accelerometers/servo-accelerometers/>. Last Accessed 29 Apr 2022
20. Bajić D, Dimić G, Lončar-Turukalo T, Milovanović B, Japundžić-Žigon N (2018) A descriptive approach to signal processing. In: ECG time series variability analysis, pp 75–86
21. Brincker R, Zhang L, Andersen P (2000) Modal identification from ambient responses using frequency domain decomposition. In: Proceedings of the 18th international modal analysis conference (IMAC), 625–630, San Antonio, Texas, USA

22. Magalhães F (2004) Identificação modal estocástica para validação experimental de modelos numéricos (Stochastic modal identification for experimental validation of numerical models). (in Portuguese), Porto, Portugal
23. Brincker R, Ventura CE, Andersen P (2001) Damping estimation by frequency domain decomposition. In: Proceedings of the international modal analysis conference-IMAC, pp 698–703, Kissimmee, Florida, USA
24. Van Overschee P, De Moor B (1996) Subspace identification for linear systems, Boston, Massachusetts, USA
25. Chauhan S (2016) Subspace algorithms in modal parameter estimation for operational modal analysis: perspectives and practices. *Conf Proc Soc Exp Mech Ser* 8:295–301
26. Peeters B, De Roeck G (1999) Reference-based stochastic subspace identification for output-only modal analysis. *Mech Syst Signal Process* 13:855–878
27. Peeters B, De Roeck G (2000) Reference based stochastic subspace identification in civil engineering. *Inverse Probl Eng* 8:47–74
28. Craig Jr RR, Kurdila AJ (2006) Fundamentals of structural dynamics. Wiley & Sons, Hoboken, New Jersey, USA
29. Ribeiro D, Bragança C, Costa C, Jorge P, Silva R, Arêde A, Calçada R (2022) Calibration of the numerical model of a freight railway vehicle based on experimental modal parameters. *Structures* 38:108–122
30. Meixedo A, Ribeiro D, Santos J, Calçada R, Todd M (2021) Progressive numerical model validation of a bowstring-arch railway bridge based on a structural health monitoring system. *J Civ Struct Heal Monit*
31. ARTeMIS (2009) ARTeMIS extractor pro-academic license. User's Manual, SVS: Aalborg, Denmark

Chapter 12

An Automated Tool for Long-Term Structural Health Monitoring Based on Vibration Tests



Daniel Soares , Rharã de Almeida Cardoso , Flávio de Souza Barbosa , and Alexandre Abrahão Cury

Abstract Structural Health Monitoring (SHM) programs play an essential role in the field of civil engineering, especially for assessing safety conditions involving large structures such as viaducts, bridges, tall buildings, towers, and old historical buildings. Typically, an SHM process needs to be based on a trustful strategy for detecting structural novelties or abnormal behaviors. Usually, such an approach is complemented with human inspection and structural instrumentation routines, where the latter requires proper hardware equipment and software tools. However, most strategies already published in this topic mainly focus on modal identification procedures and tracking their outputs i.e., structural modal parameters. Such approaches usually lead to high computational costs and can still be insensitive to minor changes in structural behavior, thus missing crucial damage scenarios in their initial manifestations. To circumvent these drawbacks, recent studies showed that the use of symbolic representations derived directly from raw time-domain data (e.g., acceleration measurements) obtained from vibration tests could provide more damage-sensitive responses with lower computational effort. The proposed methodology employs a clustering technique over such symbolic representations within a moving time-window framework and uses a single-valued index to indicate if a novelty (i.e., structural damage and/or interventions, such as maintenance/repair) is present in the acquired data. Two practical studies—a highway and a railway bridge located in France—show that the proposed tool provide an unsupervised and adaptive scheme for automated real-time SHM applications based on vibration tests.

D. Soares · R. de Almeida Cardoso · F. de Souza Barbosa · A. A. Cury (✉)
University of Juiz de Fora, Juiz de Fora, Minas Gerais, Brazil
e-mail: alexandre.cury@engenharia.ufjf.br

D. Soares
e-mail: daniel.cardoso@engenharia.ufjf.br

R. de Almeida Cardoso
e-mail: rharã.cardoso@engenharia.ufjf.br

F. de Souza Barbosa
e-mail: flavio.barbos@engenharia.ufjf.br

Keywords Structural health monitoring · Dynamic testing · Novelty detection · Unsupervised statistical learning · Real-time monitoring

12.1 Introduction

The existence of Structural Health Monitoring (SHM) programs for strategic structures like viaducts, bridges, ageing buildings, and towers are crucial to prevent disasters. Damage-related information extracted from the structural behavior may save lives and avoid great economical losses. A recent example of disaster occurred in Genoa, Italy (August 14, 2018), where a cable-stayed bridge collapsed leaving 43 people dead [1].

This example shows why SHM programs must complement and support human inspections [2–4]. Ideally, such a monitoring procedure must work automatically and continuously providing updated sensitive information about the structure's condition. Besides, to reduce maintenance costs and prevent social, physical, and economical losses from structural collapses, it is fundamental that such algorithms can readily detect abnormal dynamic behavior or even damage in its early manifestations.

As an early attempt to detect damage, many of the published techniques depended on modal information i.e., natural frequencies, damping ratios and mode shapes. Nevertheless, although modal frequencies and shapes are deeply related to the mechanical behavior of structures (mass and stiffness), they are not sensitive enough to detect small novelties in the system (e.g., early damage). The main reason is that most of these abnormalities are local and, therefore, do not impact significantly on the first vibration modes, which are estimated, in general, with best precision [5].

To avoid such constraints, instead of relying on the analysis of modal parameters, some recently published methods propose the use of raw time-domain data (e.g., acceleration series) represented by means of Symbolic Data Objects (SDOs). This type of approach is drawing special attention over the last years [6–9] due to their great power of data fusion. Indeed, such a representation allows an efficient manipulation of large amounts of data with low computational efforts while keeping the original information sufficiently preserved.

Such methods are generally based on machine learning strategies, usually represented by classification techniques. However, some of them are still dependent on long damage-free baseline periods (supervised approach) [10]. Besides, they are frequently based on the prior knowledge of the structure's behavior: past or present. Therefore, they might not be always suitable for the SHM purposes, which is the real-time unsupervised monitoring.

The present work presents a tool able to conduct a fully automated unsupervised real-time SHM method for damage (or novelty) detection. The proposed approach starts from the premise that structural novelties (i.e., structural damage and/or interventions, such as maintenance/repair) affect both time and frequency

domain responses. Thus, a special SDO comprising these two domains is used. The *k*-medoids technique is chosen due to its attested robustness [11]. Finally, aiming at detecting damage, the procedure to obtain a single-valued index is also presented [12].

The proposed methodology is assessed by two experimental tests performed on real-scaled structures subjected to ambient vibration and the results obtained are very promising for long-term SHM real-world applications.

12.2 Data Fusion and Feature Extraction

12.2.1 Extraction of Symbolic Data Objects

A usual Symbolic Data Object (SDO) applied to civil engineering SHM is the Inter-Quartile Range object [6–8]. In fact, such an SDO represents the statistical distribution of the amplitudes of the original signal (raw data) in a very compact form by simply using two values per measuring channel: the 1st and 3rd quartiles. Alternatively, a richer way to describe such data is through histograms, where a higher number of divisions (classes) implies a more detailed (yet more massive) representation.

Nevertheless, none of these SDOs considers the information contained in the frequency spectrum of the original data. Indeed, as the SDOs perform the data fusion exclusively in the time domain, they miss relevant information related to the frequency domain.

This work uses a more complete SDO that embraces both *time* and *frequency* information of the original data [12]. The *time* aspect is represented by the three quartiles of the amplitude's distribution of the raw acceleration signals. The *frequency* aspect is characterized by the three quartiles of the vibrational energy distribution expressed in the frequency spectrum of the raw acceleration measurements.

For reference purposes, the new SDO is onwards named Time-Frequency IQRM object (TF-IQRM), where IQR stands for the Inter-Quartile Range, i.e., the difference between the third and the first quartiles (Q_3 and Q_1); and M stands for the median, i.e., the second quartile (Q_2). Moreover, the superscripts *T* and *F* indicate whether the quantity refers to time or frequency domain, respectively.

Figure 12.1 illustrates how to obtain the TF-IQRM object from raw data. In this example, the signal consists in a single numerically generated acceleration time history. Let the *number of channels* and the SDO *length* be denoted by *p* and *L*, respectively. Thus, for this particular example, *p* = 1 and *L* = 10 s. The signal is sampled at f_s = 102.4 Hz, yielding *L* = 1024 sampling points.

Thus, two triplets of quartiles compose the novel SDO: one for the time domain $[Q_1^T, Q_2^T, Q_3^T]$ and the other for the frequency domain $[Q_1^F, Q_2^F, Q_3^F]$.

The quartiles related to the time domain are computed over the statistical distribution of the amplitude values of the raw signal. The upper-right plot of Fig. 12.1 shows a histogram of such a distribution along with the representation of the three

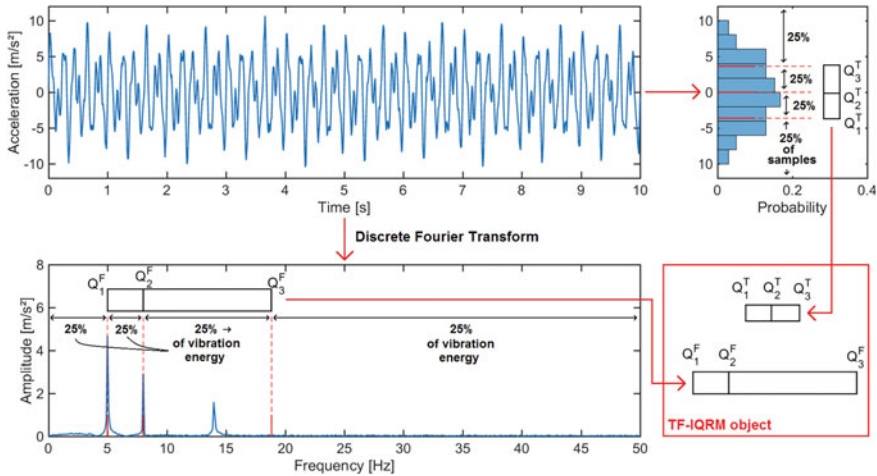


Fig. 12.1 Process to obtain the proposed SDO [12]

correspondent quartiles. This exemplifies how data fusion takes place, since only three values represent 1024 points.

The quartiles related to the frequency domain might be extracted by means of FFT (Fast Fourier Transform) or, alternatively, by any transformation such as PSD (Power Spectral Density), Prony, Levinson, among others. However, intending to keep a direct reciprocity between both domains (time and frequency) and to handle data as raw as possible, the authors have chosen to use the half-spectrum of the FFT. For instance, the present example has 1024 FFT points ($N = 2^{10}$). As already mentioned, the information concerning the energy distribution along the spectral range is expressed by its three quartiles (bottom-left plot of Fig. 12.1). Thus, besides its fusion power (1024 values down to just 3), such quartiles also allow the SDO to be sensitive to frequency shifts and redistributions of the vibration energy. In other words, the quartiles divide the spectrum into four regions with 25% of vibration energy each (analogy to the area below the curve). If the peaks are too sharp, the quartiles tend to fall near them.

Thus, for this example, the original signal containing 1024 points is symbolically represented by only six values comprising both time and frequency aspects, which constitute the TF-IQRM object.

For the case of a set of signals with an arbitrary number of channels p , the TF-IQRM object is represented by two triplets of p -dimensional vectors: one triplet for the time domain and another for the frequency domain, yielding six p -dimensional vectors. Let $Q_{k,r}$ be the k th quartile of channel $r = 1, 2, 3, \dots, p$, where p is the total number of channels of the raw data. The vectors containing the quartiles information of all channels of test i are expressed in Eqs. (12.1) and (12.2). Note that the p -dimensional vectors \mathbf{L}_i , \mathbf{M}_i and \mathbf{U}_i gather the first, second and third quartiles, respectively, of each one of the p channels.

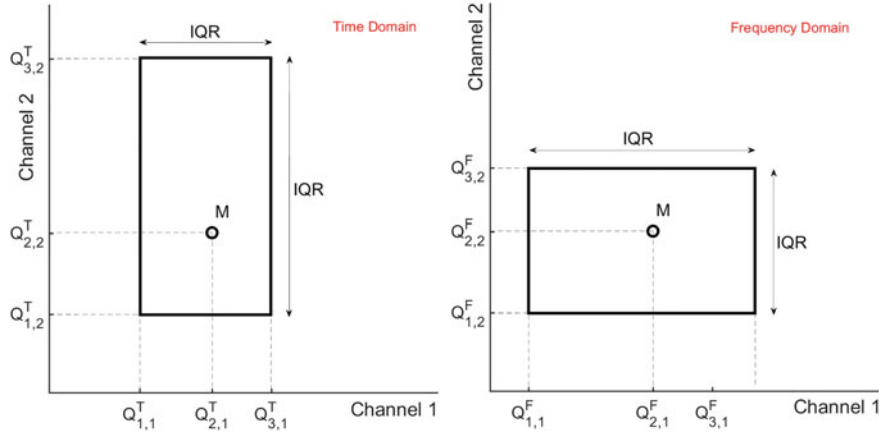


Fig. 12.2 Representation of a TF-IQRM object with two channels [12]

$$\mathbf{L}_i^T = \begin{bmatrix} Q_{1,1}^T \\ Q_{1,2}^T \\ Q_{1,3}^T \\ \vdots \\ Q_{1,p}^T \end{bmatrix}, \mathbf{M}_i^T = \begin{bmatrix} Q_{2,1}^T \\ Q_{2,2}^T \\ Q_{2,3}^T \\ \vdots \\ Q_{2,p}^T \end{bmatrix}, \mathbf{U}_i^T = \begin{bmatrix} Q_{3,1}^T \\ Q_{3,2}^T \\ Q_{3,3}^T \\ \vdots \\ Q_{3,p}^T \end{bmatrix}, \quad (12.1)$$

$$\mathbf{L}_i^F = \begin{bmatrix} Q_{1,1}^F \\ Q_{1,2}^F \\ Q_{1,3}^F \\ \vdots \\ Q_{1,p}^F \end{bmatrix}, \mathbf{M}_i^F = \begin{bmatrix} Q_{2,1}^T \\ Q_{2,2}^T \\ Q_{2,3}^T \\ \vdots \\ Q_{2,p}^T \end{bmatrix}, \mathbf{U}_i^F = \begin{bmatrix} Q_{3,1}^F \\ Q_{3,2}^F \\ Q_{3,3}^F \\ \vdots \\ Q_{3,p}^F \end{bmatrix}. \quad (12.2)$$

Geometrically, the TF-IQRM object consists in a pair of hyper-rectangles with a single point inside each one of them. The hyper-rectangles are related to both time and frequency domains. While the facets represent the interquartile range (IQR) of each channel, the point indicates the median (M). For the specific case of just two channels ($p = 2$) its geometry collapses into a pair of rectangles with a single point inside, as shown in Fig. 12.2.

12.2.2 Dissimilarity Between Symbolic Data Objects

The feature extraction procedure relies on the knowledge of the dissimilarity degree of patterns expressed in the SDOs. To do so, the distance measure $d_{i,j}$ (Eq. 12.3) between the TF-IQRM objects i and j is defined by an original symbolic metric:

$$d_{i,j} = \frac{\|\Delta_{i,j}^T\|}{\max(\overline{RMS_i}, \overline{RMS_j})} + \frac{\|\Delta_{i,j}^F\|}{N/2} \quad (12.3)$$

where N is the number of FFT points ($N/2$ is to account for the half-spectrum); $\overline{RMS_i}$ is the mean of the Root Mean Square values of all p channels of object i ; $\|\bullet\|$ is the Euclidean norm of vector \bullet ; $\Delta_{i,j}^T$ and $\Delta_{i,j}^F$ are the distance vectors, defined by Eq. (12.4):

$$\Delta_{i,j}^T = \begin{bmatrix} \|\mathbf{L}_j^T - \mathbf{L}_i^T\| \\ \|\mathbf{M}_j^T - \mathbf{M}_i^T\| \\ \|\mathbf{U}_j^T - \mathbf{U}_i^T\| \end{bmatrix}, \quad \Delta_{i,j}^F = \begin{bmatrix} \|\mathbf{L}_j^F - \mathbf{L}_i^F\| \\ \|\mathbf{M}_j^F - \mathbf{M}_i^F\| \\ \|\mathbf{U}_j^F - \mathbf{U}_i^F\| \end{bmatrix}. \quad (12.4)$$

The distance metric shown in Eq. (12.3) comprehends the sum of two dimensionless fractions. While the first one accounts for the dissimilarity in the time domain, the second one accounts for the dissimilarity in the frequency domain.

The quartiles of the frequency spectrum (Eq. (12.2)) are considered in this work as being the indexes of the FFT coefficients and, therefore, are dimensionless. One could alternatively consider such quartiles as actual frequency values (in Hz). However, in that case, the sampling frequency (f_s) should be used instead of N in Eq. (12.3). Thus, the distance metric would remain compatible in terms of units. Moreover, the proposed distance measure fulfills the requirements for being a valid symbolic metric, which are:

- Symmetry: the metric always generates a symmetric dissimilarity matrix, i.e. $d_{i,j} = d_{j,i}$ for any i and j ;
- Non-negative distances: the metric always provides values equal or greater than zero;
- The metric always provides a null distance measure when a SDO is compared to itself, i.e. $d_{i,j} = 0$ when $i = j$, which generates zeros in all diagonal elements of the distance matrix.

12.2.3 Extraction of Unidimensional Feature

The last step for the feature extraction procedure is to obtain a unidimensional quantity capable of measuring the degree of novelty present within a time-window. Such a feature is called *Novelty Index* (NI) and is herein defined as the largest distance between all possible pairs of prototypes¹ by means of the distance matrix already defined. Hence, considering a time-window containing S SDOs, the NI is computed as shown in Eq. (12.5):

¹ Each group is represented by one prototype [12], which is the cluster's medoid SDO (i.e., the object that has the minimum sum of distances to the rest of other intra-cluster objects).

$$\text{NI} = \max(d_{i,j}) \mid i, j = t_1, t_2, \dots, t_k \quad (12.5)$$

where $d_{i,j}$ is the distance calculated using Eq. (12.3) and t_1, t_2, \dots, t_k are the indexes of SDOs assigned as being the prototypes of each one of the k clusters, with $k \in [2, S - 1]$.

It is worth mentioning that the NI values are always positive since they are directly obtained from distance values.

12.2.4 Schematic Overview

To better illustrate the entire process to obtain the NI value, let us consider the following example: Fig. 12.3 shows a time-window of a two-channel signal containing 10,000 raw data points (1). The procedure starts with the extraction of the SDOs, as presented in Sect. 12.2.1. In this example, the signal is represented by 5 SDOs ($S = 5$), each one with 2000 points ($L = 10,000/5 = 2000$) (2). In the sequence, the dissimilarity between the SDOs is computed according to Sect. 12.2.2 to generate a 5×5 distance matrix (3), depicted as a gray-scaled image. The closer to white, the higher the distance between two SDOs. At this point, the choice of prototypes is performed. To do so, the k -medoids clustering technique is applied as established in Sect. 12.2.3. In this case, $k = 2$ and the chosen prototypes are the second and fourth SDOs (4). Finally, the NI extraction is performed by evaluating the largest distance between the prototypes as explained in Sect. 12.2.4. In this example, since there are only two prototypes, the distance between them is the NI itself (12.5).

12.3 Feature Classification

A powerful data fusion was achieved (as shown in Sect. 12.2) by extracting the TF-IQRM objects from raw data and proceeding to the NI computation. Thus, a time-window comprising thousands of points is represented by a single value, which is proportional to the novelty degree. However, this isolated value is insufficient to establish precisely whether there is any structural change or damage. For instance, the time-window presented in Fig. 12.4 has a NI value equal to 0.484. Is that feature pointing out to any damage (or novelty) within the analyzed time-window? The answer is provided by what is called *feature classification*.

12.3.1 Confidence Boundaries

Like what was presented in [7, 12], this work suggests the tracking of successive NI values as the time-window advances over time. Hence, as a NI series is generated,

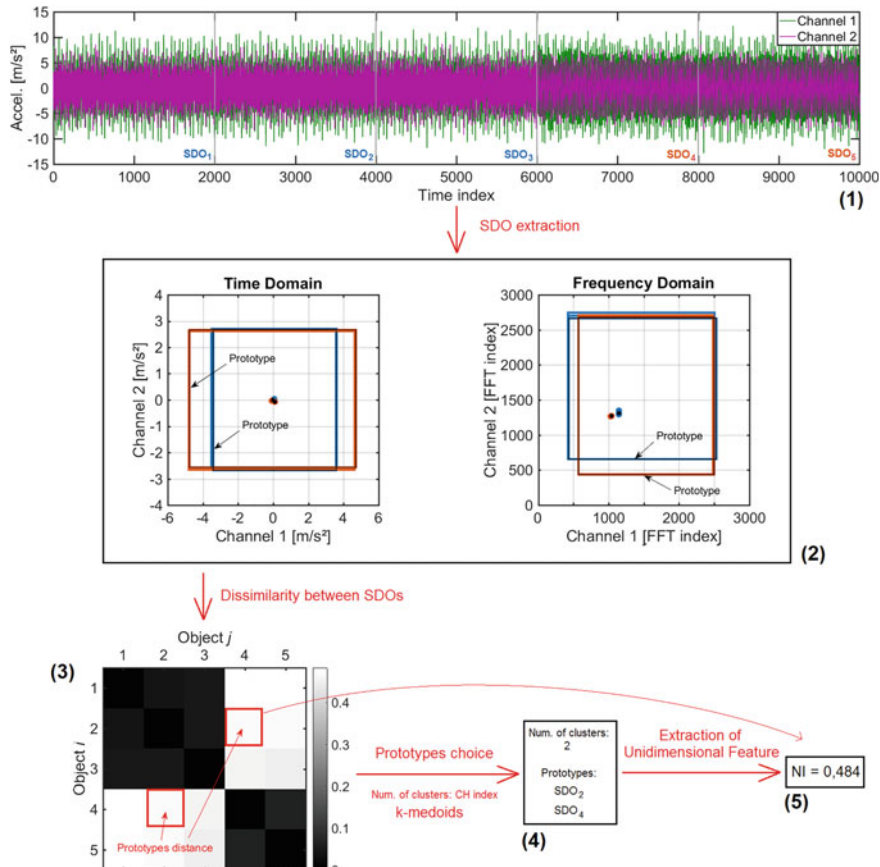


Fig. 12.3 Schematic overview of the unidimensional feature extraction [12]

an outlier analysis of their values is performed. If the newly evaluated NI is greater than the upper confidence boundary (named CB), a novelty detection is triggered.

To keep the unsupervised premise, such confidence boundary is not defined through the knowledge of a long undamaged baseline period. Instead, this limit is dynamically defined within each time-window by considering the last S values of NI as samples. It is assumed that the undamaged behavior would generate a t-Student distribution with $S - 1$ degrees of freedom of NI values, instead of normal distribution, due to the small sampling population.

Thus, the upper confidence boundary defined within the time-window with index TW is defined in Eq. (12.6):

$$\text{CB}_{TW} = \text{E[NI]}_{TW} + t_{[S-1, 99\%]} \times \frac{\text{E}[NI - \text{E[NI]}_{TW}]_{TW}}{\sqrt{S}} \quad (12.6)$$

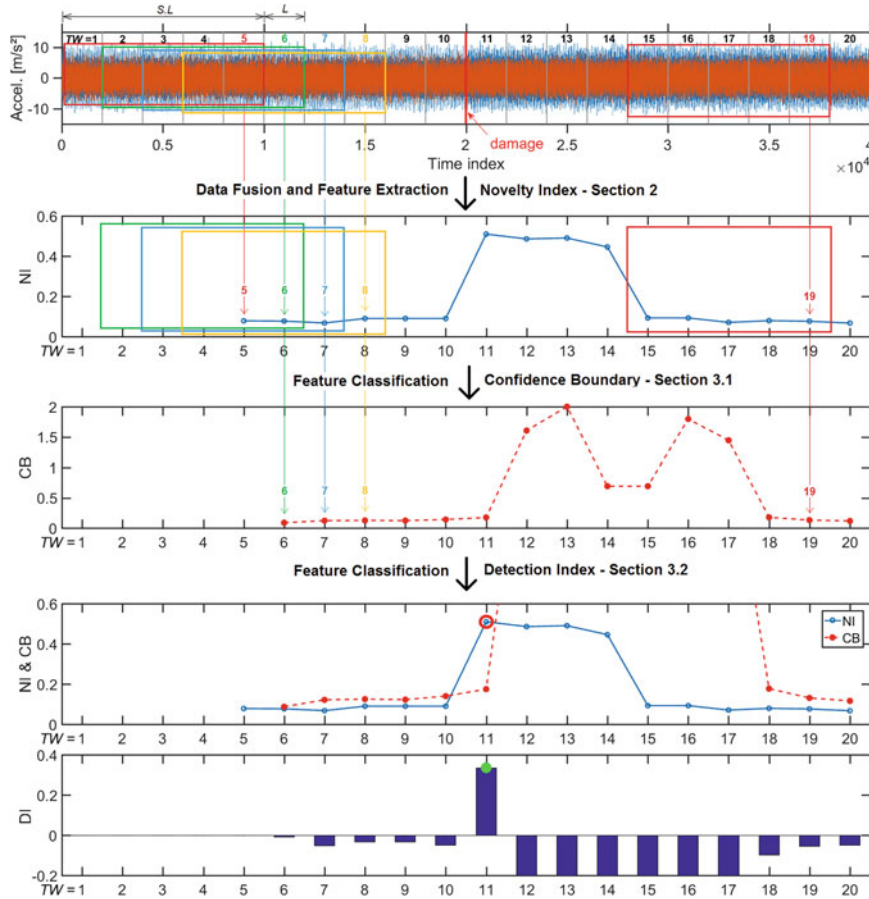


Fig. 12.4 Schematic overview of the entire methodology [12]

where $E[NI]_{TW}$ is the expected value of NI within the time-window TW ; $t_{[S-1, 99\%]}$ is the 99th percentile of a t-Student distribution with $S - 1$ degrees of freedom and $E[NI - E[NI]_{TW}]_{TW}$ is the variability, i.e., the expected value of the variation of NI values from its expected value $E[NI]_{TW}$.

For robustness, the median (or the 50th percentile) estimator is used as the expected value of the NI population once it achieves the maximum possible breakpoint i.e., 50%. In the same way, a robust estimator for the variability is adopted as being the S_n estimator proposed by Rousseeuw and Croux [13]. Such assumptions can be formally described by Eqs. (12.7) and (12.8):

$$E[NI]_{TW} = \text{med}_i(NI_i); i = TW - S + 1, \dots, TW \quad (12.7)$$

and

$$\begin{aligned} E[NI - E[NI]_{TW}]_{TW} = S_n = & 1.1926 \operatorname{med}_i \left\{ \operatorname{med}_j |NI_i - NI_j| \right\}; \\ i, j = & TW - S + 1, \dots, TW \end{aligned} \quad (12.8)$$

where {} stands for an array and 1.1926 is a factor defined in [10] with the objective of making this estimator consistent with Gaussian populations.

Hence, by substituting the statements of Eqs. (12.7) and (12.8) into Eq. (12.6), one obtains Eq. (12.9):

$$\begin{aligned} CB_{TW} = & \underbrace{\operatorname{med}_i (NI_i)}_{\text{Expected Value}} + t_{[S-1, 99\%]} \times \underbrace{\frac{1.1926 \operatorname{med}_i \left\{ \operatorname{med}_j |NI_i - NI_j| \right\}}{\sqrt{S}}}_{\text{Variability}}; \\ i, j = & TW - S + 1, \dots, TW \end{aligned} \quad (12.9)$$

12.3.2 Detection Index

Finally, the Detection Index (DI) related to newly acquired SDO with index TW is simply defined by Eq. (12.10):

$$DI_{TW} = NI_{TW} - CB_{TW} \quad (12.10)$$

Therefore, if DI_{TW} is positive, a damage (or structural novelty) is said to have occurred in the SDO with index TW . Thus, the alarm is expected to sound almost in real-time, with the maximum delay equal to L , which is the length of the newly acquired *SDO*.

The time delay until the first DI computation is called *initialization period*, rather than baseline period. It has the duration of $(S + 1)L$ and is further explored in the following section.

12.3.3 Overall Scheme of the Methodology

This section provides an illustrative example to clarify the concept behind both CB and DI values. It also summarizes the entire methodology for damage detection proposed in this work.

Let us consider the same case showed in Sect. 12.2.4 under continuous monitoring, generating a sequence of time-windows. This provides, purposely, a series of NI values. At each NI computation described in Sect. 12.2, a CB value is also computed using the “memory” of the last S NI values, as shown in Sect. 12.3.1. Whenever NI

surpasses CB, damage is immediately characterized (DI positive), as described in Sect. 12.3.2.

The history of such a continuous monitoring is depicted in Fig. 12.4, where time-windows comprising five 2-channel SDOs of 2000 points ($S = 5$ and $L = 2000$) are used to perform a clear damage detection, which occurred immediately after the acquisition of the 11th SDO. It is worth noting that the first NI value is computed only when the time-window accumulated S SDOs ($TW = 5$, displayed in red). From that moment, after L/f_s seconds, a new SDO is extracted and a new time-window is defined ($TW = 6$, displayed in green). Again, a new value of NI is computed. However, since two values are available, a CB and a DI are also calculated ($TW = 6$).

By means of the monitoring history of Fig. 12.4, it is possible to see that the NI grows so sharply right after the acquisition of the 11th SDO that it falls out of the 99% confidence interval, which alarms for a new behavior (delayed L/f_s seconds from the actual occurrence). After $S - 1$ new SDOs ($TW = 15$), when the old behavior is no longer within the time-window, the NI drops back to its usual values. This shows the adaptiveness and responsiveness of the proposed technique.

The proposed methodology focuses on the detection of discrete damage, be they small or severe. Thus, for the cases of gradually increasing damage—as those due to concrete creep or support-soil densification (foundation settlement)—even if large enough time-windows are used, the probability of detecting such gradual damage is rather small.

Another important aspect of the proposed technique is that two consecutive damage events—be they of small or large magnitude—can be detected correctly by employing short time-windows lengths. However, as an immediate consequence, false alarms are more likely to be sounded.

Finally, this methodology cannot identify the nature of an abnormal events. Thus, in the event of an alarm (be it false or positive), a maintenance action should be considered.

12.4 Case Study 1: Railway Viaduct

The studied viaduct is an embedded steel bridge located on the South-East high-speed track in France at the kilometric point 075 + 317; it crosses the secondary road 939 between the towns of Sens and Soucy in the Yonne County (see Fig. 12.5a).

The measurements previously carried out by SNCF (*Société Nationale des Chemins de Fer Français*—French National Railway Company) on this structure revealed vibrations and excessive deformation of the deck due to TGV (*Trains à Grande Vitesse*—high-speed trains) crossings. These findings led the SNCF's Department of Infrastructure to modify the support conditions of the deck—previously simply supported—by performing a mechanical embedding of the deck's ends on the abutments (see Fig. 12.5b) [14].



Fig. 12.5 **a** Overview of the viaduct during a TGV crossing; **b** Detail of the strengthening procedure taking place

A dynamic monitoring of this railway bridge was performed to characterize and to quantify the effect of the strengthening procedure between June 23rd to 26th in 2003. This strengthening procedure consisted in tightening special bearings to shift the first natural frequency (around 5 Hz) from the excitation frequency due to train crossings (around 4–5 Hz). To be effective and relevant, dynamic testing must precise the selection of the test conditions (particularly regarding the excitation source), the choice of the data to acquire on a given frequency band, the definition of the number and the localization of the sensors, the acquisition and the data processing, and the determination of the modal properties [15].

The complete instrumentation put up in place and the conditions for intervention by SITES (*Ingénierie, Instrumentation, Monitoring et Inspection*—Engineering, Instrumentation, Monitoring, and Inspection) and SNCF are detailed in the reference [16]. This section is limited to recalling the essential elements of this instrumentation, useful for understanding the calculations carried out.

The instrumentation set up at the viaduct includes the following sensors:

- 3 *vertical displacement sensors* (SVH Kyowa PD-A 0–100 cm) placed between the parapet and the deck: each displacement sensor is mounted on a support fixed on the parapet and measures the relative displacement between the parapet (supposedly fixed) and the deck.
- 8 *vertical accelerometers* and 2 *horizontal accelerometers* (longitudinal and lateral), model Kyowa AS-1 GB ($\pm 9.807 \text{ m/s}^2$, 0.5 mV/V) under the deck: each accelerometer is mounted on a support fixed under the deck at the level of the beams.
- 2 *temperature sensors* (Pt100) respectively below and above the parapet.
- 2 Q.Bridge acquisition systems over the tracks: each Q.Bridge measures the axle loads at the entry and exit of the structure.

The supports were both glued and mechanically kept by different assemblies which allow adjusting the orientation of each sensor [16]. Both displacement sensors



Fig. 12.6 Displacement sensors and accelerometers (view from below the deck)

and accelerometers were connected by cables running under the deck to a connection box. Such box was fixed on a wall at about 3 m from the ground (Fig. 12.6).

The sensor supports, cables and the connection box remained fixed on the structure while all the sensors, with the exception of the Q.Bridges, and the acquisition chain were installed and then removed during each measurement campaign.

For a merely informative purpose, the mean values and respective ± 1 standard deviations of the first four natural frequencies of the structure are presented in Table 12.1. It is possible to observe the frequency values before and after the structural reinforcement.

In this specific work, only the data registered by the 8 vertical piezoelectric accelerometers is used. The instrumentation plan is shown in Fig. 12.7.

The sampling frequency was fixed at 4096 Hz. The signal analyses due to train crossings highlighted a good repeatability. Each time the train passed over the viaduct, 2 s of forced vibrations were recorded. This is equivalent to $L = 8192$ classical data points per channel (Fig. 12.8). The monitoring campaign consisted in 13 tests before and 13 tests after the structural intervention. The complete acceleration history can be seen in Fig. 12.9.

This application aims to test if the proposed tool is suitable to detect changes in the structure's behavior. It is important to emphasize that no modal identification or data normalization procedures are performed previously. The idea is to observe if

Table 12.1 Natural frequencies of the viaduct before and after the strengthening [15]

#	Frequency (Hz)	
	Before strengthening	After strengthening
1	5.848 ± 0.242	6.461 ± 0.267
2	8.507 ± 0.322	8.592 ± 0.415
3	13.017 ± 0.305	13.078 ± 0.296
4	16.850 ± 0.502	17.142 ± 0.507

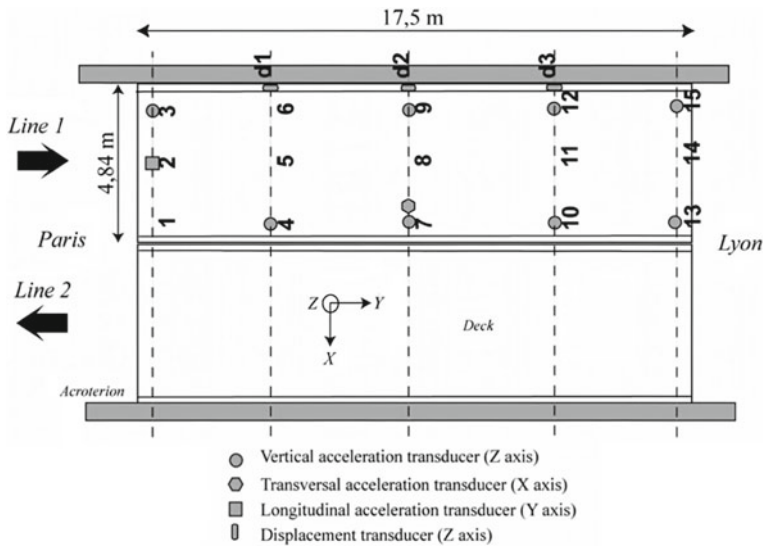


Fig. 12.7 Instrumentation plan of the vertical accelerometers

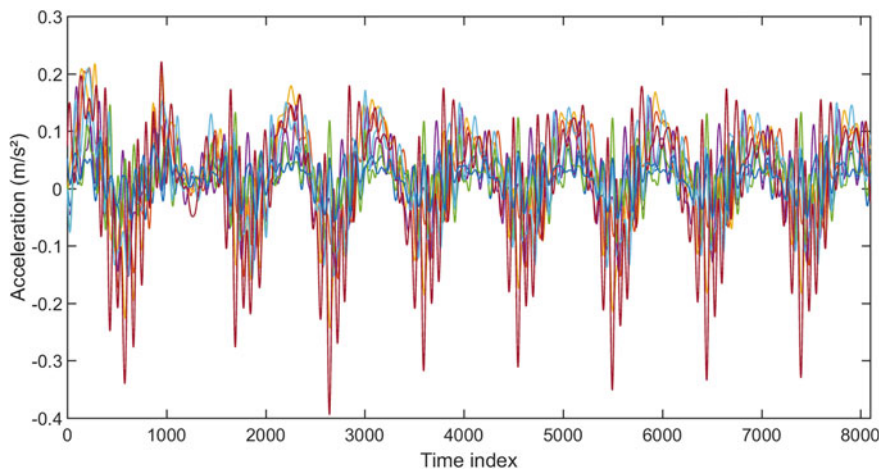


Fig. 12.8 Acceleration data acquired during a single train passage

the proposed approach is robust enough to detect novelties even in the presence of noise, ambient and environmental effects. The feature extraction and classification are carried out at each time-window directly from the raw signals provided by the eight vertical accelerometers.

It is noticeable that false alarms are more prone to occur as the SDO length decreases. Such a phenomenon is quite natural, since the SDO is carrying little information. Consequently, the use of short SDOs leads to many alarms (positive

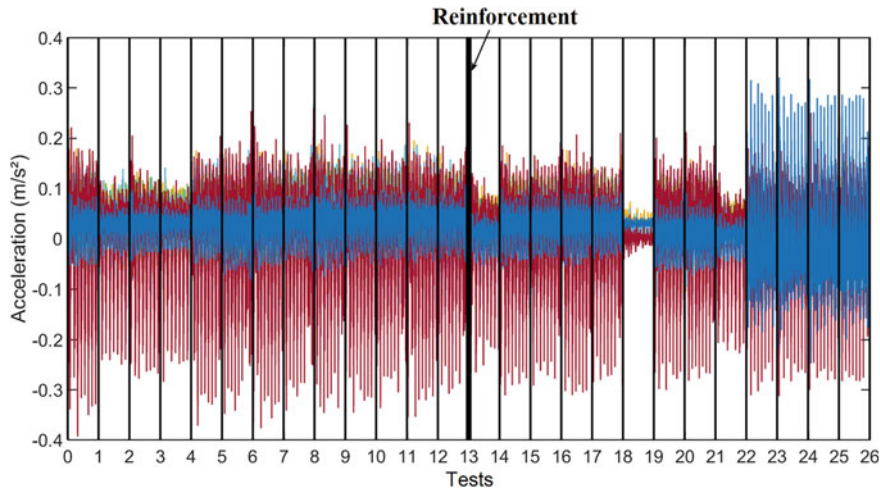


Fig. 12.9 Complete raw data history showing each test boundary (one test per train pass)

DIs), be they real or false. However, this type of SDOs has the advantage of better accusing the occurrence of damage in a shorter time delay, almost instantaneously. Conversely, the use of longer SDOs leads to more accuracy, i.e., the rate of real alarms compared to false alarms rises significantly. Still, as they surpass a certain length, which is difficult to determine, they tend to be prone to miss small damage scenarios. These explanations highlight the essence of the behavior of the detection method when one adopts different SDO lengths.

Due to the difficult to choose the length of the SDO (L), a set of different predefined values of L is tested. By doing this, an alarm tends to be real if more than 50% of the cases have at least one positive value of DI for the same test. The other parameters, i.e., the number of SDO per time-window (S) and the number of FFT terms (N) are kept fixed as 5 and 2^{13} , respectively. For this application, the proposed approach considers 9 different TF-IQRM object lengths (L): 0.125; 0.25; 0.50; 0.75; 1.00; 1.25; 1.50; 1.75 and 2.00 s.

As Fig. 12.10 shows, the proposed tool has correctly pointed out that 89% of the cases have an object with positive DI value that intercepts the test number 14 (from 26 to 28 s), which is the first test containing the data expressing the new behavior. Moreover, no other test had more than 50% of detection rate, which proves the tool's robustness. Despite being an unsupervised approach, the first instants must be used as a short period of training (or initialization) so that the method can “learn” about the structure's behavior. The larger the size of the object, the longer the initialization period.

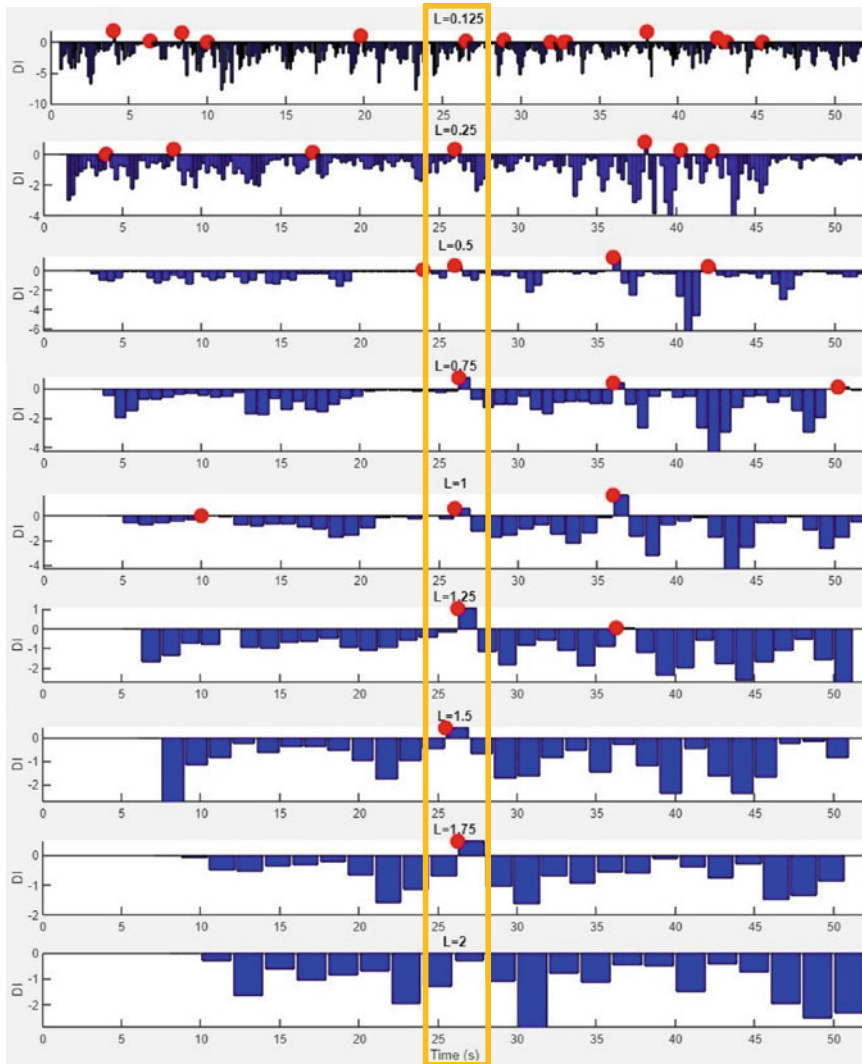


Fig. 12.10 *Detection Indexes for the 9 different SDO lengths*

12.5 Case Study 2: Highway Bridge

The PI-57 bridge (Fig. 12.11) is a double-deck bridge located near the town of Senlis in France, crossing the Oise river, and carrying the A1 motorway connecting Paris to Lille. The bridge, a 116.50 m long, cast-in-place, post-tensioned segmental structure built in 1965, consists of three continuous spans of 18.00, 80.50, 18.00 m [17]. The two lateral spans play the role of counterweights.



Fig. 12.11 Monitored bridge over Oise River, France

This slender and elegant structure experienced various problems and distress during and after its construction resulting in localized cracking and increasing deflection in the central part. These problems were due mainly to insufficient prestressing because of lowering shrinkage and creep effects, and a limited knowledge regarding thermal stresses at the construction time. Because of the potential risk of cracking in the deck, the numerical studies showed that the long-term integrity could be affected if corrective measures were not taken immediately. Based on these technical evaluations and considering the structure's importance, the Société des Autoroutes du Nord et de l'Est de la France (SANEF), the concessionary motor-way company, decided to strengthen the two decks. Additional longitudinal prestressing would correct the lack of sufficient prestressing and the reinforcement work was scheduled in the summer of 2009. The strengthening consists in reducing the tensile stresses under live loads to 1.5 MPa at the bottom part of the bridge cross-sections. These tensile stresses may reach 5.10 MPa at the mid-span cross-section. The external prestressing must at least induce 6.60 MPa as compressive stresses. From calculations performed by the ACOGEC design office under the supervision of the SANEF motorway company, a straight profile for the external prestressing cables has been chosen. The anchorages are realized on the backside of the cross-girders located on the bridge piles. The total prestressing force has been evaluated to 32,000 kN corresponding to eight 19T15S cables. With this strengthening the displacement at mid-span moves from -2.44 to -0.69 cm under SLS dead and live load effects. A small longitudinal displacement is expected (4.02 mm). No extra-displacements occur on the piles.

To check on one hand the variability of the structural behavior due to thermal effects and on the other hand to evaluate the efficiency of the strengthening procedure, a vibration-based monitoring was conducted: it consisted in installing accelerometers before and after reinforcement. The first campaign of measurements took place between November 21st, 2008 and April 3rd, 2009. The second campaign, after reinforcement, started on November 21st, 2009 and ended on April 3rd, 2010. Dynamic tests were performed under ambient excitation: the traffic was used as a source of excitation.

Sixteen piezo-electric accelerometers (Brüel & Kjær 4507B-005 with sensitivity 1 V/g, frequency range from 0.4 to 6000 Hz, maximum operational level ± 5 g, temperature range from -54 to 100 °C) and seven temperature sensors (Pt100 class B) were installed on the most deficient bridge deck (Lille/Paris—Fig. 12.12). The data acquisition system was composed of two separate data acquisition systems. For the acceleration recording, a data programmable controller Gantner E-PAC DL was used and connected to an 8 GB USB flash drive. Data was transferred by a TCP/IP modem. Measuring modules e-bloxx Gantner A2-1 connected the piezo-electric sensors to the E-PAC DL controller. For the temperature recording, a data logger Gantner IDL100 was used and data was transferred by a GSM modem. Accelerations were filtered within the 0–30 Hz frequency range and sampling was set to 0.004 s during 5 min.

For making amenable the data processing and avoiding any loss of information in the case of internet breakage, data is only recorded every 3 h over a 24 h period and stored on a buffer hard disk.

For the first campaign, 972 tests were recorded. The second campaign had a total of 1164 tests recorded. Sixteen accelerometers measured vertical accelerations and other three measured longitudinal accelerations. The instrumentation scheme allows identifying flexural vertical modal shapes, torsional and longitudinal vibration modes. Temperature measurements were made on seven different locations across a bridge deck cross-section (Fig. 12.13).

For illustrative purposes, the mean values and respective standard deviations of the first four natural frequencies of the structure are presented in Table 12.2.



Fig. 12.12 Accelerometers (left) and temperature sensors placed inside the bridge's cross section

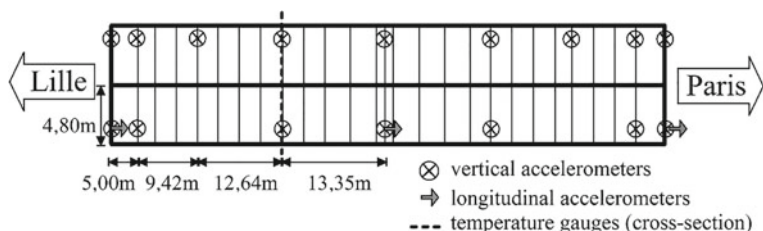


Fig. 12.13 Instrumentation plan

Table 12.2 Natural frequencies of the bridge before and after the reinforcement [17]

#	Frequency (Hz)	
	Before strengthening	After strengthening
1	2.23 ± 0.053	2.29 ± 0.067
2	4.89 ± 0.173	4.95 ± 0.088
3	6.84 ± 0.111	6.93 ± 0.161
4	8.48 ± 0.173	8.51 ± 0.135
5	11.00 ± 0.165	11.08 ± 0.176

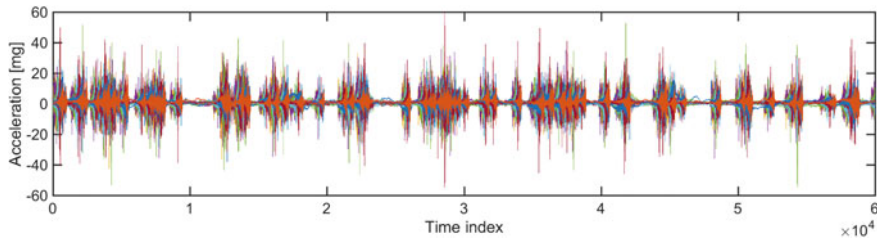


Fig. 12.14 Typical 4-min signal acquired at every hour

For the application of the methodology described in Sects. 12.2 and 12.3, the number of SDOs per time-window is kept unchanged ($S=5$). The same is done with the number of FFT points ($N=2^{13}$). Also, 11 different TF-IQRM object lengths (L) ranging from 1 to 11 min, equally spaced by one minute, are considered.

Figure 12.14 shows a typical 5-min acceleration signal registered by the 16 accelerometers. This is the typical package of information, obtained every three hours, fused in TF-IQRM symbolic objects.

Figure 12.15 shows the resulting graphics using the 11 values of L . Here, only 50 tests before the reinforcement (from March 26th, 2009 to April 3rd, 2009) and 50 tests after the reinforcement (from October 13th, 2009 to October 19th, 2009). The change of the structural state occurs over time 12,000 s (200 min), that is the middle of the graphics.

It is important to note that the cycles of day-and-night, which impacts temperature and traffic levels (environmental factors), did not influence the methodology performance. This is quite an interesting result, since no signal normalization procedure is employed by the proposed technique (except for the use of the RMS value, implicit in the symbolic metric). These results indicate that 8/11 (73%) of the cases had a positive DI value intercepting the first signal right after the reinforcement (October 13th, 2009). No other signal had more than 50% detection.

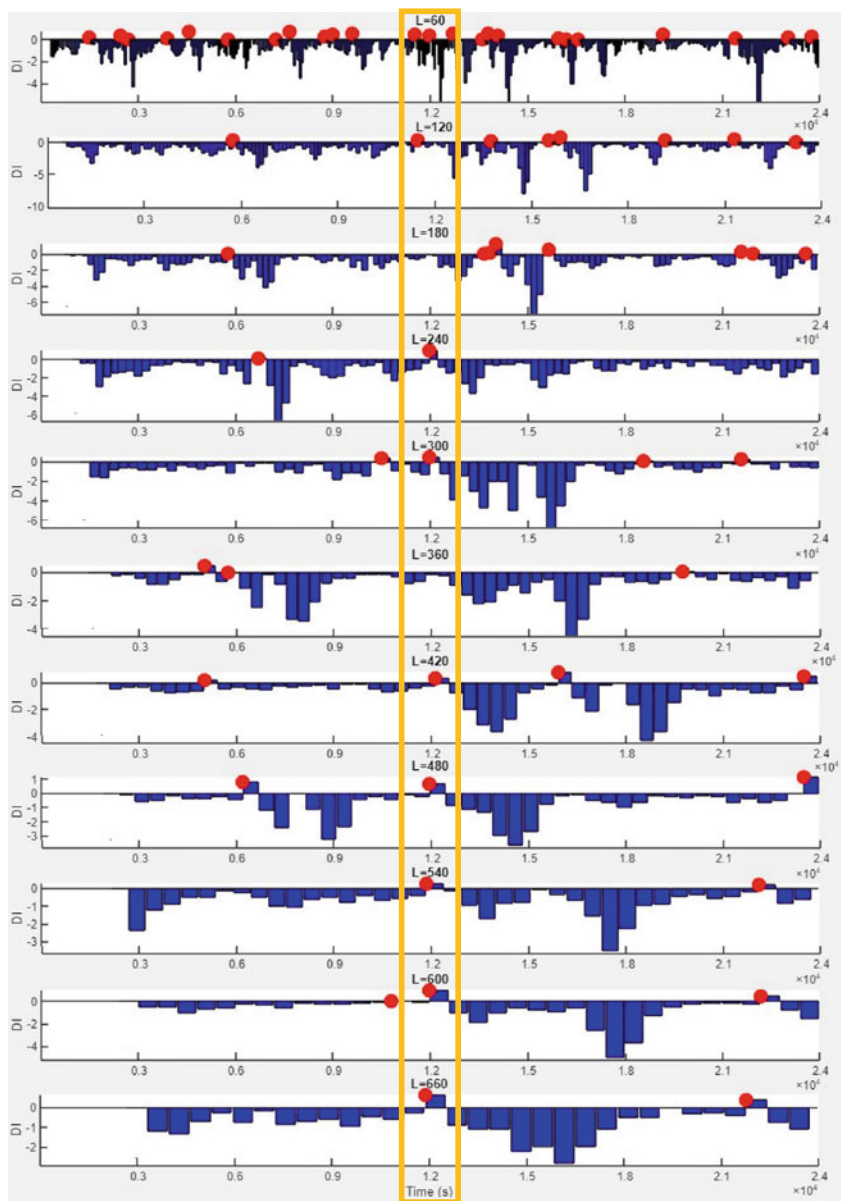


Fig. 12.15 *Detection Indexes for the 11 different SDO lengths*

12.6 Final Remarks

This work presented a tool able to perform a fully automated real-time unsupervised damage detection on structures subjected to ambient vibration. The continuous acquisition of signals is transformed into packages of compact information expressed by the proposed novel symbolic object, called TF-IQRM. Such an original representation embraces both time and frequency responses of structural dynamic measurements. Then, these objects are used to feed a procedure of pattern recognition (k -medoids clustering) within a moving time-window to generate single-valued features (NI), which indicates the degree of structural novelty. By tracking the evolution of such an index, an outlier analysis is performed yielding the Detection Index (DI), which is statistically analyzed based on continuous parallel monitoring with different lengths of symbolic objects. Such an index can indicate the current structure's condition, i.e., damaged, or undamaged.

To assess the proposed approach, two real-case experimental applications were explored. The results obtained have shown that the tool was capable of handling environmental factors, such as temperature, traffic, wind, among others. Even without an explicit normalization step, the algorithms precisely detected the novelties, which in these cases are the structural strengthening.

Hence, since the proposed technique is also sensitive to small damage (usually invisible to human inspections) and rather insensitive to environmental/operational scenarios, this method represents an important aid to maintenance schedules for preventive actions.

Acknowledgements The authors would like to thank CAPES (Coordenação de Aperfeiçoamento de Pessoal de Nível Superior), CNPq (Conselho Nacional de Desenvolvimento Científico e Tecnológico), grants “304329/2019-3” and “311576/2018-4”, and FAPEMIG (Fundação de Amparo à Pesquisa do Estado de Minas Gerais), grants “PPM-0001-18” and “PPM-00106-17”, for the financial support. The authors also thank IFSTTAR (former LCPC—Laboratoire Central des Ponts et Chaussées), SANEF (Société des Autoroutes du Nord et de l'Est de la France, project 0560V407) and SNCF (Société Nationale des Chemins de fer Français) for the data used in this paper (project 01V0527 RGCU “Evaluation dynamique des ponts”).

References

1. Glanz J, Pianigiani G, White J, Patanjali K (2018) Genoa bridge collapse: the road to tragedy. New York Times. <https://www.nytimes.com/interactive/2018/09/06/world/europe/genoa-italy-bridge.html>. Last Accessed 26 Oct 2020
2. Fan W, Qiao P (2011) Vibration-based damage identification methods: a review and comparative study. Struct Health Monit 10(1):83–111
3. Sony S, Laventure S, Sadhu A (2019) A literature review of next-generation smart sensing technology in structural health monitoring. Struct Control Health Monit 26(3)
4. Sadhu A, Narasimhan S, Antoni J (2017) A review of output-only structural mode identification literature employing blind source separation methods. Mech Syst Signal Process 94:415–431

5. Cardoso R, Cury A, Barbosa F (2017) A robust methodology for modal parameters estimation applied to SHM. *Mech Syst Signal Process* 95:24–41
6. Santos J, Crémona C, Orcesi A, Silveira P (2017) Early damage detection based on pattern recognition and data fusion. *J Struct Eng* 143(2)
7. Santos J, Orcesi A, Crémona C, Silveira P (2015) Baseline-free real-time assessment of structural changes. *Struct Infrastruct Eng Mainten Manag Life-Cycle Perform* 11(2):145–161
8. Cardoso R, Cury A, Barbosa F, Gentile C (2019) Unsupervised real-time SHM technique based on novelty indexes. *Struct Control Health Monit* 26(7):e2364
9. Alves V, Cury A, Roitman N, Magluta C, Cremona C (2015) Novelty detection for SHM using raw acceleration measurements. *Struct Control Health Monit* 22(9):1193–1207
10. Alves V, Cury A, Roitman N, Magluta C, Crémona C (2015) Structural modification assessment using supervised learning methods applied to vibration data. *Eng Struct* 99:439–448
11. Kaufman L, Rousseeuw P (2009) Finding groups in data: an introduction to cluster analysis. Wiley & Sons Inc., Hoboken, New Jersey
12. Cardoso RA, Cury A, Barbosa F (2019) Automated real-time damage detection strategy using raw dynamic measurements. *Eng Struct* 196
13. Rousseeuw P, Croux C (1993) Alternatives to the median absolute deviation. *J Am Stat Assoc* 88(424):1273–1283
14. Pissot J, Martin P (1998) Surveillance accélérométrique des tabliers à poutrelles enrobées—Ligne TGV Paris-Sud-Est—Pont Rail 75+317. Rapport SNCF R 6770-98-01
15. Cury A, Crémona C, Diday E (2010) Application of symbolic data analysis for structural modification assessment. *Eng Struct* 32(3):762–775
16. Ducret D, Caron H, Boufridi N (2003) Programme de Recherche Evaluation Dynamique des Ponts—Instrumentation et Mesures Dynamiques sur le Pont-Rail SNCF du PK 075+317 de la Ligne à Grande Vitesse Paris Sud-Est—Campagne de Mesures no 1. Rapport SITES R 03 PS 15400
17. Cury A, Cremona C, Dumoulin J (2012) Long-term monitoring of a PSC box girder bridge: operational modal analysis, data normalization and structural modification assessment. *Mech Syst Signal Process* 33:13–37

Part III

Buildings

Chapter 13

Innovative Approach on Building Pathology Testing and Analysis



Nuno M. M. Ramos  and Pedro F. Pereira 

Abstract The continuous innovation in construction introduces new materials and components that often cannot be analysed with standard testing techniques. Moreover, the lack of information on reference values may prevent the adequate interpretation of the test results. This chapter is focused on the application of innovative in-situ tests that address non-structural materials and components. A review of recent techniques and case studies is conducted, focusing on pathological manifestations that stem from an inadequate hygrothermal behaviour. The determination of the moisture content by non-destructive or semi-destructive techniques is, in that sense, a key example. The other aspect addressed in this chapter is the advanced monitoring of hygrothermal parameters and others that can be of relevance. It provides a clear evolution from point measurements to a continuous assessment of the building state. Hence, the implementation of advanced monitoring techniques in Building Digital Twins is described and its potential for building pathology studies in the logic of asset management is explored. By exploring the literature, the most promising approaches for specific innovative components are analysed.

Keywords Building pathology · Hygrothermal behaviour · Moisture · In-situ testing · Building digital twins

13.1 Introduction

Building pathology learnings often result from the observation and testing of anomalies in existing buildings. Construction frequently incorporates innovative materials and solutions that eventually may develop anomalies. It is important that those anomalies are rapidly detected and studied so that they are not repeated. The growing digitalization of the Architecture, Engineering and Construction (AEC) Industry

N. M. M. Ramos (✉) · P. F. Pereira
CONSTRUCT-LFC, Faculty of Engineering (FEUP), University of Porto, Porto, Portugal
e-mail: nmmr@fe.up.pt

P. F. Pereira
e-mail: fpfp@fe.up.pt

has opened the door for an in-depth analysis of the behaviour of buildings and components.

The availability of affordable sensors has enlarged the possibility of collecting large amounts of data for the characterization of buildings performance in different fields. Also, the possibility to digitally store the collected data eventually combined with remote access enables high workability of the measurement results.

The evolution of digital platforms is another strong driver to enabling the usability of collected data, allowing the development of dashboards with synthetic information derived from data analysis tools.

This chapter focus on innovative testing on building pathology that stems from an inadequate hygrothermal behaviour. The study of this specific type of anomalies can benefit from the digital evolution of the AEC, and involve practitioners, dealing with detailed technical data and building managers using synthetic information.

13.2 Building Digital Twins

The initial concept of Digital Twins (DT) was developed by Glaessgen and Stargel [1]. The concept was later applied by NASA before its dissemination amongst the scientific and technical community. The initial definition of a DT was a multiphysics and multiscale simulation with embedded statistics of a built system through a state of the art digital modelling, updated with sensor information, as a mirror of its existing twin. Different knowledge areas have adapted the concept with several variations. Manufacturing companies use digital twins to collect the life cycle data of their products and define preventive maintenance procedures (Fig. 13.1) [2]. Health applications combine wearable medical devices and DT for monitoring and diagnosis [3].

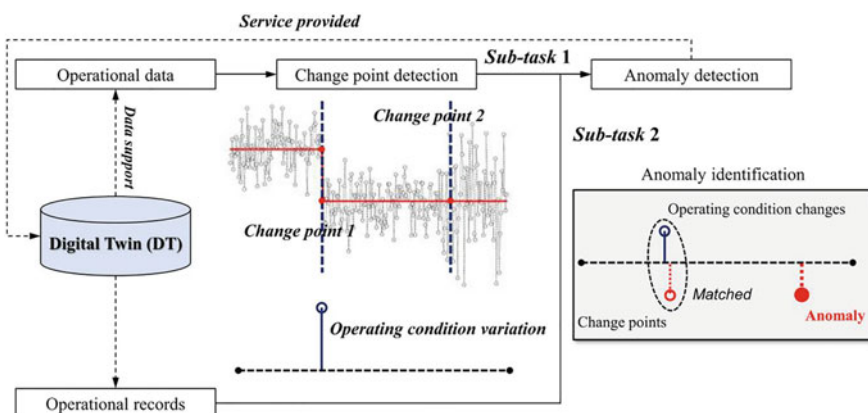


Fig. 13.1 Procedure of anomaly detection for asset monitoring [2]

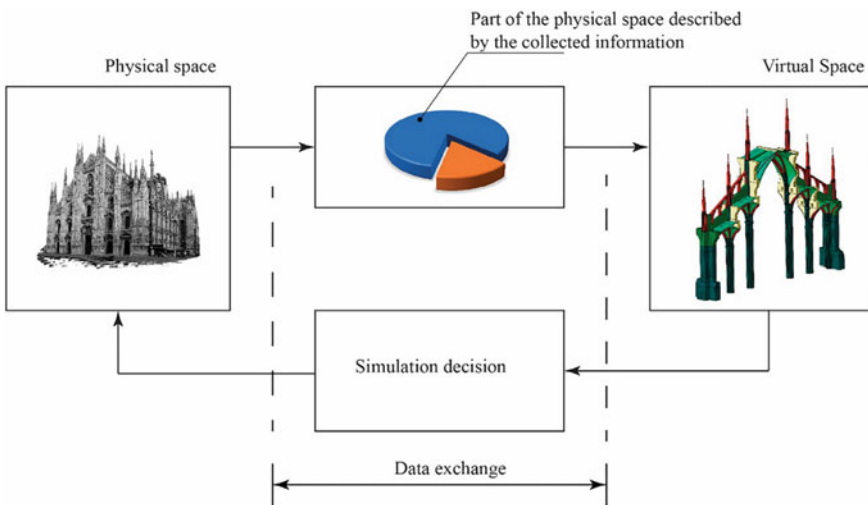


Fig. 13.2 Schematic representation of the Digital Twin concept for historical buildings [5]

The DT classification depends on applicability and complexity [3]. Complexity can include three levels: light with unnecessary details; multiphysics and multiscale model combining data and information; and autonomous systems [3].

The main features of a DT [4] imply that it will be an individualized, high-fidelity, real-time and controllable representation of the physical twin. Therefore, a DT can be divided into a triad: real and physical model; data monitored (big data); virtual reality (Fig. 13.2) [5]. However, a DT is not always a comprehensive representation of the physical model. The scope of the digital replica depends on the objectives of the developers and, above all, on the dimension of the monitoring system and the models used to create the digital replica [5].

The main challenge of DT implementation is to guarantee the capacity to continuously update the digital model to keep it similar to the physical twin. Only by doing so, monitoring, control and optimization will be possible during its life cycle. This will allow the prediction of the future state of the system, including anomalies, allowing to simulate and test preventive measures [6]. The impossibility of monitoring everything in a real building implies that the DT will only represent part of the reality. Hence, the virtual space will only replicate what is of interest to its creator (Fig. 13.2) [5]. There is a growing interest of the scientific community on DT [7]. Figure 13.3 shows the growth of the studies of this area in the scientific database “SCOPUS” in the subject areas of engineering and energy.

In the AEC industry, DT are still considered a novelty and a way of implementing the 4th industrial revolution [8]. The DT can also be seen as an evolution of BIM-enabled asset management [9]. The AEC industry is highly evolved in the field of modelling and simulation so it will be on monitoring and data communication that the industry 4.0 will find its main challenges. A continuous connection between a DT and the physical twin enables the transmission of data describing the status of the

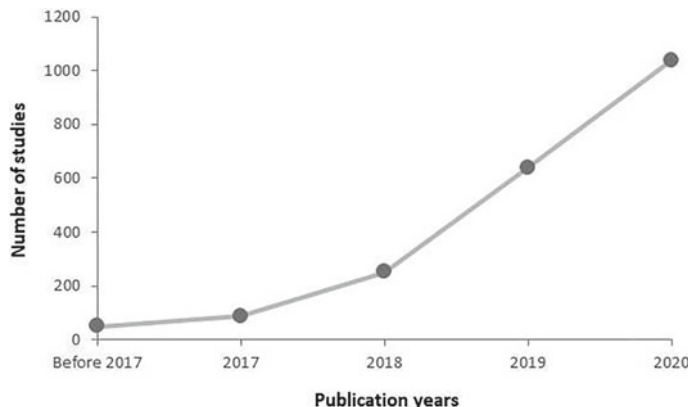


Fig. 13.3 Evolution of the documents related to “digital twins” in SCOPUS

building and its boundary conditions. The storage and treatment of a high amount of data will therefore be a requirement of a DT. It should then characterize, interpret, group and classify the data through machine-learning techniques [10].

The starting point of the construction of a DT depends on the quality and precision of the Building documentation. The continuous tracking of the building status requires the Internet of Things (IoT) as a tool for the update of the building data [11]. The integration of sensors allows real-time monitoring of the Building performance, enabling immediate action in case of an anomaly detection. The control algorithm of the building may benefit from the feedback during operation [12]. Three different areas should be continuously updated in a DT: building performance (energy, etc.); anomalies; and maintenance and refurbishment [13]. The data may be collected thru IoT sensors but some aspects of the building may be recorded in scheduled inspections as there is a limit to the data that can actually be obtained from sensors [13].

According to Khalil et al. [13] DT can keep track on the performance of different aspects: energy, thermal comfort, hygric performance, visual comfort, acoustics, indoor air quality, equipment, occupant behaviour and others (Fig. 13.4). The collected data are important to evaluate the performance of the building but also to support decisions related to renovation actions. The data alone are insufficient but they will allow detailed modelling and simulation [14].

The construction of a DT can be done with different configurations, depending on the interest of the stakeholders. Nevertheless, BIM is one of the tools that will be often used (Fig. 13.5). It occurs mainly due to the standardized format for storing semantic information introduced by BIM. It describes the Industry Foundation Classes (IFC) as a standard for hierarchical data storage [15]. In literature authors using BIM as a middleware [16–18] or the only platform among Revit to build the DT [19, 20] were found. In some works the concept of BIM is given as a synonym as DT; however, accordingly to Khajavi et al. [21] there are three great differences between these concepts. The authors highlighted that BIM was created to optimize buildings design

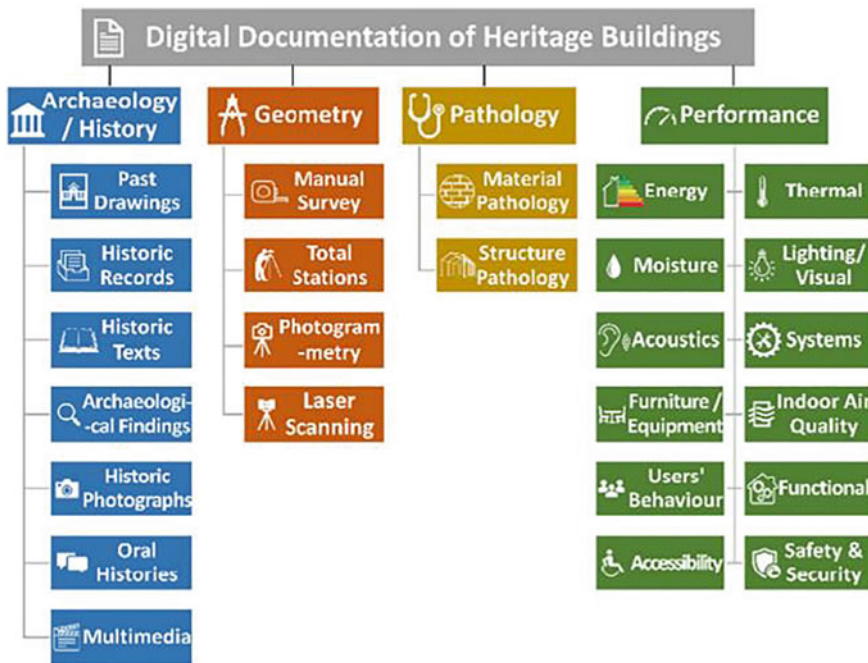


Fig. 13.4 Proposed categorisation of the documentation data of heritage buildings and their respective data capture tools [13]

and construction while DT is designed to optimize the post-occupancy phase with predicting capabilities. Therefore, BIM was not projected to work with real-time data in contrast to DT that is the online replica of the real physical building. Finally, BIM was not projected to integrate real-time data contrarily to the DT [21].

In buildings, the continuous monitoring of the structural part of the elements is a reality and is being employed in different kinds of structures, even in the form of a digital twin. Complex structures are being continuously monitored by smart sensors,

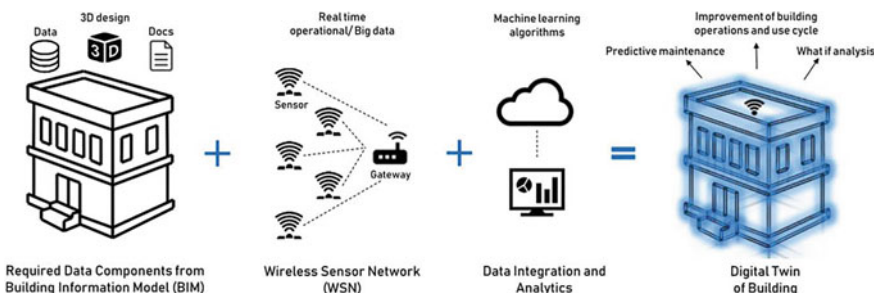


Fig. 13.5 Essential components to create a digital twin of building and difference with BIM [21]

such as bridges [22–24], wind turbine [25] and heritage [13, 14, 26]. However, the main objective of the digital twins implemented in buildings is in a perspective of the maintenance of the systems or construction elements [24, 27].

Nowadays, the first works in the area of digital twins in buildings are appearing, about non-structural elements. Using BIM processes, Revit software, Dinamo Revit as a graphical interface and a middleware IoT, Zaballos et al. [17] created a real-time monitoring system in an university Campus with sensors from Indoor Environmental Assessment (IEQ) and energy efficiency. The system has big data techniques that were used for statistical analysis. The created digital twin gave recommendations to occupants and facility managers according to the real time measured values and the indexes given by the algorithms. Zaballos et al. [17] stated that further developments are needed to achieve adaptation, learning, anticipation, and self-organization smartness levels. In the same way, Chang et al. [20] used Dinamo to collect sensor data as input and automatically redraw visualized information in BIM. In this study, an Arduino-based IoT equipment was used with temperature and relative humidity sensors. The Revit interface was used as a visualization platform to help energy-saving management decisions. Chang et al. [20] used the Dinamo to put the algorithms to calculate the PMV to analyse the thermal comfort. A similar work by Kazado et al. [19], studied three hypothesis of transforming BIM models in digital twins, Revit, Navisworks and API integrations. This study used temperature and CO₂ sensors and a platform to enable facility operators to obtain the required information. In a different study [21], an attempt was made to use a digital twin to include building life cycle management. Big databases were created with sensors in a building façade. The sensors collect light, ambient temperature and relative humidity, inside and outside the building façade. Khajavi et al. [21] used the light sensors to detect the presence of objects in front of the monitored façade and developed a framework to determine the sensor arrangement on a building façade to enable a digital twin.

Due to the technical complexity of the creation of a digital twin in a comprehensive real building scenario, at the present, only a few works were found and not holistic.

13.3 Building Pathology

The long-term performance of a building will evidence the defects that it may have, regarding design or construction errors, or the ones that arise from inadequate occupant behaviour or durability issues. In Europe, several studies compiled data regarding recurring anomalies in buildings.

In France, the SYCODÉS (SYstème de COLlecte des DÉSordres) [28] is a database that allows the identification of the most frequent building anomalies observed in French buildings. Water tightness defects represented 58% of the defects reported from 1995 to 2015. Condensation problems and indoor temperature connected problems also made it to the top ten. Regarding building components, façades and roofs are amongst the components with prevailing anomalies. In Norway [29], construction elements located in the building envelope account for almost two-thirds of all

observed defects. In Portugal, a study developed by Branco and Torres [30], analysed the most often observed anomalies in seven historic buildings. The problems with higher occurrence were due to water tightness defects and rising damp. The majority of the anomalies were moisture related.

The authors conducted recently, in the northern region of Portugal, an extensive survey on eight school buildings. The most frequently observed anomalies are presented in Fig. 13.6. The three anomalies with the highest frequency of observation are moisture related. They stand for more than 50% of the observations and are caused by rainwater infiltration (19% in roofs and 16% in façades) and surface condensation (19%). Water leaks (12%) and drain pipes malfunction (7%) are also relevant problems of the observed buildings.

A researcher from Singapore [31], studied fifty-six high-rise non-residential buildings and found that the ten most serious building anomalies humidity-related were the following (the percentages of incidence are presented in brackets): water leakage through joints (53%), corrosion of pipes (50%), spalling of concrete (47%), water leakage through cracks (42%), unevenness of tiles and poor pointing (40%), paint defects (37%), waterpoinding (35%), staining of ceiling finishes (34%), staining of vanity top (33%), and water leakage at pipe penetration (32%).

The cited studies highlight that moisture-related anomalies are very frequent in buildings. Water leakage, rising damp and interior surface condensation are the main sources of excessive moisture in building components or surfaces. The deterioration caused by moisture-related problems will assume different forms of degradation:

- Plaster and renderings (Fig. 13.7a);
- Staining and colour alteration (Fig. 13.7b);
- Detachment of renderings and plasters (Fig. 13.7c and d);
- Water run-off (Fig. 13.7e and f);
- Salt crystallization (Fig. 13.7g);
- Mould growth (Fig. 13.7h).

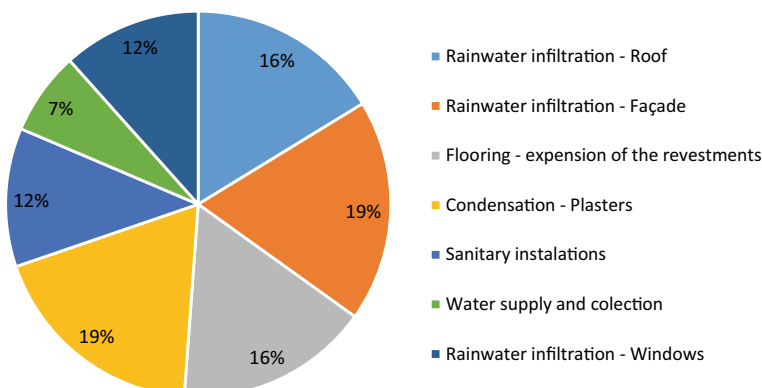


Fig. 13.6 Distribution of the main anomalies found in the surveys of schools in Portugal

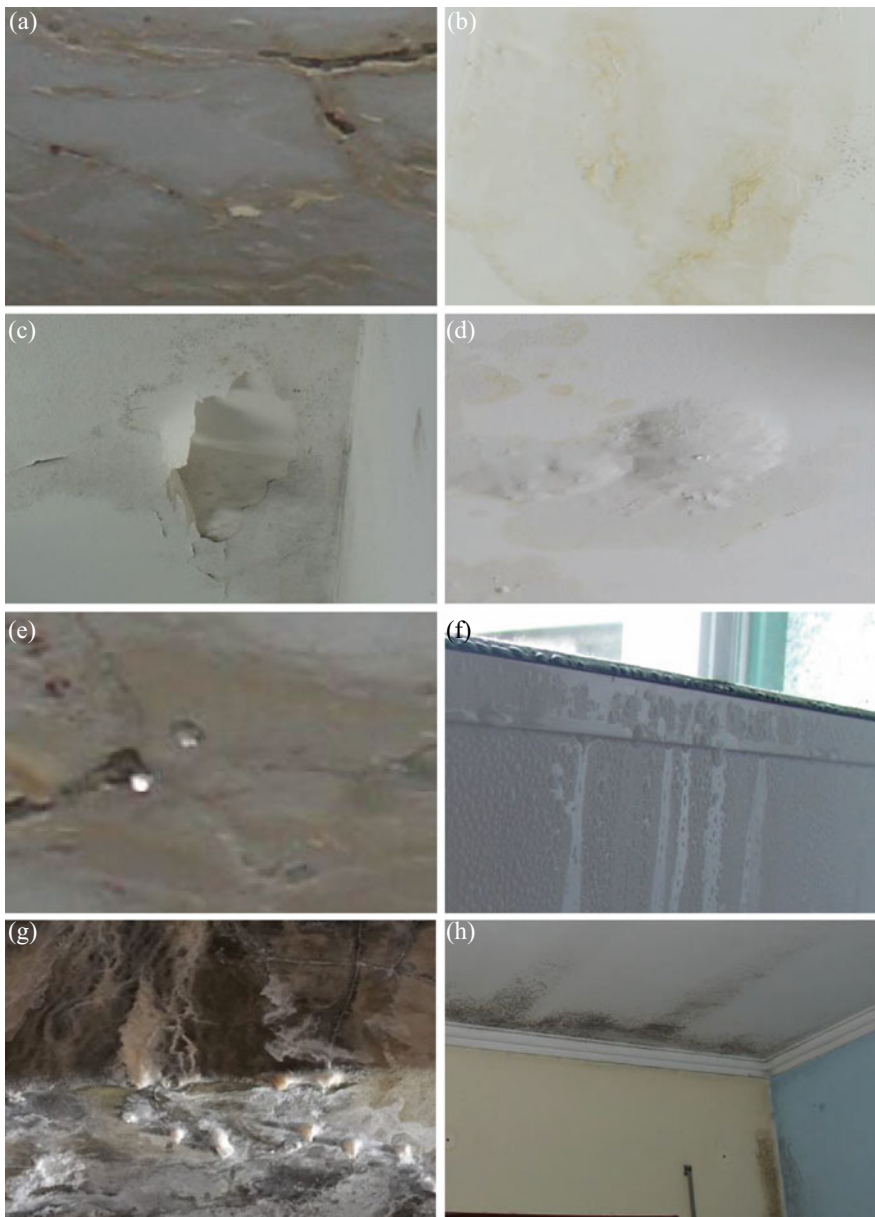


Fig. 13.7 Common moisture related anomalies observed in buildings

In most cases the non-structural anomalies addressed in this section are only corrected after evident degradation takes place (Fig. 13.7), a survey is carried out and a rehabilitation proposal is put forward. A state of the art review of inspection procedures and diagnosis methodologies was presented in Ferraz et al. [32] focusing on non-structural anomalies. The implementation of DT in buildings would allow preventive actions and anomalies would be detected before degradation was evident.

13.4 Hygrothermal-Related In-Situ Tests and Monitoring

The diagnosis of Building pathology induced by an inadequate hygrothermal behaviour largely benefits from extensive in-situ measurements and/or continuous monitoring of temperature and humidity of both indoor air and building components.

Indoor climate monitoring has seen a fast evolution in recent years due to the development of small data loggers with a high storage capacity or Wi-Fi transmission combined with innovative sensors. The case of humidity sensors is a good example of that innovation [33], as a wide technological range of solutions can be used for relative humidity sensing. The wide spread use of detailed monitoring schemes has been fuelled not so much by pathology diagnosis. Instead, energy efficiency, comfort and indoor air quality (IAQ) are more frequently the focus of advanced monitoring studies. Nevertheless, a holistic analysis of the measured parameters can also detect anomalies of the building performance [34], which could be corrected by optimizing the building enclosure and systems or improving occupant behaviour.

An adequate research plan has to be assembled if knowledge is to be extracted from monitoring efforts that generate large amounts of data, especially when IEQ is performed and the number of parameters and data series increases. An example extracted from Pereira et al. [35] is presented in Fig. 13.8. It highlights a sequence of steps where data mining processes are applied to the collected data.

The measurement of moisture content in materials has also evolved and nowadays the possibility to conduct continuous moisture monitoring exists. The work conducted by Strangfeld and Kruschwitz [36] used relative humidity (RH) sensors embedded in porous materials and Hilleborg's approach to convert the measured values into the corresponding pore saturation, enabling non-destructive monitoring of liquid water in porous materials. The possibility of using methods to determine moisture in wood in continuous monitoring was investigated by Dietsch et al. [37]. The electrical resistance method proved to be a good option, applied in different previous studies, although the researchers consider that standardization and equipment improvement is required. The study presented by Walker and Pavía [38] used T and RH probes inserted into holes drilled in an internally insulated historic brick wall, allowing to measure the effect of different thermal insulation materials on the long-term performance of each assembly. It goes in the right direction, by showing that a continuous measurement is feasible and can produce relevant information for building management such as the real U value during building operation phase.

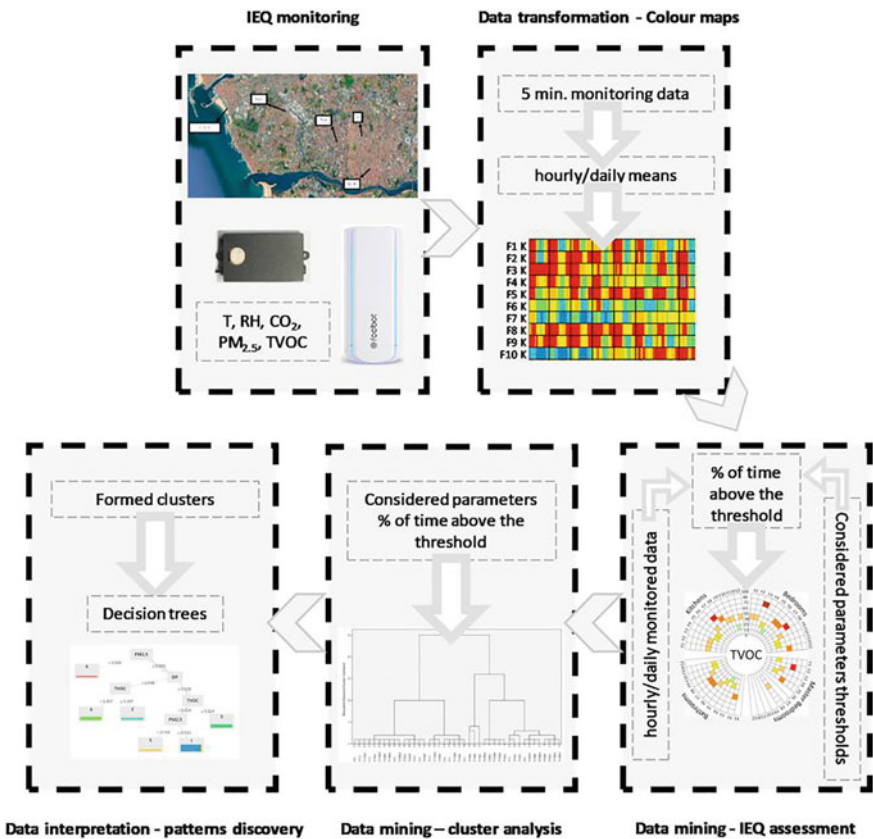
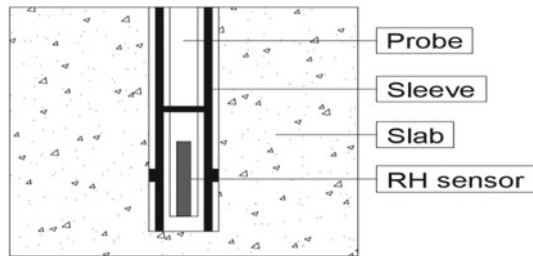


Fig. 13.8 Research plan for monitoring and knowledge discovery from IEQ data [35]

Although academic studies point to the possibility of implementing moisture monitoring of building components as a common practice, practical issues still have to be tackled. The ASTM F2170 standard [39] describes a procedure for the determination of RH in concrete floor slabs. It is used when the performance of flooring systems can be affected by moisture permeating from the concrete floor. The detailed methods described by the standard, including sensor placement details (Fig. 13.9), are important to ensure the feasibility of the readings obtained by the monitoring system.

The T and RH monitoring of buildings and building components can be combined with the monitoring of the resulting deformations. The work presented by Lohonyai et al. [40] is a good example of how a remote monitoring system is able to record deformations of masonry cavity walls and evaluate if the causes for dimensional changes and strain variation were explained by hygrothermal loads, and if whether or not they were reversible. Other studies targeted the analysis of timber components mechanical behaviour when facing T and RH variation. The behaviour of

Fig. 13.9 Example of RH probe placement according to [39]



cross-laminated timber panels [41] can be influenced by moisture induced stress, but an adequate moisture monitoring set-up would keep-track of moisture distribution patterns and detect hazardous conditions. The moisture monitoring of glulam members [41] is also feasible and the placement of sensors in the active zones of the cross-section is a good strategy to evaluate the risk of cracking. This risk can occur even in the hygroscopic range, which puts the focus on the adequate evaluation of environmental conditions in order to predict the risk level that the structures will be facing.

The range of monitoring sensors can also be expanded to other specific anomalies. The use of innovative optoelectronic mould sensors was demonstrated by Savory et al. [42], allowing the quantification of mould growth in enclosed spaces. This type of sensors can be part of post-remediation strategies included in the building maintenance plan.

Continuous monitoring can be combined with traditional Building inspection procedures that use different devices to evaluate the moisture content of Building components [43] or the connected relative humidity [44]. The technologies of InfraRed Thermography (IRT) and Ground-Penetrating Radar (GPR) for the detection and classification of moisture in interior walls were also used Garrido et al. [45]. The latter combination of techniques allows the study of both surface and internal moisture distribution. The recent evolutions on the quantification of building components defects [46, 47] also demonstrate the potential of using IRT-based automated non-destructive techniques in the study of moisture related pathology. The evolution of different experimental techniques that can be used in-situ demonstrate the potential of including the assessment of moisture-based pathology in DT.

13.5 Conclusions

Technological developments at the level of ICTs make it possible to create digital twins of the built environment. Some areas of the AEC industry have already started to implement these concepts mainly from a maintenance point of view.

The BIM tool is a perfect ally in the application of the DT concept to the AEC industry. In addition to the ability to model 3D images, powered by scan to BIM technologies already disseminated in practice, the organization and data storage

capacities are currently used by the bibliography in the construction of DT. However, there are still some areas of this industry that remain to be explored. There are separate studies on the inclusion of sensors related to energy efficiency, IAQ, thermal comfort, visual comfort, acoustic comfort and durability of construction materials, but their generalized and integrated inclusion is not yet a reality. In addition to the above, many anomalies found in buildings are humidity-related. Thus, it is considered essential that the DT of the future include this type of sensors to inform, in real time, the owners/occupants/managers about the moisture content and the relative humidity in critical areas of the construction that may be in risk of developing anomalies.

It is considered that the creation of DT is the future path that will provide energy-efficient built environments, with predictive features in order to be able to respect the occupants while maintaining quality standards at the level of IEQ, avoiding the appearance of structural and non-structural anomalies and making it possible to carry out maintenance operations before there are malfunctions.

Acknowledgements The research presented in this chapter was funded by Base Funding—UIDB/04708/2020 of the CONSTRUCT—Instituto de I&D em Estruturas e Construções—funded by national funds through the FCT/MCTES (PIDDAC) and by the project ENERGY PUSH (SOE3/P3/E0865) that is co-funded by the INTERREG SUDOE Programme through the European Regional Development Fund (ERDF).

References

1. Glaessgen E, Stargel D, The digital twin paradigm for future NASA and US Air Force vehicles. In: 53rd AIAA/ASME/ASCE/AHS/ASC structures, structural dynamics and materials conference
2. Lu Q, Xie X, Parlikad AK, Schooling JM (2020) Digital twin-enabled anomaly detection for built asset monitoring in operation and maintenance. *Autom Constr* 118:103277
3. Greif T, Stein N, Flath CM (2020) Peeking into the void: digital twins for construction site logistics. *Comput Ind* 121:103264
4. Liu M, Fang S, Dong H, Xu C (2020) Review of digital twin about concepts, technologies, and industrial applications. *J Manuf Syst*
5. Angjeliu G, Coronelli D, Cardani G (2020) Development of the simulation model for digital twin applications in historical masonry buildings: the integration between numerical and experimental reality. *Comput Struct* 238:106282
6. Autiosalo J, Vepsäläinen J, Viitala R, Tammi K (2020) A feature-based framework for structuring industrial digital twins. *IEEE Access* 8:1193–1208
7. Lim KYH, Zheng P, Chen C-H (2020) A state-of-the-art survey of digital twin: techniques, engineering product lifecycle management and business innovation perspectives. *J Intell Manuf* 31(6):1313–1337
8. Ridley J (2019) Connecting the buildings of the past to the cities of the future with digital twins. In: Proceedings of the CTBUH 10th world congress 50 forward 50 back: the recent history and essential future of sustainable cities
9. Lu Q, Xie X, Heaton J, Parlikad AK, Schooling J (2020) From BIM towards digital twin: strategy and future development for smart asset management. Springer International Publishing, Cham
10. Barricelli BR, Casiraghi E, Fogli D (2019) A survey on digital twin: definitions, characteristics, applications, and design implications. *IEEE Access* 7:167653–167671

11. Sedlmaier A, Dietl T, Harraßer J (2019) Digitizing roll forming with smart sensors. *AIP Conf Proc* 2113(1):170017
12. Poli T, Mainini AG, Speroni A, Blanco Cadena JD, Moretti N (2020) The effect of real-time sensing of a window on energy efficiency, comfort, health and user behavior. In: Daniotti B, Gianinetto M, Della Torre S (eds) *Digital transformation of the design, construction and management processes of the built environment*. Springer International Publishing, Cham, pp 291–296
13. Khalil A, Stravoravdis S, Backes D (2020) Categorisation of building data in the digital documentation of heritage buildings. *Appl Geomat*
14. Jouan P, Hallot P (2020) Digital twin: research framework to support preventive conservation policies. *ISPRS Int J Geo Inf* 9(4):228
15. Mayer H (2018) Digitalization of legacy building data-preparation of printed building plans for the BIM Process. In 7th international conference on smart cities and green ICT systems (SMARTGREENS 2018). Portugal, pp 304–310
16. Lu Q, Parlidak AK, Woodall P, Ranasinghe GD, Xie X, Liang Z, Konstantinou E, Heaton J, Schooling J (2020) Developing a digital twin at building and city levels: case study of West Cambridge campus. *J Manag Eng* 36(3):05020004
17. Zaballos A, Briones A, Massa A, Centelles P, Caballero V (2020) A smart campus' digital twin for sustainable comfort monitoring. *Sustainability* 12(21):9196
18. Teizer J, Wolf M, Golovina O, Perschewsk M, Propach M, Neges H-M, König M (2017) Internet of Things (IoT) for integrating environmental and localization data in Building Information Modeling (BIM)
19. Kazado D, Kavcic M, Eskicioglu R (2019) Integrating Building Information Modeling (BIM) and sensor technology for facility management. *Electron J Inf Technol Constr* 24:440
20. Chang K-M, Dzeng R-J, Wu Y-J (2018) An automated IoT visualization BIM platform for decision support in facilities management. *Appl Sci* 8(7):1086
21. Khajavi SH, Motlagh NH, Jarabion A, Werner LC, Holmström J (2019) Digital twin: vision, benefits, boundaries, and creation for buildings. *IEEE Access* 7:147406–147419
22. Kaewunruen S, Sresakoolchai J, Zhou Z (2020) Sustainability-based lifecycle management for bridge infrastructure using 6D BIM. *Sustainability* 12(6):2436
23. Shao S, Zhou Z, Deng G, Du P, Jian C, Yu Z (2020) Experiment of structural geometric morphology monitoring for bridges using holographic visual sensor. *Sensors* 20(4):1187
24. Shim C-S, Dang N-S, Lon S, Jeon C-H (2019) Development of a bridge maintenance system for prestressed concrete bridges using 3D digital twin model. *Struct Infrastruct Eng* 15(10):1319–1332
25. Grosse CU (2019) Monitoring and inspection techniques supporting a digital twin concept in civil engineering. In: *Sustainable construction materials and technologies*
26. Sangiorgio V, Martiradonna S, Uva G, Fatiguso F (2017) An information system for masonry building monitoring. In: 2017 IEEE international conference on service operations and logistics, and informatics (SOLI)
27. Errandonea I, Beltrán S, Arrizabalaga S (2020) Digital twin for maintenance: a literature review. *Comput Ind* 123:103316
28. AQC (2016) SYCODÉS pathologies. In: Estingoy P (ed) *Agence Qualité construction*
29. CIB (2013) A state-of-the-art report on building pathology. In: de Freitas VP (ed) *CIB-W086-building pathology*
30. Branco D, Torres I (2009) Humidade em Construções Históricas. In: PATORREB, Porto, pp 583–588
31. Chew MYL (2005) Defect analysis in wet areas of buildings. *Constr Build Mater* 19(3):165–173
32. Ferraz GT, de Brito J, de Freitas VP, Silvestre JD (2016) State-of-the-art review of building inspection systems. *J Perform Constr Facil* 30(5):04016018
33. Farahani H, Wagiran R, Hamidon MN (2014) Humidity sensors principle, mechanism, and fabrication technologies: a comprehensive review. *Sensors* 14(5):7881–7939
34. Sharmin T, Güll M, Li X, Ganey V, Nikolaidis I, Al-Hussein M (2014) Monitoring building energy consumption, thermal performance, and indoor air quality in a cold climate region. *Sustain Cities Soc* 13:57–68

35. Pereira PF, Ramos NMM, Ferreira A (2020) Room-scale analysis of spatial and human factors affecting indoor environmental quality in Porto residential flats. *Build Environ* 186:107376
36. Strangfeld C, Kruschwitz S (2018) Monitoring of the absolute water content in porous materials based on embedded humidity sensors. *Constr Build Mater* 177:511–521
37. Dietsch P, Franke S, Franke B, Gamper A, Winter S (2015) Methods to determine wood moisture content and their applicability in monitoring concepts. *J Civ Struct Heal Monit* 5(2):115–127
38. Walker R, Pavía S (2018) Thermal and moisture monitoring of an internally insulated historic brick wall. *Build Environ* 133:178–186
39. ASTM_F2170 (2016) Standard test method for determining relative humidity in concrete floor slabs using in situ probes. In: ASTM International, West Conshohocken
40. Lohonyai AJ, Korany Y, Güll M (2015) Remote field monitoring of thermal and moisture deformations in masonry cavity wall building envelopes. *J Perform Constr Facil* 29(3):04014072
41. Franke B, Franke S, Schiere M, Müller A (2019) Moisture content and moisture-induced stresses of large glulam members: laboratory tests, in-situ measurements and modelling. *Wood Mat Sci Eng* 14(4):243–252
42. Savory E, Dooreleyers M, Spiler K, Li E, Sabarinathan J, Scott JA (2018) Evaluation of an optoelectronic mould sensor for use in building health monitoring and in post-remediation performance assessment. *Sustain Cities Soc* 36:311–318
43. Duarte R, Flores-Colen I, de Brito J, Hawreen A (2020) Variability of in-situ testing in wall coating systems-Karsten tube and moisture meter techniques. *J Build Eng* 27:100998
44. Torres MIM, de Freitas VP (2007) Treatment of rising damp in historical buildings: wall base ventilation. *Build Environ* 42(1):424–435
45. Garrido I, Solla M, Lagüela S, Fernández N (2020) IRT and GPR techniques for moisture detection and characterisation in buildings. *Sensors* 20(22):6421
46. Tejedor B, Barreira E, Almeida RMSF, Casals M (2021) Automated data-processing technique: 2D map for identifying the distribution of the U-value in building elements by quantitative internal thermography. *Autom Constr* 122:103478
47. Barreira E, Almeida RMSF, Simões ML, Rebelo D (2020) Quantitative infrared thermography to evaluate the humidification of lightweight concrete. *Sensors* 20(6):1664

Chapter 14

Testing for New Requirements for Building Coatings



Paulina Faria and M. Rosário Veiga

Abstract Coatings are an important part of buildings in terms of performance, costs and time needed to be applied, repaired and replaced. They are requested to perform several functions, starting with the protection of the substrates and, therefore, durability of the coated building elements. With the increased concern on ecological performance, energy conservation and economic efficiency, the durability of the coatings themselves and several innovative requirements, such as contributing to lightning, comfort, health (indoors and outdoors) and safety, are also very important nowadays. Therefore, innovative tests have recently been defined, usually designed to reproduce the real actions while other tests have been adapted from tests designed for other materials. The new tests have to be optimized and validated before being formally adopted. This chapter addresses several building coating requirements, namely some which only recently are attracting research. Many innovative tests to assess new requirements and tests that were adapted to properly assess coatings performance are described and are briefly discussed to contribute to advances in research and to the identification of gaps.

Keywords Durability · Hygroscopicity · Pollutant release and capture · Self-cleaning · Visual comfort · Weathering

14.1 Introduction

Building coatings have different requirements based on their application, outdoor or indoor in walls, roofs, ceilings and floors. Their main function is to protect the substrate, acting as sacrificial systems, while providing good aesthetic appearance. Therefore, their durability is expected to be shorter than the one of the substrates.

P. Faria

CERIS, Department of Civil Engineering, NOVA School of Science and Technology,
Universidade NOVA de Lisboa, Lisbon, Portugal
e-mail: paulina.faria@fct.unl.pt

M. R. Veiga

Department of Buildings, National Laboratory for Civil Engineering, 1700-066 Lisbon, Portugal
e-mail: rveiga@lnec.pt

Coatings are frequently composed by different layers, as the cases of innovative organic-based floor coatings [1], external thermal insulation composite system (ETICS, also known as external insulation finishing systems—EIFS) [2] and traditional painted renders and plasters (differences defined for instance by EN 998-1 [3], being a render to apply outdoors and a plaster to apply indoors), or include diverse elements, as the case of ventilated cladding systems for façades, composed by façade cladding supported by an intermediate sub-structure, defining a continuous air layer and possibly with insulation adhered to the wall [4, 5], or roofing with elements to support insulation and traditional ceramic tiles.

Those materials and products that compose the systems are important so they should accomplish common technical requirements, depending on the application. For instance, a render or a plaster, traditional building elements very common since antiquity, need to have good adhesion to the wall that constitutes the substrate; if painted, the paint system must provide good adhesion to the mortar surface. The mechanical strength of plasters and renders must be enough to provide durability but without inducing mechanical stress on the substrate surface [6]; therefore, it should never be higher than the one of the substrates. The mechanical performance of a render should ensure that: it can deform slightly, together with minor deformation of the walls, without cracking; it can resist to abrasion of particles suspended by wind, with or without rain. Similar situation occurs to plasters coating walls in terms of resistance to cracking, and they must resist to furniture shocks and to abrasion due to indoor usage. In terms of water vapor permeability, the plasters and renders should never act as a vapor barrier, as they need to allow the migration of moisture without blocking it in the substrate. And this is particularly important for plasters and renders applied on historic buildings, were rising damp may probably exist.

A render must be applied on a wall in a way that, together with that wall, the rainy water does not access the indoor space. That is why, in the past, renders were adapted to massive thick walls: in rainy periods some of the water could migrate from the outdoor surface to the interior of the wall but, when the rain stopped, the moisture front reversed the direction of progression, and the wall could dry. For this, the render (including its finishing) should ensure some protection from water absorption but also be water vapor permeable, and the wall (based on its composition) should be thick enough for the local climate. However, with climate changes even historic walls that performed well for centuries may have problems nowadays, as tropical rainy periods, when high amount of water falls in a very short period, seem to occur in non-tropical regions, and non-adapted historic walls. Complementary materials and systems for protection may be needed and, therefore, tested to ensure compatibility. A possibility may be the use of limewashes with hydrophobic natural agents, such as natural fats or oils [7]. Frequently, the water vapor permeability is not achieved when new renders with cementitious mortars are applied for inappropriate repair of old walls.

Additional requirements for some coatings, such as the ones applied on the exterior envelope of buildings, included since the twentieth century, were related to insulation, both thermal and acoustic, and comfort for occupants. In the last decades, thermal insulation became directly related with energy efficiency. Once again, the

need of insulation materials in the envelope coating systems is not independent of the substrate where they are applied, and the substrates may be significantly diverse.

Another requirement associated to coatings is safety in case of fire, as indoor coatings can directly interfere with indoor safety, namely time to evacuate, and outdoor coatings are related to propagation to all the building [8].

In the present century, concerns related to embodied energy of the coatings and life cycle and life cost analysis also became important, both for new construction and retrofitting [9], and are influenced by the type, application and maintenance of coatings, that in turn implicate their durability. As coatings are exposed mainly to usage indoors and to weathering outdoors, protecting the substrate they cover, their durability should not only be assessed directly but has also to guaranty it does not jeopardize the protective function.

Furthermore, many other aspects also called attention only more recently, namely those related to: self-cleaning capacity of the surfaces, to decrease maintenance costs; reflective properties affecting both aesthetic quality, energy efficiency for comfort and sometimes also increase durability; hygroscopic capacity available to equilibrate indoor relative humidity; safety during the use, to decrease the risk of accidents; reduction of toxic products release to avoid polluting rainwater running down from roofs and facades; reduction of pollutant gases release to the indoor air from the coating materials themselves; capacity for indoor pollutants capture. To improve hygroscopic capacity and reduce embodied energy, there is a tendency to include residues and by-products, namely bio-based, to produce building coating products, replacing raw materials. However, the introduction of bio-based materials may increase the possibility of biological colonization, which is another aspect to control.

Some of these requirements appear because of the use of new materials and technologies; others because of new concerns, namely with health, ecology and energy efficiency. All these relatively new requirements for building coatings must be assessed in complement to common technical ones. Therefore, innovative testing procedures are being developed and used for testing new materials and products, such as the simulation of collecting and toxicological analysis of run-off water from roofs and facades, to avoid pluvial water contamination, or the hygroscopic and moisture buffer tests for indoor plasters applied on walls and ceilings, or the safety against slippery when using indoor floor coatings in public areas.

The tests methodology, their advantages and drawbacks, influence of expected results in design, will be discussed, defining the best possibilities so far and showing the problems that still need to be addressed.

14.2 Building Coating Requirements

14.2.1 General Remarks

As mentioned before, many requirements are strongly important for coatings, as they are in contact with indoor environment or with weathering conditions. Some are already well standardized, such as the need of adequate adhesion of renders and plasters to a substrate. However, even some well standardized requirements may have problems to be assessed and results compared, such as the case of the latter. Therefore, in this and the following section requirements and standardized methods for coatings will only be addressed whenever problems may exist. Although the sections are not exhaustive, most of the requirements and test methods addressed will be innovative, adapted or very recently considered to be a concern.

14.2.2 Aesthetics and Lightning

Aesthetics is an important requirement for coatings, either outdoors and indoors, particularly on walls, ceiling and floors. Aesthetic related properties can change during the coating lifetime and, therefore, those probable future changes should also be assessed. They can include cracking, stains and other colour changes, gloss and texture. For instance, natural materials, such as wood used as exterior cladding, should be tested for natural aging, so that the change in colour can be expected and accepted.

Indoors coatings are also related with lightning, namely by the surface colour and reflectivity. Testing and modelling about indoor lightning is addressed in Chap. 17.

14.2.3 Acoustic and Thermal Insulation

Acoustic requirements are needed for façade walls, roofs and also for walls and floors between neighbours, and may be important both for airborne sound insulation and impact sound insulation. When considering walls, floors and roofs, airborne sound insulation is particularly important for low weight walls, floors and roofs, as the mass effect is reduced. However, insulation requirements are needed to insulate indoor space of building from outdoor noise, from common areas, from neighbours and even between rooms. For impact sound insulation, there should be a discontinuity (namely a layer composed by a resilient material) between the walls and the structure that supports it, and particularly a discontinuity in the floor, between the structure and the surface. That discontinuity depends on the type of structure and the coating system and can be placed in different ways and using diverse materials. One possibility is

that the coating itself is resilient and, therefore, complementary discontinuity is not mandatory.

For indoor acoustic comfort, the indoor surfaces of furniture, occupation (and people surface) and coatings have a high influence. Reverberation time should be adequate for the indoor use and to indoor volume. Therefore, the surface absorption of coating surfaces must be known and, eventually, controlled.

Although common tests exist to assess the acoustic performance of coatings and other building products and elements, specific innovative tests are addressed in Chap. 15.

Concerning thermal insulation performance, standardized tests exist for thermal insulation materials and even for building elements. However, the performance is not only due to the insulation material used but also to the way it is applied. For instance, if the insulation material presents open pores, it should be applied with protection from moisture and liquid water. Otherwise, its thermal conductivity will drastically increase, decreasing the thermal resistance it may provide. An insufficient thermal insulation of building elements frequently is the cause of anomalies, such as the ones due to surface moisture condensation and biological colonization. Therefore, innovative testing is sometimes required for innovative insulation materials and buildings systems.

14.2.4 Performance in Case of Fire

The performance in case of fire is very important for indoor and outdoor coatings. No toxic gases should be released by the coatings, and the substrate they are supposed to protect, and the dissemination of the fire should be contained so that building occupants can have conditions to get away from the building if a fire occurs. Therefore, testing the reaction to fire of materials used to coat indoor walls, ceilings and floors, and the resistance to fire of the systems where they are applied is extremely important. As fire can propagate from floor to floor, and in buildings with exterior thermal insulation composite systems or ventilated cladding systems or rainscreen facades the rise of heated air and ventilation can propagate toxic smoke, the performance of exterior coatings needs also to be tested [8, 10].

To assess fire safety when applying and using coatings, standardized and expensive tests assess the reaction of building materials and systems to fire and allow evaluating if they can be applied exposed or need additional coatings. Simplified tests are sometimes preliminarily performed, namely, to assess the reaction of bio-based building insulation materials [11]. To assess the resistance to fire of building elements standardized sophisticated tests are performed because of the need of preserving the integrity of structural and compartmentation elements during enough time for acting concerning fire extinction or people extraction.

Although standardized tests of reaction and resistance to fire are not addressed in this chapter, complementary ways to assess people's behaviour in case of fire are addressed in Chap. 16.

14.2.5 Biological Colonization

The biological colonization often occurs indoors when relative humidity (RH) is high, which is frequent in many tropical countries with constant high RH, and in Mediterranean countries where heating is reduced (or intermittent) and ventilation during the heating season is frequently not enough. In the latter case it is common to have development of moulds particularly in the indoor surface of inefficiently insulated façade walls and roofs, and they occur due to indoor surface condensation of water vapor in high RH environment.

When indoor coatings are produced with bio-based materials, such as plasters with incorporation of natural organic fibres, it is mandatory that the drying of those fresh plasters occur with strong ventilation, particularly if the plasters are highly hygroscopic.

The application of paints to control biological development is not always adequate. That can be the case of roofs with ceramic tiles. In fact, after the tiles are applied on a roof, the painting to control biological development can only be applied on the exposed surfaces of the tiles. Frequently, those paints reduce the water vapor permeability of the tiles and, doing so, the water absorbed by the tiles will be kept inside its porous microstructure for much longer. During that period, it can freeze and thaw many times, and that may contribute to reduce the durability of the tiles, that begin to delaminate and to lose cohesion. Also damage to the ceramic roof tiles occurs when they are not applied with a ventilated space underneath, for instance they are directly applied immediately on top of a thermal insulation board instead of supported by two small section battens.

Biological development is also common on exterior walls, both when thermal insulation is insufficient, namely when associated to thermophoresis (Fig. 14.1a). However, biological development can occur even when thermal insulation exists, such as in facades coated with ETICS with low direct exposure to sun or with concentrated rainwater runoffs due to inadequate façade details (Fig. 14.1b).

14.2.6 Hygroscopicity

Hygroscopicity of indoor coatings is the capacity they have to adsorb water vapor from the indoor air and to desorb it when the air gets drier. Commonly that capacity depends on the properties of the exposed surface and, therefore, it mainly depends on the coating. If a coating can have that capacity cyclically, it can act passively (without energy consumption) as a moisture buffer, contributing to equilibrate indoor RH. Therefore, the coating can contribute to thermal comfort, as it depends not only on temperature but also on RH, and to reduce building pathology associated to high RH. Human health is negatively influenced when extreme RH occurs; in fact, dry RH induces voice problems, while high RH contribute to respiratory diseases. Therefore, hygroscopicity can also contribute to occupants' health.

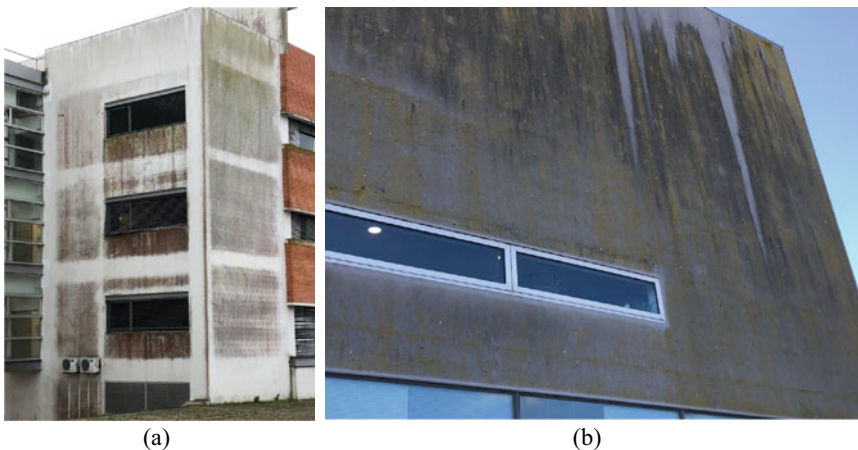


Fig. 14.1 Thermophoresis due to insufficient thermal insulation in North and West façade walls of a building with a reinforced concrete structure (a) and biological development of lichens in a North exposed facade coated with ETICS coloured grey, with very low exposure to sun (b), not far from the Atlantic Ocean, in Portugal

Timber and many wood-based coating products, as well as clay-based products, such as earth-based walls and clay plasters [12, 13] are known for being highly hygroscopic when compared to other similar products. For instance, the hygroscopicity of gypsum plasters and boards and air lime plasters is much lower.

For highly hygroscopic plasters the effect of bio-fibres on hygroscopicity is not significant, but the contrary occurs for non-highly hygroscopic building coatings. Therefore, bio-fibres are being tested on non-highly hygroscopic indoor coatings to improve that capacity. As bio-fibres are vulnerable to biological development, frequently tests include both characteristics.

14.2.7 *Reflective and Thermochromic Coatings*

Reflective properties of coatings, affecting both visual comfort and energy efficiency of buildings, are another important research subject, again both for facades and roofs. A reflective coating, such as a paint system or a glazed ceramic cladding, can reduce thermal heat during the cooling season. However, that increased reflection for instance in a façade or a roof would not be beneficial during the heating season.

In turn, thermochromic coatings are able of tuning their solar reflectivity to adapt to the climatic conditions where they are applied. Therefore, the application of these coatings can be beneficial both in cooling and heating seasons, as their surface change colour depending on the temperature, adapting the performance.

These materials are the focus of research and can be divided in non-dye-based, and dye-based applications [14], with different transition mechanisms. Thermochromic films are also developed for glazed windows and facades.

14.2.8 Self-cleaning Capacity, Photocatalytic Activity and Hydrophobicity

The self-cleaning capacity is important for all types of coatings and particularly for outdoor ones with difficult and expensive access to be cleaned. Examples can be glazed windows and other glazed coating panels. Several studies are being held, developing innovative building self-cleaning and antifouling products, namely that can be applied as protective treatments simultaneously with hydrophobic action [15].

Many of these products depend on photocatalytic activity [16], commonly based on the application of titanium oxide (TiO_2), and some may also have the capacity to capture pollutants. However, this performance is limited due to the absorption dependence on UV light. Other studies try to overcome the daylight limitation implementing catalytic memory on the coating products [17].

The hydrophobicity of coatings may be also important namely indoors to reduce stains and facilitate cleaning.

14.2.9 Protection Capacity from Water and Moisture

Protection capacity from water is a common requirement for building envelope elements and is different from materials hydrophobicity. The substrate and its coatings must ensure that the water (and moisture) does not reach the indoor space. Therefore, this requirement is particularly important for roofs, flat or with a slope, but also for façade walls.

For flat roofs the requirement is achieved using adequate drainage system and a waterproofing system (polymeric or bituminous) applied on a very low slope. The waterproofing system should be protected from UV radiation to ensure longer durability. To increase its durability, if possible, it should also be thermally insulated, with an insulation layer placed on top of the waterproofing system. In this case, for an effective thermal insulation of the flat roof, the insulation material should not absorb water, thus it should have a closed porosity.

For roofs with significant slope and coated by ceramic roof tiles (a traditional roof system with several millennia), the use of waterproofing systems is not commonly needed, so that moisture produced indoor can migrate through the roof. However, the use of a water vapor permeable membrane with some resistance to water absorption is recommendable, to avoid some rainwater leakage in the case that a roof tile can break and need some time to be replaced.

For façade walls produced with brick or block masonry, or with monolithic walls, two choices can occur, depending on the type of wall and on the coating: single wall with a coating of low water permeability that ensures the water does not reach the interior; alternatively, a medium/high water permeable coating may be applied, such as a render if a double wall is used. In this case, the double wall should define an air void layer in between, where the water migrating from outdoors can reach and be collected and drained, without reaching the indoor wall of the double wall system. The latter system is known for decades, and the barrier to the water migration is physical, considering that the air void, the collecting of the migrating water and its drainage is efficient. In this type of double walls, the insulation material should occupy only partially the air gap, being attached to the inside wall leaf and leaving a continuous air thickness between the exterior surface of the insulation and the interior surface of the exterior wall leaf. In these facades, as the insulation material is located inside the double wall, it is common (although not positive) that thermal bridges occur in structural elements and, therefore, they should be thermally insulated too. In case the thermal insulation is applied on the exterior surface of the structural elements (columns/pillars, beams), that must be compatibilized with the coating, as the adherence of a render is not facilitated to most insulation materials.

Coatings for single façade walls are more diverse, and can be applied: adhered to the wall, such as ETICS or thermal renders, with chemical waterproof finishing systems that guarantee that the water is not absorbed by the insulation layer; without contacting the wall and defining an air gap between the coating and the thermal insulation, which is adhered to the exterior surface of the wall, such as the case of “ventilated” cladding systems, where claddings are suspended on an intermediate structure (in turn attached to the wall which can be composed by a masonry leaf), coating the wall surface but physically preventing rainwater from accessing the wall due to the ventilated air gap. In both these cases, the thermal (and acoustic) insulation materials are applied on the exterior surface of the single leaf walls, preferably in a continuous layer, eliminating thermal bridges.

When both thermal and acoustic requirements are needed within the same building element, an insulation material should be chosen to accomplish both requirements. However, not all insulation materials are able to accomplish both acoustic and thermal requirements, and to be applied in all situations; therefore, justified choice is needed.

Depending on the building element, the insulation material can be included in the element itself (such as when applied inside a “double” wall composed by two walls, air gap and insulation layer) or applied in the coating system. Only the latter case will be addressed in this chapter.

Thermal bridges and insufficient thermal insulation of envelope elements induce to building pathology, with anomalies due to water condensation on the indoor surfaces of coatings. Those condensations are sometimes mistaken with water coming from outdoors, and frequently are associated to biological development.

14.2.10 Release of Toxics that Pollute Run-Off Water

In the last decades, the release of toxic products that can pollute rainwater running down from roofs and facades became another important research topic for coating systems and the surface materials that are applied. As mentioned in Chap. 5, the release of dangerous substances from construction products into soil, ground water and surface water is addressed by a specific work group of CEN/TC 351.

Toxic elements can be released namely by biocides included in roof tiles, paints, industrial rendering mortars, treated wood claddings and waterproofing roof membranes, to prevent from biological colonization [18]. In Europe, the use of biocides is regulated by the biocidal product regulation [19], so each formulated product that includes an active biocidal ingredient needs registration. The runoff is also linked with the durability of the biocidal effect. So testing is necessary for both assessments.

14.2.11 Indoor Pollutants Release and Capture

As people spend a large part of the day indoors, modern and retrofitted indoor environments are being more airtight than before, the levels of indoor pollutants reach higher values. As poor indoor quality negatively affects occupants' health, it is important that the coatings applied indoors (as well as furniture and equipment) do not release pollutants or toxic compounds. In terms of indoor pollution, primary emissions can be considered those that occur directly from a coating material, while secondary emissions can be those resulting from physical, biological or chemical transformations that occur once the coating is applied in the building [20], such as chemical reactions occurring when the coating is in contact with oxidants. For instance, ozone reactions with building coatings may result in secondary emissions of aliphatic aldehydes and other reaction products [20]. Other examples of toxic compounds are volatile organic compounds (VOC) that can exist in some glues used for the application of wall and floor coatings, to produce some composites for indoor cladding, or even in paints, although the limit levels have nowadays been drastically reduced. As mentioned in Chap. 5, the emissions of dangerous substances from construction products into indoor air is addressed by a specific work group of CEN/TC 351.

A relatively recent subject of research is to assess the contribution that indoor coatings can have to capture indoor pollutants, namely VOC mentioned before, NO_x [21] or CO₂ produced by buildings occupants [22]. The large areas of coatings in a room may have a significative contribution and large research should proceed on this subject.

14.2.12 Synthesis of Coating Requirements

Many more requirements exist for building coatings. Some depend largely on the type of coatings. It is the case of adhesion to a substrate, which is important for coatings applied directly attached to the support. For coatings like renders and plasters, with or without finishing by ceramic tiles, natural or artificial stone claddings adhered to the mortar layer, as well as for ETICS and thermal renders, both the adhesion to the substrate and between layers are extremely important characteristics. Another is the case of abrasion, varying for outdoor and indoor coatings as the action to simulate when testing is different. Another example is the bending strength, that can be particularly important for claddings applied defining an air gap layer (such as on ventilated cladding systems for façades).

Many of the coating requirements addressed in this section are commonly evaluated, such as the cases of acoustic and thermal insulation. For some of these common requirements, standardized test procedures are established. However, sometimes new materials are developed and appear in the market and, for some, adaptation or even specific methods are needed even to test for common requirements. For other requirements, only recently they have been the focus of attention and, in that case, specific test methods need to be developed to assess them.

The durability of coatings, although not innovative, is a requirement that gains importance to ensure eco-efficiency and, more important than the coating durability itself, is the contribution to the durability of all the building element.

In the following section, tests for not so common building coating requirements, innovative tests even if for common requirements and tests which were adapted from some products to others, are addressed.

14.3 Innovative and Adapted Tests for Building Coatings

14.3.1 Tests for Aesthetics, Lighting, Reflective and Thermochromic Coatings

Aesthetics is related to many aspects; for coatings, namely to cracking, stains, changes in colour, gloss, texture. Therefore, tests are performed for assessment of new coatings and the same after natural or artificial aging, to evaluate changes. Frequently, namely when the existent coating has lost partially its performance, such as surface cohesion, consolidants and other protective finishings can be applied. The aesthetic changes resulting from those protective applications are also assessed.

Stereo-zoom observations using microscopes can detect microcracks and stains.

For changes in colour, both colorimeters and spectrophotometers can be applied and a scale considering the CIELAB colour space (L^* , a^* , b^*) is commonly used. The L^* coordinate corresponds to the lightness, ranging from 0 (black) to 100 (white), a^* is the red/green coordinate and b^* is the yellow/blue coordinate. The observer angle

and area are defined by the equipment used. For aged coatings, the global colour difference (ΔE) is calculated considering the values of ΔL^* , Δa^* and Δb^* [23].

Surface gloss measurements can be performed with specular gloss meters. A defined angle for measurement should be defined. Texture can be assessed by surface roughness measurements. A surface profile gauge can be used. Some standards for paint systems, such as the NP 4505 [24] may be used, although adaptations are sometimes needed for other coating systems.

To assess the contribution of coatings for lighting different complementary methods can be used [25]. Reflectance under controlled daylight conditions can be measured in a “test room” under diffuse light (without direct sunlight incidence), using the method of a spatial integrated visible radiant flux under steady state conditions, with an integrating sphere, coated inside with a high luminous diffuse finishing with circa 80% of reflectance. Another method is the angle-dependent luminance-based reflectance using a chromameter to measure the luminance in the laboratory, with different angles of incidence and viewing of the light. The luminance-based reflectance under controlled daylight conditions in a “test-room” is a third method, that can also be performed outdoors, under real-sky conditions, with a chromameter [25]. Measurements under real sky conditions are more realistic although less reproducible.

Reflection spectra of coatings can be assessed by UV/Vis/NIR spectrophotometer with defined wavelength accuracy, that can collect specular and diffuse reflections. Both coloured and colourless phases of the coatings can be measured, with defined wavelength range, namely 250–2500 nm [14, 26].

Thermocouples can be attached to the surface of the coatings, and kept in a climatic chamber to control the surface temperature, lower to test for the coloured phase, and higher for the colourless phase [27]. The solar spectrum [28] can be provided by ASTM E490-22 [29] and solar reflectance can be calculated by ASTM E903-96 [30].

14.3.2 Tests for Self-cleaning, Photocatalytic Activity and Hydrophobicity

Several tests can be performed to assess self-cleaning and photocatalytic activity of coatings. When protective surface products are applied, to assess compatibility and treatment effectiveness, the following tests can be performed.

Colour changes—Induced by the application of protective treatments, and by stain degradation; the changes can be assessed by:

- visual observation using a simple colour chart;
- colorimeter or spectrophotometer, using CIELAB coordinates allowing to quantify the changes.

All these tests can be performed in laboratory and, with portable equipment, in situ.

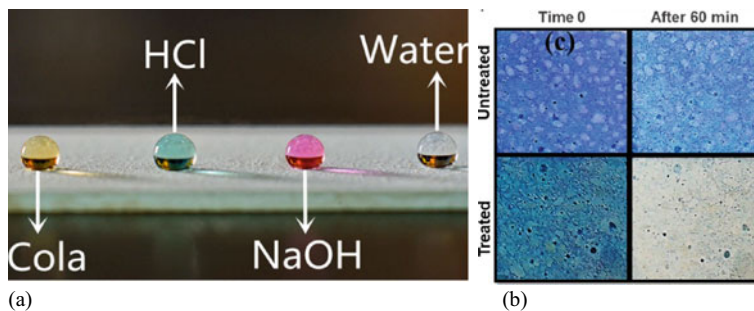


Fig. 14.2 Liquid-repellence of a coated surface towards Cola, HCl, NaOH and water droplets [32] (a); untreated and treated with TiO₂-based self-cleaning product surfaces just after stained with Methylene Blue and after 60 min of irradiation [16] (b)

Photocatalytic activity—Adapting ISO 10678 [31] test procedure using a solution of methylene blue in ethanol, and irradiation in a solar degradation chamber, namely according to Khannyra et al. [16] (Fig. 14.2b).

Self-cleaning effect—Using a deposit of a solution of carbon black pigment in chloroform Khannyra et al. [16] and assessing after irradiation.

To assess the degree of hydrophobicity and its durability, namely when it is ensured by a surface treatment, the following tests can be performed.

Hydrophobicity—The water contact angle (WCA) and contact angle hysteresis (CAH) are evaluated before and after the application of hydrophobic treatment or in coating products formulated with those hydrophobic agents, in comparison with reference products and control specimens (Fig. 14.2a).

Durability of hydrophobicity—The tests are performed before and after natural or artificial aging, namely by UV radiation (Fig. 14.2b) and after abrasion or erosion (Fig. 14.3).

To assess the durability of protective surface products applied on the coatings, the following tests can be performed.

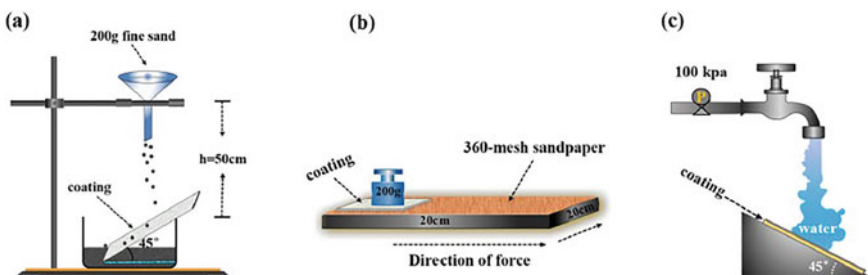


Fig. 14.3 Testing the durability of protective surface coatings for **a** sand impact, **b** sandpaper abrasion, **c** water impact erosion [15]

Peeling test—Based on Drdácký et al. [33] and adapted by Parracha et al. [34], this simple test allows to assess the adhesion of the treated surface to the substrate or to underlayers. A scotch tape with defined reference, size and weight is glued to the surface with a defined pressure, during a defined period of time, using a resilient tissue such as neoprene to homogenize a defined pressure on the tape; the tape is peeled and the visual observation of particles adhered to the tape qualitatively provides comparative results (and can be used *in situ*), while the difference of weight of the tape (before and after peeling) provides quantitative results in laboratory.

Aging—The effect of the protective treatment can be assessed after sand impact, sandpaper abrasion, water impact on erosion (Fig. 14.3), acid/alkali solution immersion, other artificial aging or after natural weatherability.

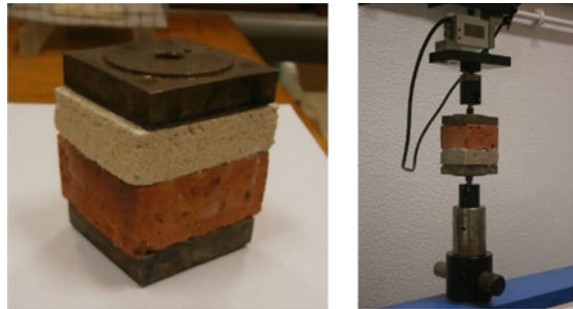
14.3.3 Testing Mechanical Performance

Several tests can be performed to assess coatings mechanical performance. These tests should be chosen depending on the coating system. For instance, adhesion is important for coatings attached to a substrate, while bending tests are mandatory for claddings to apply on ventilated systems for façades, the latter using a common test procedure. Abrasion or impact actions are different for indoor and outdoor coatings, the latter using common test procedures.

Adhesion—Adhesion to the substrate is a very important characteristic of ETICS, renders and plasters, because lack of adhesion results in total loss of functionality and, even worse, may become a safety risk, as the fall of render fragments from the façades or of plaster pieces from ceilings and higher zones of walls can seriously hurt the users of those spaces. The assessment of this characteristic is standardized for example in the European system [35, 36], using pull-off tests. However, for low strength coatings, such as those based in lime or in earth, this method can be too aggressive, because the vibration of the drilling machine may be enough to detach weak mortars, or to significantly interfere with their adhesion. Thus, adapted methods have been developed. An adapted method used for lime-based renders [37] and as well for lime-based bonding mortars for old ceramic tiles [38] consists of applying the lime-based mortar to be studied, with a thickness of 20 ± 2 mm (based on the average thickness usually applied in practice), on a porous ceramic brick piece of surface dimensions 6×6 cm, using a mould in order to get a flat surface. After 90 days of the mortars' application, two metallic plates with the same area are glued, on each side of the sample (Fig. 14.4) and connected to an electromechanical tensile testing device. A constant tension of 5 N/s is applied on the plates until failure of the system and allows to determine the adhesion strength through direct division by the area of the metallic plates.

In Santos et al. [37] the results of the method are compared with the results of bond strength by the method of EN 1015-12 [35]. It is found that the average values

Fig. 14.4 Prepared sample and testing adhesion of a lime-based coating to a substrate



obtained are rather similar; however, with the direct tensile method the variation coefficient is much lower (29% vs. 73%) and null values are eliminated.

Abrasion—Abrasion is important when eco-efficient, not so common coatings are applied. That may be the case of clay plasters, known for not having high mechanical performance, although comparable to very durable air lime plasters [12]. The DIN 18947 [39] details a simple abrasion test that can be used also to other coatings.

14.3.4 Tests for Weathering

Durability of buildings coatings are conditioned by many different factors, that depend on their microstructures and on their contexts (e.g. exterior or interior, type of substrate, etc.). Climatic and environmental actions are probably the most relevant actions affecting durability, and they are very different depending on the geographical situation and on the type of exposition. Thus a great diversity of weathering tests has been developed to simulate those actions, some more general and some for specific conditions. Usually, those tests consist of exposing the coatings to extreme conditions in repeated cycles. For example, for porous coatings, freeze-thaw cycles, heat-freeze cycles, cycles of salt saturation by partial immersion in salty water followed by drying, and cycles of combinations of these actions are used, based on existent standards and guides for different materials [36, 40–43] and adapted to each specific situation, for example by using applications on a defined substrate or by adjusting the duration and intensity of cycles to the climatic conditions in presence [23, 44–47]. For polymeric coatings and coloured coatings in general, UV cycles are also used, again both directly from existent standards [48] or adapted, in duration and type of specimens, to the specific type and context of the coating [49]. These tests are often well adapted to relative evaluation by comparison with a reference, but they are not well enough correlated with natural weathering [2], so they need more work and experience to be used to estimate the rate of degradation and the durability of a coating in absolute terms.

14.3.5 Testing the Protection from Water, Moisture and Salts

Protection from water and moisture can be tested differently, depending on the type of coating and substrate. Traditional methods can be applied, such as using moisture meters, usual for wood-based coatings for walls and floors, or standardized tests for roof tiles [50]. To assess moisture, the method consisting of the extraction of a small sample and weight it before and after drying in an oven is only valid if the extraction method itself does not dry the sample nor wet it either.

For many coating materials and products, the protection from water and moisture can be assessed by traditional testing of capillarity water absorption and drying [51], particularly important for porous building materials of cultural heritage. The latter can be an alternative to the water vapor permeability test because it assesses both the liquid and the vapor drying phases. When testing façade coatings, the Karsten tube absorption test [52] can be used. For coatings vulnerable to water, such as clay-based renders and plasters, specific tests exist and some are addressed in Chap. 3.

As coatings are used to protect the substrate, it is sometimes important to assess if they effectively provide protection from water or on the contrary, they hinder the evaporation of water already existent inside the walls. This a common problem in historic massive walls, that receive rising capillary water from the soil which may be kept inside the masonry if low capillary external coatings are used (for example cement renders or acrylic paintings). In fact, in those walls, not only the vapor drying phase but also the liquid drying phase is needed. To assess this effect a test was developed consisting of applying the coating to be tested on a thick porous substrate; saturating the substrate by immersion in water; sealing the base of the substrate and lateral faces of substrate and coating, and monitoring the drying through the coating [53]—Fig. 14.5.

Infrared thermography can be used to assess damaged on adhered coating systems [54]. Moisture in walls can be easily identified during the day as areas with lower temperatures because of the evaporative cooldown. However, when moisture presence and detachment occur at the same time, it is possible that the thermal differential

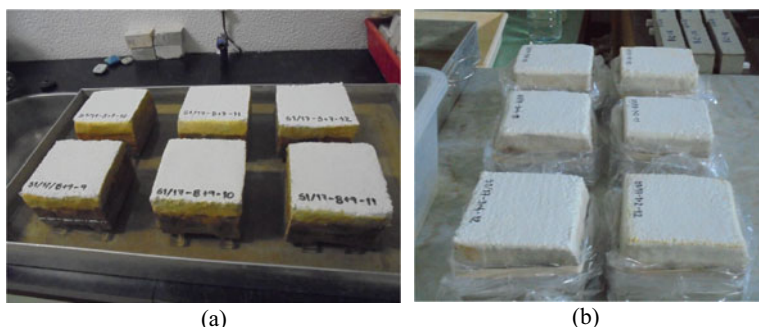


Fig. 14.5 Test to assess water vapor transport from a substrate to the coating: **a** saturation of the substrate; **b** drying through the coating system

is null, hindering the identification of both anomalies. Therefore, testing should be performed under different conditions, namely after rainy days and under dry conditions, as the opposite behaviours will reinforce the results. The same testing equipment can also be used to assess lack of watertightness on waterproofing systems of flat roofs, apart from the traditional use to detect thermal bridges.

Moisture and water are commonly associated to damage induced by salts, as they are hygroscopic and water soluble. If the salts are always below the dissolution relative humidity, they remain stable, crystalized; if they are always above that relative humidity, they are also stable, dissolved. Therefore, testing moisture is sometimes a way to know if salts attack is possible. Depending on the building material and product, different tests to assess resistance to salts attack may be performed. Different kinds of cycles have been defined for different uses, mainly based on total or partial immersion of coating samples or systems in salty solutions followed by drying, which induces crystallization and consequent damage. For the protection of the substrate (the wall) the coating should promote the removal of the salts from the substrate. This is particularly important for historic porous walls, that must be preserved. Thus, some of these tests allow to analyse both the resistance of the coating material to salt crystallization and its protection of the substrate [55]. Recommendation for an accelerated test procedure for assessing the resistance of inorganic porous building materials to salt crystallization is being defined by a RILEM Technical committee [56, 57]. The referred test procedure developed by the TC 271-ASC proposes a new approach to salt crystallization test for the assessment of the behaviour of porous building materials. It considers the need to accumulate a certain amount of salt to activate the damage. This procedure consists of two phases: a first phase, in which salts are introduced in the material and accumulate close to the evaporation surface, and a second phase, in which damage propagates because of repeated dissolution and crystallization cycles, induced by re-wetting with liquid water and by RH changes.

The test procedure considers damage due to sodium sulphate and sodium chloride, both tested as single salts, with two concentrations each: sodium sulphate—1 and 5% (weight of Na_2SO_4 /weight solution); sodium chloride—5 and 10% (weight NaCl /weight solution). These concentrations were chosen as being high enough to cause damage but still realistic salt content in the material. The contamination with salt solution occurs via capillary absorption through the bottom surface of the specimen, i.e., through the surface opposite to the evaporative surface. The propagation phase is different for each salt.

For sodium sulphate it consists of 4 cycles, each one with duration of 2 weeks, with the following composition: 4 h cooling of the specimens at room conditions ($T = 22^\circ\text{C}$; $\text{RH} = 45\%$); removal of the sealing from the bottom surface; rewetting with water (80% of the initial water weight) by capillarity from the bottom surface at room conditions; sealing of the bottom surface with paraffin film; drying at room conditions up to 24 h from the start of the re-wetting; drying for 312 h (13 days) at $40^\circ\text{C}/15\%$ RH. The weight of the specimens should be recorded at least at the end of each 2-week cycle.

For sodium chloride the propagation phase consists of 3 cycles, each cycle with a duration of 3 weeks and is composed by: 24 h hygroscopic adsorption at $20^\circ\text{C}/95\%$

RH; 12 h drying at 20 °C/50% RH; 44 h drying at 40 °C/15% RH; 24 h hygroscopic adsorption at 20 °C/95% RH; 12 h drying at 20 °C/50% RH; 44 h drying at 40 °C/15% RH; 24 h hygroscopic adsorption at 20 °C/95% RH; 12 h drying at 20 °C/50% RH; 44 h drying at 40 °C/15% RH; 4 h cooling at room conditions (22 ± 2 °C/45% RH); removal of the sealing from the bottom surface; rewetting with water from the bottom surface with 50% water amount used for the initial contamination; sealing of the bottom surface with paraffin film; 1 h storage of the specimens at RH > 95% (in order to allow for salt dissolution); 264 h drying at 40 °C/15% RH. The weight of the specimens should be recorded at least at the end of each 3-week cycle.

The whole procedures are still being fine-tuned by the TC 271-ASC, namely through round robin tests with different substrates in several laboratories of the members. The TC 271-ASC expects to publish the final procedure still in 2022. However, not being specific for coatings, this test procedure does not consider the interaction between a coating and its substrate.

14.3.6 Tests for Hygroscopicity, Water Vapor Permeability and Drying

There are several protocols to assess hygroscopicity, important for indoor coating, and a review for plasters is presented by Ranesi et al. [58]. The DIN 18947 [39] can be used to evaluate adsorption capacity, while the ISO 24353 [59] can be used to assess both adsorption and desorption, using a one-step procedure.

Other researchers use the Dynamic Vapour Sorption (DVS) equipment [60, 61], which is a gravimetric technique measuring the amount of water that is adsorbed by a sample at equilibrium, rapidly assessing the sorption isotherms instead of proceeding according to the EN ISO 12571 [62], which is a long timely test. The limitation of the DVS is the very low weight of the samples to test, which are only representative of homogeneous materials or composites with small aggregates. For the EN ISO method, air velocity in the test chamber may affect results.

A common method to assess the moisture buffer value is the NORDTEST [63], from consecutive cycles of adsorption/desorption of indoor coating samples, although environmental conditions may not be the best suited for non-Northern countries.

A common test for indoor and outdoor coatings, namely to assess their compatibility with the substrate in terms of moisture transport, is the water vapor permeability test. Specifically for rendering and plastering mortars, this test is specified in the EN 1015-19 [64], although other standards exist for building materials in general. However, only the vapor migration is tested, while the drying test, specified in the EN 16322 [51], addresses both the liquid and vapor migration phases. Therefore, results of drying capacity (drying rates in the 1st and 2nd drying phases, and drying index) provide complementary data to what happens on site when a coating is wet and dries.

For all these tests and the ones of the previous sub-section, the porous structure of renders and plasters under test is particularly important, as it varies when the mortars are tested after being applied in an impermeable mould or in contact with a porous substrate. Therefore, results would more closely reproduce real cases if the tested samples were moulded in contact with a porous substrate, before being extracted [65, 66].

14.3.7 Tests for Biological Colonization Susceptibility

Biological colonization is favoured by persistent moisture, often due to rain runoffs (in the exterior), water infiltrations (in the interior) or by condensations (in exterior, for example on ETICS, or interior, for example on cold surfaces). This phenomenon may thus be mitigated by improving the construction detailing, watertightness and thermal insulation. However, it is also related with susceptibility to biologic growth of the building materials, namely of coatings, which are very exposed to moisture and to contamination while being also very visible. Thus, it is important to evaluate the susceptibility to biological colonization of coatings. To assess the susceptibility to mould growth a method adapted from ASTM D 5590-17 [67] and ASTM C 1338-19 [68] has been used for ETICS [69] and as well for painting systems and renders [70] and for earth plasters [71]. *Aspergillus niger* and *Penicillium funiculosum* are selected as representative biodeterioration agents due to their widespread presence in interior and outdoor environments. The method consists on using strains from these species, which, on the cases analysed, were collected from the fungal culture collection of the Portuguese National Laboratory for Civil Engineering (LNEC) to obtain a mixed fungal suspension. The suspension is then uniformly applied on the surface of previously sterilized specimens of the coating to test and on controls of filter paper and surrounding culture media composed by 4% malt and 2% agar, which are needed to validate the results. The inoculated specimens are kept in a conditioned chamber at $T = 22 \pm 1^\circ\text{C}$ and $70 \pm 5\%$ RH for a period of four weeks. Each week, the specimens are visually analysed and classified for mould growth using the following scale 0 to 4:0 – no growth; 1 – <10% growth; 2 – 10–30% growth; 3 – 30–60% growth; 4 – >60% growth. At the end of the exposure time, the specimens are removed from the containers and the final percentage of contaminated surface is evaluated by combining visual observations and observations with a stereo microscope.

14.3.8 Tests the Release of Toxics that Pollute Run-Off Water and Soil

To assess the release of toxic products to rainwater running along the building roofs and facades, samples of that runoff water are collected and analysed for toxic elements detection. The EN 16105 [72] addresses how to test the release of substances from paints and varnishes used in coatings in intermittent contact with water, and can be adapted to other coatings, such as roof tiles or renders. The toxicity to the soil can also be tested [18].

14.3.9 Tests for Indoor Pollutants Release and Capture

There are several protocols to assess indoor pollutants release during the application of coatings, such as the one defined by Spee and Huizer [1] for safety assessment when applying floor coatings. For flooring, the EN 14041 [73] addresses this characteristic. The EN 16516 [74] defines how to assess the released emissions of dangerous substances into indoor air, and can be used for several coatings, although it is not exhaustive for all types of pollutants that can have high contents indoors, and so, negatively affect occupants health. Room scale chamber experiments such as those used by Gall et al. [20] to determine ozone deposition velocities and reaction product formation rates for indoor coating products under varying environmental conditions can be used. Comparison with small scale chamber experiments reported for the same test materials may validate these less expensive tests [20]. The release of pollutants from building coatings, such as VOCs, can also be tested together with the development of bacterial communities, such as performed by Mhuireach et al. [75].

Being a recent subject of research, and the existence of several pollutants indoors, testing procedures to assess pollutants capture are still under development and much less validated tests exist in comparison to pollutants release tests. The following tests are examples of what has been applied to assess pollutants capture by outdoor coatings.

Capture of CO₂—The capture of CO₂ by coatings can be performed by thermogravimetric analysis (TGA/DTG), testing samples before (without) and after exposure to CO₂, simulating levels that can occur indoors. This technique has been used by Santos et al. [22] to compare the capture of CO₂ of earth and gypsum plasters. A higher mass loss variation was associated to higher capture capacity.

Capture of NO—The evaluation of NO photooxidation or photocatalytic remediation for surfaces treated with innovative materials and for innovative coating products can be performed according to the ISO 22197–1 [76], as adapted by Mills et al. [77]. The content of NO conversion, NO_x removal, generation of NO₂ and selectivity of the generated NO₂ can be calculated [16]. Alternatively, flow tube photo-reactor can also be used to assess NO_x remediation, namely by photocatalytic paints [78].

14.4 Concluding Remarks

Coatings are an important part of buildings in terms of functions to accomplish and requirements to fulfil, cost and time needed for application, repair and replace. This part of building elements plays the protection and image of surface envelope of buildings, outdoors and indoors. They perform several functions, starting with the protection of the substrates and, therefore, durability of the building systems. With the increased concern on energy efficiency and eco-efficiency in general, the durability of the building elements protected by the coatings, as well as durability of the coatings themselves, are important. In addition, several other requirements are mandatory nowadays, such as the ones contributing to reduce energy consumption on lightning, cooling and heating, ensuring comfort. Furthermore, also complementary requirements to the more common ones should place coatings as important contributors to health and safety. Innovative coating materials and coating products with incremental innovation also appear in the market, intending to contribute for new requirements. Therefore, innovative tests are being defined while other tests have been adapted to allow assessing the performance of building coatings.

Not being totally exhaustive, due to publishing limitations, this chapter presents the most important requirements for coatings and describes and briefly discusses the tests which allow to assess them. Some of the new tests described (innovative or adapted) provide assessment methods for the reflectivity and contribution to lighting indicators, for self-cleaning and photocatalytic effect and for hydrophobicity, for adhesion in case of low strength coatings, for abrasion of partially soluble materials. Additionally tests for weathering of coatings and to evaluate their protection ability concerning water, moisture and salts are also referred. Finally, tests for the susceptibility to biological colonization, the release of toxics and pollutants and as well the potential to pollutants capture are also indicated.

Apart from applying some of these test methods, it is also expected that the examples described will allow readers to optimize the tests referred and contribute to evaluate their validity. In turn that will contribute to enlarge the range of test methods to assess building coatings. Well defined and more accurate testing, used worldwide, will provide tools to a better choice of materials by the users and to the improvement of these building elements by the industry of construction products.

Acknowledgements The first author would like to acknowledge the support of FCT for the partial funding of this work under the strategic project UIDB/04625/2020 from the research unit CERIS.

References

1. Spee T, Huizer H (2017) Comparing REACH chemical safety assessment information with practice-a case-study of polymethylmethacrylate (PMMA) in floor coating in The Netherlands. Int J Hyg Environ Health 220(7):1190–1194

2. Parracha JL, Borsoi G, Veiga R, Flores-Colen I, Nunes L, Viegas CA, Moreira LM, Dionísio A, Gomes MG, Faria P (2022) Durability assessment of external thermal insulation composite systems in urban and maritime environments. *Sci Total Environ* 849:157828
3. EN 998:2016 (2016) Specification for mortar for masonry-part 1: rendering and plastering mortar. CEN
4. ETAG 034:2012 (2012) Guideline for European technical approval of kits for external wall claddings. Part 1: ventilated cladding kits comprising cladding components and associated fixings. European Organisation for Technical Approvals (EOTA)
5. Shafaghat A, Keyvanfar A (2022) Dynamic façades design typologies, technologies, measurement techniques, and physical performances across thermal, optical, ventilation, and electricity generation outlooks. *Renew Sustain Energy Rev* 167:112647
6. Veiga MR, Velosa A, Magalhães A (2007) Evaluation of mechanical compatibility of renders to apply on old walls based on a restrained shrinkage test. *Mater Struct* 40(10):1115–1126
7. Nunes, C, Faria P, Garcia N (2022) Limewashes with vegetable oils: water transport characterization. In: Bokan-Bosiljkov V, Padovnik A, Turk T, Štukovnik P (eds) HMC 2022-6th historic mortars conference. University of Ljubljana, Ljubljana, Slovenia, pp 179–190. ISBN 978-961-6884-77-8
8. Ma X, Tu R, An W, Xu L, Luo S, Wang J, Tang F (2020) Experimental study of interlayer effect induced by building facade curtain wall on downward flame spread behavior of polyurethane. *Appl Therm Eng* 167:114694
9. Göswein V, Silvestre JD, Monteiro CS, Habert G, Freire F, Pittau F (2021) Influence of material choice, renovation rate, and electricity grid to achieve a Paris Agreement-compatible building stock: a Portuguese case study. *Build Environ* 195:107773
10. Peck G, Jones N, McKenna ST, Glockling JLD, Harbottle J, Stec AA, Hull TR (2021) Smoke toxicity of rainscreen façades. *J Hazard Mater* 403:123694
11. Antunes A, Faria P, Brás A, Silva V (2019) Rice husk-earth based composites: a novel bio-based panel for buildings refurbishment. *Constr Build Mater* 221:99–108
12. Lima J, Faria P, Veiga R (2021) Comparison of an earth mortar and common binder mortars for indoor plastering. In: Horszczaruk E, Brzozowski P (eds) ICSEFCM2021-2nd international conference on sustainable, environmentally friendly construction materials. West Pomeranian University of Technology, Szczecin, Poland, pp 71–76
13. Santos T, Gomes MI, Ssantos Silva A, Ferraz E, Faria P (2020) Comparison of mineralogical, mechanical and hygroscopic characteristic of earthen, gypsum and cement-based plasters. *Constr Build Mater* 254:119222
14. Fabiani C, Castaldo VL, Pisello AL (2020) Thermochromic materials for indoor thermal comfort improvement: finite difference modeling and validation in a real case-study building. *Appl Energy* 262:114147
15. Jiang L, Hou P, He S, Han M, Xiang P, Xiao T, Tan X (2022) The robust superhydrophobic SiO₂/Diatomite/PDMS/KH-570/Me-MQ composite coating for self-cleaning application of building surface. *Colloids Surf A* 634:127936
16. Khannyra S, Mosquera MJ, Addoub M, Gil MLA (2021) Cu-TiO₂/SiO₂ photocatalysts for concrete-based building materials: self-cleaning and air de-pollution performance. *Constr Build Mater* 313:125419
17. Mokhtarifar M, Nguyen DT, Sakar M, Lucotti A, Asa M, Kaveh R, Diamanti MV, Pedeferri MP, Do TO (2022) Smart protection of surfaces during day-night by a novel composite self-cleaning coating with catalytic memory. *J Environ Chem Eng* 10(1):106891
18. Bollmann UE, Fernandez-Calvin D, Brandt KK, Storgaard MS, Sanderson H, Bester K (2017) Biocide runoff from building facades: degradation kinetics in soil. *Environ Sci Technol* 51(7):3694–3702
19. European Parliament and Council (2012) Regulation EU No 528/2012 concerning the making available on the market and use of biocidal products. *Off J Eur Communities Legis* L167:1–122
20. Gall E, Darling E, Siegel JA, Morrison GC, Corsi RL (2013) Evaluation of three common green building materials for ozone removal, and primary and secondary emissions of aldehydes. *Atmos Environ* 77:910–918

21. Maqbool Q, Czerwinska N, Giosue C, Sabbatini S, Ruello ML, Tittarelli F (2022) New waste-derived TiO₂ nanoparticles as a potential photocatalytic additive for lime based indoor finishings. *J Clean Prod* 373:133853
22. Santos T, Santos Silva A, Gomes MI, Faria P (2022) Evaluation of the hygroscopic and CO₂ capture capacities of earth and gypsum-based plasters. In: Bokan-Bosiljkov V, Padovnik A, Turk T, Štukovnik P (eds) HMC 2022-6th historic mortars conference. Ljubljana, Slovenia, pp 249–257. ISBN 978-961-6884-77-8
23. Parracha J, Borsoi G, Flores-Colen I, Veiga MR, Nunes L (2022) Impact of natural and artificial ageing on the properties of the multilayer external wall thermal insulation systems. *Constr Build Mater* 317:125834
24. NP 4505:2012 (2012) Paints and varnishes. Paints for exterior surfaces of buildings. Classification and requirements. IPQ (in Portuguese)
25. Barbero-Barrera M, Santos AJC, Veiga MR (2019) The appearance and luminous properties of lime and gypsum pastes: a comparative analysis of different methods of measurement. *Constr Build Mater* 221:562–572
26. Zhang Y, Zhai X (2019) Preparation and testing of thermochromic coatings for buildings. *Sol Energy* 191:540–548
27. Zhang Y, Zhu Y, Yang J, Zhai X (2020) Energy saving performance of thermochromic coatings with different colors for buildings. *Energy Build* 215:109920
28. Hu J, Yu X (2019) Design and characterization of energy efficient roofing system with innovative TiO₂ enhanced thermochromic films. *Constr Build Mater* 223:1053–1062
29. ASTM E490-22 (2022) Standard solar constant and zero air mass solar spectral irradiance tables. ASTM
30. ASTM E903-20 (2020) Standard test method for solar absorptance, reflectance, and transmittance of materials using integrating spheres. ASTM
31. ISO 10678:2010 (2010) Fine ceramics (advanced ceramics, advanced technical ceramics)—determination of photocatalytic activity of surfaces in an aqueous medium by degradation of methylene blue. ISO
32. Wang X, Ding H, Wang C, Zhou R, Li Y, Li W, Ao W (2021) Self-healing superhydrophobic A-SiO₂/N-TiO₂@HDTMS coating with self-cleaning property. *Appl Surf Sci* 567:150808
33. Drdácký M, Lesák J, Rescic S, Slízková Z, Tiano P, Valach J (2012) Standardization of peeling tests for assessing the cohesion and consolidation characteristics of historic stone surfaces. *Mater Struct* 45:505–520
34. Parracha JL, Pereira AS, Velez da Silva R, Almeida N, Faria P (2019) Efficacy of iron-based bioproducts as surface biotreatment for earth-based plastering mortars. *J Clean Prod* 237:117803
35. EN 1015-12:2016—Methods of test for mortars for masonry—part 12: determination of adhesive strength of hardened rendering and plastering mortars to the substrate. CEN
36. EAD 040083-00-0404:2019 (2019) European Assessment document of external thermal insulation composite systems (ETICS) with rendering. EOTA
37. Santos AR, Veiga MR, Santos Silva A, De Brito J (2020) Tensile bond strength of lime-based mortars: the role of the microstructure on their performance assessed by a new non-standard test method. *J Build Eng* 29:101136
38. Botas S, Veiga MR, Velosa A (2017) Bond strength in mortar/ceramic tile interface-testing procedure and adequacy evaluation. *Mater Struct* 50:211
39. DIN 18947: 2018 (2018) Earth plasters—earth plasters—requirements, test and labelling. DIN
40. EN 1015-21:2002 (2002) Methods of test for mortar for masonry. Part 21: determination of the compatibility of one-coat rendering mortars with substrates. CEN
41. ASTM C 666-97 (2017) Standard test method for resistance of concrete to rapid freezing and thawing. ASTM
42. ASTM D 559-2003 (2003) Standard test methods for wetting and drying compacted soil-cement mixtures. ASTM
43. EN 12370:2020 (2020) Natural stone test methods—determination of resistance to salt crystallization. CEN

44. Fragata A, Veiga MR, Velosa A (2016) Substitution ventilated render systems for historic masonry: salt crystallization tests evaluation. *Constr Build Mater* 102(1):592–600
45. Maia J, Ramos NMM, Veiga MR (2019) A new durability assessment methodology of thermal mortars applied in multilayer rendering systems. *Constr Build Mater* 222:654–663
46. Bochen J (2015) Weathering effects on physical e chemical properties of external plaster mortars exposed to different environments. *Constr Build Mater* 79:192–206
47. Santos AR, Veiga MR, Santos Silva A, Matias L, Brito J (2018) Durability and compatibility of lime-based mortars: the effect of aggregates. *Infrastructures* 3:34
48. EN ISO 16474-2:2013 (2013) Paints and varnishes—methods of exposure to laboratory light sources—part 2: xenon-arc lamps. CEN
49. Parracha J, Borsoi G, Veiga MR, Flores-Colen I, Nunes L, Garcia A, Ilharco L, Dionísio A, Faria P (2021) Effects of hydrothermal, UV and SO₂ accelerated ageing on the durability of ETICS in urban environments. *Build Environ* 204:108151
50. EN 539-1:2005 (2005) Clay roofing tiles for discontinuous laying-determination of physical characteristics-part 1: impermeability test. CEN
51. EN 16322:2014 (2014) Conservation of Cultural Heritage-Test Methods-Determination of drying properties. CEN
52. EN 16302:2014 (2014) Conservation of cultural heritage-test methods-measurement of water absorption by pipe method. CEN
53. Veiga MR, Rodrigues P, Santos D, Pereira J (2018) Polysiloxane-based paint system: evaluation of compatibility with old building walls. In: Proceedings of the construction congress, Porto, FEUP, November 21–23. (in Portuguese)
54. Lourenço T, Matias L, Faria P (2017) Anomalies detection in adhesive wall tiling systems by infrared thermography. *Constr Build Mater* 148:419–428
55. Fragata A, Veiga MR, Velosa A (2021) Performance of a salt-accumulating substitution lime render for salt laden historic masonry walls. *Heritage* 4:3879–3891
56. Lubelli B, Cnudde V, Diaz-Goncalves T, Franzoni E, van Hees R, Ioannou I, Menendez B, Nunes C, Siedel H, Stefanidou M, Verges-Belmin V, Viles H (2019) Towards a more effective and reliable salt crystallization test for porous building materials: state of the art. *Mater Struct* 51:55
57. Lubelli B, RILEM TC 271-ASC members (2021) A new accelerated laboratory test for the assessment of the durability of materials with respect to salt crystallization. In Lubelli B, Kamat A, Quist W (eds) Proceedings of the 5th SWBSS-international conference on salt weathering of buildings and stone sculptures. TU Delft, pp 55–68
58. Ranesi A, Veiga MR, Faria P (2021) Laboratory characterization of relative humidity dependent properties for plasters: a systematic review. *Constr Build Mater* 304:124595
59. ISO 24353:2008 (2008) Hygrothermal performance of building materials and products-determination of moisture adsorption/desorption properties in response to humidity variation. ISO
60. Lagouin M, Laborel-Préneron A, Magniont C, Geoffroy S, Aubert J-E (2022) Moisture buffer capacity of a bilayer bio- and geo-based wall. *Constr Build Mater* 329:127209
61. Fabbri A, McGregor F, Costa I, Faria P (2017) Effect of temperature on the sorption curves of earthen materials. *Mater Struct* 50:253
62. EN ISO 12571:2021 (2021) Hygrothermal performance of building materials and products-determination of hygroscopic sorption properties. CEN
63. Rode C, Peuhkuri RH, Mortensen LH, Hansen KK, Time B, Gustavsen A, Harderup LE (2005) Moisture buffering of building materials. Technical University of Denmark, Department of Civil Engineering
64. EN 1015-19:1998 (1998) Methods of test for mortar for masonry-part 19: determination of water vapour permeability of hardened rendering and plastering mortars. CEN
65. Veiga MR, Vilhena A (2019) Support for the rehabilitation of S. Francisco do Penedo fortress, in Luanda. 2nd phase—study of repair and conservation mortars to be applied in the intervention. Report 191/2019. Lisbon, LNEC. (in Portuguese)

66. Bellei P, Arromba J, Flores-Colen I, Veiga R, Torres I (2021) Influence of brick and concrete substrates on the performance of renders using in-situ testing techniques. *J Build Eng* 43:102871
67. ASTM D 5590-17 (2017) Determining the resistance of paint films and related coatings to fungal defacement by accelerated four-week agar plate assay. ASTM
68. ASTM C 1338-19 (2019) Standard test method for determining fungi resistance of insulation materials and facings. ASTM
69. Parracha J, Borsoi G, Flores-Colen I, Veiga MR, Nunes L, Dionísio A, Gomes G, Faria P (2021) Performance parameters of ETICS: correlating water resistance, bio-susceptibility and surface properties. *Constr Build Mater* 272:121956
70. Brazão Farinha C, Nunes L, Brito J, Veiga MR (2018) Effect of organic residues on moulds development on mortars. In: *Construção 2018*. Porto, FEUP. (in Portuguese)
71. Santos T, Nunes L, Faria P (2017) Production of eco-efficient earth-based plasters: influence of composition on physical performance and bio-susceptibility. *J Clean Prod* 167:55–67
72. EN 16105:2011 (2011) Paints and varnishes-laboratory method for determination of release of substances from coatings in intermittent contact with water. CEN
73. EN 14041:2018 (2018) Resilient, textile, laminate and modular multilayer floor coverings—essential characteristics. CEN
74. EN 16516:2017 (2017) Construction products: assessment of release of dangerous substances—determination of emissions into indoor air. CEN
75. Mhuireach GÁ, Dietz L, Griffiths W, Horve PF, Laguerre A, Northcutt D, Vandegrift R, Gall E, Van Den Wymelenberg K (2021) Differing effects of four building materials on viable bacterial communities and VOCs. *Dev Built Environ* 7:100055
76. ISO 22197-1:2016 (2016) Fine ceramics (advanced ceramics, advanced technical ceramics)—test method for air-purification performance of semiconducting photocatalytic materials—part 1: removal of nitric oxide. ISO
77. Mills A, Burns L, O'Rourke C, Elouali S (2016) Kinetics of the photocatalysed oxidation of NO in the ISO 22197 reactor. *J Photochem Photobiol A* 321:137–142
78. Gandolfo A, Bartolomei V, Gomez Alvarez E, Tlili S, Gligorovski S, Kleffmann J, Wortham H (2015) The effectiveness of indoor photocatalytic paints on NO_x and HONO levels. *Appl Catal B* 166–167:84–90

Chapter 15

New Trends in Acoustic Testing in Buildings



Julieta António , António Tadeu , and João Dias Carrilho

Abstract Acoustic testing techniques are traditionally and most often used to characterise construction materials and construction elements, either to certify compliance with building codes for noise transmission or to check desired architectural acoustic properties. New metamaterials that are being developed with acoustic applications in mind include metal, ceramic and gel foams, porous asphalt and smart sound-absorbing materials that exceed the acoustic performance achievable with conventional materials. Some of these new materials have interesting nonlinear behaviour that requires new testing approaches for their acoustic characterisation and to fully explore their capabilities. Acoustic-based, non-invasive techniques are extremely useful for monitoring the health of built structures, to detect and characterise defects such as cracks and voids, and to locate sources through acoustic imaging. Experimental evaluation of the acoustic behaviour of materials and composite structures is particularly important when it comes to validating numerical models of acoustic propagation, whether for a single material or for extremely complex structures. New trends in low-cost instrumentation technology, such as disposable sensors or direct sensor-ADC interfaces, and large-scale autonomous monitoring systems such as passive acoustic monitoring (PAM) also have potentially very interesting applications in the built environment. The purpose of this chapter is to provide an interdisciplinary overview of the latest developments and emerging techniques in acoustic testing, focusing particularly on existing and possible future applications in the field of civil engineering.

J. António () · A. Tadeu

CERIS, Department of Civil Engineering, University of Coimbra, Coimbra, Portugal
e-mail: julieta@dec.uc.pt

A. Tadeu

e-mail: tadeu@itecons.uc.pt

J. António · A. Tadeu · J. D. Carrilho

Itecons, Coimbra, Portugal

e-mail: joao.carrilho@itecons.uc.pt

J. D. Carrilho

CERIS, University of Coimbra, Coimbra, Portugal

Keywords Acoustic testing · New materials · Composite structures · Instrumentation

15.1 Introduction

In its broadest sense, acoustics encompasses the body of scientific knowledge concerned with the generation, propagation, and reception of mechanical waves and sound effects. Contrary to electromagnetic waves, mechanical waves require a medium to exist in, which can be a single solid, liquid, or gaseous phase or a mixture of phases. Mechanical waves support oscillation frequencies in ranges that can theoretically range up to the THz in liquids and solids. In air, it is common to split the frequency range into 3 main ranges: sound is the name given to the nominal frequency range to which the normal human ear is sensitive, between 20 Hz and 20 kHz; infrasound is the range below 20 Hz; and ultrasound is the range above 20 kHz and up to an estimated upper limit of 5 GHz.

It can be said that acoustics is everywhere. According to Lindsay's Wheel of Acoustics [1] the scope of acoustics covers four broad fields: Engineering (architectural, mechanical, electrical and chemical); Earth Sciences (oceanography, physics of earth and atmosphere); Life Sciences (physiology, and medicine); and Arts (visual arts, music, speech and psychology). The present chapter focuses on engineering acoustics, that is to say, on the relationship of environmental and indoor noise with comfort and health.

There is evidence across different scientific studies on the effect of environmental noise (such as road traffic noise, railway noise, aircraft noise, wind-turbine noise) on quality of life, wellbeing, and mental health [2]. Auditory effects (such as hearing impairment and tinnitus) and nonauditory effects (such as cardiovascular issues, poor quality of life, mental health, annoyance, cognitive impairment, and poor sleep) are some of the outcomes. Analysis of the available data shows that 65% of Europeans living in major urban areas are exposed to daytime noise levels greater than 55 dB, and more than 20% to night-time noise levels greater than 50 dB [3].

Various mitigation and preventive measures and tools have been used to prevent noise, which may require limiting it at the source, controlling the sound transmission path, protecting the receiver's site, and land-use planning. Of these possible measures, the most effective is to reduce noise emissions at the source. In this context, different regulations have been devised to impose noise level limits for road traffic, railway, and aircraft noise, and that caused by equipment (such as heating and ventilation systems). Regarding the control of the sound transmission path, acoustic barriers are often placed in the vicinity of dwellings close to the traffic source. In terms of protection at the receiver's site, this approach is mainly used for local sources of noise [4]. Land-use and urban planning measurements are the main tools for noise control. Numerical algorithms might be required to predict the noise impact caused by road traffic, railways, airports, and similar sources while noise level limits can be imposed for various zones and building types, and noise mapping assessment carried out.

Besides the noise generated outside, the indoor noise has to be accounted for, which can cause loss of productivity, illness, and even mortality. Within this context, the airborne sound insulation of slabs, walls, doors, and windows, the impact sound insulation of slabs, and the acoustic quality of confined spaces are very relevant.

In some cases, the acoustic excitation produced by impact sources is used as a tool in non-destructive testing to identify eigenfrequencies, eigenmodes, and damping ratios. Resonant techniques can be used to detect specific defects such as voids, cracks, delamination, lack of bonding, and changes in rigidity. In addition, various methods can detect changes in components relative to referenced ones. Acoustic emission is a technique used in the field of structural integrity assessment using fracture mechanics. It investigates the behaviour of defects under stress. Under these conditions, a sudden release of energy can occur, part of which will be converted to elastic waves. These waves are recorded by piezoelectric transducers and used to indicate the state of the defect.

The present chapter describes active research and development areas and identifies trends and directions, all concerning acoustic testing. More specifically, an attempt is made to relate the new trends of acoustic testing, given the appearance of new materials (such as metamaterials) and new methods of construction (such as smart shutters in windows), the existence of a more significant number of sources, the appearance of new acoustic equipment for measurement, and changed noise (such as that generated by electric vehicles and drones).

This chapter is organised as follows: first, the acoustic sources are characterised; then, the characterisation of materials, building elements, building equipment, and soundscape is discussed; finally, new trends in acoustic sensing are presented and discussed.

15.2 Characterisation of Noise Sources

Environmental noise, also known as noise pollution, refers normally to unwanted sound, generated and present in the outdoor environment. The most common sources of environmental noise originate in transport systems, industrial sites and recreational activities such as musical events.

In many regions of the world, the approach to mitigating environmental noise has matured into standard assessment procedures and concerted regulatory action. In the European Union (EU), for instance, the Environmental Noise Directive (END) was published in 2002 [5]. It details a harmonised plan of action focusing on 3 key areas: determining exposure to environmental noise; informing the public; and reducing environmental noise where necessary while preserving the good quality of areas which already had low environmental noise.

The END introduced the requirement that EU member states periodically monitor and report the degree of exposure of their general population to environmental noise. This is achieved by producing municipality-wide strategic noise maps, based on semi-empirical source strength correlations and propagation models, and validated with

on-site measurements where necessary. Strategic noise mapping is a highly regarded and perhaps one of the most successful instruments available to EU policy makers. However more than 30% of noise mapping data required is still not available and gap-filling algorithms must be used to produce estimates for a complete, Europe-wide, picture of the environmental noise problem [6].

Despite their wider importance as a policy instrument, strategic noise maps are nevertheless created primarily from model calculations and from complementary short-term measurements, and one should expect some shortcomings in their ability to capture the reality of the noise environment, depending on the greater or lesser fidelity of the models implemented. The identification of some of these shortcomings, has driving the latest research trends towards novel approaches to environmental noise assessment.

One particular difficulty that has raised the concern of several authors over the years is determining the building facade wall correction, as prescribed in ISO 1996-2 [7], and its influence on the accuracy of strategic noise maps. The END considers the ISO 1996 standards [7, 8] as a reference in the development of noise maps, and particularly in the determination of exposure from measurements at building facades. Barrigón Morillas et al. [9] reviewed experimental works from several authors and found measured values for the facade wall correction that deviate considerably from the values established in ISO 1996-2 [7], along with indications as to how these deviations could influence the accuracy of strategic noise maps. Zagubień and Wolniewicz [10] have recently revisited this problem, having found a building facade reflection correction lower than 1 dB, compared with the 3 dB correction prescribed by ISO 1996-2 [7], and proposed an alternative technique for locating the measurement microphone, although strictly for checking compliance with noise limits.

Of the different types of noise, those with low frequency content are those more difficult to attenuate. Low frequency noise is common as background noise in urban environments and as an emission of different artificial sources such as road traffic, aircraft, industrial machinery, artillery and mining explosions, and air movement machinery including wind turbines, compressors, and ventilation or air-conditioning units [11]. Compared with other types of noise, it is more difficult to attenuate due to its efficient propagation and the poor ability of building structures and hearing protectors to attenuate it. Thus, the effects of low frequency noise exposure in humans have been a topic of concern and investigation over the years. A review of the literature between 2016 and 2019 about low-frequency noise and its main effects on human health was performed by Alves et al. [12]. Most of the papers analysed mention effects on sleep disorders, discomfort, sensitivity to and irritability caused by noise, annoyance, hearing loss, and cardiovascular diseases.

Representative measurements of low frequency noise inside dwellings can be very challenging. Measurements are very dependent on the microphone position because of standing waves, and specialized equipment and expertise are needed. Additionally, the source of noise can be unknown and can be emitted intermittently, or the complaints are at night, making the measurement procedure more difficult.

To overcome these difficulties, a low-frequency measurement device was developed to be easily used by the occupants of dwellings [13]. Following simple guidelines, they can make recordings at times when the low-frequency noise typifies what they experience. The device is based on the Raspberry pi platform connected to a USB measurement microphone. As the microphone is not factory-calibrated, a custom-made microphone calibrator was also constructed to ensure calibrated measurements. Recordings and pictures of the measurement setup are automatically uploaded to a central server. Close collaboration with the occupants was crucial to avoid communication problems.

In addition to the measurement results, the responses from complainants over a long period are extremely important when assessing low frequency noise complaints. With this in mind, an on-site measurement system of the low frequency noise and annoyance response was developed by Sato et al. [14]. The system can function for long periods (more than 24 h) without an operator and the complainant carries a wireless button that they press when they detect the low frequency noise that annoys them. The automated post-processing method produces a quantified relationship between physical noise properties and the complainant's responses. Since the system measures both objective noise and subjective response, the authors consider that some limitations and precautions should be taken into account, such as measuring subjective response, background and man-made noise, criteria, and period for measurement. However, they found that the system can be used as a tool to assess whether a complainant is affected by low-frequency components.

Adverse symptoms have also been reported when workers have been exposed to very high frequency sound (VHFS; 11.2–17.8 kHz) and ultrasound (US; >17.8 kHz) for more than 70 years. Among the reported symptoms are headache, tinnitus, fatigue, and fullness or pain in the ears [15]. The different ways in which workers and the public can be exposed to ultrasound have increased in recent years. The installation in public places of different ultrasonic devices such as pest deterrents and public address voice alarm (PAVA) monitoring systems has exposed people, without their knowledge, to ultrasounds. Several controlled studies have been performed to assess the symptoms provoked by the exposure to VHFS/US [15–17] and to measure the sound pressure levels of these sources. Fletcher et al. [15] reported the outcome of measuring the sound pressure level produced by 16 different sources, either publicly accessible or installed in busy public spaces. For some sources very high sound pressure levels were found. For instance, levels of up to 100 dB of sound pressure level (SPL) at ~20 kHz were found for pest deterrents and 84 dB of SPL at 40 kHz for a hand dryer [17].

Despite the growing interest in characterising these sources, it is evident that the procedures and equipment currently used are not the most suitable for this range of frequencies. For instance, when it comes to measuring audible sound exposure in a workplace, a hand-held sound level meter placed in a defined location at a workstation or a personal sound dosimeter is very often used.

Radosz and Pleban [18] examine the possibility of adapting standard measurement procedures for occupational noise exposure in the ultrasonic range. Requirements for measuring instruments and measurement procedures are discussed, the application of

a correction to measurement results is proposed and the need to take all components of uncertainty into account is highlighted. The correction factor allows for the effect of using a microphone's protection grid and the metrological features of the instruments on the measurement results. In the ultrasonic range, the uncertainty of measurements associated with the position of the microphone is of the utmost importance. Since the class 1 specifications for sound level meters do not cover the ultrasound range, it is proposed to use a class 1 sound meter/analyser equipped with a microphone appropriate for the frequency range to perform measurements using 1/3 octave band filters.

Based on recent developments in the field of microelectronics, Cieslak et al. [19] presented the foundations for developing a personal ultrasound exposimeter, built with commercially available electronic components and showing very good potential of being able to measure ultrasonic noise up to 100 kHz. According to their findings, this approach will make it possible to build a network of low-power and low-weight personal sound exposimeters, connected wirelessly to a central node.

A measuring system for airborne ultrasound fields has several requirements concerning spatial resolution, frequency range, dynamic range, signal-to-noise ratio and traceability. The work of Schöneweiß et al. [20] defines the technical and procedural requirements for it and applies them to develop a system setup and calibration for measuring three-dimensional, high spatial resolution scans of sound pressure levels in the laboratory. A multi-channel device for simultaneous measurement at several measuring points was implemented in order to reduce the measurement time, since a high spatial resolution is needed to characterise the high spatial variation of the ultrasound fields. The system should have a flat frequency response in the frequency interval of 6–90 kHz under free-field conditions, a dynamic range from 60 dB to the peak sound pressure level, and a signal-to-noise ratio in the measuring interval of approximately 20 dB. Moreover, the measurement conditions should be well known and their influence on the measurement repeatability and the intermediate measurement precision should be minimised.

15.3 Characterisation of Materials

Several new materials are being developed with acoustic applications in mind to exceed the acoustic performance achievable with conventional materials. Among these materials, there are the metamaterials produced in metal, ceramic, or gel foams, porous asphalt, and smart sound-absorbing materials.

A metamaterial is an artificial material with properties not found in nature. It is created by changing its micro and macrostructure or forming a composite. The presence of periodic material structural inhomogeneities in a material changes the propagation of waves. Mechanical metamaterials are used to enable the creation of an artificial medium that may confer more wave transmission attenuation than any existing classical material. These materials have been developed in different areas such as electromagnetics and acoustics [21, 22].

Metamaterials can be designed to prevent wave transmission in specific frequency ranges of electromagnetic, elastic, or acoustic waves in any direction [23, 24]. The periodic crystal-like arrangement of rods or columns generates a band gap behaviour due to wave diffraction and interference because these structures act as scattering reflectors [25]. However, at very low frequencies where wavelengths are large, an arrangement of simple structures would be too large to be applicable.

Hall et al. [26, 27] designed, modelled, and tested a set of local resonance structures (multi-resonance systems) to provide significantly higher transmission loss at low frequencies than conventional wall systems of similar size and weight. The frequency-dependent properties of single resonant units have been evaluated through dynamic testing. The resonant units were suspended and their frequency response was measured using an electrodynamic shaker to excite them, and a force transducer and an accelerometer (PCB A353 B65) recorded the input forces and output motions. Rubber bands were used to decouple the test specimen from the support structure and avoid unwanted modes of vibration. The impedance tube method was used to evaluate the transmission and reflection coefficients using plane waves. A mounting method was used that isolated the samples from the tube walls on either side, using two soft rubber rings to mitigate flanking transmission. For full-scale diffuse field testing, a room-to-room testing facility (ISO 10140-2 [28]) was implemented, using two reverberation rooms ($202\text{--}208\text{ m}^3$) separated by highly insulated sliding doors. Wall-scale local resonance structures (LRS) were built to fill the adjustable gap between these sliding doors. Two broadband pink noise sources were positioned in one of the rooms and the spatial average sound pressure and reverberation times (RT) were measured in both the emitting and receiving rooms. They concluded that systems with multiple single resonance layers with spread or staggered frequencies developed the highest peak transmission loss band gaps.

Emerson and Manimala [29] used prototypical nonlinear acoustic metamaterial waveguides, having nonlinear softening oscillator arrays patterned on a host plate, to demonstrate their potential to steer and sort waves in a tuneable frequency range towards specific regions or paths within the waveguide. In their work, the nonlinear softening response of the rubber dome springs was characterised using compression tests. Dynamic tests were performed on single resonator units to determine resonance frequencies.

Besides the metamaterials, several construction materials incorporating waste from various industries have been studied. António et al. [30] studied the mechanical, thermal and acoustic performance of composite boards made of rice husk and cork or rubber waste. To this end, small-scale tests were conducted to assess properties such as improvement in impact sound insulation, sound absorption and transmission loss. The study concluded that these composites can be used in floating floors to reduce impact sound transmission (overall sound reduction from 20 to 27 dB). At the same time, the application of the uncoated composites exhibited promising sound absorption properties, especially for composites with rubber granules which had maximum sound absorption coefficients of 0.96. The noise reduction coefficients (NRC) of all composites ranged from 0.15 to 0.45.

Marques et al. [31] developed innovative polymer-based composite materials made with rice husk and expanded cork by-products that were characterised to evaluate the influence of the different mix ratios and composite densities. Considering acoustic performance, small-scale tests were conducted to assess improvement in impact sound insulation and sound absorption. The results indicate that incorporating higher amounts of rice husk can help to improve the sound absorption performance. The results of the impact sound insulation tests also indicate that formulations with lower density and higher rice husk content are likely to improve impact sound performance. However, all mixes exhibit great potential for impact sound insulation when they are incorporated in building solutions.

Marques et al. [32] assessed the performance of sustainable building walls made from 80 and 100 kg/m³ straw bales. Experimental tests based on the procedures set out in conventional testing guidelines were designed to evaluate their hygrothermal and acoustic characteristics. The acoustic performance was first assessed by evaluating the airflow resistivity. Additionally, different constructive solutions for walls that combined rice straw bales and a variety of coatings (lime mortar, gypsum plaster board and OSB) were studied in terms of airborne sound insulation. The results confirm the benefit of using suitable coating materials as the acoustic results suggest that conventional mortar coatings could help improve the acoustic insulation performance.

15.4 Characterisation of Building Elements

The standards for measuring and predicting sound insulation in buildings are well established. However, they are regularly updated in line with new developments resulting from robust research driven by new challenges posed by the needs of both industry and designers. In a recent publication, Hopkins [33] presents recent developments and current challenges in the measurement and prediction of sound transmission in buildings.

Lately, sound insulation measurement standards have paid attention to sound insulation measurements at low frequencies. Several studies have looked at the effect of the low frequency content on neighbour noise and assessed the correlation between the subjective and objective evaluation of sound insulation [34, 35]. Low frequencies are of essential importance when evaluating sound insulation in lightweight buildings, where frequencies below 50 Hz are extremely relevant when considering impact sound insulation and annoyance [36–38].

In the laboratory, the difficulty of ensuring a diffuse field at low frequencies serves to limit the accuracy of the results. In this case sound intensity measurements [39] lead to accurate low-frequency (below 100 Hz) sound insulation assessment with good reproducibility, with a better estimate of the sound reduction index than EN ISO 10140-2 [28]. However, it appears that this methodology has not sparked the interest of the industry, perhaps because of the time and additional cost involved in carrying out the test [33].

Other alternative methodologies have been proposed, such as vibration velocity-based measurement methods to assess impact [40] or airborne [41] sound insulation. Those methodologies have advantages over the standard methods, especially in the low frequency range or in special applications with articulated boundary conditions.

Sound intensity methodology can also be used in the field to measure the sound power radiated by a separating element. However, in a building the energy radiated by flanking elements, contributing to the total sound field of the room to be compared with building regulations requirements, should be considered. For field measurements, the EN 16283 standards (parts 1, 2 and 3) [42–44] present methodologies to assess low frequency sound insulation in rooms with volumes less than 25 m³. Those standards present a lower limit of 50 Hz for low frequency measurements.

When it comes to excitation sources, the rubber ball was introduced in EN ISO 10140 [45, 46] for laboratory tests and in EN ISO 16283-2 [43] for field tests as an alternative impact source. It can be used to assess heavy, soft impacts, since the ISO tapping machine is better suited to assessing a variety of light, hard impacts.

A new part of EN ISO 10848 (Part 5) [47] was recently developed to specify measurement methods for characterising (in the laboratory) the acoustic radiation of a building element when it is directly excited by an airborne or structure-borne source. This is an example of a standard that was developed to obtain parameters that are used as input data for prediction methods like those presented in EN ISO 12354-1 [48] and EN ISO 12354-2 [49].

Developments have recently been made in the experimental vibro-acoustic testing of floors, one of which involves the characterisation of impact sources intended for use in forecasting impact sound insulation models. It has also been possible to design test conditions for situations when standard laboratory facilities cannot be used, and several studies have set out to assess the conditions of vibro-acoustic comfort and users' subjective responses to certain flooring solutions.

The impact force generated by the ISO tapping machine in wooden floors is different from that generated in bare concrete floors. Knowledge of the impact force is fundamental to develop mathematical models to predict the impact sound insulation of those floors [50, 51]. An instrumented ISO tapping machine equipped with both force and acceleration sensors was used to assess the force spectra and impulses exerted on a large range of wooden floors [52]. The experiments confirmed that the excitation driving the wooden floors depends strongly on the type of the structure, and the differences between the force spectra were noticeable in the frequencies above 500 Hz. Furthermore, the comparison of the results with force spectra found in literature from measurements on concrete and steel structures showed important differences. The authors also reported that the process of excitation with the ISO tapping machine was not transient for the wooden floors studied.

The design of multi-storey timber buildings includes impact sound performance below 100 Hz. In the low frequency range, the ISO rubber ball approaches better human excitation in this range than the ISO tapping machine. To measure and analyse the ISO rubber ball's force spectra at low frequencies Olsson and Linderholt [53] developed a prototype equipment (a test rig) for the force spectra measurements. The test rig used allowed accurate repeatability for force measurements with the

ISO rubber ball. It was found that, for the tested floors, the force spectra of the rubber ball depend on the tested floor only for frequencies above 55 Hz. This means that up to that frequency the ISO ball spectrum could be prescribed, and the impact force measurement should be measured above 55 Hz to estimate frequency response functions.

Urban buildings with open architecture have been a timber industry investment. A solution of hollow box timber floors means that a long span can be handled with efficient material consumption. However, the lack of information on the vibroacoustic behaviour of such systems complicates the building design. Conta and Homb [54] developed an experimental setup to better understand the modal behaviour and radiated sound power under impact excitation of floors of this type. A standard acoustic floor test facility cannot perform ordinary measurements because of the size of the elements and the frequency range of interest. Thus, recently developed measurement methods like the Integral Transform method had to be employed to acquire reliable data. The results show that the influence of size and boundary conditions is more expressive in the low frequency range. These results matter since this range of frequencies is responsible for the annoyance to occupants in wooden lightweight buildings.

Serviceability requirements guide the design of timber-concrete composite (TCC) floors. Motivated by the scarcity of studies in the vibration comfort of TCC under human-induced excitation, Xie et al. [55] performed dynamic experiments to obtain the fundamental frequency and damping ratio of a glulam-concrete composite floor with two different boundary conditions. They assessed the influence of walking path, step frequency, number of pedestrians, arrangement of walking loads and walking mode on the vibration response of the composite floor and concluded that during the design phase it is necessary to combine the different loading conditions and take into account the boundary conditions.

Some studies report that the objective rating of impact sound insulation of floors does not properly describe the subjective perception of sound transmission through floors. It should also be noted that standard impact sound sources do not exist in buildings. With this in mind, Hongisto et al. [56] conducted a psychoacoustic laboratory experiment to see if installing a floating floor would bring a subjective benefit in sound insulation, when using impact sources occurring naturally in dwellings. They found that the subjective rank of the floor types tested depends on the type of natural impact sound used as excitation. Furthermore, they concluded that the existing standardised single number quantities are not appropriate to rank the floors tested with the different sound types, and that there is a need to obtain objective rating methods that properly rank the floors according to the subjective perception.

Protection against noise in building codes also includes sound insulation requirements for facades. Recent research in building facades is mainly focused on the study of solutions for low frequency sound levels and new methodologies of measurement.

In some countries there are requirements for the indoor sound pressure level at low frequencies. It is usual nearby new wind power areas to check if the indoor SPL levels are not violated. Keränen et al. [57] built a special infrasound loudspeaker to make it possible to measure the level difference of facades ranging down to 5 Hz.

The study covered a wide variety of facades and construction materials in such a way that the statistical assessments allow an estimate of indoor noise levels when the outdoor SPL is known.

The loudspeaker method is one of the most used methods described in ISO 16283-3 [44] to measure the sound insulation of facades. However, an uneven sound coverage over a facade could be due to the loudspeaker directivity and the distance from the loudspeaker to the facade. To reduce these variations Asensio et al. [58] proposed a measurement setup that depends on the location of the weakest element in the facade.

Although most of the studies on the exposure-response relationship for environmental noise annoyance have been based on the sound pressure levels of outdoor sound at the most exposed facade of a dwelling, a building's facade "filters" the spectra of the transportation environmental noise and changes the annoyance experience. Thus, according to recent studies the subjective responses should be examined in both indoor and outdoor situations. Based on experiments, Ryu and Song [59] concluded that the annoyance experienced is influenced by the expectation of facade insulation, by the frequency spectrum heard, noise type, and sound level presented.

Protection against noise in buildings is generally enforced by national acoustic building regulations. Additionally, some countries have developed national acoustic classification schemes for buildings. Acoustic regulations impose minimum acoustic requirements while classification schemes define quality classes based on different intervals of acoustic comfort. However, acoustic regulations and classification schemes have developed without coordination between countries, and comparative studies have shown that acoustic descriptors and limit values differ widely [60]. Thus, the latest studies recommend consensus in using similar descriptors and classification schemes [61], such as the proposal of the international standard ISO/TS 19488 [62] on acoustic classification procedures.

Requirements for sound insulation and acoustic class criteria are expressed by objective descriptors, defined in standards, and calculated from standardised measurements. However, a holistic sound quality assessment in buildings needs both objective and subjective evaluations [63]. Thus, subjective tests are important to define subjective scales for sound quality [63] and derive indoor soundscape models capable of guiding soundscape assessment and design in residential buildings [64]. Subjective tests and surveys on dwelling satisfaction and noise annoyance can provide an important basis for settling on the requirements in legislation [65].

Listening tests are also important to assess subjective performance of auditory virtual reality (AVR) systems that allow intuitive and opportune exploration of different acoustical designs.

An audio-visual virtual reality system that allows real-time movement of the user [66] can be very important to improve the communication between acousticians and architects/stakeholders. In their work, Llopis et al. [66] use pre-computed B-format room impulse responses (IRs) for identifying the direction of incident sound. Then the IRs are convoluted with source signals, and a real-time audio processor handles the playback of the relevant signals, taking the position and head orientation of the listener into account.

15.5 Characterisation of Building Equipment

Equipment noise in buildings can be a source of discomfort to building occupants. Services equipment generates noise and also acts as a structure-borne source inducing vibrations that can propagate throughout a building's structural elements if not properly isolated.

The sound levels generated on site by structure-borne sound sources in buildings can be predicted by recent power-based input quantities defined in the revised measurement standards EN 15657 [67] and EN ISO 10848-1 [68]. Villot and Schneider [69] proposed a simple method to predict *in situ* sound levels generated by structure-borne sound sources in buildings, with the quantities defined in these standards.

The European Standard EN 15657 [67] specifies methods for estimating the structure-borne sound power produced in buildings by services equipment (sources) from measurements under laboratory conditions, using the reception plate approach. This revised version has been expanded from low-mobility receiver structures to any source-receiver mobility condition. The method is robust when the mobility of the source is significantly higher than that of the reception plate. The application of the reception plate method requires a power balance between the input power at the excitation point and the reception plate power, which is fulfilled when the reception plate is excited out-of-plane. Further research is needed when the excitation of the reception plate is in-plane, since the power balance is not achieved to a satisfactory extent in this case [70].

The data can be used as input for EN 12354-5 [71], or under certain conditions for EN ISO 12354-2 [49], to calculate the sound pressure levels produced by the same equipment when installed in buildings.

The model described in EN 12354-5 [71] is only valid for heavyweight constructions. To extend its application to lightweight buildings, Mayr et al. [72] proposed an empirical method to describe the building transmission in lightweight timber buildings where the transmission is regarded globally, including all transmission paths using a transmission function.

The 2017 version of EN ISO 10848-1 [68] extends the flanking transmission of sound between adjoining rooms to building service equipment. To estimate sound pressure levels in a receiving room due to structure-borne excitation by service equipment in a source room, two approaches are used. One is a normalised flanking equipment sound pressure level and the second is a transmission function that can be used to estimate sound pressure levels in a receiving room due to structure-borne excitation by service equipment in a source room. The first approach assumes that flanking transmission is limited to one junction (or no junction if the element supporting the equipment is the separating element), and the second considers the combination of direct (if any) and all flanking transmission paths. The transmission function is specific to the building in which it is measured and quantifies the combination of all

the transmission paths from the power injected at a source position on an element to a spatial average sound pressure level in a receiving room in a building.

For instance, a collection of transmission functions was measured in several timber buildings to provide a catalogue of data that can be used at the design stage of a building [72].

15.6 New Trends in Acoustic Sensing

Acoustic and elastic wave propagation features offer a powerful tool for sensing applications in many fields such as acoustic imaging, structural health monitoring, and defect characterisation. Depending on the wave frequency range that extends from infrasound (<20 Hz) up to ultrasound (in the GHz-band), different propagating wave modes, including longitudinal and shear waves, surface waves, plate modes, can be used in acoustic tools to characterise the media crossed by these waves [73].

Efforts are also being made to lower the cost of distributed instrumentation systems, particularly of the sensing nodes in environmental noise monitoring networks [74]. One example of this effort has been demonstrated by Mydlardz and colleagues [75], who showed that mass-produced micro-electro-mechanical systems (MEMS) microphones can be used successfully to build extremely low-cost and highly scalable IEC 61672-1 class 2 compliant environmental noise monitoring networks. In [76], Mydlardz and co-workers report on the 2-year experience of running the 55-node low-cost network deployed in the city of New York. A review on low-cost sensors for urban noise monitoring was recently published by Picaut et al. [77].

Acoustic emission is another technique used for assessing structural integrity and for health monitoring of components. The waves are recorded when the analysed component is subjected to external excitation, such as an impact. As the damage grows with the external excitation, there is a release of energy. The acoustic emission detected, and its intensity, are then used to detect defects, cracks, corrosion, allowing large structures and machines to be monitored while in operation, with minimal disruption, unlike destructive testing [78].

The design and manufacture of passive acoustic monitoring (PAM) systems have also steadily been increasing to study populations of vocally active species [79]. This method uses autonomous recording data loggers to register sounds, allowing active species surveys across spatial and temporal scales over grid-based sampling designs [80, 81]. Similar systems can be used to monitor the acoustic environment in cities [82]. One line of research that has received considerable attention is dynamic noise mapping based on a network of sensor nodes.

15.7 Conclusions

This chapter described how different acoustic testing techniques have been developed to characterise environmental noise, construction materials (including new metamaterials), and construction elements. It also presented a set of acoustic-based, non-invasive, techniques for monitoring the health of built structures, to detect and characterise defects such as cracks and voids. It has drawn attention to new trends in low-cost instrumentation technology. Finally, it also showed how passive acoustic monitoring (PAM) systems have been used to monitor the built environment. Essentially, this chapter has provided an interdisciplinary overview of the latest developments and the emerging techniques in acoustic testing, focusing mainly on current and possible future applications in civil engineering.

References

1. Lindsay RB (1964) Lindsay's wheel of acoustics. *J Acoust Soc Am* 36:2242
2. Clark C, Paunovic K (2018) WHO environmental noise guidelines for the European region: a systematic review on environmental noise and quality of life, wellbeing and mental health. *Int J Environ Res Public Health* 15:2400
3. Jarosińska D, Héroux M-È, Wilkhu P, Creswick J, Verbeek J, Wothege J, Paunović E (2018) Development of the WHO environmental noise guidelines for the European region: an introduction. *Int J Environ Res Public Health* 15:813
4. Berglund B, Lindvall T, Schwela DH (1999) Guidelines for community noise. World Health Organization, Geneva
5. EU, Directive 2002/49/EC of the European Parliament and of the Council of 25 June 2002 relating to the assessment and management of environmental noise (OJ L 189, 18.7.2002, p 12–25)
6. EEA, Noise in Europe 2020, EEA Report No22/2019. European Environment Agency. <https://www.eea.europa.eu/publications/environmental-noise-in-europe>. Last Accessed 19 June 2021
7. International Standardization Organization (2017) ISO 1996-2: acoustics-description, measurement and assessment of environmental noise-part 2: determination of sound pressure levels. International Standardization Organization, Geneva
8. International Standardization Organization (2016) ISO 1996-1: acoustics-description, measurement and assessment of environmental noise-part 1: basic quantities and assessment procedures. International Standardization Organization, Geneva
9. Barrigón Morillas JM, Montes González D, Rey Gozalo G (2016) A review of the measurement procedure of the ISO 1996 standard. Relationship with the European noise directive. *Sci Total Environ* 565:595–606
10. Zagubień A, Wolniewicz K (2021) Impact of measuring microphone location on the result of environmental noise assessment. *Appl Acoust* 172:107662
11. Berglund B, Hassmén P, Job RF (1996) Sources and effects of low-frequency noise. *J Acoust Soc Am* 99(5):2985–3002
12. Alves JA, Paiva FN, Silva LT, Remoaldo P (2020) Low-frequency noise and its main effects on human health-a review of the literature between 2016 and 2019. *Appl Sci* 10:5205
13. Pedersen CS, Møller H, Christensen F, Olesen SK, Nielsen SB (2017) A low-frequency noise measurement and recording device for occupant operation. In: McMinn T, Duncan A, (eds) *Acoustics 2017 Perth: proceedings of the annual conference of the Australian Acoustical Society: sound, science and society*. Australian Acoustical Society, Canberra

14. Sato H, Ryu J, Kurakata K (2018) Development of an on-site system for measuring the low-frequency noise and complainant's responses. *J Low Freq Noise Vib Act Control* 37(2):373–384
15. Fletcher MD, Lloyd Jones S, White PR, Dolder CN, Leighton TG, Lineton B (2018) Effects of very high-frequency sound and ultrasound on humans. Part I: adverse symptoms after exposure to audible very-high frequency sound. *J Acoust Soc Am* 144(4):2511–2520
16. Fletcher MD, Lloyd Jones S, White PR, Dolder CN, Leighton TG, Lineton B (2018) Effects of very high-frequency sound and ultrasound on humans. Part II: a double-blind randomized provocation study of inaudible 20-kHz ultrasound. *J Acoust Soc Am* 144(4):2521–2531
17. Fletcher MD, Lloyd Jones S, White PR, Dolder CN, Lineton B, Leighton TG (2018) Public exposure to ultrasound and very high-frequency sound in air. *J Acoust Soc Am* 144(4):2554–2564
18. Radosz J, Pleban D (2018) Ultrasonic noise measurements in the work environment. *J Acoust Soc Am* 144(4):2532–2538
19. Cieslak M, Kling C, Wolff A (2020) Ultrasound exposure in a workplace and a potential way to improve its measurement methodology. In: 2020 IEEE international workshop on metrology for industry 4.0 & IoT. Roma, Italy, pp 172–176
20. Schöneweiß R, Kling C, Koch C (2020) A laboratory study for occupational safety and health on the structure of airborne ultrasound fields. *Acta Acustica* 4(4):12
21. John S (1991) Localization of light. *Phys Today* 44(5):32–40
22. Kushwaha MS, Halevi P, Dobrzynski L, Djafari-Rouhani B (1993) Acoustic band structure of periodic elastic composites. *Phys Rev Lett* 71(13):2022–2025
23. Liu Z, Chan CT, Sheng P (2002) Three-component elastic wave band-gap material. *Phys Rev B* 65(16):165116
24. Cruz-Muñoz FJ, Romero A, Galván P, Tadeu A (2019) Acoustic waves scattered by elastic waveguides using a spectral approach with a 2.5D coupled boundary-finite element method. *Eng Anal Bound Elem* 106:47–58
25. Liu Z, Zhang X, Mao Y, Zhu YY, Yang Z, Chan CT, Sheng P (2000) Locally resonant sonic materials. *Science* 289(5485):1734–1736
26. Hall AJ, Dodd G, Calius EP (2020) Multiplying resonances for attenuation in mechanical metamaterials: part 1-concepts, initial validation and single layer structures. *Appl Acoust* 170:107513
27. Hall AJ, Dodd G, Calius EP (2021) Multiplying resonances for attenuation in mechanical metamaterials: part 2-multi-layer structures. *Appl Acoust* 179:108041
28. International Standardization Organization (2021) ISO 10140-2: acoustics-laboratory measurement of sound insulation of building elements-part 2: measurement of airborne sound insulation. International Standardization Organization, Geneva
29. Emerson TA, Manimala JM (2020) Passive-adaptive mechanical wave manipulation using nonlinear metamaterial plates. *Acta Mech* 231:4665–4681
30. António J, Tadeu A, Marques B, Almeida JAS, Pinto V (2018) Application of rice husk in the development of new composite boards. *Constr Build Mater* 176:432–439
31. Marques B, Tadeu A, António J, Almeida J, de Brito J (2020) Mechanical, thermal and acoustic behaviour of polymer-based composite materials produced with rice husk and expanded cork by-products. *Constr Build Mater* 239:117851
32. Marques B, Tadeu A, Almeida J, António J, de Brito J (2020) Characterisation of sustainable building walls made from rice straw bales. *J Build Eng* 28:101041
33. Hopkins C (2018) Sound transmission in buildings: recent developments and current challenges in measurement and prediction. In: Proceedings of Euronono 2018, the 11th European congress and exposition on noise control engineering. Heronissos, Crete
34. Rindel JH (2003) On the influence of low frequencies on the annoyance of noise from neighbours. In: Proceedings of InterNoise 2003. Seogwipo, Korea
35. Hagberg KG (2010) Evaluating field measurements of impact sound. *Build Acoust* 17:105–128
36. Ljunggren F, Simmons C, Hagberg K (2014) Correlation between sound insulation and occupants' perception-proposal of alternative single number rating of impact sound. *Appl Acoust* 85:57–68

37. Ljunggren F, Simmons C, Öqvist R (2017) Correlation between sound insulation and occupants' perception-proposal of alternative single number rating of impact sound, part II. *Appl Acoust* 123:143–151
38. António J, Mateus D (2015) Influence of low frequency bands on airborne and impact sound insulation single numbers for typical Portuguese buildings. *Appl Acoust* 89(1):141–151
39. European Committee for Standardization (2010) EN ISO 15186-3: acoustics-measurement of sound insulation in buildings and of building elements using sound intensity-part 3: laboratory measurements at low frequencies (ISO 15186-3:2002). European Committee for Standardization, Brussels
40. Conta S, Santoni A, Homb A (2020) Benchmarking the vibration velocity-based measurement methods to determine the radiated sound power from floor elements under impact excitation. *Appl Acoust* 169:107457
41. Roozen NB, Leclère Q, Urbán D, Méndez Echenagucia T, Block P, Rychtáriková M, Glorieux C (2018) Assessment of the airborne sound insulation from mobility vibration measurements; a hybrid experimental numerical approach. *J Sound Vib* 432:680–698
42. European Committee for Standardization (2017) EN ISO 16283-1: acoustics-field measurement of sound insulation in buildings and of building elements-part 1: airborne sound insulation-amendment 1 (ISO 16283-1:2014/Amd 1:2017). European Committee for Standardization, Brussels
43. European Committee for Standardization (2020) EN ISO 16283-2: acoustics-field measurement of sound insulation in buildings and of building elements-part 2: impact sound insulation (ISO 16283-2:2020). European Committee for Standardization, Brussels
44. European Committee for Standardization (2016) EN ISO 16283-3: acoustics-field measurement of sound insulation in buildings and of building elements-part 3: façade sound insulation (ISO 16283-3:2016). European Committee for Standardization, Brussels
45. European Committee for Standardization (2021) EN ISO 10140-3: acoustics-laboratory measurement of sound insulation of building elements-part 3: measurement of impact sound insulation (ISO 10140-3:2021). European Committee for Standardization, Brussels
46. European Committee for Standardization (2021) EN ISO 10140-5: acoustics-laboratory measurement of sound insulation of building elements-part 5: requirements for test facilities and equipment (ISO 10140-5:2021). European Committee for Standardization, Brussels
47. European Committee for Standardization (2020) EN ISO 10848-5: acoustics-laboratory and field measurement of the flanking transmission for airborne, impact and building service equipment sound between adjoining rooms-part 5: radiation efficiencies of building elements (ISO 10848-5:2020). European Committee for Standardization, Brussels
48. European Committee for Standardization (2017) EN ISO 12354-1: Building acoustics-estimation of acoustic performance of buildings from the performance of elements-part 1: airborne sound insulation between rooms (ISO 12354-1:2017). European Committee for Standardization, Brussels
49. European Committee for Standardization (2017) EN ISO 12354-2: building acoustics-estimation of acoustic performance of buildings from the performance of elements-part 2: impact sound insulation between rooms (ISO 12354-2:2017). European Committee for Standardization, Brussels
50. Tadeu A, Pereira A, Godinho L, António J (2007) Prediction of airborne sound and impact sound insulation provided by single and multilayer systems using analytical expressions. *Appl Acoust* 68(1):17–42
51. Tadeu A, António J (2001) 2.5D Green's functions for elastodynamic problems in layered acoustic and elastic formations. *Comput Model Eng Sci* 2(4):477–495
52. Lietzén J, Miettinen J, Kylliänen M, Pajunen S (2021) Impact force excitation generated by an ISO tapping machine on wooden floors. *Appl Acoust* 175:107821
53. Olsson J, Linderholt A (2020) Measurements of low frequency impact sound frequency response functions and vibrational properties of light weight timber floors utilizing the ISO rubber ball. *Appl Acoust* 166:107313

54. Conta S, Homb A (2020) Sound radiation of hollow box timber floors under impact excitation: an experimental parameter study. *Appl Acoust* 161:107190
55. Xie Z, Hu X, Du H, Zhang X (2020) Vibration behavior of timber-concrete composite floors under human-induced excitation. *J Build Eng* 32:101744
56. Hongisto V, Virjosen P, Maula H, Saarinen P, Radun J (2020) Impact sound insulation of floating floors: a psychoacoustic experiment linking standard objective rating and subjective perception. *Build Environ* 184:107225
57. Keränen J, Hakala J, Hongisto V (2019) The sound insulation of façades at frequencies 5–5000 Hz. *Build Environ* 156:12–20
58. Asensio C, Trujillo JA, Arcas G (2018) Analysis of the effects of uneven sound coverage over a facade during a sound insulation test according to the international standard ISO 16283-3. *Appl Acoust* 130:52–62
59. Ryu J, Song H (2019) Effect of building façade on indoor transportation noise annoyance in terms of frequency spectrum and expectation for sound insulation. *Appl Acoust* 152:21–30
60. Rasmussen B (2010) Sound insulation between dwellings—requirements in building regulations in Europe. *Appl Acoust* 71(4):373–385
61. Rasmussen B, Machimbarrena M (2019) Developing an international acoustic classification scheme for dwellings—from chaos & challenges to compromises & consensus? In: Proceedings of INTERNOISE 2019. Madrid, June 16–19
62. International Standardization Organization (2021) ISO/TS 19488, acoustics-acoustic classification of dwellings. International Standardization Organization, Geneva
63. Ma KW, Mak CM, Wong HM (2020) Development of a subjective scale for sound quality assessments in building acoustics. *J Build Eng* 29:101177
64. Torresin S, Albatici R, Aletta F, Babich F, Oberman T, Siboni S, Kang J (2020) Indoor soundscape assessment: a principal components model of acoustic perception in residential buildings. *Build Environ* 182:107152
65. Dümen AŞ, Bayazit NT (2020) Enforcement of acoustic performance assessment in residential buildings and occupant satisfaction. *Build Res Inf* 48(8):866–885
66. Llopis HS, Pind F, Jeong C-H (2020) Development of an auditory virtual reality system based on pre-computed B-format impulse responses for building design evaluation. *Build Environ* 169:106553
67. European Committee for Standardization (2017) EN 15657: Acoustic properties of building elements and of buildings-laboratory measurement of structure-borne sound from building service equipment for all installation conditions. European Committee for Standardization, Brussels
68. European Committee for Standardization (2017) EN ISO 10848-1: acoustics-laboratory and field measurement of flanking transmission for airborne, impact and building service equipment sound between adjoining rooms-part 1: frame document (ISO 10848-1:2017). European Committee for Standardization, Brussels
69. Villot M, Schneider M (2020) A simple method for predicting sound levels generated by structure-borne sound sources in buildings. *Appl Acoust* 165:107334
70. Schanda U, Hoßfeld M, Schöpfer F, Mayr A (2019) In-plane excitation of reception plates according to DIN EN 15657:2017. In: Ochmann M, Vorländer M, Fels J (eds) 23rd International congress on acoustics. Deutsche Gesellschaft für Akustik e.V. (DEGA), 9–13 September 2019. Aachen, Berlin, Germany, pp 1255–1262
71. European Committee for Standardization (2009) EN 12354-5: building acoustics-estimation of acoustic performance of building from the performance of elements. Part 5: sound levels due to the service equipment. Brussels: European Committee for Standardization
72. Mayr AR, Schöpfer F, Schanda U, Hopkins C (2018) Measurement and prediction of structure-borne sound transmission from machinery in timber-frame buildings. In: Proceedings of Euronoise 2018, the 11th European congress and exposition on noise control engineering. Hersonissos, Crete, pp 27–31
73. Caliendo C (2014) Latest trends in acoustic sensing. *Sensors* 14:5781–5784

74. Gontier F, Lagrange M, Aumond P, Can A, Lavandier C (2017) An efficient audio coding scheme for quantitative and qualitative large scale acoustic monitoring using the sensor grid approach. *Sensors* 17(12):2758
75. Mydlarz C, Salamon J, Bello J (2017) The implementation of low-cost urban acoustic monitoring devices. *Appl Acoust* 117(B):207–218
76. Mydlarz C, Sharma M, Lockerman Y, Steers B, Silva C, Bello JP (2019) The life of a New York City noise sensor network. *Sensors* 19(6):1415
77. Picaut J, Can A, Fortin N, Ardouin J, Lagrange M (2020) Low-cost sensors for urban noise monitoring networks-a literature review. *Sensors* 20(8):2256
78. Grossé CU, Ohtsu M, Aggelis DG, Shiotani T (eds) (2021) Acoustic emission testing. Basics for research-applications in engineering. Springer International Publishing
79. Reid DS, Wood CM, Whitmore SA, Berigan WJ, Keane JJ, Sawyer SC, Shaklee PA, Kramer HA, Kelly KG, Reiss A, Kryshak N, Gutiérrez RJ, Klinck H, Peery MZ (2021) Noisy neighbors and reticent residents: distinguishing resident from non-resident individuals to improve passive acoustic monitoring. *Glob Ecol Conserv* 28:e01710
80. Gibb R, Browning E, Glover-Kapfer P, Jones KE (2019) Emerging opportunities and challenges for passive acoustics in ecological assessment and monitoring. *Methods Ecol Evol* 10:169–185
81. Shonfield J, Bayne EM (2017) Autonomous recording units in avian ecological research: current use and future applications. *Avian Conserv Ecol* 12(1):14
82. Sheng Z, Pfersich S, Eldridge A, Zhou J, Tian D, Leung VCM (2019) Wireless acoustic sensor networks and edge computing for rapid acoustic monitoring. *IEEE/CAA J Autom Sin* 6(1):64–74

Chapter 16

State-of-the-Art and Future Insights into the Material's Fire Behaviour Tests



Miguel Chichorro Gonçalves and António Leça Coelho

Abstract Fire safety in buildings (FIS) is characterized by the multidimensionality of the contents associated with it, ranging from the behaviour of materials at high temperatures to the evacuation of people in case of fire. FIS is ensured by imposing a set of requirements translated into a legal body consisting of regulations and standardization, whose goal is to reduce the fire risk for occupants and firefighters involved in fighting a fire. The knowledge required to build up this body of law essentially derives from the theoretical evolution that has been consolidated over time. However, there are areas in which this knowledge is derived from tests carried out following standardization, as the case of construction products. In the case of European standardization, it is essential, firstly, to assess, two decades after its publication whether there is a need for adjustments to the conditions under which they are carried out. Secondly, it is necessary to identify possible gaps where the development of new knowledge derives from the performance of tests. This text addresses these two perspectives and the possible consideration of what we call virtual tests.

Keywords Safety · Fire · Buildings · Tests · Reaction · Resistance

16.1 Introduction

The multidisciplinary contents of Fire safety in buildings (FIS) imply research in many areas. It will be analysed the tests in the field of fire behaviour.

In order to provide buildings with adequate safety conditions (i.e., reducing the fire risk), a set of requirements are defined and translated into a legal body consisting of regulations and standardization.

M. C. Gonçalves
Faculdade de Engenharia, Universidade do Porto, Porto, Portugal
e-mail: miguelcg@fe.up.pt

A. L. Coelho (✉)
Universidade Lusófona do Porto, Porto, Portugal
e-mail: p901967@ulp.pt

The knowledge required to build this body of law is essentially derived from theoretical knowledge that has been consolidated over time. In the field of construction products, that knowledge must be obtained from tests carried out following published standardization.

Focusing the analysis on the European Union countries, the body of regulations currently in force regarding reaction and resistance to fire of construction products is about two decades old [1, 2].

At the end of this long period, it is pertinent to reflect on the need, or not, to change this body of regulations by identifying both inadequacies and gaps, particularly in areas where knowledge is mainly derived from tests.

In the following sections, an analysis is made of the referred normative body in the field of construction products, complemented by a reflection on possible tests to be adopted for active FIS systems and on the so-called “virtual tests” in the field of the behaviour of people in case of fire.

16.2 Tests on Reaction to Fire

This section presents a brief overview of the characteristics of the European harmonized system (EHS) for classifying the reaction to fire of construction products. The complexity and limitations of this system are analyzed, ending with a reflection on future adjustments that can be introduced in this system.

16.2.1 Brief Description of the Current EHS

Reaction to fire tests in Europe is carried out according to the EHS, implemented at the beginning of this century.

The EHS has as fundamental pillars five tests, carried out under the conditions indicated in the following European Standards (EN).

- EN ISO 1182 [3]

This standard defines the conditions for performing the non-combustibility test, whose purpose is to evaluate the production of heat and flame. The parameters determined during the test and used for classification purposes are the temperature rise due to thermal degradation of the test piece, the mass loss suffered by the test piece during the test and the duration of the test piece firing, Fig. 16.1a.

- EN ISO 1716 [4]

This standard defines the conditions for carrying out the calorimeter test, which, together with the ISO oven test, is intended to prove the zero or negligible contribution given by some materials to fire, particularly in a situation of full development of the

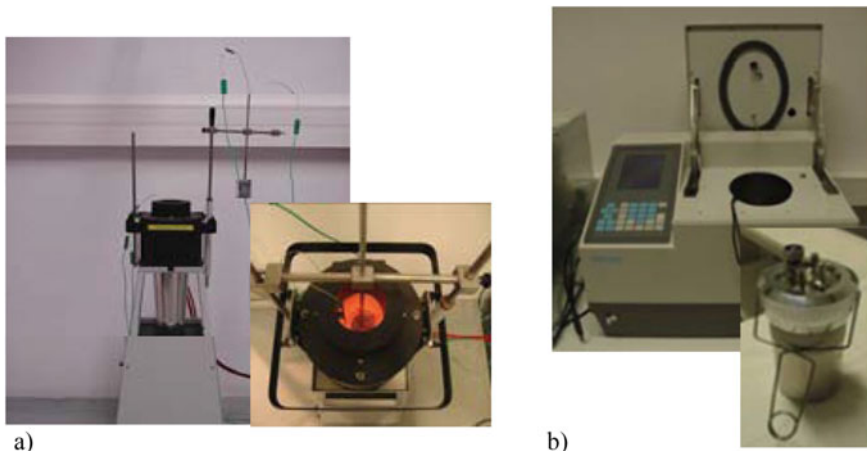


Fig. 16.1 **a** Non-combustibility test, EN ISO 1182 [3]; **b** Calorimeter test, ISO 1716 [4]

fire. The test consists of determining the calorific value of a homogeneous product at constant volume by combustion in an oxygen atmosphere of a product specimen, Fig. 16.1b.

– EN 13823 [5]

This standard defines the conditions to perform the test of the insulated burning object (OIC/SBI), whose purpose is the evaluation of several aspects of the fire performance of a specimen of significant dimensions submitted to the action of the flames of a gas burner with a rated thermal input of 30 kW.

– EN ISO 11925-2 [6]

This standard defines the conditions for conducting the small flame test, the purpose of which is to evaluate the ease of ignition of a product when subjected to the direct incidence of a small flame, such as, for example, that due to a lighter or a match.

– EN ISO 9239-1 [7]

This standard defines the conditions for performing the radiant panel test, whose purpose is to evaluate the combustion and flame propagation in a specimen of a floor covering, placed horizontally, in an identical way to the product in its final application, Fig. 16.3b.

The classification of reaction to fire of the materials obtained from the tests performed in accordance with the EHS is based on the determination of various parameters, from which the following stand out:

- temperature rise due to thermal degradation of the test specimen of EN ISO 1182 [3];
- loss in mass of the test piece during the test specimen of EN ISO 1182, [3];
- duration of ignition of the test specimen of EN ISO 1182, [3];



Fig. 16.2 **a, b** Insulated burning object (OIC/SBI), EN 13823, [5]

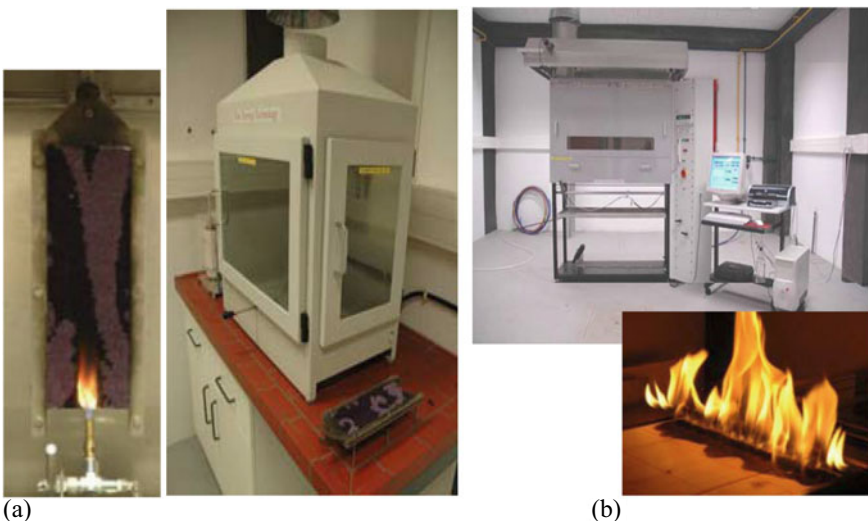


Fig. 16.3 **a** Small flame test, EN ISO 11925-2 [6]; **b** Radiant panel test, EN ISO 9239-1[7]

- high calorific power of EN ISO 1716, [4];
- the index FIGRA (1) of EN 13823, [5];
- the index SMOGRA (2) of EN 13823, [5];
- the index THR_{600s} (3) of EN 13823, [5];
- the index TSR_{600s} (4) of EN 13823, [5];
- lateral flame spread of EN 13823, [5];
- the index LFS (5) of EN 13823, [5];
- flaming droplets/particles and their duration of EN 13823, [5];
- flame spread extension (FS) of EN ISO 11952-2, [6];
- critical heat radiant flux (CHF) of EN ISO 9239-1, [7].

- (1) FIGRA: Fire Growth Rate
- (2) SMOGRA: Smoke Growth Rate
- (3) THR_{600s}: Total Heat Released in a defined period of 600s
- (4) TSR_{600s}: Total Smoke Released in a defined period of 600s
- (5) LFS: Lateral Flame Spread.

The previous overview reveals, by itself, the complexity that the EHS presents, with all the inconveniences that this generates.

In fact, this complexity makes difficult for the technicians to perceive what is really being evaluated with these tests since the parameters determined do not always allow for an evident quantification of what is being assessed, as happens, for example, with the SMOGRA.

16.2.2 Limitations of EHS

Although Commission Decision 2000/147/EC has applicability that extends to all construction products defined in the Construction Products Directive, it cannot respond to all possible situations [8].

Thus, it becomes necessary to adapt whether these limitations occur concerning specific products or reference scenarios/methods. Or, eventually, to define other criteria and test methods more suitable for the various specific situations, as well as the procedures to be adopted in such cases which are described in a Guidance Paper prepared by the EC [9].

As a consequence of this inability, several requests for the adoption of other classification methodologies have arisen, justified by the specificity of the products or the inadequacy of the methods or criteria contained in Decision 2000/147/EC.

To avoid the risk of a proliferation of such requests, which would complicate the harmonization sought in this area, decisions to initiate alternative specific studies should firstly demonstrate and then possibly accept the non-applicability of that document.

Another limitation arises from the fact that, despite the complexity of the EHS, the information that results from the tests: is insufficient to determine some quantities that make it possible to characterize the dangers arising from the fire and, in other cases, the impossibility of determining them.

When the intention is to implement a fire safety engineering, namely as regards its development and propagation, using simulators for that purpose, it is clear that the information contained in the reports and test bulletins is, in most cases, insufficient to be able to build the so-called heat sources. These heat sources are essential to model the impact of construction products on the development and propagation of fire.

The most critical limitation comes from the non-evaluation of the toxicity of the products resulting from the fire. As can be seen from the observation of the parameters indicated above, the tests focus exclusively on preventing ignition and reducing flame spread by reducing the heat release rate, ignoring the critical issue

of toxicity. Evaluating the type of toxic effluents produced by different types of fire and their physiological effects is not subject to analysis in the EHS. However, it is known that almost all fatalities in urban fires result from the intoxication of people due to the gases released.

These limitations make it advisable to envisage possible changes to the current EHS, and the following section points out two possible modifications to take place in the future.

16.2.3 Research and Development

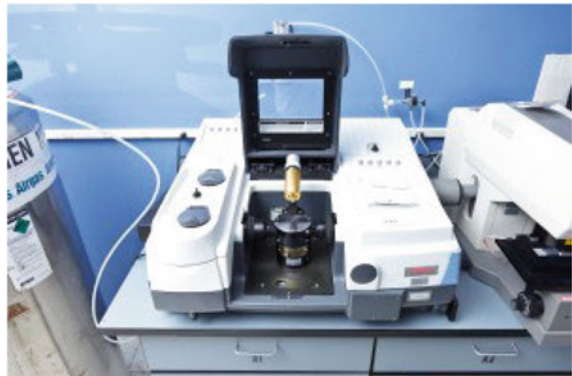
Toxicity-related tests. The technological changes that have occurred in the last decades have significantly changed the content of buildings, which were predominantly of cellulose nature, to have a strong component of materials in which synthetic polymers are present, which has made buildings much more dangerous in a fire situation.

This evidence has led to several research projects aiming at developing analytical techniques to measure the concentrations of volatile products generated in real fires. This is a complex field of investigation due to several factors, such as, for instance, the reactivity of the gas mixtures that are formed and the possibility of a rapid change of their concentration in time.

These difficulties have motivated the development of new methods or the adaptation of existing ones to analyze the gases present during combustion. A particular highlight of the research conducted on this subject is the EU-funded project (SAFIR) focused on testing and validating a Fourier transform infrared spectroscopy (FTIR) method, Fig. 16.4.

In most cases, FTIR can provide the concentration data necessary to calculate the yields of chemical species, which are essential as input for toxic hazard assessment.

Fig. 16.4 Fourier transform infrared spectroscopy



Despite its limitations in some circumstances, FTIR is the technology with the most significant potential to be used to determine a variety of gases from a single method.

Furthermore, the use of FTIR allows monitoring of how the various species develop during the fire and, in the event of the formation of a new product, identify it as toxic.

If it is subsequently identified as necessary, relevant data on the presence of this toxicant can be found in the FTIR spectra stored from previous tests.

The results of this project formed the basis of ISO 19702, [10], which provides specific recommendations for sampling systems for use in small- and large-scale measurements, for spectral resolution and for collection and use of calibration spectra.

ISO 19702, [10] lists various chemical methods for determining individual gases of toxicological importance since it is to be expected that several methods will be required to determine all the species of interest for fire risk analysis.

Other tests. As regards possible tests that may be implemented to qualify certain construction products and others that are not, tests on a real scale with a view to characterizing the impact of external building insulation, such as, for instance, cladding, should be highlighted.

Also, the evaluation of the effect of photovoltaic panels, roofs and garden facades, if their application is generalized, makes it advisable to define new tests in order to characterize the danger they can represent in terms of FIS.

16.3 Testing of Fire Resistance

16.3.1 *The Importance of Fire Resistance*

Introduction. This part of the chapter intends to do a state of the art on testing assessment of structural fire engineering, identify the knowledge gaps of fire resistance assessment, and identify the development to implement to advance technical solutions to improve the fire resistance of structures through greater use of existing technologies—specifically, the structural assessment tests on concrete, steel, and timber structures.

Fire resistance is one of the most important and old ideas in fire safety design. Since the beginning of the twenty century, more importance has been given to assessing fire resistance and its rise to ubiquity in codes and standards. As a method for independent testing of ‘fireproofing’ systems, fire resistance was formalized in the USA and subsequently in the UK. Minimum fire resistance periods were defined to allow a structure to resist fire in a compartment and became legislatively empowered in the 1950s.

Beginnings of fire testing. Fire endurance design for buildings has been based on Standard E119 of the American Society for Testing and Materials (ASTM) [11]. While numerous minor changes have been made, the time-temperature curve, the

basic test apparatus, and some criteria have remained unchanged. Component test methods established in other parts of the world have, until recently, likewise been modelled on E119 and even more recently by ISO 834 [12].

By December 31, 1992, some seventeen European countries will dismantle all barriers to the free movement of goods, people, services, and capital; a plan referred to as EC 1992. In addition to facilitating internal trade, EC 1992 will create one of the largest consumer markets in the world. To assist in product standards, the European Community has contracted with the Committee for European Standardization (CEN), they are charged with developing a unified fire testing system. Their mandate has divided the field of fire tests into two broad categories: reaction to fire and fire resistance, [2–6, 13–16].

A list of test standards currently required for assessing fire resistance in the various building components is presented.

Classification for elements with load-bearing functions and with fire-resistant compartmentalization function (Walls, floors, roof, beams, columns, balconies, stairs, walkways):

EN 13501-2 (Walls; Floors and roofs), EN 1365-1 (Walls), EN 1365-2 (Floors and roofs), EN 1365-3 (Beams), EN 1365-4 (Columns), EN 1365-5 (Balconies and Walkways), EN 1365-6 (Stairs), EN 1992(3-5.9)-1.2 (Walls; Floors and roofs), EN 1996-1.2 (Walls).

Classification for products and systems for protecting elements or parts of works with load-bearing functions:

EN 13501-2 (Ceilings without independent fire resistance; Coatings, exterior cladding, fire protection panels and boards), EN 13381-1 (Ceilings without independent fire resistance), EN 13501-3 to 7 (Coatings, exterior coatings, fire protection panels and boards).

Classification for elements or parts of works without load-bearing functions and products intended for them:

EN 13501-2 (Partitions; Ceilings with independent fire resistance; Facades and exterior walls; False floors; Seals for openings for the passage of cables and pipes; Fire doors and shutters and respective closing devices; Smoke control doors; Shutters for continuous conveyor systems by belts and rails; Conduits and ducts; Coatings for walls and roofs), EN 1634-1 (Fire doors and shutters and their closing devices), EN 1634-3 (Smoke control doors), EN 1364-1 (Partitions; Fire doors and shutters and respective closing devices), EN 1365-2 (Ceilings with independent fire resistance), EN 1365-3-6 (Facades and exterior walls), EN 1366-3.4 (Seals for cable and piping passage openings), EN 1366-5 (Conduits and ducts), EN 1366-6 (False floors), EN 1366-7 (Shutters for continuous conveyor systems on belts and rails), EN 1992(3,5,6,9)-1.2 (Partitions; Facades and exterior walls), EN 1994-1.2 (Partitions), EN 14135 (Wall and roof coatings).

Classification for products intended for ventilation systems, excluding smoke and heat exhausts:

EN 13501-3 (Ventilation ducts; Fire dampers), EN 1366-1 (Ventilation ducts), EN 1366-2 (Fire registers).

Classification for products incorporated in installations:

EN 13501-3 (Electrical and fibre optic cables and accessories; tubes and electrical cable protection systems against fire; Power or signal cables or systems with small diameter «less than 20 mm and with conductors of less than 2.50 mm²»), EN 50200 (Cables or power or signal systems with a small diameter «less than 20 mm and with conductors of less than 2.50 mm²»).

Classification for products intended for smoke control systems:

EN 13501-4 (Single-compartment smoke control ducts; Multi-compartment fire-resistant smoke control ducts; Single-compartment smoke control dampers; Multi-compartment fire-resistant smoke control dampers; Smoke-resistant barriers; Electric smoke hoods; and heat (fans), connection joints; Natural smoke and heat exhausts), EN 1363-1 (Single-compartment smoke control ducts; Multi-compartment fire-resistant smoke control ducts; Single-compartment smoke control dampers; Multi-compartment fire-resistant smoke control dampers; Smoke-resistant barriers; Electric smoke hoods; and heat (fans), connection joints; Natural smoke and heat exhausts), EN 1363-2, (Single-compartment smoke control ducts; Multi-compartment fire-resistant smoke control ducts; Multi-compartment fire-resistant smoke control dampers; Smoke-resistant barriers), ENV 1363-3 (Single-compartment smoke control ducts; Multi-compartment fire-resistant smoke control ducts; Single-compartment smoke control dampers; Multi-compartment fire-resistant smoke control dampers), EN 1366-2 (Multi-compartment fire-resistant smoke control registers), EN 1366-8 (Multi-compartment fire-resistant smoke control ducts; Multi-compartment fire-resistant smoke control registers), EN 1366-9 (Single-compartment smoke control ducts; Single-compartment smoke control dampers), EN 1366-10 (Single-compartment smoke control registers; Multi-compartment fire-resistant smoke control registers), EN 12101-1 (Smoking Barriers), EN 12101-2 (Natural smoke and heat exhausts), EN 12101-3 (Electric smoke and heat exhausts (fans), connecting joints), EN 12101-7 (Single-compartment smoke control ducts; Multi-compartment fire-resistant smoke control ducts), EN 12101-8 (Single-compartment smoke control registers; Multi-compartment fire-resistant smoke control registers), ISO 834-1 (Electric smoke and heat exhausts (fans), connecting joints).

Critics and detractors. Over time there have been many criticisms made of this approach to the fire safety design of structures. These fall into three categories:

- i. criticism of the standard heating curve (i.e., it doesn't look like a real fire, it lacks a decay phase, etc.);
- ii. criticism of standard fire testing furnaces (i.e., the furnace is a poorly controlled and variable test method, the thermal and mechanical boundary conditions are unrealistic, system effects and interactions are ignored, etc.);
- iii. criticism of the equivalent severity method (i.e., the usual approach was physically wrong and fails to account for a range of relevant factors which are now well understood to influence fire dynamics in compartments and structural outcomes in real buildings).

All these criticisms are, naturally, justified. Over decades, much research effort has gone into attempting to correct these issues whilst avoiding more substantive or fundamental changes to the existing fire resistance framework for structural fire design.

Favourable aspects.

- i. *Endurance*—Resistance remains as firmly embedded in regulations worldwide as it has ever been. Although virtually every aspect of the fire resistance framework's approach has been legitimately challenged, fire resistance is an idea with such strong inertia that it has proved extraordinarily resilient to reasoned and legitimate criticism. The standard temperature versus time curve defined (E119, ISO 834, [11, 12]) what the scientific community considered to be an extreme scenario. Thus, for all its failings, the standard furnace test does provide a form of proxy assessment of the qualities from which a structure would be likely to benefit in a real fire.
- ii. *Validity*—More than a century of testing with the standard fire testing furnaces internationally means that a considerable volume of proprietary and research literature exists regarding the performance of different structural materials and configurations. This literature has spawned a litany of design and ‘simplified’ methods for structural fire ‘design’. While these data have numerous limitations, they are clearly not devoid of value; a century of experience with the furnace as a proxy for natural fires means that engineers have learnt something about protecting structures from severe fires.
- iii. *Burnout*—The fire resistance test is only one part of the broader fire resistance framework. The idea of resisting a burnout fire has been a central philosophical aspect of the endeavour of fire resistance since its inception. Subsequent steps in the story of fire resistance have periodically reinforced the idea of designing high consequence structures to resist burnout.
- iv. *Proxy metrics of structural behaviour and performance specification*—The fact that the test is a proxy for useful structural qualities also contributes to the inertia of the fire resistance test. The test does not directly measure structural behaviour but relies on deflection as a proxy for all aspects of mechanical performance.

16.3.2 Knowledge Gaps Versus Future of Fire Resistance

Introduction. Fire has a devastating and widespread impact on the built environment: losses of human life, public and private property, and national treasure. Traditional approaches to fire protection for buildings and communities include construction restrictions (e.g., zoning and occupancy restrictions), measures to limit fire spread (e.g., passive fire protection and fire resistance rating requirements), and active fire suppression. Whereas these approaches have worked reasonably well, there are gaps in knowledge and understanding that preclude certainty in engineered structural fire protection design, and there remain instances of uncontrolled fires that have led to significant structural damage or collapse.

The confluence of technological advances in three areas: characterization of building fires, prediction of thermal effects, and calculation of structural performance, make possible the vision of a unified performance-based approach to structural fire safety and design (but at first step also of point of view of prescriptive approach).

Both the International Council for Research and Innovation in Building and Construction (Conseil International du Bâtiment, or CIB), [17] and the National Institute of Standards and Technology (NIST), [18] are working to enhance the knowledge and tools needed to improve the structural fire resistance of new buildings and retrofit of existing structures.

Those institutions established a Roadmap that would focus on the development of a multi-year, multi-institution, large-scale experimental program to support advanced computational models and their application to standards development for performance-based engineering for structural fire resistance [19].

Recommendations regarding new methods for fire resistance design of structures, an international research and development (R&D) roadmap on the fire resistance of structures are being developed to concrete, steel and timber structures. But it is equally important to analyze the current state of the art of structural fire resistance.

Knowledge gaps of fire resistance. The NIST/CIB institutions were highlighted the most important Knowledge gaps of fire resistance in terms of Performance Data; Construction Designs; Modelling Capabilities; and Societal and Regulatory [19].

Performance Data

- Lack of database to assess probabilities and risk for existing building
- Limited material property data as a function of temperature
- Standardization for determining new material properties at elevated temperature (during and after the fire)
- Lack of high-temperature properties like permeability and pore structure—that influence spalling
- Need more data on the applicability of the finite element
- Understand the partition/protection variability in standard gypsum board when exposed to standard and natural fires using probability methods
- Need to identify the conditions for self-extinguishing of charred wood
- Limited data on damage thresholds for structural systems at different fire exposure levels to develop strategies for property protection.

Construction Designs

- Instrumentation of buildings to assess performance after fire
- Fire response of post-installed reinforcement and anchoring and adhesive anchors
- Evaluation of the post-fire elements residual capacity
- Cascading impact on multiple system failures (and assembly failures)
- Indeterminate nature of spalling
- Performance of base isolation systems in fire
- Considerations of exposure from/to neighbours' fire on nearby structures
- Need more on structural loading, compatibility/commonality of finite element computational fluid dynamic codes to characterize damage for wood/concrete/steel composite construction under fire heat loading and cool down
- Need to determine PBD impact and requirements for acceptance—transition from prescriptive to performance-based design is a significant change

- Determine the fire performance of an as-built structure compared to as-tested construction.

Modelling Capabilities

- Limited use of fire dynamics simulation for moving fires
- Uncertainties both in testing and modelling
- The probabilistic approach in simulations and translation in codes of PBD and application, with a transfer path to R&D and then the application
- Models for mechanical properties of materials at different fire-damaged levels after cooling.

Societal and Regulatory

- Implementation of PBD in education, training, certification, standard fire scenarios, and test methods
- Identify hurdles anticipated when instituting performance versus prescriptive codes, local versus model code acceptance, and the translation challenges to assimilating PBD codes into building R&D and design
- Impact on PBD by current and evolving environmental laws, requirements, etc.

Vision for the future of resistance fire. The guide's focus is the development of a comprehensive, unified performance-based approach to structural fire safety and design [19]. This goal will be realized by creating information and data, tools, guidelines, and standards for structural systems exposed to fire. The transformation to PBD to evaluate the fire performance of buildings and other structures will allow the community to move beyond the prescriptive procedures presently in use and their attendant limitations. For the first time, this vision will consider fire as a design condition in the structural design process and treat fire along with other hazards on a risk-consistent basis. The attributes of this transformation will include the following:

- Generation of a database of large-scale experiments documenting the performance of structural connections, components, subassemblies, and systems under realistic fire and loading conditions for validation of analytical models
- Development of verified and validated simulation models and tools to predict structural fire performance based on fire dynamics and thermal-structural modelling
- Use of risk- and reliability-based tools and models for the prediction and specification of the fire hazard, structural fire effects, and calculation of structural response
- Development of design guidance and standards on performance-based approaches for determining fire effects on structural systems.

This broad vision of the future holds the promise of the following:

- A revolutionary transformation from the current prescriptive to new PBD
- Increased innovation and marketplace competition for new products, designs, and services

- Cost savings based on a rational and risk-consistent approach to design and the use of materials while achieving sustainability-related goals, such as reduced material use and more achievable construction programs
- It has increased public safety by understanding building responses to severe compartment fires.

R&D future. The strategy for generating the R&D agenda to move toward the vision outlined are listed in order of priority below in terms of test methodology, societal, regulatory and performance, modeling and simulation, and materials properties:

Test methodology

- Fire as a load case
- High-temperature strain and deflection measurement methods
- Conduct three-dimensional (3-D) full-scale tests on structural systems
- Conduct reliability-based analysis of fire testing, especially standard testing
- Perform compartment burnout encapsulation studies (full/partial)
- Identify and describe applicable fire scenarios.

Societal, regulatory and performance

- Stakeholder education and code development
- External demand for property protection, business continuity, and sustainability versus life safety—societal awareness of the fire “problem”
- Define acceptable performance criteria for a variety of all structures.

Modelling and simulation

- Multi-scale simulation: including heat transfer modelling in specific scenarios
- Develop connection models, including fracture for simulation of 3-D building structures under fire scenarios
- Predict the reliability of fire compartmentation
- Develop structural models for fire resistance of all structure types
- Develop models to determine the residual capacity of structures after a fire to evaluate property loss.

Materials properties

- Determine material properties of all new grades of building structural materials
- Determine material properties for different kinds of concrete during and after the cooling phase
- Calculate the residual strength of structural timber exposed to fire.

16.4 Tests in the Field of Active Systems

Regarding the active means of FIS, the automatic detection and alarm systems (ADAS), the automatic fire extinguishing systems (AFES) and the active smoke control systems (ASCS) assume prominence.

In these systems, it is necessary to ensure that they are reliable and know the consequences in terms of FIS of their installation, i.e., that allows us to quantify their performance capacity.

Ensuring that the systems are of acceptable reliability is achieved by carrying out tests.

16.4.1 ADAS-Related Tests

Concerning ADAS, to make it possible to assess the impact of these media on FIS, it is crucial to determine a parameter necessary to model this impact through tests.

This parameter may be the thermal sensitivity of the detector, sensitivity to opacity variation, or other, depending on what is to be “measured”. This response parameter must reflect the greater or lesser speed with which the detector can react to the manifestations of fire that it intends to evaluate. From its knowledge, it will be possible to determine the response time of these systems.

In the case of detectors sensitive to temperature variation, what must be “measured” is the thermal sensitivity which represents the “speed of response” of the sensitive element of the detector.

To measure this “speed of response”, the concept of “Response Time Index” (RTI) was developed. The value of the RTI is a function of the heat transfer coefficient by convention, the specific heat of the sensitive element, by the mass and surface area of the sensitive element.

To determine the “response index” following specific and pre-defined criteria, it is necessary to implement the standardization that allows the performance of tests oriented towards this objective.

The determination of the RTI based on standardized tests is fundamental to know with precision the performance capacity of these systems to quantify their impact, namely in what concerns security solutions related to building evacuation.

In the case of detectors sensitive to other manifestations arising from the fire, an identical process should occur, except for the measured index (Fig. 16.5).

16.4.2 AFES-Related Tests

So, for example, in the case of AFES, there are comprehensive tests carried out according to, for example, BS 8458:2015, [20] and AS 1851-2012, [21], which



Fig. 16.5 Automatic detection and alarm systems test

apply to the entire life cycle of these systems, giving recommendations for design, installation, water supply, commissioning, maintenance and testing.

Regarding these systems, it is also important to establish a standardization that allows tests to be carried out under controlled conditions to determine the thermal sensitivity of the sprinklers, in a similar way to that referred to in Sect. 16.4.1 for thermal detectors (Fig. 16.6).



Fig. 16.6 Automatic fire extinguishing systems test

16.4.3 ASCS—Related Tests

Concerning performance capacity, of the three systems mentioned, only that of the ASCS is known, as for each fan, its extraction capacity is known.

As far as the ASCS is concerned, the impact of the installation of these means on the FIS is not quantified, considering only that they confer greater safety to the building by their existence (Fig. 16.7).

16.5 “Virtual” Tests

It has been previously stated that the area of fire safety is characterized by a strong multidisciplinary, whose knowledge is still far from being considered stabilized, with particular emphasis on the behavioural theme.

Industry 4.0 has now emerged and is developing. This industry is very important for the field of civil engineering, as it is also evolving with Construction 4.0. Construction 4.0 is a term that should be seen as a leap in the built environment, with an increase in efficiency in production, business models and value chains. In fact, the focus of this revolution is the improvement of the efficiency and productivity of the processes, but also de safety in the AECO context. This focus becomes very important in the AECO sector since this problem that the revolution intends to solve is one that has been observed in the construction industry, which, in comparison with other industries, has been lagging due to the lack of incentive for digital transition. The transformation or technological leap is only possible through the convergence between existing technologies and emerging technologies, which are part of the industry 4.0 paradigm. Baur and Wee [22], define industry 4.0 as a ‘confluence of trends and technologies promises to reshape the things are made’, which are both digital and physical. Here we integrate the concept of construction 4.0 which has the same premise that propose for industry 4.0, but with the purpose of reshape the way the built environment assets are designed and constructed.

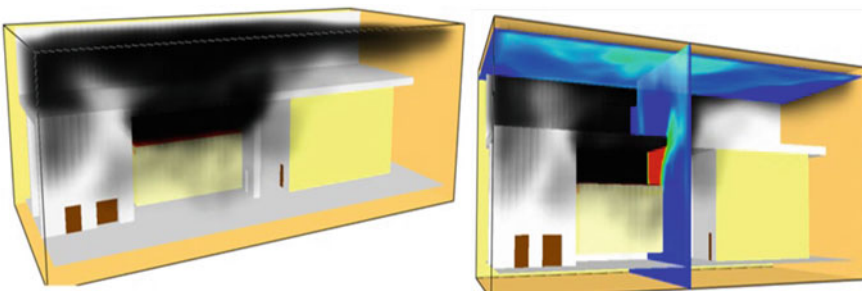


Fig. 16.7 Active smoke control systems test

Construction 4.0 combines cyber-physical systems and digital ecosystems to create a new paradigm for design and construction. To analyze Construction 4.0, we must then understand what these concepts are. Cyber-physical systems (CPS) are a fundamental driver of Industry 4.0. This concept integrates technologies that bring together the virtual world with the physical world, creating an interconnected world where intelligent objects interact with each other. The digital ecosystem concepts ‘is an interdependent group of enterprises, people and/or things that share standardized digital platforms for a mutually beneficial purpose, such as commercial gain, innovation or common interest’, [23]. In the paper ‘Construction 4.0’ of Anil Sawhney, Mike Riley, and Javier Irizarry [24] they propose a framework for the construction 4.0 which, ‘provides a mechanism via which we can:

- *Digitally model the built assets that already exist in our physical world.*
- *Design new assets in the backdrop of what already exists or plan for the retrofit and rehabilitation of existing assets using these digital models.*
- *Once these assets are digitally captured and designed, use digital and physical technologies to deliver these physical assets.*

Construction 4.0 is a framework that is a confluence and convergence of the following broad themes:

- *Industrial production: prefabrication, 3D printing, and assembly, offsite manufacture.*
- *Cyber-physical systems: robots and cobots for repetitive and dangerous processes, and drones for surveying and lifting, moving and positioning, and actuators.*
- *Digital technologies: BIM, video and laser scanning, IoT, sensors, AI and cloud computing, big data and data analytics, reality capture, Blockchain, simulation, augmented reality, data standards and interoperability, and vertical and horizontal integration.’*

The subject of fire behaviour has been the object of research studies for some decades due to the perception that had been acquired about the impact of that behaviour on the fire safety of buildings.

The impact of that behaviour on the total evacuation time of a building can be, not rarely, higher than the travel time between the place where the occupants are located and the exterior. However, knowledge acquisition in this area is strongly conditioned by the fact that it is not possible to “test” people’s behaviour in real fire situations.

Thus, the current state of knowledge results, essentially, from the analysis of surveys of diverse nature that never reflect the natural behaviour in fire situations, even when they are carried out with people who have lived that situation.

With the evolution that other areas of science have experienced in recent decades, with particular emphasis on artificial intelligence (AI) and the Internet of Things (IoT), new perspectives have opened up in terms of knowledge of human behaviour. The so-called virtual tests are essential in areas of expertise in which experimentation is strongly conditioned.

Of the possible “virtual tests”, we highlight the so-called “serious games”, which have the potential to create surrounding environments, simulating the occurrence of



Fig. 16.8 Simulator using peer designed agents concept (Silva [25])

fires. When people enter this game, they will make decisions and choices facing the conditions that the game creates, simulating situations identical to those of natural fires, allowing the acquisition of fundamental knowledge to optimize evacuation conditions and others that would not. Thus, it becomes possible to obtain any other type of experimentation through a virtual resource (Fig. 16.8).

Besides having to represent the fire with the maximum of realism, these games must also allow “transporting” the “players” to different environments since it will influence the behaviour. Thus, different settings should be recreated, such as, for example, familiar ones like the home, leisure ones like the cinema or the theatre, and working ones like offices.

On the other hand, the use of IoT can enable the transmission to the occupants, in real-time, of information about the development of the fire through the existing signage. Thus, we would move from currently static signage to another that would be dynamic and, indeed, would condition the occupants’ behaviour.

16.6 Conclusions

The main conclusions about fire reaction and fire resistance tests and virtual and active systems tests are summarized here. The measures to limit fire spread like passive fire protection and fire resistance rating requirements are some of the most traditional approaches to fire protection for buildings. However, there are gaps in knowledge and understanding here summarized that preclude certainty in engineered structural fire protection design. Also, it is summed up the actions to developed on R&D in the fire resistance to concrete, steel and timber structures.

16.6.1 Conclusions on Reaction to Fire Tests

From the analysis presented in the previous sections, it is easy to conclude the complexity of the current system and the difficulty of some of the indices that are determined to transmit sufficient information.

The non-inclusion of tests that allow measuring the toxicity conditions is also worth mentioning. The profound change that has occurred in the last decades in the contents of buildings, with the introduction of increasingly dangerous materials from the point of view of toxicity, makes it advisable that this parameter be evaluated.

16.6.2 Conclusions on Fire Resistance Tests

Gaps in knowledge of fire resistance. The following gaps in knowledge in testing and analysis for the performance in the fire of reinforced concrete structures, steel and timber were identified or are considered relevant.

Concrete

Fire exposure

To truly understand the response of concrete buildings in fires, tests of concrete structures and structural elements are required under a range of credible design fire exposures.

Structural interactions and asymmetry

Modern structures increasingly use irregular floor plates with varying span lengths, bay sizes, mixed construction materials.

Failure localizations

Failure is often initiated by localized failures or structural distress, such as discrete or splitting cracking in concrete, rupture of tensile steel reinforcement, connection or anchorage failure, shear or punching shear failure of concrete slabs, rupture of prestressing tendons, secondary moments, or unexpected shear forces exerted on columns due to lateral expansion of floor plates, heat-induced concrete spalling, etc.

Compartmentations and fire spread

The impacts of vertical and lateral deformations of structural frames on fire-stopping and both horizontal and vertical compartmentation should be studied to

preserve life safety in concrete buildings, which are becoming ever more reliant on defend-in-place life-safety strategies.

Cooling phase behavior and residual capacity

Structural actions resulting from creep, localized and/or global plastic deformation, thermal contraction, and restraint during cooling need to be better understood if designers can credibly design for burnout natural fire exposures while preventing structural collapse.

Instrumentation and measurement

More complete data are required from standard and non-standard large-scale structural fire tests. During testing, better information, particularly on strains and displacements, is needed to develop a more accurate understanding of response and provide the essential data for credible computational model development, validation, and verification.

Data for model calibration, validation and verification

Experimental data from realistic large-scale tests on concrete structures of various types are essential for calibration, validation, and verification of existing and emerging computational modelling techniques to simulate the response of concrete structures and structural elements in a fire.

Structural optimization and the use of new materials and systems.

The responses of modern concrete buildings during a fire are not well known in actual buildings.

Connections and post-installed anchors

However, there has been little effort to understand connection performance in concrete structures and develop and validate computational modelling capabilities to predict connection response and suggest best practice guidance to ensure structural robustness in a fire.

Steel. It should be noted that experiments on material properties are required to understand and model the larger-scale studies. Knowledge gaps in large-scale experiments are:

- Standardized test methods need to be developed to obtain the necessary data on steel elements' materials properties, focusing mainly on the future high grades of steel (e.g., ASTM A1077, A709) (including both heating and cooling phases).
- Accurate methods and standards need to be developed regarding test methods for assessing the bonding capability of fire protection systems (e.g., sprayed and intumescent material).

The bonding properties of protective materials to steel need to be understood to derive the necessary thermo-physical properties required for predicting the structural steel performance under fire.

Timber. Evaluating existing fire testing experience should be consulted before starting further studies. Japan has requirements for an extended time after fire resistance testing of combustible structures to evaluate possible continued charring and loss of load-bearing capacity.

Actions on R&D

Concrete

Whole structure testing and modeling

These tests are essential to validate and corroborate testing and modelling of materials credibly and small scale and large-scale structural elements. Such tests also provide an opportunity to observe possible additional structural interactions and failure modes that may have been overlooked during smaller scale or single element testing.

Property protection methodologies

Research is also of interest to study property protection aspects of concrete buildings both during and after severe fires. Tests and models are needed to allow engineers to quantify fire damage to concrete structures after different fire exposure levels. Such testing and modelling would support the development of intensity measures, damage indices, performance limits, and quantification of consequences of damage.

Hybrid testing

In the long term, validated sub-structuring methods and models need to be developed for very large whole structure testing when a large part of the 'test structure' is modelled in real-time. At the same time, a smaller portion of the structure is physically tested. For validation of the technique, whole-structure tests would be required.

Test-model based certification protocols

A long-term goal is the development of a structural certification methodology based on the complete structure response. This would be an assessment method for certification based on performing validated, credible numerical modelling of a whole structure with some minimum requirements for structural fire testing and materials characterization.

Steel

Develop advanced tools for large-scale testing

Hybrid testing has the potential to reduce costs associated with full testing systems.

Perform large-scale steel frame tests on 3D structural systems.

The most considerable absence of data is in large scale 3D structural system tests. These tests are essential to complement the smaller-scale tests that assume boundary conditions and cannot capture the response of the adjacent structure.

Perform large-scale tests on structural components

Deep plate girders and long-span truss beams

Effect of structural response on non-structural elements

Timber. The comprehensive gap analysis, leading to recommendations for future research and testing:

- Fire testing of new and innovative timber and hybrid solutions
- Full-scale/large-scale fire testing of mock-up tall timber frames
- Natural fire testing in full-scale/large-scale tall timber frames
- Economic analysis to quantify construction, operation and costs of tall timber buildings.

Emphasis on effective risk communication and education.

Large-scale experiments on timber structures are needed to support structure-fire model validation. The primary needs are to develop a design strategy for “burnout of fire compartments” to prevent structural collapse, control the vertical spread of fire, and understand the interaction between active and passive fire protection systems. This needs to be focused on developing advanced computer modelling, followed by, and supported by, experiments.

16.6.3 Conclusions on Virtual and Active Systems Tests

Research actions are mainly focused on testing in active systems and so-called virtual testing.

In the field of active systems, tests to determine parameters related to the response time of automatic fire detection systems and automatic fire extinguishing systems should be generalized.

Also, the evaluation of the effect of photovoltaic panels, roofs and garden facades, if their application is generalized, makes it advisable to define new tests to characterize the danger they can represent in terms of FIS.

Finally, in the field of human behaviour, it is considered valuable to implement, in the future, standardization establishing conditions for the validation of serious games, as otherwise, the results obtained from these applications are of limited interest.

References

1. Commission Decision of 8 February 2000 implementing Council Directive 89/106/EEC on the classification of construction products with regard to reaction to fire performance (2000/147/EC). Official Journal of the European Communities (JOCE), L 50, 2000-02-23, p 14–18
2. COMITÉ EUROPÉEN DE NORMALISATION (CEN) (2002) Fire classification of construction products and building elements. Part 1: classification using test data from reaction to fire test. Brussels, CEN. EN 13501-1
3. CEN (2002) Reaction to fire test for building products. Non-combustibility. Brussels, CEN. EN ISO 1182
4. CEN (2002) Reaction fire tests for building products. Determination of the heat of combustion). Brussels, CEN. EN ISO 1716
5. CEN (2002) Reaction to fire tests for building products. Building products excluding floorings exposed to the thermal attack by a single burning item. Brussels, CEN. EN 13823
6. CEN (2002) Reaction to fire tests—ignitability of building products subjected to direct impingement of flame. Part 2: single-flame source test. Brussels, CEN. EN ISO 11925-2
7. CEN (2002) Reaction to FIRE tests for floorings. Part 1: determination of the burning behaviour using a radiant heat source. Brussels, CEN. EN ISO 9239-1
8. International Organization standardization (ISO) (1993) Fire tests-full-scale room test for surface products. Genève, ISO. ISO 9705:1993
9. European Commission (EC), The European classification system for the reaction to fire performance of construction products. Brussels: the Commission, December 1999. Guidance Paper G
10. ISO 19702:2015, Guidance for sampling and analysis of toxic gases and vapours in fire effluents using fourier transform infrared (FTIR) spectroscopy
11. American Society for Testing and Materials (ASTM) (2000) Standard test methods for fire tests of building construction and materials. E 119, ASTM, pp 1–21
12. ISO 834-1 (1999) Fire-resistance tests-elements of building construction. Part 1: general requirements. Geneva, ISO
13. EN1991-1-2 (2002) Eurocode 1: actions on structures. Part 1–2: general rules–actions on structures exposed to fire. Brussels, CEN
14. EN1993-1-2 (2005) Eurocode 3: design of steel structures. Part 1–2: general rules–structural fire design. Brussels, CEN
15. EN1994-1-2 (2005) Eurocode 4: design of composite steel and concrete structures. Part 1–2: general rules–structural fire design. Brussels, CEN
16. EN 1995-1-2 (2004) Eurocode 5: design of timber structures. Part 1–2 general–structural fire design. European standard. CEN, Brussels
17. CIB-Council for Research and Innovation in Building and Construction. <http://www.cibworld.nl/>
18. NIST-National Institute of Standards and Technology. <http://www.nist.gov/>
19. Yang JC, Bundy M, Gross J, Hamins A, Sadek F, Raghunathan A (2015) International R&D roadmap for fire resistance of structures-summary of NIST/CIB Workshop. Fire Research Division, Engineering Laboratory, NIST Special Publication 1188
20. BS 8458:2015, Fixed fire protection systems-residential and domestic watermist systems-code of practice for design and installation
21. AS 1851-2012, Australian standard-routine service of fire protection systems and equipment
22. Baur C, Wee D (2015) Manufacturing's next act. In: McKinsey.Com (issue June). <https://www.mckinsey.com/business-functions/operations/our-insights/manufacturings-next-act>

23. Rowsell-Jones A, Lowendahl JM, Howard C, Nielsen T (2016) The 2017 CIO agenda: seize the digital ecosystem opportunity. Technical Report, Gartner Inc
24. Sawhney A, Riley M, Irizarry J (2020) Construction 4.0 introduction and overview. In: Construction 4.0 an innovation platform for the built environment, vol 53, issue 9
25. Silva JFM, Almeida JE, Pereira A, Rossetti RJF, Coelho AL (2013) Preliminary experiments with EVA-serious games virtual fire drill simulator. In: 27th EUROPEAN conference on modelling and simulation (ECMS 2013). Ålesund, Norway

Chapter 17

A Modelling Tool for Lighting Systems Based on Visual Comfort and Energy Consumption—Case Study of a Residential Building



Luis G. Baltazar  and João Tapadas

Abstract Most buildings in the European Union (EU) have lighting systems that are outdated and inefficient. To achieve the targets proposed by the EU in terms of decarbonization and energy efficiency in buildings, it is necessary to optimize and moderate the energy consumption in buildings, including the parcel of electricity consumed with lighting. An efficient lighting system in a residential building can easily be achieved through an adequate design using numerical modelling tools. Moreover, a proper lighting design is not only essential for energy efficiency but also for the visual comfort of the occupants, especially when contemporary society spends a large part of its daily life exposed to artificial light, which in turn can lead to sleep disturbance, cancer, and other health problems. This chapter presents the analysis of different lighting systems in a residential single-family building in Portugal using the DIALux modelling tool. This study involves the analysis of the existing lighting system and different solutions that can be implemented to reduce electricity consumption. Moreover, it documents several parameters which can reduce lighting demand in a residential building and highlight the need of standardization of lighting design in the residential sector. In summary, the energy savings that can be achieved by the proposed solutions were determined with this tool, including the impact of the studied parameters on the visual comfort of the residents.

Keywords Efficient lighting system · Residential building · Energy savings · DIALux · Illuminance

L. G. Baltazar 

NOVA School of Science and Technology, Universidade NOVA de Lisboa, 2825-149 Caparica, Almada, Portugal
e-mail: luis.baltazar@fct.unl.pt

J. Tapadas

Department of Civil Engineering, NOVA School of Science and Technology, Universidade NOVA de Lisboa, Lisbon, Portugal
e-mail: j.tapadas@campus.fct.unl.pt

17.1 Introduction

Over the twentieth century there was a significant growth both at the economic and technological level. The considerable progresses made in the industry and technology represents, on one hand, an important milestone in the development of humankind, but on the other, it triggered a problem in terms of energy demand and emissions of greenhouse gases from burning fossil fuels for electricity production, transports, heating, industry, etc. According to the European Environmental Agency, about 80% of the total greenhouse gas emissions in the European Union (EU) are caused by energy production, energy use by the industry, businesses, households and transports. In 2018 Portugal was the 7th country in the EU with the highest energy dependency on fossil energy, namely natural gas. To reverse this situation, the National Energy and Climate Plan (NECP) for 2021–2030 was approved [1]. The main objective of the Portuguese NECP is to addresses all five scopes of the EU Energy targets: decarbonization, energy efficiency, energy security, internal energy markets and research, innovation and competitiveness [1]. To do so, it is necessary to optimize and moderate the energy consumption in buildings. In 2019, lighting in the residential sector in EU was responsible for 15% of electric energy consumption [2], although the contribution of lighting to electricity consumption can be reduced considering that about 90% of buildings have lighting systems that are outdated and inefficient [3].

More recently, in February 2021, Portugal approved the long-term strategy for building renovation (ELPRE) for the transposition of the Directive (EU) 2018/844 of the European Parliament [4]. ELPRE encompasses a set of measures aimed at increasing energy efficiency of buildings. For instance, ELPRE tends to promote a trend towards the increase of energy efficiency of both residential and non-residential buildings with the implementation of more efficient and low consumption lighting systems. However, the importance of implementing the lighting project as a rule in residential buildings is not only related to the energy performance, but also to the visual comfort of the buildings' occupants. A proper lighting design is important since contemporary society is exposed to artificial light for a large part of the day, which in turn can lead to sleep disturbance, cancer and psychiatric disorders, as well as biological problems controlled by endogenous circadian clocks, resulting in health problems [5, 6]. Hence it is crucial to assess and implement internationally recognized visual comfort indices [7]. It should be noted that there is no agreement on the metrics to evaluate visual comfort. However, several reviews about visual comfort can be found in the literature [8–11].

Regarding the parameters associated to lighting in office buildings and services, the minimum lighting levels for various tasks carried out inside buildings are specified in standard EN 12464–1 [12]. Noteworthy, however, is the lack of standardization and adequate lighting design in the residential sector. Given this situation, this study aims to analyse different lighting systems in a residential building using the DIALux modelling tool. This study involves the analysis of the existing lighting system (based on halogen lamps) of a single-family house. Then, different solutions

(such as changing the lamp type and/or values of illuminance) that can be implemented to reduce electricity consumption will be investigated and electricity savings that will be accomplished by each solution will be calculated. The impact of the studied parameters on the visual comfort of the occupants will be considered as well.

17.2 Experimental Lighting Measurements Using HDRI Image

The quality of natural or artificial lighting in interior spaces can be measured using traditional photometric measurements, however, these methods are usually time consuming. The high dynamic range image (HDRI) appears as an alternative method to determine the values of luminance and enables to carry out fast and low-cost measurements compared to the traditional technique of point-by-point readings [13, 14]. The biggest advantage pointed to the HDRI luminance mapping is that it can be easily used in buildings where modelling is difficult due to its complex geometry and/or to effectively reproduce the aging of light-reflecting surfaces in the simulation.

The HDRI only involves a single-lens reflex camera with wide reception angle, and a computer to process the data obtained and to create the luminance map [15]. Nevertheless, to obtain luminance maps of an interior space, it is necessary to capture the whole space with the camera several times with different exposure values [16]. HDRI luminance maps provide valuable information on the quality of light and luminance distribution indoors. The luminance maps can be afterward converted to fictitious colour pictures, where each colour is associated with a luminous value. In reference [17], the authors used the HDRI method to quantify and analyse natural lighting in the dome of the church of San Lorenzo in Turin (Fig. 17.1).

These authors [17] used the HDRI mapping technique as a valuable tool to scientifically investigate the range and the quantity of light in every part of the dome (see Fig. 17.2).

From Fig. 17.2 it can be noted that blue (cold colour) represents the spots with the lowest luminance, and the warmest colour (yellow) represents the brightest locations. Several studies [15–17] indicate that the measures of luminance obtained by means of the HDRI method are generally in good agreement with those collected by the traditional measurement techniques. Notwithstanding, in situ measurement requires that it be done in different periods because daylight varies with time of day, season, and sometimes it is even impossible to carry out due to the most diverse reasons.

Moreover, to overcome some limitations and simultaneously complement the in situ photometric measurements, in the last decades, there has been a growth of different lighting simulation tools, which can be used to see how light behave in a building. In addition, one of the great possibilities of these simulation tools is that they also allow the investigation of the lighting solution that leads to the lowest energy consumption according to the use profile of the building (commercial building, office building, residential building, among others). The present study aims

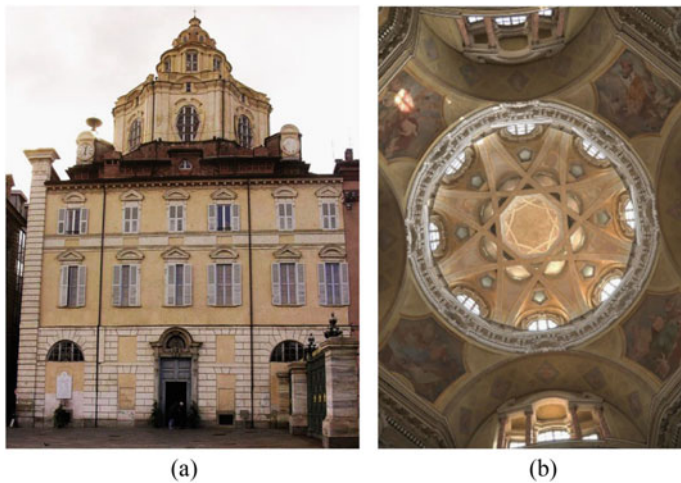


Fig. 17.1 Church of San Lorenzo: **a** entrance façade **b** interior view of the dome (adapted from [17])

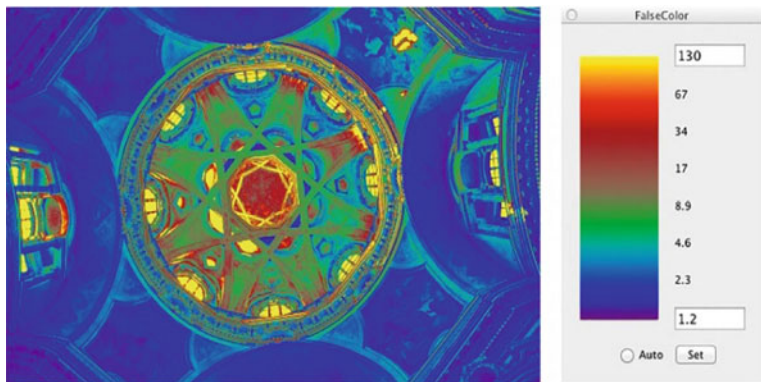


Fig. 17.2 Example of luminance map the dome Church of San Lorenzo (adapted from [17])

to demonstrate the systematic procedures of simulation of different lighting solutions in single-family house using a lighting simulation tool along with the corresponding parameters, such as glare index, illuminance, surface reflection coefficient, etc.

17.3 Case Study—Model of Residential Building

The building considered in this study is a single-family house located in the city of Lisbon, Portugal. The total floor area of the building under study is 125 m^2 split over

two floors. The first floor consists of a living room, an office, a kitchen, a bathroom, hallway and stairs. The second floor comprises four bedrooms, two toilets and a hall. Figure 17.3a and b represent the schematic plans of the zones referring to floors 1 and 2, respectively.

The building has facades oriented to the four quadrants and there is vertical glazing in the SW and NE quadrants which is beneficial for daylight utilization. However, the

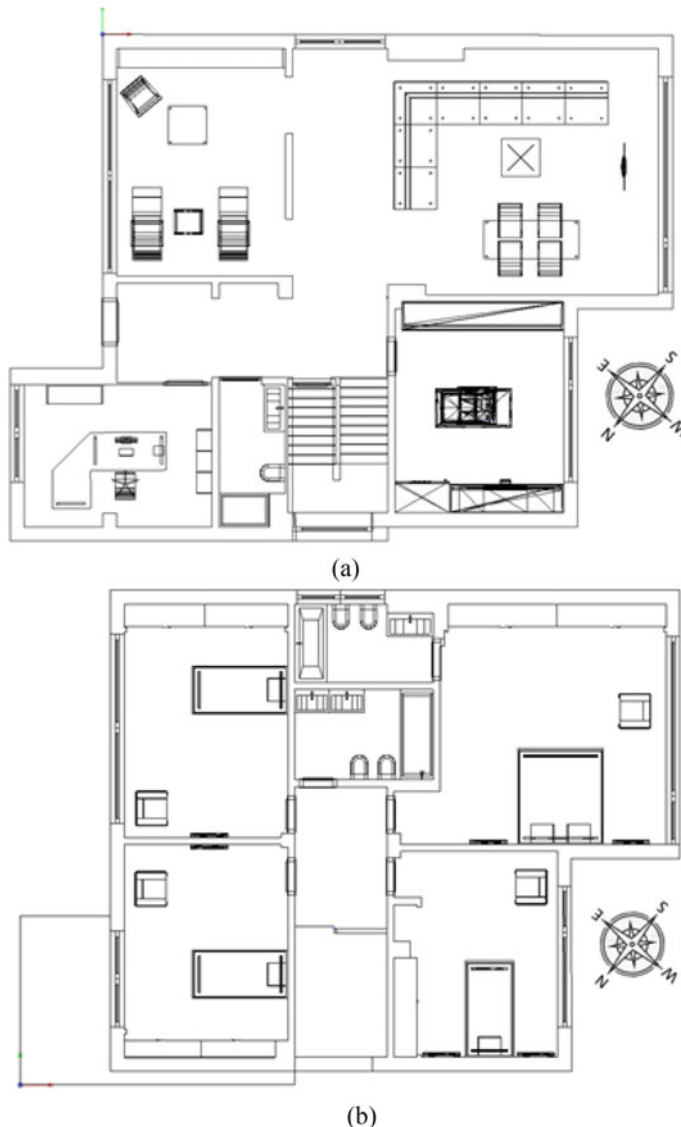


Fig. 17.3 Schematic plan of the case study: **a** floor 1; **b** floor 2

design of the windows does not include any shading system to avoid excessive solar gains in summer. Moreover, it should be noted that no renewable energy systems have been considered in this building.

17.4 Numerical Simulations and Calculation Parameters

DiaLux evo is a numerical software designed to carry out lighting simulations. This software allows you to plan, design and visualize lighting for both indoor and outdoor areas, from individual rooms to complete buildings. Its main objective is to evaluate in an integrated way the visual performance and energy efficiency of the lighting system under study.

17.4.1 Illumination Calculation Parameters

The main elements that affect the performance of a lighting system are the lamp, the luminaire, and the specificity of interior environment (such as the characteristics of the interior surfaces of the room). The lamp transforms electricity into light, the luminaire distributes the light in the room, and the room transforms this light into visible luminance by the surface reflections. Below are the most relevant parameters in designing the lighting system using the software DiaLux evo.

Reflection coefficient. The characteristics of the surfaces are decisive for the luminotechnical study, the main one being the reflectivity of the surfaces. It is easily understandable that interior walls with a light colour finish have greater light reflection compared to dark finishes. European standard EN 12464 [12] defines ranges of reflection coefficients for various interior surfaces. Considering the values for the reflection coefficient specified in the standard EN 12464, the following reflection coefficients (ρ) were defined for the different surfaces (see Table 17.1).

Illuminance. The parameter usually assumed to quantify the amount of light that reaches each surface is illuminance. In a lighting system design it is necessary to define illuminances depending on the type of activity carried out by the occupants in

Table 17.1 Reflection coefficients for interior surfaces for each building zone

Zone	Surface	Reflection coefficient [%]
Living room; offices; hall; stairs; bedrooms	Ceiling	70
	Walls	77
	Floor	50
Kitchen; bathrooms	Ceiling	70
	Walls	70
	Floor	70

Table 17.2 Ideal illuminance intervals for each building zone

Zone	Ideal illuminance range (Emd) [lux]
Living room	70
Kitchen	77
Office	50
Bathrooms	70
Hall and stairs	70
Bedrooms	70

each indoor zone. LUX is the unit of measuring the illuminance. Table 17.2 shows illuminance values for each zone depending on the activity according to other studies [18, 19].

The values in Table 17.2 were defined considering the lowest and highest values for each zone found in the literature, and then ideal illuminance intervals (Emd) were created where the lowest value represents the minimum acceptable value for optimal lighting.

Glare index. The glare produces a feeling of surplus light in the eye of the occupant and generates a feeling of discomfort. Visual comfort is defined in the standard EN 12665 [20] as a “subjective condition” and it has been addressed in the literature through some indexes that relate the needs of the occupants and the light in the indoor space, such as: the amount of light; the uniformity of light and the risk of glare [9]. The glare index (UGR) can be pointed as the main index for the evaluation of visual comfort [9]. For the correct definition of the characteristics of each zone, it is necessary to establish the maximum values of UGR. In this case, UGR values (Table 17.3) referring to standard EN 12464 [12] were adopted.

From the analysis of Table 17.3, it can be concluded that the office is the zone that presents a more conditioning glare requirement, as it is a workspace that requires greater visual demand. On the contrary, zones intended for circulation (halls and stairs) have higher maximum glare values as they are transit zones and do not require great demand in terms of vision.

All furniture elements that could interfere with the lighting project were introduced in the model (Fig. 17.4). The influence of these objects derives from the reflection produced on them.

Table 17.3 Maximum glare index for each building zone

Zone	Maximum (UGR)
Living room	22
Kitchen	22
Office	19
Bathrooms	25
Hall and stairs	28
Bedrooms	22



Fig. 17.4 View of furniture configuration in the living room

In order to consider the influence of the furniture, several calculation points were defined, to recreate in the model the spots where the occupants stay longer so as to determine the glare index of the occupants in certain places (see Figs. 17.5 and 17.6).

From Fig. 17.5, it can be seen the calculation points that were defined to study the glare felt by users when using the office. In Fig. 17.6, it is possible to observe two surfaces related to the sofas and the four points considered to study the glare on the chairs at the table. Regarding the positioning of the points under study, a height of 0.80 m above the floor level and a viewing angle range of 0 to 180° were considered. These heights were adopted to simulate the user's field of vision, trying to get as

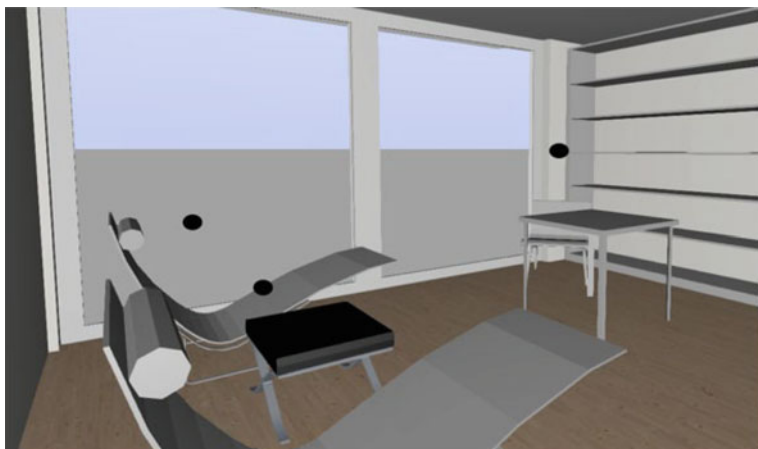


Fig. 17.5 Surfaces and calculation points in the office



Fig. 17.6 Surfaces and calculation points in the living room

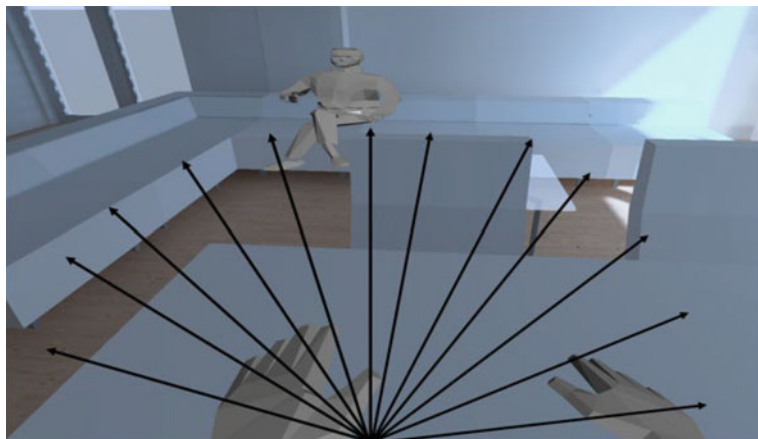


Fig. 17.7 Occupant's field of vision at dining table

close as possible to reality. Figures 17.7 and 17.8 presents the user's field of vision both when sitting at the dining table and when sitting on the sofa, respectively.

17.4.2 Evaluation of the Existing Lighting System

In order to assess the efficiency of artificial lighting, several simulations were carried out considering the existing lighting system in the case study, as well as possible solutions for improvement.

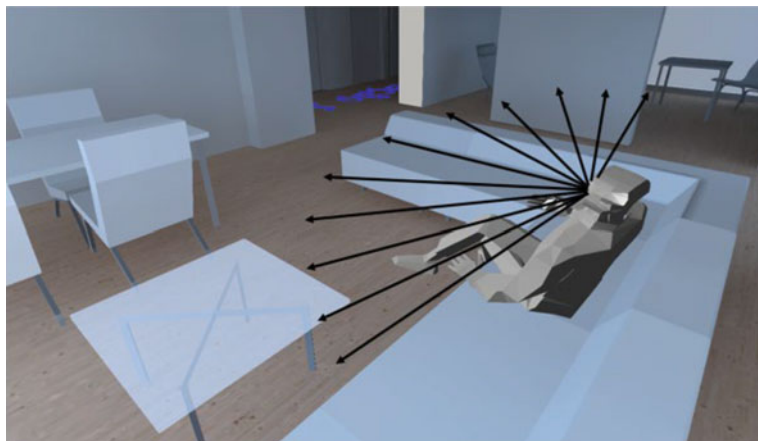


Fig. 17.8 Occupant's field of vision when sitting on the sofa

First, the implemented system was simulated for the illuminance values defined by the designer in the construction documents, evaluating the glare index felt by the occupants as well as the energy consumption of the equipment defined by the project.

Then, other simulations were thought in order to obtain improvements, having been made alterations into the Emd values and changing the lighting system. Regarding the existing lighting system in the building under study, the system consists of luminaires with direct light distribution and halogen lamps. To carry out the simulation, the halogen of lamp shown in Table 17.4 was defined in all zones of the building.

Table 17.5 shows the modelled illuminance values obtained for each zone, and these were compared with the illuminance values defined in the project.

Regarding the glare index obtained for the existing lighting system, the values are shown in Table 17.6.

By analysing the different zones, the existing lighting system causes glare in certain usage plans. Considering the values obtained for a period of use similar to the one adopted by Zhen et al. [21], the electricity consumption and costs of energy were calculated. Table 17.7 shows the consumptions and costs for the existing system, as well as the power used per m^2 for all zones.

Based on the values presented in Table 17.7, it can be stated that the power used per m^2 is around 24.5 W/m^2 . According to the study presented by Souza et al. [22]

Table 17.4 Type of lamp of the existent lighting system

Type of lamp	Power [W]	Luminous Flux [lm]	Luminous Efficiency [lm/W]	CCT [K]	IRC
Low voltage halogen lamp	35	926	26	3000	99

Table 17.5 Illuminance values obtained for the existing lighting system

	Zone	Existen illuminance (Emd) [lux]	Modelled illuminance (Emd) [lux]
Floor 1	Living room	500	521
	Kitchen	500	503
	Office	500	500
	Bathroom 1	70	341
	Hall and stairs	150	251
Floor 2	Bedroom 1	500	503
	Bedroom 2	500	546
	Bedroom 3	500	598
	Bedroom 4	500	517
	Bathroom 2	250	350
	Bathroom 3	250	403
	Hall	150	246

Table 17.6 Glare index values obtained for the existing lighting system

	Zone	Calculation point	Maximum UGR	Modelled UGR
Floor 1	Living room	Sitting at the table	22	19.6
		Reading in a chair		30.0
		Reading in a chair		29.1
	Kitchen	Standing	22	24.3
		Sitting		24.6
	Office	Standing	19	25.8
Floor 2	Bathroom 1	Standing	25	25.1
	Bedroom 1	Lying	22	19.1
		Standing		16.3
	Bedroom 2	Lying		18.8
		Standing		17.1
	Bedroom 3	Lying		18.6
		Standing		19.4
	Bedroom 4	Lying	25	19.1
		Standing		16.4
	Bathroom 2	Standing	25	21.2
	Bathroom 3	Standing		20.0
	Hall	Standing	28	13.7

Table 17.7 Consumptions and costs related to the existing lighting system

	Zone	Number of fixtures	Power [W]	Consumption [kWh/year]	Cost [€/year]
Floor 1	Living room	35	1225	750	128
	Kitchen	12	420	185	31
	Office	9	315	93	8
	Bathroom 1	2	70	7.7	1
	Hall and Stairs	5	175	45	8
Floor 2	Bedroom 1	12	420	87	14.5
	Bedroom 2	20	700	145	24
	Bedroom 3	16	560	226	19.5
	Bedroom 4	12	420	87	14.5
	Bathroom 2	3	105	7.7	1
	Bathroom 3	3	105	7.7	1
	Hall	2	70	18	3
Total				1659.1	253.5

concerning a residential building, the power per m^2 required to obtain the ideal luminance values for a halogen lighting system is around 24.9 W/m^2 .

Considering the above results, it can be said that the defined illuminance and the characteristics of the luminaires contribute to the power needed per m^2 . However, the existing lighting solution in the case study, the luminous flux of the luminaires and the illuminance values are higher than those used by the authors [22]. Thus, this comparison demonstrates that the existing lighting system has a usage power per m^2 identical to that required for systems design with lower illuminances, being by comparison more efficient.

17.4.3 Designing Lighting System Improving Visual Comfort and Energy Consumption

It is important to understand the influence of Emd on the distribution of luminaires in each zone, the electricity consumption and the cost. For that, different improvements (solutions) are here analysed. Solution 1 involves the existing lighting system, but the illuminance values were changed to the optimized ones (see Table 17.2). Given these values, the distribution of luminaires (light fixtures) per zone was carried out as illustrated in Fig. 17.9.

With the approval of long-term strategies for the renovation of buildings [4], one of the packages of measures involves the replacement of the lighting systems currently used by LED-type systems. Thus, one of the possible solutions to improve the efficiency of the case study's lighting system is the implementation of a LED-type

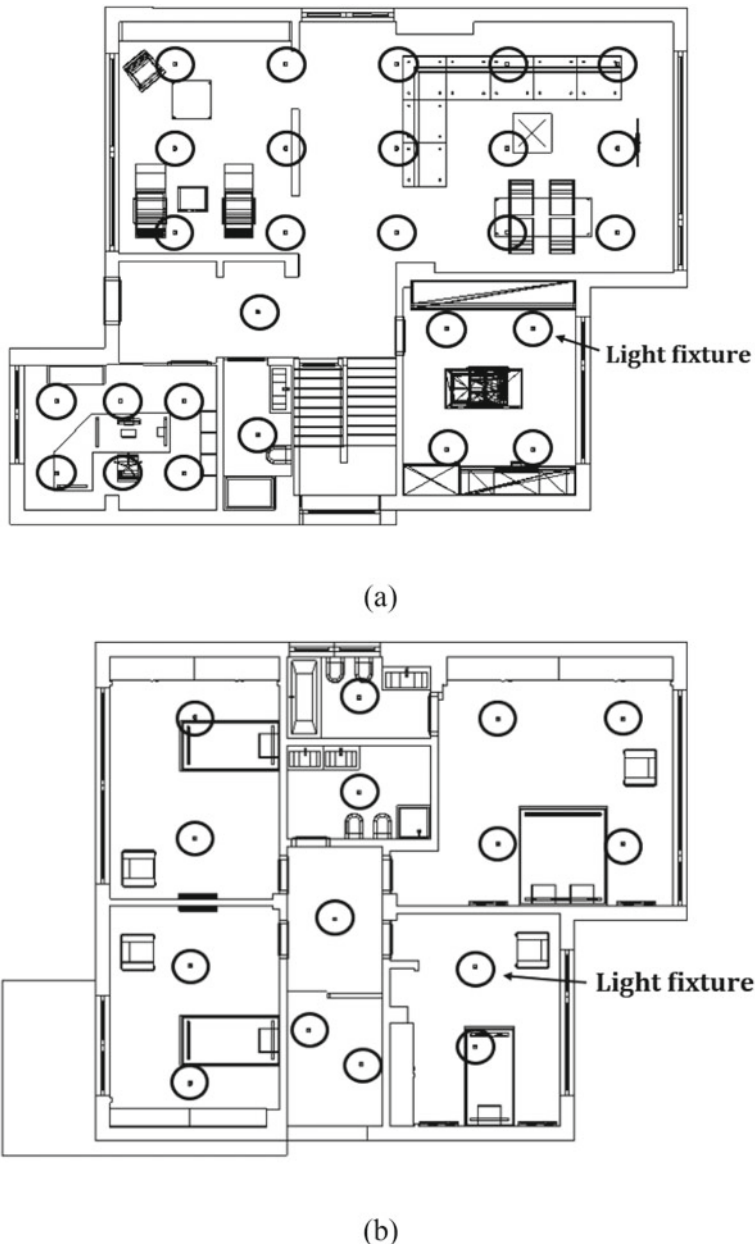


Fig. 17.9 Distribution of luminaires for solution 1: **a** floor 1; **b** floor 2

Table 17.8 Type of lamp adopted in solution 2

Type of lamp	Rated power [W]	Luminous flux [lm]	Luminous efficiency [lm/W]	CCT [K]	IRC
LED lamp	10.6	680	79	3000	80

lighting system. To carry out the improvement simulation (solution 2), the type of lamp characterized in Table 17.8 was defined in each building zone.

Then, the distribution of the luminaires throughout the building zones was defined, as shown in Fig. 17.10.

For the distribution of luminaires defined above, the Emd values were determined and compared with the optimized Emd values (see Table 17.9).

Concerning to glare index, the implementation of solution 2 allowed the maximum values for the glare index to be checked for all zones (see Table 17.10).

Solution 2 (LED-lighting system) presents glare index values, for all zones, within the defined maximum limits, which means that there is no glare felt by the occupants.

It should also be noted that it is essential to consider not only the system's efficiency but other characteristics such as colour temperature. Colour temperature of LED type luminaires may be within the range of values corresponding to 3000 K and 6000 K. Taking into account the illuminance values necessary for carrying out activities in a residential building and considering the health of the occupants, the recommended colour temperature of the lighting system is around 3000 K, thus providing a warmer environment and better visual comfort. Table 17.11 summarizes the annual energy consumption and respective cost for both simulation solutions.

By comparing solution 1 with the existing lighting solution, it can be stated that there is a clear decrease in the number of luminaires in each zone of the house, which in turn leads to a decrease in energy consumption and cost of use.

Regarding the values obtained in Table 17.11 for solution 2, the power used per m^2 is around 2.3 W/ m^2 . According to studies carried out by Souza et al. [22] and Sun et al. [23], for this type of lighting system, the power used per m^2 is around 4.6 W/ m^2 and 3.4 W/ m^2 , respectively. Comparing these values, it can be stated once more that the illuminance defined for each building zone is decisive. Relating the study by Souza et al. with solution 2, it presents lower Emd values and a lighting system with higher nominal power and lower luminous flux. Moreover, when comparing the solution 2 to the study by Sun et al., the illuminance values obtained are still lower, and the luminaires defined in the lighting system used by the authors have a lower nominal power. Thus, comparing to solution 2, even though it may not be the most efficient luminaire, the system presents a usage power per m^2 lower than the solutions studied by the authors and with a very satisfactory performance.

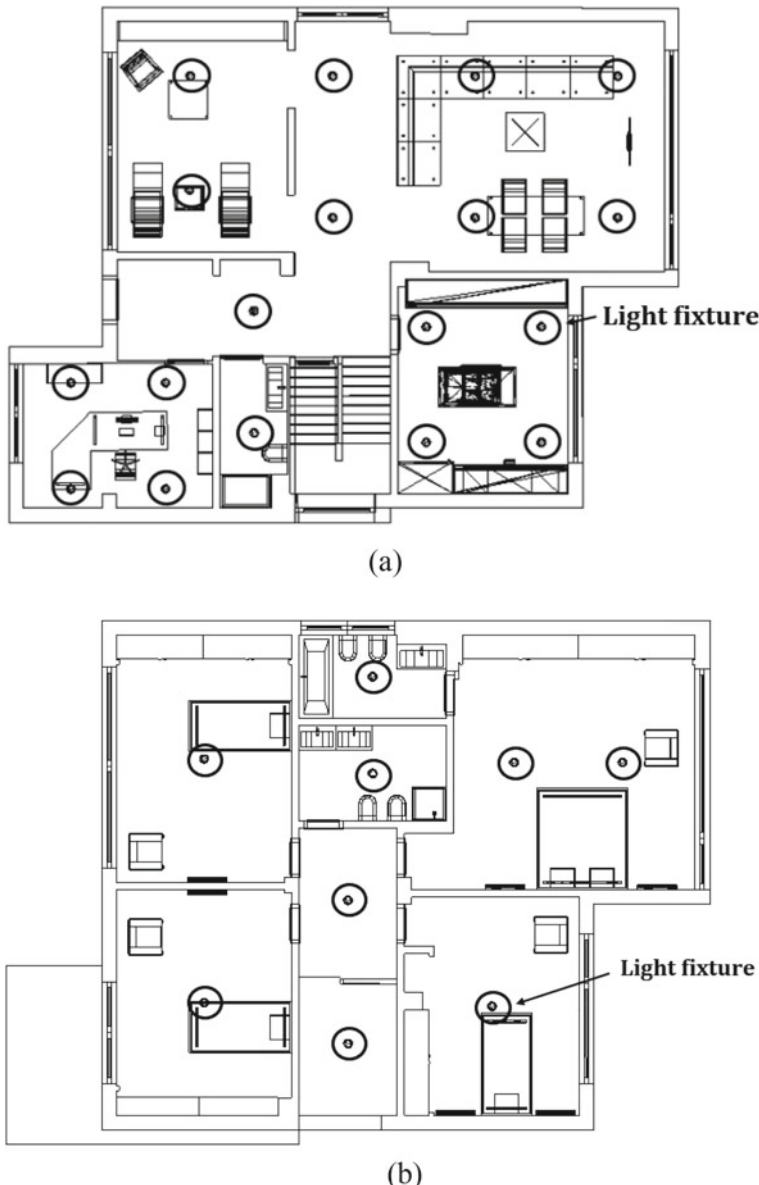


Fig. 17.10 Distribution of luminaires for solution 2: **a** floor 1; **b** floor 2

Table 17.9 Illuminance values obtained for solution 1 and 2

	Zone	Optimized illuminance (Emd) [lux]	Modelled illuminance (Emd) [lux]—solution 1	Modelled illuminance (Emd) [lux]—solution 2
Floor 1	Living room	200	224	220
	Kitchen	150–300	181	204
	Office	300	346	369
	Bathroom 1	80–150	182	200
	Hall and stairs	50–100	95.7	88.6
Floor 2	Bedroom 1	80–100	101	101
	Bedroom 2	80–100	120	91.1
	Bedroom 3	80–100	85.9	86.8
	Bedroom 4	80–100	92.7	96.8
	Bathroom 2	80–150	125	164
	Bathroom 3	80–150	145	131
	Hall	50–100	182	132

Table 17.10 Glare index values obtained for solution 1 and 2

	Zone	Calculation point	Maximum UGR	Modelled UGR solution 1	Modelled UGR solution 2
Floor 1	Living room	Sitting at the table	22	21.8	15.2
		Reading chair		23.6	12.7
		Reading chair		30.0	20.6
	Kitchen	Standing	22	27.7	21.9
	Office	Sitting	19	20.7	17.4
		Standing		25.3	19.0
Floor 2	Bathroom 1	Standing	25	27.7	23.8
	Bedroom 1	Lying	22	23.0	19.9
		Standing		22.0	14.2
	Bedroom 2	Lying		22.0	19.4
		Standing		15.5	10.0
	Bedroom 3	Lying		18.3	10.0
		Standing		21.9	15.4
	Bedroom 4	Lying		22.3	19.9
		Standing		10.0	15.5
	Bathroom 2	Standing	25	24.5	20.0
	Bathroom 3	Standing		20.9	21.2
	Hall	Standing	28	26.8	23.1

Table 17.11 Consumptions and costs for solution 1 and solution 2

Zone	Solution 1			Solution 2				
	Number of fixtures	W/m ²	Consumption [kWh/year]	Cost [€/year]	Number of fixtures	W/m ²	Consumption [kWh/year]	Cost [€/year]
Floor 1	Living room	15	9.3	325	47.2	15	2.8	96.5
	Kitchen	4	8.9	64.5	9.4	4	2.7	18.5
	Office	6	17.6	24.5	2.6	6	5.3	6.5
	Bathroom 1	1	8.9	6.9	1	1	2.7	14
Floor 2	Hall and stairs	3	14.4	32	4.6	2	2.7	2.7
	Bedroom 1	2	5.1	17.5	2.5	2	1.5	0.9
	Bedroom 2	4	5.9	32	4.6	3	1.4	0.7
	Bedroom 3	2	4.9	17.5	2.5	2	1.5	0.4
	Bedroom 4	2	4.4	17.5	2.5	2	1.3	0.4
	Bathroom 2	1	8	6.9	1	1	2.4	0.2
	Bathroom 3	1	5.9	6.9	1	1	1.8	0.2
	Hall	1	6.6	10	1.5	1	2	0.4
Total		8.3	561.2	81.5	1	2.3	154.3	22.4

17.5 Analysis of Lighting Solutions

The Emd values initially defined for this case study, when compared to the optimized values from the literature (see Table 17.2), turned out to be excessively high. It is possible to conclude that the existing Emd values require on the one hand a larger number of luminaires (Table 17.12), but on the other hand they cause glare situations with higher frequency (Table 17.6). Moreover, it can be stated that the adoption of optimized Emd values (with the same type of luminaires i.e. solution 1), allowed a decrease in electricity consumption and an annual cost of approximately 66% and 63%, respectively.

As far as the differences between solution 1 and 2 are concerned, it can be said that the implementation of a LED lighting system allows for energy and economic savings of around 90% (Table 17.13). However, converting a halogen lighting system to an LED lighting system entails material and labour costs.

In order to determine the cost of converting the existent lighting system to one of LED-based luminaires, an estimate was made of the cost of labour and material to install the luminaires in the case studied. Table 17.13 shows the values for both the cost of the luminaire and the labour cost associated with its installation.

Bearing in mind that the unit price to place each luminaire is around 60€, it is possible to determine the total cost of implementing solution 2 for the case study, which is 2398.20€.

The feasibility of implementing solution 2 system is quite important considering the building's usage profile. The zone in which the set of luminaires is active for the longest time throughout the year is the living room, with an annual period of use of 1095 h.

Table 17.12 Comparison of parameters between solution 1 and existing lighting system

	Number of luminaires	Consumption [kWh/ano]	Cost [€/year]
Existing lighting system	131	1659.1	241.1
Solution 1	42	561.2	81.5

Table 17.13 Cost of implementing an LED luminaire—adopted in solution 2

	Consumption	Unit price [€]	Total [€]
LED-based luminaire	1 ud	49.25	49.25
Electrician	0.3 h	14.52	4.36
Electrician assistant	0.3 h	12.25	3.68
Direct complementary costs	2%	133.61	2.67
			59.96

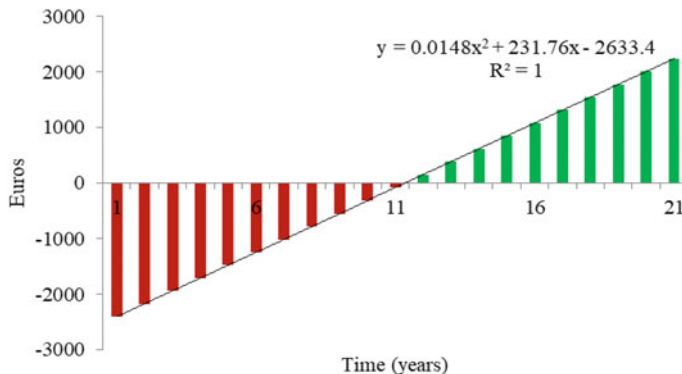


Fig. 17.11 Payback analysis for solution 2

Bearing in mind that the luminaire manufacturer optimistically describes a lifetime of 25,000 h, the lifetime for this system would be approximately 22 years. Nevertheless, it is necessary to know the payback period from the solution 2 considering the performance of the existing system and the investment required to implement this solution. The increase in the cost of electricity over the years was considered, with an annual increase of 2.3% being considered [24].

Figure 17.11 shows the energy savings obtained with the adoption of solution 2 and that break-even is reached at 11 years, meaning that in 11 years the LED-based lighting system is paid with the savings generated annually.

17.6 Conclusion

This study focused on the modelling of artificial lighting systems and had as its main objective the achievement of higher levels of electric energy savings, visual comfort, as well as the reduction of energy costs for lighting. To this end, several simulations were carried out. Regarding the glare felt by the occupants, it was found that in certain points of calculation, glare index values above the defined maximum values were obtained. Moreover, the simulation of the existing lighting system proved to have an energy consumption of 1659.1 kWh per year and a cost of use of 241.1€ per year. Such results turned out to be 6.3 times higher than the average annual cost recommended by the EU for lighting.

After analysing the existing lighting system, possible solutions for lighting performance improvement were modelled. The first iteration (solution 1) consisted of changing the illuminance values to lower ones. To do so, the existing lighting system in the case study was used, but with lower Emd values, and a consumption of 561.2 kWh per year and a usage cost of 81.5€ was obtained. It can thus be realized that, compared to the existent system, there are improvements of around 60% both in

terms of consumption and cost. This means that it is possible to get higher energy efficiency levels without the need to change the type of luminaire.

This study also demonstrates the importance of a detailed design of artificial lighting systems in residential buildings and the relevance of using modelling tools. Numerical simulation tools help to support the choice of the most suitable lighting solution according to the specifics of each building. The design of an efficient lighting solution is essential not only to reduce the electricity bill, but also to increase energy efficiency and promote lighting levels that are adequate to the visual comfort of users.

In order to achieve lower electrical energy demand and to promote cost reduction, a solution for LED-type luminaires was modelled and the consumption values of around 154.3 kWh per year and annual energy costs of 22 € were obtained which, in comparison with the existing lighting system promote a 91% reduction in electrical energy consumption.

The results obtained make it clear the benefits of an efficiently designed lighting system. This study ends with the statement that the efficient lighting systems usually involve significant costs of installation, but it has been shown that the payback time is adequate for the lifetime of the equipment and the usage profile of a residential building.

Acknowledgments This work was supported by National Funds through FCT—Portuguese Foundation for Science and Technology under the project UID/CTM/50025.

References

1. Portugal's National Energy and Climate Plan for 2021–2030, https://ec.europa.eu/energy/sites/ener/files/documents/pt_final_necp_main_pt.pdf, last accessed 2021/08/03
2. Eurostat Homepage, https://ec.europa.eu/eurostat/statistics-explained/index.php?title=Energy_consumption_in_households#Energy_consumption_in_households_by_type_of_end-use, last accessed 2021/08/10
3. Pohl W, Werner M (2010) Lighting, comfort and energy and the evaluation of the recommendations of EN 15251. Intelligent Energy Europe
4. Directive (EU) 2018/844 of the European Parliament and of the Council of 30 May 2018 amending Directive 2010/31/EU on the energy performance of buildings and Directive 2012/27/EU on energy efficiency
5. Lunn RM, Blask DE, Coogan AN, Figueiro MG, Gorman MR, Hall JE, Hansen J, Nelson RJ, Panda S, Smolensky MH, Stevens RG, Turek FW, Vermeulen R, Carreón T, Caruso CC, Lawson CC, Thayer KA, Twery MJ, Ewens AD, Garner SC, Schwingl PJ, Boyd WA (2017) Health consequences of electric lighting practices in the modern world: a report on the National Toxicology Program's workshop on shift work at night, artificial light at night, and circadian disruption. *Sci Total Environ*
6. Cho Y, Ryu SH, Lee BR, Kim KH, Lee E, Choi J (2015) Effects of artificial light at night on human health: a literature review of observational and experimental studies applied to exposure assessment. *Chronobiol Int* 32(9): 1294–1310
7. Ryckaert W, Lootens C, Geldof J, Hanselaer P (2010) Criteria for energy efficient lighting in buildings. *Energy and Buildings* 42(3): 341–347
8. Scheir GH, Hanselaer P, Bracke P, Deconick G (2015) Calculation of the unified glare rating on luminance maps for uniform and non-uniform light sources. *Build Environ* 84: 60–67

9. Bellia L, Cesarano A, Iuliano G, Spada G (2008) Daylight glare: a review of discomfort indexes. Paper presented at Visual Quality and Energy Efficiency in Indoor Lighting: Today for Tomorrow vol. 31, International workshop, Rome, Italy
10. Guo X, Houser KW (2004) A review of colour rendering indices and their application to commercial light sources. *Light Res Technol* 36(3): 183–199
11. Clear RD (2013) Discomfort glare: what do we actually know? *Light Res Technol* 45(2): 141–158
12. EN 12464–1/2002 (2002) Light and lighting—lighting of workplaces—part 1: indoor work, Eur Stand, 3: 1–43
13. Vásquez NGF, Ruttikay O, Oliveira MPL, Niero M (2016) Investigating a method to dynamic assessment of glare using the HDR technique. In: PLEA 2016: 32nd International conference on passive and low energy architecture Los Angeles. USA
14. Wienold J, Christoffersen J (2006) Evaluation methods and development of a new glare prediction model for daylight environments with the use of CCD cameras. *EnergyBuild* 38(7): 743–757
15. Bellia L, Musto M, Spada G (2011) Illuminance measurements through HDR imaging photometry in scholastic environment. *Lancet* 43:2843–2849
16. Reinhard E, Heidrich W, Debevec P, Pattanaik S, Ward G, Myszkowski K (2010) High dynamic range imaging: acquisition, display, and image-based lighting. Morgan Kaufmann, USA
17. Panahiazar S, Matkan M (2018) Qualitative and quantitative analysis of natural light in the dome of San Lorenzo. *Turin Front Archit Res* 7(1): 25–36
18. Galasiu AD, Veitch JA (2006) Occupant preferences and satisfaction with the luminous environment and control systems in daylit offices: a literature review. *Energy Build.* 38(7): 728–742
19. Ganguly T, Hajdukiewicz M, Keane M, Goggins, J (2016) Generating robust algorithms for energy efficient lighting as a performance aspect of the building operational energy optimisation framework. Civil Engineering Research in Ireland Conference, Galway, Ireland
20. EN 12665 (2018) Light and lighting—basic terms and criteria for specifying lighting requirements. Eur Stand, 1–65
21. Zhen M, Du Y, Hong F, Bian G (2019) Simulation analysis of natural lighting of residential buildings in Xi'an, China. *Sci Total Environ* 690: 197–208
22. Souza DF, Silva PPF, Fontenele LFA, Barbosa GD, Oliveira Jesus M (2019) Efficiency, quality, and environmental impacts: a comparative study of residential artificial lighting. *Energy Reports*, 5, 409–424
23. Sun WS, Tsuei CH, Huang YH (2011) Simulating the illuminance and efficiency of the LEDs used in general household lighting. *Phys Procedia* 19: 244–248
24. European Commission Homepage. Energy prices and costs in Europe. https://ec.europa.eu/energy/data-analysis/energy-prices-and-costs_en, last accessed 2021/08/24